

Advanced Electrochemical Reforming of Methanol for Hydrogen Production

by

Caroline R. Cloutier

M.A.Sc., Metals and Materials Engineering, University of British Columbia, 2006
B.A.Sc., Chemical Engineering, Environmental Option, Co-op, University of Ottawa, 1999.

A THESIS SUBMITTED IN PARTIAL FULFILLMENT OF THE REQUIREMENTS FOR THE
DEGREE OF

DOCTOR OF PHILOSOPHY

in

The Faculty of Graduate Studies

(Chemical & Biological Engineering)

THE UNIVERSITY OF BRITISH COLUMBIA
(Vancouver)

December, 2011

@ Caroline R. Cloutier, 2011

Abstract

The issue of efficient, low-cost, sustainable hydrogen (H_2) production is one of the barriers to the adoption of a H_2 economy. In this thesis, the electrochemical production of H_2 from liquid methanol (CH_3OH) in acidic aqueous media was studied in a proton exchange membrane (PEM) electrolyser in the static mode at low temperatures. A baseline study showing the influence of CH_3OH concentration, catalyst, catalyst support, operating temperature and operating mode was established. A theoretical thermodynamic analysis of the system was carried out as a function of temperature, and the limiting current densities, kinetic parameters, including the Tafel slopes and current exchange density, and apparent activation energies were determined. The effect of electrochemical promotion (EP) was investigated to see if it can increase the efficiency and performance of H_2 production through electrochemical processes.

The electrochemical promotion of electrocatalysis (EPOE) was investigated by carrying out the electrolysis in triode and tetrode operation. It was shown to improve the PEM electrolysis in the galvanostatic and potentiostatic modes. A decrease in electrolysis voltage or an increase in electrolysis current proportional to the current or potential imposed in the auxiliary circuit was observed when the auxiliary current or potential was opposite to the electrolyser circuit current or potential. The effect was observed using catalytic and non-catalytic non-precious electrolyser electrode materials. It was postulated that triode and tetrode operation enhanced the electro-oxidation rate through electrochemical pumping and spillover of protons. With this novel electrolysis configuration, electrolysis cost reduction may be achieved through the use of non-precious electrolyser anode materials and/or improving electrolyser performance.

The electrochemical promotion of catalysis (EPOC) was also investigated for the catalytic reforming of CH_3OH at low temperature with Pt-Ru/C and Pt-Ru/ TiO_2 . The synthesized Pt-Ru/ TiO_2 was characterized physico-chemically and electrochemically. Powder catalytic CH_3OH reforming tests showed that both catalysts can be used to generate H_2 . EPOC experiments were conducted on gas diffusion electrodes (GDEs) in galvanostatic control. Under the experimental conditions, only supplying H^+ to the catalyst

working electrode surface resulted in only in a Faradaic enhancement of the catalytic activity for the low temperature reforming of CH_3OH , which appears to be a purely electrophilic behaviour.

Preface

The literature review, design of the experimental set-up, experimental data collection and analysis was conducted by Caroline R. Cloutier under the supervision of Dr. David P. Wilkinson. The material covered in *Chapter 2* was published:

- Cloutier, C. R., and Wilkinson, D. P., "Electrolytic Production of Hydrogen from Aqueous Acidic Methanol Solutions", *Int. J. H₂ Energy*, 35, (2010) 3967-3984.

Co-op student Jason Gao co-produced the data used in Fig. 2.6 (e) in *Chapter 2* under the supervision of Caroline R. Cloutier. Some of the material covered in *Chapter 3* was published in a conference proceeding and another paper has been submitted for publication:

- Cloutier, C. R., and Wilkinson, D. P., "Triode Operation of a Proton Exchange Membrane (PEM) Electrolyser", *ECS Transactions*, 25 (23), (2010) 47-57.
- Cloutier, C. R., and Wilkinson, D. P., "Electrochemical Promotion of Aqueous Acidic Methanol PEM Electrolysis in Triode and Tetraode Operation", (submitted).

A manuscript based on the content of *Chapter 4* is in preparation. The initial and final drafts of this thesis were prepared by Caroline R. Cloutier, with revisions edited and approved by Dr. David P. Wilkinson. The thesis proposal and the thesis manuscript were reviewed by the Ph.D. Committee, which included Dr. David Wilkinson, Dr. Elöd Gyenge, Dr. Walter Mérida, and Dr. David Dreisinger.

Table of Contents

Abstract	ii
Preface	iv
Table of Contents	v
List of Tables	x
List of Figures	xii
Nomenclature	xvii
List of Acronyms	xxi
Acknowledgements	xxiv
Dedication	xxvi
Chapter 1: Introduction	1
1.1 Background	1
1.1.1 Alternative fuels.....	1
1.1.2 Technology gap	3
1.1.3 Proposed solution.....	3
1.1.4 A sustainable closed loop system.....	4
1.2 Thesis overview	6
1.2.1 Justification.....	6
1.2.2 Research objectives.....	7
1.2.3 Layout.....	8
1.3 Literature review	10
1.3.1 Heterogeneous catalysis.....	10
1.3.1.1 Steam reforming.....	11
1.3.1.2 Liquid phase reforming.....	12
1.3.1.3 Hydrogen spillover in heterogeneous catalysis.....	13
1.3.1.4 Catalyst local heating.....	14
1.3.2 Proton exchange membrane fuel cell.....	15
1.3.2.1 Membrane electrode assembly.....	16
1.3.2.2 Overvoltage.....	17
1.3.2.3 Hydrogen proton exchange membrane fuel cell.....	18
Hydrogen purity requirements.....	19
1.3.2.4 Direct methanol fuel cell.....	20
Anodic methanol oxidation.....	21
Methanol crossover.....	22
1.3.2.5 Indirect methanol fuel cell.....	23
1.3.3 Proton exchange membrane electrolysis.....	24
1.3.3.1 Proton exchange membrane water electrolysis.....	24
1.3.3.2 Depolarized proton exchange membrane water electrolysis.....	26
Methanol depolarized electrolysis.....	27
Applications of depolarized methanol electrolysis.....	32

1.3.4 Electrochemical promotion of heterogeneous catalysis.....	34
1.3.4.1 Theory.....	35
1.3.4.2 Parameters.....	39
1.3.4.3 Electrochemical promotion of methanol oxidation.....	41
1.3.4.4 Electrochemical promotion using protonic electrolytes.....	42
1.3.4.5 Applications for the electrochemical promotion of catalysis.....	44
1.3.5 Electrochemical promotion of electrocatalysis.....	47
Chapter 2: Electrocatalysis Baseline Study	49
2.1 Synopsis.....	49
2.2 Experimental.....	50
2.2.1 Materials.....	50
2.2.2 Equipment.....	51
2.2.3 Electrochemical measurements.....	54
2.2.4 Characterization.....	54
2.3 Results and discussion.....	57
2.3.1 Thermodynamic evaluation of methanol reforming at low temperatures.....	57
2.3.2 Electrolysis polarizations.....	62
2.3.2.1 Cell voltage stability.....	62
2.3.2.2 Effect of methanol concentration and anode catalyst.....	64
2.3.2.3 Effect of dry purged cathode.....	71
2.3.2.4 Effect of temperature.....	73
2.3.2.5 Anode Tafel kinetics.....	76
2.3.2.6 Activation energy.....	85
2.4 Summary.....	87
Chapter 3: Electrochemical Promotion of Electrocatalysis (EPOE).....	88
3.1 Synopsis.....	88
3.2 Overview.....	89
3.3 Experimental.....	93
3.3.1 Materials and membrane electrode assembly.....	93
3.3.2 Glass cell for triode and tetrode operation.....	95
3.3.3 Electrochemical measurements.....	97
3.3.4 Stability of carbon containing electrolyser ring electrodes.....	101
3.4 Triode or tetrode operation evaluation expressions.....	103
3.4.1 Triode or tetrode operation evaluation in the galvanostatic mode.....	103
3.4.2 Triode or tetrode operation evaluation in the potentiostatic mode.....	105
3.5 Results and discussion.....	106
3.5.1 Galvanostatic characterization.....	106
3.5.1.1 Triode and tetrode operation in galvanostatic control.....	106
3.5.1.2 Parallel and reverse operation in galvanostatic control.....	107
3.5.1.3 Electrolyser ring electrode material in galvanostatic control.....	109
3.5.1.4 Electrolyser voltage ratio, power enhancement ratio and power gain ratio in galvanostatic control.....	111
3.5.1.5 Benefits of starting in triode operation in galvanostatic control.....	114
3.5.2 Potentiostatic characterization.....	116
3.5.2.1 Triode configuration in potentiostatic control.....	116
3.5.2.2 Tetrode configuration in potentiostatic control.....	118
3.5.2.3 Counter electrode potential measurements in potentiostatic control.....	119
3.5.2.4 Electrolyser ring electrode material in potentiostatic control.....	121
3.5.2.5 Electrolyser rate enhancement ratio, power gain ratio and Faradaic efficiency in potentiostatic control.....	123
3.5.3 Durability investigation.....	126
3.5.3.1 Long-term triode and tetrode operation in galvanostatic control.....	126
3.5.3.2 Methanol concentration change over time in long-term triode or tetrode	

galvanostatic control.....	128
3.5.3.3 Long-term tetrode operation in mixed potentiostatic and galvanostatic control...	130
3.5.3.4 Methanol concentration change over time in long-term tetrode operation in mixed potentiostatic and galvanostatic control.....	132
3.5.4 Mechanism investigation.....	134
3.5.4.1 Electrolytic contact of auxiliary electrodes in potentiostatic control	134
3.5.4.2 Effect of acid concentration and conductivity on triode operation in potentiostatic control.....	136
3.5.4.3 Effect of triode operation on membrane conductivity in potentiostatic control....	138
3.5.4.4 Effect of electrolyser working electrode ring geometry in potentiostatic control..	139
3.5.4.5 Effect of proton flux lines direction in potentiostatic control.....	140
3.5.4.6 Effect of the electrochemical surface area of the carbon fibre paper electrolyser working electrode in potentiostatic control.....	143
3.5.4.7 Effect of triode operation using non-noble non-carbon containing working electrode materials in potentiostatic control.....	144
3.5.4.8 Proposed mechanism.....	153
3.6 Summary.....	156
Chapter 4: Catalysis and Electrochemical Promotion of Catalysis (EPOC).....	157
4.1 Synopsis.....	157
4.2 Experimental.....	160
4.2.1 Materials.....	160
4.2.2 Catalyst synthesis.....	160
4.2.3 Pt-Ru/TiO ₂ physicochemical characterization.....	162
4.2.3.1 Scanning electron microscopy.....	162
4.2.3.2 Energy-dispersive X-ray spectroscopy.....	162
4.2.3.3 Transmission-electron microscopy.....	163
4.2.3.4 X-ray diffraction.....	163
4.2.3.5 X-ray photoelectron spectrometry.....	164
4.2.3.6 Inductively coupled plasma optical emission spectrometry.....	164
4.2.3.7 Brunauer, Emmett and Teller surface area and Baret-Joyner-Halenda pore size and volume analysis.....	164
4.2.4 Pt-Ru/TiO ₂ electrochemical characterization.....	165
4.2.5 Apparatus.....	166
4.2.5.1 Powder catalysis.....	166
4.2.5.2 GDE catalysis and electrochemical promotion of catalysis.....	171
4.3 Results and discussion.....	173
4.3.1 Pt-Ru/TiO ₂ physicochemical characterization.....	173
4.3.1.1 SEM images.....	173
4.3.1.2 EDX measurements.....	174
4.3.1.3 TEM images.....	175
4.3.1.4 XRD measurements.....	177
4.3.1.5 XPS measurements.....	180
4.3.1.6 ICP-OES measurements.....	181
4.3.1.7 BET surface area and BJH pore size and volume analysis.....	182
4.3.2 Pt-Ru/TiO ₂ electrochemical characterization.....	184
4.3.3 Powder catalysis.....	192
4.3.4 GDE catalysis and electrochemical promotion of catalysis.....	199
4.4 Summary.....	214
Chapter 5: Conclusions.....	216
5.1 Electrocatalysis baseline study.....	216
5.2 Electrochemical promotion of electrocatalysis (EPOE).....	218
5.2.1 Galvanostatic and potentiostatic characterization.....	218

5.2.2 Durability investigations.....	219
5.2.3 Mechanism investigations.....	220
5.3 Electrochemical promotion of catalysis (EPOC).....	221
5.3.1 Catalyst synthesis and characterization.....	222
5.3.2 Powder catalysis.....	222
5.3.3 GDE catalysis and electrochemical promotion of catalysis.....	223
5.4 Potential application, significance and impact of research findings.....	224
5.4.1 Potential applications.....	224
5.4.2 Significance and impact.....	228
5.5 Recommendations for further research.....	230
5.5.1 Electrocatalysis baseline study.....	230
5.5.2 Electrochemical promotion of electrocatalysis (EPOE).....	231
5.5.3 Electrochemical promotion of catalysis (EPOC).....	234
References.....	236
Appendix A: Publications, presentations, and posters.....	250
A.1 Publications.....	250
A.2 Presentations.....	250
A.3 Posters.....	250
Appendix B: Methanol electro-oxidation mechanism.....	251
B.1 Methanol electro-oxidation parallel pathways.....	251
B.2 Methanol electro-oxidation mechanism on Pt.....	251
B.3 Methanol electro-oxidation mechanism on Pt-Ru.....	252
B.4 References.....	252
Appendix C: Efficiency and economic comparison of H₂ production.....	254
C.1 Objective.....	254
C.2 System definition.....	254
C.3 Block diagrams.....	254
C.4 Feedstock processing.....	256
C.4.1 Methanol production.....	256
C.4.2 Sodium borohydride production.....	257
C.5 Hydrogen production.....	257
C.5.1 Electrolysis.....	258
C.5.2 Catalytic steam reforming.....	259
C.5.3 Sodium borohydride hydrolyser.....	260
C.6 Efficiency analysis.....	260
C.7 Economic analysis.....	262
C.7.1 Capital cost.....	264
C.7.2 Feedstock cost.....	265
C.7.3 Energy cost.....	265
C.7.4 Carbon cost.....	266
C.7.5 Economic analysis summary.....	267
C.8 Conclusion.....	268
C.9 References.....	269
Appendix D: Supplemental EPOC and EPOE theory.....	271
D.1 EPOC rules.....	271
D.2 Chemisorption on a transition metal.....	273
D.3 Kirchhoff's first law for triode and tetrode operation.....	275
D.3.1 Triode fuel cell.....	275
D.3.2 Triode electrolyser.....	276
D.3.3 Tetrode electrolyser.....	276
D.4 References.....	277

Appendix E: Experimental procedures.....	278
E.1 Catalyst electrode preparation.....	278
E.1.1 Cathode carbon sublayer composition calculation.....	278
E.1.2 Anode and cathode catalyst ink composition calculation.....	279
E.1.3 Catalyst ink preparation procedure.....	281
E.1.4 Electrode spraying procedure.....	282
E.2 Platinization procedure.....	283
E.3 Silicon ring preparation.....	284
E.4 Nafion membrane conditioning.....	285
E.5 Determination of CH ₃ OH concentration.....	286
E.6 RDE catalyst ink preparation.....	289
E.7 Pt-Ru/TiO ₂ preparation.....	290
E.8 References.....	294
Appendix F: Electrochemical techniques.....	295
F.1 Cyclic voltammetry.....	295
F.1.1 Pt-C catalyst electrochemical surface area determination.....	296
F.1.2 Pt-Ru/C catalyst electrochemical surface area determination.....	300
F.2 Electrochemical impedance spectroscopy.....	303
F.3 Determination of the open circuit voltage.....	305
F.4 Current - potential transients.....	306
F.5 Rotating disk electrode.....	309
F.6 References.....	311
Appendix G: Thermodynamic data and sample calculations.....	313
G.1 Thermodynamic data.....	313
G.2 Thermodynamic sample calculations.....	313
G.2.1 Liquid phase.....	313
G.2.2 Gas phase.....	315
G.2.3 System efficiency calculation.....	320
G.2.4 Effect of pressure in the gas phase.....	321
G.2.5 Effect of anode and cathode pressure in the liquid phase.....	322
G.3 References.....	323
Appendix H: Electrochemical data and sample calculations.....	324
H.1 Power consumption.....	324
H.2 CO ₂ emissions and H ₂ production rate.....	324
H.3 Proton diffusion limited H ₂ production – back envelope calculation.....	326
H.4 Overall system efficiency.....	328
H.5 References.....	330

List of Tables

Table 1.1	Methanol properties.....	2
Table 1.2	Relevant methanol electrochemical reforming membrane reactors.....	28
Table 1.3	Vapour phase methanol oxidation EPOC studies with oxide conductors.....	42
Table 1.4	Vapour/gaseous phase EPOC studies using protonic conducting electrolytes.....	43
Table 1.5	EPOC studies in aqueous systems.....	44
Table 2.1	Electrochemical characterization of supported and unsupported catalysts studied.....	56
Table 2.2	Literature Tafel kinetic parameters for the electro-oxidation of methanol and water on Pt and Pt-Ru catalysts.....	78
Table 2.3	Tafel kinetic parameters from current work for the electro-oxidation of methanol and water on Pt and Pt-Ru catalysts.....	80
Table 2.4	Activation energy data for the electro-oxidation of methanol on Pt and Pt-Ru catalysts.....	86
Table 3.1	List of possible half-cell reactions and their standard potentials.....	92
Table 3.2	IR corrected on-set potentials for CFP samples with and without Pt black at varying CH ₃ OH concentrations.....	102
Table 3.3	Effect of auxiliary WE _{aux} potential ($U_{aux, we}$) on the rate enhancement ratio (ρ_e) (Pt auxiliary WE _{aux} , 2 mg/cm ² Pt/C CE, $U_{elec, we} = 0.52$ V vs. SHE).....	123
Table 3.4	IR corrected on-set potential for different electrolyser and auxiliary WE _{aux} materials at varying CH ₃ OH concentrations.....	148
Table 3.5	Effect of auxiliary WE _{aux} potential ($U_{aux, we}$) on the rate enhancement ratio (ρ_e) using Au plated 316 SS components (2 mg/cm ² Pt/C CE, $U_{elec, we} = 0.52$ V vs. SHE)....	150
Table 4.1	Scherrer's crystallite size for selected peaks from the carbon, Pt-Ru/C, TiO ₂ and Pt-Ru/TiO ₂ XRD patterns.....	179
Table 4.2	ICP-OES results for H ₂ reduced Pt-Ru/TiO ₂ before and after ball milling and Pt-Ru/C.....	182
Table 4.3	BET surface areas of the Pt-Ru/TiO ₂ materials synthesized, as well as commercial TiO ₂ and Pt-Ru/C materials.....	183
Table 4.4	On-set potentials for the forward and reverse CH ₃ OH oxidation on different catalytic surfaces (2 M CH ₃ OH in 0.5 M H ₂ SO ₄).....	187
Table 4.5	Peak potentials for the forward and reverse CH ₃ OH oxidation on different catalytic surfaces (2 M CH ₃ OH in 0.5 M H ₂ SO ₄).....	187
Table 4.6	List of CV studies on unsupported and supported Pt, Pt-Ru and TiO ₂ available in the literature.....	188
Table 4.7	Literature powder catalysis CH ₃ OH reforming production rates at low temperature (0.5 g Pt-Ru/TiO ₂ , 10 wt% metal, Pt:Ru 1:1 a/o, 60 ml of 2 M CH ₃ OH).....	196
Table 4.8	Powder catalysis CH ₃ OH reforming production rates (0.5 g catalyst, 20 wt% Pt-Ru, Pt:Ru 1:1 a/o, 20 ml of 2 M CH ₃ OH in 0.5 M H ₂ SO ₄ , 75 ±1°C).....	196
Table 4.9	Imposed currents or potentials on selected chemical reactions subjected to EPOC.....	200
Table 4.10	Average H ₂ unpromoted production rates for GDE catalysis of CH ₃ OH at low temperature (2.01 cm ² , 4 mg/cm ² Pt-Ru/C or Pt-Ru/TiO ₂ , 20 wt% Pt-Ru, Pt:Ru 1:1 a/o, 80 ml of 2 M CH ₃ OH in 0.5 M H ₂ SO ₄ electrolyser anolyte, 80 ml of 0.5 M H ₂ SO ₄ electrolyser catholyte, 75±1°C).....	204
Table 4.11	Faradaic H ₂ production rate, measured H ₂ production rates, Faradaic efficiencies and EPOC efficiencies for the GDE catalytic reforming of CH ₃ OH at low temperature (2.01 cm ² , 4 mg/cm ² Pt-Ru/C, 20 wt% Pt-Ru, Pt:Ru 1:1 a/o, 80 ml of 2 M CH ₃ OH in 0.5 M H ₂ SO ₄ , 75±1°C).....	210
Table C.1	High level comparison of four H ₂ generation process schemes.....	258
Table C.2	Efficiency comparison of four H ₂ generation process schemes.....	261

Table C.3	Cost comparison of four H ₂ generation process schemes.....	268
Table E.1	Cathode carbon sublayer calculation spreadsheet.....	279
Table E.2	Anode catalyst ink composition calculation spreadsheet.....	280
Table E.3	Cathode catalyst ink composition calculation spreadsheet.....	281
Table E.4	Precursor salt addition calculation spreadsheet for the impregnation method.....	291
Table F.1	Total metal area results comparison for electrode degradation evaluation.....	300
Table G.1	Thermodynamic data.....	313
Table G.2	Empirical coefficients for Shomate equations.....	317
Table H.1	Direct methanol reformer electrochemical active surface area as a function of proton diffusion coefficient in Nafion, based on H ₂ production for a 100 kW PEMFC at a voltage of 0.6 V.....	328

List of Figures

Figure 1.1	(a) Schematic diagram of conventional methanol synthesis combined with a DMR and a PEMFC (b) Schematic diagram of a future sustainable system comprising a DMR and PEMFC.....	5
Figure 1.2	Schematic diagram of a methanol electrochemical reforming membrane cell (Modified from patent DE 197007384 [112]).....	29
Figure 1.3	Schematic diagram of an alcohol electrolyser (Modified from Hu <i>et al.</i> [7] with permission from Elsevier).....	30
Figure 1.4	Schematic diagram of a metal catalyst-electrode deposited on (a) an oxide-conducting solid electrolyte, and (b) a proton-conducting solid electrolyte (Modified from Vayenas <i>et al.</i> [18] with permission from Springer).....	37
Figure 1.5	Schematic diagram of a triode fuel cell electrical circuit.....	47
Figure 2.1	Schematic diagram of (a) the electrochemical glass cell, (b) the MEA components (c) the MEA holder.....	52
Figure 2.2	Picture of (a) the electrochemical glass cell, (b) the MEA holder.....	53
Figure 2.3	Theoretical thermodynamic efficiency and theoretical cell voltage as a function of temperature (1 atm) for a DMR and PEM water electrolyser.....	61
Figure 2.4	Electrolysis cell voltage stability with respect to current density (16 M CH ₃ OH in 0.5 M H ₂ SO ₄ electrolyser anolyte, 0.5 M H ₂ SO ₄ electrolyser catholyte, 4 mg/cm ² Pt-Ru/C anode, 2 mg/cm ² Pt/C cathode, 23 ±2°C).....	62
Figure 2.5	IR corrected electrolysis cell voltage repeatability as a function of geometric current density in the stable and unstable regions (2 M CH ₃ OH in 0.5 M H ₂ SO ₄ electrolyser anolyte, 0.5 M H ₂ SO ₄ electrolyser catholyte, 2 mg/cm ² Pt/C anode and cathode, 23 ±2°C).....	63
Figure 2.6	Effect of methanol concentration on the IR corrected electrolysis cell voltage as a function of geometric current density for different anode catalysts (a) 4 mg/cm ² Pt-Ru/C, (b) 2 mg/cm ² Pt/C, (c) 4 mg/cm ² Pt-Ru black, (d) 2 mg/cm ² Pt black, (e) well-defined Pt disk (0, 1, 2, 6 or 16 M CH ₃ OH in 0.5 M H ₂ SO ₄ electrolyser anolyte, 0.5 M H ₂ SO ₄ electrolyser catholyte, 23 ±2°C).....	66
Figure 2.7	Dependence of limiting geometric current densities for the oxidation of methanol and water on the CH ₃ OH concentration for various anode catalysts (0, 1, 2, 6 or 16 M CH ₃ OH in 0.5 M H ₂ SO ₄ electrolyser anolyte, 0.5 M H ₂ SO ₄ electrolyser catholyte, 23 ±2°C).....	67
Figure 2.8	Effect of CH ₃ OH concentration on the individual electrode potential (0, 1, 2, 6 or 16 M CH ₃ OH in 0.5 M H ₂ SO ₄ electrolyser anolyte, 0.5 M H ₂ SO ₄ electrolyser catholyte, 4 mg/cm ² Pt-Ru/C anode, 2 mg/cm ² Pt/C cathode, 23 ±2°C).....	68
Figure 2.9	Effect of the IR corrected voltage on electrolysis for Pt/C and Pt black anode catalysts as a function of real electrochemical current density (0, 2, or 16 M CH ₃ OH in 0.5 M H ₂ SO ₄ electrolyser anolyte, 0.5 M H ₂ SO ₄ electrolyser catholyte, 23 ±2°C).....	70
Figure 2.10	Effect of dry N ₂ purged cathode on the IR corrected electrolysis cell voltage as a function of geometric current density (0 or 1 M CH ₃ OH in 0.5 M H ₂ SO ₄ electrolyser anolyte, wet electrolyser catholyte: 0.5 M H ₂ SO ₄ , dry electrolyser catholyte: N ₂ purge electrolyser, 4 mg/cm ² Pt-Ru/C anode, 2 mg/cm ² Pt/C cathode, 23 ±2°C).....	71
Figure 2.11	Effect of dry N ₂ purged cathode and a wet cathode on the (a) anode potential and (b) cathode potential, as a function of geometric current density (0 or 1 M CH ₃ OH in 0.5 M H ₂ SO ₄ electrolyser anolyte, wet electrolyser catholyte: 0.5 M H ₂ SO ₄ , dry electrolyser catholyte: N ₂ purge, 4 mg/cm ² Pt-Ru/C anode, 2 mg/cm ² Pt/C cathode, 23 ±2°C).....	72
Figure 2.12	Effect of CH ₃ OH concentration on the IR corrected electrolysis cell voltage as a function of geometric current density for different temperatures (a) 23 ±2°C (b) 50 ±1°C (c) 75 ±1°C (0, 2 or 16 M CH ₃ OH in 0.5 M H ₂ SO ₄ electrolyser anolyte, 0.5 M H ₂ SO ₄ electrolyser catholyte, 4 mg/cm ² Pt-Ru/C anode, 2 mg/cm ² Pt/C cathode).....	75
Figure 2.13	Tafel plot of the IR corrected anodic overpotential as a function of the log of the geometric current density (0, 2, or 16 M CH ₃ OH in 0.5 M H ₂ SO ₄ electrolyser anolyte, 0.5	

	M H ₂ SO ₄ electrolyser catholyte, 4 mg/cm ² Pt black anode, 2 mg/cm ² Pt/C cathode, 23 ±2°C).....	76
Figure 3.1	Schematic diagram of the triode electrolyser electrical circuit.....	89
Figure 3.2	Side view of membrane electrode assemblies in different configurations: (a) triode, normal operation, common CE (b) like (a) with auxiliary WE _{aux} away from surface (c) like (a) in inverted operation, and (d) tetrode, normal operation, independent CEs.....	90
Figure 3.3	Schematic drawing of auxiliary Teflon™ cap with apertures.....	94
Figure 3.4	Front view of the triode or tetrode operation working electrode components.....	94
Figure 3.5	Apparatus for triode and tetrode electrolysis (a) electrochemical glass cell, (b) auxiliary electrode	96
Figure 3.6	Picture of the electrochemical glass cell set-up in triode operation.....	97
Figure 3.7	Potentiostatic working electrode potential experimental settings relative to the standard half-cell electrochemical potentials.....	98
Figure 3.8	Schematic diagram of EPOE testing system connections for (a) galvanostatic triode operation, (b) potentiostatic triode operation (c) galvanostatic tetrode operation, and (d) potentiostatic tetrode operation.....	99
Figure 3.9	IR-corrected forward anodic potential sweep (5 mV/s, 0, 2 or 16 M CH ₃ OH in 0.5 M H ₂ SO ₄ electrolyser anolyte, 0.5 M H ₂ SO ₄ electrolyser catholyte, CFP with and without 2 mg/cm ² Pt black WE, Pt flag CE, 23 ±1°C).....	101
Figure 3.10	Triode effect in galvanostatic control (CFP electrolyser ring WE _{elec} , Pt auxiliary WE _{aux} , 2 mg/cm ² Pt/C CE, 2 M CH ₃ OH in 0.5 M H ₂ SO ₄ electrolyser anolyte, 0.5 M H ₂ SO ₄ electrolyser catholyte, $i_{elec, cell} = 1.25 \text{ mA/cm}^2$, $i_{aux, cell} = -50 \text{ mA/cm}^2$).....	107
Figure 3.11	Effect of varying $i_{aux, cell}$ on the electrolyser circuit voltage in galvanostatic control (a) parallel operation (b) reverse operation (4 mg/cm ² Pt-Ru black electrolyser ring WE _{elec} , Pt auxiliary WE _{aux} , 2 mg/cm ² Pt/C CE, 2 M CH ₃ OH in 0.5 M H ₂ SO ₄ electrolyser anolyte, 0.5 M H ₂ SO ₄ electrolyser catholyte, $i_{elec, cell} = 1.25 \text{ mA/cm}^2$, $i_{aux, cell} = -50 \text{ mA/cm}^2$).....	108
Figure 3.12	Effect of varying $i_{aux, cell}$ on the electrolyser circuit voltage in galvanostatic control (a) 4 mg/cm ² Pt-Ru black electrolyser ring WE _{elec} , (b) CFP electrolyser ring WE _{elec} (Pt auxiliary WE _{aux} , 2 mg/cm ² Pt/C CE, 2 M CH ₃ OH in 0.5 M H ₂ SO ₄ electrolyser anolyte, 0.5 M H ₂ SO ₄ electrolyser catholyte, $i_{elec, cell} = 1.25 \text{ mA/cm}^2$).....	110
Figure 3.13	Effect of $i_{aux, cell}$ on $U_{elec, cell}$ and on the triode voltage ratio (R) (a) 4 mg/cm ² Pt-Ru black electrolyser ring WE _{elec} (b) CFP electrolyser ring WE _{elec} (Pt auxiliary WE _{aux} , 2 mg/cm ² Pt/C CE, 2 M CH ₃ OH in 0.5 M H ₂ SO ₄ electrolyser anolyte, 0.5 M H ₂ SO ₄ electrolyser catholyte, $i_{elec, cell} = 1.25 \text{ mA/cm}^2$).....	112
Figure 3.14	Power enhancement ratio ($\rho_{elec, cell}$) and power gain ratio ($\gamma_{elec, cell}$) as a function of the auxiliary circuit current density (a) 4 mg/cm ² Pt-Ru black electrolyser ring WE _{elec} (b) CFP electrolyser ring WE _{elec} (Pt auxiliary WE _{aux} , 2 mg/cm ² Pt/C CE, 2 M CH ₃ OH in 0.5 M H ₂ SO ₄ electrolyser anolyte, 0.5 M H ₂ SO ₄ electrolyser catholyte, $i_{elec, cell} = 1.25 \text{ mA/cm}^2$).....	113
Figure 3.15	Benefits of starting in triode operation in galvanostatic control (CFP ring electrolyser WE _{elec} , Pt auxiliary WE _{aux} , 2 mg/cm ² Pt/C CE, 2 M CH ₃ OH in 0.5 M H ₂ SO ₄ electrolyser anolyte, 0.5 M H ₂ SO ₄ electrolyser catholyte, $i_{elec, cell} = 50, 75 \text{ mA/cm}^2$, $i_{aux, cell} = -5 \text{ A/cm}^2$).....	115
Figure 3.16	Triode effect in potentiostatic control (CFP electrolyser ring WE _{elec} , Pt auxiliary WE _{aux} , 2 mg/cm ² Pt/C CE, 2 M CH ₃ OH in 0.5 M H ₂ SO ₄ electrolyser anolyte, 0.5 M H ₂ SO ₄ electrolyser catholyte, $U_{elec, we} = 0.52 \text{ V vs. SHE}$).....	116
Figure 3.17	Triode and tetrode effect in potentiostatic control (4 mg/cm ² Pt-Ru black electrolyser ring WE _{elec} , 2 mg/cm ² Pt/C electrolyser CE _{elec} , Pt auxiliary WE _{aux} and CE _{aux} , 2 M CH ₃ OH in 0.5 M H ₂ SO ₄ electrolyser anolyte, 0.5 M H ₂ SO ₄ electrolyser catholyte, $U_{elec, we} = 0.52 \text{ V vs. SHE}$).....	119
Figure 3.18	Triode effect in potentiostatic control (a) geometric current density (b) counter electrode potential (4 mg/cm ² Pt-Ru black electrolyser ring WE _{elec} , 2 mg/cm ² Pt/C electrolyser CE, Pt auxiliary WE _{aux} , 2 M CH ₃ OH in 0.5 M H ₂ SO ₄ electrolyser anolyte, 0.5 M H ₂ SO ₄ electrolyser catholyte, $U_{elec, we} = 0.52 \text{ V vs. SHE}$).....	120
Figure 3.19	Tetrode effect in potentiostatic control (a) geometric current density (b) counter electrode potential (4 mg/cm ² Pt-Ru black electrolyser ring WE _{elec} , 2 mg/cm ² Pt/C	

	electrolyser CE _{elec} , Pt auxiliary WE _{aux} and CE _{aux} , 2 M CH ₃ OH in 0.5 M H ₂ SO ₄ electrolyser anolyte, 0.5 M H ₂ SO ₄ electrolyser catholyte, $U_{elec, we} = 0.52$ V vs. SHE)...120
Figure 3.20	Effect of varying $U_{aux, we}$ on different electrolyser ring WE _{elec} materials in potentiostatic control (a) 0 M CH ₃ OH in 0.5 M H ₂ SO ₄ electrolyser anolyte, 0.5 M H ₂ SO ₄ electrolyser catholyte and (b) 2 M CH ₃ OH in 0.5 M H ₂ SO ₄ electrolyser anolyte, 0.5 M H ₂ SO ₄ electrolyser catholyte (2 mg/cm ² Pt black, 4 mg/cm ² Pt-Ru black, and CFP electrolyser WE _{elec} , Pt auxiliary WE _{aux} , 2 mg/cm ² Pt/C CE, $U_{elec, we} = 0.52$ V vs. SHE).....122
Figure 3.21	Power gain ratio ($\gamma_{elec, cell}$) as a function of $U_{aux, we}$ (CFP electrolyser ring WE _{elec} and 4 mg/cm ² Pt-Ru black electrolyser ring WE _{elec} , Pt auxiliary WE _{aux} , 2 mg/cm ² Pt/C CE, 2 M CH ₃ OH in 0.5 M H ₂ SO ₄ electrolyser anolyte, 0.5 M H ₂ SO ₄ electrolyser catholyte, $U_{elec, we} = 0.52$ V vs. SHE).....125
Figure 3.22	Durability test in normal, triode and tetrode electrolysis in galvanostatic control (CFP electrolyser ring WE _{elec} , Pt auxiliary WE _{aux} , 2 mg/cm ² Pt/C CE, 2 M CH ₃ OH in 0.5 M H ₂ SO ₄ electrolyser anolyte, 0.5 M H ₂ SO ₄ electrolyser catholyte, $i_{elec, cell} = 1.25$ mA/cm ² , $i_{aux, cell} = -50$ mA/cm ²).....127
Figure 3.23	Methanol concentration as a function of time as predicted by Faraday's law, and during normal, triode, and tetrode electrolysis in galvanostatic control (CFP electrolyser ring WE _{elec} , Pt auxiliary WE _{aux} , 2 mg/cm ² Pt/C CE, 2 M CH ₃ OH in 0.5 M H ₂ SO ₄ electrolyser anolyte, 0.5 M H ₂ SO ₄ electrolyser catholyte, $i_{elec, cell} = 1.25$ mA/cm ² , $i_{aux, cell} = -50$ mA/cm ²).....129
Figure 3.24	Potentiostatic electrolyser circuit control and galvanostatic auxiliary circuit control durability test in tetrode electrolysis (CFP electrolyser ring WE _{elec} , Pt auxiliary WE _{aux} , 2 mg/cm ² Pt/C CE _{elec} , Pt auxiliary CE _{aux} , 2 M CH ₃ OH in 0.5 M H ₂ SO ₄ electrolyser anolyte, 0.5 M H ₂ SO ₄ electrolyser catholyte, $U_{elec, we} = 1$ V vs. SHE, $i_{aux, cell} = -20$ mA/cm ²).....131
Figure 3.25	Methanol concentration as a function of time as predicted by Faraday's law and as measured during potentiostatic electrolyser circuit control and galvanostatic auxiliary circuit control in tetrode electrolysis (CFP electrolyser ring WE _{elec} , Pt auxiliary WE _{aux} , 2 mg/cm ² Pt/C CE _{elec} , and Pt auxiliary CE _{aux} , 2 M CH ₃ OH in 0.5 M H ₂ SO ₄ electrolyser anolyte, 0.5 M H ₂ SO ₄ electrolyser catholyte, $U_{elec, we} = 1$ V vs. SHE, $i_{aux, cell} = -20$ mA/cm ²).....133
Figure 3.26	Effect of varying $U_{aux, we}$ on the electrolyser current density in tetrode operation (a) Pt auxiliary WE _{aux} 1 cm away from surface (b) Pt auxiliary CE _{aux} 1 cm away from surface (CFP electrolyser ring WE _{elec} , 2 M CH ₃ OH in 0.5 M H ₂ SO ₄ electrolyser anolyte, 0.5 M H ₂ SO ₄ electrolyser catholyte, $U_{elec, we} = 0.52$ V vs. SHE).....135
Figure 3.27	Nafion [®] N-117 membrane conductivity and solution conductivity as a function of sulphuric acid concentration.....136
Figure 3.28	Effect of varying $U_{aux, we}$ on the electrolyser current density (CFP electrolyser ring WE _{elec} , Pt auxiliary WE _{aux} , 2 mg/cm ² Pt/C CE, 0 M CH ₃ OH in 0.05 or 5 M H ₂ SO ₄ electrolyser anolyte, 0.5 M H ₂ SO ₄ electrolyser catholyte, $U_{elec, we} = 0.52$ V vs. SHE)...137
Figure 3.29	Resistance measurement over time in normal electrolysis and in triode electrolysis (CFP electrolyser ring WE _{elec} , Pt auxiliary WE _{aux} , 2 mg/cm ² Pt/C CE, 2 M CH ₃ OH in 0.5 M H ₂ SO ₄ electrolyser anolyte, 0.5 M H ₂ SO ₄ electrolyser catholyte, $U_{elec, we} = 0.52$ V vs. SHE, $U_{aux, we} = -0.59$ V vs. SHE).....139
Figure 3.30	Effect of varying $U_{aux, we}$ on the $i_{elec, cell}$ for different electrolyser ring WE _{elec} gap distances (CFP electrolyser ring WE _{elec} , 2 M CH ₃ OH in 0.5 M H ₂ SO ₄ electrolyser anolyte, 0.5 M H ₂ SO ₄ electrolyser catholyte, $U_{elec, we} = 0.52$ V vs. SHE).....140
Figure 3.31	Effect of varying $U_{aux, we}$ on the current density in tetrode operation (a) inverted CEs (CFP ring WE _{elec} , Pt rod WE _{aux} , Pt rod CE _{elec} , Pt/C CE _{aux}) (b) inverted WEs (Pt rod WE _{elec} , CFP ring WE _{aux} , Pt/C ring CE _{elec} , Pt rod CE _{aux}), (2 M CH ₃ OH in 0.5 M H ₂ SO ₄ electrolyser anolyte, 0.5 M H ₂ SO ₄ electrolyser catholyte, $U_{elec, we} = 0.52$ V vs. SHE)...142
Figure 3.32	Effect of electrolyser ring CFP WE _{elec} carbon SA on $i_{elec, cell}$ (2 M CH ₃ OH in 0.5 M H ₂ SO ₄ electrolyser anolyte, 0.5 M H ₂ SO ₄ electrolyser catholyte, $U_{elec, we} = 0.52$ V vs. SHE)...144
Figure 3.33	IR corrected forward anodic potential sweeps (a) 316 SS auxiliary WE _{aux} (b) 316 SS mesh electrolyser ring WE _{elec} (c) Au plated 316 SS auxiliary WE _{aux} (d) Au plated 316 SS mesh electrolyser ring WE _{elec} (e) Pt auxiliary WE _{aux} (5 mV/s, 0, 2, or 16 M CH ₃ OH in 0.5 M H ₂ SO ₄ , Pt flag CE, 23 ± 1°C).....147
Figure 3.34	Effect of varying $U_{aux, we}$ on (a) Au plated 316 SS electrolyser ring WE _{elec} , Pt auxiliary WE _{aux} , 0 M CH ₃ OH in 0.5 M H ₂ SO ₄ electrolyser anolyte, 0.5 M H ₂ SO ₄ electrolyser catholyte, (b) Au plated 316 SS electrolyser ring WE _{elec} , Pt auxiliary WE _{aux} , 2 M CH ₃ OH

	in 0.5 M H ₂ SO ₄ electrolyser anolyte, 0.5 M H ₂ SO ₄ electrolyser catholyte, (c) Au plated 316 SS electrolyser ring WE _{elec} , Au plated 316 SS auxiliary WE _{aux} , 0 M CH ₃ OH in 0.5 M H ₂ SO ₄ electrolyser anolyte, 0.5 M H ₂ SO ₄ electrolyser catholyte, (d) Au plated 316 SS electrolyser ring WE _{elec} , Au plated 316 SS auxiliary WE _{aux} , 2 M CH ₃ OH in 0.5 M H ₂ SO ₄ electrolyser anolyte, 0.5 M H ₂ SO ₄ electrolyser catholyte (triode, Pt/C CE, $U_{elec, we} = 0.52$ V vs. SHE).....	149
Figure 3.35	Power gain ratio ($\gamma_{elec, cell}$) as a function of $U_{aux, we}$ (a) 0 M CH ₃ OH, (b) 2 M CH ₃ OH (Au plated 316 SS components, 2 mg/cm ² Pt/C CE, 2 M CH ₃ OH in 0.5 M H ₂ SO ₄ electrolyser anolyte, 0.5 M H ₂ SO ₄ electrolyser catholyte, $U_{elec, we} = 0.52$ V vs. SHE).....	152
Figure 3.36	Schematic diagram of the proposed triode/tetrode mechanism in reverse electrolysis operation.....	154
Figure 4.1	Schematic diagram of the experimental set-up used for the catalytic reforming of liquid CH ₃ OH using catalyst powders.....	167
Figure 4.2	Schematic diagram of experimental set-up used for the catalytic CH ₃ OH reforming and the electrochemical promotion of catalytic CH ₃ OH reforming using GDEs.....	171
Figure 4.3	Picture of the experimental set-up used for the catalytic CH ₃ OH reforming and the electrochemical promotion of catalytic CH ₃ OH reforming using GDEs (a) auxiliary equipment (b) glass cell configuration.....	172
Figure 4.4	SEM image of 20 wt% metal Pt-Ru/TiO ₂ (WD 15.2 mm, 20.0 kV, x2.0 k).....	173
Figure 4.5	EDX spectra for Pt-Ru/TiO ₂ (a) 10 wt% metal, (b) 20 wt% metal.....	174
Figure 4.6	TEM images of 20 wt% Pt-Ru/TiO ₂ (a) direct mag. 200000x and (b) direct mag. 600000x (20 wt% Pt-Ru, H ₂ reduction method, ball milled 60 min., HV = 100.0 kV).....	176
Figure 4.7	X-ray diffraction data for (a) Carbon and 20 wt% Pt-Ru/C, and (b) TiO ₂ and 20 wt% Pt-Ru/TiO ₂	177
Figure 4.8	Survey XPS spectrum of 20 wt% Pt-Ru/TiO ₂	181
Figure 4.9	Pt-Ru/TiO ₂ BJH desorption pore volume distribution.....	184
Figure 4.10	Cyclic voltammograms of (a) Pt, (b) Pt-Ru/C on GC, and (c) Pt-Ru/TiO ₂ on GC (2 M CH ₃ OH in 0.5 M H ₂ SO ₄ , 23 ± 2°C, 50 and 75 ± 1°C, 50 mV/s, no rotation).....	186
Figure 4.11	H ₂ production rate as a function of time (ambient to 100 ± 1°C, 0.5 g catalyst, 20 wt% Pt-Ru, Pt:Ru 1:1 a/o, 20 ml of 2 M CH ₃ OH in 0.5 M H ₂ SO ₄).....	193
Figure 4.12	H ₂ production rate as a function of time (ambient to 75 ± 1°C, 0.5 g catalyst, 20 wt% Pt-Ru, Pt:Ru 1:1 a/o, 20 ml of 2 M CH ₃ OH in 0.5 M H ₂ SO ₄).....	194
Figure 4.13	H ₂ production as a function of temperature (0.5 g catalyst, 20 wt% Pt-Ru, Pt:Ru 1:1 a/o, 20 ml of 2 M CH ₃ OH in 0.5 M H ₂ SO ₄).....	195
Figure 4.14	CH ₃ OH partial pressure as a function of time (a) Pt-Ru/C, (b) Pt-Ru/TiO ₂ (ambient to 75 ± 1°C, 0.5 g catalyst, 20 wt% Pt-Ru, Pt:Ru 1:1 a/o, 20 ml of 2 M CH ₃ OH in 0.5 M H ₂ SO ₄).....	198
Figure 4.15	H ₂ production rate and electrolysis cell voltage as a function of time during unpromoted and promoted catalysis (2.01 cm ² , 4 mg/cm ² Pt-Ru/TiO ₂ , 20 wt% Pt-Ru, Pt:Ru 1:1 a/o, 80 ml of 2 M CH ₃ OH in 0.5 M H ₂ SO ₄ electrolyser anolyte, 80 ml of 0.5 M H ₂ SO ₄ electrolyser catholyte, 75 ± 1°C).....	202
Figure 4.16	H ₂ production rate and electrolysis cell voltage as a function of time during unpromoted and promoted catalysis (2.01 cm ² , 4 mg/cm ² Pt-Ru/C, 20 wt% Pt-Ru, Pt:Ru 1:1 a/o, 80 ml of 2 M CH ₃ OH in 0.5 M H ₂ SO ₄ electrolyser anolyte, 80 ml of 0.5 M H ₂ SO ₄ electrolyser catholyte, 75 ± 1°C).....	203
Figure 4.17	Schematic diagram of the reverse electrolyser electrical circuit and of the proposed EPOC mechanism for the catalytic reforming of methanol.....	205
Figure 4.18	H ₂ production rate and electrolyser current as a function of time during unpromoted and promoted catalysis (2.01 cm ² , 4 mg/cm ² Pt-Ru/C, 20 wt% Pt-Ru, Pt:Ru 1:1 a/o, 80 ml of 2 M CH ₃ OH in 0.5 M H ₂ SO ₄ electrolyser anolyte, 80 ml of 0.5 M H ₂ SO ₄ electrolyser catholyte, 75 ± 1°C).....	207
Figure 4.19	H ₂ production rate and electrolyser current as a function of time during unpromoted and promoted catalysis (2.01 cm ² , 4 mg/cm ² Pt-Ru/C, 20 wt% Pt-Ru, Pt:Ru 1:1 a/o, 80 ml of 2 M CH ₃ OH in 0.5 M H ₂ SO ₄ electrolyser anolyte, 80 ml of 0.5 M H ₂ SO ₄ electrolyser catholyte, 75 ± 1°C).....	208
Figure 4.20	Absolute Faradaic efficiency as a function of (a) average cell voltage, and (b) average	

	working electrode potential (2.01 cm ² , 4 mg/cm ² Pt-Ru/C, 20 wt% Pt-Ru, Pt:Ru 1:1 a/o, 80 ml of 2 M CH ₃ OH in 0.5 M H ₂ SO ₄ electrolyser anolyte, 80 ml of 0.5 M H ₂ SO ₄ electrolyser catholyte, 75 ±1°C).....	211
Figure 4.21	Catalytic H ₂ production rate as a function of average working electrode potential (2.01 cm ² , 4 mg/cm ² Pt-Ru/C, 20 wt% Pt-Ru, Pt:Ru 1:1 a/o, 80 ml of 2 M CH ₃ OH in 0.5 M H ₂ SO ₄ electrolyser anolyte, 80 ml of 0.5 M H ₂ SO ₄ electrolyser catholyte, 75 ±1°C)....	212
Figure 4.22	Electrophilic behaviour of the catalytic reaction rate as a function catalyst WE potential (Modified from Vayenas <i>et al.</i> [18] with permission from Springer).....	213
Figure 5.1	Example of working electrode scale-up design for triode or tetrode operation (a) single auxiliary working electrode, (b) multiple auxiliary working electrodes.....	226
Figure 5.2	Diagram showing possible electrolysis circuit current reversal under triode or tetrode operation.....	227
Figure B.1	Methanol electro-oxidation parallel pathways.....	251
Figure B.2	Methanol electro-oxidation bi-functional mechanism on Pt-Ru.....	252
Figure C.1	Block diagrams of four H ₂ generation process schemes (a) PEM methanol electrolyser, (b) PEM water electrolyser, (c) methanol steam reforming, and (d) sodium borohydride hydrolysis.....	255
Figure D.1	CO chemisorption on a transition metal. Molecular orbitals and density of states before (a, b) and after (c, d). Effect of varying Φ and E_F on electron back donation (c) and donation (d) (Modified from Vayenas <i>et al.</i> [1] with permission from Springer).....	274
Figure D.2	Application of Kirchhoff's first law for fuel cell triode operation.....	275
Figure D.3	Application of Kirchhoff's first law for triode electrolysis in parallel operation.....	276
Figure D.4	Application of Kirchhoff's first law for triode electrolysis in reverse operation.....	276
Figure D.5	Application of Kirchhoff's first law for tetrode electrolysis in reverse operation.....	277
Figure E.1	Electrolysis in dilute sulphuric acid.....	283
Figure E.2	Lead-free platinization.....	284
Figure F.1	Picture of a three-port glass cell for cyclic voltammetry.....	295
Figure F.2	Cyclic voltammogram (2.01 cm ² , 2 mg/cm ² Pt/C, 5 mV/s, 0.5 M H ₂ SO ₄ , Pt flag CE, 23 ± 2°C).....	298
Figure F.3	Cyclic voltammograms for a fresh catalyst sample, a used catalyst sample, and an oxidized catalyst sample (2.01 cm ² , 2 mg/cm ² Pt/C, 5 mV/s, 0.5 M H ₂ SO ₄ , Pt flag CE, 23 ± 2°C).....	299
Figure F.4	Cyclic voltammogram (4 mg/cm ² Pt-Ru, 5 mV/s, 0.5 M H ₂ SO ₄ , Pt flag CE, 23 ± 2°C).....	302
Figure F.5	Typical Nyquist plots for a fresh MEA at varying methanol concentration (initial frequency of 1x10 ⁵ Hz to final frequency of 0.01 Hz, 4 mg/cm ² Pt-Ru/C anode, 2 mg/cm ² Pt/C cathode, 0, 1, 2, 6 or 16 M CH ₃ OH in 0.5 M H ₂ SO ₄ electrolyser anolyte, 0.5 M H ₂ SO ₄ electrolyser catholyte).....	304
Figure F.6	MEA resistance as a function of methanol concentration for various MEA conditions (4 mg/cm ² Pt/Ru anode, 2 mg/cm ² Pt cathode, N-117, 0.5 M H ₂ SO ₄ electrolyte and catholyte).....	304
Figure F.7	H-cell set-up for OCV measurements.....	306
Figure H.1	Power consumption as a function of cell voltage for different CH ₃ OH concentrations (0, 1, 2, 6 or 16 M CH ₃ OH in 0.5 M H ₂ SO ₄ electrolyser anolyte, 0.5 M H ₂ SO ₄ electrolyser catholyte, 4 mg/cm ² Pt-Ru anode, 2 mg/cm ² Pt cathode, 23 ±2°C).....	324
Figure H.2	Rate of CO ₂ emission and volumetric rate of H ₂ evolution rate in function of the cell Voltage (2 M CH ₃ OH in 0.5 M H ₂ SO ₄ electrolyser anolyte, 0.5 M H ₂ SO ₄ electrolyser catholyte, 4 mg/cm ² Pt-Ru or 2 mg/cm ² Pt anode, 2 mg/cm ² Pt cathode, 23 ±2°C)....	326

Nomenclature

i) Arabic symbols

Symbol	Description	Units
a	Activity	dimensionless
a	Tafel constant	V
A	Absorbance	dimensionless
A_{Geom}	Active cell geometric area	cm ²
Ar	Pre-exponential factor	1/s
b	Tafel slope	V/dec
B	Levich parameter	mA.s ^{1/2} /cm ²
c	Charge	C
C	Concentration	M
C^o	Bulk concentration	M
Cal	Calibration number	dimensionless
cal_f	Calibration factor	dimensionless
C_C	Carbon tax	\$/tonC
C_{CAP}	Capital cost	\$/y/GJ
C_E	Energy cost	\$/GJ
C_F	Feed cost	\$/GJ
C_{H2}	Hydrogen cost	\$/GJ
C_{OM}	Operation and maintenance cost	\$/GJ
C_p^o	Standard heat capacity	J/molK
D	Diffusion coefficient	m/s ²
e	Charge of an electron	C
E	Operating cell voltage	V
E^o	Standard reversible cell voltage	V
E_a	Anodic potential	V
E_A	Activation energy	kJ/mol
E_A^o	Open circuit activation energy	eV
E_a^o	Standard anodic potential	V
E_c	Cathodic potential	V
E_c^o	Standard cathodic potential	V
E_e	Thermodynamic equilibrium (reversible) cell voltage	V
E_{ff}	Efficiency	GJ produced/GJ feedstock
E_p	Peak potential	V
f_{Nafion}	Fraction of Nafion in solution	dimensionless
f_{PTFE}	Fraction of PTFE in solution	dimensionless
F	Faraday constant	C/mol
FCR	Fixed charge rate on capital	1/y
Fr	Molar flow rate	mmol/min.
$FWHM$	Full width half max	radians
i	Current density	mA/cm ²
i_o	Exchange current density	mA/cm ²
$i_{aux, cell}$	Auxiliary current density in triode or tetrode operation	mA/cm ²
$i_{elec, cell}$	Electrolyser current density in triode or tetrode operation	mA/cm ²
i_k	Kinetic current density	mA/cm ²
I_L	Limiting current density	mA/cm ²
I	Total current	A
I_o	Exchange current of the metal-solid electrolyte interface	A

Symbol	Description	Units
I_{aux}	Auxiliary circuit current	A
$I_{aux, cell}$	Auxiliary current in triode or tetrode operation	A
$I_{aux, cell}^o$	Auxiliary current in normal operation	A
I_{elec}	Electrolyser circuit current	A
$I_{elec, cell}$	Electrolyser current in triode or tetrode operation	A
$I_{elec, cell}^o$	Electrolyser current in normal electrolysis	A
$I'_{elec, cell}$	Calculated electrolyser current based on measured CH_3OH concentration changes in triode or tetrode operation	A
I_{Far}	Net Faradaic fuel consuming current	A
I_{fc}	Fuel cell current	A
I_r	Reversible current	A
l	Path length of light in solution	cm
k	Shape factor	dimensionless
k_A	Reaction rate constant	1/s
L_{cat}	Catalyst loading	mg/cm ²
L_{Csub}	Carbon sublayer loading	mg/cm ²
m	Mass	g
M_i	Mass rate of species i	g/s
n	Number of electrons	electrons
NH^+	Protonic migration flux	mol/m ² .s
N_i	Molar rate of species i	mol/cm ² .s
N_G	Number of moles of catalyst on the metal surface	moles of metal
N_s	Total number of squares	dimensionless
P	Pressure	atm
$P_{aux, cell}$	Auxiliary power in triode or tetrode operation	W
P_C	Carbon emissions	TonC/GJ
P_e	Electric power	W
$P_{elec, cell}$	Electrolyser power in triode or tetrode operation	W
$P_{elec, cell}^o$	Electrolyser power in normal operation	W
P_i	Promotion index	dimensionless
P_p	Partial pressure	atm
Q_b	Background charge	C
Q_{cv}	H ₂ adsorption charge	C
Q_{exp}	Total charge measured	C
Q_{UDP}	Underpotential deposition charge	C
r	Electrochemically promoted catalytic reaction rate	mol/s
r^o	Open circuit unpromoted catalytic reaction rate before EPOC experiment	mol/s
r'	Open circuit unpromoted catalytic reaction rate after EPOC experiment	mol/s
r_e	Electrochemical reaction rate	mol/s
$r_{elec, cell}$	Electrochemically promoted electrochemical reaction rate	mol/s
$r_{elec, cell}^o$	Unpromoted electrochemical reaction rate	mol/s
r_F	Faradaic reaction rate	mol/s
$r_e H^+$	Electrochemical proton reaction rate	mol/s
R	Universal gas constant	J/mol·K
R	Triode or tetrode voltage ratio	dimensionless
Re	Reynolds number	dimensionless
R_s	Ohmic resistance	ohm
s	Number of moles of species	moles
S_d	Standard deviation	dimensionless
t	Time	(s)
T	Temperature	°C or K
$U_{aux, cell}$	Auxiliary cell voltage in triode or tetrode operation	V

Symbol	Description	Units
$U_{aux, we}$	Auxiliary WE potential in triode or tetrode operation	V
$U_{aux, cell}^{\circ}$	Auxiliary cell voltage in normal operation	V
$U_{elec, cell}$	Electrolyser cell voltage in triode or tetrode operation	V
$U_{elec, we}$	Electrolyser WE potential in triode or tetrode operation	V
$U_{elec, cell}^{\circ}$	Electrolyser cell voltage in normal operation	V
U_{fc}	Fuel cell voltage	V
$U_{rev, cell}$	Reversible cell voltage	V
U_{WR}	Working electrode potential with respect to a reference electrode	V
U_{WC}	Working electrode potential with respect to a counter electrode	V
V	Voltage	V
V_i	Volumetric rate of species i	m ³ /h
V_r	Volumetric flow rate	ml/h
W	X-ray wavelength	nm
W_o	Instrumentation broadening	radians
Y	Molar fraction	dimensionless
Z	Absolute impedance	ohm
Z'	Real portion of the impedance	ohm
Z''	Imaginary portion of the impedance	ohm

ii) Greek symbols

Symbol	Description	Units
α_a	Anodic transfer coefficient	dimensionless
α_H	Enthalpic parameter	dimensionless
β	Symmetry factor	dimensionless
ΔC_p	Change in heat capacity	J/molK
ΔG	Gibbs free energy of reaction	kJ/mol
ΔG°	Standard Gibbs free energy of reaction	kJ/mol
ΔG_f°	Standard Gibbs free energy of formation	kJ/mol
ΔH°	Standard enthalpy of reaction	kJ/mol
ΔH_f°	Standard enthalpy of formation	kJ/mol
ΔH_f^T	Change in enthalpy of combustion at temperature T	kJ/mol
ΔH_j	Binding energy or enthalpy of adsorption	kJ/mol
$\Delta N_{mol,g}$	Number of mole of gaseous species in the products minus in the reactants	mol
$\Delta P_{elec, cell}$	Change in electrolyser power output in triode or tetrode operation	W
ΔQ_D	Ru oxide charge gain	μ C
ΔQ_H	H ₂ adsorption charge loss	μ C
Δr	Electrochemically induced change in catalytic reaction rate	mol/s or g equivalents/s
ΔS°	Standard entropy of reaction	kJ/molK
ΔS_f°	Standard entropy of formation	kJ/molK
$\Delta \Phi_w$	Change in the work function of the working electrode	eV

Symbol	Description	Units
ΔU_{WR}	Overpotential between the working electrode catalyst and a reference electrode	V
ΔV_g	Change in volume of gaseous components	l
ε	Molar extinction coefficient	l/mol.cm
$\gamma_{elec, cell}$	Electrolyser cell power gain ratio	dimensionless
η	Overpotential	V
η_a	Anodic overpotential	V
η_c	Cathodic overpotential	V
η_{conc}	Concentration overpotential	V
η_E	Voltage efficiency	dimensionless
η_{EPOC}	EPOC production rate efficiency	dimensionless
η_{fuel}	Fuel efficiency	dimensionless
η_i	Current efficiency	dimensionless
η_{max}	Thermodynamic efficiency	%
$\eta_{max, system}$	System thermodynamic efficiency	%
$\eta_{overall}$	Overall system efficiency	dimensionless
η_{ohm}	Ohmic overvoltage	V
η_s	Charge transfer or activation overpotential	V
λ	Fuel utilization or stoichiometry	%
Λ	Rate enhancement factor or Faradaic efficiency	dimensionless
τ	Mean size of the crystalline domains	nm
θ_B	Bragg angle	radians
θ_f	Coverage of the promoting ion on the catalyst surface	dimensionless
μ_e	electrochemical potential of an electron at infinite separation from a metal	KJ
ρ_e	Electrolyser rate enhancement ratio	dimensionless
$\rho_{elec, cell}$	Electrolyser power enhancement ratio	dimensionless
v	Scan rate	V/s
Φ	Work function	eV
Ψ	Outer potential	V
ω	Angular velocity	1/s

List of Acronyms

Acronyms	Definition
AC	Alternating current
ACS	American Chemical Society
AES	Atomic emission spectroscopy
APR	Aqueous phase reforming
ATR	Autothermal reforming
BET	Brunauer-Emmett-Teller
BEV	Buttler-Erdey-Gruz-Volmer equation
BJH	Barrett-Joyner-Halenda
BPG	Barium-praseodymium-gadolinium oxide
BSE	Back-scattering electron
BZY	Barium-zirconium-yttrium oxide
C	Carbon
CE	Counter electrode
CE _{aux}	Auxiliary counter electrode
CE _{elec}	Electrolyser counter electrode
CFP	Carbon fibre paper
CNT	Carbon nanotube
CPO	Catalytic partial oxidation
CV	Cyclic voltammetry
D	Thermal decomposition
DC	Direct current
DI	Deionised water
DHE	Dynamic hydrogen electrode
DHRFC	Direct hydrogen redox fuel cell
DMFC	Direct methanol fuel cell
DMR	Direct methanol reformer
DOE	Department of energy
DOS	Density of state
EATR	Electrochemical autothermal reforming
ECSA	Electrochemical surface area
EDS	Energy dispersive X-ray spectroscopy
EDX	Energy dispersive X-ray spectroscopy
EIS	Electrochemical impedance spectroscopy
EMR	Electrochemical membrane reactor
EP	Electrochemical promotion
EPOC	Electrochemical promotion of catalysis
EPOE	Electrochemical promotion of electrocatalysis
ESCA	Electron spectroscopy for chemical analysis
F	Fuel
FC	Fuel cell
FCV	Fuel cell vehicle
FWHM	Full width half max
GB	Global behaviour
GC	Glassy carbon
GDE	Gas diffusion electrode
GDL	Gas diffusion layer
GHG	Green house gas

Acronyms	Definition
HER	Hydrogen evolution reaction
HHV	Higher heating value
HP	High performance
HPLC	High performance liquid chromatography
ICE	Internal combustion engine
ICP	Induced couple plasma
ICPMS	Induced couple plasma mass spectrometry
ID	Inner diameter
IMFC	Indirect methanol fuel cell
IR	Current resistance
I-R	Infra-red
ITO	Indium tin oxide
IV	Inverted volcano
LCR	Inductance capacitance resistance
LDH	Layered double hydroxide
LHV	Lower heating value
MCFC	Molten carbonate fuel cell
MEA	Membrane electrode assembly
MEPR	Membrane electrochemically promoted reactor
MPL	Micro-porous layer
MS	Mass spectrometer
MSE	Mercury-mercurous sulphate electrode
NEMCA	Non-Faradaic electrochemical modification of catalytic activity
OCV	Open circuit voltage
OD	Outer diameter
OES	Optical emission spectrometry
ORR	Oxygen reduction reaction
OSR	Oxidative steam reforming
PBI	Polybenzimidazole
PE+	Purely electrophilic
PE-	Purely electrophobic
PEM	Proton exchange membrane
PEMFC	Proton exchange membrane fuel cell
PGM	Precious group metal
PSA	Pressure swing adsorption
PTFE	Polytetrafluoro-ethylene
PZC	Point of zero charge
RDE	Rotating disk electrode
RE	Reference electrode
RMFC	Reformed methanol fuel cell
SA	Surface area
SCY	Strontia-ceria-ytterbia
SMSI	Strong metal-support interactions
SE	Secondary electron
SEM	Scanning electron microscopy
SHE	Standard hydrogen electrode
SOFC	Solid oxide fuel cell
SR	Steam reforming
SS	Stainless steel
SSE	Silver-silver chloride electrode
STP	Standard temperature and pressure

Acronyms	Definition
TEM	Transmission-electron microscopy
TMA	Total platinum area
TNT	Titanium dioxide nanotube
TPB	Triple phase boundary
UPD	Under potential deposition
UV	Ultra-violet
V	Volcano
WE	Working electrode
WE _{aux}	Auxiliary working electrode
WE _{elec}	Electrolyser working electrode
WGS	Water gas shift
XPS	X-ray photoelectron spectroscopy
XRD	X-ray diffraction
YSZ	Yttria-stabilized zirconia

Acknowledgements

I wish to thank my supervisor Professor Dr. David Wilkinson for his mentorship, guidance, and support, without which this work would not have been possible. Our discussions helped my progression as a scientific researcher through the strengthening and development of skills that will last a lifetime. I am also very grateful for his encouragement to participate in various learning opportunities throughout the completion of this degree, which contributed to my development at many different levels. I would like to extend my sincere appreciation to my Ph.D. Committee members, Professors Dr. Elöd Gyenge, Dr. Walter Mérida, and Dr. David Dreisinger, for their insightful comments. Additionally, I am grateful to Dr. Ken-Ichiro Ota, from Yokohama National University, for allowing the study of the low temperature contact glow discharge of water during the summer of 2008, Dr. Phillippe Vernoux from the Université Claude Bernard Lyon 1, for hosting the 3rd international training school on the electrochemical promotion of catalysis, Dr. Elena Baranova, from the University of Ottawa, as well as Dr. Constantinos Vayenas, from Patras University, for interesting discussions on electrochemical promotion.

Many thanks to the National Sciences and Engineering Research Council of Canada, the Marie Curie Action Project and the European Union, the Japan Society for the Promotion of Science, the Pacific Century, Scott Paper, the University of British Columbia, my supervisor for scholarships and research assistantships, as well as my family for financial aid in times of need.

I would like to address a special thank you to Dr. Kevin Smith for allowing me to use the mass spectrometer in the Catalysis Laboratory, and to Dr. Farnaz Sotoodeh for providing assistance with it. I would like to acknowledge the technical staff at the Bio-imaging laboratories, at the Materials Engineering Department's Electron Microscope Laboratory, at the Chemistry Department's Structural Chemistry Facility, at the National Research Council for Fuel Cell Innovations, and at Cansci Glass Inc. I wish to thank the staff in the Chemical and Biological Engineering Department administration office, store and workshop for their valuable help. I am very grateful to my friends and research colleagues at the Chemical and Biological Engineering Department, at the Clean Energy Research Center, as well as at

the National Research Council for Fuel Cell Innovations for their aid in this endeavour, and for an enjoyable and supportive work environment. I would also like to acknowledge my friends at the West Coast Symphony Orchestra and all my musically inclined friends for helping me maintain harmony and balance in my life.

Last but not least, I wish to express my deepest gratitude to my father, Michel Cloutier, for his unconditional love, continuous encouragement and support over the years, and to my beloved mother, Colette C. Cloutier and grandmother, Jeanne H. Crégheur, whose passing affected me beyond words. Warm acknowledgements to the loved ones who helped me while completing this thesis, especially Rick Harkness, and to all the people who encouraged me in difficult times. Without you, I could not have done this.

Dedication

To whom I own all things.

To my father, and to the memory of my mother (12/15/2005) and grandmother (12/12/2010).

You gave me the opportunity to study science and music, you taught me to be strong, and you inspired me to achieve academic excellence. This work is the fruit of the years of support and encouragement you provided me, and for which I will never be able to thank you enough.

I complete this thesis in your honour.

~~~~~

À ceux et celles à qui je dois tout.

À mon père, ainsi qu'à la mémoire de ma mère (12/15/2005) et de ma grand-mère (12/12/2010).

Vous m'avez incité à poursuivre mes études en sciences et en musique, vous m'avez appris à être forte et persévérante, et vous avez été mon inspiration dans la poursuite de l'excellence et de la réussite. Ce travail est le fruit de votre soutien et de vos encouragements. Je vous en suis infiniment reconnaissante.

Je vous rends hommage en complétant cette thèse.

# Chapter 1: Introduction

## 1.1 Background

### 1.1.1 Alternative Fuels

The increased global energy demand and environmental challenges we are facing drive efforts in clean energy research. A peak in conventional non-renewable oil production before 2030 appears imminent [1]. The burning of fossil fuels generates green house gases (GHG), which are considered to be the major contribution to climate change. The escalating need to reduce our fossil fuel dependency for increased energy security and to reduce GHG emissions for a cleaner environment, elevate pure hydrogen ( $H_2$ ) as a promising energy fuel for the future. Switching to  $H_2$  as an energy carrier for energy production could alleviate many environmental concerns related to the combustion of fossil fuels [2].

Fuel cells (FCs) are electrochemical devices capable of continuously converting the chemical energy of a fuel into electricity. Hydrogen and fuel cells could provide an efficient sustainable alternative to fossil-fuel based technologies. Hydrogen can be stored or readily used in various applications. It can serve as a chemical reagent in hydrogenation processes and in the production of fertilizers, it can be directly combusted in an internal combustion engine (ICE), or used to feed fuel cells. Fuel cell systems can achieve 2 to 3 times greater overall energy efficiencies than conventional gasoline ICE when fuel production is not taken into account [3]. There is no doubt that fuel processing plays an important role in fuel cell development. The strong interest in  $H_2$  has led to the search for various methods to deliver it in a convenient way. However, the issues of  $H_2$  production, distribution, compression, safety, and public acceptance, limit the large scale adoption of  $H_2$  as an energy carrier. The scientific development of practical fuelling technologies is required to close these existing gaps and facilitate the introduction of a  $H_2$  economy. Although  $H_2$  is the most abundant element on earth, it is not available in its elemental form in sufficient amounts, thus, it needs to be extracted from other sources. It can be produced from primary fossil energy sources which, even if combined with efficient carbon sequestration, emit various pollutants.

In addition, the anticipated decrease in oil reserves will result in crude oil price increases. Therefore, ways to produce H<sub>2</sub> from non-fossil sources need to be developed. Until then, H<sub>2</sub> applications will mostly depend on hydrocarbon fuel processing for H<sub>2</sub> generation.

Alternative fuels, such as liquid alcohols, could serve as a bridge between gasoline and gaseous H<sub>2</sub>. These alternative fuels possess high energy densities and can be easily stored and distributed through the existing gasoline infrastructure. It has also been argued that alcohols are the next liquid fuels to use after the depletion of petroleum resources [4]. Methanol (CH<sub>3</sub>OH) is a readily-available electroactive alcohol, which can be economically mass-produced catalytically from non-renewable resources, such as natural gas, and coal, and from renewable resources, such as gasified biomass. It may also be electro-catalytically generated from CO or CO<sub>2</sub> [5, 6]. Table 1.1 summarizes some important properties of CH<sub>3</sub>OH.

Table 1.1: Methanol properties.

| Properties                      | Methanol |
|---------------------------------|----------|
| Energy density [kWh/kg]/[kWh/l] | 6.4/4.6  |
| Boiling point [°C]              | 64.7     |
| Freezing point [°C]             | -97      |
| Flash point [°C]                | 11       |
| Toxicity – Oral [mg/kg]         | 14.3     |

In addition, methanol possesses a higher hydrogen to carbon ratio than gasoline (octane, C<sub>8</sub>H<sub>18</sub>), i.e., 4 vs. 2.25, respectively. Although CH<sub>3</sub>OH can be used directly in a fuel cell or combustion process to generate electricity, it will be explained that its electrolysis could be an efficient and economical H<sub>2</sub> production method to ease H<sub>2</sub> transportation and storage issues with minimum infrastructure changes.

### 1.1.2 Technology Gap

There exist four categories of H<sub>2</sub> production technologies: biological, chemical, electrochemical and thermal [7]. Most H<sub>2</sub> is currently produced by the well-established catalytic steam reforming (SR) process of hydrocarbon based fuels, which requires temperatures ranging from 250 to 1545°C, depending on the fuel [8, 9]. Reforming can be carried out externally, integrated with a fuel cell, or done directly inside a fuel cell such as a molten-carbonate fuel cell (MCFC, 600–700°C) or a solid oxide fuel cell (SOFC, 600–1000°C). On-board gasoline SR was originally believed to be the best way of generating H<sub>2</sub> for transportation, but it was determined that it did not offer clear advantages over other available technologies, such as gasoline ICE and battery hybrids [10]. The practical issues of durability, size and weight, resistance to vibration, cold-start, transient response, and H<sub>2</sub> purity concerns, complicates the application of SR for H<sub>2</sub> generation in transportation. Combining SR with low temperature H<sub>2</sub> proton exchange membrane (PEMFC) technology is also restricted by the low tolerance of the H<sub>2</sub> PEMFC anode catalyst to the residual CO present in the reformed fuel feed.

### 1.1.3 Proposed solution

As described later in this thesis, there may be various applications for a low temperature H<sub>2</sub> production processes. One of them is the production of H<sub>2</sub> for direct combustion or for a PEMFC inside a vehicle. An approach to achieving the ultimate performance targets, including start-up time and energy, may be to conduct on-board reforming at temperatures lower than that of conventional steam reforming (SR) processes. Electrocatalysis can be used to extract H<sub>2</sub> from CH<sub>3</sub>OH at low temperatures (20-80°C) [11-12]. Methanol catalytic reforming can also be conducted in the liquid phase at lower temperatures (72–200°C) [13–16]. It will be seen that, using new electrochemical approaches, the electrocatalytic or catalytic CH<sub>3</sub>OH reforming process may result in reduced energy consumption over comparable existing technologies. To the author's knowledge, no studies have verified if these low temperature alcohol electrocatalytic or catalytic reforming processes could meet the on-board fuel processing targets and if their adoption could facilitate the implementation of a H<sub>2</sub> economy. This thesis focuses on the catalytic and electrocatalytic oxidation of CH<sub>3</sub>OH at low temperatures, i.e., below 200°C.

#### 1.1.4 A sustainable closed loop system

Low temperature CH<sub>3</sub>OH oxidation technologies may meet the short-to-medium term demand for H<sub>2</sub>, until it can be effectively produced without releasing significant CO<sub>2</sub>. Figure 1.1 (a) shows an example of how conventional methanol synthesis processes can be combined with a direct methanol reformer (DMR) and a PEMFC. For example, without going into the details of the reaction mechanism, syngas can be produced by methane steam reforming (SR):



The water-gas shift (WGS) reaction is used to adjust the CO to H<sub>2</sub> ratio for the synthesis of CH<sub>3</sub>OH.



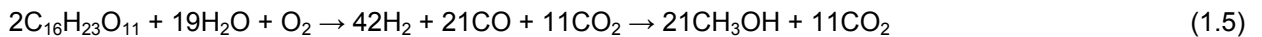
Methanol is synthesized from the highly selective conversion of the synthesis gas generated.



However, as CO is used in the CH<sub>3</sub>OH synthesis, the WGS reaction reverses, producing more CO. Therefore, the overall reactions, which produces CH<sub>3</sub>OH from syngas can be summarised in the following overall reaction:



Biomass gasification can also be used to produce CH<sub>3</sub>OH. For example, wood biomass can be gasified to syngas, which can in turn be synthesized to CH<sub>3</sub>OH.



In this case the process is carbon neutral as the  $\text{CO}_2$  generated is used to produce biomass by photosynthesis. Ideally, the system would exclusively depend on renewable resources: the methanol could be originating from biomass, while the electricity required for direct current (DC) voltage supply could originate from solar, wind, hydro, tidal, or geothermal energy. Figure 1.1 (b) demonstrates how, in the future, the system could be made sustainable when paired with solar energy and an electrochemical synthesis process. The  $\text{CH}_3\text{OH}$  would be synthesized from  $\text{CO}_2$ , generated by the DMR, i.e., methanol electrolyser, and  $\text{H}_2\text{O}$ , generated by a PEMFC. The current efficiency for the electro-synthesis of  $\text{CH}_3\text{OH}$  using  $\text{RuO}_2/\text{TiO}_2$  nanotube composite electrodes was reported to be about 60% [17]. It may appear to be simpler to produce  $\text{H}_2$  and  $\text{O}_2$  directly from water using solar energy, however, the scheme presented in Fig. 1.1 could also use  $\text{CO}_2$  from external sources (dashed line), such as fossil fuel combustion, and contribute to the reduction of GHG from other existing processes.

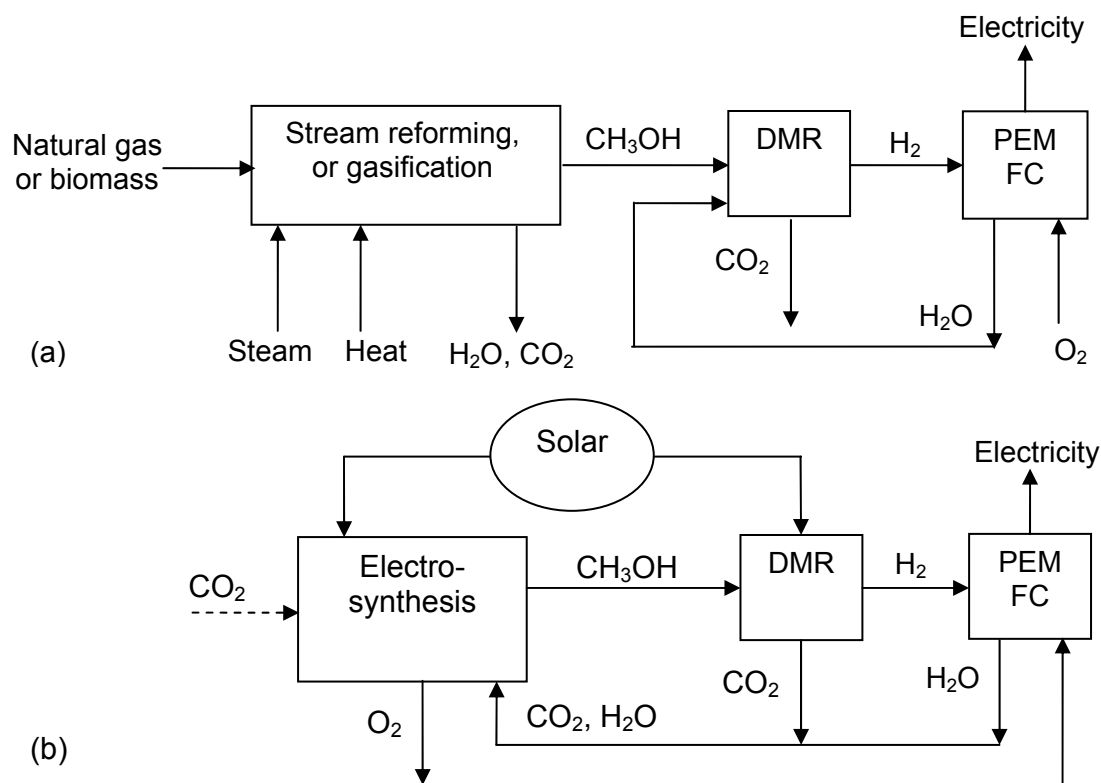


Figure 1.1: (a) Schematic diagram of conventional methanol synthesis combined with a DMR and a PEMFC (b) Schematic diagram of a future sustainable system comprising a DMR and PEMFC.

In this thesis, it will be seen that electrochemical promotion can be applied to improve the current or voltage efficiency of electrochemical processes. Over the long term, this research may benefit the creation of a sustainable energy system for the production of H<sub>2</sub> from renewable methanol originating from biomass. Over the short term, the findings of this research are more likely to impact the development of transitional low temperature CH<sub>3</sub>OH based H<sub>2</sub> generation technologies, utilizing energy sources currently available.

## **1.2 Thesis overview**

### **1.2.1 Justification**

Ideally, the CH<sub>3</sub>OH and water catalytic or electrocatalytic H<sub>2</sub> production process should possess a higher efficiency than other currently available technologies. The non-Faradaic enhancement of catalytic activity (NEMCA), also referred to as the electrochemical promotion (EP) of catalysis (EPOC), was identified as a novel approach to improve the overall performance of catalytic chemical reactions. This phenomenon has been shown to enhance the rate of a variety of catalytic reactions [18]. A new EP approach, known as triode operation, has been shown to affect the overpotential of electrodes in fuel cells [19]. This approach is analogous to EPOC, except that an electrochemical reaction is promoted instead of a catalytic one. We denote it as the electrochemical promotion of electrocatalysis (EPOE). In this thesis, both of these approaches, i.e., EPOC of the catalytic reforming of CH<sub>3</sub>OH, and EPOE of the electrocatalytic reforming of CH<sub>3</sub>OH and water, were investigated at low temperature. The application of EP, through the synergy of solid-state electrochemistry and catalysis, could be a key to efficient fuel processing technologies for H<sub>2</sub> production. As EP is a fairly new topic, many cutting-edge research opportunities still remain. This thesis provides valuable information on the effect of EP on the electrocatalytic and catalytic reforming of CH<sub>3</sub>OH and water at low temperature, i.e., ambient to 75°C, and gives insights for further improvements. Applying this new electrochemical engineering technique might eventually lead to the development of a ground-breaking H<sub>2</sub> production technology, which could have a tremendous market impact on the energy and transportation sectors, as well as on the environment.

### 1.2.2 Research objectives

The main objective of this research was to improve the state-of-the-art methanol and water electrochemical and chemical reforming processes by rendering them more thermodynamically and kinetically attractive. Investigating the thermodynamic and kinetic characteristics of H<sub>2</sub> production via catalytic and electrocatalytic methanol liquid phase reforming involved the following goals:

- 1) Evaluate the influence of different operating conditions, such as CH<sub>3</sub>OH concentration (0 to 16 M), and low temperatures (25 to 75°C), as well as the performance of different electro-catalysts (Pt, Pt-Ru) on the electrochemical reforming of CH<sub>3</sub>OH in acidic media;
- 2) Determine the effect of EPOE on the electrolysis of CH<sub>3</sub>OH and water using different triode and tetrode configurations and materials in the galvanostatic and potentiostatic modes;
- 3) Synthesize, characterize, and evaluate the catalytic and electrocatalytic capabilities of Pt-Ru/TiO<sub>2</sub>;
- 4) Determine the effect of EPOC on the low temperature catalytic reforming of CH<sub>3</sub>OH in acidic media.

This applied research project comprises several innovative contributions, which, to the author's knowledge, have not been reported in the literature to date. For example, there have been no scientific papers on:

- 1) The passive electrochemical reforming or electrolysis of CH<sub>3</sub>OH and water in the liquid phase;
- 2) The use of the triode and tetrode configuration in the electrolysis mode;
- 3) The application of triode and tetrode operation in the potentiostatic control;
- 4) The operation of a tetrode in the mixed galvanostatic and potentiostatic control;
- 5) The low temperature catalytic reforming of CH<sub>3</sub>OH and water using Pt-Ru/C;
- 6) The application of EP on the low temperature catalytic reforming of CH<sub>3</sub>OH and water using proton-conducting electrolytes.

This thesis provides a better understanding of the chemical and electrochemical CH<sub>3</sub>OH reforming processes at low temperature, as well as valuable information on possible ways to improve their effectiveness, particularly through electrochemical promotion.

### 1.2.3 Layout

This study was achieved by drawing from knowledge in electrochemical, chemical, and material engineering. Six key topics were identified: catalytic reforming, electrochemical membrane reactors, H<sub>2</sub> pumping, direct fuel cells, proton-conducting electrolytes, and electrochemical promotion. Only the most essential information is discussed in the literature review, which completes *Chapter 1* and starts in *Section 1.3*.

*Chapter 2* constitutes a baseline study of the electrochemical reforming of methanol and water using a proton exchange membrane (PEM) electrolyser and extends the existing knowledge of this system, which is presently limited as will be seen in *Section 1.3.3*. A theoretical thermodynamic evaluation demonstrating that the electrochemical reforming systems could become thermodynamically favourable under certain operating conditions is presented. The investigation of the kinetic aspect of alcohol electrochemical reforming systems was valuable in determining if the electrochemical reaction occurs at a rate of practical interest. The characteristics of the alcohol electrochemical reformer were determined under various conditions and using different membrane electrode assembly (MEA) compositions. The content of this Chapter is based on a publication and is reprinted from the International Journal of H<sub>2</sub> Energy, 35, C. R. Cloutier, and D. P. Wilkinson, "Electrolytic Production of Hydrogen from Aqueous Acidic Methanol Solutions", 3967-3984, Copyright (2010), with permission from Elsevier.

*Chapter 3* describes the electrochemical promotion of electrocatalysis in triode and tetrode operation in the galvanostatic and potentiostatic mode. This new application was developed based on fuel cell triode operation knowledge presented in *Section 1.3.5*. The effects of electrochemical promotion on the electrolysis of methanol and water are evaluated under various conditions and different design configurations. The results obtained are used to compare the energetics of triode and tetrode electrolysis versus conventional electrolysis. It will be demonstrated that the application of electrochemical promotion on the electrochemical reforming of alcohols can lead to the elimination of the need for anodic noble metal catalysts. Part of the work presented in this Chapter was published and reprinted from the ECS Transactions, 25 (23), C. R. Cloutier, and D. P. Wilkinson, "Triode Operation of a

Proton Exchange Membrane (PEM) Electrolyser", 47-57, Copyright (2010), with permission from the Electrochemical Society. Another more complete article was also recently submitted for publication.

*Chapter 4* contains a baseline low temperature chemical reforming study. The electrochemical promotion of low temperature liquid phase catalytic reforming of methanol and water requires that the chosen catalyst, in addition to being a chemical catalyst, is also an electrocatalyst for the methanol and water electrochemical reforming reaction. To achieve this requirement, Pt-Ru/TiO<sub>2</sub> was synthesized, characterized and tested for its catalytic reforming capabilities. Also in this *Chapter*, the effect of EP on the catalytic reforming of CH<sub>3</sub>OH and water was evaluated using the commercial Pt-Ru/C CH<sub>3</sub>OH electro-oxidation catalyst and the synthesized Pt-Ru/TiO<sub>2</sub>. The results obtained are used to compare the energetics and viability of the electrochemically enhanced low temperature CH<sub>3</sub>OH and water reforming systems versus conventional low temperature catalytic reforming, CH<sub>3</sub>OH and water PEM electrolysis. The content of *Chapter 4* is the basis for a journal submission currently in preparation.

*Chapter 5* summarizes the research outcomes of *Chapters 2 to 4*. Possible applications are described and the significance and impact of the work is discussed. Finally, recommendations for future work are given. *Appendices A to J* contain detailed information which is supporting but not essential to the thesis. *Appendix A* contains a list of publications, presentations, and posters which resulted from this research. The mechanism for the electro-oxidation of methanol on Pt and Pt-Ru is shown in *Appendix B*. *Appendix C* contains an efficiency and economic comparison of H<sub>2</sub> production methods. Some EPOC rules and triode equation derivations are provided in *Appendix D*. *Appendix E* contains experimental procedures used to carry out this work while *Appendix F* contains background information on the various electrochemical techniques employed. *Appendices G and H* contain thermodynamic and electrochemical data, and sample calculations.

## 1.3 Literature Review

### 1.3.1 Heterogeneous catalysis

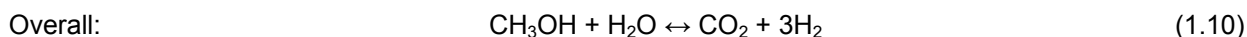
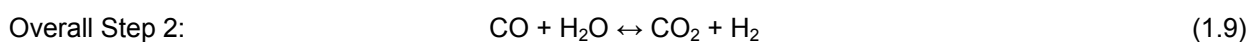
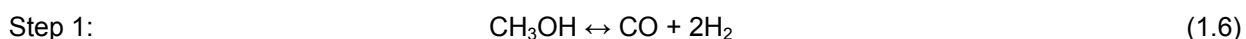
In heterogeneous catalysis, the reactant(s) phase differs from that of the catalyst. Most of the time, the reactants are in the liquid or gaseous phase, and the catalyst is in the solid phase. The main stages of heterogeneous catalysis includes (1) the diffusion of the reactant(s) to the catalyst surface (2) the adsorption of the reactants on the catalyst active site through the formation of chemical bonds, (3) after chemical reaction, desorption of the products formed from the catalyst surface, and (4) product(s) diffusion away from the catalyst surface. Heterogeneous catalysis is often the most important step in the synthesis of petrochemicals, pharmaceuticals, chemicals, and in environmental applications.

A catalyst is a substance which is not consumed in a chemical reaction, but accelerates its rate. In heterogeneous catalysis, the diffusion and adsorption of reactants to the catalyst surface is crucial for the chemical reaction to occur. Catalysts can reduce the activation energy required for a chemical reaction to take place. Most metal catalysts used in heterogeneous catalysis are transition metals. Their electronic structure impacts the interactions between the reactants and the catalyst as electronically unsaturated metal atoms allow electrons to be accepted by available d orbitals.

Most hydrogen is produced by the heterogeneous catalytic reforming of fossil fuels [20]. Three main vapour phase production paths exist for the generation of H<sub>2</sub> from methanol: thermal decomposition (D), steam reforming (SR), and catalytic partial oxidation (CPO). Autothermal reforming (ATR), also referred to as oxidative steam reforming (OSR), combines the SR with the CPO reactions. Of these processes, only SR is discussed, as it produces the highest H<sub>2</sub> concentration. Methanol can be converted to H<sub>2</sub> at lower temperatures than other hydrocarbons, making it possible to catalytically reform it by aqueous phase reforming (APR) or liquid phase reforming.

### 1.3.1.1 Steam reforming

The catalytic SR of CH<sub>3</sub>OH is an endothermic reaction, which is conducted at temperatures ranging from 250 to 350°C [6]. Heat is needed to attain a reasonable CH<sub>3</sub>OH conversion. The SR process starts with the splitting of CH<sub>3</sub>OH into CO and H<sub>2</sub>, followed by the exothermic water gas shift (WGS) reaction (Eq. 1.9), as per the following chemical reactions, which do not describe the details of the reaction mechanism:



The enthalpy of the overall reaction at standard conditions is  $\Delta H^\circ = 49.2$  kJ/mol. It will be later explained that the overall CH<sub>3</sub>OH chemical reforming reaction is the same as the overall electrochemical reaction for the electrolysis of CH<sub>3</sub>OH in a proton exchange membrane (PEM) electrolyser. Catalysts commonly used for the steam reforming of CH<sub>3</sub>OH are composed of copper supported on zinc oxides, such as CuO/ZnO and CuO/ZnO/Al<sub>2</sub>O<sub>3</sub>, in which Al<sub>2</sub>O<sub>3</sub> can be added for thermal stability [21]. Different Cu-Al catalysts of varying Cu contents have been investigated for the production of H<sub>2</sub> from CH<sub>3</sub>OH. A maximum H<sub>2</sub> production efficiency of 78 mol% was obtained for the SR reaction at 250°C using a catalyst containing 27.8 wt% Cu and calcined at 700°C [22]. Since the WGS reaction (Eq. 1.9) is reversible, CO can be generated. The activity of layered double hydroxide (LDH) catalysts containing various metal combinations was evaluated for the SR of CH<sub>3</sub>OH at 150–400 °C and atmospheric pressure [23]. Again, the most favourable LDH for the SR of CH<sub>3</sub>OH was Cu-Al based. A WO<sub>3</sub>/CeO<sub>2</sub>/YSZ nanocomposite catalyst was used for the reforming of CH<sub>3</sub>OH, with and without H<sub>2</sub>O, at temperatures ranging from 100 to 300°C [24]. In both cases, the only product was CO<sub>2</sub>, which formed at

room temperature when H<sub>2</sub>O was present. The SR CO<sub>2</sub> emissions need to be suppressed by concentrating and sequestering CO<sub>2</sub>, which results in energy losses.

### 1.3.1.2 Liquid phase reforming

The terms aqueous phase reforming (APR) are used to designate the reforming of aqueous solutions composed of direct biomass products, such as methanol, ethylene glycol, glycerol, sugars and sugar alcohols (sorbitol, etc.). Biomass is a renewable carbon-containing fuel, which can be obtained from a variety of sources such as animal, agricultural, and municipal wastes. In this process, a feed of oxygenated hydrocarbons, having a limited volatility and a C:O ratio of 1:1, is catalytically converted with liquid H<sub>2</sub>O over a heterogeneous catalyst at temperatures around 230°C to produce H<sub>2</sub> and CO<sub>2</sub> [25]. This single-step catalytic process is achievable at conditions where the WGS reaction is favourable, making it possible to generate H<sub>2</sub> with low amounts of CO. The APR process consumes less energy than the conventional SR process, as it does not require the vaporization of the oxygenated hydrocarbon and water feeds. Platinum metal has a high activity for the dehydrogenation of CH<sub>3</sub>OH, so typically, Pt/Al<sub>2</sub>O<sub>3</sub> is used for APR, while other promising materials include Pt and Ni-Sn based catalysts [26-28]. Bimetallic catalysts were shown to result in higher activities for the APR reaction than monometallic catalysts [25]. It was noted that the oxygenated hydrocarbons have various aqueous phase reforming reaction pathways, resulting in catalyst selectivity challenges. The process selectivity depends on many factors, including the catalytic metal, the support, the solution pH, the feed and the operating conditions [25]. The CO species adsorbed at the catalyst surface result in low catalytic activity and are partially removed by the WGS to form CO<sub>2</sub>. The development of heterogeneous catalysts comprising metals, metal alloys, support and WGS reaction promoters, which are stable under APR conditions, is still under way.

There are only a limited number of studies focusing on the aqueous phase catalytic reforming of CH<sub>3</sub>OH, which do not originate from biomass sources. Hence, these processes are not referred too as APR in the literature. This liquid phase reforming reaction was first studied on a Ru/C catalyst with external heating at 100-200°C [13]. Compared to Pt-based catalysts, commercial Cu/ZnO reforming catalysts were found to have no activity under liquid phase reaction conditions, although their activity is high for

the steam reforming reaction. Silica-supported Pt-Ru catalysts were also investigated at 77 to 84°C at ambient pressure, and CH<sub>3</sub>OH dehydrogenation was determined to be the rate limiting step of the reaction [14]. The formation of CO<sub>2</sub> over Pt-Ru/SiO<sub>2</sub> did not proceed via HCHO decomposition, and partly-dehydrogenated CH<sub>3</sub>OH (CH<sub>2</sub>OH\*) was determined to be the initial reaction intermediate, from which H<sub>2</sub> and CO<sub>2</sub> were formed through HCOOCH<sub>3</sub> and HCOOH as successive reaction intermediates. The catalytic activity and selectivity towards CO<sub>2</sub> increased with basic oxide catalyst supports and decreased with acidic catalyst supports [29]. Platinum was most active for liquid phase H<sub>2</sub> production reforming when supported on TiO<sub>2</sub>. In addition, Pt-Ru/SiO<sub>2</sub> resulted in an even greater activity than Pt/SiO<sub>2</sub>. The addition of Ru to Pt/SiO<sub>2</sub> accelerated the reaction of the formaldehyde (H<sub>2</sub>CO) intermediate to form methyl formate (HCOOCH<sub>3</sub>), as the product formation rate was not restricted in the presence of CO. The dehydrogenation of CH<sub>3</sub>OH was reported as the rate determining reaction. Ir-Re/SiO<sub>2</sub> catalysts were also studied at 105°C and resulted in an activity comparable to Pt-Ru/SiO<sub>2</sub> [15]. The highest activity for the catalytic reforming of liquid CH<sub>3</sub>OH was obtained with Pt-Ru/TiO<sub>2</sub> between 77 and 84°C [16]. It proceeded through the partially dehydrogenated HCOOCH<sub>3</sub> and HCOOH intermediates through a mechanism similar to that obtained using Pt-Ru/SiO<sub>2</sub>.

### 1.3.1.3 Hydrogen spillover in heterogeneous catalysis

Spillover is defined as a phenomenon in which species activated on one phase are transported, usually across a surface, to another phase where they may then participate directly or indirectly in catalysis [30]. The second surface should not normally adsorb or form the active species which are adsorbed or formed on the first surface under the same conditions. The species spilled on the second surface may (1) diffuse on the surface, (2) diffuse or react in the bulk, (3) react on or with the surface, (4) create sites capable of adsorption or catalysis [30]. Spillover can extend from the initial accepting surface to adjacent surfaces in direct or indirect contact with the source of spillover, or the surface that initially accepted the spillover species. This means that spillover species can be transferred over long distances, i.e., over millimetre and centimetre distances [30]. Spillover constitutes an important mechanistic step which can occur during adsorption in heterogeneous catalysis and was found to be involved in many surface reactions and transport phenomena.

H<sub>2</sub> spillover from a metal to an oxide or carbon surface was extensively studied because most heterogeneous catalysts comprise metal particles supported on high surface area carbon or oxides, and because H<sub>2</sub> is involved in many catalytic reactions. It is the fastest spillover process and may occur at room temperature [30]. H<sub>2</sub> spillover has been demonstrated on several supported metals, which are known to adsorb H<sub>2</sub> dissociatively. A model assuming the dynamic equilibrium of two coexisting activated H<sub>2</sub> spillover species (H atoms and H<sup>+</sup> ions) was proposed to explain the synergy between the components of bifunctional catalysts [31]. It was concluded that the nature of the activated hydrogen species depended on the physico-chemical properties of the catalyst [32]. For the promotion of acidic catalysis, the spillover species is proposed to be part of the active site as H<sup>+</sup> [28]. The principles of H<sub>2</sub> spillover have been applied to the design of highly selective and active catalysts from physical mixtures [33].

The spillover of H<sub>2</sub> over macroscopic distances was exploited in the design of a dual-bed reactor comprising two separate zones of metal and bimetallic catalysts. Using this design, activities 2.7 times greater than that of the noble metal alone were achieved, demonstrating that a catalytic reaction may occur at different reactive sites as the activating species moved via surface diffusion [34]. Indirect catalyzed hydrogenation was shown to occur via a mechanism in which H<sub>2</sub> is activated on a metal catalyst, desorbed in an activated form, which may then react with a second reactant not in contact with the catalyst [35]. The deactivation kinetics of H<sub>2</sub> spillover in the gas phase was found to be a first-order reaction, which is accelerated by glass surfaces [36]. The effect of H<sub>2</sub> spillover through the gas phase on the hydrogenation of methane was studied on graphite and activated carbon using various independent methods [37]. Studies of the H<sub>2</sub> spillover to the carbon support of metal catalysts demonstrated that the uptake and spillover of H<sub>2</sub> was greater for Ru containing catalysts than for Pt/C catalysts [38].

#### **1.3.1.4 Catalyst local heating**

Catalysts can be thermally heated locally by using heating elements or by the passage of an electric current. The selective oxidation of CH<sub>3</sub>OH was investigated at temperatures ranging from 100 to 350°C on indium tin oxide (ITO). The study was carried out by (1) thermally heating the catalyst with a ceramic heating element, (2) by heating the catalyst through ohmic heating due to the passage of an electric

current, and (3) by thermal heating followed by ohmic heating [39]. It was found that the electrically activated and thermally heated catalyst was much more active than the non-electrically activated but thermally heated catalyst. The electrically activated catalyst was active even after the current was cut-off. This phenomenon was thought to be analogous to the EPOC effect, which is described in more details in *Section 1.3.4*. However, it was determined that the mechanism was different in this case, as reversing the catalyst electrical leads did not affect the reaction kinetics or selectivity, and the catalyst was still active after the current was cut-off, and the reaction took place on ITO deposited on a porous insulating surface and not on a metal deposited on a solid ion conducting electrolyte. An electrically heatable device using electrically conductive non-metallic materials [40] and a process for the electrically activated transformation of chemical and material compositions have been proposed [41]. Electrically activated catalysis was also studied for the steam reforming of methane at 600°C [42]. A conversion of 76% H<sub>2</sub> was obtained upon passing a current through the catalyst, while a conversion of 66% was obtained upon thermal heating only. More detailed investigations are required to elucidate the reasons behind the catalyst activity enhancement observed.

### **1.3.2 Proton exchange membrane fuel cell**

The electrochemical operating principles of FCs are similar to those of batteries as neither requires combustion. However, fuel cells can effectively convert chemical energy into electrical energy as long as a fuel is supplied, so they do not require recharging like batteries. They are quiet and flexible devices, which convert a fuel to electricity and heat through a spontaneous electrochemical reaction. H<sub>2</sub> fuel cells were initially developed for the space program for providing electricity and drinking water to astronauts. As they can produce electrical energy efficiently and can generate less emissions than combustion engines, various types of FCs are being considered for many applications. Most FC research is focused on the development of direct H<sub>2</sub> and direct liquid fuel cells. Only low temperature proton exchange (or polymer electrolyte) membrane (PEM) fuel cells are discussed in this thesis.

### 1.3.2.1 Membrane electrode assembly

The membrane electrode assembly (MEA) forms the core of a PEMFC. It is usually inserted between flow field plates, which allow current flow and reactant and product distribution. The MEA comprises a PEM, which separates an anodic electrode from a cathodic electrode. The most common PEM is a perfluorinated ion exchange membrane from DuPont, which is referred to as Nafion<sup>®</sup>. The mobile ion of this sulphonated fluoro-polymer is H<sup>+</sup>. This acidic polymer is an excellent gas separator and electrical insulator, and has good chemical resistance and mechanical strength. However, it dehydrates at temperatures exceeding 100°C and loses its proton conductivity. Therefore, Nafion<sup>®</sup> membranes must be kept humidified to maintain their high proton conductivity. The presence of cationic contaminants also affects the mechanical properties and the protonic conductivity of Nafion<sup>®</sup> [43, 44]. Due to these shortcomings, work has been done on the development of other proton conducting electrolyte membranes for PEMFC applications, such as ceramics [45-50], composite [51-54], other polymers [55-57], and metal coated polymers [58, 59].

The anode and cathode of fuel cells are usually composed of electroactive Pt group metal (PGM) based catalysts. As platinum has a high cost and a low abundance, precious metal nanoparticles are often dispersed or supported on larger carbon particles to reduce the amount of Pt needed while increasing the electrochemically active surface area (ECSA) of the catalyst. ECSA losses deteriorate the PEMFC performance. Improving the catalyst activity, utilization and stability are important topics in PEMFC research. The main approaches taken to reduce or replace Pt while maintaining PEMFC performance and efficiency are to reduce the noble metal loading or use less expensive noble metals [60], or explore using non-Pt electrocatalysts [61, 62]. Changing the carbon catalyst support is also looked at as it may affect the catalyst activity and lead to the partial reduction of the Pt loading [63].

A triple phase boundary (TPB) between the electrolyte, reactants and catalyst is required for an electrochemical reaction to occur. Different methods can be used to create this three-dimensional electrochemical reaction zone. The most common is the application of an ink comprised of a polymer electrolyte solution and electrocatalytic particles. Thin films of catalyst inks usually contain an electrolyte ionomer binder (typically Nafion<sup>®</sup>), and supported or unsupported nanocatalyst Pt particles. A three

phase contact between the H<sub>2</sub>, protons and solid catalyst is obtained by applying this electronically connected ink coating onto a porous conducting carbon substrate or a membrane. The three main methods consist of applying an ink onto (1) a Teflon film which is transferred by decal to the membrane through a hot pressing process [64] (2) a porous conducting carbon substrate (gas diffusion layer, GDL) to form a gas diffusion electrode (GDE) [65], or (3) onto each side of the membrane to form a catalyst-coated membrane (CCM) [66].

### 1.3.2.2 Overvoltage

In fuel cells, the operating voltage,  $E$  (V), is always greater than the standard reversible cell voltage,  $E^\circ$  (V):

$$E^\circ = -\frac{\Delta G^\circ}{nF} \quad (1.11)$$

where  $\Delta G^\circ$  (kJ/mol) is the change in Gibbs free energy of reaction,  $n$  is the number of electrons participating in the reaction, and  $F$  is Faraday's constant (96485 C/mol). When not operating at standard conditions, the thermodynamic equilibrium (reversible) cell voltage at non-standard temperature and pressure,  $E_e$  (V), can be estimated with the Nernst equation:

$$E_e = E^\circ - \frac{2.303RT}{nF} \text{Log} \left( \frac{\prod_j a_{Red,j}^{s_{r,j}}}{\prod_j a_{Ox,j}^{s_{o,j}}} \right) \quad (1.12)$$

where  $R$  is the ideal gas constant (8.314 J/molK),  $T$  is the temperature (K), and  $a$  is the activity (dimensionless). The excess amount of electrical energy required for the electrocatalytic process to occur is known as overvoltage,  $\eta$  (V). It is the difference between the operating cell voltage,  $E$ , and the equilibrium cell voltage,  $E_e$ :

$$\eta = E - E_e \quad (1.13)$$

The overvoltage represents the sum of the cell efficiency losses which are mainly due to the activation overvoltage or charge transfer overvoltage,  $\eta_s$ , the concentration overvoltage,  $\eta_{conc}$ , and the ohmic overvoltage,  $\eta_{ohm}$ .

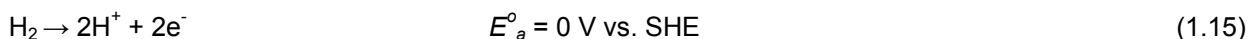
$$E = E_e - |\eta_s| - |\eta_{conc}| - |\eta_{ohm}| \quad (1.14)$$

The activation overvoltage and the concentration overvoltage in Eq. 1.14 can be separated in their anodic and cathodic components. If so, the absolute values in Eq. 1.14 are then removed, and the anodic component is subtracted as it is a positive value, while the cathodic component is added, as it is a negative value. The activation overvoltage is related to the activity of the electrode surface which affects the charge transfer process for a particular electrochemical reaction. The concentration overvoltage is linked to the change in the mass transport of reactants to the electrode surface as the electrochemical reaction proceeds. The ohmic resistance is caused by the PEM/electrocatalyst interface resistance, as well as the bulk resistance and the ionic conductor's resistance to the transport of electrons. Other losses include fuel crossover and internal currents [67]. The power output and thermodynamic efficiency of electrochemical systems depend on the minimization of overpotential losses at the anode and/or cathode. Significant overpotentials will result in inefficient electrocatalysis and restrict the commercialization of electrochemical devices as they are often not sufficiently cost-effective. For this reason, research efforts are concentrated towards the minimization of overvoltage losses, which is crucial to the development of effective electrocatalytic processes.

### 1.3.2.3 Hydrogen proton exchange membrane fuel cell

The H<sub>2</sub> PEMFC uses H<sub>2</sub> as the fuel and O<sub>2</sub> as the oxidant. The oxidation occurs at the anode and the reduction occurs at the cathode. The electrons pass through an external electrical circuit while the protons diffuse through the membrane. The overall reaction is the sum of the anodic and cathodic reactions. The PEMFC electrochemical reactions are as follows:

Anode half-cell reaction:



Cathode half-cell reaction:



Overall reaction:



Note that throughout this thesis, the convention of reversing the  $E_a^\circ$  values reported for the half-cell reactions written as electro-oxidation was adopted. The subscript “*a*” designate the standard potential of the half-cell reaction occurring on the anode, while the subscript “*c*” designate the standard potential of the half-cell reaction occurring on the cathode. The standard reversible cell voltage,  $E^\circ$ , based on thermodynamics is 1.23 V. The rate limiting process is the cathode oxygen reduction reaction (ORR), which suffers from kinetic limitations. For this reason, a larger quantity of catalyst is needed for the slow ORR cathodic reaction compared than for the fast  $\text{H}_2$  anodic reaction. The  $\text{H}_2$  PEMFC has significant water management issues, which need to be continuously addressed to reach stable operation, and for this reason, their operation is usually limited to temperatures around 60-90°C.

### Hydrogen purity requirements

The PEMFC electrodes usually contain a Pt catalyst, which promotes the reactions occurring at the electrodes. The electrocatalytic properties of Pt are greatly affected by contaminants, which adsorb to the surface of the catalyst and prevent  $\text{H}_2$  adsorption onto the catalyst surface [68]. At temperatures below 150°C, CO strongly adsorbs onto Pt and poisons the  $\text{H}_2$  reaction. This CO poisoning effect occurs at concentrations of CO as low as 5-100 ppm (0.0005-0.01%) in the  $\text{H}_2$  inlet stream, depending on the catalyst loading [69]. A tolerance to CO levels of 100 ppm or more would greatly simplify the PEMFC

fuelling system when H<sub>2</sub> is produced by catalytic reforming processes. Typically, the H<sub>2</sub> fuel stream needs to contain less than 10 ppm of CO in order to be fed directly to a PEMFC.

Different options exist to overcome electrocatalyst CO poisoning in the PEMFC [70]. These include increasing the cell operating temperature, which weakens the CO bond to the Pt active sites and reduces the catalyst's sensitivity to CO poisoning. It is also possible to remove CO from the reformat using advanced fuelling system design or membranes for CO separation. Preferential oxidation reactors or H<sub>2</sub> separation membranes containing Pd-based alloys or proton-conducting ceramics can be used to remove CO. For example, Pt-alloy catalysts can preferentially oxidize CO and selectively remove it [71]. Other methods are the introduction of oxidant in the H<sub>2</sub> fuel feed stream, referred to as O<sub>2</sub> bleeding, or the use of cyclic operation to clean the surface from adsorbed species.

#### 1.3.2.4 Direct methanol fuel cell

The direct methanol fuel cell (DMFC) is the most advanced type of direct liquid fuel cell. In a DMFC, a diluted aqueous solution of CH<sub>3</sub>OH is fuelled directly to the anode of a PEM fuel cell, while air or O<sub>2</sub> is supplied to the cathode, as per the following electrochemical reactions:

Anode half-cell reaction:



Cathode half-cell reaction:



Overall reaction:



The DMFC has a standard reversible cell voltage of 1.21 V. The MEA arrangement for the DMFC is similar to that for the H<sub>2</sub> PEMFC. When liquid CH<sub>3</sub>OH mixtures are used as the fuel, the membrane can maintain high humidification levels, but cross-over of the liquid CH<sub>3</sub>OH can be a problem. While the cathode reaction of the PEMFC suffers from poor kinetics, in the DMFC, the anode and the cathode reactions both result in kinetic losses. Thus, the two main issues which restrict the performance of DMFCs are the poor anodic CH<sub>3</sub>OH oxidation kinetics, and CH<sub>3</sub>OH crossover.

### **Anodic methanol oxidation**

The slow CH<sub>3</sub>OH oxidation kinetics at the electrode/electrolyte interface in acidic media limits the electrochemical reaction rate. The high activation overpotentials observed are mostly caused by the complex anodic electrochemical reaction mechanism [4]. Possible CH<sub>3</sub>OH electro-oxidation pathways are illustrated in *Appendix B*. The direct electrochemical oxidation of CH<sub>3</sub>OH on Pt occurs in multiple stages, which include various adsorbed intermediates. Strongly adsorbed CO remains un-oxidized at the surface and blocks the electrode active sites from adsorbing reaction intermediates which are formed during the oxidation process [4, 72]. The poisoning species which deactivates the electrode surface is CO. It is the rate limiting component for the electro-oxidation of CH<sub>3</sub>OH.

Typical methods used to prevent CO poisoning in DMFCs include modifying the anode electrocatalyst structure/composition (e.g., Pt-Ru) to enhance the reaction rate, adding oxygen in the fuel (O<sub>2</sub> bleeding), using cyclic operation, and increasing the operating temperature. It was found that adding a second component to Pt prevented the formation of strongly adsorbed CO by accelerating its oxidation kinetic at lower potentials. To date, the preferred anode material for the electrochemical oxidation of CH<sub>3</sub>OH is an optimized Pt-Ru binary electrocatalyst [73]. The presence of Ru results in the oxidation of CO via the formation of adsorbed hydroxide ions at low potential and the lowering of the oxidation potential of CO [72]. The bi-functional mechanism for CH<sub>3</sub>OH electro-oxidation on Pt-Ru is described in *Appendix B*. Binary metal-oxide Pt catalysts, which are poor electrical conductors, were also studied to promote the electrochemical oxidation of CH<sub>3</sub>OH [74]. It was reported that Pt-WO<sub>3</sub> electrodes are more active and resistant to poisoning than Pt or Pt-Ru alloy catalysts [75]. In this work, Pt and Pt-Ru supported and unsupported catalysts will be employed.

## Methanol crossover

Methanol is fully miscible, i.e., a highly soluble molecule which readily mix with water. Nafion<sup>®</sup> membranes are permeable to CH<sub>3</sub>OH. In DMFCs, water and CH<sub>3</sub>OH molecules are transferred through the membrane by diffusion due to the driving force of concentration gradients between the anode and the cathode. They are also transferred through the PEM by electro-osmotic drag, as induced by the movement of protons, and by hydraulic pressure gradients which is usually small compared to the two other crossover mechanisms. In a flowing-electrolyte DMFC, diffusion is replaced by convection-diffusion [76]. Water diffusion can be neglected in a well-humidified membrane. However, CH<sub>3</sub>OH diffusion cannot be neglected because a CH<sub>3</sub>OH concentration gradient develops between the anode and the cathode. The diffusive flux and electro-osmotic drag of CH<sub>3</sub>OH are both directed from the anode to the cathode. While anodic gaseous CO<sub>2</sub> results from the electro-oxidation of CH<sub>3</sub>OH, cathodic gaseous CO<sub>2</sub> is usually attributed to the combustion of the crossed-over CH<sub>3</sub>OH with O<sub>2</sub>. However, it was shown that anodic permeation CO<sub>2</sub> to the cathode by diffusion and convection due to electro-osmosis also occurs in DMFC, and is not negligible [77]. The anodic CO<sub>2</sub> permeation was determined to be 20% of the total cathodic flux in a DMFC at room temperature.

Methanol crossover from the anode to the cathode results not only in fuel waste, but also reduces the voltage and Faradaic efficiency of DMFCs [78, 79]. This crossover phenomenon lowers the DMFC performance at higher fuel concentrations [80]. For this reason, there is an optimum CH<sub>3</sub>OH concentration to use at specific DMFC operating conditions [81]. With Nafion<sup>®</sup>, the crossover typically decreases with decreasing operating temperatures and concentrations, increasing cathodic pressure, increasing membrane thickness and equivalent weight, as well as increasing current density.

Typical measures to minimize CH<sub>3</sub>OH crossover and its effects include the optimization of the proton-conducting membrane structure and composition, the use of oxygen reduction electrocatalysts insensitive to CH<sub>3</sub>OH at the cathode, and the improvement of electrochemical oxidation catalyst utilization and optimization of the cell operating conditions. Modifying the CH<sub>3</sub>OH membrane permeability without decreasing its ionic and/or electrical conductivity is not a simple process [79]. High

temperature (120-200°C) acid-doped polybenzimidazole (PBI) membranes have high conductivities [82] and improve DMFC cell performance by decreasing CH<sub>3</sub>OH crossover [83].

### 1.3.2.5 Indirect methanol fuel cell

The indirect methanol fuel cell (IMFC), also referred to as the reformed methanol fuel cell (RMFC), is the combination of a H<sub>2</sub> PEMFC with an upstream catalytic CH<sub>3</sub>OH SR. This approach has the benefits of both the high electrochemical activity of H<sub>2</sub>, as well as the convenience of liquid CH<sub>3</sub>OH storage and distribution. However, as mentioned earlier, the SR product stream needs to be purified before H<sub>2</sub> can be fed to the PEMFC. Any remaining un-recoverable H<sub>2</sub> is combusted with air. As the IMFC system typically operates at higher temperatures than the DMFC, heat losses have to be properly managed. Due to the energetic inefficiencies associated with the catalytic CH<sub>3</sub>OH SR, the IMFC tends to be larger, heavier, and have longer start-up times than the DMFC [84]. For this reason, most research is directed towards the DMFC instead of the more complex IMFC system.

Feeding liquid CH<sub>3</sub>OH directly to the anode of a DMFC eliminates the need for a fuel processor, but, as discussed earlier, the full potential of the DMFC is hindered by the slow CH<sub>3</sub>OH electro-oxidation kinetics, and CH<sub>3</sub>OH crossover. To reduce the effect of crossover, the operation of DMFCs is limited to low CH<sub>3</sub>OH concentrations, which renders their performance more suitable for low power density applications. As the H<sub>2</sub> PEMFC can attain higher power densities than the DMFC, the DMFC's low power density would require improvements to be competitive with the IMFC. The IMFC process could become a more interesting option if a low temperature CH<sub>3</sub>OH fuel reforming process could be developed.

The drive cycle dynamic response and efficiency of an IMFC's CH<sub>3</sub>OH SR has been investigated [85, 86]. A study from the Los Alamos National Laboratory compared the trade-offs of using a PEMFC, DMFC or an IMFC for portable power applications [87]. Ishihara *et al.* compared the energy of an IMFC with that of a DMFC and determined that, at a current density of 600 mA/cm<sup>2</sup>, the DMFC needed to operate at a minimum voltage of 0.5 V to have a greater energy efficiency than the IMFC [88]. Brown compared seven fuels, including CH<sub>3</sub>OH, gasoline and H<sub>2</sub>, as possible H<sub>2</sub> sources for PEMFC for use in fuel cell

vehicles (FCVs) [89]. Lattner *et al.* compared CH<sub>3</sub>OH based fuel processors using commercial catalysts for PEMFC systems [90]. A high-level efficiency and economic comparison of some H<sub>2</sub> production methods is provided in *Appendix C*.

### 1.3.3 Proton exchange membrane electrolysis

The principle of electrolysis has been known since the early 19<sup>th</sup> century. It consists in the separation of chemically-bonded elements and substances by the passage of an electric current. The electrochemical decomposition of water is the most practical electrolytic process for the production of pure H<sub>2</sub> and O<sub>2</sub>. Existing H<sub>2</sub> electrolytic production methods include alkaline electrolysis, PEM electrolysis, ceramic oxide electrolysis, and photoelectrolysis. PEM water electrolysis was developed over the last decades [91]. It is an acidic process which possesses many benefits over traditional alkaline electrolysis: it results in higher energy efficiencies and power densities, and it is a simple system that can operate at low temperature and high pressure [92, 93]. It has been used in the industrial gas markets for H<sub>2</sub> production, in the military and aerospace markets for O<sub>2</sub> production, and is now close to entering new emerging energy markets, such as H<sub>2</sub> vehicle refuelling [94]. It represents an attractive technology for portable applications due to its compactness and its ability to effectively produce pure H<sub>2</sub> on demand.

#### 1.3.3.1 Proton exchange membrane water electrolysis

PEM water electrolyzers are the reverse of H<sub>2</sub> PEMFCs. Water is split into oxygen and protons at the anode. The protons travel through the proton conducting membrane and combine with electrons at the cathode to form H<sub>2</sub> via the hydrogen evolution reaction (HER). The water electrolysis electrochemical reactions are as follows:

Anodic half-cell reaction:



Cathodic half-cell reaction:



Overall reaction:



Water electrolysis is an endothermic reaction with a positive Gibbs free energy, which results in a negative standard equilibrium cell voltage of -1.23 V. It is a power sink which requires electrical energy input to extract H<sub>2</sub> from water. The amount of potential/current applied controls the electrocatalytic reaction rate as per Faraday's law. Commercial PEM water electrolyzers operate between 60-80°C. Although there exists significant opportunities for the development of H<sub>2</sub>O electrolysis systems, they remain economically limited by the high overall cost required to split H<sub>2</sub>O. While the H<sub>2</sub>O electrolyser operating costs may be more affordable where electricity prices are low, the cost of electricity greatly fluctuates with geographical location. When combined with renewable sources, PEM H<sub>2</sub>O electrolysis becomes a possible pathway to zero pollution fuelling [95]. To render the electrochemical generation of H<sub>2</sub> as economic as the production of hydrocarbon fuels, significant research advancements are needed to reduce the high energetic cost of H<sub>2</sub>O splitting, increase its operating efficiency, and reduce its capital cost.

The core structure of PEM water electrolyzers is similar to that of H<sub>2</sub> PEMFC and they are subject to similar overpotential losses. Fortunately, some of the challenges encountered in PEMFCs, such as cooling and water management, do not apply to PEM electrolyzers as there is a constant contact with H<sub>2</sub>O. The anode, where the electro-oxidation of water to oxygen occurs, has a high activation overpotential and represents the largest portion of the PEM water electrolyser losses. Like in the case of the PEMFC, various PEM water electrolysis research approaches are taken to address the concerns related to catalytic activity, electronic conductivity and stability. Non-noble metal catalysts corrode and Pt forms a conducting oxide film when in contact with the acidic Nafion<sup>®</sup> membranes. Pt has a low

overpotential at low current densities, but its resistance must be reduced at high current densities. The performance of the membrane and electrocatalysts is crucial to maintain high electrolyser efficiencies at high current densities. Since the development of dimensionally-stable anodes (DSA), the anode of PEM electrolysers usually comprises noble metal oxides (Ir, Ru) combined with oxides of non-noble metal (Sn, Ti) as electrocatalysts. These anodes usually possess large active surface areas. However, it was reported that there may be a poor contact between the catalyst layer and the PEM electrolyte because of high open porosity, and that the thin-film electrocatalyst layer technique, also used in PEMFCs, may be a preferred option [96]. Fujishima *et al.* photo-electrochemically produced H<sub>2</sub> using n-type semiconductor TiO<sub>2</sub> at the electrolyser anode [97]. Composite membranes based on Nafion<sup>®</sup> and TiO<sub>2</sub> or Nafion<sup>®</sup> and SiO<sub>2</sub> were also developed to improve the membrane conductivity for high temperature PEM electrolysis [98, 99]. Some PEM water electrolysers are commercially available. Hydrogenics Corporation's HyLYZER<sup>™</sup> consists of 7 PEM cells which can generate up to 1 Nm<sup>3</sup>/h of 99.99% H<sub>2</sub> at a stack efficiency of 4.9 kWh/Nm<sup>3</sup> and ambient temperature (5 to 35°C) [100]. Its maximum power consumption is 7.2 kW, when all equipment is included. The H-Tec EL 30 electrolyser has a maximum H<sub>2</sub> production rate between 0.3 m<sup>3</sup>/h (13 cells) and 3.6 m<sup>3</sup>/h (144 cells) at ambient temperatures ranging from 4 to 50 °C [101]. Their rated power range is from 1.8 to 20 kW, but no information is given about the EL 30 bar electrolysers efficiencies. It is not clear if these commercial electrolysers operate at lower currents to attain greater efficiencies. While reduction in the electrical energy required for the electrolysis may be obtained by reducing the overpotential losses, it is not possible to operate the electrolysis system at voltage more positive than the H<sub>2</sub>O electrolysis reversible cell voltage at standard conditions. Further energy cost reductions might be achieved through depolarized electrolysis methods as described below.

### **1.3.3.2 Depolarized proton exchange membrane water electrolysis**

Increasing the electrolysis efficiency and reducing the reversible cell voltage can be accomplished by substituting the O<sub>2</sub> evolution reaction (Eq. 1.16) with another anodic reaction taking place at a lower potential than that of O<sub>2</sub> evolution. This technique, called anodic depolarization, consists of depolarizing the H<sub>2</sub>O electrolysis anodic electro-oxidation reaction by oxidizing a fuel, which forms oxidized species along with H<sup>+</sup> ions and electrons [102]. The electro-oxidation of the chosen depolarization fuel must have more favourable thermodynamics than the O<sub>2</sub> evolution reaction, i.e., a smaller reversible standard

cell voltage,  $E^\circ$ . In addition,  $E^\circ$  and the operating electrolyser cell voltage in normal operation,  $U_{elec, cell}^\circ$  would both be further reduced, if the chosen anodic electro-oxidation involved the transfer of more than two electrons. Therefore, depolarized electrolysis may result in reduced energy consumption, hence cost reductions, over conventional water electrolysis. Depolarization fuels studied in the past include coal [103], glucose ( $C_6H_{12}O_6$ ) [104], sulphur dioxide ( $SO_2$ ) [105, 106], methanol ( $CH_3OH$ ) [107, 108], and ferrous ions ( $Fe^{2+}$ ) [109]. Only the case of methanol depolarization is discussed here.

### Methanol depolarized PEM electrolysis

Methanol is a particularly attractive water electrolysis depolarizer for the generation of  $H_2$ . The DMR or  $CH_3OH$  PEM electrolyser is analogous to a DMFC as the anodic reaction is the electrochemical oxidation of  $CH_3OH$  in both cases. Consequently, most issues taking place at the electrodes during  $CH_3OH$  depolarized water PEM electrolysis are encountered at the DMFC anode. The electrochemical reactions are as follows:

Anode half-cell reaction:



Cathode half-cell reaction:



Overall reaction:



The overall reaction for  $CH_3OH$  catalytic reforming process (Eq. 1.10) is the same as for the electrochemical  $CH_3OH$  reforming process (Eq. 1.26). The standard reversible cell voltage required to

drive the CH<sub>3</sub>OH depolarized PEM electrolysis (Eq. 1.26), is much less (minimum 0.016 V) than for water PEM electrolysis (minimum of 1.23 V). Like in the PEM water electrolysis case, the amount of electrical energy required mainly depends on the anodic activation overvoltage. This is because the H<sub>2</sub> evolution reaction is very rapid, and the CH<sub>3</sub>OH oxidation is rate limiting. The electrolyzer electrode where the electro-oxidation of CH<sub>3</sub>OH occurs causes most of the overpotential in this electrochemical system. As in the case of the DMFC anode, the anodic activation overvoltage of the CH<sub>3</sub>OH depolarized water electrolyser results from the poor alcohol electro-oxidation kinetics of the complex reaction mechanism involving adsorbed intermediates. In CH<sub>3</sub>OH electrolysis, CH<sub>3</sub>OH crossing over to the cathode will not be oxidized, but will result in a fuel loss, which should be minimized. It appears that no scientific papers were published on the CH<sub>3</sub>OH depolarization of PEM water electrolysis in acidic media until 2007. However, there was some prior activity on this topic in the patent literature. Some electrochemical reforming membrane reactors for the electrochemical reforming of CH<sub>3</sub>OH investigated are described in Table 1.2.

Table 1.2: Relevant methanol electrochemical reforming membrane reactors.

| Reactant               |                   | Product                          | Solid Electrolyte            | Porous Electrode                    | Temperature | Reference |
|------------------------|-------------------|----------------------------------|------------------------------|-------------------------------------|-------------|-----------|
| Electron Donor         | Electron Acceptor |                                  |                              |                                     | [°C]        |           |
| CH <sub>3</sub> OH (l) | H <sup>+</sup>    | H <sub>2</sub> , CO <sub>2</sub> | Aqueous NaOH or KOH [6-12 M] | Pt/C                                | 23-60       | [110]     |
| CH <sub>3</sub> OH     | H <sup>+</sup>    | H <sub>2</sub> , CO <sub>2</sub> | -                            | -                                   | -           | [111]     |
| CH <sub>3</sub> OH (g) | H <sup>+</sup>    | H <sub>2</sub> , CO <sub>2</sub> | Nafion <sup>®</sup>          | Pt, Pt/Ru anode, Pd-Ag foil cathode | 50-100      | [112]     |

The electrochemical production of H<sub>2</sub> from CH<sub>3</sub>OH in the presence of a base, such as NaOH or KOH, was carried out at Pt/C electrodes [110]. The inclusion of a base permitted the generation of H<sub>2</sub> without emission of greenhouse gas and without the need to separate H<sub>2</sub> from the other gaseous products. However, the resulting carbonate ion by-product needs to be dealt with. An electrochemical reformer and fuel cell system was developed to reform organic fuels into H<sub>2</sub> and CO<sub>2</sub> [111]. It uses electricity

and/or thermal energy to supply the necessary reaction energy to convert the fuel to  $H_2$ . There is no mention of the operating temperature, and of the type of electrode or electrolyte used. An electrochemical process to reform a mixture of  $CH_3OH$  and water at temperatures between 50 and  $100^\circ C$  was proposed [112]. As shown in Fig. 1.2, the methanol electrochemical reforming membrane cell operating in the gas phase resembles a DMFC.

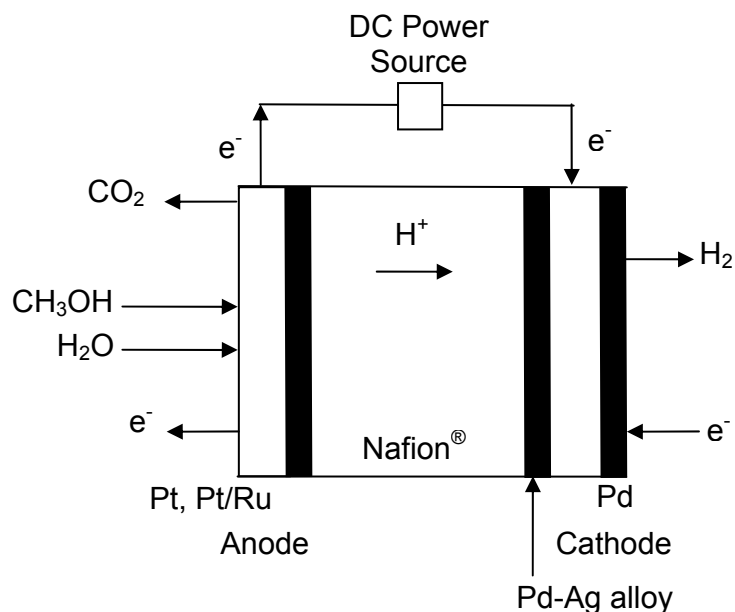


Figure 1.2: Schematic diagram of a methanol electrochemical reforming membrane cell (Modified from patent DE 197007384 [112]).

A polymeric proton-conducting membrane and Pt or Pt/Ru catalysts were used. A Pd-Ag foil was hot-pressed on the cathode polymer side of the membrane to prevent water and  $CH_3OH$  crossover. A cell voltage between 300 and 500 mV was sufficient to generate  $H_2$ .

There are three Japanese patents pertaining to the electrolysis of alcohols: two of them relate to the electrolysis of alcohols in conjunction with a PEMFC, which is similar to an entirely electrochemical version of an IMFC [113, 114], and the other describes an organic electrolytic synthesis in the presence of a base [115]. The first American patent on the generation of  $H_2$  production by electrolysis of organic solutions dates from 2001 [116]. It was later followed by a patent on the electrolytic production of  $H_2$  in

the presence of a base [110]. Narayanan *et al.* last re-amended their original 2001 US patent in 2006 [117].

An example of a PEM CH<sub>3</sub>OH electrolyser in transient operation is shown in Fig. 1.3. The anode chamber is continuously fed with un-acidified CH<sub>3</sub>OH aqueous solution, which is recycled using a pump. The cathode chamber is purged with argon. The anode catalyst is Pt or Pt-Ru/C and, typically, the cathode catalyst is Pt/C, but the performance of a Pt-WC/C catalyst has also been investigated. The electrolysis of CH<sub>3</sub>OH resulted in an absolute voltage of 0.4 V to 1 V at the same current density depending on the cathode catalyst used [7, 118]. The current collectors and diffusion layers were made of carbon paper. As Nafion<sup>®</sup> 117 was the electrolyte, the CH<sub>3</sub>OH electrolyser was operational at temperatures up to 120°C.

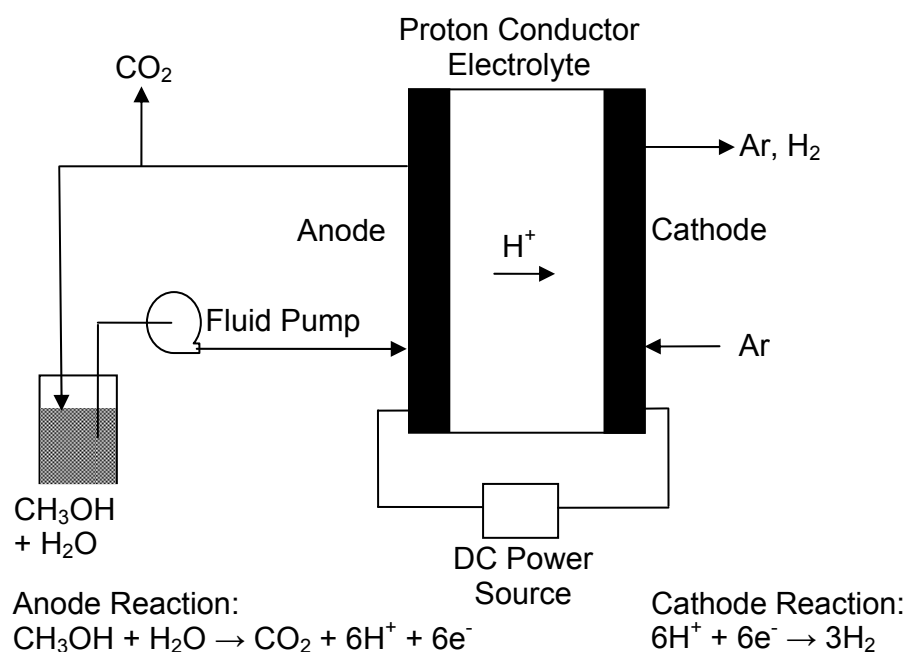


Figure 1.3: Schematic diagram of an alcohol electrolyser (Modified from Hu *et al.* [7] with permission from Elsevier).

At low current densities, the voltage reached a steady-state approximately an hour after electrolysis started. At higher current densities, a rapid drop in negative voltage was observed. The drop happened because the applied current could not be sustained with only the oxidation of CH<sub>3</sub>OH and drifted to a

value where  $O_2$  evolution could also occur [118]. Hu *et al.* reported that the electrolysis voltage did not depend on the  $CH_3OH$  concentration at concentrations greater than 2 M and at temperatures below  $60^\circ C$  [7]. The explanation given was that at  $CH_3OH$  concentrations exceeding 2 M,  $CH_3OH$  crossover to the cathode resulted in a mixed potential which reduced the activity of the electrocatalyst. Shen *et al.* reported that the electrolyser voltage was about the same at  $CH_3OH$  concentrations between 2 and 4 M, and that the voltage was greater outside this concentration range [11]. Again, this was explained by mass transport limitations at low  $CH_3OH$  concentrations, and by  $CH_3OH$  crossover to the cathode, which supposedly created a mixed potential, at higher  $CH_3OH$  concentrations.

Yet, Take *et al.* confirmed that the voltage did not depend on the  $CH_3OH$  concentration, but only on the current density [118]. However, the limiting current density at which the voltage rapidly decreases varies with  $CH_3OH$  concentration. It attained a maximum value when the methanol-water ratio was equal to 1 [118]. In the same study, it was also established that the oxidation of crossover methanol in the cathode compartment does not occur. The  $CO_2$  in the cathode exhaust is not produced at the cathode because no  $O_2$  is supplied at the cathode. In fact, any cathodic  $CO_2$  permeated from the anode in a similar manner as to that previously discussed for DMFCs. The  $CO_2$  permeation rate diminished with increasing anode  $CH_3OH$  concentrations and increased with increasing current densities. Also like for the DMFC, the water and  $CH_3OH$  would also cross over to the cathode at permeation rate which decreased as the current density increased. Take *et al.* verified that the  $CH_3OH$  crossover rate escalated with increasing  $CH_3OH$  concentrations, while the water permeation rate was not affected [118]. The water and  $CH_3OH$  at the cathode can be separated from the  $H_2$  produced by molecular sieves. However, since it was found that the permeated water-methanol solution concentration was almost the same as the solution supplied to the anode, the permeated solution was recycled back to the anode. The flow rate of the  $H_2$  produced increased proportionally to the current density and came close to the theoretical  $H_2$  production rates [118]. The electrolysis voltage became more positive with increasing temperature as the mass transport and the kinetics are more favourable and the activation and concentration polarizations are reduced. For example, the voltage at  $80^\circ C$  was reduced by half compared to the voltage at  $20^\circ C$  [11].

## Applications of depolarized methanol PEM electrolysis

The CH<sub>3</sub>OH PEM electrolysis H<sub>2</sub> production has advantages over conventional CH<sub>3</sub>OH steam reforming as it may result in reduced energy consumption. First, the single-reactor CH<sub>3</sub>OH electrochemical reforming process has the potential to be conducted in the liquid phase at a lower operating temperature and at higher overall system efficiencies compared to a conventional high-temperature multi-reactor SR system. Secondly, since the production of H<sub>2</sub> from depolarized electrolysis should result in lower power consumption than H<sub>2</sub> production from water electrolysis. Therefore, its large scale commercialization might not be as significantly energetically restrained as that of water electrolysis. Narayanan *et al.* estimated that H<sub>2</sub> production from the electrolysis of CH<sub>3</sub>OH would cost about 50% less compared to that of water, even when the cost of CH<sub>3</sub>OH is taken into account [117]. An efficiency, energy and economical comparison of various H<sub>2</sub> production methods is presented in *Appendix C*.

Although CO<sub>2</sub> is produced whether CH<sub>3</sub>OH is thermally or electrochemically reformed, it is more localized and concentrated in the electrochemical reforming process than in the chemical reforming process. For this reason, electrochemical reforming may result in more effective CO<sub>2</sub> capture for sequestration and in lower CO<sub>2</sub> disposal cost in many applications. The cost of CO<sub>2</sub> capture and disposal for various coal-fired generation technologies ranges from 1.1 to 4.9 cent/kWhe and 0.6 to 6.7 cent/kWhe, respectively [119]. In some cases, it may be desirable to combine the CO<sub>2</sub> produced with the H<sub>2</sub> generated at high temperature and pressure to obtain methane, as per the Sabatier reaction:



Alternatively, other depolarized water PEM electrolysis processes using compounds which do not produce CO<sub>2</sub>, such as the ferrous ions (Fe<sup>2+</sup>), could be evaluated for H<sub>2</sub> production.

Methanol electrolysis could effectively be used as part of systems cogenerating chemical energy and electrical energy, which may include a H<sub>2</sub> PEMFC, as long as the amount of energy required to generate H<sub>2</sub> does not exceed the energy resulting from using the H<sub>2</sub> produced. A system composed of an efficient electrochemical CH<sub>3</sub>OH electrolyser providing H<sub>2</sub> to a PEMFC could be more advantageous than a

DMFC because it might be possible to use higher concentration fuel mixtures in a system combining a CH<sub>3</sub>OH electrolyser with a H<sub>2</sub> PEMFC than in a DMFC. Without taking the storage and infrastructure issues into account, the overall performance of a system composed of a CH<sub>3</sub>OH electrolyser and a H<sub>2</sub> PEMFC is expected to be less than a system in which gaseous H<sub>2</sub> tanks directly feeds a PEMFC, but greater than that for a IMFC. The system combining the principles of H<sub>2</sub> pumping and autothermal reforming referred to as electrochemical autothermal reforming (EATR) [120, 121] could be modified to include an electrochemical reformer in order to simultaneously produce H<sub>2</sub> and useful heat. The resulting higher temperatures would render the thermodynamic and kinetic aspects of the electrochemical CH<sub>3</sub>OH oxidation more attractive.

The prompt start-up and shut-down time of PEM electrolysers and their ease of scalability render them appropriate to generate pure H<sub>2</sub> for portable and stationary applications. Having similar scalability limits as PEMFCs, multiple PEM electrolysis cells can be put into stacks. Currently, some of the largest PEM electrolysis stacks commercially available have a rated power of 14 to 20 kW [101]. The combination of an electrochemical alcohol reformer and a fuel cell system could potentially be made compact, light and simple enough for use in small low power applications, which usually do not justify the cost of a separate fuel processor. It could be developed into a portable fuelling option for high and low power output PEMFCs, as well as for micro-fuel cell power sources, and used to power laptops, cell phones and other small portable devices. Under thermodynamically favourable operating conditions, the direct electrochemical CH<sub>3</sub>OH reformer could be used as a stand-alone H<sub>2</sub> generation unit for H<sub>2</sub> combustion engine vehicles or FCVs requiring fuelling at local electrochemical stations. Distributed H<sub>2</sub> production at a H<sub>2</sub> refuelling station constitutes an attractive option to supply H<sub>2</sub> to FC vehicles, allowing the supply to match the demand as more H<sub>2</sub> vehicles are driven. As it has clear advantages over high temperature SR, the low temperature CH<sub>3</sub>OH electrochemical reformer may meet the DOE on-board fuel processing targets for automotive applications. It may represent an attractive on-board H<sub>2</sub> storage alternative to high pressure H<sub>2</sub> storage in FCVs, as the H<sub>2</sub> could be produced at the PEMFC's demand. A CH<sub>3</sub>OH fuel processor and fuel cell system could be optimized to give maximum power density as an off-grid generator system for back-up and remote power applications for the telecommunications, utilities and military sectors. As it requires less energy to electrolyse CH<sub>3</sub>OH than water, and depending on the source of CH<sub>3</sub>OH, CH<sub>3</sub>OH electrolysis may be a preferred option to produce H<sub>2</sub> during off-peak hours so

electricity can be provided by H<sub>2</sub> PEMFCs during high grid loads or blackouts. Based on these examples, it can be seen that an efficient CH<sub>3</sub>OH electrochemical reformer has a significant market potential.

### **1.3.4 Electrochemical promotion of heterogeneous catalysis**

Catalysts typically consist of an active metal or metal oxide phase, a support, and one or more promoters. The promoters affect the properties of the supports or of the active phase [122]. The metal-support interactions between catalytic nanoparticles and their support is a well studied heterogeneous catalysis concept. A special type of heterogeneous catalysis, in which the catalyst properties are modified by the application of an electric field, was discovered in 1980, and was reported as a new electrochemically induced catalytic effect in 1988 [123, 124]. It was found that solid electrolytes or active catalyst supports may be used to modify the catalytic properties of metals and metal oxides. Applying polarization controls the surface work function by creating promoters and modifying their quantity on the catalyst surface, which in turns affects the adsorption, amount, and surface diffusion properties of reaction intermediates [125].

The multidisciplinary principles of this phenomenon combine features of heterogeneous catalysis and electrocatalysis as the working electrode is used to catalyze a chemical reaction and an electrochemical reaction simultaneously. Two types of processes occur at electrodes: Faradaic and non-Faradaic [126]. In Faradaic processes, the electrons transferred across the metal-solution interface cause an oxidation or reduction reaction to occur at a rate proportional to the current. Under unfavourable thermodynamic and kinetic conditions, charge transfer reactions may not occur. However, non-Faradaic processes like adsorption or desorption may occur. The structure of the electrode-solution interface may then be altered by changing the current or potential, or the solution composition [126]. In the electrical promotion of catalysis, most of the yield is obtained through the heterogeneous catalytic reaction, and is non-Faradaic. The superimposed electrochemical reaction used to control and improve the catalytic properties of the electrode surface result in the Faradaic part of the yield [125].

### 1.3.4.1 Theory

The non-Faradaic electrochemical modification of catalytic activity (NEMCA), also called the electrochemical promotion of catalysis (EPOC), is ascribed to the modification of the catalytic activity of metals on ionic conducting substrates. It is obtained upon variation of the potential on the working electrode, which is used as an electrode and as a catalyst for the heterogeneous catalytic reaction under study [127]. The application of a current ( $\pm 5-50 \text{ mA/cm}^2$ ) or voltage ( $\pm 1-2 \text{ V}$ ) between the catalyst working electrode WE and a counter electrode CE, also deposited on the solid electrolyte, polarizes the catalyst and changes its work function. This property correlates the electrocatalytic and catalytic reaction rates with the properties of the catalyst involved. The catalyst work function is directly proportional to the catalyst electrode overpotential, which is the extent of polarization at the metal catalyst [128]. The work function,  $\Phi$  (eV), is the minimum energy required to remove an electron from the interior of a solid to a position just outside. It is defined as:

$$-\Phi = \mu_e - e\Psi \quad (1.28)$$

where  $\mu_e$  is the electrochemical potential of an electron at infinite separation from a metal, i.e., at the Fermi level (KJ),  $e$  is the charge of an electron (C), and  $\Psi$  is the outer potential (V), which represents the work required to bring a charge from infinity to a point just outside a charged phase and is equal to zero if there is no net charge on the metal surface. It was determined that the changes in the catalyst surface work function closely follow the changes in potential difference under galvanostatic or potentiostatic transients for a large number of systems [129]. The change in the work function of the catalyst surface,  $\Delta\Phi_w$  (eV), can be controlled in situ by an applied potential,  $U_{WR}$  (V) as per the following relationship:

$$e\Delta U_{WR} = \Delta\Phi_w \quad (1.29)$$

where  $\Delta U_{WR}$  (V) is the overpotential between the working electrode catalyst and a reference electrode [130]. The catalyst potential is represented by  $U_{WR}$  and is defined as the catalyst WE potential with

respect to a reference electrode (RE) while  $U_{WC}$  represents the cell voltage and is defined as the catalyst-working electrode potential with respect to a counter CE.

Vayenas *et al.* qualitatively explained this effect by the scheme represented in Fig. 1.4 for a metal-electrode deposited on an oxide-conducting and proton-conducting solid electrolyte. For a system where the solid electrolyte mobile ions are  $H^+$ , the reaction at the electrode surface would be:



The migration of ions to or from the ion conducting solid electrolyte from or to the catalyst surface is called backspillover, in analogy with the term spillover, which refers to migration from a metal to a support [129]. This backspillover of ions forms neutral spillover dipoles which establish an effective chemical double layer over the entire catalyst surface which is exposed to the reactants. Hence, EPOC is catalysis in the presence of an electrochemically controllable double layer at the catalyst/reactant interface [18]. The charged double layers are accumulations of charges on a surface, which are either formed due to diffusion effects, reactions between electrons in the electrodes and ions in the electrolyte, or results from applied currents or voltages. The classical metal-solid electrolyte double layer and the effective double layer resulting from the current or potential controlled ion migration are indicated in Fig. 1.4 (a) and (b) for an oxide conductor and for a proton conductor, respectively.

All EPOC studies to date have been carried out using gaseous reactants. The electrocatalytic reaction takes place at the catalyst-solid electrolyte-gas three phase boundaries (TPB) while the catalytic reaction with no charge transfer takes place at the metal-gas interface [128]. Here, the term catalytic refers to a chemical reaction and the term electrocatalytic refers to an electrochemical reaction which includes charge transfer. The electrochemically-induced protonic current supplies promoting  $H^+$  ions to the catalytically-active metal-gas interface but do not directly affect the catalytic reaction rate [131]. It is the effective chemical double layer which interacts electrochemically with covalent chemisorbed reactants and reaction intermediates by lowering their energy and modifying their binding strength.

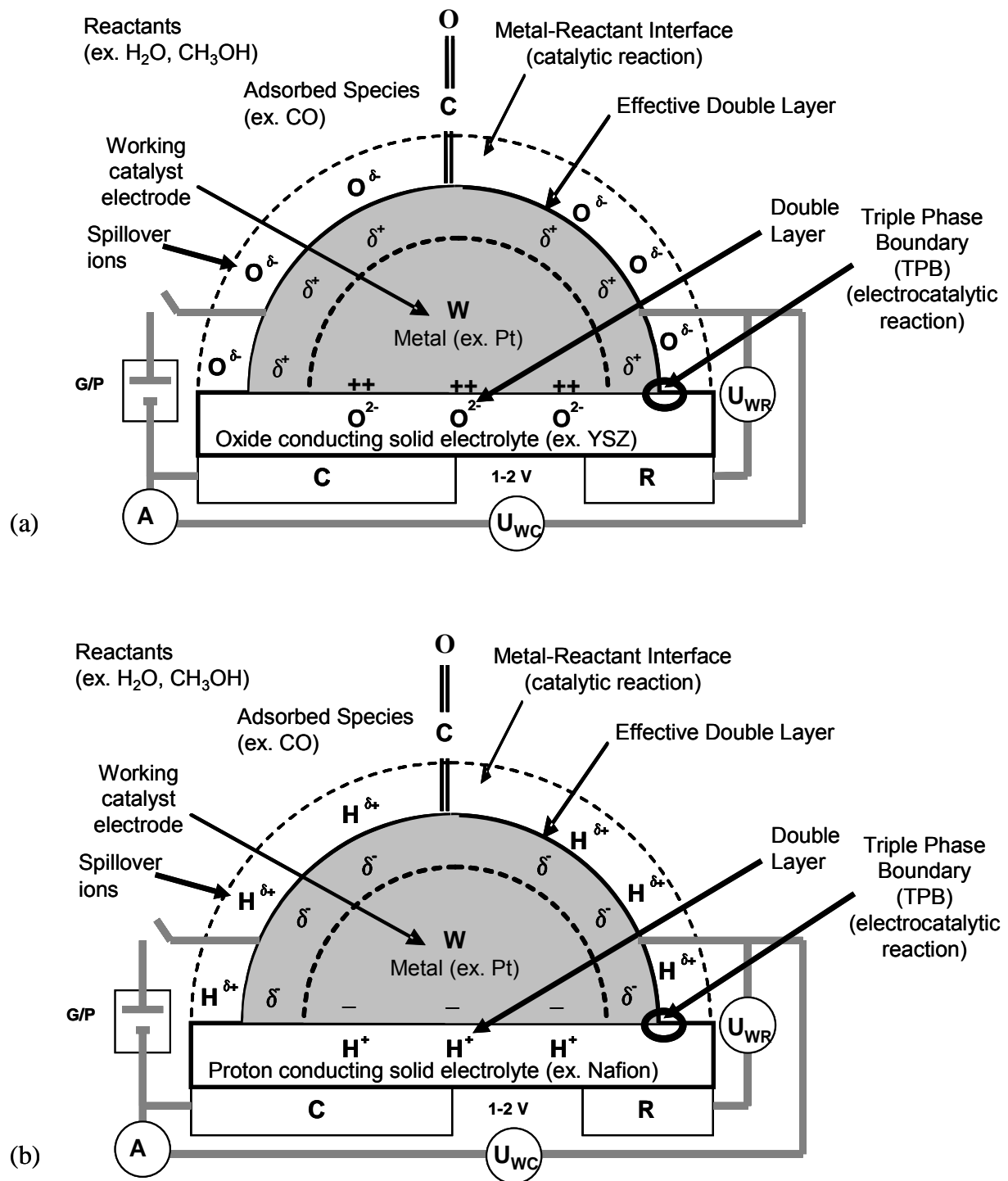


Figure 1.4: Schematic diagram of a metal catalyst-electrode deposited on (a) an oxide-conducting solid electrolyte, and (b) a proton-conducting solid electrolyte (Modified from Vayenas *et al.* [18] with permission from Springer).

A change in the strength of the chemisorptive bonds can be induced upon polarization of the metal-solid electrolyte interface. The corresponding decrease in overpotential can enhance the catalytic reaction rate at the gas-metal interface in a very pronounced and reversible manner [18]. This induced exponential catalytic rate non-Faradaic enhancement is analogous to the Buttlar-Erdey-Gruz-Volmer (BEV) equation for high electrode overpotentials, highlighting the resemblances between electrochemistry and heterogeneous catalysis [127].

Some of the rules of EPOC are listed in *Appendix D*. Supplying  $H^+$  with a proton conductor (positive voltage application) is equivalent to removing  $O^{2-}$  with an oxide conductor (negative voltage application) as they both decrease the catalyst work function. An electron donor is defined as a compound that gives electrons during its oxidation, while an electron acceptor is defined a compound which accepts electrons during its reduction. As per the first rule of EPOC, adding electropositive promoters, such as  $H^+$ , weaken the chemisorptive bond of electron donor (negatively charged) adsorbates and strengthen the chemisorptive bond of electron acceptor (positively charged) adsorbates. This first principle has been experimentally confirmed and rationalized on an electrostatic and quantum mechanic basis as per Eq. 1.26. The binding energy or enthalpy of adsorption,  $\Delta H_j$ , is related linearly to the change in work function,  $\Delta\Phi_w$ , as follows:

$$\Delta|\Delta H_j| \approx \alpha_{H_j} \cdot \Delta\Phi_w \quad (1.31)$$

where  $\alpha_{H_j}$  is a parameter which is positive for electropositive (electron donor) adsorbates, and negative for electronegative (electron acceptor) adsorbates [18]. Although not a general fundamental equation, Vayenas *et al.* are not aware of any exceptions to the physical meaning which Eq. 1.26 conveys, i.e., that  $\Delta H_j$ , and hence, the coverage of an electron acceptor/donor adsorbate decreases/increases with increasing work function, and thus, decreasing Fermi level,  $E_F$ . More details on this can be found in *Appendix D*. It is known that  $CH_3OH$  will be an electron donor (O bonding) on surfaces with high work functions and will be an electron acceptor (CO bonding) on surfaces with low work functions [18]. It was also established that the strength of the CO metal bond was reduced by the addition of electronegative modifiers (e.g.,  $O^{2-}$ ) as it decreases the activation energy of CO desorption [18].

Varying the potential and work function of the catalyst affects the heterogeneous reaction catalytic rate and the activation energy of the reaction. There is a linear variation in the activation energy,  $E_A$  (kJ/mol):

$$E_A = E_A^o + \alpha_H \cdot \Delta\Phi_w \quad (1.32)$$

where  $\alpha_H$  is the enthalpic parameter, a constant, which is usually negative for electrophobic reactions (donor reactions), and  $E_A^o$  is the open circuit activation energy value (eV). Hence, the activation energy of an electron acceptor (positively charged) decreases linearly with decreasing work function [18]. Reactions for which the activation energy decreases with increases in the catalyst work function are termed electrophobic, and when the opposite occurs, the reactions are termed electrophilic.

#### 1.3.4.2 Parameters

The magnitude of EPOC is described by some important parameters: the rate enhancement factor, the rate enhancement ratio, and the promotion index. Normally, the electrochemical reaction rate,  $r_e$  (mol/s), is given by Faraday's law:

$$r_e = \frac{i \cdot A_{Geom}}{nF} = \frac{I}{nF}, \quad (1.33)$$

where  $i$  is the applied current density ( $A/cm^2$ ),  $A$  is the active geometric surface area ( $cm^2$ ),  $I$  is the applied current (A),  $n$  is the number of electrons transferred, and  $F$  is the Faraday constant (C/mol). Following the established EPOC terminology conventions, in the non-Faradaic enhancement case, this equation becomes:

$$\Delta r = \Lambda \cdot \frac{I}{nF}, \quad (1.34)$$

where  $\Delta r$  is the non-Faradaic electrochemically induced change in the catalytic reaction rate (mol/s) [132], and is equal to the difference between the promoted catalytic reaction rate,  $r$  and the unpromoted catalytic reaction rate,  $r_0$ . Here,  $n$  represents the number of electrons promoting the electrochemical reaction at the triple phase boundary. Hence, it is equal to 2 in the case of an oxide conductor and equal to 1 in the case of a proton conductor, as per the following electrochemical reactions:



Rearranging equation 1.29, and knowing that for a proton conductor  $n = 1$ , the dimensionless rate enhancement factor, also referred to as the Faradaic efficiency,  $\Lambda$ , is defined as:

$$\Lambda = \frac{nF\Delta r}{I}, \quad (1.37)$$

For catalytic oxidation reactions,  $\Lambda > 1$  implies an electrophobic (donor reaction) behaviour for which the rate increases with increasing catalyst work function, while  $\Lambda < -1$  implies an electrophilic (acceptor reaction) behaviour for which the rate increases with decreasing catalyst work function. For a pure electrocatalyst,  $\Lambda$  is always unity [18].

There are four types of global catalytic reaction  $r$  vs.  $\Phi$  behaviours over the entire experimentally accessible  $\Phi$  range: purely electrophobic ( $\partial r/\partial\Phi > 0$ ), purely electrophilic ( $\partial r/\partial\Phi < 0$ ), volcano type ( $\partial r/\partial\Phi > 0$  followed by  $\partial r/\partial\Phi < 0$ ), and inverted volcano-type ( $\partial r/\partial\Phi < 0$  followed by  $\partial r/\partial\Phi > 0$ ). All purely electrophobic reactions are positive order in electron donor and zero or negative order in electron acceptor. All purely electrophilic reactions are positive order in electron acceptor and zero or negative order in electron donor. Volcano-type reactions are always in positive order for one reactant and purely negative order in the other. Inverted volcano-type reactions are positive in both reactants [18]. The EPOC global behaviour rules are listed in *Appendix D*.

A reaction is electrochemically promoted when  $|A| > 1$  and it is electrocatalyzed when  $|A| \leq 1$ . The exchange current of the metal-solid electrolyte interface,  $I_0$  (A), can be extracted from Tafel plots and used to estimate the expected magnitude of the absolute value of the rate enhancement factor as per:

$$|\Lambda| \approx \frac{nFr_0}{I_0} \quad (1.38)$$

where  $r_0$  is the open circuit unpromoted catalytic reaction rate (mol/s) [133]. This expression defines the applicability limit of EPOC: when the absolute value of the rate enhancement factor well exceeds unity, EP is observed and the kinetic efficiency is enhanced. For a reaction to be electrochemically-promoted, the open circuit catalytic rate,  $r_0$ , must be greater than  $I_0/nF$  and the catalytic reaction must be faster than the electrocatalytic one [127]. The fact that  $I_0$  increases exponentially with temperature in conjunction with the fact that  $\Lambda$  is inversely proportional to  $I_0$  explains why most EPOC studies are restricted to lower temperatures [134]. The dimensionless rate enhancement ratio,  $\rho$ , is defined as the ratio of the promoted to unpromoted catalytic rate:

$$\rho = \frac{r}{r_0}, \quad (1.39)$$

where  $r$  is the electrochemically promoted catalytic reaction rate (mol/s).

#### 1.3.4.3 Electrochemical promotion of methanol oxidation

The EPOC effect has been demonstrated for a variety of catalytic reactions, including the  $\text{CH}_3\text{OH}$  oxidation on oxide-conducting ceramics. Table 1.3 summarizes the rate enhancement factors and rate enhancement ratios reported for  $\text{CH}_3\text{OH}$  oxidation EPOC studies. All studies listed in Table 1.3 were conducted using gaseous reactants. The most pronounced rate enhancements were typically observed at the lowest temperature examined [128]. It is important to remark that most EPOC catalytic oxidation reaction studies were conducted via oxygen pumping using solid oxide ion conductors.

Table 1.3: Vapour phase methanol oxidation EPOC studies with oxide conductors.

| Reactant<br>Electron<br>Donor | Electron<br>Acceptor | Product                                   | Electrolyte | Catalyst | T<br>[°C]   | $\Lambda$         | $\rho$ | Global<br>Behaviour<br>(GB)* | Ref.  |
|-------------------------------|----------------------|-------------------------------------------|-------------|----------|-------------|-------------------|--------|------------------------------|-------|
| CH <sub>3</sub> OH            | O <sub>2</sub>       | H <sub>2</sub> CO,<br>CO <sub>2</sub>     | YSZ         | Pt       | 250-<br>320 | 100               | -      | PE-                          | [136] |
| CH <sub>3</sub> OH            | O <sub>2</sub>       | H <sub>2</sub> CO,<br>CO <sub>2</sub>     | YSZ         | Ag       | 500         | -95.5             | 2      | PE+                          | [137] |
| CH <sub>3</sub> OH            | O <sub>2</sub>       | H <sub>2</sub> CO,<br>CO <sub>2</sub>     | YSZ         | Pt       | 250-<br>500 | -                 | 2.5    | -                            | [132] |
| CH <sub>3</sub> OH            | O <sub>2</sub>       | H <sub>2</sub> CO,<br>CO, CH <sub>4</sub> | YSZ         | Ag       | 550-<br>750 | -25               | 6      | PE+                          | [138] |
| CH <sub>3</sub> OH            | O <sub>2</sub>       | H <sub>2</sub> CO,<br>CO <sub>2</sub>     | YSZ         | Pt       | 300-<br>500 | 1x10 <sup>4</sup> | 4, 15  | IV                           | [18]  |
| CH <sub>3</sub> OH            | O <sub>2</sub>       | H <sub>2</sub> CO,<br>CO <sub>2</sub>     | YSZ         | Pt       | 400-<br>500 | -10               | 3      | PE+                          | [18]  |

\*GB: global behaviour, PE-: purely electrophobic, PE+: purely electrophilic, IV: inverted volcano, V: volcano. Note: Although EPOC was mostly studied on oxidation reactions, it has been applied to many hydrogenation and dehydrogenation reactions.

#### 1.3.4.4 Electrochemical promotion using protonic electrolytes

The use of the electrochemical promotion of heterogeneous catalyst surfaces has been investigated on various reactions with proton-conducting electrolytes. The EPOC effect was observed at high temperatures using proton-conducting ceramics, and also at low temperatures using Nafion<sup>®</sup> as a protonic polymer electrolyte. Table 1.4 summarizes the findings of EPOC studies using protonic conductors.

All studies in Table 1.4 were conducted using gaseous reactants. No EPOC studies on the electrochemical reforming of CH<sub>3</sub>OH using proton-conducting electrolytes have been reported in the literature. By comparing the rate enhancement factors and rate enhancement ratios reported in Table 1.3 and Table 1.4, it can be generally concluded that, to date, it seems that there are less reactions having a high rate enhancement factor with proton conductors than with solid oxide ion conductors. Table 1.5 lists the few EPOC studies which have been carried out in alkaline aqueous media.

Table 1.4: Vapour/gaseous phase EPOC studies using protonic conducting electrolytes.

| Reactant                        |                               | Product                                                             | Electrolyte                                                                           | Catalyst | T<br>[°C]       | $\Lambda$          | $\rho$   | GB* | Ref.              |
|---------------------------------|-------------------------------|---------------------------------------------------------------------|---------------------------------------------------------------------------------------|----------|-----------------|--------------------|----------|-----|-------------------|
| Electron Donor                  | Electron Acceptor             |                                                                     |                                                                                       |          |                 |                    |          |     |                   |
| C <sub>2</sub> H <sub>4</sub>   | O <sub>2</sub>                | CO <sub>2</sub>                                                     | Ba <sub>3</sub> Ca <sub>1.18</sub><br>Nb <sub>1.82</sub> O <sub>9-a</sub>             | Pt       | 250<br>-<br>350 | -1340              | 4        | PE+ | [139]             |
| H <sub>2</sub>                  | N <sub>2</sub>                | NH <sub>3</sub>                                                     | CaIn <sub>0.1</sub> Zr <sub>0.9</sub><br>O <sub>3-a</sub>                             | Fe       | 440             | 6                  | $\infty$ | PE+ | [13,<br>140]      |
| C <sub>2</sub> H <sub>4</sub>   | O <sub>2</sub>                | CO <sub>2</sub>                                                     | CaIn <sub>0.1</sub> Zr <sub>0.9</sub><br>O <sub>3-a</sub>                             | Pt       | 385<br>-<br>470 | -3x10 <sup>4</sup> | 5        | PE+ | [18]              |
| NH <sub>3</sub>                 |                               | N <sub>2</sub> , H <sub>2</sub>                                     | CaIn <sub>0.1</sub> Zr <sub>0.9</sub><br>O <sub>3-a</sub>                             | Fe       | 530<br>-<br>600 | 150                | 3.6      | PE- | [18]              |
| H <sub>2</sub>                  | N <sub>2</sub>                | NH <sub>3</sub>                                                     | SrCe <sub>0.95</sub> Yb <sub>0.05</sub><br>O <sub>3-a</sub><br>(SCY)                  | Pd       | 550<br>-<br>750 | ~ 1-2              | -        | -   | [141]             |
| CH <sub>4</sub>                 | -                             | C <sub>2</sub> H <sub>6</sub> ,<br>C <sub>2</sub> H <sub>4</sub>    | SCY                                                                                   | Ag       | 750             | -                  | 8        | PE- | [18, 128]         |
| H <sub>2</sub>                  | CO <sub>2</sub>               | H <sub>2</sub> O,<br>CO                                             | SrZr <sub>0.90</sub> Y <sub>0.10</sub><br>O <sub>3-a</sub>                            | Cu       | 550<br>-<br>750 | < 1                | -        | -   | [142]             |
| C <sub>2</sub> H <sub>4</sub>   | O <sub>2</sub>                | CO <sub>2</sub>                                                     | Gd-doped<br>BaPrO <sub>3</sub><br>(BPG) and<br>Y-doped<br>BaZrO <sub>3</sub><br>(BZY) | Pt       | 400<br>-<br>600 | ~ 1                | 1.3      | PE+ | [143]             |
| H <sub>2</sub>                  | C <sub>2</sub> H <sub>4</sub> | C <sub>2</sub> H <sub>6</sub>                                       | CsHSO <sub>4</sub>                                                                    | Ni       | 150<br>-<br>170 | 300                | 2        | PE+ | [18, 144]         |
| C <sub>2</sub> H <sub>4</sub>   | O <sub>2</sub>                | CO <sub>2</sub>                                                     | Nafion <sup>®</sup><br>117                                                            | Pd/C     | -               | 6                  | 1230     | -   | [145]             |
| H <sub>2</sub>                  | O <sub>2</sub>                | H <sub>2</sub> O                                                    | Nafion <sup>®</sup><br>117                                                            | Pt       | 25              | 20                 | 6        | V   | [18, 146]         |
| 1-C <sub>4</sub> H <sub>8</sub> | -                             | C <sub>4</sub> H <sub>10</sub> ,<br>2-C <sub>4</sub> H <sub>8</sub> | Nafion <sup>®</sup><br>117                                                            | Pd       | 70              | -28                | 40       | PE+ | [18, 147,<br>148] |

\*GB: global behaviour, PE-: purely electrophobic, PE+: purely electrophilic, IV: inverted volcano, V: volcano.

Table 1.5: EPOC studies in aqueous systems.

| Electron Donor | Reactant       |                   | Product          | Electrolyte           | Catalyst | T [°C] | $\Lambda$ | $\rho$ | GB* | Ref.  |
|----------------|----------------|-------------------|------------------|-----------------------|----------|--------|-----------|--------|-----|-------|
|                | Electron Donor | Electron Acceptor |                  |                       |          |        |           |        |     |       |
| H <sub>2</sub> |                | O <sub>2</sub>    | H <sub>2</sub> O | 0.1 M KOH             | Pt       | 25-50  | 20        | 6      | PE- | [18]  |
| H <sub>2</sub> |                | O <sub>2</sub>    | H <sub>2</sub> O | 0.01-0.5 M KOH / LiOH | Pt       | -      | 7.2       | -      | PE- | [135] |

\*GB: global behaviour, PE-: purely electrophobic, PE+: purely electrophilic, IV: inverted volcano, V: volcano.

It is important to note that, for H<sub>2</sub> oxidation using Pt as a catalyst in aqueous media, non-Faradaic rate changes were only obtained in alkaline aqueous solutions. Only Faradaic changes were observed in acidic solutions as the catalytic rates were much higher than those measured in the alkaline aqueous solutions [135]. This was attributed to the larger electrocatalytic activity measured in acidic aqueous solutions. In aqueous media, the concentration of electrolyte affects the magnitude of EPOC [135]. It was also reported that the low temperatures of aqueous electrochemistry may have limited the number of reactions where non-Faradaic enhancements may have been obtained, as the open circuit catalytic activity,  $r_o$ , must be measurable to obtain an EPOC effect [132]. No EPOC studies on the electrochemical reforming of liquid CH<sub>3</sub>OH in acidic media have been reported in the literature.

#### 1.3.4.5 Applications for the electrochemical promotion of catalysis

Currently, there is a strong industrial interest in developing commercial EP applications with most efforts focused on lab-scale EPOC research. The acceptance and understanding of EPOC is still limited [125]. The use of EPOC in commercial applications depends on technical and economical aspects: material cost minimization, ease of electrical connection, efficient and compact reactor design [149]. Although applied research efforts are needed to develop industrial EPOC applications, fundamental research is still required to improve commercialization possibilities. For example, low temperature EPOC with aqueous electrolytes has a tremendous potential for many applications but has not been thoroughly studied in the literature. Suitable chemical processes for industrial EPOC applications are slow processes, which can be activated through the use of EPOC, and processes requiring low investments,

as it would reduce the market entry risks for the first commercial EPOC application. EPOC has been recognized as a mean to facilitate the commercialization of fuel cells [125, 149]. H<sub>2</sub> production and utilization was identified as a potential niche market where EP could find an open field opportunity for industrialization [149].

A compact and flexible EPOC reactor design will minimize heat losses, maximize efficiencies, and facilitate the practical utilization of EPOC in industrial settings. To reduce application implementation costs, an efficient EPOC reactor design based on established technologies which have simple electrical connections, and use inexpensive materials would need to be developed. Durability, lifetime, and scalability are other aspects which will need to be addressed to develop a practical EPOC reactor [149]. To date, most EPOC reactor designs have been based on heterogeneous catalysis reactors and fuel cells. Simplified EPOC reactors may be obtained through single chamber reactors and bipolar systems. Scalable liquid electrolyte EPOC reactors designs may be obtained based on scrubber technologies [127].

Most EPOC studies have been conducted in electrochemical membrane reactors (EMR) using solid electrolytes [150]. Two main types of catalytic-electrocatalytic reactors have been used: double-chamber reactors and single-chamber reactors. In the double-chamber reactor, the catalyst WE is exposed to the catalytic reactants and products, while the CE and RE are exposed to a reference gas in a separate compartment. This design possesses an accurate RE but is difficult to scale-up. The EPOC effect has also been studied in continuous flow single-chamber reactors containing three electrodes (WE, CE and RE), which are all exposed to the reactants and products in order to promote the rate of catalytic reactions. The CE and RE are both made of catalytically-inert materials so that no catalytic reaction occurs on their surface. The single-chamber reactor requires the use of a quasi-reference electrode, which may cause inaccuracies in measuring the catalyst potential, but is easier to scale-up.

It was shown that direct electrical contact to the catalyst electrode is not necessary to induce EP in a bipolar monolithic reactor [151]. EPOC can be induced without external potential application by using the potential difference developed between the catalyst WE and a catalytically-inert CE. This single pellet wireless configuration was used to demonstrate the effect of EPOC on the oxidation of CH<sub>3</sub>OH at

250°C with an oxide ion-conducting electrolyte [132]. A change in the CH<sub>3</sub>OH consumption rate was obtained by using the RE as a CE, and short-circuiting it with the WE. A potential difference developed between the CE and the WE, and resulted in a current flow between two electrodes [136]. The wireless EPOC for the oxidation of CH<sub>3</sub>OH in a mixed-reactant single-chamber alkaline fuel cell has been patented [152, 153]. The design of EPOC reactors based on this wireless EPOC concept may lead to simpler designs.

Yiokari *et al.* evaluated the effect of EPOC on the synthesis of NH<sub>3</sub> via the Haber-Bosh process, using proton conducting ceramic catalyst pellets [154]. This study was the first to use an industrial catalyst, to be carried out at high pressure (50 atm), and it was the first attempt at an EPOC scale-up. St-Pierre *et al.* employed EPOC in an electrolytic cell to purify a reformat stream H<sub>2</sub> feeding a PEMFC [155]. EPOC can efficiently be carried out on thin sputtered metal films which possess stability and endurance. Balomenou *et al.* conducted development work on a high temperature membrane electrochemically promoted reactor (MEPR), which is a hybrid between a monolithic honeycomb catalytic reactor and a planar flat or ribbed plate SOFC for the EPOC of the catalytic oxidation of hydrocarbons [156, 157]. In this scalable reactor design, two external electrical connections are needed to dynamically control the applied current/potential required to induce EPOC to the catalyst film plates and only one gas stream containing all reactants and products was used.

The benefits of EPOC were also applied to the treatment of automotive exhaust in catalytic converters to reduce CO emissions [158-161]. EPOC studies were extended to non-redox systems and Salazar *et al.* electrochemically enhanced the isomerization reaction of olefin by over a thousand fold in a PEMFC using Pd/C catalyst at the cathode [162]. Sapountzi *et al.* have shown that EPOC could efficiently purify the H<sub>2</sub> stream from the CO formed during the H<sub>2</sub> production from hydrocarbons or alcohols, by electrochemically enhancing the water-gas-shift reaction or by improving the selectivity towards CO oxidation [163]. EPOC was used in the development of a catalytic system for the after-treatment of diesel exhaust. The unit combustion, tested on a commercial diesel engine, was found to be satisfactory for soot but not for NO<sub>x</sub>, and its Faradaic efficiency was estimated to be 66 [149]. More recently, a method using EPOC in a tubular reactor at temperatures from 150 to 600°C was developed to improve the reaction kinetics of biofuel production from biomass [164].

### 1.3.5 Electrochemical promotion of electrocatalysis

Recently, a new engineering solution analogous to EPOC was developed to enhance electrochemical reactions instead of chemical ones. Hence we refer to it as the electrochemical promotion of electrocatalysis (EPOE). This approach, involving a third electrode, is referred to in the literature as triode operation. Balomenou *et al.* have shown that it can enhance the power output of fuel cells [19, 165]. A dual-chamber triode fuel cell arrangement was designed to study the application of EP in fuel cells using gaseous reactants. It comprised three electrodes: the fuel cell anode WE, the fuel cell cathode CE, and an auxiliary CE. The fuel cell anode WE was also the auxiliary WE. The electrodes were in electrolytic contact and form two electrical circuits as shown on Fig. 1.5. The fuel cell circuit consisted of the fuel cell anode WE and the fuel cell cathode CE. The auxiliary circuit consisted of the auxiliary WE, which was also the anode WE of the fuel cell circuit, and the auxiliary CE.

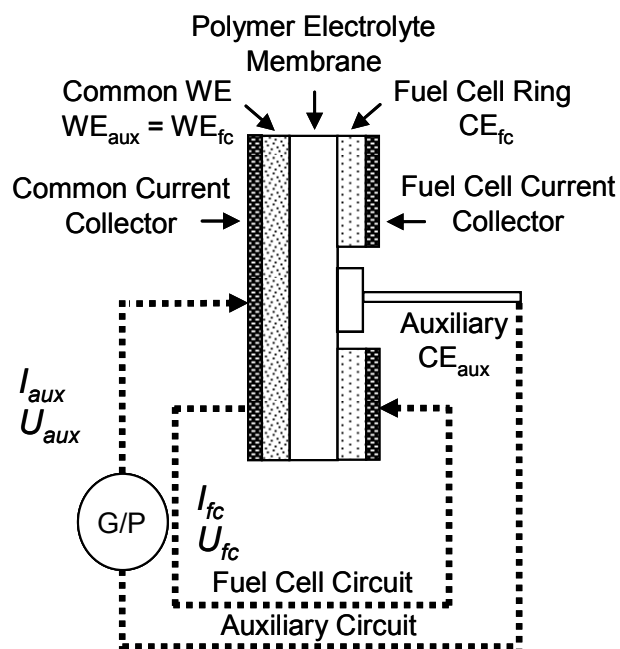


Figure 1.5: Schematic diagram of a triode fuel cell electrical circuit.

The net Faradaic fuel-consuming current,  $I_{far}$ , is the difference between the fuel cell current,  $I_{fc}$ , and the auxiliary circuit current,  $I_{aux}$  [14]. When the auxiliary circuit is not used, the fuel cell operates normally. When a current is supplied in the auxiliary circuit, the fuel cell anode and cathode are forced to operate under a controlled potential [14, 166]. It was reported that the triode improvement resulted from using

the auxiliary circuit potential to keep the fuel cell anode (or cathode) at a corrosion-type potential inaccessible during normal fuel cell operation.

At the new WE operating potential resulting from triode operation, the surface coverage of the promoting species and the adsorption of adsorbates is modified. In some cases, the reaction at the WE surface is enhanced in triode operation as it is no longer limited by the supply and adsorption of the fuel. Triode operation is advantageous under high anodic and cathodic overpotentials [14]. The application of EPOE resulted in gains similar to that obtained in classical EPOC experiments. The only results available in the literature pertain to triode operation of an SOFC and a PEMFC using gaseous reactants. Balamenou *et al.* obtained power enhancement ratios up 8, i.e., efficiencies over 700% for a SOFC operating on dry H<sub>2</sub>, ethane or methane at 400-750°C in triode operation [14]. In this case, the low anodic potential created in triode operation decreased the surface coverage of O<sup>2-</sup>, increased the adsorption of H<sub>2</sub>, CO, or CH<sub>4</sub>, and enhanced the rate of the anodic oxidation. In SOFC's, the solid electrolyte ohmic resistance contribution typically exceeds that of the electrodes, and as the use of the auxiliary circuit diminishes the ohmic losses between the fuel cell anode and cathode, triode operation can enhance the fuel cell performance [14]. Triode operation was also shown to improve the efficiency of a PEMFC running on pure H<sub>2</sub> or H<sub>2</sub> poisoned with CO, using an anode feed of humidified H<sub>2</sub>/CO/He or H<sub>2</sub>/CO<sub>2</sub>/CO/N<sub>2</sub> at 30°C [165]. Using 4 mg/cm<sup>2</sup> of a Pt-Ru/C anode catalyst and 4 mg/cm<sup>2</sup> of a Pt black cathode catalyst, the application of a current of 0.09-0.5 mA to the auxiliary circuit enhanced the power enhancement ratio of a CO-poisoned PEMFC by a factor of 5 [165]. The enhancement was attributed to the electrolytic H<sup>+</sup> supplied by the auxiliary circuit, which decreased the coverage of adsorbed CO and enhanced the membrane conductivity due to additional H<sup>+</sup> pumping. Vayenas *et al.* [166] developed the triode gas phase fuel cell and battery concept as it is an advantageous alternative method to conduct electrochemical reactions in non-liquid systems. It appears that no EPOE studies have been carried out using liquid phase reactants and that triode operation has not been evaluated in the electrolysis mode to date. In this thesis, the EPOE effect was evaluated in triode and tetrode operation using liquid phase reactants and in the electrolysis mode for the first time.

## Chapter 2: Electrocatalysis Baseline Study

### 2.1 Synopsis

As discussed in *Section 1.3.3*, all published work relevant to CH<sub>3</sub>OH electrolysis or DMR was carried out in a recycle operation mode or in a flowing mode, in which an un-acidified CH<sub>3</sub>OH aqueous solution is pumped to the anode, while the H<sub>2</sub> produced at the cathode was continuously purged with Ar. In this *Chapter*, the electrochemical production of H<sub>2</sub> from the PEM electrolysis of liquid CH<sub>3</sub>OH in acidic aqueous media was investigated in the static mode (non-flowing, stirred). Experiments were carried out in a two-compartment glass cell with a MEA composed of a Nafion<sup>®</sup> 117 membrane and gas diffusion electrodes (GDE). This glass cell configuration allowed for the separate measurements of the anodic and cathodic potential contributions to the overall cell voltage. Most tests were conducted with 0.5 M H<sub>2</sub>SO<sub>4</sub> in the anode and cathode compartment, but the effect of having a dry N<sub>2</sub> purge cathode was also investigated. Methanol electrolysis was studied at concentrations ranging from 0 to 16 M, where 0 M corresponds to water electrolysis. The characteristics of the CH<sub>3</sub>OH - H<sub>2</sub>O electrolysis were described and compared to that of the H<sub>2</sub>O electrolysis under the same acidic conditions. The influence of supported (carbon) and unsupported (black) conventional fuel cell catalysts (Pt and Pt-Ru), operating temperatures (23, 50 and 75°C) and operating modes (dry and wet cathode) on the electrocatalytic reforming of CH<sub>3</sub>OH and water were evaluated. A theoretical thermodynamic analysis of the system was conducted and the limiting current densities, kinetic parameters, including the Tafel slopes and current exchange density, and apparent activation energies were determined. Additional electrochemical sample calculations can be found in *Appendix H*. The work presented in this section was published and is reprinted from the *International Journal of H<sub>2</sub> Energy*, 35, C. R. Cloutier, and D. P. Wilkinson, "Electrolytic Production of Hydrogen from Aqueous Acidic Methanol Solutions", 3967-3984, Copyright (2010), with permission from Elsevier.

## 2.2 Experimental

### 2.2.1 Materials

Certified electronic grade CH<sub>3</sub>OH, and American Chemical Society (ACS) certified plus H<sub>2</sub>SO<sub>4</sub>, both from Fisher Scientific, were used with deionised (DI) H<sub>2</sub>O having a resistivity of 18 MΩcm to make up the solutions. The H<sub>2</sub>O associated with H<sub>2</sub>SO<sub>4</sub> was taken into account when making the CH<sub>3</sub>OH solutions. Behmann *et al.* [167] stated that the addition of CH<sub>3</sub>OH to H<sub>2</sub>SO<sub>4</sub> and H<sub>2</sub>O mixtures containing less than 18 M H<sub>2</sub>SO<sub>4</sub> had no influence on the dissociation behaviour of H<sub>2</sub>SO<sub>4</sub> in the ternary mixture, and had dissociation behaviour is similar to that of the H<sub>2</sub>SO<sub>4</sub> and H<sub>2</sub>O binary system. Hence the dissociation behaviour of H<sub>2</sub>SO<sub>4</sub> will be the same for all the aqueous acidic CH<sub>3</sub>OH solution concentration used in this study. Ultra high-purity H<sub>2</sub> and N<sub>2</sub> gases from Praxair were used in some tests. Potassium dichromate salt (K<sub>2</sub>Cr<sub>2</sub>O<sub>4</sub>) reagent plus ≥ 99.5 % from Sigma-Aldrich was used for the spectrophotometric studies with a Shimadzu UV Vis spectrophotometer (UV mini 1240). A supporting electrolyte concentration of 0.5 M H<sub>2</sub>SO<sub>4</sub> was used in the anode and cathode cell compartments in most tests, unless otherwise indicated. A volume of 80 ml of solution was used in the anode and cathode cell compartments in most tests, unless otherwise indicated.

Nafion<sup>®</sup> 117 (Ion Power Inc.), was selected as the solid polymer proton exchange membrane. Conditioning was conducted by first boiling the membrane in a solution of 3 wt% H<sub>2</sub>O<sub>2</sub> (certified, Fisher Scientific), for 30 minutes, then boiling it in DI H<sub>2</sub>O for 30 minutes and finally, boiling it in 0.5 M H<sub>2</sub>SO<sub>4</sub> for 30 minutes. It was rinsed with DI between each boiling step and then cut to shape and stored in DI H<sub>2</sub>O until used. Toray<sup>™</sup> carbon paper, TGPH-060, with 20 wt% Teflon<sup>®</sup> (PTFE) wet-proofing from BASF Fuel Cell Inc., was used as the gas diffusion layer (GDL). A micro-porous layer (MPL) consisting of a 1 mg/cm<sup>2</sup> coating composed of carbon black and 20 wt% PTFE was sprayed on top of the cathode GDL surface, to form a double-layer gas diffusion layer. No MPL was used on the anode side.

Conventional CH<sub>3</sub>OH fuel cell noble metal electrocatalysts were employed: 20 wt% high performance (HP) Pt supported on Vulcan XC-72 and 20 wt% HP Pt:Ru alloy (1:1 atomic ration (a/o)) supported on

Vulcan XC-72, both from E-TEK, Pt black (99.9+%, fuel cell grade) and Ru black (99.9%) both from Sigma Aldrich, and Pt:Ru alloy (1:1 a/o) from Alfa Aesar. The anode Pt-Ru catalyst loading was 4 mg/cm<sup>2</sup>, while the cathode Pt loading was only 2 mg/cm<sup>2</sup>, as the cathode half-cell reaction is simple and straightforward compared to the anodic half-cell reaction. The catalyst inks were composed of the supported catalyst powder, 30 wt% of a proton conductive ionomer in solution (Nafion<sup>®</sup>, 5 wt% perfluorosulfonic acid-PTFE copolymer, Alfa Aesar), H<sub>2</sub>O and isopropanol (IPA, 2-propanol certified ACS plus from Fisher Scientific). Catalyst inks were prepared and sprayed with an Accuspray<sup>®</sup> air gun (Model 07HS, ISAAC Series HVLP Spray), on one side of the GDL, forming a gas diffusion electrode (GDE). More details of the ink preparation and spraying procedure are given in *Appendix E*. A planar Pt disk (0.25 mm, 99.99%<sup>+</sup> Pt foil, Goodfellow Cambridge Limited) of a 2.01 cm<sup>2</sup> area was used as an anode catalyst in some experiments for comparison purposes. The current collectors were made from an annealed 0.25 mm thick Nb foil, 99.9% pure from Sigma-Aldrich.

## 2.2.2 Equipment

All experiments were conducted in a dual-chamber borosilicate glass (Pyrex) cell composed of two chambers as shown in Fig. 2.1 and 2.2, which was built by CanSci Glass Products Ltd. Various ports permitted the inclusion of reference electrodes, thermocouples, and gas spargers or bubblers in the anode or cathode compartments. Slight internal bevels were provided in the upper part of the anode and cathode compartments to facilitate the gas exit. The CO<sub>2</sub> gas forming at the anode and H<sub>2</sub> gas forming at the cathode were vented to atmosphere in all experiments.

The MEA holder contained different layers: the membrane electrode assembly, the current collectors, two silicon sealing rings and a PTFE spacer ring, as shown in Fig. 2.1 (b). The MEA holder was machined in polyetherimide (ULTEM 1000) by Core Tools Ltd. and is shown in Fig. 2.1 (c). Its central opening had a circular active geometric area of 2 cm<sup>2</sup>. The silicon rings were made in house using a procedure described in *Appendix E*. A 25 mm diameter membrane sample was sandwiched between the anodic and cathodic 16 mm diameter GDE samples. Two niobium current collectors (25 mm OD, 16 mm ID), having a thin current collecting metal cross through their circular openings were placed on each side of the MEA. Silicone seal rings (25 mm OD, 16 mm ID, 1 mm thickness) made in house were

placed on each side of the current collectors. Finally, a PTFE spacer ring (54273 AMG06, 25 mm OD, 16 mm ID, 1 mm thickness) was placed as the last layer on the cathode side to reduce friction when turning the cap to close the MEA holder.

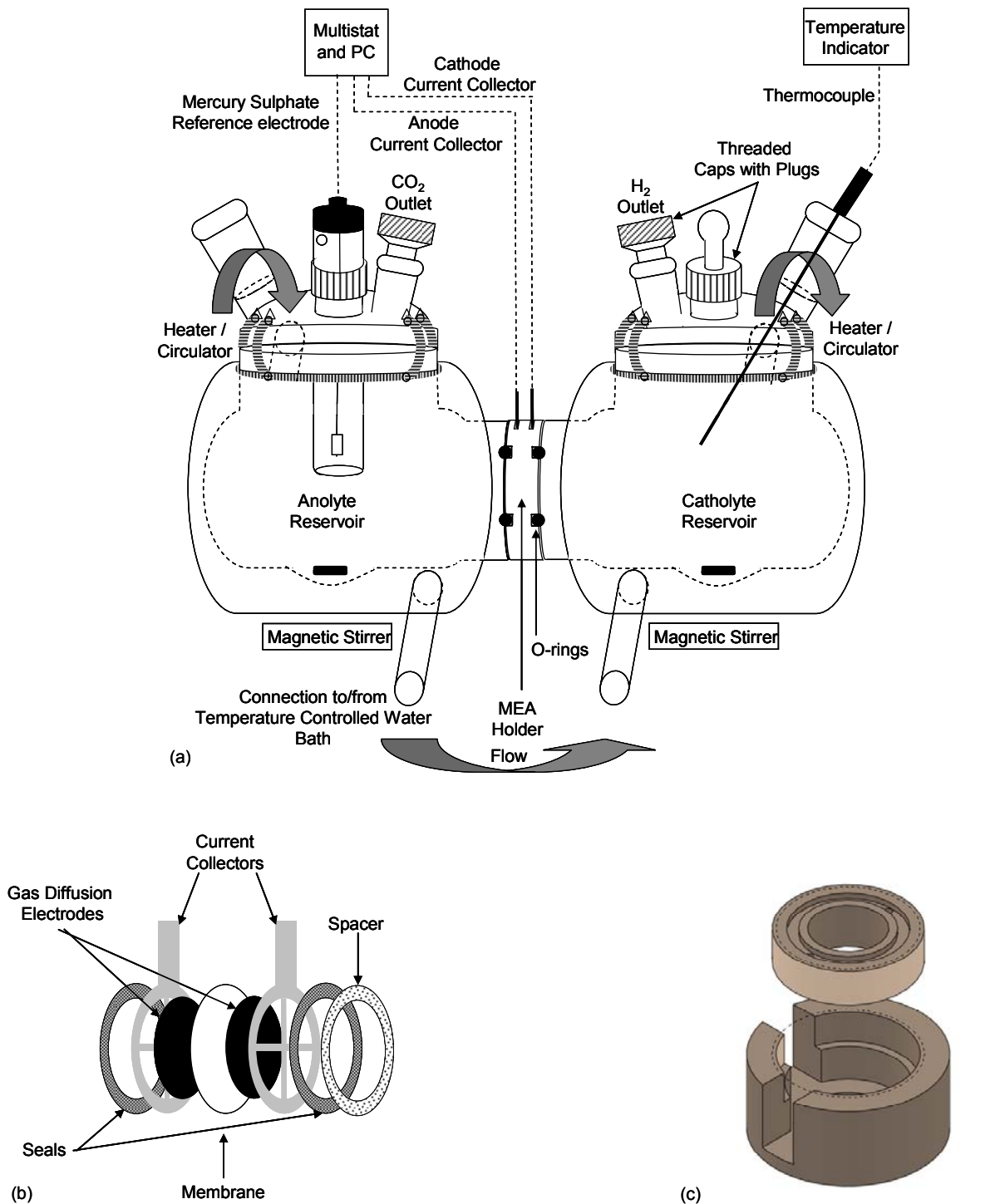


Figure 2.1: Schematic diagram of (a) the electrochemical glass cell, (b) the MEA components (c) the MEA holder.

The glass cell, MEA holder and O-rings were joined and held together using a screw clamping apparatus. It was designed to press the thick flat ends of the glass cell compartments together and ensured alignment of the glass compartments. This permitted the application of a uniformly distributed force to seal the glass cell flanges to the MEA holder O-rings. All experiments carried out at room temperature were conducted in ambient air ( $23^{\circ}\text{C} \pm 2^{\circ}\text{C}$ ). For experiments at  $50$  and  $75^{\circ}\text{C} \pm 1^{\circ}\text{C}$ ,  $\text{H}_2\text{O}$  was circulated within the double wall of the glass cell and the temperature was controlled by a Haake DC-30 immersion circulator. Thermocouples were used to monitor the temperature in each of the glass cell compartments.

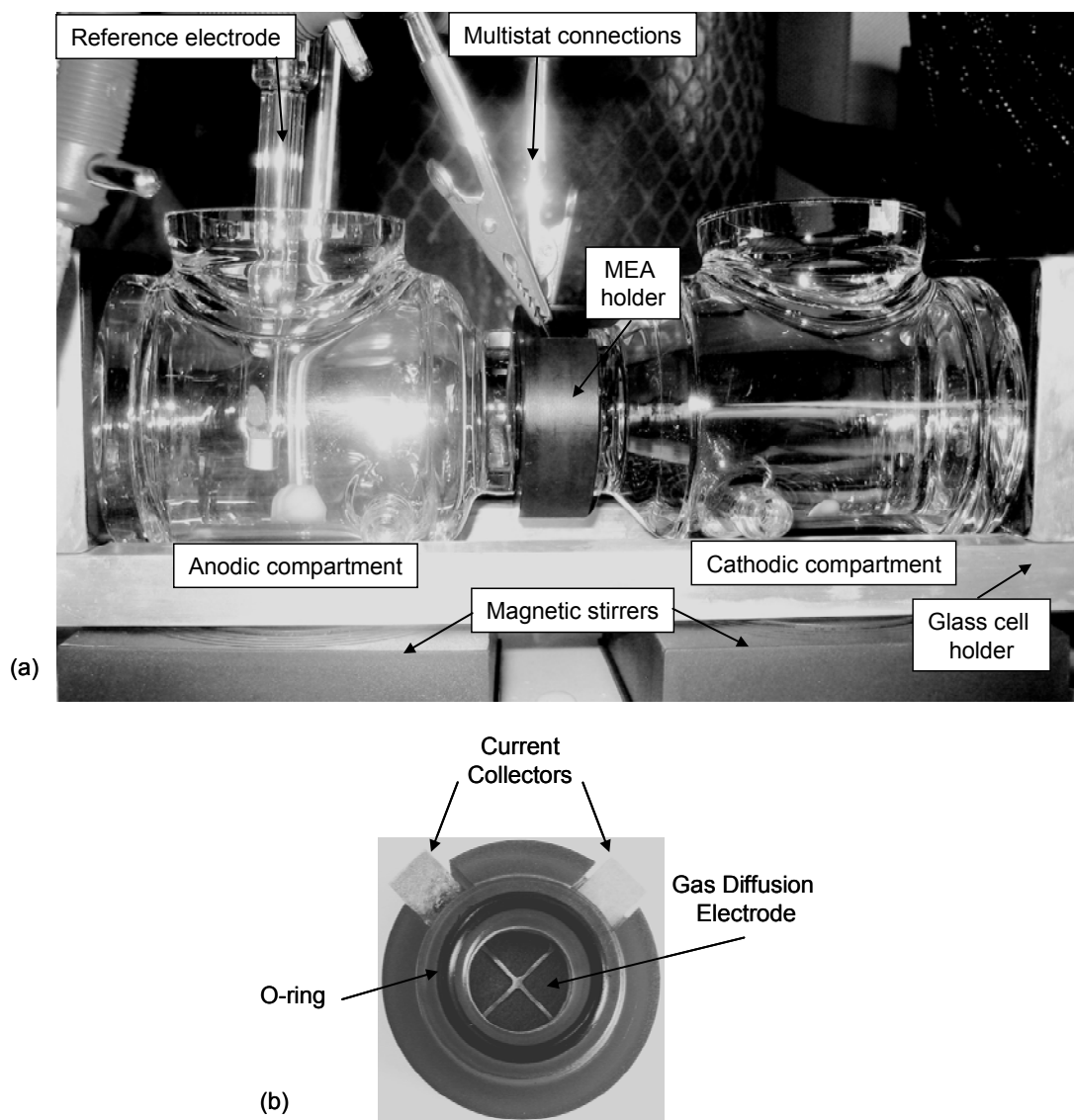


Figure 2.2: Picture of (a) the electrochemical glass cell, (b) the MEA holder.

### 2.2.3 Electrochemical measurements

All electrochemical measurements were carried out at steady-state using a multistat (Solartron Analytical, Model 1470E) connected to a computer, using CoreWare software. A single junction mercury-mercurous sulphate (MSE, Hg/Hg<sub>2</sub>SO<sub>4</sub>, Radiometer Analytical) reference electrode located in the anode compartment was used for all experiments at ambient temperature. At 50 and 75°C, a double junction silver/silver chloride (SSE, Ag/AgCl, Radiometer Analytical) reference electrode was used, with 0.5 M H<sub>2</sub>SO<sub>4</sub> in its outer compartment, as it is more stable than the MSE at higher temperatures. This is because the MSE has an outer porous plug tip while the SSE electrode outer tip is a porous glass frit, which limits the ion migration to increase with temperature. The reference electrode was placed in the anode compartment. All voltages are reported versus the standard hydrogen electrode (SHE). All electrolysis experiments were conducted in the galvanostatic, current-controlled mode. More information on the electrochemical technique used to obtain current/potential transients is given in *Appendix F*. AC impedance measurements were carried out with an impedance/gain phase analyzer (Solartron Analytical, Model 1260A) to obtain the MEA and solution resistance. Measurements were performed with an AC amplitude of 10 mV, in the frequency range of 10<sup>-3</sup> to 10<sup>7</sup> Hz. More details on this electrochemical technique can be found in *Appendix F*. As the measured potential values were affected by the ohmic drop, they were corrected for the current resistance (IR) before kinetic parameter information was extracted. Using this technique, it was confirmed that the MEA resistance increased with increasing CH<sub>3</sub>OH concentration, MEA usage and electrode degradation due to carbon oxidation.

### 2.2.4 Characterization

Cyclic voltammetric techniques were used to determine the true active electrochemical surface area (ECSA) of the catalysts in a conventional three electrode single chamber electrochemical cell, using a platinized Pt counter electrode (CE) (see *Appendix E* for platinization procedure), an Ag/AgCl double junction reference electrode (RE), and various working electrodes (WE). The platinization procedure employed can be found in *Appendix E*. The ECSA of the various Pt catalyst working electrodes (WEs) was estimated from the H<sub>2</sub> adsorption charge on the cyclic voltammograms [168], while that of Pt-Ru catalysts was estimated by the copper under potential deposition (UPD) method [169, 170]. More details

on the CV technique employed can be found in *Appendix F*. The average total Pt area (TPA) and ECSA values obtained by H<sub>2</sub> adsorption or Cu UPD for the different catalysts are summarized in Table 2.1. The values reported represent the average of three tests conducted on three different catalyst samples of the same batch of GDE. The Brunauer, Emmett and Teller (BET) surface area (SA) from the catalyst powder certificate of analysis were provided for comparison purposes only. The BET estimated ECSA exceeded the measured ECSA in all cases. The experimentally determined values were later used in the estimation of kinetic parameters and in Fig. 2.9. For the pure Pt disk, a surface roughness factor of 4 was assumed, giving an ECSA of 8 cm<sup>2</sup>/g Pt. These techniques were also used to confirm that the catalyst electrochemical area decreases with increasing utilization and carbon oxidation of the catalyst support.

Table 2.1: Electrochemical characterization of supported and unsupported catalysts studied.

| Catalyst    | BET SA*<br>[m <sup>2</sup> /g] | Typical BET SA Range<br>[m <sup>2</sup> /g] | Actual Loading<br>[mg/cm <sup>2</sup> ] | Geometric Area<br>[cm <sup>2</sup> ] | Total metal area (TMA) by Different Methods   |                                                   |                                       | Electrochemical Surface Area (ECA) by Different Methods |                                                      |                                          |
|-------------|--------------------------------|---------------------------------------------|-----------------------------------------|--------------------------------------|-----------------------------------------------|---------------------------------------------------|---------------------------------------|---------------------------------------------------------|------------------------------------------------------|------------------------------------------|
|             |                                |                                             |                                         |                                      | Roughness Factor of 4<br>[cm <sup>2</sup> Pt] | H <sub>2</sub> adsorption<br>[cm <sup>2</sup> Pt] | Cu UPD<br>[cm <sup>2</sup> Pt and Ru] | Roughness Factor of 4<br>[cm <sup>2</sup> /g Pt]        | H <sub>2</sub> adsorption<br>[cm <sup>2</sup> /g Pt] | Cu UPD<br>[cm <sup>2</sup> /g Pt and Ru] |
| Pt-Ru/C     | 130                            | 120-140                                     | 4.01                                    | 2.01                                 | -                                             | -                                                 | 562                                   | -                                                       | -                                                    | 140                                      |
| Pt-Ru/C     | 130                            | 120-140                                     | 3.99                                    | 2.01                                 | -                                             | -                                                 | 562                                   | -                                                       | -                                                    | 140                                      |
| Pt/C        | 180                            | 160-200                                     | 2.04                                    | 2.01                                 | -                                             | 3929                                              | -                                     | -                                                       | 1926                                                 | -                                        |
| Pt/C        | 180                            | 160-200                                     | 2.01                                    | 2.01                                 | -                                             | 3746                                              | -                                     | -                                                       | 1863                                                 | -                                        |
| Pt-Ru black | 86.65                          | 80-90                                       | 3.98                                    | 2.01                                 | -                                             | -                                                 | 69                                    | -                                                       | -                                                    | 17                                       |
| Pt black    | 29                             | 25 to 34                                    | 2.06                                    | 2.01                                 | -                                             | 248                                               | -                                     | -                                                       | 120                                                  | -                                        |
| Pt disk     | -                              | -                                           | -                                       | 2.01                                 | 8                                             | -                                                 | -                                     | 8                                                       | -                                                    | -                                        |

\* From catalyst powder vendor certificate of analysis.

## 2.3 Results and Discussion

### 2.3.1 Thermodynamic evaluation of methanol reforming at low temperatures

A theoretical thermodynamic analysis was carried out for a DMR in acidic media and a water PEM electrolyser as a function of temperature. The effect of pressure on the theoretical cell voltage and thermodynamic efficiency was found to be negligible compared to the effect of temperature, and hence is not discussed here. The thermodynamic information for the species involved, including the standard Gibbs free energy of formation ( $\Delta G_f^\circ$ ), the standard enthalpy of formation ( $\Delta H_f^\circ$ ), the standard entropy of formation ( $\Delta S_f^\circ$ ), and the heat capacity ( $C_p^\circ$ ), are available in the literature [171, 172] and are listed in *Appendix G*. These values were used to establish the theoretical cell voltage ( $E_e$ ) and theoretical thermodynamic efficiency ( $\eta_{max}$ ) as a function of temperature (25 to 150°C) assuming a constant pressure (1 atm). Examples of the thermodynamic calculations for the DMR electrochemical reactions in the liquid phase and in the gas phase are provided in *Appendix G*. The standard Gibbs free energy associated with the electrochemical reaction is given by:

$$\Delta G^\circ = \sum_i s_i \Delta G_{i,f}^\circ (\text{products} - \text{reactants}) \quad (2.1)$$

The standard enthalpy of the electrochemical reaction can be calculated by:

$$\Delta H^\circ = \sum_i s_i \Delta H_{i,f}^\circ \quad (2.2)$$

Similarly, assuming that the entropy is independent of pressure, the standard entropy of formation of the electrochemical reaction can be determined by:

$$\Delta S^\circ = \sum_i s_i \Delta S_{i,f}^\circ \quad (2.3)$$

The standard reversible cell voltage can then be calculated by Eq. 1.6. Various Shomate equations of the form

$$C_p = a_o + \sum_{n=1}^N a_n T^{b_n} \quad (2.4)$$

based on empirical data, were used to evaluate the heat capacity of the various species as a function of temperature. Over the temperature range of 25 to 50°C, the average change in the  $C_p$  values was about 8 % for methanol in the liquid phase, and over the temperature range of 100 to 150°C, the change in the  $C_p$  value was about 2 % for water in the gas phase, respectively. As demonstrated in *Appendix G*, the heat capacities hence obtained were used to evaluate the molar enthalpy and entropy of formation at temperature  $T$ , assuming a constant pressure, are given by:

$$\Delta H_T = \Delta H^o + \int_{298}^T C_p dT \quad (2.5)$$

$$\Delta S_T = \Delta S^o + \int_{298}^T \frac{1}{T} C_p dT \quad (2.6)$$

For  $\text{CH}_3\text{OH}$  electrolysis, over the temperature range of 25 to 50°C, the temperature correction was about 1 % for the  $\Delta S_T$  value in the liquid phase and over the temperature range of 76.7 to 150°C, and the temperature correction was about 2 % for the  $\Delta S_T$  value in the gas phase. The reversible cell voltage approximated as a function of temperature by:

$$E_e = E^o + (T - 298) \cdot \left( \frac{\Delta S_T}{nF} \right) \quad (2.7)$$

And the corresponding Gibbs free energy of formation was calculated:

$$\Delta G_T = -nFE_e \quad (2.8)$$

Finally, the maximum thermodynamic efficiency,  $\eta_{max}$ , can be calculated, at a temperature T and 1 atm, as per:

$$\eta_{max} = \left( \frac{\Delta G^T}{\Delta H^T} \right) \cdot 100 \quad (2.9)$$

These theoretical calculations assume that there is no gas forming before the fuel boiling point is reached and that there is no liquid present after the fuel boiling point is attained. The boiling point of the CH<sub>3</sub>OH-H<sub>2</sub>O mixture will change depending on the concentration. For the DMR thermodynamic calculations an equimolar mixture of H<sub>2</sub>O and CH<sub>3</sub>OH, which has a boiling point of 76.7°C, was assumed. The effect of the electrolyte is also ignored. The CO<sub>2</sub> released at the anode of the DMR was assumed to be in the gas phase at all temperatures.

It is important to note that the sign of the thermodynamic efficiency for the electrolysis systems can be positive or negative, depending on the temperature at which the system is evaluated. For both electrolysis systems, the enthalpy of formation was positive for the temperature range studied, indicating that both overall reactions are endothermic. The Gibbs free energy of formation for the water electrolysis system is positive (> 0) under the entire temperature range studied, indicating that the electrolysis of water is non-spontaneous. Hence, the thermodynamic efficiency of water electrolysis was positive at all temperature studied. Although, the methanol electrolysis Gibbs free energy of formation was positive at 25°C, indicating that the reaction is non-spontaneous at this temperature, the Gibbs free energy of formation was negative (< 0) at higher temperatures, indicating that the reaction became spontaneous. Under these conditions, the thermodynamic efficiency was a negative value.

As shown in Fig. 2.3, the PEM H<sub>2</sub>O electrolyser resulted in a positive theoretical thermodynamic efficiency over the entire temperature range studied, while that of the DMR was positive at 25°C and became negative at higher temperatures. The theoretical thermodynamic efficiencies determined for the PEM H<sub>2</sub>O electrolyser indicate that work is required on the system in order to generate H<sub>2</sub> under these conditions. The theoretical thermodynamic efficiencies determined for the DMR indicate that the system

requires work input to generate H<sub>2</sub> at 25°C, but that work is generated by the system at higher temperatures.

As shown in Fig. 2.3, for both systems, the theoretical cell voltage became less negative as temperature increased. In the case of the DMR, the theoretical cell voltage even became positive as temperature increased. It was determined that the DMR Gibbs free energy of formation and theoretical cell voltage of methanol electrolysis become positive at a temperature of about 41°C. Hence, according to thermodynamics at temperatures greater than 50°C, the DMR should be a spontaneous source of electricity, as well as H<sub>2</sub>. However, favourable reaction thermodynamics do not imply that the reaction is kinetically favourable. The Gibbs free energy of formation and theoretical cell voltage of the PEM H<sub>2</sub>O electrolyser, on the other hand, do not become positive over the temperature range investigated, i.e., up to 150°C. The thermodynamic analysis demonstrates which electrochemical reactions can occur spontaneously at specific conditions and equilibrium, but does not provide any kinetic information about the electrochemical reactions. The actual amount of electrical energy which will be required to generate H<sub>2</sub> is equal to the Gibbs free energy of the electrochemical reaction plus the losses in the system.

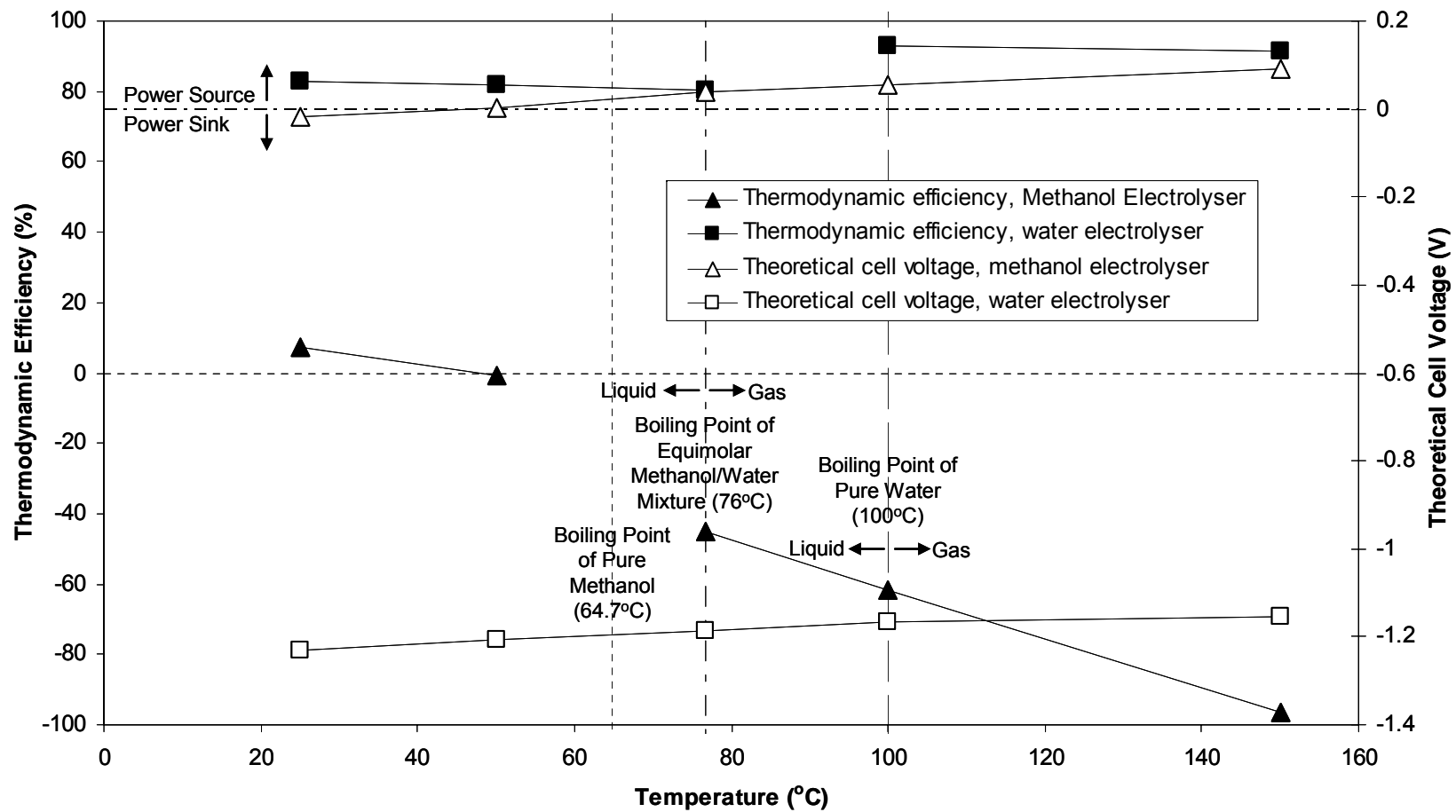


Figure 2.3: Theoretical thermodynamic efficiency and theoretical cell voltage as a function of temperature (1 atm) for a DMR and PEM water electrolyser.

## 2.3.2 Electrolysis Polarizations

### 2.3.2.1 Cell voltage stability

Typical responses obtained for different electrolysis current densities are shown in Fig. 2.4. The open circuit voltage (OCV) for the reaction was measured in an H-cell as described in *Appendix F*. At low current densities, steady-state was rapidly reached and the CH<sub>3</sub>OH electrolysis voltage stabilized. At high current densities, the CH<sub>3</sub>OH oxidation current alone was insufficient to sustain the high current density. The electrolysis voltage dropped off until water oxidation and carbon oxidation started to occur.

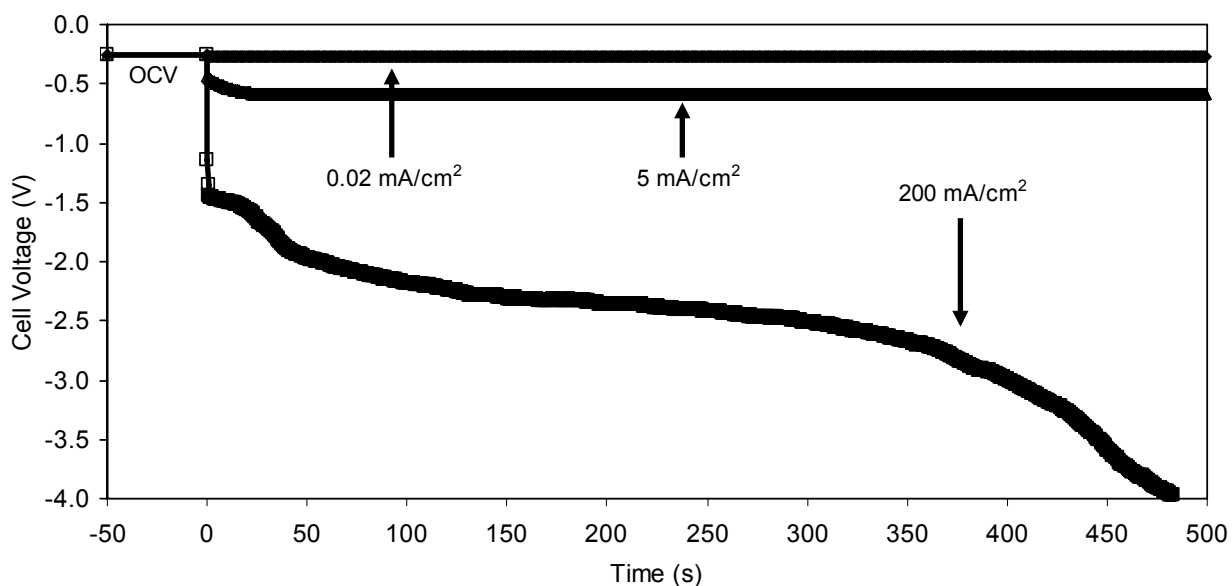


Figure 2.4: Electrolysis cell voltage stability with respect to current density (16 M CH<sub>3</sub>OH in 0.5 M H<sub>2</sub>SO<sub>4</sub> electrolyser anolyte, 0.5 M H<sub>2</sub>SO<sub>4</sub> electrolyser catholyte, 4 mg/cm<sup>2</sup> Pt-Ru/C anode, 2 mg/cm<sup>2</sup> Pt/C cathode, 23 ± 2°C).

Water electrolysis starts to occur at voltages below -1.23 V vs. SHE, and carbon oxidation, e.g., the anode oxidation catalyst support starts to oxidize at a cell voltage of about -1.8 V vs. SHE. Hence, a limiting current density is reached for the electro-oxidation of CH<sub>3</sub>OH beyond which no stable cell voltage measurements could be obtained. Although the experiments were done in the static mode, this effect has also been observed for CH<sub>3</sub>OH electrolysis in the active mode [118]. Voltage measurements were

recorded at current densities where steady-state was reached, i.e., when the change in cell voltage was less than 20 mV over five minutes. The region of cell voltage stability varied as a function of current density, CH<sub>3</sub>OH concentration, temperature and the type of anode electrocatalyst. In the limiting current density region, steady-state could not be reached.

Figure 2.5 shows an example of the electrolysis test repeatability in the different regions. In the stable region, the electrolysis polarization curve is very reproducible. The experiments conducted in the forward direction, from small current densities to large current densities, in the backward direction, from large current densities to small current densities, and in a random order of current densities all resulted in very similar voltages at a particular current density. When the test was started backward from a point in the unstable region, the results were still reproducible, but the error for the first data point in the stable region was slightly larger. When the test was started at a current density where the safety limit of -4 V was reached, irreversible damage was observed as the catalyst was oxidized and precious metal was lost from its surface. This was also verified by conducting cyclic voltammetric experiments on fresh, used, and oxidized supported catalyst coupons.

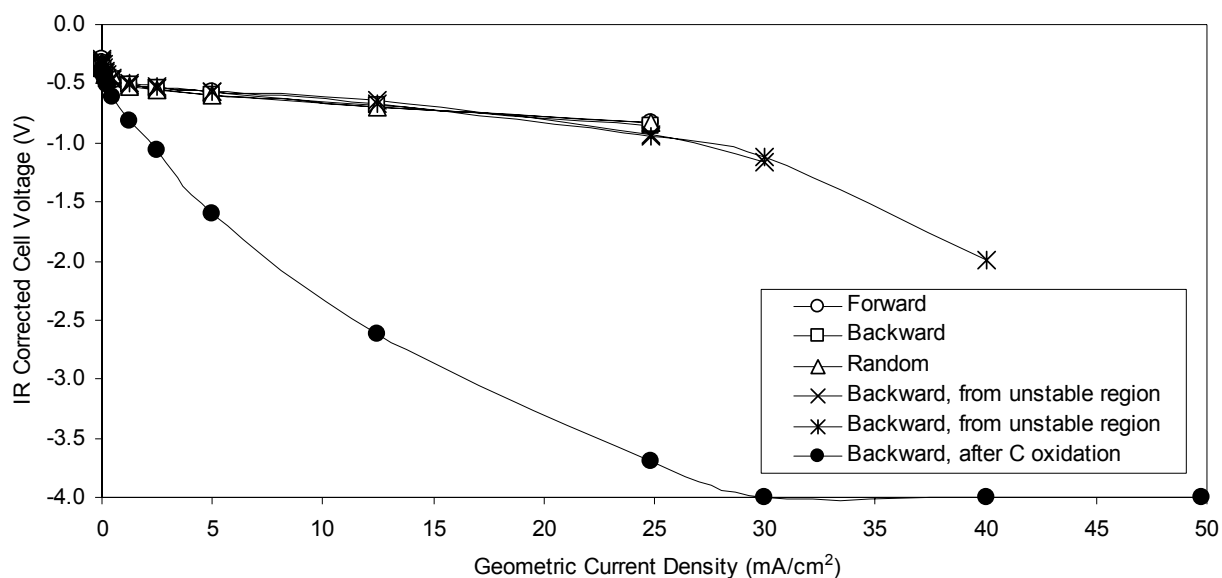


Figure 2.5: IR corrected electrolysis cell voltage repeatability as a function of geometric current density in the stable and unstable regions (2 M CH<sub>3</sub>OH in 0.5 M H<sub>2</sub>SO<sub>4</sub> electrolyser anolyte, 0.5 M H<sub>2</sub>SO<sub>4</sub> electrolyser catholyte, 2 mg/cm<sup>2</sup> Pt/C anode and cathode, 23 ±2°C).

The data points shown in the figures represent the arithmetic average of values obtained for a minimum of three different samples. The calculated standard deviation,  $S_d$ , representing the upper and lower limits, was typically in the range of 10 mV but closer to 200 mV in the limiting current region. In the limiting current density region, voltage values were unstable and were empirically obtained by linear interpolation between the last stable data points and the safety limit, which was set at -4 V.

### 2.3.2.2 Effect of methanol concentration and anode catalyst

In order to investigate the effect of CH<sub>3</sub>OH concentration on the polarization curve, the anode compartment CH<sub>3</sub>OH concentration was varied from 0 to 16 M (i.e., 0, 1, 2, 6, 16 M), with 0 M representing H<sub>2</sub>O electrolysis. Figure 2.6 shows the dependence of the cell voltage corrected for the ohmic losses on the current density for different CH<sub>3</sub>OH concentrations and represent typical electrolysis polarization curves. They show open-circuit voltages (OCV) less than the equilibrium cell voltage likely due to fuel cross-over; activation control at lower current densities resulting in a sharp initial decrease in cell voltage as the current density increases; a subsequent linear slow voltage decrease with current density due to ohmic control followed by a rapid decrease in cell voltage due to mass transport limitations. The limiting current densities,  $i_L$ , are reached in the transport control region when the fuel is used at a rate equal to its maximum transport supply rate. At the limiting current density, voltages where other competing reactions can occur, such as H<sub>2</sub>O electrolysis and/or carbon oxidation, were reached. As can be seen in Fig. 2.6, the  $i_L$  value varied with CH<sub>3</sub>OH concentration. At low current densities (<12 mA/cm<sup>2</sup>), the CH<sub>3</sub>OH concentration did not impact the cell voltage significantly, while at higher current densities, lower overpotentials were obtained at higher CH<sub>3</sub>OH concentrations. As expected, for CH<sub>3</sub>OH oxidation the required electrolytic voltages were significantly less than for H<sub>2</sub>O electrolysis at the same current density. In contrast with active CH<sub>3</sub>OH electrolysis studies where the anode reactants are continuously flowing, the static system electrolytic polarizations are more sensitive to CH<sub>3</sub>OH concentration. Hu *et al.* [7] reported that the electrolysis performance was not dependent on the CH<sub>3</sub>OH concentration at concentrations greater than 2 M at 60°C, but that the concentration polarization was obvious at high current densities for concentrations lower than 1 M. In another study, by Shen *et al.* [11], the voltage losses for CH<sub>3</sub>OH electrolysis were reported to be almost the same in the 2-4 M range, while the voltage losses were greater at concentrations lower or higher than this range. At low CH<sub>3</sub>OH

concentrations, high current densities could not be sustained. At high CH<sub>3</sub>OH concentrations, less voltage was required to hold the same current densities and higher current densities could be sustained. Methanol permeation from the anode compartment to the cathode compartment will increase with increasing CH<sub>3</sub>OH concentrations and will decrease fuel efficiency. However, in the system under study, CH<sub>3</sub>OH present in the cathode compartment can not be oxidized at the reducing cathode potentials observed during electrolysis. In their study, Hu *et al.* attributed the poor electrolysis performance at high CH<sub>3</sub>OH concentration to the creation of a mixed potential at the cathode, which in turn reduced its electrocatalytic activity. Other phenomena such as adsorption and catalyst site blockage were not considered but are possible. As the concentration of CH<sub>3</sub>OH increases, the solution conductivity will decrease, and the mass transfer limitations will decrease, which will affect rate of CH<sub>3</sub>OH electrolysis.

As the data presented in Fig. 2.6 is for catalysts having different ECSAs, it is not possible to make a direct comparison of the performance of the three-dimensional catalysts studied for the electrolysis of CH<sub>3</sub>OH or H<sub>2</sub>O on a geometric current density basis. Nevertheless, Fig. 2.6 (e) clearly demonstrates that the well-defined low electrochemical surface area non-porous Pt disk did not perform as well as the dispersed three-dimensional electrode catalysts. Furthermore, it can be seen that the Pt disk electrode, for which no carbon is present, was able to sustain greater current densities for H<sub>2</sub>O electrolysis than for CH<sub>3</sub>OH oxidation. Interestingly, for the 1 M CH<sub>3</sub>OH case with the well-defined Pt disk at low current densities, two different potential values were obtained for the same current density. In this system, proton conductivity of the MEA was provided by the electrolyte in the cathodic compartment. The bi-stability was observed in multiple tests which were performed separately at the same conditions. This phenomenon was also observed for a PEM fuel cell running at 37°C using H<sub>2</sub> partial pressure less than 1.5 kPa, and 4 mg/cm<sup>2</sup> Pt-Ru black anode and a 4 mg/cm<sup>2</sup> Pt black cathode [173]. It was attributed to the total resistance of Nafion<sup>®</sup>, which is split in an ohmic component, due to proton migration in the membrane's aqueous phase, and a non-ohmic one, due to proton tunnelling in the membrane.

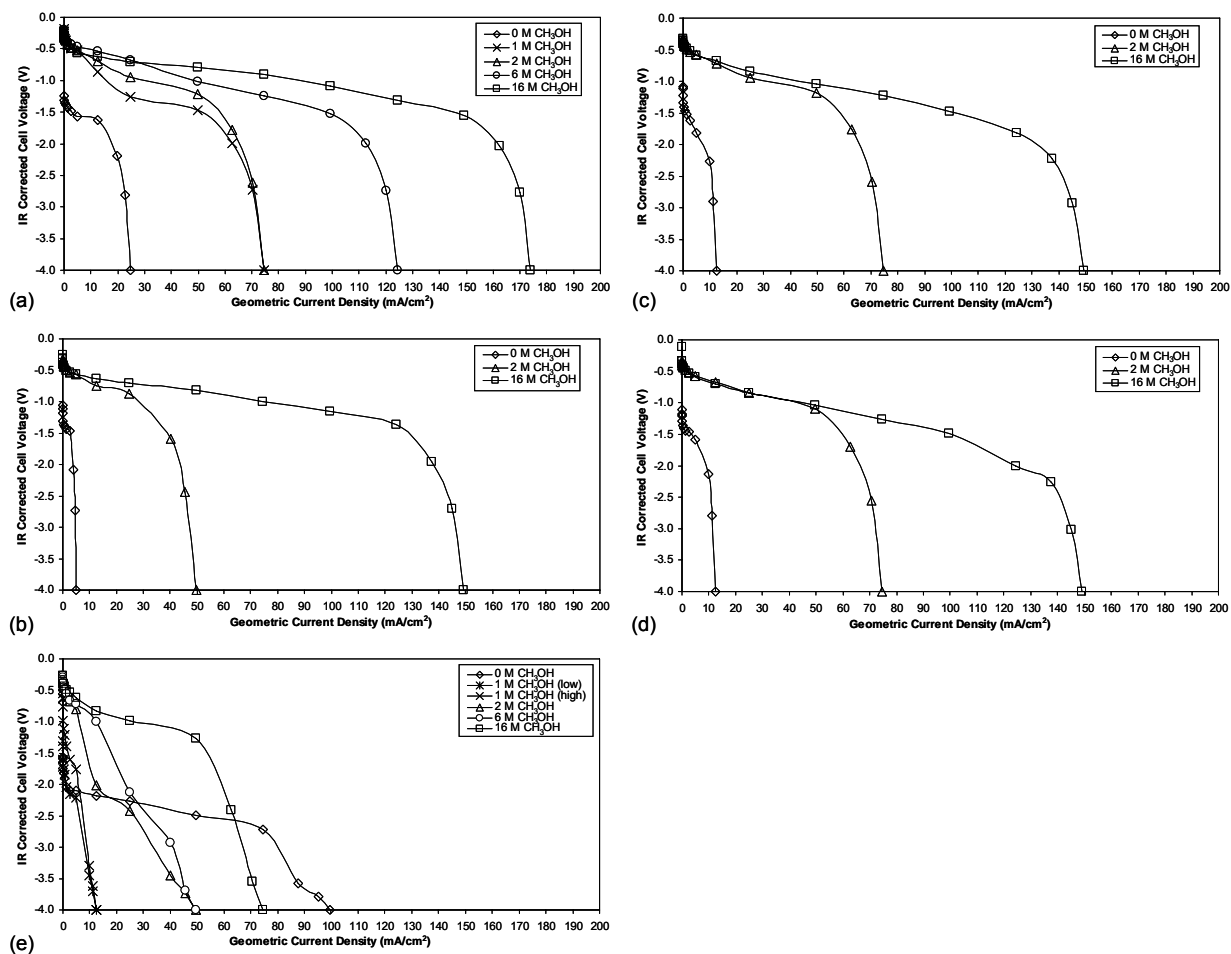


Figure 2.6: Effect of methanol concentration on the IR corrected electrolysis cell voltage as a function of geometric current density for different anode catalysts (a) 4 mg/cm<sup>2</sup> Pt-Ru/C, (b) 2 mg/cm<sup>2</sup> Pt/C, (c) 4 mg/cm<sup>2</sup> Pt-Ru black, (d) 2 mg/cm<sup>2</sup> Pt black, (e) well-defined Pt disk (0, 1, 2, 6 or 16 M CH<sub>3</sub>OH in 0.5 M H<sub>2</sub>SO<sub>4</sub> electrolyser anolyte, 0.5 M H<sub>2</sub>SO<sub>4</sub> electrolyser catholyte, 23 ± 2°C).

Figure 2.7 shows that the  $i_L$  values varied with the  $\text{CH}_3\text{OH}$  concentration and the type of anode catalyst used.

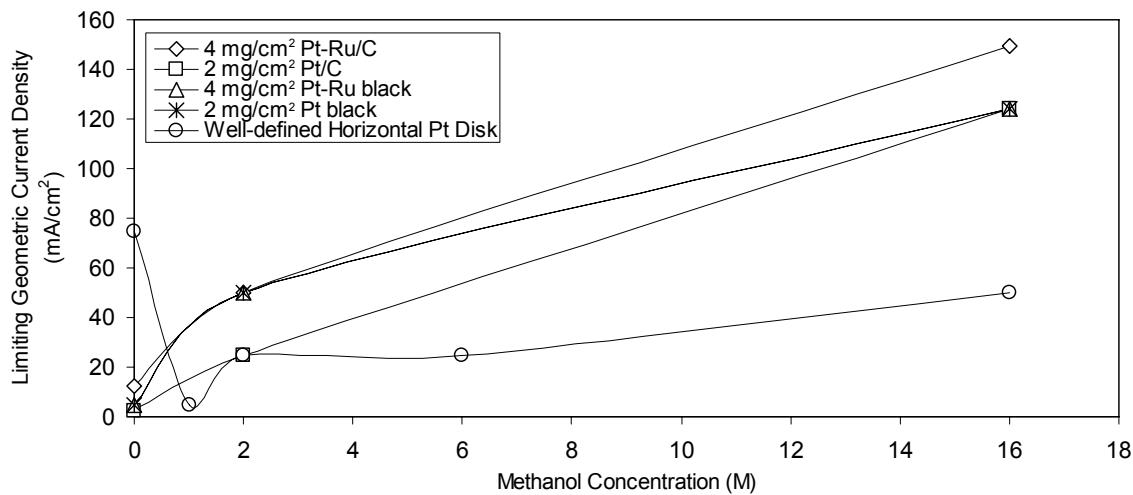


Figure 2.7: Dependence of limiting geometric current densities for the oxidation of methanol and water on the  $\text{CH}_3\text{OH}$  concentration for various anode catalysts (0, 1, 2, 6 or 16 M  $\text{CH}_3\text{OH}$  in 0.5 M  $\text{H}_2\text{SO}_4$  electrolyser anolyte, 0.5 M  $\text{H}_2\text{SO}_4$  electrolyser catholyte,  $23 \pm 2^\circ\text{C}$ ).

For  $\text{CH}_3\text{OH}$  oxidation, the largest limiting current densities were reached with the Pt-Ru/C catalyst. For  $\text{H}_2\text{O}$  electrolysis, the largest limiting current density was reached with the well-defined Pt disk. However, the  $i_L$  values obtained for this catalyst are lower in the case of  $\text{CH}_3\text{OH}$  oxidation than for  $\text{H}_2\text{O}$  oxidation. Although this well-defined Pt catalyst is not affected by carbon oxidation thus allowing higher current densities to be achieved, its low electrochemical surface area was strongly affected by CO adsorption in the case of  $\text{CH}_3\text{OH}$  oxidation. The  $i_L$  values for the Pt/C catalyst were lower than the one for the unsupported catalyst at low concentrations, while the  $i_L$  values were similar to the unsupported catalyst ones at high concentration. The  $i_L$  values for the 4 mg/cm<sup>2</sup> Pt-Ru black catalyst and for the 2 mg/cm<sup>2</sup> Pt black catalyst were within the same range. It would be expected that the supported catalysts, which possess higher active areas, would result in higher limiting current densities. Yet, this was not observed for Pt/C and Pt black. Take *et al.* [118] determined limiting current densities for an active  $\text{CH}_3\text{OH}$  electrolysis electrolytic cell using 5.4 cm diameter Pt catalyst samples (real surface area of 23 cm<sup>2</sup>) at the anode and cathode, of 130 mA/cm<sup>2</sup> for 1 M  $\text{CH}_3\text{OH}$ , 170 mA/cm<sup>2</sup> for 2 M  $\text{CH}_3\text{OH}$ , 210 mA/cm<sup>2</sup> for 6 M

CH<sub>3</sub>OH, and 260 mA/cm<sup>2</sup> for 16 M CH<sub>3</sub>OH. These reported values are greater than the limiting geometric current densities shown in Fig. 2.7 for the same CH<sub>3</sub>OH concentrations using the 2 mg/cm<sup>2</sup> supported or unsupported Pt catalyst. In the passive mode, the transport of the fuel to the electrode is slower and its access to the electrode is more restrained by the CO<sub>2</sub> production. This resulted in lower limiting current densities compared to the active mode.

Figure 2.8 shows the individual IR corrected anode potential and cathode potential, respectively, obtained for stable voltage values before the limiting current density region. The change in cathode potential is insignificant compared to the change in anode potential. As the cathode potential remained more or less the same, it can be deduced that the increase in cell voltage required is mainly due to the anode. It can also be seen that higher CH<sub>3</sub>OH concentrations reduce the anode overpotential.

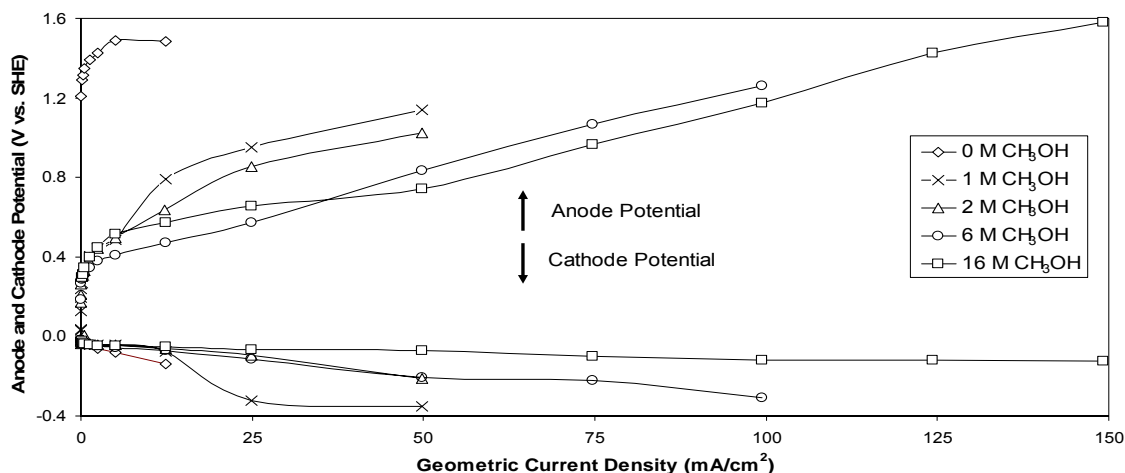
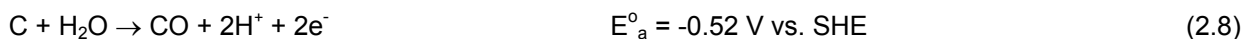
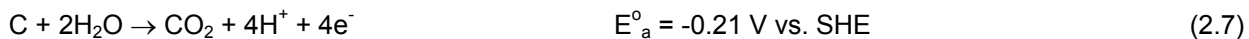


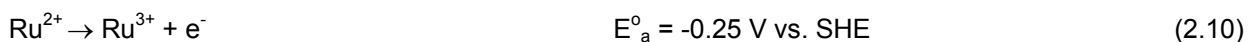
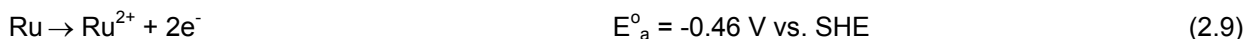
Figure 2.8: Effect of CH<sub>3</sub>OH concentration on the individual electrode potential (0, 1, 2, 6 or 16 M CH<sub>3</sub>OH in 0.5 M H<sub>2</sub>SO<sub>4</sub> electrolyser anolyte, 0.5 M H<sub>2</sub>SO<sub>4</sub> electrolyser catholyte, 4 mg/cm<sup>2</sup> Pt-Ru/C anode, 2 mg/cm<sup>2</sup> Pt/C cathode, 23 ± 2°C).

As shown in Fig. 2.8, the electrolysis of H<sub>2</sub>O in 0.5 M H<sub>2</sub>SO<sub>4</sub> commences at the anode at a potential of about 1.3 V vs. SHE (Eq. 1.21). At anode potentials equal to and greater than this value for the CH<sub>3</sub>OH oxidation reaction, the current efficiency is not 100 %, as there is a current loss due to the H<sub>2</sub> evolution

reaction. Beyond this point, the H<sub>2</sub>O electrolysis current density should be subtracted from the CH<sub>3</sub>OH electro-oxidation current density. At higher cell voltages, the current density is also increasingly sustained by carbon corrosion. According to thermodynamics, carbon can be oxidized on the anode at a standard potential of -0.21 V vs. SHE:



However, the carbon oxidation is kinetically-inhibited and it does not usually begin until a potential of about 1.8 V vs. SHE is reached at the anode [174]. Beyond this potential, the cell current density is increasingly sustained by carbon corrosion. This was confirmed by the observation of a decrease in cell voltage after re-utilization of catalysts which were subjected to anode potentials greater than this value. The degradation of the catalyst carbon support and the consequent loss in electrochemical surface area was also confirmed by cyclic voltammetry (refer to Appendix F for more details). Furthermore, Ru can dissolve at anodic potentials greater than the standard potential of -0.25 V vs. SHE, as per the following electrochemical reactions:



Hence, as the absolute current density increases and the anode potential become more positive, a decrease in the CH<sub>3</sub>OH oxidation performance due to Ru loss can also be anticipated. However, this is likely kinetically limited, similar to the case of carbon oxidation. The impact of Ru dissolution and crossover on the performance of a PEMFC and on the functionality of the anode was studied in the literature [175].

Figure 2.9 compares the performance of Pt/C and Pt black catalysts on a real electrochemical current density basis for different CH<sub>3</sub>OH concentrations. Both catalysts had the same catalyst loading of 2 mg Pt/cm<sup>2</sup> and a Nafion<sup>®</sup> content of 30 wt%, even though the optimized amount of ionomer required for the unsupported catalyst is likely different than for the supported catalyst.

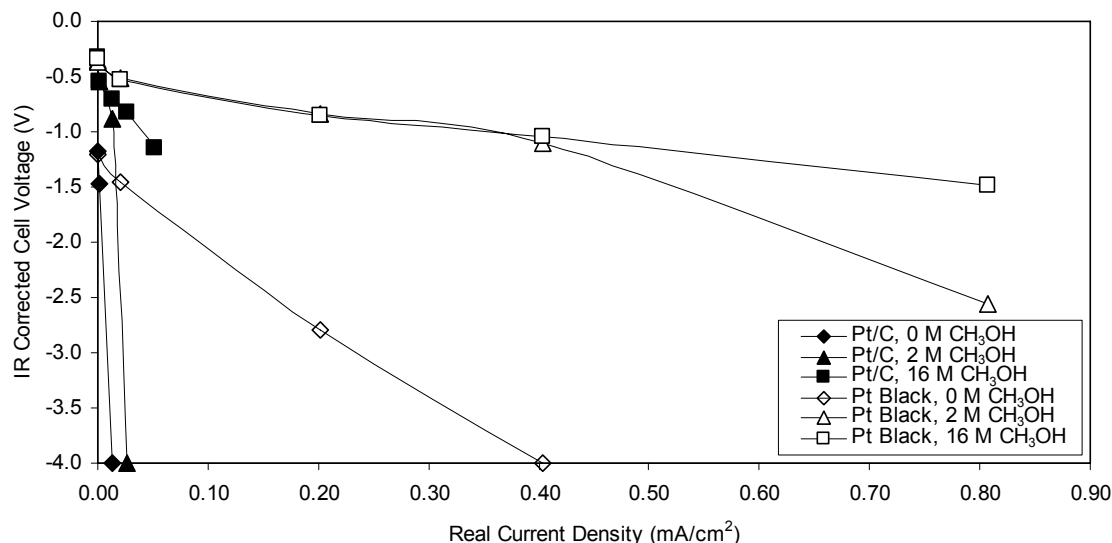


Figure 2.9: Effect of the IR corrected voltage on electrolysis for Pt/C and Pt black anode catalysts as a function of real electrochemical current density (0, 2, or 16 M CH<sub>3</sub>OH in 0.5 M H<sub>2</sub>SO<sub>4</sub> electrolyser anolyte, 0.5 M H<sub>2</sub>SO<sub>4</sub> electrolyser catholyte, 23 ± 2°C).

The Pt black catalyst had a much smaller ECSA than the Pt/C catalyst. It is possible that the non-optimized Nafion<sup>®</sup> content partly contributed to a decrease in the surface area of the unsupported catalyst. However, the required applied voltage to oxidize H<sub>2</sub>O or CH<sub>3</sub>OH was less for the Pt black catalyst than for the Pt/C catalyst at the same current density. Thus, the Nafion<sup>®</sup> loading used did not restrain the access to the active surface sites of the black catalyst and did not render it less active than the Pt/C catalyst. Moreover, the Pt black catalyst was able to sustain higher real current densities than the Pt/C catalyst at the same CH<sub>3</sub>OH concentration. It appears that carbon oxidation started to occur at lower real current densities for the Pt/C electrode than for the Pt black electrode. This suggests that the carbon of the supported catalyst oxidizes before the carbon of the carbon fibre paper on which the both catalysts were sprayed start to oxidize.

### 2.3.2.3 Effect of dry purged cathode

Experiments were also conducted with a dry cathode, which was purged with  $N_2$  gas, to confirm the feasibility of this possible design simplification. Figure 2.10 compares the polarization curves for a DMR running with the cathode compartment filled with 0.5 M  $H_2SO_4$  and for one with a dry cathode compartment purged with  $N_2$ . The cell voltage became more negative for the DMR operating with a dry purged cathode compartment compared to the DMR with a cathode compartment containing 0.5 M  $H_2SO_4$ .

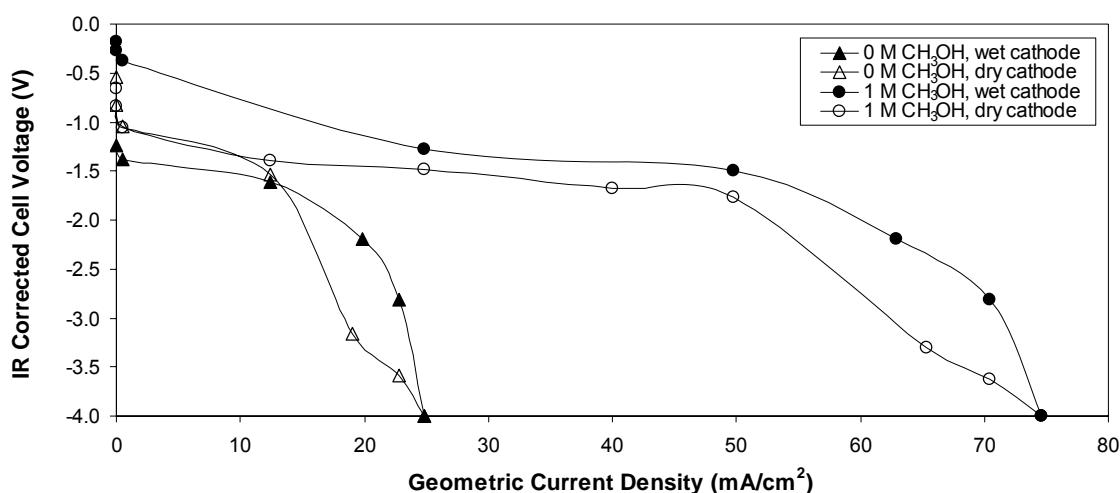


Figure 2.10: Effect of dry  $N_2$  purged cathode on the IR corrected electrolysis cell voltage as a function of geometric current density (0 or 1 M  $CH_3OH$  in 0.5 M  $H_2SO_4$  electrolyser anolyte, wet electrolyser catholyte: 0.5 M  $H_2SO_4$ , dry electrolyser catholyte:  $N_2$  purge electrolyser, 4 mg/cm<sup>2</sup> Pt-Ru/C anode, 2 mg/cm<sup>2</sup> Pt/C cathode, 23 ± 2°C).

In the case of  $CH_3OH$  electrolysis, slightly more voltage is required to drive the electrochemical reaction when the cathode does not contain any electrolytic solution. In both cases, the required voltage for the dry and wet cases were within 10 % at high current densities and similar limiting current densities were attained in the dry and wet cathode case for 0 and 1 M  $CH_3OH$ . However, the AC impedance (*Appendix F*) results indicated that the ohmic resistance across the MEA can be up to about 55 % higher in the dry cathode case compared to the wet cathode one, i.e., 0.22  $\Omega$  versus 0.1  $\Omega$  for 1 M  $CH_3OH$ . This indicates

humidification of the membrane by diffusion of H<sub>2</sub>O from the liquid anode side to the dry cathode side in this case might be insufficient to maintain the membrane conductivity. Of course, membrane humidification could be improved by decreasing the membrane thickness and pressurizing the anode side, for example. Fig. 2.11 shows the corresponding anode and cathode potentials respectively, for the wet and dry cathode cases. The cathode potential remained largely unaffected by the wet or dry cathode operation compared to the anode potential. No tests were carried out using humidified N<sub>2</sub>.

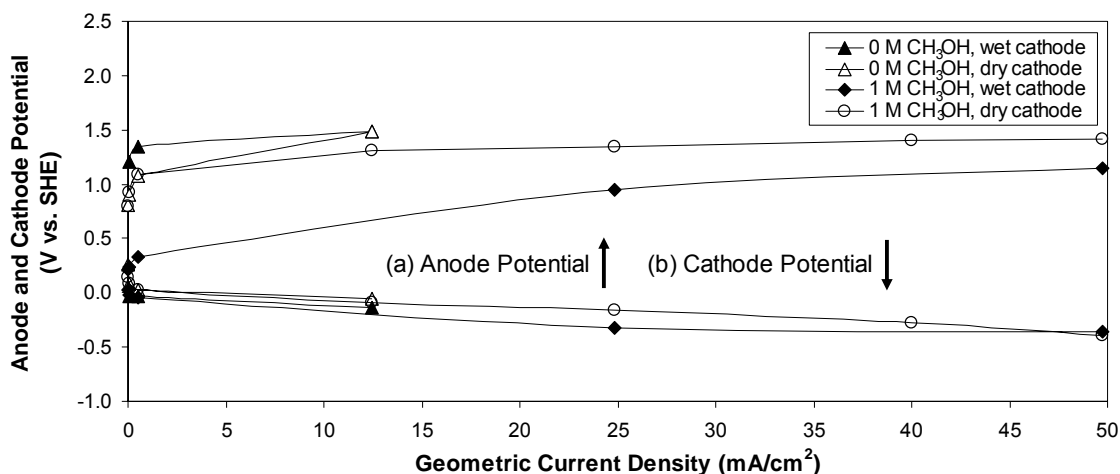


Figure 2.11: Effect of dry N<sub>2</sub> purged cathode and a wet cathode on the (a) anode potential and (b) cathode potential, as a function of geometric current density (0 or 1 M CH<sub>3</sub>OH in 0.5 M H<sub>2</sub>SO<sub>4</sub> electrolyser anolyte, wet electrolyser catholyte: 0.5 M H<sub>2</sub>SO<sub>4</sub>, dry electrolyser catholyte: N<sub>2</sub> purge, 4 mg/cm<sup>2</sup> Pt-Ru/C anode, 2 mg/cm<sup>2</sup> Pt/C cathode, 23 ± 2°C).

Fig. 2.11 shows that for CH<sub>3</sub>OH electrolysis the anode potential was significantly larger with the dry purged cathode than with the wet cathode. The CH<sub>3</sub>OH cross-over and MEA resistance are likely greater in the dry N<sub>2</sub> case. It is not clear why the anode potential is larger in the dry cathode case. At high enough current densities in both modes, the anode potential is high enough that H<sub>2</sub>O electrolysis will also occur in parallel. Using a dried N<sub>2</sub> purged cathode compartment seems to represent a possible design simplification for the liquid CH<sub>3</sub>OH electrochemical reformer.

#### 2.3.2.4 Effect of temperature

The effect of temperature was studied for CH<sub>3</sub>OH and H<sub>2</sub>O electrolysis using the 4 mg/cm<sup>2</sup> Pt-Ru/C catalyst. As can be seen in Fig. 2.12, increasing the operating temperature significantly improved the Pt-Ru/C electrode kinetics of the CH<sub>3</sub>OH electrolysis. There was a large improvement in the electrolyser performance for all catalyst types with temperature. For example, for the 16 M CH<sub>3</sub>OH solution and a current density of 150 mA/cm<sup>2</sup>, the cell voltage was -1.55 V, -1.26 V and -0.87 V corresponding to temperatures of 23, 50 and 75°C, respectively. Hence, there was a reduction in the electrolyser cell voltage of 31 % between 50 and 75°C. The reduced electrolytic overpotentials resulted from an improvement in the mass transport and in the electrode kinetics at the higher temperature. Compared to the limiting current density at 23°C, at 50°C, the limiting current density was about 25 mA/cm<sup>2</sup> higher in the case of the 2 M CH<sub>3</sub>OH solution, and 50 mA/cm<sup>2</sup> higher in the case of the 16 M CH<sub>3</sub>OH solution. However, the increase in limiting current densities between 50 and 75°C was not significant, and a similar limiting current was obtained at both temperatures in the case of water and CH<sub>3</sub>OH electrolysis. This is not in agreement with what has been previously observed for active CH<sub>3</sub>OH electrolysis systems [7, 11]. For example, Shen *et al.* [11] using a 2.5 mg/cm<sup>2</sup> Pt-Ru/C anode and a 1.5 mg/cm<sup>2</sup> Pt/C cathode in a 2 M CH<sub>3</sub>OH active system shown that over the temperature range of 50 to 80°C, the electrolysis cell voltage at 80°C was reduced to half of the electrolysis cell voltage at 50°C. There is no indication in this paper that measures were taken to prevent CH<sub>3</sub>OH loss to the vapour phase. However, as a closed-loop CH<sub>3</sub>OH-H<sub>2</sub>O anode feeding system, it can be assumed that any CH<sub>3</sub>OH evaporating would be condensing back in the CH<sub>3</sub>OH-H<sub>2</sub>O storage tank, and that the concentration of CH<sub>3</sub>OH fed to the anode is constant. In our static system set-up, the anolyte is not constantly replenished and any CH<sub>3</sub>OH evaporating is loss. This may explain why the electrolyser cell voltage did not decrease as significantly as for active systems between 50 and 75°C in our experiments.

As the 16 M CH<sub>3</sub>OH solution has a boiling point of 76.7°C, and our study uses a non-flowing system, a partial loss of solution to the vapour phase was possible. Using a K<sub>2</sub>Cr<sub>2</sub>O<sub>7</sub> reduction technique combined with spectrophometric measurements, which is described in *Appendix E*, it was verified that, the CH<sub>3</sub>OH concentration change for a 16 M CH<sub>3</sub>OH at 75°C was less than 2 M over the period of time for which polarization measurements were taken. This small concentration change might partly explain why the

limiting current density was similar at 50 and 75°C in the case of the 16 M CH<sub>3</sub>OH solution. Another possible explanation may be that there is a greater crossover rate of CH<sub>3</sub>OH at 16 M CH<sub>3</sub>OH, which may affect the kinetics of the H<sub>2</sub> production at the cathode. However, in the case of H<sub>2</sub>O electrolysis, while minor improvements in the anode kinetics were observed with increasing temperature, the limiting current also remained the same over the temperature range of 23 to 75°C studied. Therefore, CH<sub>3</sub>OH crossover can not explain why similar limiting current densities were obtained for the electrolysis of 2 and 16 M CH<sub>3</sub>OH at 50 and 75°C. Nevertheless, it may be preferable to operate the CH<sub>3</sub>OH electrolyser at higher temperatures as less current would be wasted for secondary reactions and performance is better under these conditions.

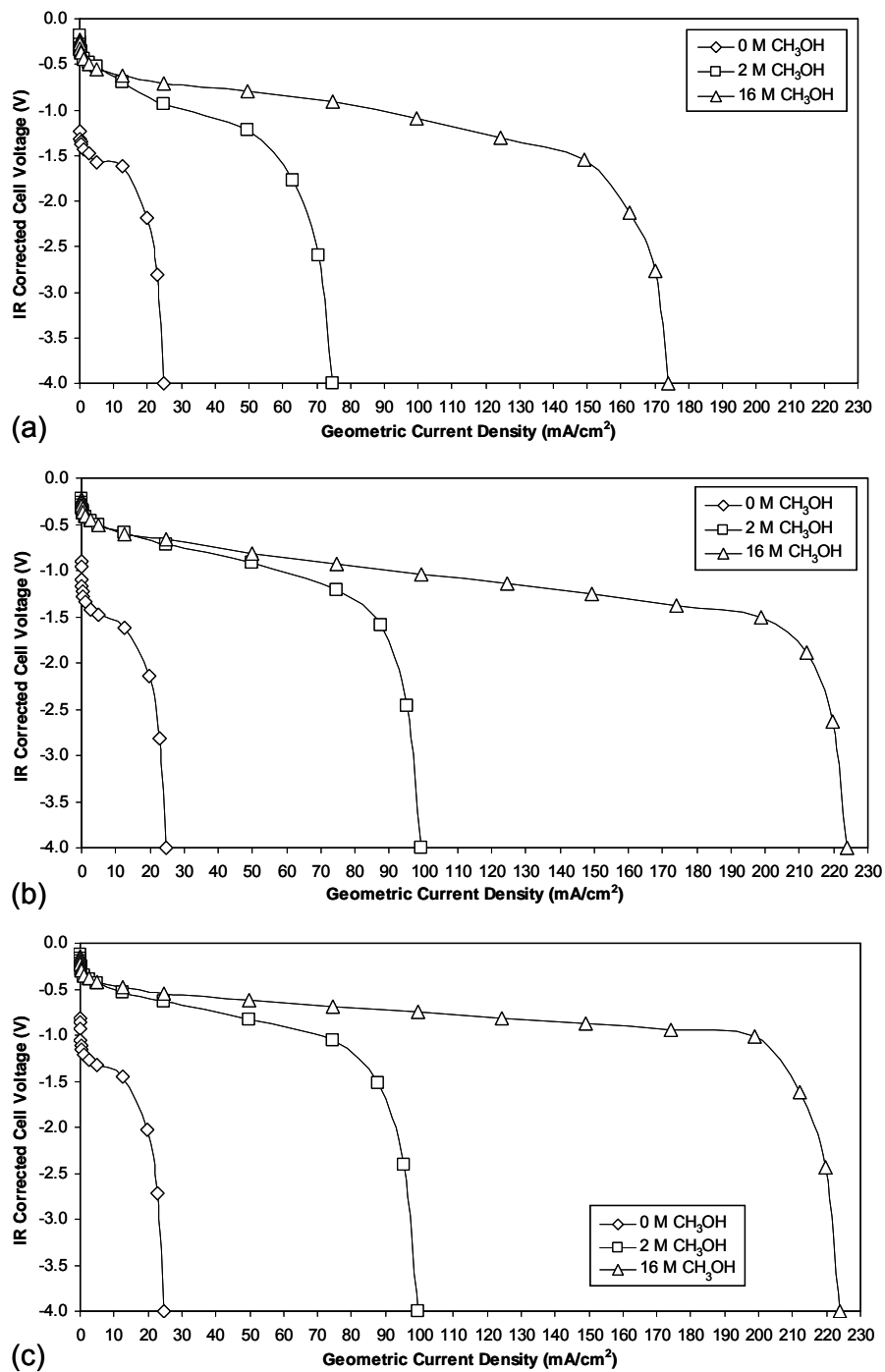


Figure 2.12: Effect of CH<sub>3</sub>OH concentration on the IR corrected electrolysis cell voltage as a function of geometric current density for different temperatures (a) 23 ± 2°C (b) 50 ± 1°C (c) 75 ± 1°C (0, 2 or 16 M CH<sub>3</sub>OH in 0.5 M H<sub>2</sub>SO<sub>4</sub> electrolyser anolyte, 0.5 M H<sub>2</sub>SO<sub>4</sub> electrolyser catholyte, 4 mg/cm<sup>2</sup> Pt-Ru/C anode, 2 mg/cm<sup>2</sup> Pt/C cathode).

### 2.3.2.5 Anode Tafel kinetics

In the case  $\text{CH}_3\text{OH}$  and  $\text{H}_2\text{O}$  electrolysis, the anodic reaction kinetics is slow, resulting in a high overpotential. The overvoltage at the cathode is negligible compared to the overvoltage at the anode. The Butler-ERdey-Grutz-Volmer (BEV) equation can be simplified to the Tafel equation as per a well-known treatment described elsewhere [126, 176] and in more details in *Appendix F*. The anodic form of the Tafel equation was used to make Tafel plots ( $\log(i)$  vs.  $\eta_a$ ) from which the Tafel slope and the Tafel constant were extracted to obtain kinetic information on the  $\text{CH}_3\text{OH}$  and  $\text{H}_2\text{O}$  electrolysis. Fig. 2.13 shows an example of the IR corrected anode overpotential vs. log of the geometric current density for different  $\text{CH}_3\text{OH}$  concentrations, demonstrating the linearity of the Tafel lines obtained.

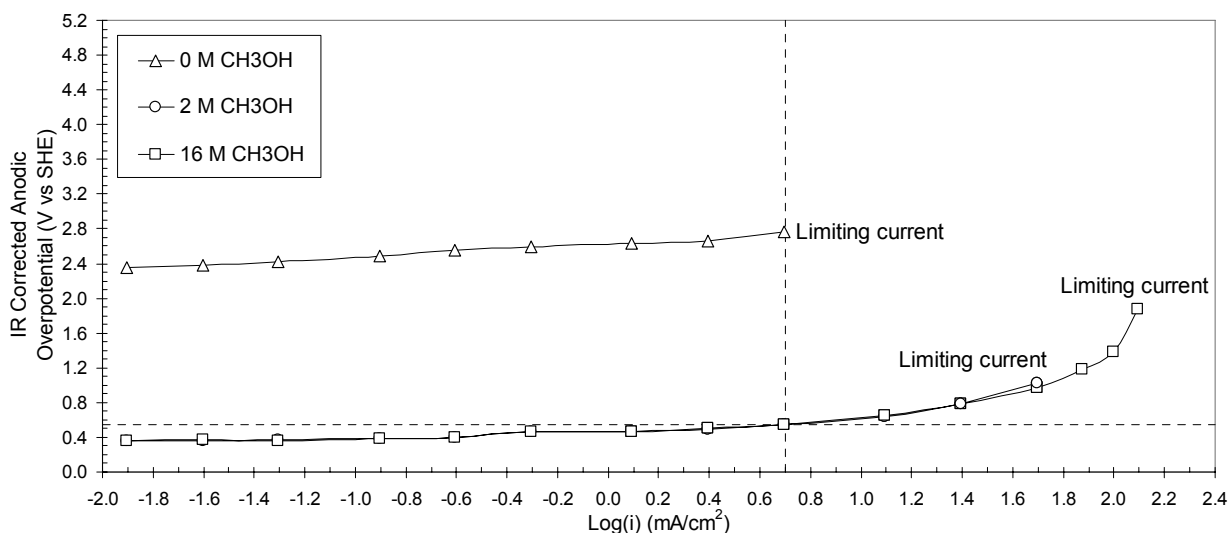


Figure 2.13: Tafel plot of the IR corrected anodic overpotential as a function of the log of the geometric current density (0, 2, or 16 M  $\text{CH}_3\text{OH}$  in 0.5 M  $\text{H}_2\text{SO}_4$  electrolyser anolyte, 0.5 M  $\text{H}_2\text{SO}_4$  electrolyser catholyte, 4 mg/cm<sup>2</sup> Pt black anode, 2 mg/cm<sup>2</sup> Pt/C cathode, 23 ± 2°C).

The slope of the anodic Tafel curves for the  $\text{CH}_3\text{OH}$  electrolysis changed at about 0.6 V for the Pt and Pt-Ru catalysts, indicating two distinct kinetic control regions. Wu *et al.* [177] have reported that these two regions represent two different reaction mechanisms. In the first region, where  $\eta_a < \sim 0.6$  V vs. SHE, the splitting of the first C-H bond with the first electron charge transfer reaction is the rate-determining

step, while in the second region, where  $\eta_a > \sim 0.6$  V vs. SHE, the reaction between the adsorbed CO on Pt sites is the rate-determining step [178]. For H<sub>2</sub>O electrolysis on the other hand, only one apparent slope was obtained over the entire potential range for the different catalysts studied. Hence, it is likely that there is only one reaction mechanism over the entire region. However, Kinoshita [179] reported that two distinct Tafel slopes were obtained for most metal oxide based catalysts studied in 1 N H<sub>3</sub>PO<sub>4</sub> at 25°C. They reported a low Tafel slope value at low current densities and a high Tafel slope value at high current densities.

Tafel parameters reported in the literature for Pt and Pt-Ru catalysts for CH<sub>3</sub>OH and H<sub>2</sub>O electrolysis, along with the values obtained in this study, are summarized in Table 2.2 and 2.3, respectively. For the case of the 4 mg/cm<sup>2</sup> Pt-Ru anode, the exchange current density values,  $i_o$ , were approximated by using twice the ECSA determined for the 2 mg/cm<sup>2</sup> Pt catalyst, as well as the ECSA determined through Cu UPD, for comparison purposes. This is indicated by the superscript <sup>1</sup> and <sup>3</sup>, respectively, as indicated in the legend provided at the bottom of Table 2.3.

Table 2.2: Literature Tafel kinetic parameters for the electro-oxidation of methanol and water on Pt and Pt-Ru catalysts.

| Method              | Catalyst    | Electrode Description                                   | Experimental Conditions               |                          |        | Anode Overpotential         |         | Tafel Slope |         | Exchange Current Density |                       | Ref.  |
|---------------------|-------------|---------------------------------------------------------|---------------------------------------|--------------------------|--------|-----------------------------|---------|-------------|---------|--------------------------|-----------------------|-------|
|                     |             |                                                         | [H <sub>2</sub> SO <sub>4</sub> ] [M] | [CH <sub>3</sub> OH] [M] | T [°C] | η <sub>a</sub> [mV vs. SHE] | Zone I  | Zone II     | Zone I  | Zone II                  | Zone I                |       |
| IR, P.              | Pt (111)    | 0.2 cm OD spheres                                       | 0.1                                   | 0.2                      | 20     | <422                        | -       | 119         | -       | 1.00x10 <sup>-2</sup>    | -                     | [180] |
| IR, P.              | Pt (110)    | 0.2 cm OD spheres                                       | 0.1                                   | 0.2                      | 20     | <422                        | -       | 123         | -       | 1.00x10 <sup>-2</sup>    | -                     | [180] |
| IR, P.              | Pt (100)    | 0.2 cm OD spheres                                       | 0.1                                   | 0.2                      | 20     | <422                        | -       | 63          | -       | 1.00x10 <sup>-2</sup>    | -                     | [180] |
| IR, P.              | Pt (111)    | 0.2 cm OD spheres                                       | 0.1                                   | 0.2                      | 20     | <422                        | -       | 106         | -       | 6.31x10 <sup>-6</sup>    | -                     | [181] |
| IR, P.              | Pt (110)    | 0.2 cm OD spheres                                       | 0.1                                   | 0.2                      | 20     | <422                        | -       | 123         | -       | 6.31x10 <sup>-6</sup>    | -                     | [181] |
| M, P.               | Pt/C        | 14 μg/cm <sup>2</sup> , Nafion <sup>®</sup> film on GC. | 0.5                                   | 0.5                      | 60     | <550                        | -       | 80          | -       | -                        | -                     | [182] |
| P.                  | Pt black    | 5.6 and 4.2 mg/cm <sup>2</sup> , on N-315.              | 0.5                                   | 1                        | 16-20  | 400-700                     | 400-700 | 100-140     | 100-140 | -                        | -                     | [181] |
| R <sub>s</sub> , P. | Pt black    | 5.6 and 4.2 mg/cm <sup>2</sup> , on N-315.              | 0.5                                   | 1                        | 16-20  | <500                        | >600    | 60          | 120     | 4.00x10 <sup>-8</sup>    | 1.55x10 <sup>-6</sup> | [183] |
| R <sub>s</sub> , P. | Pt/C        | 40 wt%, on GC.                                          | 0.5                                   | 0.1-2                    | 30-80  | <650                        | -       | 80-94       | -       | 2.00x10 <sup>-8</sup>    | -                     | [184] |
| IR, G.              | Pt-Ru/C     | 40 wt%, 1:1, 3.2 mg/cm <sup>2</sup> , on GC.            | 0.5                                   | 0.5                      | 40-70  | <550                        | >550    | 108-128     | 300-700 | 5.24x10 <sup>-5</sup>    | 8.95x10 <sup>-4</sup> | [177] |
| IR, G.              | Pt-Ru/C     | 40 wt%, 1:1, 3.2 mg/cm <sup>2</sup> , on GC.            | 0.5                                   | 0.5                      | 40     | <550                        | >550    | 128         | 525     | 2.51x10 <sup>-4</sup>    | 7.41x10 <sup>-4</sup> | [177] |
| IR, G.              | Pt-Ru/C     | 40 wt%, 1:1, 3.2 mg/cm <sup>2</sup> , on GC.            | 0.5                                   | 0.5                      | 40     | <550                        | >550    | 123         | 647     | 3.51x10 <sup>-5</sup>    | 8.19x10 <sup>-4</sup> | [177] |
| IR, G.              | Pt-Ru/C     | 40 wt%, 1:1, 3.2 mg/cm <sup>2</sup> , on GC.            | 0.5                                   | 0.5                      | 40     | <550                        | >550    | 116         | 465     | 1.48x10 <sup>-6</sup>    | 2.24x10 <sup>-4</sup> | [177] |
| IR, G.              | Pt-Ru/C     | 40 wt%, 1:1, 3.2 mg/cm <sup>2</sup> , on GC.            | 0.5                                   | 0.5                      | 70     | <550                        | >550    | 114         | 650     | 1.64x10 <sup>-5</sup>    | 2.27x10 <sup>-3</sup> | [177] |
| IR, G.              | Pt-Ru/C     | 40 wt%, 1:1, 3.2 mg/cm <sup>2</sup> , on GC.            | 0.5                                   | 0.5                      | 70     | <550                        | >550    | 124         | 777     | 1.00x10 <sup>-5</sup>    | 1.00x10 <sup>-3</sup> | [177] |
| IR, G.              | Pt-Ru/C     | 40 wt%, 1:1, 3.2 mg/cm <sup>2</sup> , on GC.            | 0.5                                   | 0.5                      | 70     | <550                        | >550    | 108         | 537     | 1.93x10 <sup>-7</sup>    | 3.16x10 <sup>-4</sup> | [177] |
| M, P.               | Pt-Ru/C     | 14 μg/cm <sup>2</sup> , Nafion <sup>®</sup> film on GC. | 0.5                                   | 0.5                      | 60     | <550                        | -       | 195         | -       | -                        | -                     | [182] |
| R <sub>s</sub> , P. | Pt-Ru black | 5.6 and 4.2 mg/cm <sup>2</sup> , on N-315.              | 0.5                                   | 1                        | 16-20  | <500                        | >600    | 70          | 163     | 2.88x10 <sup>-7</sup>    | 2.88x10 <sup>-6</sup> | [183] |
| R <sub>s</sub> , P. | Pt-Ru/C     | 30 wt%, 1:1, on GC                                      | 0.5                                   | 0.1-2                    | 30-80  | <650                        | -       | 140-192     | -       | 4.50x10 <sup>-12</sup>   | -                     | [184] |

| Method                  | Catalyst         | Electrode<br>Description                               | Experimental Conditions           |                      |        | Anode Overpotential   |         | Tafel Slope |         | Exchange Current Density   |                        | Ref.  |
|-------------------------|------------------|--------------------------------------------------------|-----------------------------------|----------------------|--------|-----------------------|---------|-------------|---------|----------------------------|------------------------|-------|
|                         |                  |                                                        | [H <sub>2</sub> SO <sub>4</sub> ] | [CH <sub>3</sub> OH] | T      | $\eta_a$ [mV vs. SHE] |         | b [mV/dec]  |         | $i_0$ [A/cm <sup>2</sup> ] |                        |       |
|                         |                  |                                                        | [M]                               | [M]                  | [°C]   | Zone I                | Zone II | Zone I      | Zone II | Zone I                     | Zone II                |       |
| R <sub>s</sub> , IR, V. | Pt-Ru/C          | 40 wt%, 1:1, 1 mg/cm <sup>2</sup> , on TGPH-60.        | 1                                 | 1                    | 20-80  | <750                  | -       | 159-169     | -       | -                          | -                      | [185] |
| V.                      | Pt-Ru/C          | 1.5 mg/cm <sup>2</sup> , carbon cloth with GDL, N-117. | 0.5                               | 0.1, 1               | 20-45  | -                     | -       | 60          | -       | -                          | -                      | [186] |
| V.                      | Pt/C             | 1.5 mg/cm <sup>2</sup> , carbon cloth with GDL, N-117. | 0.5                               | 0.1, 1               | 25     | -                     | -       | 80          | -       | -                          | -                      | [186] |
| V.                      | Pt/C             | 1.5 mg/cm <sup>2</sup> , carbon cloth with GDL, N-117. | 0.5                               | 0.1, 1               | 45     | -                     | -       | 90          | -       | -                          | -                      | [186] |
| R.                      | Pt               |                                                        | 0.5                               | 1                    | Room T | -                     | -       | 125         | -       | -                          | -                      | [187] |
| F, P.                   | Pt/C             | 20 wt%, 50-100 ug/cm <sup>2</sup> , on GC.             | 0.5                               | 0.1                  | 100    | >330                  | -       | 83          | -       | -                          | -                      | [188] |
| R                       | Pt (oxide free)  | -                                                      | 0.1 N                             | -                    | -      | -                     | -       | 70          | -       | 2.00x10 <sup>-11</sup>     | -                      | [179] |
| G                       | Pt               | -                                                      | 1 N                               | -                    | 25     | -                     | -       | 65          | -       | 1.00x10 <sup>-9</sup>      | -                      | [179] |
| G                       | Pt black         | -                                                      | 20 wt%                            | -                    | 70     | -                     | -       | 65          | -       | 4.00x10 <sup>-10</sup>     | -                      | [179] |
| R                       | Pt               | -                                                      | 0.05                              | -                    | 25     | -                     | -       | 145         | -       | 3.00x10 <sup>-6</sup>      | -                      | [179] |
| -                       | Ru               | -                                                      | 1 N                               | -                    | 25     | -                     | -       | 80          | -       | 1.00x10 <sup>-12</sup>     | -                      | [179] |
| -                       | Pt               | -                                                      | 1 N                               | -                    | 20     | -                     | -       | 107         | -       | 7.60x10 <sup>-10</sup>     | -                      | [179] |
| -                       | Pt (111)         | -                                                      | 1 N                               | -                    | 20     | -                     | -       | 120         | -       | 3.70x10 <sup>-10</sup>     | -                      | [179] |
| -                       | Pt (100)         | -                                                      | 1 N                               | -                    | 20     | -                     | -       | 114         | -       | 6.40x10 <sup>-10</sup>     | -                      | [179] |
| -                       | Pt               | -                                                      | 1 N                               | -                    | 80     | -                     | -       | 90          | -       | 1.30x10 <sup>-11</sup>     | -                      | [179] |
| -                       | Pt-Ru            | 50 atom % Ru                                           | 1 N                               | -                    | 80     | -                     | -       | 120         | -       | 1.80 x10 <sup>-8</sup>     | -                      | [179] |
| -                       | Ru               | -                                                      | 1 N                               | -                    | 80     | -                     | -       | 41          | -       | 5.10 x10 <sup>-9</sup>     | -                      | [179] |
| P                       | RuO <sub>2</sub> | -                                                      | 1                                 | -                    | -      | -                     | -       | 30-40       | 50-65   | 5-15 x10 <sup>-9</sup>     | -                      | [179] |
| P, IR                   | RuOx             | -                                                      | 1 N                               | -                    | 25     | -                     | -       | 32          | 42      | 7.00 x10 <sup>-13</sup>    | 1.00x10 <sup>-11</sup> | [179] |

Legend: all italic values are average values estimated from graphs, F = flow through, G = galvanostatic mode (constant current applied vs. time, monitor V vs. time), IR = IR corrected current density, M = mass specific current density, P = potentiostatic mode (constant potential applied vs. time, monitor I vs. time), R = Rotating disk electrode using the Levich method, R<sub>s</sub> = real surface area current density, V = voltammetry.

Table 2.3: Tafel kinetic parameters from current work for the electro-oxidation of methanol and water on Pt and Pt-Ru catalysts.

| Method | Catalyst    | Electrode<br>Description                                      | Experimental Conditions           |                      |      | Anode Overpotential   |         | Tafel Slope |         | Exchange Current Density   |                         |
|--------|-------------|---------------------------------------------------------------|-----------------------------------|----------------------|------|-----------------------|---------|-------------|---------|----------------------------|-------------------------|
|        |             |                                                               | [H <sub>2</sub> SO <sub>4</sub> ] | [CH <sub>3</sub> OH] | T    | $\eta_a$ [mV vs. SHE] |         | b [mV/dec]  |         | $i_o$ [A/cm <sup>2</sup> ] |                         |
|        |             |                                                               | [M]                               | [M]                  | [°C] | Zone I                | Zone II | Zone I      | Zone II | Zone I                     | Zone II                 |
| G, IR. | Pt-Ru/C     | 50:50, 4 mg/cm <sup>2</sup> , on TGPH-60, N-117. <sup>1</sup> | 0.5                               | 0                    | 23   | <600                  | >600    | 125.90      | 125.90  | 7.33x10 <sup>-16</sup>     | 7.33x10 <sup>-16</sup>  |
| G, IR. | Pt-Ru/C     | 50:50, 4 mg/cm <sup>2</sup> , on TGPH-60, N-117. <sup>1</sup> | 0.5                               | 1                    | 23   | <600                  | >600    | 134.50      | 557.9   | 9.77x10 <sup>-8</sup>      | 1.27x10 <sup>-4</sup>   |
| G, IR. | Pt-Ru/C     | 50:50, 4 mg/cm <sup>2</sup> , on TGPH-60, N-117. <sup>1</sup> | 0.5                               | 2                    | 23   | <600                  | >600    | 159.70      | 649.20  | 3.46x10 <sup>-7</sup>      | 1.50x10 <sup>-4</sup>   |
| G, IR. | Pt-Ru/C     | 50:50, 4 mg/cm <sup>2</sup> , on TGPH-60, N-117. <sup>1</sup> | 0.5                               | 6                    | 23   | <600                  | >600    | 191.6       | 1407.8  | 2.89x10 <sup>-6</sup>      | 1.60x10 <sup>-3</sup>   |
| G, IR. | Pt-Ru/C     | 50:50, 4 mg/cm <sup>2</sup> , on TGPH-60, N-117. <sup>1</sup> | 0.5                               | 16                   | 23   | <600                  | >600    | 186.40      | 274.60  | 8.22 x10 <sup>-7</sup>     | 1.03x10 <sup>-5</sup>   |
| G, IR. | Pt/C        | 50:50, 4 mg/cm <sup>2</sup> , on TGPH-60, N-117. <sup>1</sup> | 0.5                               | 0                    | 23   | <600                  | >600    | 176.60      | 176.60  | 1.94x10 <sup>-12</sup>     | 1.94x10 <sup>-12</sup>  |
| G, IR. | Pt/C        | 50:50, 4 mg/cm <sup>2</sup> , on TGPH-60, N-117. <sup>1</sup> | 0.5                               | 2                    | 23   | <600                  | >600    | 113.40      | 447.80  | 1.42x10 <sup>-8</sup>      | 7.53x10 <sup>-5</sup>   |
| G, IR. | Pt/C        | 50:50, 4 mg/cm <sup>2</sup> , on TGPH-60, N-117. <sup>1</sup> | 0.5                               | 16                   | 23   | <600                  | >600    | 104.40      | 284.90  | 5.40x10 <sup>-9</sup>      | 2.19x10 <sup>-5</sup>   |
| G, IR. | Pt-Ru black | 50:50, 4 mg/cm <sup>2</sup> , on TGPH-60, N-117. <sup>3</sup> | 0.5                               | 0                    | 23   | <600                  | >600    | 244.80      | 244.80  | 4.40x10 <sup>-9</sup>      | 4.40x10 <sup>-9</sup>   |
| G, IR. | Pt-Ru black | 50:50, 4 mg/cm <sup>2</sup> , on TGPH-60, N-117. <sup>3</sup> | 0.5                               | 2                    | 23   | <600                  | >600    | 144.80      | 701.60  | 5.45x10 <sup>-6</sup>      | 1.16x10 <sup>-2</sup>   |
| G, IR. | Pt-Ru black | 50:50, 4 mg/cm <sup>2</sup> , on TGPH-60, N-117. <sup>3</sup> | 0.5                               | 16                   | 23   | <600                  | >600    | 156.10      | 527.90  | 1.20x10 <sup>-5</sup>      | 7.13x10 <sup>-3</sup>   |
| G, IR. | Pt black    | 2 mg/cm <sup>2</sup> . <sup>4</sup>                           | 0.5                               | 0                    | 23   | <600                  | >600    | 150.30      | 150.30  | 1.19x10 <sup>-12</sup>     | 1.19x10 <sup>-12</sup>  |
| G, IR. | Pt black    | 2 mg/cm <sup>2</sup> . <sup>4</sup>                           | 0.5                               | 2                    | 23   | <600                  | >600    | 147.20      | 640.60  | 3.10x10 <sup>-6</sup>      | 5.03x10 <sup>-3</sup>   |
| G, IR. | Pt black    | 2 mg/cm <sup>2</sup> . <sup>4</sup>                           | 0.5                               | 16                   | 23   | <600                  | >600    | 142.00      | 522.30  | 2.11x10 <sup>-6</sup>      | 2.74x10 <sup>-3</sup>   |
| G, IR. | Pt Disk     | 0.25 mm thick, 99.99% <sup>+</sup> Pt. <sup>2</sup>           | 0.5                               | 0                    | 23   | <600                  | >600    | 120.60      | 120.6   | 6.54x10 <sup>-77</sup>     | 6.54x10 <sup>-27</sup>  |
| G, IR. | Pt Disk     | 0.25 mm thick, 99.99% <sup>+</sup> Pt. <sup>2</sup>           | 0.5                               | 1                    | 23   | <600                  | >600    | 400.30      | 400.30  | 7.75x10 <sup>-7</sup>      | 7.75x10 <sup>-7</sup>   |
| G, IR. | Pt Disk     | 0.25 mm thick, 99.99% <sup>+</sup> Pt. <sup>2</sup>           | 0.5                               | 1                    | 23   | <600                  | >600    | 49.30       | 408.70  | 1.19x10 <sup>-15</sup>     | 6.60x10 <sup>-5</sup>   |
| G, IR. | Pt Disk     | 0.25 mm thick, 99.99% <sup>+</sup> Pt. <sup>2</sup>           | 0.5                               | 2                    | 23   | <600                  | >600    | 143.90      | 325.20  | 1.29x10 <sup>-5</sup>      | 2.37x10 <sup>-3</sup>   |
| G, IR. | Pt Disk     | 0.25 mm thick, 99.99% <sup>+</sup> Pt. <sup>2</sup>           | 0.5                               | 6                    | 23   | <600                  | >600    | 145.50      | 393.90  | 3.70x10 <sup>-5</sup>      | 8.68x10 <sup>-3</sup>   |
| G, IR. | Pt Disk     | 0.25 mm thick, 99.99% <sup>+</sup> Pt. <sup>2</sup>           | 0.5                               | 16                   | 23   | <600                  | >600    | 155.30      | 533.20  | 1.24x10 <sup>-4</sup>      | 4.49x10 <sup>-2</sup>   |
| G, IR. | Pt-Ru/C     | 50:50, 4 mg/cm <sup>2</sup> , on TGPH-60, N-117. <sup>1</sup> | 0.5                               | 0                    | 50   | <600                  | >600    | 359.60      | 359.60  | 5.83x10 <sup>-12</sup>     | 5.83 x10 <sup>-12</sup> |
| G, IR. | Pt-Ru/C     | 50:50, 4 mg/cm <sup>2</sup> , on TGPH-60, N-117. <sup>1</sup> | 0.5                               | 2                    | 50   | <600                  | >600    | 145.40      | 140.00  | 4.52x10 <sup>-10</sup>     | 3.08 x10 <sup>-4</sup>  |
| G, IR. | Pt-Ru/C     | 50:50, 4 mg/cm <sup>2</sup> , on TGPH-60, N-117. <sup>1</sup> | 0.5                               | 16                   | 50   | <600                  | >600    | 126.20      | 216.10  | 3.10x10 <sup>-10</sup>     | 3.34x10 <sup>-8</sup>   |

| Method | Catalyst | Electrode<br>Description                                      | Experimental Conditions           |                      |      | Anode Overpotential   |         | Tafel Slope |         | Exchange Current Density   |                        |
|--------|----------|---------------------------------------------------------------|-----------------------------------|----------------------|------|-----------------------|---------|-------------|---------|----------------------------|------------------------|
|        |          |                                                               | [H <sub>2</sub> SO <sub>4</sub> ] | [CH <sub>3</sub> OH] | T    | $\eta_a$ [mV vs. SHE] |         | b [mV/dec]  |         | $i_o$ [A/cm <sup>2</sup> ] |                        |
|        |          |                                                               | [M]                               | [M]                  | [°C] | Zone I                | Zone II | Zone I      | Zone II | Zone I                     | Zone II                |
| G, IR. | Pt-Ru/C  | 50:50, 4 mg/cm <sup>2</sup> , on TGPH-60, N-117. <sup>1</sup> | 0.5                               | 0                    | 75   | <600                  | >600    | 325.50      | 325.50  | 1.43x10 <sup>-11</sup>     | 1.43x10 <sup>-11</sup> |
| G, IR. | Pt-Ru/C  | 50:50, 4 mg/cm <sup>2</sup> , on TGPH-60, N-117. <sup>1</sup> | 0.5                               | 2                    | 75   | <600                  | >600    | 206.10      | 285.90  | 2.98x10 <sup>-7</sup>      | 1.59x10 <sup>-6</sup>  |
| G, IR. | Pt-Ru/C  | 50:50, 4 mg/cm <sup>2</sup> , on TGPH-60, N-117. <sup>1</sup> | 0.5                               | 16                   | 75   | <600                  | >600    | 215.10      | 222.30  | 2.93x10 <sup>-7</sup>      | 2.98x10 <sup>-7</sup>  |
| G, IR. | Pt-Ru/C  | 50:50, 4 mg/cm <sup>2</sup> , on TGPH-60, N-117. <sup>3</sup> | 0.5                               | 0                    | 23   | <600                  | >600    | -           | -       | 3.01x10 <sup>-24</sup>     | 3.01x10 <sup>-24</sup> |
| G, IR. | Pt-Ru/C  | 50:50, 4 mg/cm <sup>2</sup> , on TGPH-60, N-117. <sup>3</sup> | 0.5                               | 2                    | 23   | <600                  | >600    | -           | -       | 5.77x10 <sup>-6</sup>      | 8.24x10 <sup>-4</sup>  |
| G, IR. | Pt-Ru/C  | 50:50, 4 mg/cm <sup>2</sup> , on TGPH-60, N-117. <sup>3</sup> | 0.5                               | 16                   | 23   | <600                  | >600    | -           | -       | 1.33x10 <sup>-5</sup>      | 2.22x10 <sup>-2</sup>  |
| G, IR. | Pt-Ru/C  | 50:50, 4 mg/cm <sup>2</sup> , on TGPH-60, N-117. <sup>3</sup> | 0.5                               | 0                    | 50   | <600                  | >600    | -           | -       | 7.90x10 <sup>-11</sup>     | 7.90x10 <sup>-11</sup> |
| G, IR. | Pt-Ru/C  | 50:50, 4 mg/cm <sup>2</sup> , on TGPH-60, N-117. <sup>3</sup> | 0.5                               | 2                    | 50   | <600                  | >600    | -           | -       | 6.12x10 <sup>-9</sup>      | 4.17x10 <sup>-3</sup>  |
| G, IR. | Pt-Ru/C  | 50:50, 4 mg/cm <sup>2</sup> , on TGPH-60, N-117. <sup>3</sup> | 0.5                               | 16                   | 50   | <600                  | >600    | -           | -       | 4.20x10 <sup>-9</sup>      | 4.53x10 <sup>-7</sup>  |
| G, IR. | Pt-Ru/C  | 50:50, 4 mg/cm <sup>2</sup> , on TGPH-60, N-117. <sup>3</sup> | 0.5                               | 0                    | 75   | <600                  | >600    | -           | -       | 1.93x10 <sup>-10</sup>     | 1.93x10 <sup>-10</sup> |
| G, IR. | Pt-Ru/C  | 50:50, 4 mg/cm <sup>2</sup> , on TGPH-60, N-117. <sup>3</sup> | 0.5                               | 2                    | 75   | <600                  | >600    | -           | -       | 4.03x10 <sup>-6</sup>      | 2.15x10 <sup>-5</sup>  |
| G, IR. | Pt-Ru/C  | 50:50, 4 mg/cm <sup>2</sup> , on TGPH-60, N-117. <sup>3</sup> | 0.5                               | 16                   | 75   | <600                  | >600    | -           | -       | 3.98x10 <sup>-6</sup>      | 4.03x10 <sup>-6</sup>  |

Legend: all italic values are average values estimated from graphs, F = flow through, G = galvanostatic mode (constant current applied vs. time, monitor V vs. time), IR = IR corrected current density, M = mass specific current density, P = potentiostatic mode (constant potential applied vs. time, monitor I vs. time), R = Rotating disk electrode using the Levich method, R<sub>s</sub> = real surface area current density, V = voltammetry.

<sup>1</sup>Based on the electrochemical surface area of a 2 mg/cm<sup>2</sup> Pt/C catalyst determined by H<sub>2</sub> adsorption, <sup>2</sup> Geometric surface area assuming a roughness factor of 4, <sup>3</sup>Based on the electrochemical surface area of a 4 mg/cm<sup>2</sup> Pt-Ru black catalyst determined by Cu UPD, <sup>4</sup>Based on the electrochemical surface area of a 2 mg/cm<sup>2</sup> Pt black catalyst determined by H<sub>2</sub> adsorption.

A proper comparison with the literature is difficult due to differences in the experimental conditions and whether geometric or real surface area was used. The type of electrolyte, the electrolyte and CH<sub>3</sub>OH concentration, as well as the catalyst loading used varied among the studies and most Tafel parameters available were mainly obtained using single-compartment cells without membranes. In general, the reported Tafel slope using Pt-Ru catalysts ranged from 70 to 128 mV/dec at low overpotentials, and ranged from 75 to 777 mV/dec at high overpotentials. This is comparable to the 4 mg/cm<sup>2</sup> Pt-Ru/C catalyst Tafel slopes obtained at low CH<sub>3</sub>OH concentrations, but smaller than the ones obtained at high CH<sub>3</sub>OH concentrations in our work. Amongst different systems for which Tafel slopes were reported, the one used by Aramat *et al.* [183] seems to be the closest to our system. Tafel data was obtained using a two-compartment cell for unsupported catalyst coated with Nafion<sup>®</sup> 315 at 16-20°C in 1 M CH<sub>3</sub>OH and 0.5 M H<sub>2</sub>SO<sub>4</sub>. The Tafel slopes were in the range of 100-140 mV/dec for Pt black- Nafion<sup>®</sup> 315 in the overvoltage range of 0.4 to 0.7 V vs. SHE, 70 mV/dec for Pt-Ru black-N315 at  $\eta_a < 0.5$  V vs. SHE and 163 mV/dec for the same catalyst at  $\eta_a > 0.6$  V vs. SHE. The Tafel slopes obtained in our work using a 2 mg/cm<sup>2</sup> Pt black GDE anode and N117 membrane, were in agreement with the Pt-N315 reported values for  $\eta_a < 0.6$  V vs. SHE and CH<sub>3</sub>OH concentrations equal to or lower than 2 M. However, the Tafel slope values obtained in this study for CH<sub>3</sub>OH electrolysis with the Pt black catalyst at greater CH<sub>3</sub>OH concentrations and at  $\eta_a > 0.6$  V vs. SHE are up to four times higher than the ones reported in the literature. This may be linked to a change in the rate determining step at higher potentials, as it is known that CO stripping from an unsupported Pt-Ru catalyst surface normally occurs at potentials ranging from about 0.5 to 0.7 V vs. SHE at 25°C [189, 190].

Tafel slopes were also evaluated as a function of temperature using the 4 mg/cm<sup>2</sup> Pt-Ru/C anode at three different CH<sub>3</sub>OH concentrations. Zhang *et al.* [184] reported that at low temperatures, non-linearity is due to CO poisoning, while at high temperature, it is due to concentration polarization. They also noticed that Tafel slope data reported in the literature conflictingly increase or decrease with increasing temperature. This was attributed to different rate determining steps. In our study, the Tafel slopes values obtained for Pt-Ru/C were larger at ambient temperature than at 50°C, and the values obtained for the same catalyst at 75°C were the largest of all. Although it might be possible that the catalyst went through degradation at higher temperature, it is also possible that operation at 50°C is more desirable for

the Pt-Ru/C catalyst as it improves its activity for the electrolysis of CH<sub>3</sub>OH. From an efficiency standpoint, faster oxidation kinetics might allow the use of higher CH<sub>3</sub>OH concentrations. In general, reported Tafel slope values for Pt-Ru/C varied between 108 to 195 mV/dec in the temperature range of 60 to 80°C [177, 182, 184, 185], compared to experimental values obtained in this study which ranged from 126 to 215 mV/dec between 50 to 75°C. For  $\eta_a < 0.6$  V, the Tafel slopes obtained at 75°C and 2 to 16 M CH<sub>3</sub>OH averaged 211 mV/dec. This seems to be in reasonable agreement with the 192 mV/dec reported on 30 wt% Pt-Ru/C on glassy carbon at 80°C and low CH<sub>3</sub>OH concentration in a single compartment cell [184].

The effect of CH<sub>3</sub>OH concentration on the kinetic parameters seems to be complex and no clear trend could be established for the change in  $b$  and  $i_o$  values as a function of increasing CH<sub>3</sub>OH concentration. However, it can be observed that at ambient conditions and low overpotentials, the lowest Tafel slopes were obtained using the Pt/C anode, while the greatest Tafel slopes were obtained using the Pt-Ru/C anode. It was suggested by Zhang *et al.* [184] that high  $b$  values on Pt-Ru/C are due to the initial dissociative dehydrogenation of CH<sub>3</sub>OH while low  $b$  values for Pt/C are due to the oxidation of CO rather than an adsorption process. Based on the real surface area of a 2 mg/cm<sup>2</sup> catalyst determined by H<sub>2</sub> adsorption, at 2 M CH<sub>3</sub>OH and for  $\eta_a < 0.6$  V, the  $b$  value obtained in this study was about 30% larger for Pt-Ru/C than for Pt/C, and the  $i_o$  value was about 96 % smaller for Pt/C than for Pt-Ru/C. Under those conditions, the oxidation of CH<sub>3</sub>OH may occur faster on Pt-Ru/C than on Pt/C. For the same conditions, but at  $\eta_a > 0.6$  V, the  $b$  value obtained was also about 30 % larger for Pt-Ru/C than for Pt/C. Similarly, the value of  $i_o$  was about still 96 % smaller for Pt/C than for Pt-Ru/C. The  $i_o$  value determined based on the ECSA of the 4 mg/cm<sup>2</sup> Pt-Ru/C catalyst obtained by Cu UPD was even larger. Based on this, it is likely that Pt-Ru/C possesses a superior catalytic activity for the electrolysis of CH<sub>3</sub>OH than Pt/C. This difference was not observed between the Pt-Ru black and Pt black anodes at ambient conditions, which had similar Tafel slopes at all concentrations. For pure Pt, at CH<sub>3</sub>OH concentrations of 1 M or less, reported Tafel slopes ranged from 63 to 125 mV/dec below 0.6 V, and no Tafel data was reported for Pt above 0.6 V. As previously mentioned in *Section 2.3.2.2*, bi-stability was observed for the well-defined Pt case at 1 M CH<sub>3</sub>OH and two Tafel slopes were calculated. In the same potential range, it seems that

the Tafel value obtained for the more positive curve (49 mV/dec) is in much better agreement with the literature than the one obtained for the more negative curves (400 mV/dec).

The Tafel slope value of 121 mV/dec obtained for H<sub>2</sub>O electrolysis using the well-defined Pt disk is in agreement with the reported value range of 65 to 145 mV/dec at 20-25°C, however the corresponding  $i_0$  value is 100 % smaller than the ones reported in the literature. For H<sub>2</sub>O electrolysis, the Tafel slope was about 60 % larger for the Pt-Ru black catalyst than for the Pt black catalyst, which would indicate that Pt black is more favourable to H<sub>2</sub>O electrolysis than Pt-Ru black. However, the  $i_0$  value obtained was three orders of magnitude larger for Pt-Ru black than for Pt black. It was the largest  $i_0$  value obtained compared to all other catalysts tested for H<sub>2</sub>O electrolysis. Based on this, it seems like Pt-Ru black is a more favourable catalyst than Pt black for H<sub>2</sub>O electrolysis. The latter is in agreement with Miles *et al.* [191], who reported that Pt-Ru black was a better catalyst than Pt black for the O<sub>2</sub> evolution reaction in 0.1 M H<sub>2</sub>SO<sub>4</sub> at 80°C. They attributed this to the formation of an oxide film which decreased the Pt surface catalytic activity towards O<sub>2</sub> evolution. For H<sub>2</sub>O electrolysis at ambient conditions, the Pt/C catalyst had a  $b$  40 % greater than that for the Pt-Ru/C catalyst, and its  $i_0$  was 4 orders of magnitude smaller. This indicates that, under these conditions, Pt-Ru/C is more active for H<sub>2</sub>O electrolysis than Pt/C. The Tafel slopes for H<sub>2</sub>O electrolysis with the Pt-Ru/C at 50 and 75°C, were about 60 % higher than when using the same catalyst at ambient conditions.

The kinetic parameters reported for electrolysis are varied and often contradictory. It is important to note that at IR corrected anodic overpotentials greater than 0.6 V, mass transport effects are not negligible. Hence, the kinetic parameters extracted in this region do not likely represent true kinetic behaviour and have to be considered with caution as mass transport effects could explain some of the variability in reported results. A low overpotential, which is desired to use energy efficiently and to operate as close as possible to equilibrium, can be obtained by choosing a catalyst material and system resulting in a  $b$  value as small as possible and an  $i_0$  value as large as possible for the desired electrochemical reaction.

### 2.3.2.6 Activation energy

The activation energy was determined for CH<sub>3</sub>OH electrolysis using the Pt-Ru/C catalyst. It can be determined from the Arrhenius equation:

$$\ln(i_o) = \ln(i_o^0) - \frac{E_A}{RT} \quad (2.11)$$

where  $i_o^0$  is the absolute exchange current density of the reaction, which represents the maximum  $i_o$  at infinite temperature, i.e.,  $i_{o(T \rightarrow \infty)}$ . Using the exchange current densities based on the ECSA estimated from the intercept of the Tafel Plots, Arrhenius plots ( $\log(i_o)$  vs.  $1/T$ ) were constructed for various CH<sub>3</sub>OH concentrations in the linear kinetic Tafel region (<0.6 V) and in the region just above 0.6 V, where the effect of mass transfer starts to appear. The apparent activation energy,  $E_a$ , was determined from the slope ( $-E_a/R$ ) of the fitted linear trends. The values obtained, as well as some values reported in the literature, are included in Table 2.4. In agreement with the literature [184], over the concentration range studied, the larger the CH<sub>3</sub>OH concentration, the larger was the resulting  $E_a$  value. The  $E_a$  values obtained with the Pt-Ru/C anode in the kinetic region below 0.6 V are significantly lower than the smallest values reported in the literature, although the  $E_a$  values reported in the literature were obtained in single compartment cells and not using MEAs as in the present study. Zhang *et al.* [184] have reported that small  $E_a$  values (20-30 kJ/mol) obtained at low CH<sub>3</sub>OH concentrations (0.1-0.5 M), indicate that CO surface diffusion is the rate determining step. These researchers obtained larger  $E_a$  values (51-84 kJ/mol), at higher CH<sub>3</sub>OH concentrations (1, 2 M) representing a change in the rate determining step. At  $E_a$  values of about 60 kJ/mol, the dissociative adsorption of CH<sub>3</sub>OH is the rate determining step, while at  $E_a$  values around 70 kJ/mol, CO oxidation is the rate determining step. In this study, the  $E_a$  values obtained in the region below 0.6 V vs. SHE for 2 and 16 M CH<sub>3</sub>OH are both below 30 kJ/mol. This might signify that, under those conditions, CO surface diffusion is the rate determining step. The  $E_a$  values obtained in the region above 0.6 V vs. SHE for 2 and 16 M CH<sub>3</sub>OH are 50 and 154 kJ/mol, respectively. Although there were no changes in the rate determining step for the electrolysis of CH<sub>3</sub>OH on Pt-Ru/C as

a function of CH<sub>3</sub>OH concentration in the low potential region, there might be one in the high potential region.

Table 2.4: Activation energy data for the electro-oxidation of methanol on Pt and Pt-Ru catalysts.

| Catalyst   | Anode Description                                                                                                    | Concentration                         |                          | Temperature Range [°C] | Anode Overpotential $\eta_a$ [V vs. SHE] |         | Activation Energy $E_a$ [kJ/mol] |         | Ref.         |
|------------|----------------------------------------------------------------------------------------------------------------------|---------------------------------------|--------------------------|------------------------|------------------------------------------|---------|----------------------------------|---------|--------------|
|            |                                                                                                                      | [H <sub>2</sub> SO <sub>4</sub> ] [M] | [CH <sub>3</sub> OH] [M] |                        | Zone I                                   | Zone II | Zone I                           | Zone II |              |
| Pt-Ru      | 50:50                                                                                                                | 0.5                                   | 1                        | 17-50                  | 0.50                                     | -       | 60                               | -       | [186]        |
| Pt         | -                                                                                                                    | 0.5                                   | 1                        | 17-50                  | 0.50                                     | -       | 30                               | -       | [192]        |
| Pt(100)-Ru | -                                                                                                                    | 0.5                                   | 0.6                      | 0-65                   | 0.25                                     | -       | 61 ± 11                          | -       | [192]        |
| Pt(100)-Ru | -                                                                                                                    | 0.5                                   | 0.6                      | 0-65                   | 0.31                                     | -       | 53 ± 7                           | -       | [192]        |
| Pt(100)-Ru | -                                                                                                                    | 0.5                                   | 0.6                      | 0-65                   | 0.37                                     | -       | 65 ± 4                           | -       | [192]        |
| Pt(110)-Ru | -                                                                                                                    | 0.5                                   | 0.6                      | 0-65                   | 0.25                                     | -       | 38 ± 4                           | -       | [192]        |
| Pt(110)-Ru | -                                                                                                                    | 0.5                                   | 0.6                      | 0-65                   | 0.31                                     | -       | 50 ± 5                           | -       | [192]        |
| Pt(110)-Ru | -                                                                                                                    | 0.5                                   | 0.6                      | 0-65                   | 0.37                                     | -       | 47 ± 8                           | -       | [192]        |
| Pt(111)/Ru | Deposited Ru from 2x10 <sup>-4</sup> M Ru(NO)(NO <sub>3</sub> ) <sub>3</sub> in 0.5 M H <sub>2</sub> SO <sub>4</sub> | 0.5                                   | 0.6                      | 0-65                   | 0.25                                     | -       | 84 ± 10                          | -       | [192]        |
| Pt(111)/Ru | Deposited Ru from 2x10 <sup>-4</sup> M Ru(NO)(NO <sub>3</sub> ) <sub>3</sub> in 0.5 M H <sub>2</sub> SO <sub>4</sub> | 0.5                                   | 0.6                      | 0-65                   | 0.31                                     | -       | 66 ± 7                           | -       | [192]        |
| Pt(111)/Ru | Deposited Ru from 2x10 <sup>-4</sup> M Ru(NO)(NO <sub>3</sub> ) <sub>3</sub> in 0.5 M H <sub>2</sub> SO <sub>4</sub> | 0.5                                   | 0.6                      | 0-65                   | 0.37                                     | -       | 56 ± 5                           | -       | [192]        |
| Pt(111)/Ru | 5X10 <sup>-5</sup> M RuCl <sub>3</sub> in 0.1 M HClO <sub>4</sub>                                                    | 0.5                                   | 0.6                      | 0-65                   | 0.25                                     | -       | 70 ± 7                           | -       | [192]        |
| Pt(111)/Ru | 5X10 <sup>-5</sup> M RuCl <sub>3</sub> in 0.1 M HClO <sub>4</sub>                                                    | 0.5                                   | 0.6                      | 0-65                   | 0.31                                     | -       | 56 ± 5                           | -       | [192]        |
| Pt(111)/Ru | 5X10 <sup>-5</sup> M RuCl <sub>3</sub> in 0.1 M HClO <sub>4</sub>                                                    | 0.5                                   | 0.6                      | 0-65                   | 0.37                                     | -       | 54 ± 4                           | -       | [192]        |
| Pt-Ru/C    | 30 wt%, 1:1                                                                                                          | 0.5                                   | 0.1, 0.5, 1, 2           | 30-80                  | -                                        | -       | 54-84                            | -       | [184]        |
| Pt/C       | 40 wt%                                                                                                               | 0.5                                   | 0.1, 0.5, 1, 2           | 30-80                  | -                                        | -       | 23-78                            | -       | [184]        |
| Pt-Ru/C    | 40 wt%, 1:1                                                                                                          | 1                                     | 1                        | 20-80                  | -                                        | -       | 33.6                             | -       | [185]        |
| Pt-Ru/C    | 3.2 mg/cm <sup>2</sup>                                                                                               | 0.5                                   | 0.5                      | 23-70                  | -                                        | -       | 62.5                             | -       | [174]        |
| Pt-Ru/C    | 50:50, 4 mg/cm <sup>2</sup>                                                                                          | 0.5                                   | 2                        | 23-75                  | <0.60                                    | >0.60   | 12.1                             | 59.72   | Current work |
| Pt-Ru/C    | 50:50, 4 mg/cm <sup>2</sup>                                                                                          | 0.5                                   | 16                       | 23-75                  | <0.60                                    | >0.60   | 27.46                            | 154.12  | Current work |

## 2.4 Summary

It was thermodynamically and experimentally demonstrated that H<sub>2</sub> production from CH<sub>3</sub>OH electrolysis in aqueous acidic media is significantly more effective than the H<sub>2</sub> production from acidic H<sub>2</sub>O electrolysis. The theoretical thermodynamic evaluation proved that alcohol electrochemical reforming systems could become thermodynamically-favourable under certain operating conditions. It was estimated that in the liquid phase CH<sub>3</sub>OH electrolysis becomes thermodynamically favourable at about 41°C. However, it was demonstrated that at 50 and 75°C, the kinetics were not favourable and energy was still required to electrochemically generate H<sub>2</sub> from the acidic aqueous CH<sub>3</sub>OH solution with all catalysts. The kinetics of the PEM electrolyser were investigated for the first time under static conditions, i.e., stirred solutions, but no flow-through or recycling systems were investigated. For all catalysts studied, it was possible to operate the CH<sub>3</sub>OH electrolyser at much greater current densities than the H<sub>2</sub>O electrolyser. The electrolysis has to be carried-out at currents ( $< i_L$ ) and voltages ( $> -1.8$  V) that avoid carbon oxidation or more stable materials comprising no carbon should be used. In acidic aqueous media and for all operating conditions, carbon oxidation and catalyst degradation prevented the DMR or PEM electrolyser from sustaining higher currents in the vicinity of the limiting current. Operating the CH<sub>3</sub>OH electrolyser with a dry cathode, purged with N<sub>2</sub> resulted in similar cell voltage requirements for electrolysis, particularly at high current densities. Very limited kinetic data was found to describe similar electrochemical systems in the literature. Only two studies were found to report kinetic data on catalyzed membranes or electrodes with membranes in the literature. All data available focusing on the electro-oxidation of CH<sub>3</sub>OH was determined for low concentrations of CH<sub>3</sub>OH ( $< 2$  M). The Tafel kinetic analysis carried out revealed that Pt-Ru binary catalysts enhance the kinetics of the CH<sub>3</sub>OH oxidation. The activation energy obtained with the MEA was found to be in the same range as previously reported values for similar systems. A comprehensive baseline study was established for future comparison with other PEM electrolysers.

## Chapter 3: Electrochemical Promotion of Electrocatalysis (EPOE)

### 3.1 Synopsis

In this Chapter, the use of electrochemical promotion in triode and tetrode operation was investigated as a method to improve the kinetics of the direct aqueous acidic CH<sub>3</sub>OH PEM electrolyser or reformer studied in *Chapter 2*. To the author's knowledge, the application of electrochemical promotion of electrocatalysis concept described in *Section 1.3.5* to the electrolysis mode remains an unexplored area which requires more research. This Chapter consists of a comprehensive study of the triode and tetrode electrolysis concept, and addresses aspects of this knowledge gap. Triode and tetrode operation was shown to have an electrochemical promotion effect on the PEM electrolysis of liquid CH<sub>3</sub>OH and water for H<sub>2</sub> production in a non-flowing system at ambient conditions in the galvanostatic mode and in the potentiostatic mode. A decrease in electrolysis voltage requirements proportional to the current or potential imposed in the auxiliary circuit was observed only when the auxiliary current or potential was opposite to the electrolyser circuit current or potential. The effect was observed with catalytic and non-catalytic electrolyser ring working electrode and auxiliary working electrode materials. It was shown that the improvement obtained was not caused by intrinsic membrane or solution conductivity enhancements during triode operation and was not due to carbon oxidation of the carbon fibre paper at the electrolyser ring electrode. Some design aspects of the triode and tetrode electrolyser were investigated in order to further elucidate the mechanism causing the enhancements observed. The need for electrode contact with the electrolyte was investigated, as well as the effect of the electrolyser working electrode ring geometry, the orientation of the proton flux lines, and the use of a high-surface area carbon electrolyser working electrode were studied. It appears that triode and tetrode operation enhanced the electro-oxidation through the electrochemical pumping of protons and proton spillover. Triode and tetrode operation may lead to electrolysis cost reduction through the use of smaller amounts or no precious metal catalyst at the working electrodes while maintaining an adequate performance. Part of the work presented in this section was published and reprinted from the ECS Transactions, 25 (23), C. R. Cloutier,

and D. P. Wilkinson, "Triode Operation of a Proton Exchange Membrane (PEM) Electrolyser", 47-57, Copyright (2010), with permission from the Electrochemical Society.

### 3.2 Overview

Similar to the triode fuel cell, the triode electrolyser is composed of three electrodes: the electrolyser electrode, an auxiliary electrode, and a counter electrode (CE). Three electrodes form two electrical circuits: (a) the electrolyser circuit, which includes the electrolyser ring electrode and the CE, and (b) the auxiliary circuit, which includes the auxiliary electrode and the CE. The electrolyser ring electrode and the auxiliary electrode serve as the working electrodes (WE) of each respective circuit while the CE is the same for both circuits. A typical PEM triode electrolyser arrangement is shown in Fig. 3.1. The electrolyser  $WE_{elec}$  and the auxiliary  $WE_{aux}$ , are not physically or conductively connected to one another, i.e., electrons are not traveling between the WEs of both circuits. Therefore, the anodic or cathodic current of an electrolyser circuit electrode can not be added to the anodic or cathodic current of an auxiliary circuit electrode to form a total anodic or cathodic current. Both circuits are power sinks as under the studied conditions, their respective electrochemical reactions are not spontaneous, and they require the input of current or voltage to occur.

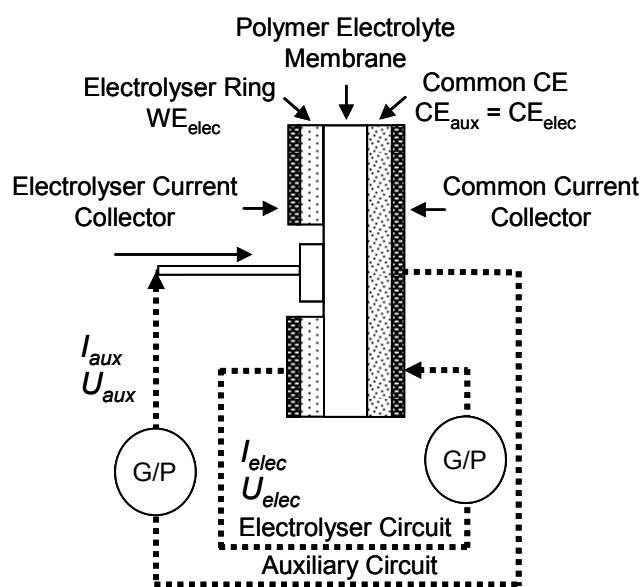


Figure 3.1: Schematic diagram of the triode electrolyser electrical circuit.

Examples of MEA side views of some of the different system configurations studied are illustrated in Fig. 3.2. The location of the auxiliary  $WE_{aux}$ , the electrolyser ring  $WE_{elec}$ , and the CE is shown. In normal operation, the electrolyser circuit uses the ring electrode while the auxiliary circuit uses the centered electrode. In inverted operation, the auxiliary circuit uses the ring electrode while the electrolysis circuit uses the centered electrode. Tetrode operation is similar to the triode concept, except that it uses a fourth auxiliary counter electrode. In tetrode operation, the electrolyser circuit and the auxiliary circuit are completely independent from one another. Triode tests were reproduced in the tetrode mode to confirm that the triode circuits were independent and not interacting.

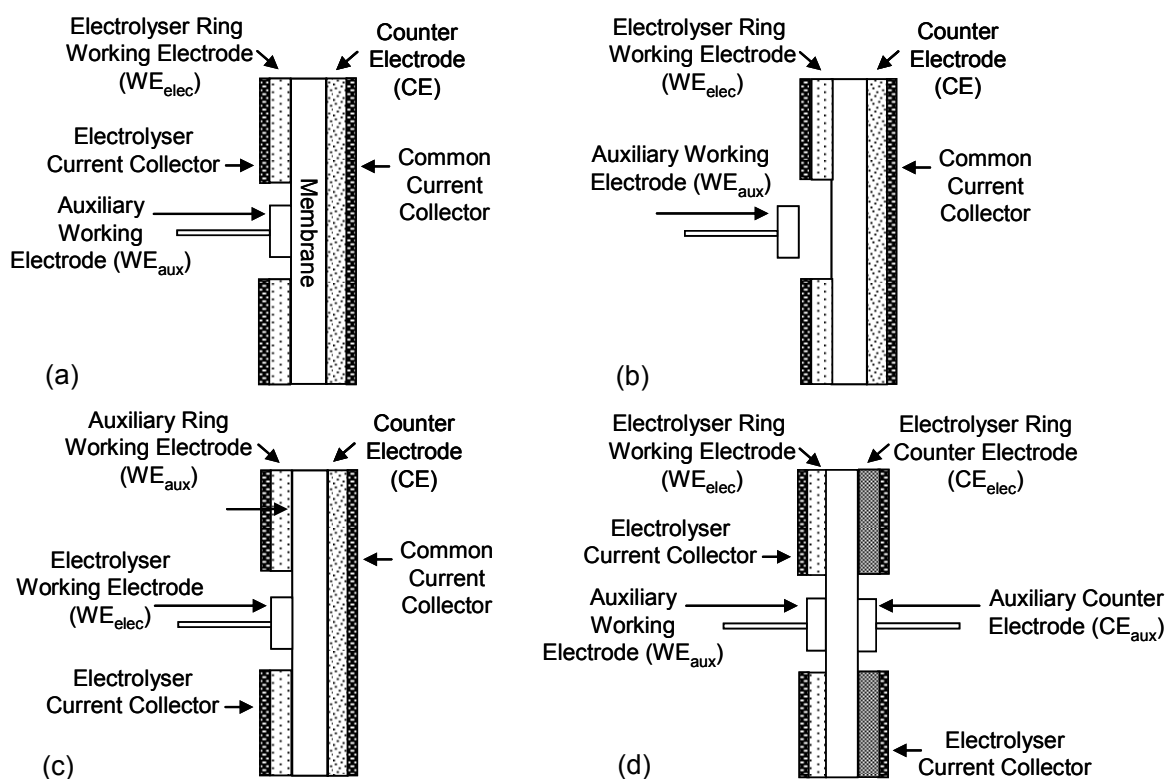


Figure 3.2: Side view of membrane electrode assemblies in different configurations: (a) triode, normal operation, common CE (b) like (a) with auxiliary  $WE_{aux}$  away from surface (c) like (a) in inverted operation, and (d) tetrode, normal operation, independent CEs.

The operation of the triode or tetrode configuration consists of promoting the electrolysis reaction through the use of an auxiliary circuit to impose electrolytic currents or potentials. When the auxiliary circuit is not used, the electrolyser operates in the conventional electrolysis mode. However, when it is used in

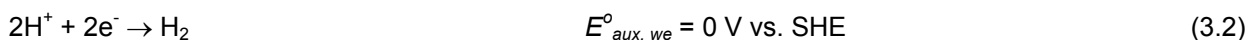
the galvanostatic mode, the auxiliary circuit affects the potential of the anode and the cathode of the primary electrolyser circuit. Balomenou *et al.* [19] showed that by applying Kirchhoff's first law, to the WE of a fuel cell triode, a simple equation can be derived to explain the circuit current relationships in triode operation. Details on how this equation was derived can be found in *Appendix D*. For triode or tetrode electrolysis, this relationship becomes:

$$I_{elec} = I_{Far} + I_{aux} \quad (3.1)$$

where  $I_{elec}$  is the electrolyser circuit current,  $I_{Far}$  is the net Faradaic fuel-consuming current, and  $I_{aux}$  is the auxiliary circuit current. According to this formula, when the auxiliary circuit is not used, then  $I_{aux} = 0$ , and  $I_{elec} = I_{Far}$ . Therefore, in triode or tetrode operation,  $I_{Far}$  corresponds to the current remaining after subtracting the auxiliary circuit current. In the galvanostatic mode, the fixed value of the imposed electrolyser circuit current is always positive, while the varying value of the imposed auxiliary current can be positive or negative. Therefore, in triode or tetrode operation, the magnitude of  $I_{aux}$  will affect  $I_{Far}$ .

The auxiliary circuit current can operate in the same direction as the electrolyser (parallel) or in a direction opposite to the electrolyser (reverse). In other words, the polarity of the auxiliary WE can be changed to be in anodic or in cathodic operation. The polarity of the auxiliary WE may affect the potential of the electrolyser circuit WE. In either cases, (Eq. 3.1) remains valid, as the sign of  $I_{aux}$  will be positive or negative for parallel or reverse operation, respectively. When the auxiliary circuit polarity is the same as the electrolyser circuit polarity, the triode electrolyser is in parallel operation. The electrolyser and the auxiliary circuits are operated like two electrolysers in parallel and the electrolysis anodic electrochemical reaction (Eq. 1.24) occurs on both electrodes in the anodic compartment of the cell in conjunction with H<sub>2</sub>O oxidation or O<sub>2</sub> evolution reaction if the potential is large enough (Eq. 1.21). That is, when the auxiliary circuit current polarity is opposite to the polarity of the electrolyser current, i.e., in the direction opposite to the electrolyser. Hence, this configuration is similar to having two electrolysis circuits in parallel, but working in directions opposite from one another. In this case, the normal electrolysis anodic electrochemical reactions (Eq. 1.24) and (Eq. 1.21) still occur at the electrolyser

electrode in the anodic cell compartment, but the electrochemical reaction occurring at the auxiliary WE<sub>aux</sub> in the anodic cell compartment will now be the H<sub>2</sub> evolution reaction (HER):



The H<sub>2</sub> evolution reaction independently occurring on the electrolyser CE (Eq. 1.25) and on the auxiliary WE<sub>aux</sub> (Eq. 3.2), has a low overvoltage compared to the electrochemical oxidation of CH<sub>3</sub>OH (Eq. 1.24) or H<sub>2</sub>O (Eq. 1.21) occurring on the electrolyser ring WE<sub>elec</sub>. The rate limiting step of the electro-oxidation reaction, in this case CH<sub>3</sub>OH electro-oxidation on the electrolyzer ring WE<sub>elec</sub>, will be the system's most sensitive electrochemical reaction to changes in current or potential, thus it will be most sensitive to electrochemical promotion. Table 3.1 summarizes all the possible half-cell reactions (all written in the reduction sense) which may occur at the various electrodes of the electrolyser and auxiliary circuits in triode or tetrode operation, along with their respective standard potential.

Table 3.1: List of possible half-cell reactions and their standard potentials.

| Half-cell reaction                                                                              | Standard cell potential |
|-------------------------------------------------------------------------------------------------|-------------------------|
|                                                                                                 | E° (V vs. SHE)          |
| $\text{H}_2\text{O} \rightarrow 1/2\text{O}_2 + 2\text{H}^+ + 2\text{e}^-$                      | -1.23                   |
| $\text{C} + \text{H}_2\text{O} \rightarrow \text{CO} + 2\text{H}^+ + 2\text{e}^-$               | -0.52                   |
| $\text{Ru} \rightarrow \text{Ru}^{2+} + 2\text{e}^-$                                            | -0.46                   |
| $\text{Ru}^{2+} \rightarrow \text{Ru}^{3+} + \text{e}^-$                                        | -0.25                   |
| $\text{C} + 2\text{H}_2\text{O} \rightarrow \text{CO}_2 + 4\text{H}^+ + 4\text{e}^-$            | -0.21                   |
| $\text{CH}_3\text{OH} + \text{H}_2\text{O} \rightarrow \text{CO}_2 + 6\text{H}^+ + 6\text{e}^-$ | -0.016                  |
| $\text{H}_2 \leftrightarrow 2\text{H}^+ + 2\text{e}^-$                                          | 0                       |

The experiments in this research were mainly carried out in normal operation (no electrochemical promotion) and in reverse operation (with electrochemical promotion). In normal operation, the electrolyser circuit or the auxiliary circuit were studied separately and independently, without triode or tetrode operation. Normal operation is indicated with the superscript "0", as previously done in the triode

fuel cell literature, and to be consistent with EPOC studies. Tests were conducted in the triode operating mode unless otherwise indicated. The electrolyser and auxiliary WEs located in the glass cell compartment in which an acidified water solution with or without CH<sub>3</sub>OH resides (Fig. 3.5) are referred to as the electrolyser ring WE<sub>elec</sub> and as the auxiliary WE<sub>aux</sub>, respectively.

In this study, the triode and tetrode operation of a PEM electrolyser was evaluated in the liquid phase, at low temperature and in the static mode. Results were obtained galvanostatically and potentiostatically, and in some cases, with independent CE measurements. The triode concept was evaluated with respect to the electrolysis of CH<sub>3</sub>OH and H<sub>2</sub>O in acidic media with various anodic materials and confirmed with tetrode operation. The possibility of carrying out the triode or tetrode electrolysis with non-precious materials was demonstrated for the first time in a liquid system. The use of the tetrode configuration is also reported for the first time. Finally, a preliminary mechanism is suggested for the electrochemical promotion of a low temperature PEM electrolyser.

### 3.3 Experimental

#### 3.3.1 Materials and membrane electrode assembly

The materials used are the same as the ones previously described in *Section 2.2.1*. The CE had a MPL consisting of a 1 mg/cm<sup>2</sup> coating composed of carbon black and 20 wt% PTFE was sprayed on top of the CE GDL surface, bonded to the membrane. No MPL was used for the GDE used in the WE compartment. The same electrocatalysts were used and the loadings were the same as in the previous Chapter. The electrolyser ring WE<sub>elec</sub> was a 4 mg/cm<sup>2</sup> Pt-Ru black GDE or a 2 mg/cm<sup>2</sup> Pt black GDE, while the electrolyser CE was a 2 mg/cm<sup>2</sup> Pt/C GDE. For the non-precious electrolyser ring WE<sub>elec</sub> experiments, a simple CFP was employed as the GDE. Those experiments were conducted to demonstrate that triode and tetrode effects can be obtain without noble metal catalysts on the electrolyser ring WE<sub>elec</sub>. The MEA was similar to the one previously used in *Chapter 2*, except that the GDE geometries were different. For triode operation, the electrolyser WE<sub>elec</sub> was cut in a ring using die cutters (Arkwel Industries Ltd.) with a 16 mm OD. Different ID sizes were tested for the electrolyser ring

$WE_{elec}$ , but unless otherwise indicated, a ring with a 6.35 mm ID was employed. For tetrode operation, the electrolyser CE was also cut into a ring of the same dimensions. The auxiliary  $WE_{aux}$  (for triode operation) or auxiliary  $CE_{aux}$  (also needed for tetrode operation) consisted of a 15 cm long 0.5 mm OD Pt wire (99.99%, Goodfellow Cambridge Limited) which was sealed in a cylindrical glass tube, and which was welded at the end to the center of a circular Pt surface of 3.18 mm OD. The alignment of the auxiliary electrodes, i.e.  $WE_{aux}$  (and  $CE_{aux}$ ) with the center of the MEA was guided by the aperture inner diameter of the tip of the Teflon™ cap as indicated on Fig. 3.3.

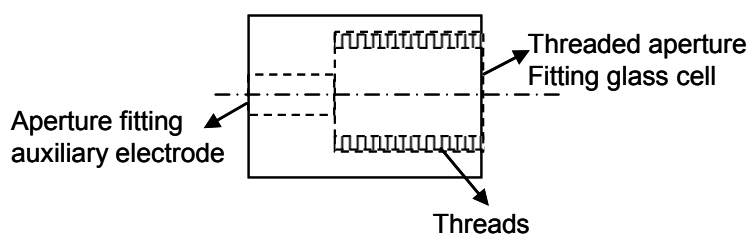


Figure 3.3: Schematic drawing of auxiliary Teflon™ cap with apertures.

Marks were made on the side of the rod to help ensure that the length and positioning was consistent for each experiment. Tightening of the caps ensured consistent contact pressure between the auxiliary and the MEA. The resistance of the electrolyser circuit (standard deviation of about 0.2 ohm) and of the auxiliary circuit (standard deviation of about 2 ohm) was measured by AC impedance for each experiment. A front view of the WEs used in triode operation is shown in Fig. 3.4.

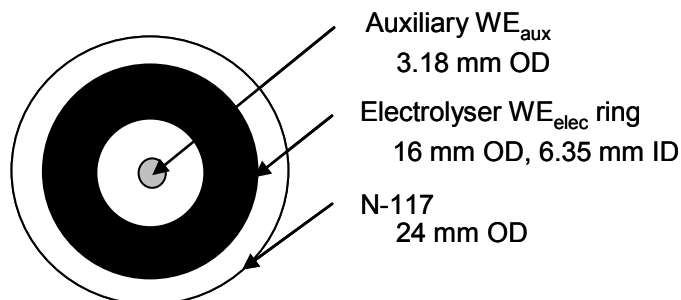


Figure 3.4: Front view of the triode or tetrode operation working electrode components.

### 3.3.2 Glass cell for triode and tetrode operation

The design of the dual-chamber glass cell described in *Section 2.2.2* was modified by CanSci Glass Products Ltd. for triode and tetrode electrolysis, as shown in Fig. 3.5 and 3.6. Ports located at the center-end of the glass cell compartments were added for the auxiliary electrodes used in triode or tetrode operation. The auxiliary electrodes were centered with the electrolyser MEA through the use of Teflon caps with apertures as was shown in Fig. 3.3. A new screw clamping apparatus was designed to hold the glass cells, MEA holder and O-rings compressed together to allow the insertion of the auxiliary electrode(s). In this Chapter, all experiments were conducted at room temperature in ambient air ( $23^{\circ}\text{C} \pm 1^{\circ}\text{C}$ ).

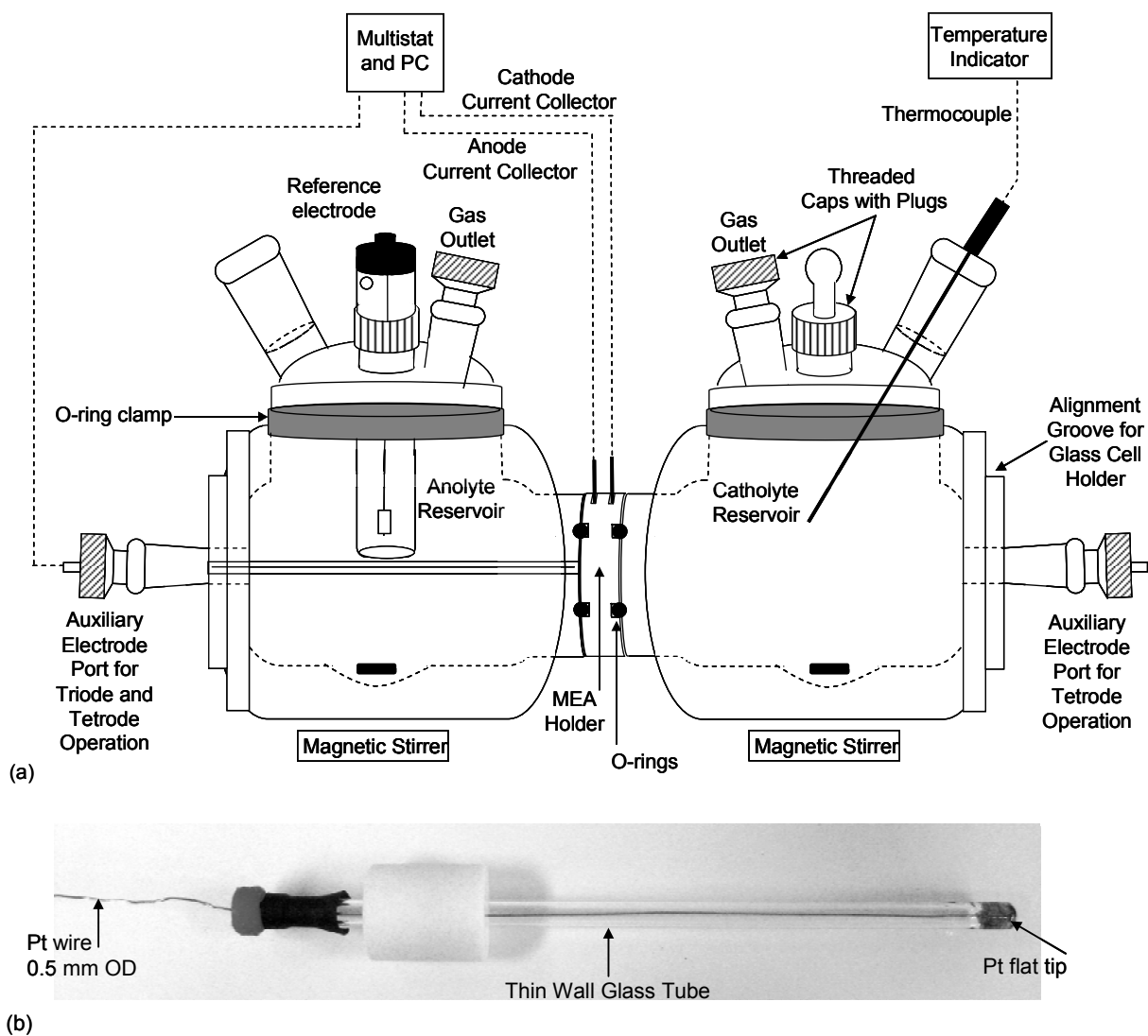


Figure 3.5: Apparatus for triode and tetraode electrolysis (a) electrochemical glass cell, (b) auxiliary electrode.

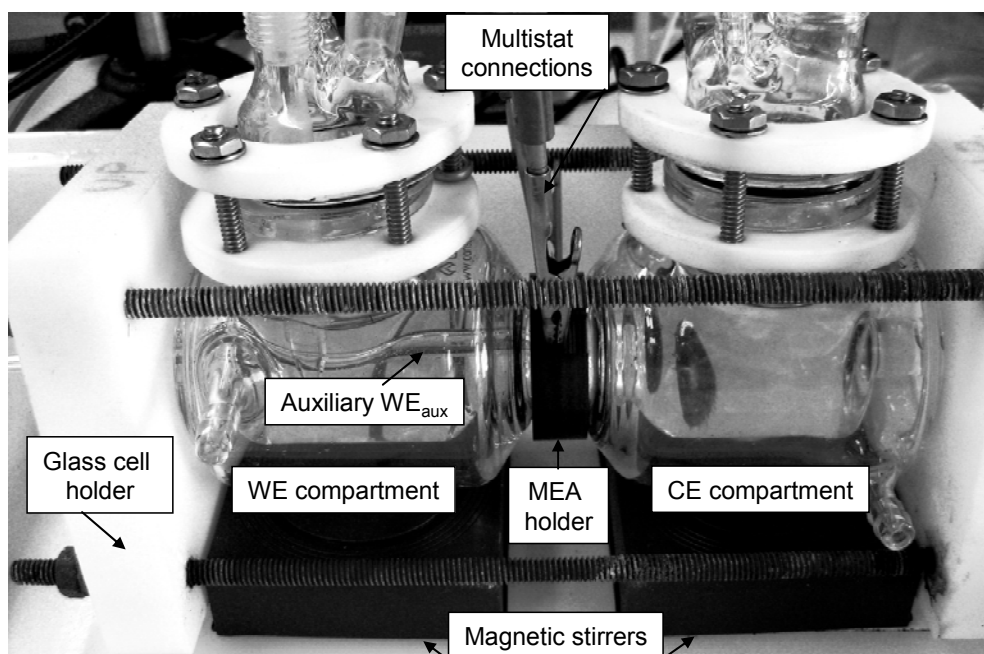


Figure 3.6: Picture of the electrochemical glass cell set-up in triode operation.

### 3.3.3 Electrochemical measurements

Electrochemical measurements were conducted using the same equipment as described in *Section 2.2.3*. Each circuit for triode or tetrode was independently controlled with different channels of the Multistat, i.e., the current or potential at one of the circuits was fixed while the current or potential of the other circuit was varied in increments. The experiments were either conducted in the galvanostatic, current-controlled mode (0.01 to 1700 mA/cm<sup>2</sup>) or in the potentiostatic, potential-controlled mode (-0.6 to 1.6 V vs. SHE). It is the first time potentiostatic control is used for triode operation. A schematic representation of the electrochemical potentials is provided in Fig. 3.7. The  $WE_{elec}$  and  $WE_{aux}$  potential settings (dashed lines) for the potentiostatic control experiments are showed along with the electrochemical half-cell reaction standard potentials. As the electrochemical half-cell reactions are kinetically inhibited, they will not start to occur until larger potentials are applied. It will be seen that, in the potentiostatic mode, triode or tetrode enhancements were only obtained when the  $WE_{aux}$  was in the potential range of -0.6 to 0.52 V vs. SHE. For the galvanostatic experiments,  $U_{elec, cell}$  is measured, and not  $U_{elec, we}$ , however, it was verified that  $U_{elec, we}$  is approximately equal to  $U_{elec, cell}$ , as  $U_{elec, ce}$  is close to 0 V vs. SHE.

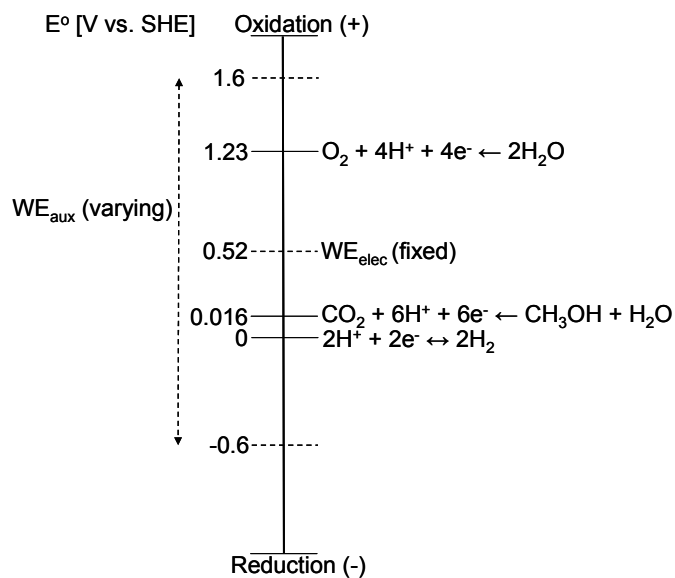


Figure 3.7: Potentiostatic working electrode potential experimental settings relative to the standard half-cell electrochemical potentials.

A schematic diagram representing the various independently controlled Multistat connections used in the galvanostatic and potentiostatic modes is shown in Fig. 3.8. In some cases, a digital multimeter (Fluke 179) was used to independently monitor the common CE potential in triode operation, or the  $CE_{elec}$  potential in tetrode operation. As per its instruction manual, the input resistance of this digital multimeter is listed as  $> 10\text{ M}\Omega$ , which is greater than the resistance of the circuit monitored. The digital multimeter impedance was high enough to avoid polarization of the reference electrode, i.e., it was sufficient to ensure that the reference electrode was subjected to a very limited measuring current. Furthermore, it did not appear to affect the accuracy of the voltage measurements, as the circuit operation was not disturbed when the multimeter was turned on or off during normal, triode or tetrode electrolysis operation.

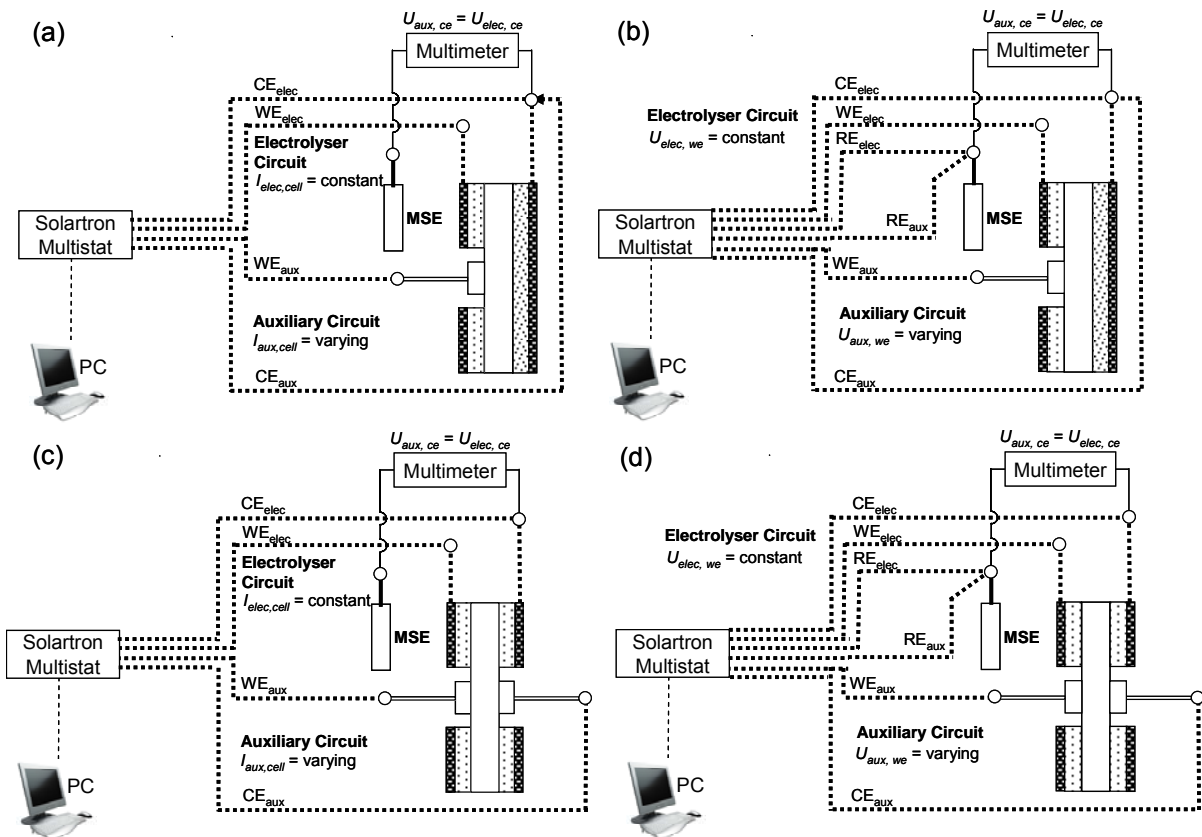


Figure 3.8: Schematic diagram of EPOE testing system connections for (a) galvanostatic triode operation, (b) potentiostatic triode operation (c) galvanostatic tetraode operation, and (d) potentiostatic tetraode operation.

In galvanostatic and potentiostatic triode operation, line interactions were avoided by grounding the auxiliary circuit through the grounding of the electrolyzer circuit. Galvanostatic experiments were conducted in three steps: (a) the electrolyser circuit was turned on first and held at a current where electrolysis occurs for 500 s, (b) the auxiliary circuit was turned on for 500 s, and (c) the auxiliary circuit was turned off for 500 s for system relaxation during which only the electrolyser circuit was still kept running. These three steps were repeated for each auxiliary current increment tested. All potentiostatic experiments were also conducted in three testing steps: (a) the electrolyser circuit was turned on by itself ( $U_{elec, cell}^0$ ) (b) the electrolyser circuit was turned off, and the auxiliary circuit was turned on by itself ( $U_{aux, cell}^0$ ), and (c) both circuits, the electrolyser and the auxiliary circuits, were turned on simultaneously, i.e., the system was in triode operation ( $U_{elec, cell}$  and  $U_{aux, cell}$ ). The system relaxation step was to re-start (a) for the next experiment. Segment (a) repeatedly resulted in the same values between each

experiment. Segment (b) was carried out to evaluate if there was a difference between  $I_{aux, cell}^0$  when the auxiliary circuit was operated alone, and  $I_{aux, cell}$ , when the system was in triode or tetrode operation. Each potentiostatic testing segment ran for 200 s instead of 500 s to speed-up the experiments, as this time was found to be sufficient for the current to attain a stable value in normal, triode or tetrode operation ( $\pm 0.002$  A). In tetrode operation, (Fig. 3.2 (d)) the electrolyser circuit and the auxiliary circuit used separate CEs. This allowed grounding of both circuits separately. Clearly, in tetrode operation, both circuits were independent and without electronic connection. The possibility of running a circuit in the galvanostatic mode while running the other in the potentiostatic mode was also evaluated in tetrode operation. As enhancements were obtained in both the triode and tetrode cases, it was further confirmed that the effects observed in the triode case were not an artefact of the experimental setup.

Most AC impedance measurements were conducted in the same manner as described in *Section 2.2.3* and in *Appendix F*. The measurements were obtained after the system reached equilibrium, i.e., at relaxation when no current or potential were applied to the electrolyser or auxiliary circuits. In general, the resistance in the auxiliary circuit was greater than that of the electrolyser circuit. In *Section 3.5.4.3*, a high-precision inductance capacitance resistance (LCR) meter (GW Instek, LCR-821) was used at a frequency of 100 kHz to record the MEA AC impedance while the multistat controlled the electrolyser in the potentiostatic mode. During these 1000 s tests, current measured by the multistat remained constant, even if the LCR meter was turned on/off to take a resistance measurement every 100 s. The perturbation of the LCR meter on the measured current was 1.5 mA at the most. In the galvanostatic mode, after the electrolyzer reached steady-state, i.e., when the change in cell potential was less than 20 mV over several minutes, AC impedance measurements were recorded every 100 s over a period of 1000 s. In most tests, AC impedance measurements were obtained with the Solartron impedance/gain phase analyzer after the system reached equilibrium, i.e., at relaxation when no current or potential were applied to the electrolyzer or auxiliary circuits.

Cyclic voltammetry (CV) experiments were conducted at ambient temperature ( $23 \pm 2^\circ\text{C}$ ) on electrodes and substrates in a single compartment 3-electrode glass cell, which was cleaned with a concentrated  $\text{H}_2\text{SO}_4\text{-HNO}_3$  (vol/vol, 3:1) mixture and rinsed with DI water between tests. A platinized Pt flag CE and a MSE RE equipped with a Luggin capillary were employed.  $\text{N}_2$  was bubbled using a sparger to de-aerate

the 0, 2 and 16 M CH<sub>3</sub>OH solutions for a few minutes. Ten conditioning potential sweep scans were carried out at 100 mV/s to ensure stability, after which two characterization potential sweep scans were conducted at 5 mV/s, all over the potential range from H<sub>2</sub> evolution to carbon oxidation. Double-sided conductive carbon tape (SPI Supplies) was used to ensure a strong electrical connection between the GDE WE and the alligator clip. More information on the CV technique can be found in *Appendix F*.

### 3.3.4 Stability of carbon containing electrolyser ring electrodes

Cyclic voltammetric measurements over a wide potential range were conducted in a three electrode system in order to verify at which potential carbon oxidation starts to occur on different electrolyser ring electrode materials in various electrolysis solutions. Figure 3.9 shows the forward anodic potential sweeps only for Pt black and CFP 2.01 cm<sup>2</sup> circular samples. The cyclic voltammograms were corrected for ohmic resistance. A high on-set potential towards the oxidation of carbon is desired for an optimized electrolyser ring electrode.

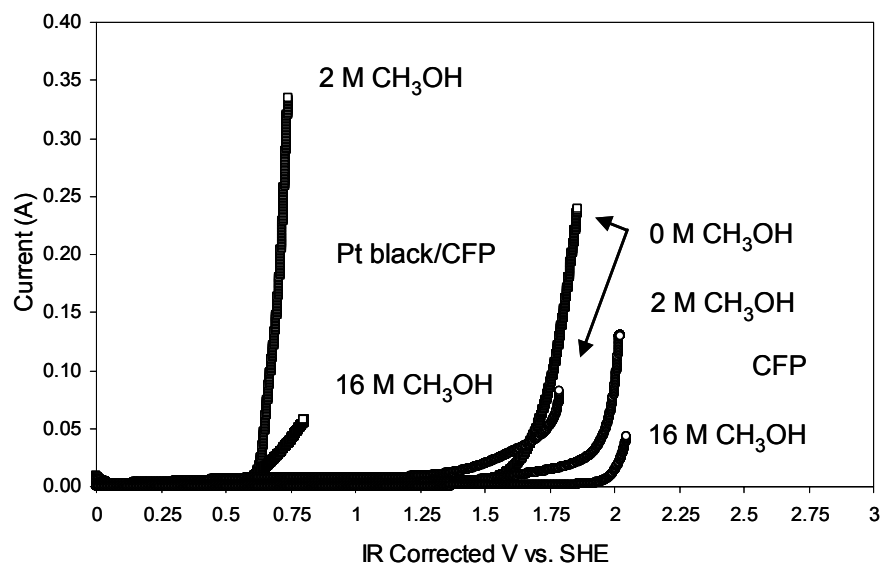


Figure 3.9: IR-corrected forward anodic potential sweep (5 mV/s, 0, 2 or 16 M CH<sub>3</sub>OH in 0.5 M H<sub>2</sub>SO<sub>4</sub> electrolyser anolyte, 0.5 M H<sub>2</sub>SO<sub>4</sub> electrolyser catholyte, CFP with and without 2 mg/cm<sup>2</sup> Pt black WE, Pt flag CE, 23 ± 1°C).

The on-set potential values obtained are summarized in Table 3.2.

Table 3.2: IR corrected on-set potentials for CFP samples with and without Pt black at varying CH<sub>3</sub>OH concentrations.

| [CH <sub>3</sub> OH]<br>[M] | 2 mg/cm <sup>2</sup> Pt black/CFP<br>[V vs. SHE] | CFP<br>[V vs. SHE] |
|-----------------------------|--------------------------------------------------|--------------------|
| 0                           | 1.70                                             | 1.86               |
| 2                           | 0.60                                             | 1.96               |
| 16                          | 0.65                                             | 2.00               |

The on-set potential values obtained on the CFP correspond to the potential at which carbon oxidation starts to occur in the different solutions according to the electrochemical anodic half-cell oxidation reaction (Eq. 2.7). It is known that carbon oxidation is kinetically-inhibited and begins to oxidize at a WE voltage around 1.8 V vs. SHE in the presence of Pt [174]. Water is the source of oxygen for the formation of CO<sub>2</sub> in carbon corrosion. Therefore, it is expected that carbon corrosion will be slower at higher CH<sub>3</sub>OH concentrations, since less H<sub>2</sub>O molecules are available for carbon corrosion. Lim *et al.* [193] have reported that the electrochemical corrosion of carbon in the gas phase is dependent on humidity and cell temperature, and that the presence of O<sub>2</sub> had little effect at a H<sub>2</sub> PEMFC temperature of 90°C. It is also known that Pt can accelerate the corrosion rate of the electrocatalyst carbon support, and cause permanent carbon loss, loss of catalytic activity, as well as structural collapse of a H<sub>2</sub> PEMFC cathode [194]. Hence, it is not expected that carbon corrosion will start at the same potential for the Pt black and CFP electrolyser ring WEs. In our system, the kinetics of carbon corrosion in the absence of an electrocatalyst was slow. It did not start until WE potentials of about 1.86 V vs. SHE or greater were reached. In most galvanostatic experiments, the electrolyser cell current density was maintained at 1.25 mA/cm<sup>2</sup>. At this current density,  $U_{elec, cell}$  was sufficient for the electro-oxidation reactions of interest to occur on the electrolyser WE while avoiding the carbon corrosion potential region. Also, the electrolyser circuit was operated in normal electrolysis between every triode case and, as  $U_{elec, cell}$  was stable, this provided further evidence that no degradation of the CFP electrode occurred. In all potentiostatic experiments, the electrolyser ring WE potential was maintained at 0.52 V vs. SHE. At this

potential, carbon oxidation is not an issue for H<sub>2</sub>O electrolysis or CH<sub>3</sub>OH electrolysis on Pt black or on CFP. The auxiliary WE potential was varied from -0.6 to 1.6 V vs. SHE, but since it is made of pure Pt, carbon oxidation was not a concern. No SEM microscopic visual corrosion of the CFP electrodes was observed after the triode and tetrode experiments were run in the galvanostatic or potentiostatic mode.

### 3.4 Triode or Tetrode operation evaluation expressions

#### 3.4.1 Triode or tetrode operation evaluation in the galvanostatic mode

The electrolyser triode or tetrode voltage ratio,  $R$ , is defined as

$$R = \frac{U_{elec, cell}}{U_{rev, cell}} \quad (3.3)$$

where  $U_{elec, cell}$  is the potential resulting from operating the electrolyser in galvanostatic triode or tetrode operation and  $U_{rev, cell}$  is the reversible cell voltage, i.e., -1.23 V for the liquid phase electrolysis of H<sub>2</sub>O and -0.016 V for the liquid phase electrolysis of CH<sub>3</sub>OH at 25°C, which can be thermodynamically calculated from

$$U_{rev, cell} = -\frac{\Delta G}{nF} \quad (3.4)$$

where  $\Delta G$  is the Gibbs free energy of reaction [J/mol],  $n$  is the number of electrons and  $F$  is Faraday's constant [C/mol]. This equation is equivalent to (Eq. 1.11). Balomenou and Vayenas [19] have shown that in triode fuel cell operation, it is possible for the fuel cell to produce power with a potential difference between the anode and cathode,  $U_{elec, cell}$ , at least 50 % greater than  $U_{rev, cell}$ . This is not possible for normal fuel cell operation, where the fuel cell voltage,  $U_{fc}$  is always less than  $U_{rev, cell}$ . Equations for the power enhancement ratio and the power gain ratio have also been developed for fuel cell triode operation [19, 164]. These types of equations are not available in the literature for electrolysis operation.

Similar equations were derived in this thesis work for triode or tetrode electrolysis operation. The electrolyser power enhancement ratio,  $\rho_{elec, cell}$ , can be defined as

$$\rho_{elec, cell} = \frac{P_{elec, cell}}{P_{elec, cell}^o} = \frac{|I_{elec, cell}| \cdot U_{elec, cell}}{|I_{elec, cell}^o| \cdot U_{elec, cell}^o} \quad (3.5)$$

where  $P_{elec, cell}$  is the power of the electrolyser in triode or tetrode operation and  $P_{elec, cell}^o$  is the power of the electrolyser in normal operation. For fuel cell triode operation, all  $\rho_{elec, cell}$  values reported were positive [19, 165]. In normal electrolysis,  $U_{elec, cell}^o$  is always negative, however, depending on the operating conditions, in triode or tetrode electrolysis operation,  $U_{elec, cell}$  can be negative or positive. To observe this sign change, the sign of the potential values in Eq. 3.5 were taken into account. In order to compare the power consumption of the electrolyser to that of the auxiliary circuit during triode or tetrode operation, the electrolyser power gain ratio,  $\gamma_{elec, cell}$ , can be defined as

$$\gamma_{e, cell} = \frac{\Delta P_{elec, cell}}{P_{aux, cell}} = \frac{P_{elec, cell} - |P_{elec, cell}^o|}{|P_{aux, cell}|} = \frac{U_{elec, cell} \cdot I_{elec, cell} - |U_{elec, cell}^o \cdot I_{elec, cell}^o|}{|U_{aux, cell} \cdot I_{aux, cell}|} \quad (3.6)$$

where  $\Delta P_{elec, cell}$  is the change in the power output of the electrolyser in triode or tetrode operation due to the operation of the auxiliary circuit and  $P_{aux, cell}$  is the power consumed in the auxiliary circuit. The power gain ratio indicates when it is advantageous to use the auxiliary circuit for triode or tetrode operation. In normal electrolysis, the main electrolyser current is positive and the electrolysis cell voltage is negative. In reverse triode or tetrode operation, the auxiliary circuit is also in electrolysis, but in the opposite direction to the main electrolyser. When the auxiliary circuit is operating independently by itself, the auxiliary current is negative and the auxiliary cell voltage is positive. Triode or tetrode galvanostatic operation may affect the sign of the electrolyser cell voltage, but the auxiliary cell voltage should remain positive. Therefore, absolute values are required to make interpretation of the results more straightforward. When  $\gamma_{elec, cell} < -1$ , the power gained by operating the electrolyser in triode or tetrode exceeds the power consumed in the auxiliary circuit. Even if  $\gamma_{elec, cell} > -1$ , resulting in a net power loss, there may still be an advantage if a non-precious surface is used at the electrolyser  $WE_{elec}$ .

### 3.4.2 Triode or tetrode operation evaluation in the potentiostatic mode

Prior to our studies, potentiostatic triode or tetrode operation had not been reported in the literature. The electrolyser power enhancement ratio and the electrolyser power gain ratio,  $\gamma_{elec, cell}$  as previously defined (Eq. 3.5 and 3.6), can be used in the potentiostatic operating mode as well. Based on the EPOC theory, the rate enhancement ratio is defined as the ratio of the promoted catalytic rate,  $r_p$ , over the unpromoted catalytic rate,  $r^o$ . Similarly, for the electrochemical promotion (EP) of an electrochemical reaction, the electrolyser rate enhancement ratio,  $\rho_e$ , can be defined as

$$\rho_e = \frac{r_{elec, cell}}{r_{elec, cell}^o} = \frac{I_{elec, cell}}{I_{elec, cell}^o} \quad (3.7)$$

which is the same as the current improvement ratio. In EPOC studies, promotional rate enhancement ratio values in the range of 10 to 100 are common [18]. Based on EPOC theory, (Eq. 1.37) the Faradaic efficiency,  $\Lambda$ , of the triode or tetrode electrolyser  $H_2$  production using a protonic solid electrolyte for which  $n = 1$ , is a ratio which can be defined as

$$\Lambda = \frac{\left( |r_{elec, cell}| - |r_{elec, cell}^o| \right)}{\left( \frac{|I_{aux, cell}|}{nF} \right)} \quad (3.8)$$

If the absolute value of  $\Lambda$  exceeds unity, the change in the electrochemical rate is non-Faradaic. In this case, the  $H_2$  production rate when the electrolyser is in triode or tetrode operation would exceed the  $H_2$  production rate when the electrolyser is operating normally. This could be verified by measuring the rates or currents experimentally. Normally, pure electrocatalysis is limited to an absolute value of  $\Lambda \leq 1$ .

## 3.5 Results and discussion

Triode operation experiments were conducted in the galvanostatic and potentiostatic mode, with some testing in tetrode operation. Analysis of the triode and tetrode effects on the electrolysis of H<sub>2</sub>O and CH<sub>3</sub>OH in the galvanostatic and potentiostatic modes follows.

### 3.5.1 Galvanostatic characterization

#### 3.5.1.1 Triode and tetrode operation in galvanostatic control

Figure 3.10 shows an example of a triode experiment conducted in the galvanostatic mode in reverse operation. The experiment started by imposing a normal electrolyser current  $i_{elec, cell}^o$  on the electrolysis circuit. At this time, the auxiliary circuit was not active and  $i_{aux, cell}$  was equal to zero. The initial values of the electrolyser and the auxiliary circuit potentials,  $U_{elec, cell}^o$  and  $U_{aux, cell}^o$ , were then recorded. Then the auxiliary circuit was set to a pre-determined value  $i_{aux, cell}$  not equal to zero, and triode operation started. Triode operation was held for 500 s. During this time, the values of the electrolyser and auxiliary circuit potentials changed to  $U_{elec, cell}$  and  $U_{aux, cell}$  respectively, while the imposed electrolyser circuit current  $i_{elec, cell}$  remained the same as in normal electrolysis, i.e.,  $i_{elec, cell} = i_{elec, cell}^o$ . When the auxiliary circuit was turned off, triode operation stopped and both circuit potentials returned to their original normal electrolysis values, indicating that the triode effect is reversible.

In this galvanostatic triode electrolysis experiment, the electrolyzer circuit current was fixed so that the electro-oxidation of CH<sub>3</sub>OH occurs on the electrolyzer ring WE<sub>elec</sub>, while the auxiliary WE<sub>aux</sub> current was varied in increments. A current of 1.25 mA/cm<sup>2</sup> was chosen to operate the electrolyser above the carbon oxidation potential region, and to avoid the limiting current in 2M CH<sub>3</sub>OH for various WE<sub>elec</sub> materials studied for CH<sub>3</sub>OH electro-oxidation in *Chapter 2* (Fig. 2.6). In the case presented in Fig. 3.10, the triode electrolyzer was operated in reverse operation, i.e., the auxiliary circuit applied current was opposite to the electrolyzer circuit applied current. As mentioned in the *Section 3.3.3*, a wide range of  $i_{aux, cell}$  values was studied. In general, the value of  $i_{elec, cell}$  was less than that of  $i_{aux, cell}$  because the geometric surface

area of the electrolyser ring  $WE_{elec}$  ( $1.69 \text{ cm}^2$ ) is much greater than the geometric surface area of the auxiliary  $WE_{aux}$  ( $0.08 \text{ cm}^2$ ), and because the resistance in the auxiliary circuit is greater than that in the electrolyser circuit.

The tetrode configuration is similar to the triode configuration, except that the auxiliary CE is independent from the electrolyser CE (see Fig. 3.2 (d)). Four distinct electrodes are used to form two completely independent circuits. Investigations of the tetrode configuration in the potentiostatic and galvanostatic modes revealed that the effect obtained in tetrode operation was similar to that observed in triode operation.

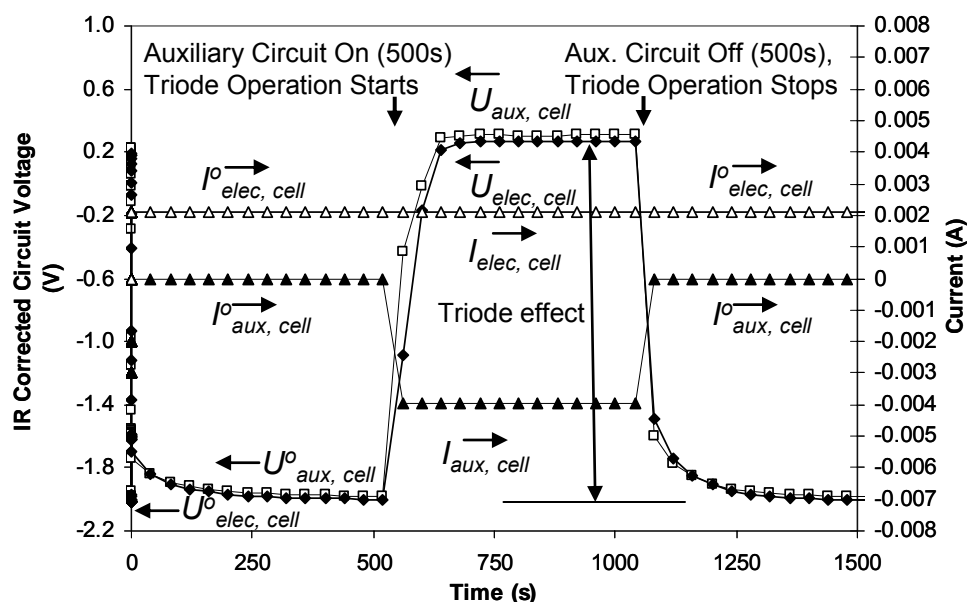


Figure 3.10: Triode effect in galvanostatic control (CFP electrolyser ring  $WE_{elec}$ , Pt auxiliary  $WE_{aux}$ ,  $2 \text{ mg/cm}^2$  Pt/C CE,  $2 \text{ M CH}_3\text{OH}$  in  $0.5 \text{ M H}_2\text{SO}_4$  electrolyser anolyte,  $0.5 \text{ M H}_2\text{SO}_4$  electrolyser catholyte,  $i_{elec, cell} = 1.25 \text{ mA/cm}^2$ ,  $i_{aux, cell} = -50 \text{ mA/cm}^2$ ).

### 3.5.1.2 Parallel and reverse operation in galvanostatic control

Figure 3.11 shows an example of triode electrolysis operation in the parallel and reverse direction. In parallel operation, Fig. 3.11 (a), the electrolyser potential remained the same whether the auxiliary circuit was operating or not. In reverse operation, Fig. 3.11 (b), the electrolyser potential was enhanced. Using

the auxiliary circuit to apply a current opposite to the electrolyser circuit current reduced the electrolyser voltage requirements. The enhancement in the electrolyser potential was proportional to the auxiliary current applied. Under certain conditions, the electrolyser potential became positive as a result of triode operation. Triode electrolysis appears to be only beneficial in when the auxiliary circuit is operated in reverse compared to the electrolyser circuit. All subsequent galvanostatic experiments were carried out in the reverse electrolysis mode.

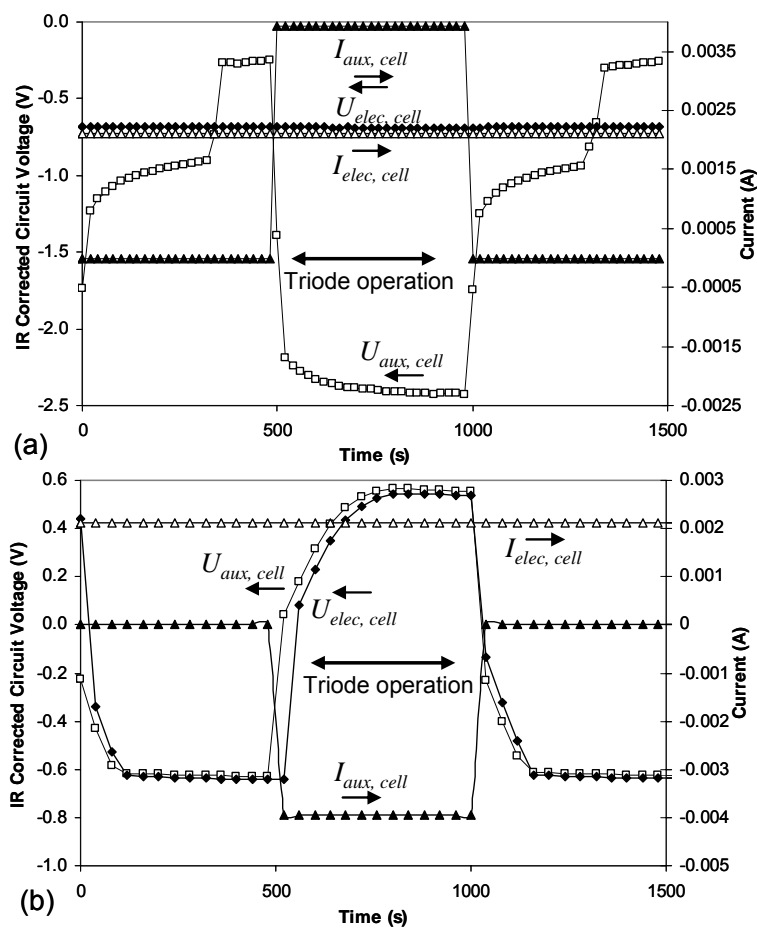


Figure 3.11: Effect of varying  $I_{aux, cell}$  on the electrolyser circuit voltage in galvanostatic control (a) parallel operation (b) reverse operation (4 mg/cm<sup>2</sup> Pt-Ru black electrolyser ring WE<sub>elec</sub>, Pt auxiliary WE<sub>aux</sub>, 2 mg/cm<sup>2</sup> Pt/C CE, 2 M CH<sub>3</sub>OH in 0.5 M H<sub>2</sub>SO<sub>4</sub> electrolyser anolyte, 0.5 M H<sub>2</sub>SO<sub>4</sub> electrolyser catholyte,  $i_{elec, cell} = 1.25$  mA/cm<sup>2</sup>,  $i_{aux, cell} = -50$  mA/cm<sup>2</sup>).

### 3.5.1.3 Electrolyser ring electrode material in galvanostatic control

Fig. 3.12 demonstrates the effect of triode operation on an unsupported noble metal electrocatalyst and on a CFP. In both cases, the  $U_{elec, cell}$  increased as the applied  $I_{aux, cell}$  was increased, but the  $U_{elec, cell}$  enhancement was not linearly proportional to the increase in the applied  $I_{aux, cell}$ . At sufficiently high auxiliary currents, the sign of the electrolyzer potential reversed and became positive as a result of triode operation. At this point, it may be possible that the electrolyser is driven in the opposite direction because the auxiliary current is driving the electrolysis circuit.

The auxiliary cell voltage,  $U_{aux, cell}$ , followed the electrolyser cell voltage,  $U_{elec, cell}$ , in all cases, even when the auxiliary circuit was at open circuit, i.e., while the electrolyser was in normal operation. When the auxiliary circuit was run by itself, a positive  $U_{aux, cell}^o$  value was obtained. In inverted triode operation, i.e., when the auxiliary WE<sub>aux</sub> is the ring as shown in Fig. 3.2 (c),  $U_{aux, cell}$  was close to zero while at open circuit in normal electrolysis, and did not equal  $U_{elec, cell}$  while in triode operation. This suggests that in normal triode operation,  $U_{aux, cell}^o$  and  $U_{aux, cell}$  were affected by the current line distribution on the WE plane, as the CE potential is the same in both cases.

The half-cell reaction occurring on the auxiliary WE<sub>aux</sub> during enhanced triode operation is the production of H<sub>2</sub> (Eq. 3.2). In order to determine the effect of this H<sub>2</sub> production on the triode improvement, the auxiliary WE<sub>aux</sub> was moved 1 cm away from the membrane surface, while still producing H<sub>2</sub> at the same rate. In triode operation, at the same electrolyser and auxiliary currents, there was a 67 % loss in the electrolyser circuit potential when the auxiliary WE<sub>aux</sub> was pulled 1 cm away from the membrane surface. Further information on this potentiostatic test is provided in *Section 3.5.4.1*. In addition, in galvanostatic normal electrolysis, 500s of continuous H<sub>2</sub> saturation of the WE glass cell compartment solution only resulted in a 3 % improvement in the electrolyser WE<sub>elec</sub> circuit potential compared to when no H<sub>2</sub> was provided. In both cases, the electrolysis improvement obtained via direct H<sub>2</sub> production is much less significant compared to when the auxiliary WE<sub>aux</sub> is in physical contact with the membrane in triode operation. A greater resistance was measured in the auxiliary circuit when it was pulled away, but not in the electrolyser circuit. This increase in the auxiliary circuit resistance is due to the solution resistance between the auxiliary WE<sub>aux</sub> and the membrane surface. Since auxiliary WE<sub>aux</sub> contact with the solid

electrolyte is required to observe any significant triode effects, the triode improvement must be resulting from an electrochemical pumping of protons rather than from the generation of  $H_2$ . Further confirmation of this is provided in Section 3.5.4.1.

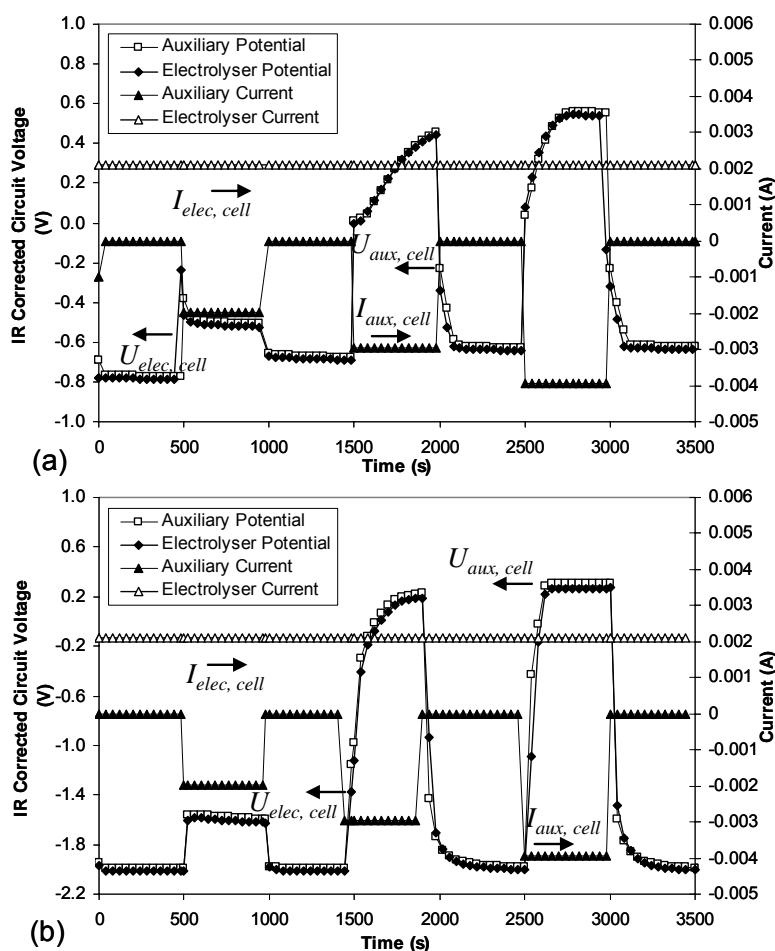


Figure 3.12: Effect of varying  $I_{aux, cell}$  on the electrolyser circuit voltage in galvanostatic control (a) 4 mg/cm<sup>2</sup> Pt-Ru black electrolyser ring  $WE_{elec}$ , (b) CFP electrolyser ring  $WE_{elec}$  (Pt auxiliary  $WE_{aux}$ , 2 mg/cm<sup>2</sup> Pt/C CE, 2 M  $CH_3OH$  in 0.5 M  $H_2SO_4$  electrolyser anolyte, 0.5 M  $H_2SO_4$  electrolyser catholyte,  $i_{elec, cell} = 1.25$  mA/cm<sup>2</sup>).

As expected, when a CFP was used as the electrolyser ring  $WE_{elec}$ , as shown in Fig. 3.12 (b), the electrolyser current, without triode operation, resulted in a more negative electrolyser potential than when a noble metal electrocatalyst was present on the electrolyser ring  $WE_{elec}$  as shown in Fig. 3.12 (a). However, the beneficial triode effect was also observed on CFP and the electrolyser potential

enhancement observed ( $U_{elec, cell} - U_{elec, cell}^0$ ), i.e., the electrolyser voltage in triode less the baseline electrolyser voltage, was similar to the one observed on Pt-Ru black. No CFP anode ring damage was observed before and after multiple triode tests. The auxiliary current was turned on and off numerous times, and the electrolyser potential without triode operation returned to the same original value, indicating the absence of carbon oxidation in the process. This confirms that the application of an auxiliary current activated a process which made the electrolyser CFP ring  $WE_{elec}$  surface electrocatalytically active. On CFP, no apparent capacitive effect was observed indicating that the change in surface charge concentration was completely reversible. This was not the case for Pt-Ru/C, for which the  $WE_{elec}$  surface charge concentration after triode operation did not return to its original value in normal operation. It appears that, triode operation promotes the electrolysis by electrochemically modifying the localised  $H^+$  species surface concentration. It was also verified that a comparable triode effect can be obtained using an auxiliary  $WE_{aux}$  made of a non-catalytic material, such as Au plated SS in *Section 3.5.4.7*. In this case, protons are transported through the membrane, but no  $H_2$  is generated at the auxiliary  $WE_{aux}$  surface. Additional experimental details on this are provided in *Chapter 4*.

#### **3.5.1.4 Electrolyser voltage ratio, power enhancement ratio and power gain ratio in galvanostatic control**

The electrolyser potential in triode operation,  $U_{elec, cell}$ , and the electrolyser triode voltage ratio,  $R$  (dimensionless), were determined for different auxiliary circuit current densities. The results obtained for the Pt-Ru black ring and the CFP ring are shown in Fig. 3.13 (a) and (b), respectively.

For both anode materials, the value of  $U_{elec, cell}$  went from being negative to being positive as the auxiliary circuit current density was increased to more negative values. This means that, in triode operation, the electrolyser can become a power source when the auxiliary circuit current reaches a certain value. The triode voltage trend was similar to the one of  $U_{elec, cell}$  but the signs were reversed as  $U_{rev, cell}$  is negative. At  $i_{aux, cell} = -0.01 \text{ A/cm}^2$ , the value of  $R$  obtained for the CFP ring was about 2.8 times greater than the one obtained for the Pt-Ru black ring  $WE_{elec}$ . At  $i_{aux, cell} = -0.05 \text{ A/cm}^2$ , the  $R$  value was two times greater for the electrolyser using a Pt-Ru black ring  $WE_{elec}$  than for the electrolyser using a CFP ring  $WE_{elec}$ . Triode operation reduces some of the overvoltage losses and allows operating at voltages lower than

$U_{rev, cell}$ , which is not possible in normal electrolysis. Balomenou *et al.* [165] have shown for an SOFC fuel cell operating on 2 % dry CH<sub>4</sub>, an increase in the fuel cell voltage,  $U_{fc}$ , of 33 % greater than  $U_{rev, cell}$  at a fixed auxiliary current of -0.5 mA and a fuel cell current of 0.2 mA at 700°C using Pt electrodes. The improvements obtained at low temperature in the current electrolysis study are of a similar magnitude. It was possible to operate the electrolyser in triode mode at 27 % and 13 % less voltage than  $U_{rev, cell}$  on a Pt-Ru black ring WE<sub>elec</sub> and a CFP ring WE<sub>elec</sub>, respectively. It appears that this is the first time such overvoltage reductions have been reported in a low temperature triode electrolysis system.

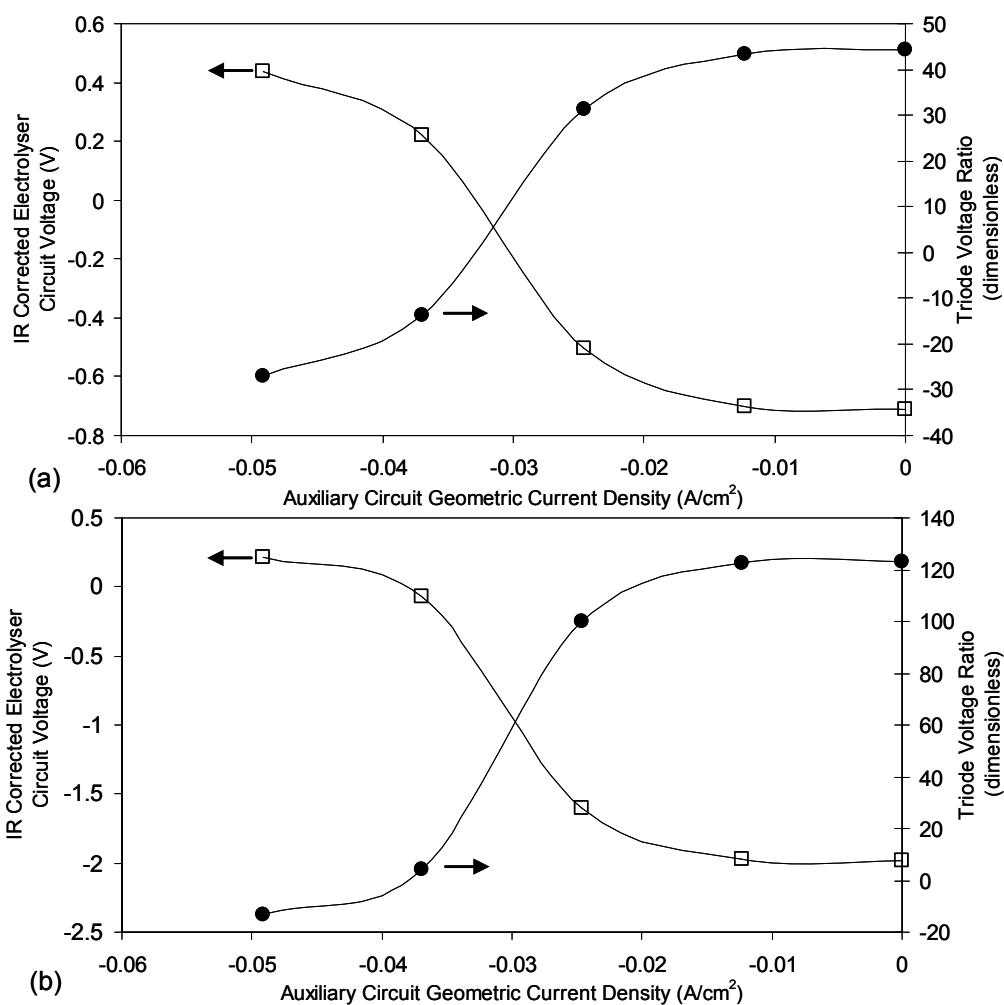


Figure 3.13: Effect of  $i_{aux, cell}$  on  $U_{elec, cell}$  and on the triode voltage ratio ( $R$ ) (a) 4 mg/cm<sup>2</sup> Pt-Ru black electrolyser ring WE<sub>elec</sub> (b) CFP electrolyser ring WE<sub>elec</sub> (Pt auxiliary WE<sub>aux</sub>, 2 mg/cm<sup>2</sup> Pt/C CE, 2 M CH<sub>3</sub>OH in 0.5 M H<sub>2</sub>SO<sub>4</sub> electrolyser anolyte, 0.5 M H<sub>2</sub>SO<sub>4</sub> electrolyser catholyte,  $i_{elec, cell} = 1.25$  mA/cm<sup>2</sup>).

The electrolyser power enhancement ratio,  $\rho_{elec, cell}$ , (dimensionless) and the electrolyser power gain ratio,  $\gamma_{elec, cell}$ , (dimensionless), are shown in Fig. 3.14.

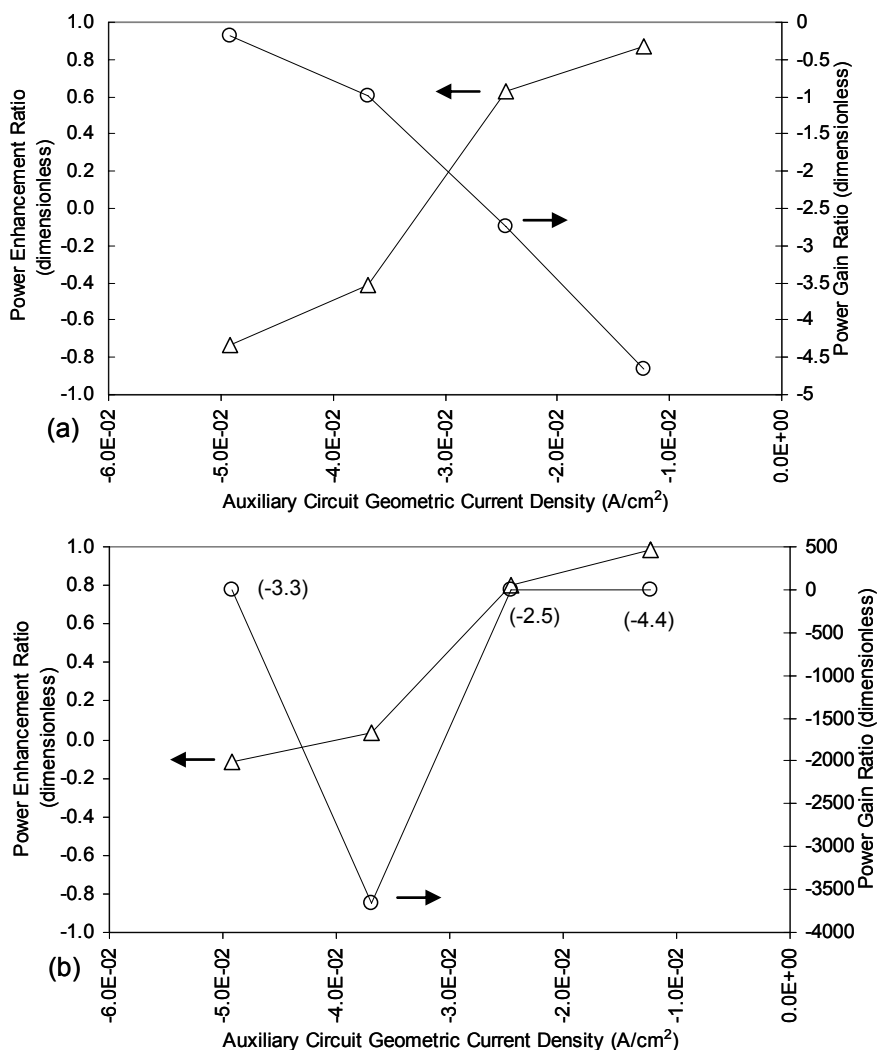


Figure 3.14: Power enhancement ratio ( $\rho_{elec, cell}$ ) and power gain ratio ( $\gamma_{elec, cell}$ ) as a function of the auxiliary circuit current density (a) 4 mg/cm<sup>2</sup> Pt-Ru black electrolyser ring WE<sub>elec</sub> (b) CFP electrolyser ring WE<sub>elec</sub> (Pt auxiliary WE<sub>aux</sub>, 2 mg/cm<sup>2</sup> Pt/C CE, 2 M CH<sub>3</sub>OH in 0.5 M H<sub>2</sub>SO<sub>4</sub> electrolyser anolyte, 0.5 M H<sub>2</sub>SO<sub>4</sub> electrolyser catholyte,  $i_{elec, cell} = 1.25$  mA/cm<sup>2</sup>).

Under the conditions studied, the power enhancement ratio,  $\rho_{elec, cell}$ , did not exceed unity in any case, indicating that less power was needed in triode electrolysis than in normal electrolysis. The reduction in the triode power requirements became more significant as the applied auxiliary current density was

increased. While the normal electrolysis cell voltage is always negative, the triode electrolysis cell voltage became positive once a sufficiently large auxiliary current density was applied. This explains the  $\rho_{elec, cell}$  sign changes observed. At large auxiliary current densities,  $\rho_{elec, cell}$  was more favourable for the Pt-Ru black electrolyser ring  $WE_{elec}$  than for the CFP ring  $WE_{elec}$ . The catalytic surface responded better than the non-catalytic one to the changes imposed by the auxiliary circuit.

The power gain ratio did not reach positive values under the conditions studied, indicating that, in all cases, the power required to operate the electrolyser in triode mode was less than the power required to operate under normal electrolysis. In some cases,  $\gamma_{elec, cell}$  reached values less than -1, signifying that the reduction in the power requirements in triode electrolysis was greater than that consumed in the auxiliary circuit. This was the case at low auxiliary current densities for the Pt-Ru black electrolyser ring  $WE_{elec}$  and for all CFP electrolyser ring  $WE_{elec}$  cases studied. For the Pt-Ru black electrolyser ring  $WE_{elec}$ , a maximum  $\gamma_{elec, cell}$  was observed at  $i_{aux, cell} = -0.012 \text{ A/cm}^2$  and for the CFP electrolyser ring  $WE_{elec}$ , a maximum  $\gamma_{elec, cell}$  was observed at  $i_{aux, cell} = -0.037 \text{ A/cm}^2$ . The maximum decrease in the power requirements was three orders of magnitude larger for the CFP electrolyser ring  $WE_{elec}$  than for the Pt-Ru black electrolyser ring  $WE_{elec}$ . Thus, it is clear that for the non-noble CFP  $WE_{elec}$  case, the decrease in power requirements caused by triode operation significantly exceeded the power sacrificed in the auxiliary circuit. Such high power gain ratios have not been reported previously.

### 3.5.1.5 Benefits of starting in triode or tetrode operation in galvanostatic control

At a sufficiently high electrolysis current, the electrolyser cell may reach voltages where CFP oxidation can occur ( $\sim 1.8 \text{ V vs. SHE}$ ) on the electrolyser ring  $WE_{elec}$ . Figure 3.15 illustrates that triode operation may be a possible way to prevent electrolyser ring  $WE_{elec}$  electrocatalyst degradation through CFP or any other material corrosion.

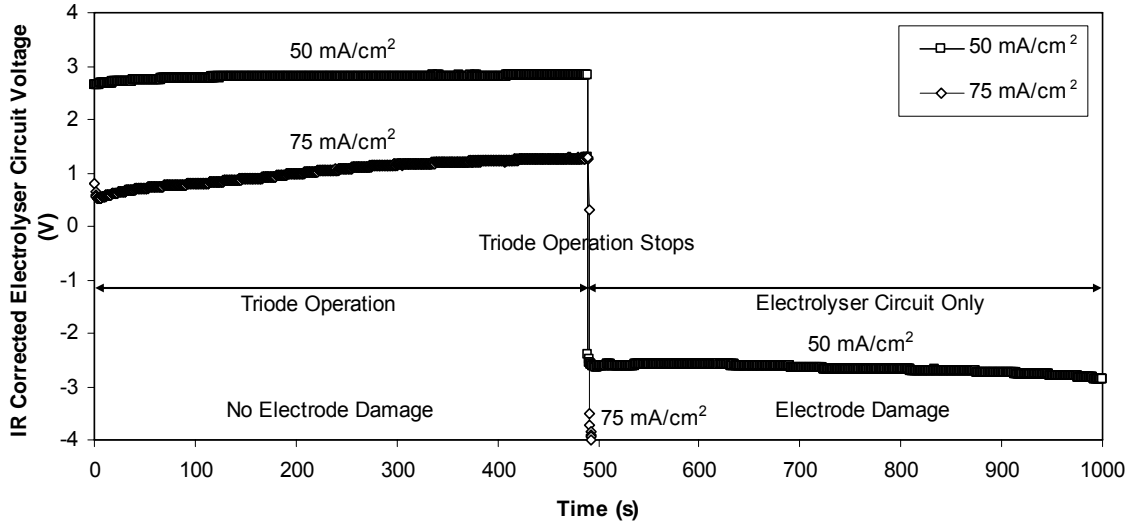


Figure 3.15: Benefits of starting in triode operation in galvanostatic control (CFP ring electrolyser  $WE_{elec}$ , Pt auxiliary  $WE_{aux}$ , 2 mg/cm<sup>2</sup> Pt/C CE, 2 M CH<sub>3</sub>OH in 0.5 M H<sub>2</sub>SO<sub>4</sub> electrolyser anolyte, 0.5 M H<sub>2</sub>SO<sub>4</sub> electrolyser catholyte,  $i_{elec, cell} = 50, 75 \text{ mA/cm}^2$ ,  $i_{aux, cell} = -5 \text{ A/cm}^2$ ).

As can be observed in Fig. 3.15, when the electrolyser operates at  $i_{elec, cell} = 50 \text{ mA/cm}^2$  and the auxiliary circuit operates at a high current density of  $-5000 \text{ mA/cm}^2$ , the electrolyser cell voltage is about 2.7 V. When the auxiliary circuit is shut-off, the electrolyser cell voltage drops to about -3 V and the CFP electrolyser ring  $WE_{elec}$  is irreversibly damaged. Similarly, when the electrolyser operates at  $i_{elec, cell} = 75 \text{ mA/cm}^2$  and the auxiliary circuit operates at the same current density, the electrolyser cell voltage is around 1 V. When the auxiliary circuit is shut-off, the electrolyser voltage drops to a value less than -4 V, i.e., reaching the chosen instrument set voltage safety limit, and the CFP electrolyser ring  $WE_{elec}$  is irreversibly destroyed. In *Chapter 2*, it was shown that, in normal PEM electrolysis, there exists a limiting current density for the electro-oxidation of CH<sub>3</sub>OH beyond which no stable cell voltage measurements can be obtained as the electrocatalyst carbon support is oxidized and precious metal is lost from the electrode surface. In both triode operation cases here, the imposition of a high auxiliary current density, where the triode effect is more significant, prevented the electrolyser ring  $WE_{elec}$  from damage through carbon oxidation. At a lower auxiliary current density, where the triode effect is not as significant, no beneficial effect was observed, and the electrolyser ring  $WE_{elec}$  was irreversibly damaged at higher electrolyser current densities.

### 3.5.2 Potentiostatic characterization

#### 3.5.2.1 Triode configuration in potentiostatic control

The electrolyser triode configuration with a common CE was also studied in potentiostatic control. Fig. 3.7 showed the working electrode potential settings and the electrochemical half-cell reactions occurring on the working electrodes. An example of a triode experiment carried out in the potentiostatic mode and demonstrating the effect of step changes in the auxiliary  $WE_{aux}$  potential varying from -0.6 to 1.6 V vs. SHE is provided in Fig. 3.16. As no triode operation measurements have been previously conducted in the potentiostatic mode according to the previously existing literature, this new graphical representation of the results requires explanation.

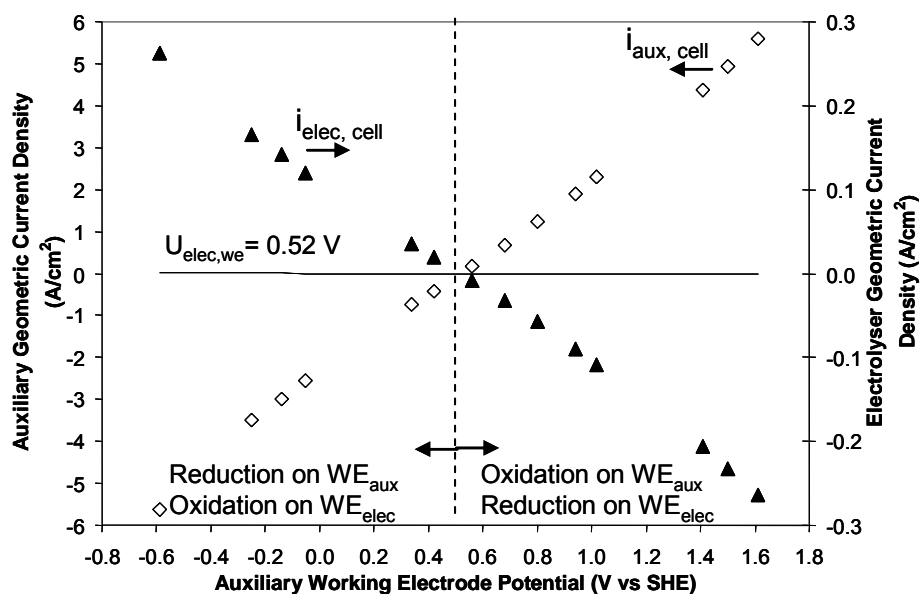


Figure 3.16: Triode effect in potentiostatic control (CFP electrolyser ring  $WE_{elec}$ , Pt auxiliary  $WE_{aux}$ , 2 mg/cm<sup>2</sup> Pt/C CE, 2 M CH<sub>3</sub>OH in 0.5 M H<sub>2</sub>SO<sub>4</sub> electrolyser anolyte, 0.5 M H<sub>2</sub>SO<sub>4</sub> electrolyser catholyte,  $U_{elec, we} = 0.52$  V vs. SHE).

The electrolyser ring  $WE_{elec}$  potential,  $U_{elec, we}$ , was maintained at 0.52 V vs. SHE (0 electrolyser current at this potential) as indicated by the horizontal dashed line. This potential value was chosen based on the fundamental study of the PEM electrolysis system discussed in *Chapter 2* because it is far removed

from the potential for carbon oxidation and it is below the onset potential for CH<sub>3</sub>OH oxidation. Cyclic voltammetry results shown in Fig. 3.9 also supported this decision. The electrolyser circuit was operated alone between each set of tests and the potential always returned to the same value between tests. This confirms that there was no carbon degradation between the tests. Furthermore, no apparent damage to the electrode was visually observed after the entire test sequence. The same potential value was used for CH<sub>3</sub>OH and H<sub>2</sub>O electrolysis, although larger electrolyser ring WE<sub>elec</sub> potential values ( $U_{elec,we}$  up to ~1.5 V vs. SHE) could be used in the case of H<sub>2</sub>O electrolysis. The auxiliary WE<sub>aux</sub> potential,  $U_{aux,we}$ , was varied and is represented on the x-axis.

A vertical dashed line divides the reverse triode operation data for the WEs into two potential regions. On the right hand side, CH<sub>3</sub>OH oxidation occurs on the auxiliary WE<sub>aux</sub>, and reduction (H<sub>2</sub> production) occurs on the electrolyser ring WE<sub>elec</sub>. On the left hand side, CH<sub>3</sub>OH oxidation occurs on the electrolyser ring WE<sub>elec</sub> and reduction (H<sub>2</sub> production) occurs on the auxiliary WE<sub>aux</sub>. The electrolyser geometric current density,  $i_{elec,cell}$  and the auxiliary current density,  $i_{aux,cell}$ , are indicated. As can be seen on Fig. 3.16, at the set voltage of 0.52 V vs. SHE, in normal electrolysis operation,  $i_{elec,cell}^0$  is close to zero. In triode operation, when  $U_{aux,we} = U_{elec,we}$ ,  $i_{elec,cell}$  is close to zero. On the right hand side of the vertical dashed line, triode operation does not have a positive effect on the desired electrolyser current compared to normal operation. When electro-oxidation occurs on both WEs, no  $i_{elec,cell}$  enhancements are observed, which is consistent with the parallel operation findings in the galvanostatic mode described earlier in Section 3.3.1. On the left hand side of the vertical dashed line, triode operation has a beneficial effect on the desired electrolyser current. When  $U_{aux,we}$  reaches the reduction region, i.e., < 0.52 V vs. SHE,  $i_{elec,cell}$  becomes positive. Under these conditions, the electro-reduction reaction occurring on the auxiliary WE<sub>aux</sub> enhances the electro-oxidation reaction occurring on the electrolyser ring WE<sub>elec</sub>. Therefore, focus is made on the region where triode operation appears to be beneficial to the electrolyser. At  $U_{aux,we}$  lower than -0.8 V vs. SHE, it may be possible that, eventually, the driving force of the electrolyser electrochemical oxidation,  $i_{elec,cell}$ , becomes so large as to create excessive CO<sub>2</sub> evolution, which would block the active catalyst surface WE<sub>elec</sub> from the solution and decrease the overall PEM electrolyser performance.

During some triode tests, the common CE potential was measured against a second MSE reference electrode located in the glass cell CE compartment. The common CE potential is generally not reported during triode operation in the literature. However, it is important to know how the potential of both individual electrodes is influenced under these test conditions, as per the diagram of the electrochemical half-cell potential presented in Fig. 3.7. During triode operation, the CE potential is forced to a common value for the electrolyser and auxiliary circuits. For some tests, it was verified that the potential of the CE when the electrolyser or the auxiliary circuit were operated separately and alone, i.e.,  $U_{elec, ce}^o$  or  $U_{aux, ce}^o$ , was constant between each  $U_{aux, we}$  increments throughout the entire course of the triode experiment, as was shown in Fig. 3.7 (b) and 3.8 (b). This confirms that the carbon of the common CE was not oxidized by the auxiliary circuit during the course of the triode experiment. It was also verified that  $U_{aux, ce}^o$  and  $U_{aux, ce}$ , as well as  $U_{elec, ce}^o$  and  $U_{elec, ce}$  did not change much during triode operation. However, small discrepancies were observed when  $U_{aux, we}^o$  was less or equal to -0.14 V vs. SHE, i.e., when the auxiliary WE<sub>aux</sub> was in the H<sub>2</sub> production region, where the mixed potential effect at the common CE becomes more apparent. At these auxiliary WE potentials, H<sub>2</sub> evolution starts to occur at the auxiliary WE<sub>aux</sub> and the mixed potential at the common CE becomes more apparent.

### 3.5.2.2 Tetraode configuration in potentiostatic control

The tetraode configuration is similar to the triode configuration, except that the auxiliary CE<sub>aux</sub> is independent from the electrolyser CE<sub>elec</sub> (Fig. 3.2 (d)). Four distinct electrodes are used to form two independent circuits. Investigations of the tetraode configuration in potentiostatic control using a Pt-Ru black electrolyser WE<sub>elec</sub>, as shown in Fig. 3.17, revealed that the effect obtained in tetraode operation was less but similar to that observed in triode operation using the same WE<sub>elec</sub> material. This can be also observed by comparing Fig. 3.17 (Pt-Ru black electrolyser WE<sub>elec</sub>) and Fig. 3.16 (CFP electrolyser WE<sub>elec</sub>). Thus, the EPOC effect is independent of the electrolyser WE<sub>elec</sub> material, which does not need to be catalytic.

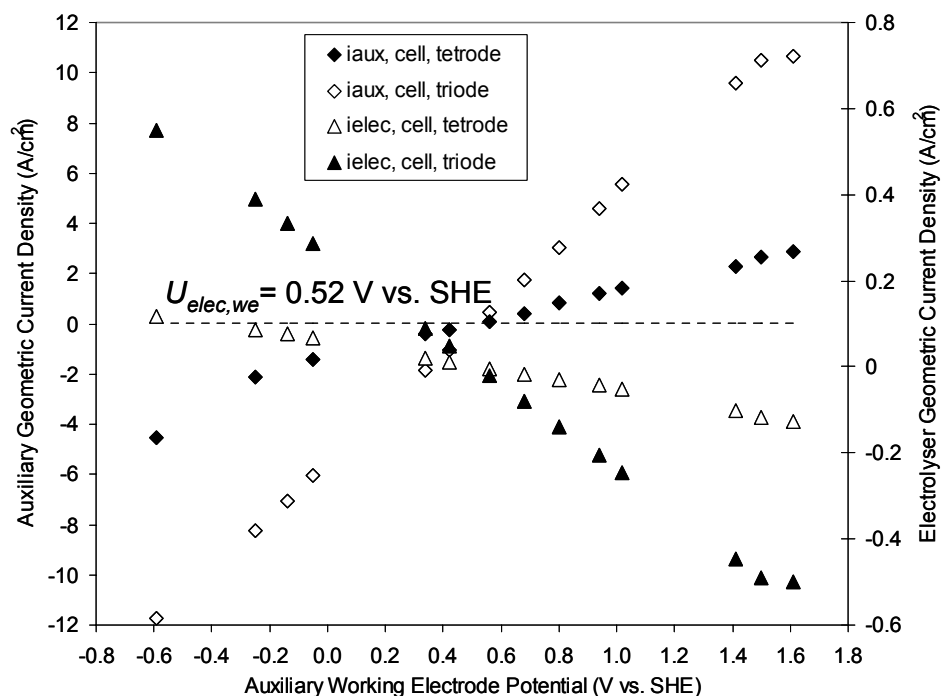


Figure 3.17: Triode and tetrode effect in potentiostatic control (4 mg/cm<sup>2</sup> Pt-Ru black electrolyser ring WE<sub>elec</sub>, 2 mg/cm<sup>2</sup> Pt/C electrolyser CE<sub>elec</sub>, Pt auxiliary WE<sub>aux</sub> and CE<sub>aux</sub>, 2 M CH<sub>3</sub>OH in 0.5 M H<sub>2</sub>SO<sub>4</sub> electrolyser anolyte, 0.5 M H<sub>2</sub>SO<sub>4</sub> electrolyser catholyte,  $U_{elec, we} = 0.52$  V vs. SHE).

The difference in the tetrode results compared to the triode results may be attributed to the fact that the tetrode CEs have different surface areas, and that the resistance in the auxiliary circuit is greater in the tetrode case than in the triode case.

### 3.5.2.3 Counter electrode potential measurements in potentiostatic control

For the tests presented in Fig. 3.18, the potential of the counter electrode(s) was measured independently with a multimeter. For the triode case shown in Fig. 3.18, the common counter electrode potential was first measured when the electrolyser was operated normally, then the common counter electrode potential was measured when only the auxiliary circuit was operating, and finally, it was measured when both circuits were in operation, i.e., triode electrolysis. Similarly, for the tetrode case

shown in Fig. 3.19, the potential of both counter electrodes,  $CE_{elec}$  and  $CE_{aux}$ , was measured in normal electrolysis, then when only the auxiliary circuit was operating, and then during tetrode operation.

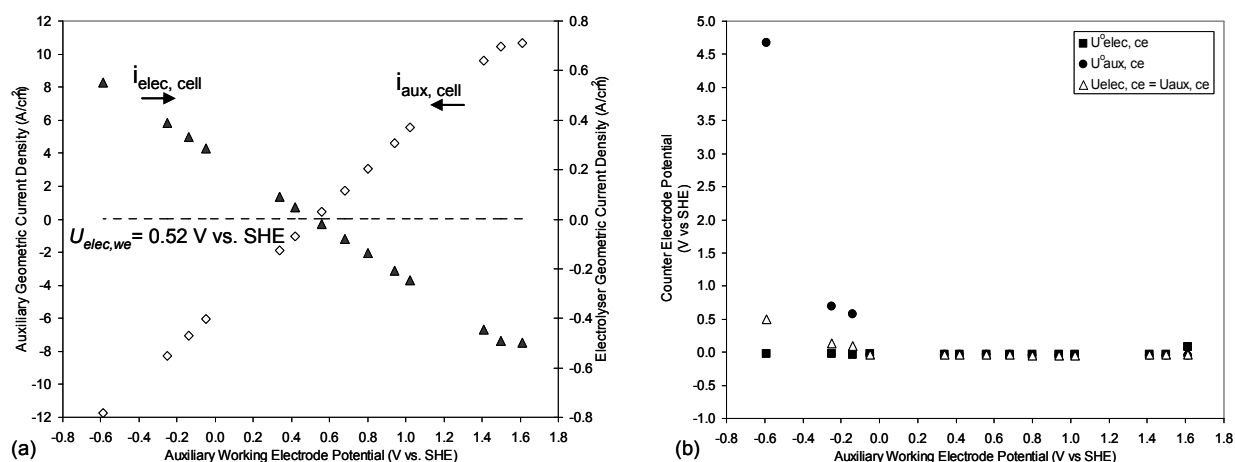


Figure 3.18: Triode effect in potentiostatic control (a) geometric current density (b) counter electrode potential ( $4 \text{ mg/cm}^2$  Pt-Ru black electrolyser ring  $WE_{elec}$ ,  $2 \text{ mg/cm}^2$  Pt/C electrolyser CE, Pt auxiliary  $WE_{aux}$ ,  $2 \text{ M CH}_3\text{OH}$  in  $0.5 \text{ M H}_2\text{SO}_4$  electrolyser anolyte,  $0.5 \text{ M H}_2\text{SO}_4$  electrolyser catholyte,  $U_{elec, we} = 0.52 \text{ V vs. SHE}$ ).

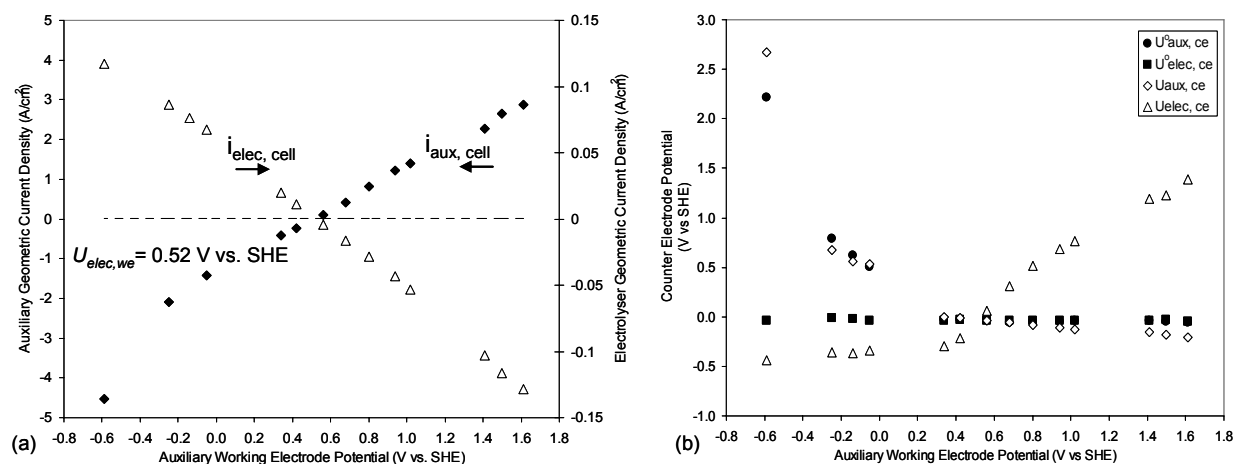


Figure 3.19: Tetrode effect in potentiostatic control (a) geometric current density (b) counter electrode potential ( $4 \text{ mg/cm}^2$  Pt-Ru black electrolyser ring  $WE_{elec}$ ,  $2 \text{ mg/cm}^2$  Pt/C electrolyser  $CE_{elec}$ , Pt auxiliary  $WE_{aux}$  and  $CE_{aux}$ ,  $2 \text{ M CH}_3\text{OH}$  in  $0.5 \text{ M H}_2\text{SO}_4$  electrolyser anolyte,  $0.5 \text{ M H}_2\text{SO}_4$  electrolyser catholyte,  $U_{elec, we} = 0.52 \text{ V vs. SHE}$ ).

As shown on Fig. 3.18 (b), in the triode case, the common counter electrode potential was close to zero in normal electrolysis. When the auxiliary circuit was operated alone, the common counter electrode potential was positive, as the system operates in reverse electrolysis, and the common counter electrode then behaves as an anode. In triode electrolysis at an electrolyser  $WE_{elec}$  potential of 0.52 V vs. SHE and an auxiliary  $WE_{aux}$  potential of -0.6 V vs. SHE, the common CE reached an intermediate potential of 0.5 V vs. SHE. Therefore, when operating the triode at this particular auxiliary  $WE_{aux}$  potential, the proton flux likely travels from the positive  $WE_{elec}$  to the negative  $WE_{aux}$  in the WE compartment, and possibly from the common CE to the  $WE_{aux}$  through the membrane.

As shown on Fig. 3.19 (b), in the tetrode case, when each circuit was operated separately, the respective potential of the independent CEs potentials was similar as the ones measured in the triode case. However, in tetrode operation at an electrolyser  $WE_{elec}$  potential of 0.52 V vs. SHE and an auxiliary  $WE_{aux}$  potential of -0.6 V vs. SHE, the electrolyser  $CE_{elec}$  potential decreased to about -0.5 V vs. SHE, while the auxiliary  $CE_{aux}$  potential increased to about 2.75 V vs. SHE. When operating the tetrode at this particular auxiliary  $WE_{aux}$  potential, the proton flux may still travel from the positive  $WE_{elec}$  to the negative  $WE_{aux}$  in the WE compartment, but also from the positive  $WE_{elec}$  to the negative  $CE_{elec}$  through the membrane, and from the positive  $CE_{aux}$  to the negative  $WE_{aux}$  through the membrane.

#### 3.5.2.4 Electrolyser ring electrode material in potentiostatic control

Different electrolyser ring electrode materials were compared in triode operation for  $H_2O$  electrolysis and  $CH_3OH$  electrolysis. Figure 3.20 shows that, in triode operation, Pt was a superior catalyst for  $H_2O$  electrolysis while Pt-Ru was a superior catalyst for  $CH_3OH$  electrolysis. The enhancement in the electrolyser geometric current density resulting from triode operation was more significant for the electrocatalysts than for the CFP at a given auxiliary  $WE_{aux}$  potential and was greater for  $CH_3OH$  electrolysis than for  $H_2O$  electrolysis. The current enhancement trend was comparable for all catalysts and for both  $H_2O$  and  $CH_3OH$  electrolysis, indicating that the mechanism behind the improvement observed in triode operation is similar for different electrolyser ring  $WE_{elec}$  materials and electro-oxidation reaction mechanisms. Like the galvanostatic experiments indicated, it appears that triode operation promoted the electro-oxidation by influencing the  $H^+$  concentration at the  $WE_{elec}$  surface.

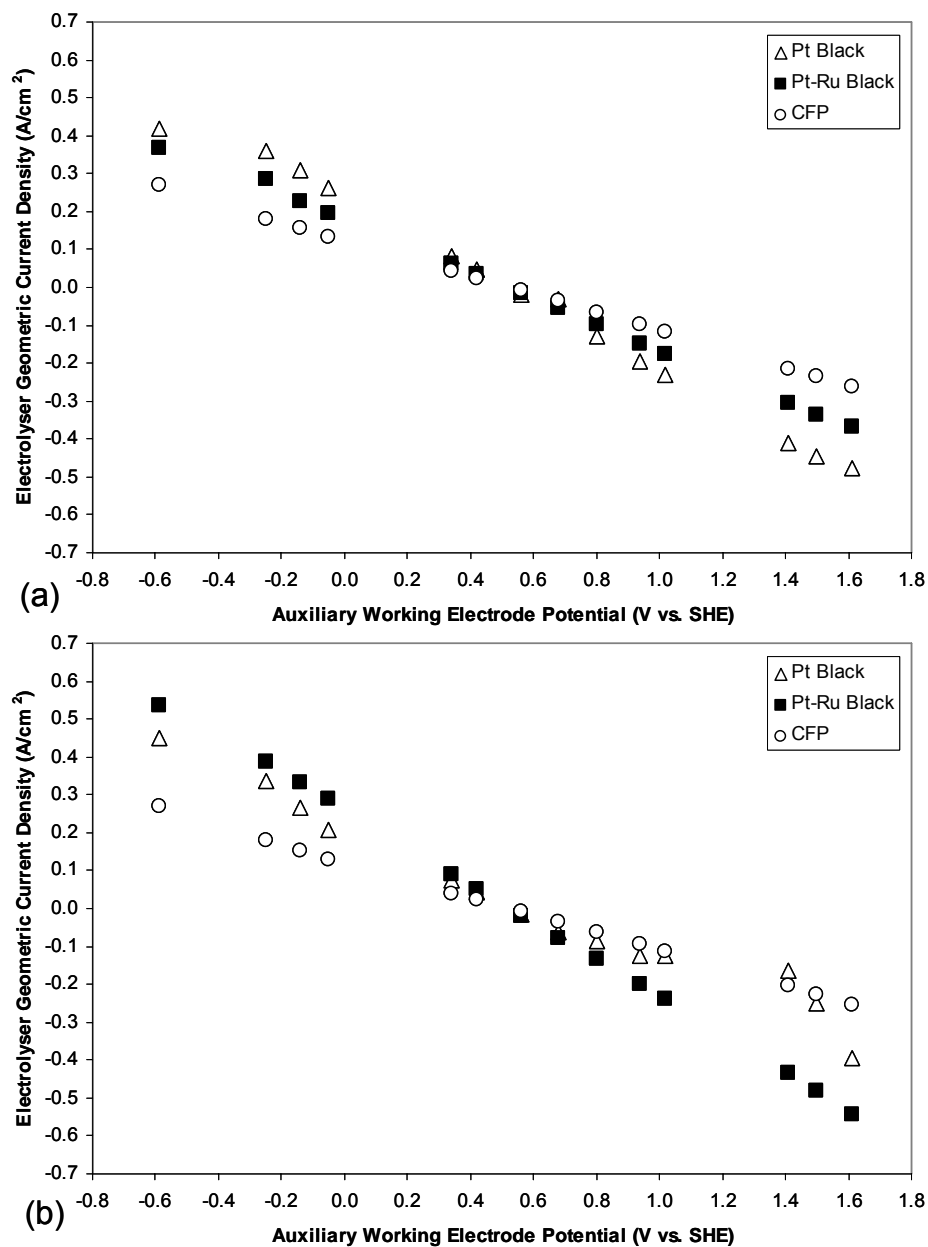


Figure 3.20: Effect of varying  $U_{aux, we}$  on different electrolyser ring  $WE_{elec}$  materials in potentiostatic control (a) 0 M CH<sub>3</sub>OH in 0.5 M H<sub>2</sub>SO<sub>4</sub> electrolyser anolyte, 0.5 M H<sub>2</sub>SO<sub>4</sub> electrolyser catholyte and (b) 2 M CH<sub>3</sub>OH in 0.5 M H<sub>2</sub>SO<sub>4</sub> electrolyser anolyte, 0.5 M H<sub>2</sub>SO<sub>4</sub> electrolyser catholyte (2 mg/cm<sup>2</sup> Pt black, 4 mg/cm<sup>2</sup> Pt-Ru black, and CFP electrolyser  $WE_{elec}$ , Pt auxiliary  $WE_{aux}$ , 2 mg/cm<sup>2</sup> Pt/C CE,  $U_{elec, we} = 0.52$  V vs. SHE).

### 3.5.2.5 Electrolyser rate enhancement ratio, power gain ratio and Faradaic efficiency in potentiostatic control

Table 3.3 list some of the dimensionless rate enhancement ratios,  $\rho_e$ , obtained for H<sub>2</sub>O and CH<sub>3</sub>OH electrolysis on different electrolyser ring WE<sub>elec</sub> materials under the selected experimental conditions in triode operation and potentiostatic control. In most cases,  $\rho_e$  (Eq. 3.7) exceeded the typical catalytic rate enhancement ratios reported for EPOC studies, which are usually in the range of 10 to 100. Once the auxiliary WE<sub>aux</sub> potential reached values in the H<sub>2</sub> production region, a peak  $\rho_e$  was eventually reached in most cases. It occurred at different auxiliary WE<sub>aux</sub> potentials for the different electrolyser ring WE<sub>elec</sub> surfaces studied. The maximum  $\rho_e$  was less significant on Pt-Ru black and Pt black than on the CFP, for which it was an order of magnitude greater than on the catalytic WE<sub>elec</sub> surfaces.

Table 3.3: Effect of auxiliary WE<sub>aux</sub> potential ( $U_{aux, we}$ ) on the rate enhancement ratio ( $\rho_e$ ) (Pt auxiliary WE<sub>aux</sub>, 2 mg/cm<sup>2</sup> Pt/C CE,  $U_{elec, we} = 0.52$  V vs. SHE).

| Electrolyser ring WE <sub>elec</sub><br>[CH <sub>3</sub> OH]<br>[M] | $U_{aux, we}$<br>[V vs. SHE] | 4 mg/cm <sup>2</sup> Pt-Ru black | 2 mg/cm <sup>2</sup> Pt black<br>$\rho_e$<br>[Dimensionless] | CFP   |
|---------------------------------------------------------------------|------------------------------|----------------------------------|--------------------------------------------------------------|-------|
| 0                                                                   | 0.42                         | 692                              | 31                                                           | 1621  |
| 0                                                                   | -0.05                        | 5242                             | 164                                                          | 10072 |
| 0                                                                   | -0.14                        | 1646                             | 305                                                          | 13278 |
| 0                                                                   | -0.25                        | 1903                             | 422                                                          | 2750  |
| 0                                                                   | -0.59                        | 675                              | 485                                                          | 2950  |
|                                                                     |                              |                                  |                                                              |       |
| 2                                                                   | 0.42                         | 22                               | 42                                                           | 2655  |
| 2                                                                   | -0.05                        | 94                               | 288                                                          | 17270 |
| 2                                                                   | -0.14                        | 71                               | 1014                                                         | 25518 |
| 2                                                                   | -0.25                        | 66                               | 1005                                                         | 5900  |
| 2                                                                   | -0.59                        | 89                               | 620                                                          | 3053  |

In triode H<sub>2</sub>O electrolysis, Pt-Ru black resulted in a greater  $\rho_e$  than Pt black, while in triode CH<sub>3</sub>OH electrolysis, Pt black resulted in a greater  $\rho_e$  than Pt-Ru black. This is contrary to that observed in *Chapter 2* under normal electrolysis conditions, for which Pt black was a better catalyst for H<sub>2</sub>O electrolysis than Pt-Ru black, while Pt-Ru black was a better catalyst for CH<sub>3</sub>OH electrolysis than Pt black. It is possible that the CO adsorption is affected during triode or tetrode operation and that the effectiveness of the bi-functional mechanism of the Pt-Ru black electrolyser WE<sub>elec</sub> catalyst is surpassed by the triode or tetrode effect. The CFP electrolyser ring WE<sub>elec</sub> maximum  $\rho_e$  attained was about two times more pronounced for CH<sub>3</sub>OH electrolysis than for H<sub>2</sub>O electrolysis. For the CFP electrolyser ring WE<sub>elec</sub>, after reaching a maximum,  $\rho_e$  dropped sharply as  $U_{aux, we}$  was further increased. This was not the case for the Pt black and Pt-Ru black electrolyser ring WE<sub>elec</sub>, as the  $\rho_e$  decreased more gradually as  $U_{aux, we}$  increased after it reached its peak. This may indicate that the peak  $\rho_e$  was not linked to carbon oxidation. In fact, stability tests were conducted for an hour at the peak  $\rho_e$  for the CFP electrolyser ring WE<sub>elec</sub> in 2 M CH<sub>3</sub>OH at  $U_{aux, we} = -0.14$  V vs. SHE and within 20 min. and  $\rho_e$  stabilized to 10 % of its peak value.

It seems that the H<sup>+</sup> supplied through triode or tetrode operation affected the electrochemical oxidation occurring at the WE<sub>elec</sub> surface, independently of the material used for the WE<sub>elec</sub>. It also appears that the beneficial effect obtained in triode or tetrode operation is independent of the electrochemical reaction occurring at the WE<sub>elec</sub>, as rate enhancements were observed for both, H<sub>2</sub>O electrolysis as well as CH<sub>3</sub>OH electrolysis, which follow two different reaction mechanisms. Although it is possible that the work function of the WE<sub>elec</sub> surface was affected in triode or tetrode operation in the galvanostatic mode, and may have affected the adsorption strength of species at the WE<sub>elec</sub> surface, and reduce the activation energy required for the electrochemical oxidation of H<sub>2</sub>O or CH<sub>3</sub>OH to occur, this is not possible in the potentiostatic mode, as the WE<sub>elec</sub> potential was fixed to a constant value throughout the entire duration of the triode or tetrode experiment.

Figure 3.21 shows the triode electrolyser power gain ratio,  $\gamma_{elec, cell}$ , which is also dimensionless. The values obtained for  $\gamma_{elec, cell}$  were calculated for the cases where the common CE potential was monitored separately, because the cell voltages were required for the analysis. Most  $\gamma_{elec, cell}$  were negative indicating that the power required to operate in triode electrolysis was less than that required to operate

in normal electrolysis. In some cases,  $\gamma_{elec, cell}$  reached values less than -1, suggesting that the decrease in the electrolyser power requirement in triode operation exceeded the power consumed in the auxiliary circuit.

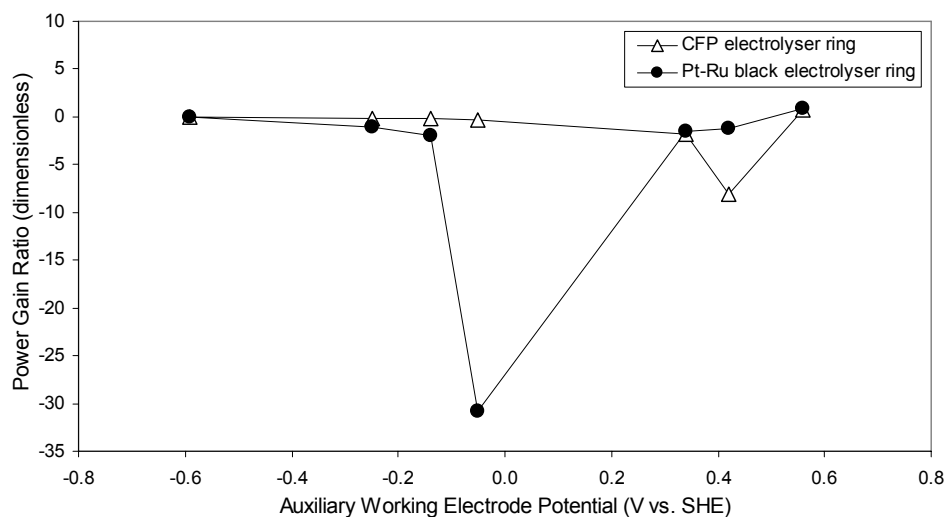


Figure 3.21: Power gain ratio ( $\gamma_{elec, cell}$ ) as a function of  $U_{aux, we}$  (CFP electrolyser ring  $WE_{elec}$  and 4 mg/cm<sup>2</sup> Pt-Ru black electrolyser ring  $WE_{elec}$ , Pt auxiliary  $WE_{aux}$ , 2 mg/cm<sup>2</sup> Pt/C CE, 2 M CH<sub>3</sub>OH in 0.5 M H<sub>2</sub>SO<sub>4</sub> electrolyser anolyte, 0.5 M H<sub>2</sub>SO<sub>4</sub> electrolyser catholyte,  $U_{elec, we} = 0.52$  V vs. SHE).

The maximum  $\gamma_{elec, cell}$  obtained was -30.78 for the Pt-Ru black electrolyser ring WE at  $U_{aux, we} = -0.05$  V vs. SHE and -8.15 for the CFP electrolyser ring  $WE_{elec}$  at  $U_{aux, we} = 0.42$  V vs. SHE. The range of  $U_{aux, we}$  for which  $\gamma_{elec, cell} < -1$  was larger for the Pt-Ru black than for the CFP electrolyser ring  $WE_{elec}$ . The power gain ratios obtained with the CFP electrolyser ring  $WE_{elec}$  in the potentiostatic control were not as significant as the ones obtained in the galvanostatic mode as the auxiliary circuit current densities studied were larger in the potentiostatic mode than in the galvanostatic control. This indicates that larger triode enhancements can be obtained when the imposed auxiliary currents/potentials are very small.

Finally, it was verified that the triode Faradaic efficiency of H<sub>2</sub> production,  $\Lambda$ , averaged from 0.90 to 1.001 for all electrolyser ring  $WE_{elec}$  materials potentiostatically evaluated for the electrolysis of 0 and 2 M CH<sub>3</sub>OH. The largest  $\Lambda$  obtained using Pt-Ru black electrolyser ring  $WE_{elec}$  was 1.18 in H<sub>2</sub>O electrolysis at  $U_{aux, we} = -0.25$  V vs. SHE and 1.07 in CH<sub>3</sub>OH electrolysis at  $U_{aux, we} = -0.59$  V vs. SHE. Although  $\Lambda$

exceeded unity, it can be argued that these values fall within experimental error. According to the Faradaic efficiency definition, the overall triode electrolysis process is Faradaic in nature and the behaviour observed is related to electrocatalysis. However, when comparing the electrolyser circuit in normal electrolysis to the electrolyser circuit in triode electrolysis, it can be said that the current (or potential) of the electrolyser circuit in triode electrolysis exceeds what would be expected from Faraday's law in normal electrolysis.

### **3.5.3 Durability investigation**

#### **3.5.3.1 Long-term triode and tetrode operation in galvanostatic control**

Durability experiments were conducted in triode and tetrode operation in the galvanostatic mode using a CFP electrolyser ring  $WE_{elec}$  at the same operating conditions as for Fig. 3.10. Similar to the prior galvanostatic tests, the electrolyser circuit was first operated by itself for 500 s. The auxiliary circuit was turned on and triode or tetrode operation was held for 3 or 5 hours. After this, the auxiliary circuit was stopped and normal electrolysis was carried-out for 500 s to confirm that the electrolyser circuit came back to its original potential values. The triode or tetrode effect attained a stable maximum about 800 s after the auxiliary circuit was turned on. Triode or tetrode operation was stable for the rest of the experiment, and normal electrolysis before and after the triode or tetrode operation was consistent in all cases. Figure 3.22 shows the durability test results obtained for 3 hours of normal, triode or tetrode operation under galvanostatic control.

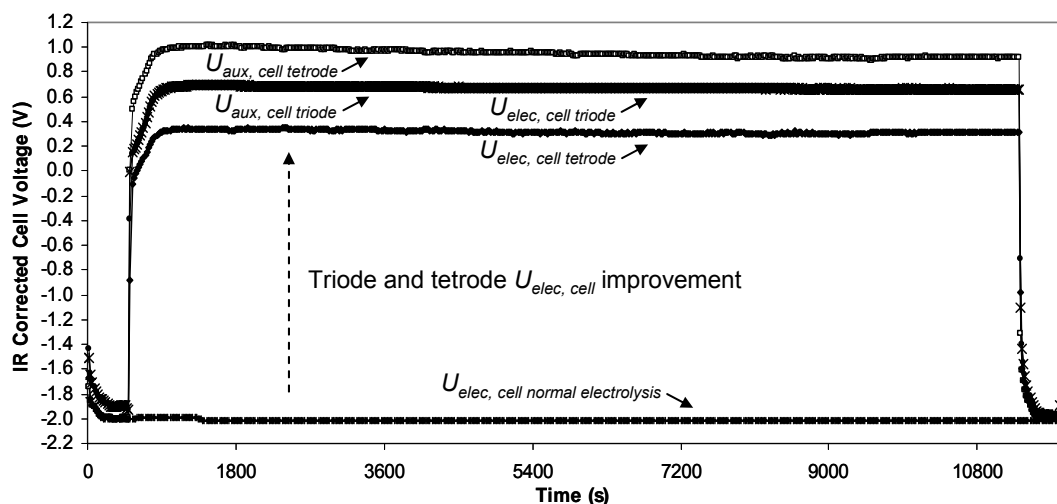


Figure 3.22: Durability test in normal, triode and tetrode electrolysis in galvanostatic control (CFP electrolyser ring  $WE_{elec}$ , Pt auxiliary  $WE_{aux}$ ,  $2 \text{ mg/cm}^2$  Pt/C CE,  $2 \text{ M CH}_3\text{OH}$  in  $0.5 \text{ M H}_2\text{SO}_4$  electrolyser anolyte,  $0.5 \text{ M H}_2\text{SO}_4$  electrolyser catholyte,  $i_{elec, cell} = 1.25 \text{ mA/cm}^2$ ,  $i_{aux, cell} = -50 \text{ mA/cm}^2$ ).

These tests were also repeated for 5 hours of operation. They demonstrated that triode and tetrode electrolysis is reliable over extended periods of operation without any signs of degradation, even when no precious metal catalysts are used on the electrolyser ring  $WE_{elec}$ . As Fig. 3.22 indicates, the measured  $U_{aux, cell, triode}$  differed from the  $U_{aux, cell, tetrode}$  because the auxiliary  $CE_{aux}$ , and the electrolyser  $CE_{elec}$  have different surface areas in the triode than in the tetrode case, as described on Fig. 3.2 (d). The IR corrected  $U_{elec, cell, triode}$  and  $U_{elec, cell, tetrode}$  measured in triode and tetrode operation were almost the same. At the resulting triode and tetrode enhanced  $U_{elec, cell}$  values, the oxidation of  $\text{CH}_3\text{OH}$  on the electrolyser ring  $WE_{elec}$  is promoted, while carbon corrosion is avoided. Although the potential of the common CE in triode operation, or of the  $CE_{aux}$  and  $CE_{elec}$  in tetrode operation was not monitored for the galvanostatic control experiments presented in Fig. 3.22, it is known from other triode and tetrode experiments that the potential of the counter electrode(s) does not vary significantly during triode or tetrode electrolysis. Thus, the working electrode(s) potential is close to the cell voltage.

### 3.5.3.2 Methanol concentration change over time in long-term triode or tetrode galvanostatic control

During the normal, triode or tetrode electrolysis durability tests, samples of the analyte solution were taken at 30 min. intervals. The samples were diluted for analysis by a  $K_2Cr_2O_7$  reduction technique used in combination with spectrophotometric measurements as in *Chapter 2*, and described in *Appendix E* in order to determine the change in  $CH_3OH$  concentration over time. The dilution effect of sample extractions over time was taken into account in the  $CH_3OH$  concentration calculations and in the Faradaic  $CH_3OH$  concentration predictions.

The methodology was validated by measuring the  $CH_3OH$  concentration change over time in normal electrolysis in the galvanostatic control. The  $CH_3OH$  concentration did not change significantly over the course of the normal electrolysis, and agreed with that predicted by Faraday's law under the same conditions. Faraday's law predicts that, at the normal electrolysis current employed, the change in  $CH_3OH$  concentration would be about 0.001 % over 3 hours. The concentration results also confirm that there was no significant  $CH_3OH$  evaporation over time due to reduced volume of reactant as solution samples were drawn out at ambient conditions. It was also verified that, when running the auxiliary circuit by itself in tetrode configuration under the same experimental conditions and for the same time period, the  $CH_3OH$  concentration did not change over the duration of the experiment.

Results obtained for the three hour normal, triode and tetrode electrolysis are shown on Figure 3.23. The  $K_2Cr_2O_7$  technique did not detect any significant  $CH_3OH$  concentration changes over the first hour of the experiment. However, after the first hour, the triode and tetrode  $CH_3OH$  concentration measurement trends indicate a decrease in the  $CH_3OH$  concentration over time during triode and tetrode electrolysis, even though no catalyst was present on the electrolyser ring  $WE_{elec}$ .

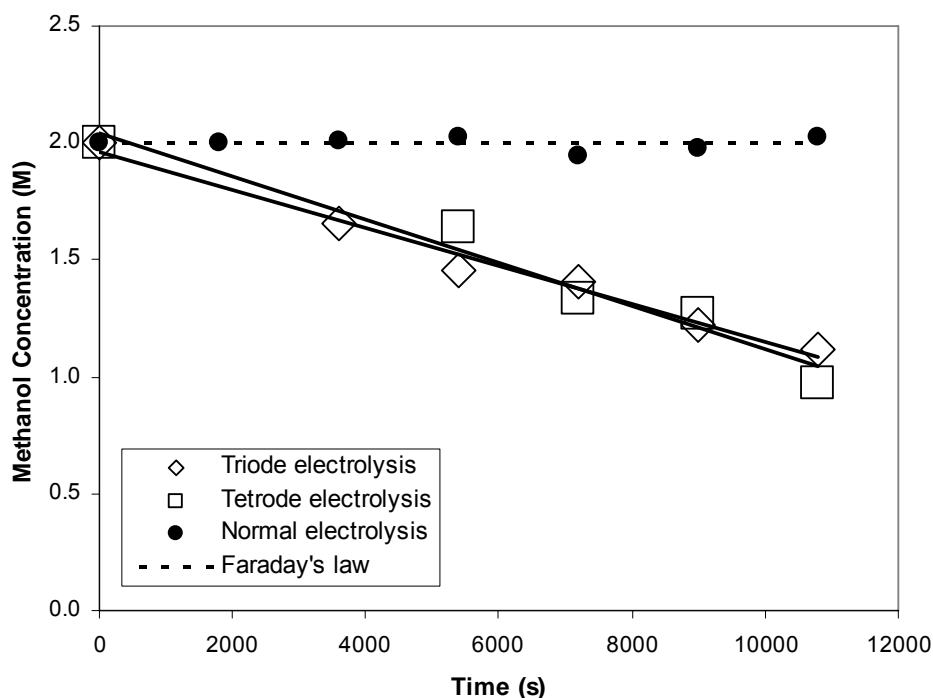


Figure 3.23: Methanol concentration as a function of time as predicted by Faraday's law, and during normal, triode, and tetraode electrolysis in galvanostatic control (CFP electrolyser ring  $WE_{elec}$ , Pt auxiliary  $WE_{aux}$ , 2 mg/cm<sup>2</sup> Pt/C CE, 2 M CH<sub>3</sub>OH in 0.5 M H<sub>2</sub>SO<sub>4</sub> electrolyser anolyte, 0.5 M H<sub>2</sub>SO<sub>4</sub> electrolyser catholyte,  $i_{elec, cell} = 1.25$  mA/cm<sup>2</sup>,  $i_{aux, cell} = -50$  mA/cm<sup>2</sup>).

The slope of the concentration plots revealed that the measured CH<sub>3</sub>OH consumption was within 10 % for the triode and the tetraode operation cases. The CH<sub>3</sub>OH concentration measurements indicate that, in triode or tetraode operation, CH<sub>3</sub>OH was consumed at a rate exceeding the imposed electrolysis current. That is, the CH<sub>3</sub>OH consumption rate attained in triode and tetraode electrolysis exceeded what was expected from Faraday's Law for normal electrolysis. It is possible to calculate the electrolysis circuit current density equivalent to the CH<sub>3</sub>OH consumption rate,  $i'_{elec, cell}$ . For the triode operation case,  $i'_{elec, cell}$  was 2130 mA/cm<sup>2</sup>, and for the tetraode operation case,  $i'_{elec, cell}$  was 1911 mA/cm<sup>2</sup>. Both are three orders of magnitude greater than the imposed  $i_{elec, cell}$  of 1.25 mA/cm<sup>2</sup> (2.11 mA). This calculated current density even exceeds the sum of the imposed  $i_{elec, cell}$  and the imposed  $i_{aux, cell}$  of -50 mA/cm<sup>2</sup> (4 mA). The difference between the calculated CH<sub>3</sub>OH consumption rates and the one expected from the current density imposed may be explained by an increase in the low temperature catalytic reforming reaction rate which may result from an EPOC effect, as the  $WE_{elec}$  potential, hence its work function, was affected.

This non-Faradaic effect would imply that the catalytic reaction rate exceeds the rate of  $H^+$  transport, which is equal to the rate of the electrochemical reaction. The EPOC effect will be discussed further in *Chapter 5*. Another possible explanation is that the auxiliary current is indirectly contributing, fully or partly, to the electrochemical oxidation of methanol by pulling protons away from the  $WE_{elec}$  surface.

In the case of  $H_2O$  electrolysis, the absorption strength of the  $H_2O$  molecules at the  $WE_{elec}$  surface may have decreased, rendering it easier to be electro-oxidized. In the case of  $CH_3OH$  electrolysis, this in-situ  $WE_{elec}$  surface potential change may help the removal of  $WE_{elec}$  surface adsorbed CO, which normally constitutes the rate limiting step of  $CH_3OH$  oxidation. The effect would be similar if the species adsorbed to the  $WE_{elec}$  surface were contaminants or poison, catalytic or not in nature. Surface contaminants reduce the Faradaic efficiency and hinder the  $WE_{elec}$ 's performance. The  $WE_{elec}$  surface adsorption limits mass transfer, affects the reaction mechanism, and impacts the double-layer capacitance. When CO is removed from the surface, a recovery in performance is expected, like it was seen in the case of triode or tetrode electrolysis.

### **3.5.3.3 Long-term tetrode operation in mixed potentiostatic and galvanostatic control**

Long-term durability electrolysis experiments were also conducted in tetrode operation with a CFP electrolyser ring  $WE_{elec}$  in mixed control. For these tests, the tetrode circuits were controlled differently in order to demonstrate the advantage of the complete independence of the electrolyser and of the auxiliary circuits. The electrolyzer circuit was controlled potentiostatically, while the auxiliary circuit was independently controlled galvanostatically. This is not possible in triode operation, for which both circuits have to be controlled in the same operating control, i.e., both in galvanostatic or both in potentiostatic control, as there would be grounding interferences for mixed control as a common CE is used.

The testing methodology employed was similar to the one used in the tests where both circuits were controlled galvanostatically. The electrolyzer circuit was operated by itself in normal electrolysis for 500 s before the auxiliary circuit was turned on. In these tests, tetrode operation was held for 30 minutes instead of 500 s. The auxiliary circuit was then turned off and re-started again for another 30 minutes. The shut-down times, which did not exceed two minutes, are indicated by the vertical dotted lines in Fig.



of tetrode operation. Consequently, it was demonstrated that, in tetrode operation, it is possible to control the electrolyzer circuit potentiostatically while independently controlling the auxiliary circuit galvanostatically for extended periods of time, and with multiple start-ups and shut-downs of the auxiliary circuit.

### 3.5.3.4 Methanol concentration change over time in long-term tetrode operation in mixed potentiostatic and galvanostatic control

The regular shut-down times of the long-term durability tetrode electrolysis tests carried out in mixed control permitted the withdrawal of anolyte solution from the Wes compartment for CH<sub>3</sub>OH concentration analysis. The extracted samples were diluted and analyzed using the same K<sub>2</sub>Cr<sub>2</sub>O<sub>7</sub>/spectrophotometric technique as before. The CH<sub>3</sub>OH concentration measured at different times during the experiments carried-out in Fig. 3.24 are shown in Fig. 3.25. Although not shown here, the tetrode electrolysis mixed control durability test carried out in Fig. 3.24 was also repeated at  $U_{elec,we} = 0.52$  V vs. SHE and  $i_{aux,cell} = -5$  mA/cm<sup>2</sup>, and the trend obtained for the CH<sub>3</sub>OH concentration change over time was very similar.

The CH<sub>3</sub>OH concentration changes measured during mixed control tetrode operation significantly exceeded that measured in normal electrolysis. The calculated electrolyzer circuit current equivalent to the measured CH<sub>3</sub>OH consumption rate obtained in tetrode operation,  $i'_{elec, cell}$ , was calculated to be 189 mA/cm<sup>2</sup>, which is within 20 % of the average measured  $I_{elec, cell}$  obtained in tetrode operation, which is 237 mA/cm<sup>2</sup>. Note that the power enhancement ratio,  $\rho_{elec, cell}$ , (Eq. 3.5) and electrolyzer power gain ratio,  $\gamma_{elec, cell}$ , (Eq. 3.6) could have been calculated with  $I_{elec, cell}$  and by replacing  $I_{elec, cell}$  by  $i'_{elec, cell}$  if the electrolyzer CE<sub>elec</sub> potential would have been monitored during the experiments. This would have allowed  $U_{elec,cell}$  to be calculated, as  $U_{elec,we}$  was fixed. Under the tetrode mixed control conditions, the electrolyzer rate enhancement ratio,  $\rho_e$  (Eq. 3.7, dimensionless), can be calculated since it is the ratio of the electrolyzer current in tetrode operation to the electrolyzer current in normal operation. For the tetrode test carried out in at  $U_{elec, we} = 1$  V vs. SHE, and  $i_{aux, cell} = -20$  mA/cm<sup>2</sup>, it was calculated to be 1600 using  $i'_{elec, cell}$  and 2011 using  $I_{elec, cell}$ . In EPOC studies, promotional rate enhancement ratio values in the range of 10 to 100 are common [18].

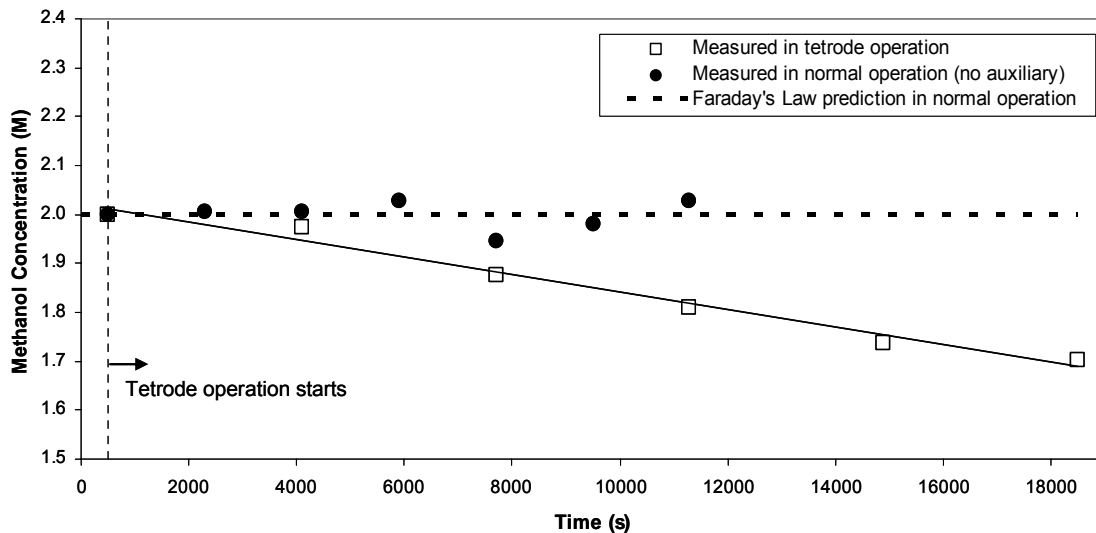


Figure 3.25: Methanol concentration as a function of time as predicted by Faraday's law and as measured during potentiostatic electrolyser circuit control and galvanostatic auxiliary circuit control in tetrode electrolysis (CFP electrolyser ring  $WE_{elec}$ , Pt auxiliary  $WE_{aux}$ , 2 mg/cm<sup>2</sup> Pt/C  $CE_{elec}$ , and Pt auxiliary  $CE_{aux}$ , 2 M CH<sub>3</sub>OH in 0.5 M H<sub>2</sub>SO<sub>4</sub> electrolyser anolyte, 0.5 M H<sub>2</sub>SO<sub>4</sub> electrolyser catholyte,  $U_{elec, we} = 1$  V vs. SHE,  $i_{aux, cell} = -20$  mA/cm<sup>2</sup>).

The Faradaic efficiency,  $\Lambda$  (Eq. 3.8, dimensionless), is the ratio of the current gain attained in tetrode electrolysis vs. normal electrolysis over the auxiliary current. For the tetrode test carried out at  $U_{elec, we} = 1$  V vs. SHE,  $i_{aux, cell} = -20$  mA/cm<sup>2</sup>, it was 160 using  $I'_{elec, cell}$  and 192 using  $I_{elec, cell}$ . As  $\Lambda$  exceeded unity, the change in the electrochemical reaction rate is non-Faradaic as the H<sub>2</sub> production rate in tetrode electrolysis exceeded the attainable H<sub>2</sub> production rate when the electrolyzer was operating normally. These results provided further evidence that the CH<sub>3</sub>OH consumption rate obtained in triode and tetrode electrolysis exceed what can be obtained from normal electrolysis.

The change in CH<sub>3</sub>OH concentration measured over time in tetrode operation was much more significant for the case for which the electrolyser circuit was controlled galvanostatically, then for the case for which the electrolyser circuit was controlled potentiostatically, i.e., by fixing the  $WE_{elec}$  potential. In the galvanostatic control case, the electrolyser current density was fixed at 1.25 mA/cm<sup>2</sup>, while in the mixed control case, the electrolyser  $WE_{elec}$  potential was fixed at 1 V vs. SHE, which corresponded to a current density of 237 mA/cm<sup>2</sup> in tetrode operation. Based on this, it would be expected that the CH<sub>3</sub>OH

consumption rate in mixed control would exceed the CH<sub>3</sub>OH consumption rate in galvanostatic control. However, it was not the case. As it was mentioned earlier, the significant enhancement in the CH<sub>3</sub>OH consumption rate obtained in galvanostatic control may be linked to an EPOC effect which lowered the activation energy for the catalytic CH<sub>3</sub>OH reforming reaction at the electrolyser ring WE<sub>elec</sub> potential attained during the application of EPOE. Thus, combining these phenomena, it may be possible to carry out the catalytic reforming of CH<sub>3</sub>OH at ambient conditions using non-precious metal at the electrolyser ring WE<sub>elec</sub>. The EPOC phenomenon will be discussed in more details in *Chapter 5*.

### **3.5.4 Mechanism investigation**

#### **3.5.4.1 Electrolytic contact of auxiliary electrodes in potentiostatic control**

As explained earlier, when the auxiliary WE<sub>aux</sub> is in reduction, H<sub>2</sub> is generated, and when the auxiliary WE<sub>aux</sub> is in oxidation, O<sub>2</sub> and/or CO<sub>2</sub> are generated. It was noticed that, when the contact between the auxiliary WE<sub>aux</sub> and the membrane was poor, an enhancement was still observed, but to a lesser extent. For this reason, the effect of generating the same amounts of H<sub>2</sub> or O<sub>2</sub>, but 1 cm away from the membrane surface was examined in triode and tetrode operation. Results for tetrode operation are shown in Fig. 3.26.

As shown in Fig. 3.26 (a), when the auxiliary WE<sub>aux</sub> located in the CH<sub>3</sub>OH or water electro-oxidation compartment was pulled 1 cm away from the membrane surface, no effect on the electrolyser geometric current density could be observed, even when the area in front of the auxiliary WE<sub>aux</sub> was saturated with H<sub>2</sub>. The auxiliary WE<sub>aux</sub> needs to be in ionic contact with the membrane in order to observe the beneficial triode effect. Thus, triode or tetrode enhancements can not be achieved with molecular H<sub>2</sub> and therefore appear to be protonic in nature. When bubbling an equivalent amount of H<sub>2</sub> away from the electrolyser ring WE<sub>elec</sub> surface, no similar enhancement effect was obtained. The increased availability of H<sup>+</sup> may contribute to enhance the protonic conductivity of the membrane in triode operation. This will be looked at in *Section 3.5.4.2*.

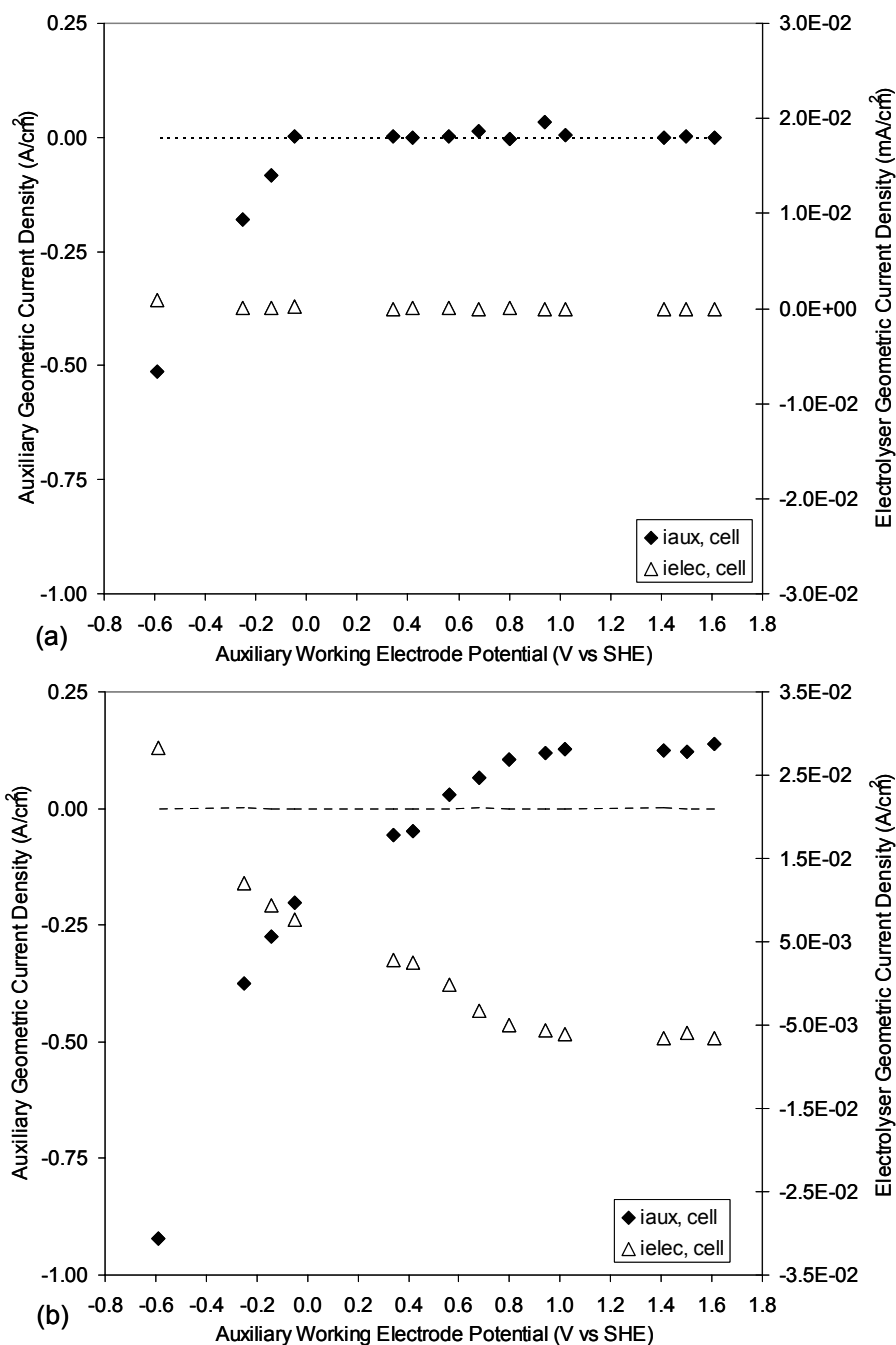


Figure 3.26: Effect of varying  $U_{aux, we}$  on the electrolyser current density in tetrode operation (a) Pt auxiliary  $WE_{aux}$  1 cm away from surface (b) Pt auxiliary  $CE_{aux}$  1 cm away from surface (CFP electrolyser ring  $WE_{elec}$ , 2 M  $CH_3OH$  in 0.5 M  $H_2SO_4$  electrolyser anolyte, 0.5 M  $H_2SO_4$  electrolyser catholyte,  $U_{elec, we} = 0.52$  V vs. SHE).

In tetrode operation, the independent auxiliary  $CE_{aux}$  was pulled 1 cm away from the surface. As shown on Fig. 3.26 (b), a slight enhancement was observed but it was not as significant as when the  $CE_{aux}$  was in electrolytic contact with the membrane, probably due to an increase in the circuit resistance. Hence, it appears that the auxiliary  $CE_{aux}$  does not need to be in electrolytic contact with the membrane.

### 3.5.4.2 Effect of acid concentration and conductivity on triode operation in potentiostatic control

Water electrolysis was conducted on a CFP electrolyser ring  $WE_{elec}$  using 0.05, 0.5 and 5 M  $H_2SO_4$  as the electrolyte in the WE compartment in order to evaluate the effect of  $H^+$  concentration with and without the auxiliary circuit. Figure 3.27 shows the effect of acid concentration on membrane and solution conductivity. The enhancements obtained in conductivity are in a similar range to other data reported in the literature [195-197]. The intrinsic increases in conductivity with increasing electrolyte concentration are not significant enough to account for the triode operation enhancement observed.

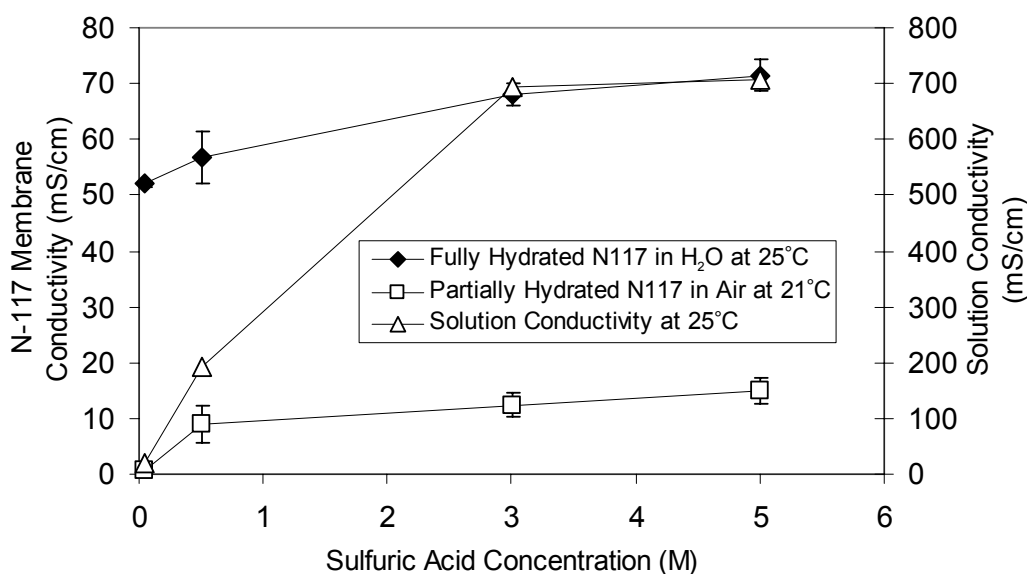


Figure 3.27: Nafion<sup>®</sup> N-117 membrane conductivity and solution conductivity as a function of sulphuric acid concentration.

In general it is assumed that there is sufficient supporting electrolyte to transfer the ions from the bulk of the solution to the electrode surface by diffusion. Potentiostatic mode results for water electrolysis with different acid concentrations are shown in Fig. 3.28. They were obtained under different conditions than

the tests carried out in the galvanostatic mode in Fig. 3.11 b). As explained earlier, in the potentiostatic mode,  $U_{elec, we}$  was set to 0.52 V vs. SHE to avoid carbon corrosion of the electrolyser CFP ring  $WE_{elec}$ . It was verified that changing this value to 0.6 or 0.7 V vs. SHE did not affect the results significantly.

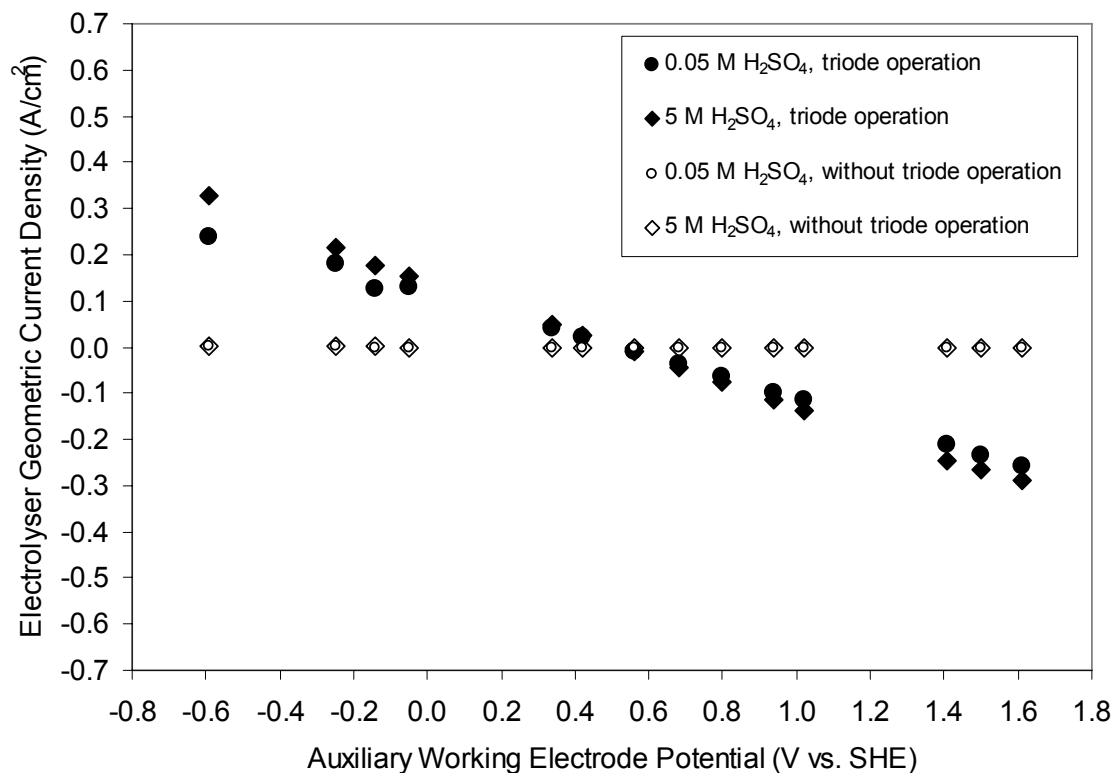


Figure 3.28: Effect of varying  $U_{aux, we}$  on the electrolyser current density (CFP electrolyser ring  $WE_{elec}$ , Pt auxiliary  $WE_{aux}$ , 2 mg/cm<sup>2</sup> Pt/C CE, 0 M CH<sub>3</sub>OH in 0.05 or 5 M H<sub>2</sub>SO<sub>4</sub> electrolyser anolyte, 0.5 M H<sub>2</sub>SO<sub>4</sub> electrolyser catholyte,  $U_{elec, we} = 0.52$  V vs. SHE).

Fig. 3.28 indicates that, in the potentiostatic mode, the relative difference between  $U_{elec, we}$  and  $U_{aux, we}$  had a direct influence on the magnitude of the triode enhancement obtained. This is in agreement with the galvanostatic results obtained in (Fig. 3.24 b)). In the galvanostatic mode or in the potentiostatic mode, the relative difference between the current/potential of the electrolyser circuit to the current/potential of the auxiliary circuit has an impact on the triode enhancement obtained. Most importantly, Fig. 3.28 demonstrates that increasing the electrolyte concentration or solution pH had no significant effect when the triode was not in use and resulted in only slight enhancements in triode operation. Consequently, the triode enhancement can not be primarily attributed to an increase in the

bulk  $H^+$  concentration of the electrolyte in the entire WE compartment. This indicates that the largest part of the performance enhancement is related to localized effects at the electrodes rather than the electrolyte.

#### **3.5.4.3 Effect of triode operation on membrane conductivity in potentiostatic control**

Electrochemical impedance spectroscopy (EIS) measurements were performed while operating the electrolyser in normal potentiostatic control for triode operation. These measurements were taken to determine if the resistance of the MEA decreased in triode electrolysis compared to normal electrolysis. It was previously suggested that during triode fuel cell operation, the conductivity of the Nafion<sup>®</sup> polymer improved by lowering the overpotential for proton tunnelling between the membrane sulphonated groups (proton tunnelling was reported to increase exponentially with potential), which would improve proton migration through the membrane [173, 198]. The data points shown in Fig. 3.29 represent the average of three different tests for normal and triode electrolysis.

The measurements taken before 200 s indicate that the MEA resistance is less in triode electrolysis than in normal electrolysis. However, after 200 s, the resistance stabilizes and the MEA resistance is on average about 0.03 ohms larger for triode electrolysis compared to normal operation. It confirms that the membrane conductivity does not improve due to the  $H^+$  flux produced by the auxiliary circuit. Therefore, the beneficial effect observed for triode operation appears to be limited to the working electrode surfaces only.

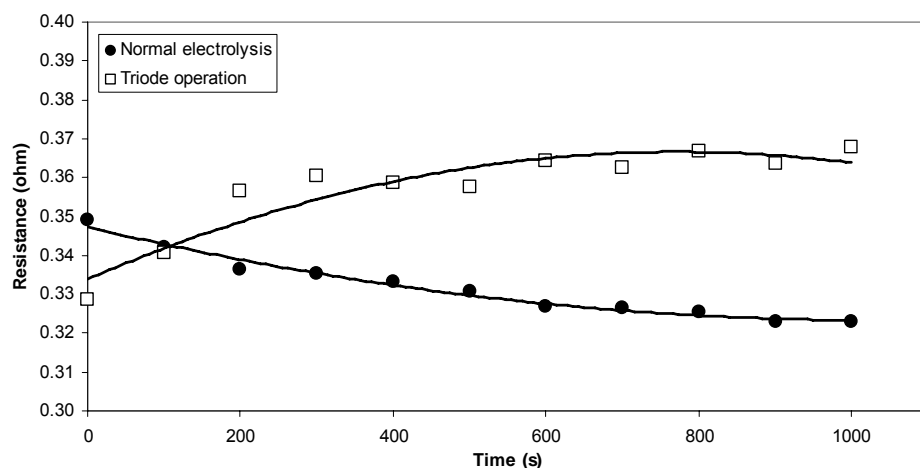


Figure 3.29: Resistance measurement over time in normal electrolysis and in triode electrolysis (CFP electrolyser ring  $WE_{elec}$ , Pt auxiliary  $WE_{aux}$ ,  $2 \text{ mg/cm}^2$  Pt/C CE,  $2 \text{ M CH}_3\text{OH}$  in  $0.5 \text{ M H}_2\text{SO}_4$  electrolyser anolyte,  $0.5 \text{ M H}_2\text{SO}_4$  electrolyser catholyte,  $U_{elec, we} = 0.52 \text{ V vs. SHE}$ ,  $U_{aux, we} = -0.59 \text{ V vs. SHE}$ ).

#### 3.5.4.4 Effect of electrolyser working electrode ring geometry in potentiostatic control

Various triode arrangements geometries could be considered, but the discussion is limited to the cell configuration described in *Section 3.1.2*. The impact of the electrolyser ring  $WE_{elec}$  dimension was evaluated by changing the gap distance between the auxiliary  $WE_{aux}$  Pt disk and electrolyser ring  $WE_{elec}$ . In Fig. 3.30, the effect of a small gap distance (3.18 mm) was compared to a larger gap distance (6.73 mm).

More significant enhancements were observed when the gap distance between the electrolyser ring  $WE_{elec}$  and the auxiliary  $WE_{aux}$  Pt disk was smaller. A larger distance might negatively affect the spillover of proton charges from the auxiliary  $WE_{aux}$  to the electrolyser ring  $WE_{elec}$ . The gap size effect was more important in the case of  $2 \text{ M CH}_3\text{OH}$  than in the case of  $\text{H}_2\text{O}$  electrolysis. Hence, the spillover of protons appears to enhance the complex electro-oxidation mechanism of  $\text{CH}_3\text{OH}$  depolarized  $\text{H}_2\text{O}$  electrolysis and have less effect on the mechanism of  $\text{H}_2\text{O}$  electrolysis.

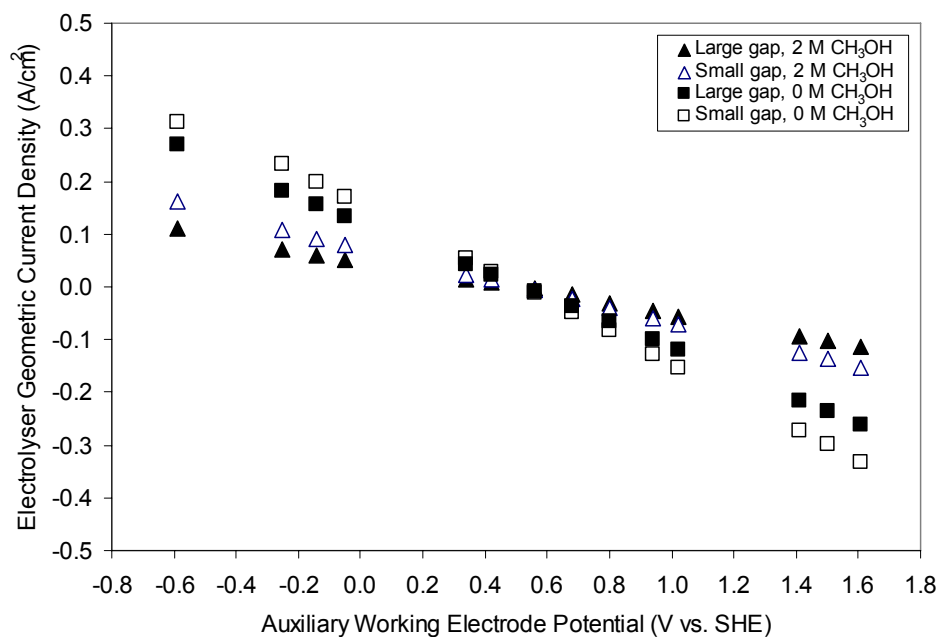


Figure 3.30: Effect of varying  $U_{aux, we}$  on the  $i_{elec, cell}$  for different electrolyser ring  $WE_{elec}$  gap distances (CFP electrolyser ring  $WE_{elec}$ , 2 M  $CH_3OH$  in 0.5 M  $H_2SO_4$  electrolyser anolyte, 0.5 M  $H_2SO_4$  electrolyser catholyte,  $U_{elec, we} = 0.52$  V vs. SHE).

### 3.5.4.5 Effect of proton flux line direction in potentiostatic control

The effect of changing the proton flux lines direction through the MEA was investigated in tetrode operation in the potentiostatic mode. For a normal electrolyser with a single electrolyser ring  $WE_{elec}$  and electrolyser  $CE_{elec}$ , the current lines are straight. The electrolyser current lines will be different when an auxiliary  $WE_{aux}$  is added and used in the reverse direction. The local  $H^+$  concentration around the auxiliary  $WE_{aux}$  may be higher, and a concentration gradient of protons might result over the entire surface, with the peak in  $H^+$  concentration on the auxiliary  $WE_{aux}$ . In addition,  $CH_3OH$  crossover from the electrolyser ring  $WE_{elec}$  to the electrolyser  $CE_{elec}$  might be hindered by the proton flux from the  $CE_{aux}$  to the auxiliary  $WE_{aux}$ . Fig. 3.31 shows the effect of inverting the CEs or inverting the WEs in tetrode operation. In Fig. 3.31 (a), the auxiliary  $CE_{aux}$  is the ring and the electrolyser  $CE_{elec}$  is the Pt rod. In Fig. 3.31 (b) the auxiliary  $WE_{aux}$  is the ring and the electrolyser  $WE_{elec}$  is the Pt rod.

In general, a weak to no effect was observed when the current lines were intersecting each other. A slight effect was observed when the CEs were inverted; however, it is so small that it is not significant. The beneficial tetrode effect was not obtained when the WEs were inverted. It is likely that, when the large CFP WE ring is the  $WE_{aux}$ , less  $H^+$  is generated per surface area than when the  $WE_{aux}$  is the smaller Pt rod tip surface area. Consequently, it is possible that there is less  $H^+$  spilling over from the CFP ring  $WE_{aux}$  to the Pt  $WE_{elec}$  than when it is spilling over from the Pt  $WE_{aux}$  to the CFP ring  $WE_{elec}$ . Also, it is possible that the misalignment of the electric fields generated when the WEs or CEs are inverted creates dynamic transport issues through the solid electrolyte (crossover,  $H_2O$  transport, etc.), while the alignment of the electric fields improves the transport and kinetics of the electron transfer reaction at the  $WE_{elec}$  surface.

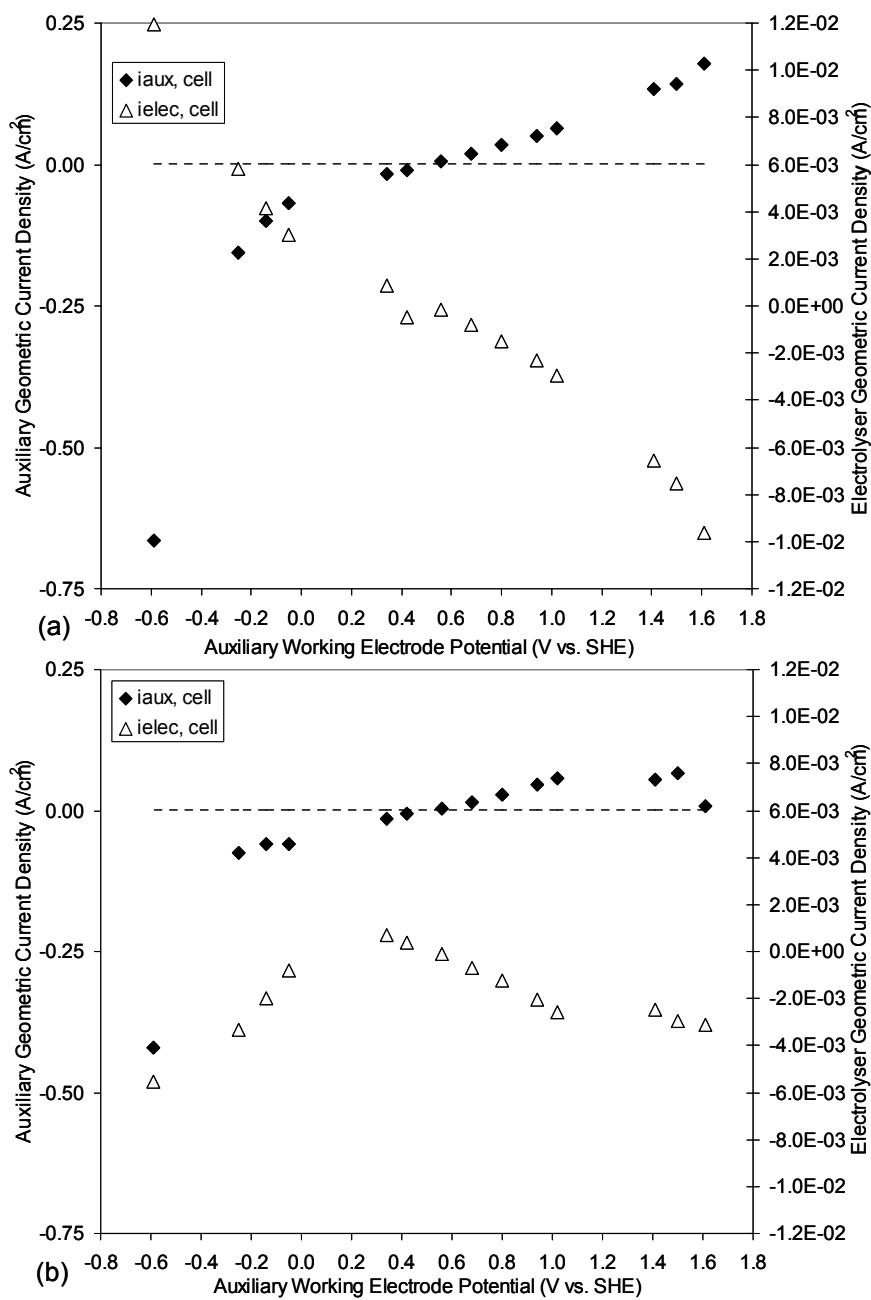


Figure 3.31: Effect of varying  $U_{aux, we}$  on the current density in tetrode operation (a) inverted CEs (CFP ring WE<sub>elec</sub>, Pt rod WE<sub>aux</sub>, Pt rod CE<sub>elec</sub>, Pt/C CE<sub>aux</sub>) (b) inverted WEs (Pt rod WE<sub>elec</sub>, CFP ring WE<sub>aux</sub>, Pt/C ring CE<sub>elec</sub>, Pt rod CE<sub>aux</sub>), (2 M CH<sub>3</sub>OH in 0.5 M H<sub>2</sub>SO<sub>4</sub> electrolyser anolyte, 0.5 M H<sub>2</sub>SO<sub>4</sub> electrolyser catholyte,  $U_{elec, we} = 0.52$  V vs. SHE).

#### 3.5.4.6 Effect of the electrochemical surface area of the carbon fibre paper electrolyser working electrode in potentiostatic control

The use of triode and tetrode electrolysis in the absence of PGM catalyst at the electrolyser ring  $WE_{elec}$  was demonstrated in *Sections 3.5.1* and *3.5.2*. It was also confirmed that no CFP corrosion was occurring over the operating potential region used during the galvanostatic and potentiostatic tests. In all experiments so far, a simple plane carbon fibre paper was employed as the electrolyser ring  $WE_{elec}$ . In this section, an MPL at a loading of  $1 \text{ mg/cm}^2$  (composed of carbon black and 20 wt% PTFE) was sprayed on the CFP surface and was tested as the electrolyser ring  $WE_{elec}$  to investigate the influence of the surface area and CFP surface morphology. Figure 3.32 compares the results obtained with this three-dimensional high surface area CFP electrolyser ring  $WE_{elec}$  to the ones obtained with the planar CFP fibre paper electrolyser ring  $WE_{elec}$ .

Using a high surface area 3-dimensional CFP based electrolyser ring  $WE_{elec}$  did not improve the operation of the triode electrolyser significantly compared to when a lower surface area carbon based electrolyser ring  $WE_{elec}$  was used. The maximum improvement in electrolyser geometric current density obtained was about 16 % at the maximum  $U_{aux, we}$  value of -0.6 V vs. SHE in the  $H_2$  production region. The pore structure of the carbon based surface might have affected the chemisorption strength of adsorbed species. It would be expected that a structure with more pores and channels would lead to a larger triple phase boundary (TPB) which would in turn improve its activity. Microscopic surface analysis measurement techniques would be required to confirm exactly how  $H^+$  catalyzed the carbon based surfaces.

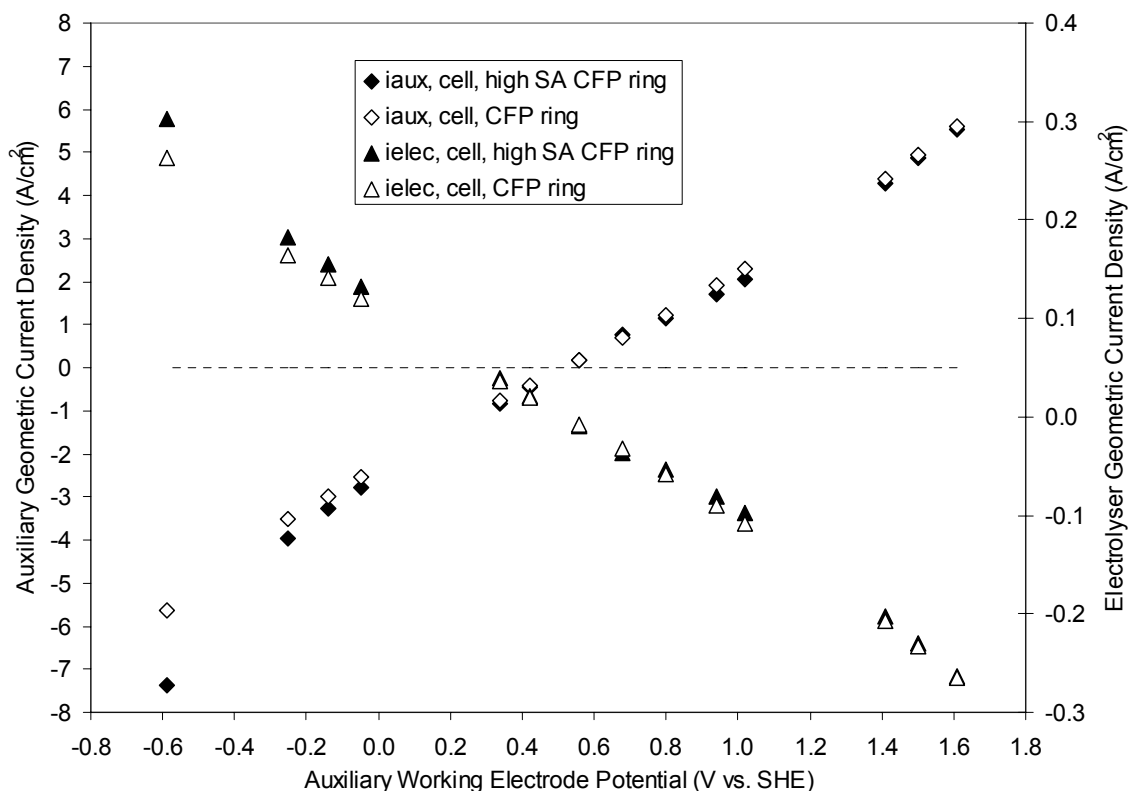


Figure 3.32: Effect of electrolyser ring CFP  $WE_{elec}$  carbon SA on  $i_{elec, cell}$  (2 M  $CH_3OH$  in 0.5 M  $H_2SO_4$  electrolyser anolyte, 0.5 M  $H_2SO_4$  electrolyser catholyte,  $U_{elec, we} = 0.52$  V vs. SHE).

### 3.5.4.7 Effect of triode operation using non-noble non-carbon containing working electrode materials in potentiostatic control

Triode and tetrode operation were shown to promote the electrocatalytic properties of the CFP electrolyser ring  $WE_{elec}$ . Carbon oxidation, which could affect the CFP electrolyser ring  $WE_{elec}$ , was avoided by restricting the electrolyser operating voltage range. However, in the potentiostatic mode, it was possible to subject the auxiliary  $WE_{aux}$  material (Pt) to a wider range of potentials than the electrolyser ring  $WE_{elec}$  material (CFP or noble metal catalyst GDE). It may be possible to operate the electrolyser over a wider range of currents/potentials if a suitable carbon-free electrolyser ring  $WE_{elec}$  material can be used. The possibility of conducting the electro-oxidation of  $CH_3OH$  on a non-precious carbon-free electrolyser ring  $WE_{elec}$  was investigated in triode operation.

In order to achieve this, appropriate materials needed to be selected. Ideally, the electrolyser ring  $WE_{elec}$  material would exhibit corrosion resistance over a wide range of electrolyser ring  $WE_{elec}$  currents/potentials in 0.5 M  $H_2SO_4$ . In addition to conducting electricity and possessing a good stability, the electrolyser ring  $WE_{elec}$  material should allow for the migration and spreading of the  $H^+$  ions generated at the auxiliary  $WE_{aux}$  surface. In addition, material corrosion or degradation may negatively impact the PEM conductivity due to ion contamination. Pourbaix diagrams demonstrate in which state a material will be at equilibrium at specific pH values and potentials, but do not provide information about the material surface kinetics for a particular electrochemical reaction. Ideally, based on the potentiostatic studies carried out in *Section 3.5.2*, the electrolyser material would be immune or form a passive film at a pH of 0 (0.5 M  $H_2SO_4$ ) and at anodic potential of  $\geq 0.5$  V vs. SHE at ambient conditions. Similarly, in reverse operation, the ideal auxiliary  $WE_{aux}$  material would be immune or form a passive film at a pH of 0 in a potential range  $\leq 0.5$  V vs. SHE at ambient conditions. Grade 316 SS is an austenitic SS, which contains Mo for higher corrosion resistance. According to its Pourbaix diagram, at pH = 0 and potentials greater than -1 V vs. SHE, the 16 to 18 % of Cr contained in the 316 SS will eventually start leaching out, and the 316 SS will corrode [199]. However, gold is stable at pH = 0, up to potentials of about 1.4 V vs. SHE [200]. Different materials can be used for the triode electrolyser ring  $WE_{elec}$  than for the auxiliary  $WE_{aux}$ . For example, the electrolyser ring  $WE_{elec}$  could be an electrochemically etched fine titanium mesh, as Ti is passive at potentials greater than 0 V vs. SHE [201]. In the same triode experiment, the auxiliary  $WE_{aux}$  rod could be made of niobium, which does not exhibit corrosion at potentials less than -0.3 V vs. SHE [202], if the auxiliary  $WE_{aux}$  is operated in the  $H_2$  production region at potentials lower than this value.

All experiments were conducted in a 0 or 2 M  $CH_3OH$  acidic anolyte and a 0.5 M  $H_2SO_4$  catholyte, for which more information was provided in *Chapter 2*. For carbon free non-precious electrolyser ring  $WE_{elec}$  experiments a corrosion resistant 316 SS woven wire cloth (McMaster-Carr) with a mesh size of 400 x 400, a wire diameter of 0.025 mm, individual opening dimensions of 0.038 mm x 0.038 mm and an open area of 36 % was used. In order to further protect the 316 SS mesh from corrosion and evaluate a different metal, for some tests, it was electrochemically plated with a 2.5  $\mu m$  Ni barrier layer followed by a 5  $\mu m$  layer of 24K Au (Acme Plating & Silver Shop Ltd.). For the non-precious metal carbon free auxiliary  $WE_{aux}$  experiments, a corrosion-resistant 3.18 mm OD 316 SS rod (passivated and annealed,

McMaster-Carr). In some cases, it was plated with Ni and Au as for the 316 SS mesh electrolyser ring  $WE_{elec}$ . The auxiliary rod was enclosed in a transparent PTFE heat shrink tubing (McMaster-Carr), leaving only the tip exposed.

Like in *Section 3.3.4*, CV measurements were conducted in a single compartment cell comprising a three electrode system to confirm carbon-free electrode material stability in water and  $CH_3OH$  acidic solutions and obtain their on-set potentials. The electrodes tested comprised Pt, 316 SS and Au plated 316 SS electrolyser ring  $WE_{elec}$  and auxiliary  $WE_{aux}$  rod materials. Fresh components were used for every different solution, since conducting CVs over a wide potential range may have been destructive to the 316 SS and to the Au plated 316 SS surfaces. Figure 3.33 shows the forward anodic potential sweeps only. The CVs were all corrected for ohmic resistance from impedance measurements taken after the CV was performed. In some cases, this resulted in a slight overcorrection of the cyclic voltammogram at high potentials.

The current was more stable for the rods, than for the electrolyser ring  $WE_{elec}$  meshes, which have a greater surface area exposed to the solution. For the 316 SS mesh, it seems that two different electrochemical processes are occurring. This was not the case for the Au plated 316 SS mesh. Also, in  $H_2O$  electrolysis, the current was noticeably smaller on the Au plated 316 SS mesh than on the non-plated one. This seems to indicate that there is significant corrosion happening for the non-plated 316 SS mesh. For convenience, the IR corrected on-set potential values obtained for the selected non-carbon containing materials, i.e., 316 SS and Au plated 316 SS electrolyser ring  $WE_{elec}$  components, as well as the Pt auxiliary  $WE_{aux}$  are summarized in Table 3.4, along with the IR corrected on-set potential previously obtained for Pt black and CFP electrolyser ring  $WE_{elec}$  at varying  $CH_3OH$  concentrations.

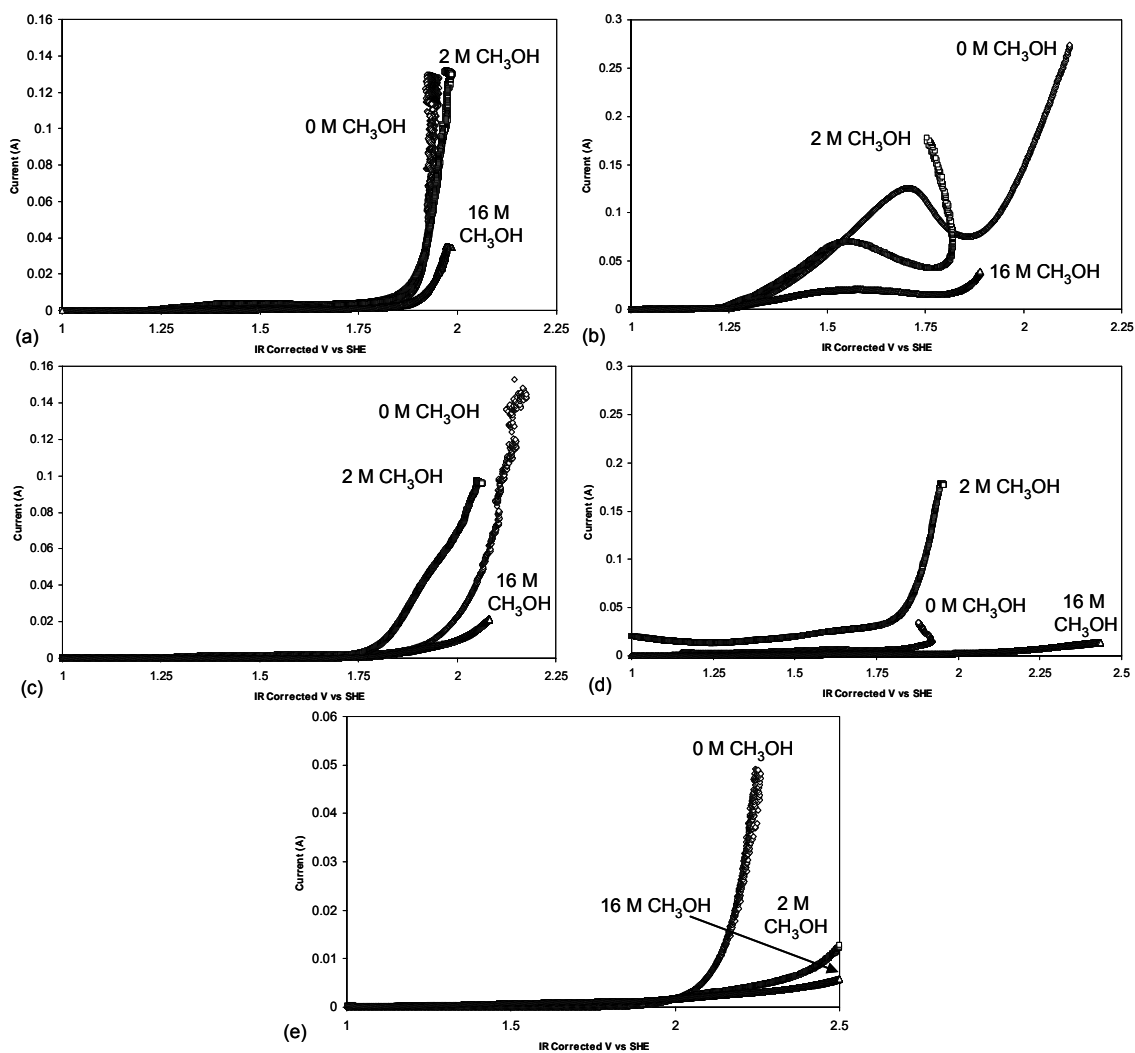


Figure 3.33: IR corrected forward anodic potential sweeps (a) 316 SS auxiliary WE<sub>aux</sub> (b) 316 SS mesh electrolyser ring WE<sub>elec</sub> (c) Au plated 316 SS auxiliary WE<sub>aux</sub> (d) Au plated 316 SS mesh electrolyser ring WE<sub>elec</sub> (e) Pt auxiliary WE<sub>aux</sub> (5 mV/s, 0, 2, or 16 M CH<sub>3</sub>OH in 0.5 M H<sub>2</sub>SO<sub>4</sub>, Pt flag CE, 23 ± 1°C).

Table 3.4: IR corrected on-set potential for different electrolyser and auxiliary WE<sub>aux</sub> materials at varying CH<sub>3</sub>OH concentrations.

| [CH <sub>3</sub> OH]<br>[M] | Electrolyser ring WE <sub>elec</sub> |      |             |                                      | Auxiliary WE <sub>aux</sub> |            |                      |
|-----------------------------|--------------------------------------|------|-------------|--------------------------------------|-----------------------------|------------|----------------------|
|                             | Pt black*                            | CFP* | 316 SS mesh | Au plated 316 SS mesh<br>[V vs. SHE] | Pt rod                      | 316 SS rod | Au plated 316 SS rod |
| 0                           | 1.70                                 | 1.86 | 1.34        | 1.87                                 | 2.17                        | 1.93       | 2.06                 |
| 2                           | 0.60                                 | 1.96 | 1.26        | 1.83                                 | 1.90                        | 1.90       | 1.81                 |
| 16                          | 0.65                                 | 2.00 | 1.23        | 2.05                                 | 1.86                        | 1.90       | 1.88                 |

\*From Table 3.2.

By comparing the values listed, it can be seen that only the Au plated 316 SS mesh had a greater on-set potential than the Pt black but was close to that of the CFP for H<sub>2</sub>O electrolysis. In CH<sub>3</sub>OH solutions, the on-set potential of the Au plated 316 SS mesh was about 1.3 V greater than that of Pt black but close to that of the CFP. In H<sub>2</sub>O electrolysis, the on-set potential of the 316 SS rod was 0.24 V less than that of the Pt rod, but 0.59 V greater than for the 316 SS mesh. It appears that corrosion is occurring on the 316 SS surface (particularly the mesh), probably preferentially at the ring edges, which were cut-off. This was visually confirmed after carrying the experiments. During the CVs of 316 SS components, the solution gradually became more yellow over time, indicating that Cr was leaching out. It is also possible that any of the components may contain impurities which may be electrochemically active contaminants. The contaminants leaching out likely negatively impact the kinetics of the electro-oxidation, electrolyte conductivity, and in turn, hinder the electrochemical performance of the system. Therefore, it is important to ensure components are stable and relatively free of contaminants. The addition of an Au coating on the 316 SS mesh moved its on-set potential value close to that of the CFP. Thus, the Au plated 316 SS components are more stable than 316 SS components. All potentiostatic triode experiments were conducted at potentials below the on-set potential values listed in Table 3.4. The tests carried out using 316 SS components are not reported as they were inconclusive due to corrosion issues. Therefore, only the results obtained using Au plated 316 SS components are discussed in this Section.

Various Au plated 316 SS combinations with the CFP electrolyser ring  $WE_{elec}$  and the Pt auxiliary  $WE_{aux}$  were studied in the potentiostatic mode as shown in Fig. 3.34. The operating range of the triode electrolyser was limited to auxiliary  $WE_{aux}$  potentials from -0.2 to 1.02 V vs. SHE.

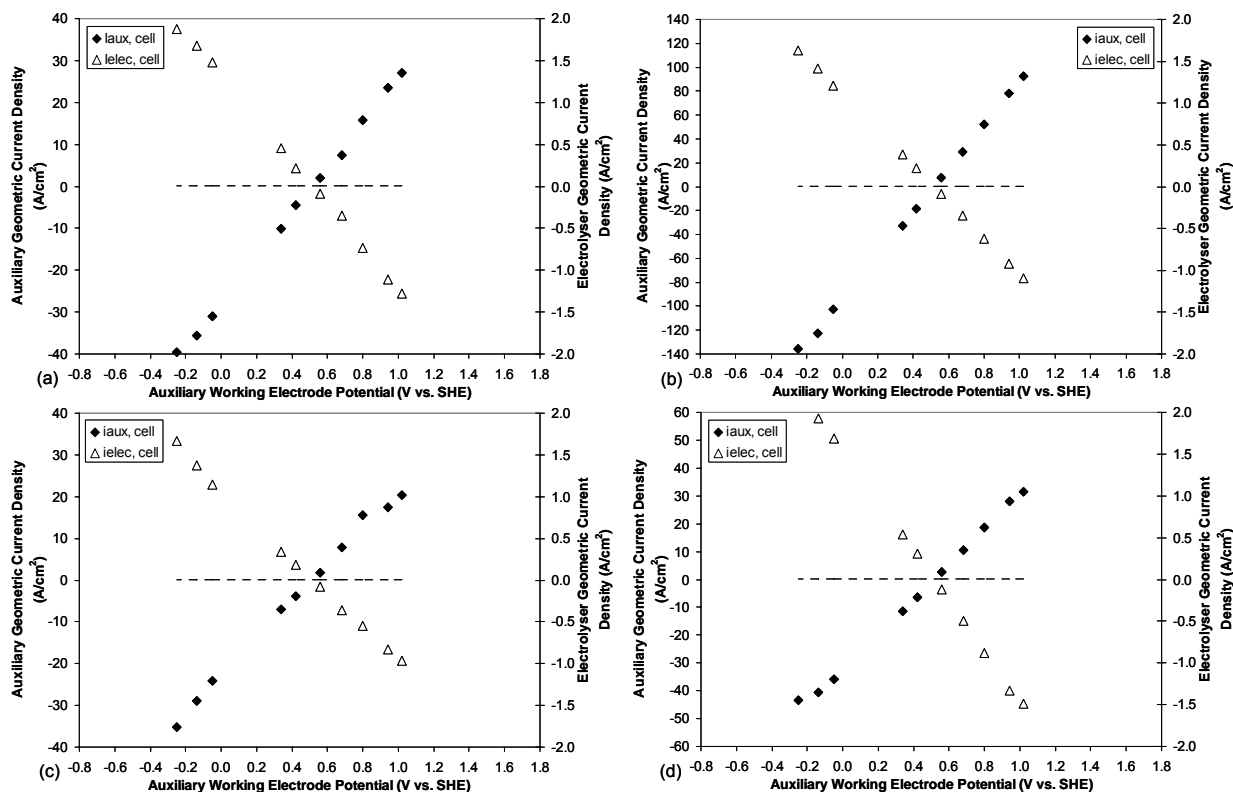


Figure 3.34: Effect of varying  $U_{aux, we}$  on (a) Au plated 316 SS electrolyser ring  $WE_{elec}$ , Pt auxiliary  $WE_{aux}$ , 0 M  $CH_3OH$  in 0.5 M  $H_2SO_4$  electrolyser anolyte, 0.5 M  $H_2SO_4$  electrolyser catholyte, (b) Au plated 316 SS electrolyser ring  $WE_{elec}$ , Pt auxiliary  $WE_{aux}$ , 2 M  $CH_3OH$  in 0.5 M  $H_2SO_4$  electrolyser anolyte, 0.5 M  $H_2SO_4$  electrolyser catholyte, (c) Au plated 316 SS electrolyser ring  $WE_{elec}$ , Au plated 316 SS auxiliary  $WE_{aux}$ , 0 M  $CH_3OH$  in 0.5 M  $H_2SO_4$  electrolyser anolyte, 0.5 M  $H_2SO_4$  electrolyser catholyte, (d) Au plated 316 SS electrolyser ring  $WE_{elec}$ , Au plated 316 SS auxiliary  $WE_{aux}$ , 2 M  $CH_3OH$  in 0.5 M  $H_2SO_4$  electrolyser anolyte, 0.5 M  $H_2SO_4$  electrolyser catholyte (triode, Pt/C CE,  $U_{elec, we} = 0.52$  V vs. SHE).

By comparing Fig. 3.34 (a) and (c), it can be observed that, at a  $U_{aux, we}$  of -0.25 V vs. SHE, the difference in the auxiliary geometric current density and in the electrolyser geometric current density obtained in the case of the Au plated electrolyser ring  $WE_{elec}$  with the Pt auxiliary  $WE_{aux}$  or with the Au plated 316 SS auxiliary  $WE_{aux}$  was within experimental error, i.e., 12 %. Thus, in 0 M  $CH_3OH$ , there were no major

differences observed when the auxiliary  $WE_{aux}$  was made of Pt or Au plated 316 SS. However, there is a difference in electrochemical activity on these materials for  $CH_3OH$  oxidation and for  $H_2O$  oxidation, i.e., the on-set potentials are different. The greatest triode effects were obtained at  $U_{aux, we}$  in the reduction potential region when using an Au plated 316 SS electrolyzer ring  $WE_{elec}$  and a Pt auxiliary  $WE_{aux}$  in 2 M  $CH_3OH$ , as shown in Fig. 3.34 (b). Thus, the auxiliary  $WE_{aux}$  and the electrolyser ring  $WE_{elec}$  do not need to be catalytic materials in order to observe the triode effect on the electrolyser ring  $WE_{elec}$ .

Table 3.5 summarizes the  $\rho_e$  values obtained in triode electrolysis as the  $U_{aux, we}$  was varied when using different combinations of Au plated 316 SS WEs components. In general, the  $\rho_e$  values increases as  $U_{aux, we}$  increased. All peak  $\rho_e$  were observed when  $U_{aux, we}$  was -0.14 V vs. SHE or lesser, i.e., in the  $H_2$  evolution region.

Table 3.5: Effect of auxiliary  $WE_{aux}$  potential ( $U_{aux, we}$ ) on the rate enhancement ratio ( $\rho_e$ ) using Au plated 316 SS components (2 mg/cm<sup>2</sup> Pt/C CE,  $U_{elec, we} = 0.52$  V vs. SHE).

| WE <sub>elec</sub> and WE <sub>aux</sub> Material |                              | Au plated<br>316 SS WE <sub>elec</sub> ,<br>Pt WE <sub>aux</sub> | Au plated<br>316 SS WE <sub>elec</sub> ,<br>Au plated<br>316 SS WE <sub>aux</sub> | CFP WE <sub>elec</sub> ,<br>Au plated<br>316 SS WE <sub>aux</sub> |
|---------------------------------------------------|------------------------------|------------------------------------------------------------------|-----------------------------------------------------------------------------------|-------------------------------------------------------------------|
| [CH <sub>3</sub> OH]<br>[M]                       | $U_{aux, we}$<br>[V vs. SHE] |                                                                  | $\rho_e$<br>[Dimensionless]                                                       |                                                                   |
| 0                                                 | 0.42                         | 42                                                               | 265                                                                               | 23                                                                |
| 0                                                 | 0.34                         | 189                                                              | 4294                                                                              | 53                                                                |
| 0                                                 | -0.05                        | 818                                                              | 17405                                                                             | 157                                                               |
| 0                                                 | -0.14                        | 869                                                              | 18519                                                                             | 255                                                               |
| 0                                                 | -0.25                        | 756                                                              | 21624                                                                             | 491                                                               |
| -----                                             |                              |                                                                  |                                                                                   |                                                                   |
| 2                                                 | 0.42                         | 489                                                              | 222                                                                               | 79                                                                |
| 2                                                 | 0.34                         | 929                                                              | 475                                                                               | 28                                                                |
| 2                                                 | -0.05                        | 3201                                                             | 1674                                                                              | 954                                                               |
| 2                                                 | -0.14                        | 3819                                                             | 1781                                                                              | 1603                                                              |
| 2                                                 | -0.25                        | 5638                                                             | 2040                                                                              | 360                                                               |

The  $\rho_e$  for the Au plated 316 SS electrolyser ring  $WE_{elec}$  and Pt auxiliary  $WE_{aux}$  combination were the same order of magnitude as the ones reported in Table 3.2 for various electrolyser ring  $WE_{elec}$  materials and the same  $WE_{aux}$ . It appears that most of the fluctuation in  $\rho_e$  values reported are caused by differences in the material surface properties, conductivities and structures. The Au plated 316 SS mesh electrolyser ring  $WE_{elec}$  possesses large pores and likely has a smaller ECSA compared to the electrolyser CFP gas diffusion ring  $WE_{elec}$ . Therefore, it is probable that the protons generated by the Pt auxiliary  $WE_{aux}$  are only reaching the inner edge of the  $WE_{elec}$  ring and do not spread out evenly over the entire Au plated 316 SS electrolyser mesh ring  $WE_{elec}$  surface during triode electrolysis, explaining why the  $\rho_e$  values obtained were greater for the CFP electrolyser ring  $WE_{elec}$  than for the Au plated 316 SS electrolyser ring  $WE_{elec}$ . While the entire surface of the mesh ring  $WE_{elec}$  is considered for normal electrolysis, the promoted electro-oxidation of water or  $CH_3OH$  may be limited to the inner edge of the electrolyser mesh ring  $WE_{elec}$ . Therefore,  $H^+$  spillover to the electrochemical oxidation sites may be more restricted for the Au plated 316 SS electrolyser ring  $WE_{elec}$  mesh than for the CFP, which has a denser and more connected structure.

The Au plated 316 SS WEs material combination for which the largest  $\rho_e$  was obtained occurred when both, the electrolyser and the auxiliary were made of Au plated 316 SS in 0 M  $CH_3OH$ . According to this, the Au plated 316 SS ring  $WE_{elec}$  and  $WE_{aux}$  combination results in greater triode enhancements for  $H_2O$  electrolysis than for  $CH_3OH$  depolarized electrolysis. It was shown in Table 3.3, for the same Pt auxiliary  $WE_{aux}$  material, the electrolyser ring  $WE_{elec}$  with precious metals, which are known to be catalytic to the electro-oxidation of  $H_2O$  or  $CH_3OH$ , did not result in larger triode enhancements than that obtained for the CFP, which is not catalytic during normal electrolysis. Therefore, larger  $\rho_e$  values are expected when the electrolyser ring  $WE_{elec}$  surface is non-catalytic to the electro-oxidation of  $H_2O$  or  $CH_3OH$ , which is the case for Au plated 316 SS components. In 2 M  $CH_3OH$ , using a Au plated 316 SS electrolyser ring  $WE_{elec}$  with the Pt auxiliary  $WE_{aux}$  resulted in a  $\rho_e$  about two times greater than when using a Au plated 316 SS electrolyser ring  $WE_{aux}$ . Similarly, also in 2 M  $CH_3OH$  and with the Pt auxiliary  $WE_{aux}$ , using a CFP electrolyser ring  $WE_{elec}$  resulted in a  $\rho_e$  26 times greater than when using the Au plated 316 SS electrolyser ring  $WE_{elec}$  at  $U_{aux, we} = -0.14$  V vs. SHE. This demonstrates that it may be possible to use a  $WE_{elec}$  and  $WE_{aux}$  combination made of non-precious, non-carbon containing materials to gain the triode electrochemical promotion effect, as it is the proton pumping which is important.

Since the common CE potential was independently measured, it was possible to calculate the power gain ratio,  $\gamma_{elec, cell}$  (Eq. 3.6). Figure 3.35 shows  $\gamma_{elec, cell}$  variation with  $U_{aux, we}$  for the various WE material combinations studied in 0 and 2 M  $\text{CH}_3\text{OH}$ .

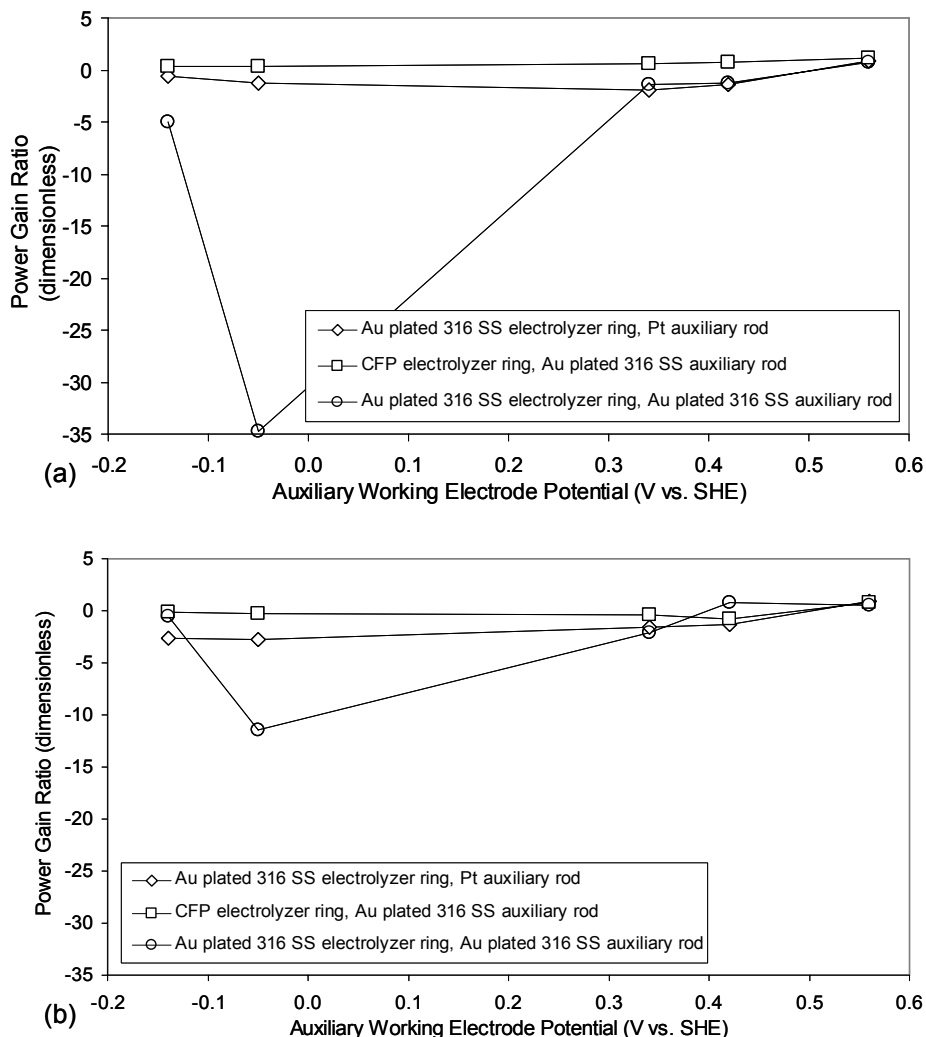


Figure 3.35: Power gain ratio ( $\gamma_{elec, cell}$ ) as a function of  $U_{aux, we}$  (a) 0 M  $\text{CH}_3\text{OH}$ , (b) 2 M  $\text{CH}_3\text{OH}$  (Au plated 316 SS components,  $2 \text{ mg/cm}^2$  Pt/C CE, 2 M  $\text{CH}_3\text{OH}$  in 0.5 M  $\text{H}_2\text{SO}_4$  electrolyser anolyte, 0.5 M  $\text{H}_2\text{SO}_4$  electrolyser catholyte,  $U_{elec, we} = 0.52 \text{ V vs. SHE}$ ).

All  $\gamma_{elec, cell}$  were less than unity and some  $\gamma_{elec, cell}$  were negative, indicating that the power required to operate in triode electrolysis was less than that required to operate in normal electrolysis. Negative  $\gamma_{elec, cell}$  values were obtained for the Au plated 316 SS electrolyser ring  $\text{WE}_{elec}$  and Pt auxiliary  $\text{WE}_{aux}$  combination. Peak  $\gamma_{elec, cell}$  values less than -1 were obtained which demonstrate that it is possible that

the decrease in the electrolyser power requirement during triode operation exceeds the power consumed in the auxiliary circuit. When both WEs were made of Au plated 316 SS, the peak  $\gamma_{elec, cell}$  obtained was -35 in 0 M CH<sub>3</sub>OH and -12 in 2 M CH<sub>3</sub>OH at a  $U_{aux, we}$  of -0.05 V vs. SHE, i.e., when the auxiliary WE<sub>aux</sub> is in the reduction region. In all cases, including the results obtained on Fig. 3.21 and 3.35, a maximum  $\gamma_{elec, cell}$  seems to be located between a  $U_{aux, we}$  of -0.14 and 0.42 V vs. SHE.

The average absolute value of the Faradaic efficiency of H<sub>2</sub> production,  $\Lambda$ , (Eq. 3.8) were in the range of 0.8 to 1.02 for the different WEs materials combinations evaluated in the reverse potentiostatic mode for the CH<sub>3</sub>OH depolarized H<sub>2</sub>O electrolysis and normal H<sub>2</sub>O electrolysis. According to this, the triode electrolysis process using carbon-free non-precious WEs materials would be Faradaic and electrocatalytic in nature. However, in normal H<sub>2</sub>O electrolysis,  $\Lambda$  exceeded unity when the auxiliary WE<sub>aux</sub> potential was -0.05 and -0.14 V vs. SHE for the CFP electrolyser ring WE<sub>elec</sub> and Au plated 316 SS WE<sub>aux</sub> combination indicating some non-Faradaic activity.

#### **3.5.4.8 Proposed mechanism**

A number of tests were done to determine what triggers the performance enhancement obtained in triode and tetrode electrolysis when in reverse operation, and its effect on the electrolyser ring WE<sub>elec</sub> surface. A general triode mechanism was proposed as shown in the schematic of Fig. 3.36 based on the information acquired from the tests conducted in reverse operation to date. Additional experiments to further clarify the mechanism are recommended *Section 5.5.2*.

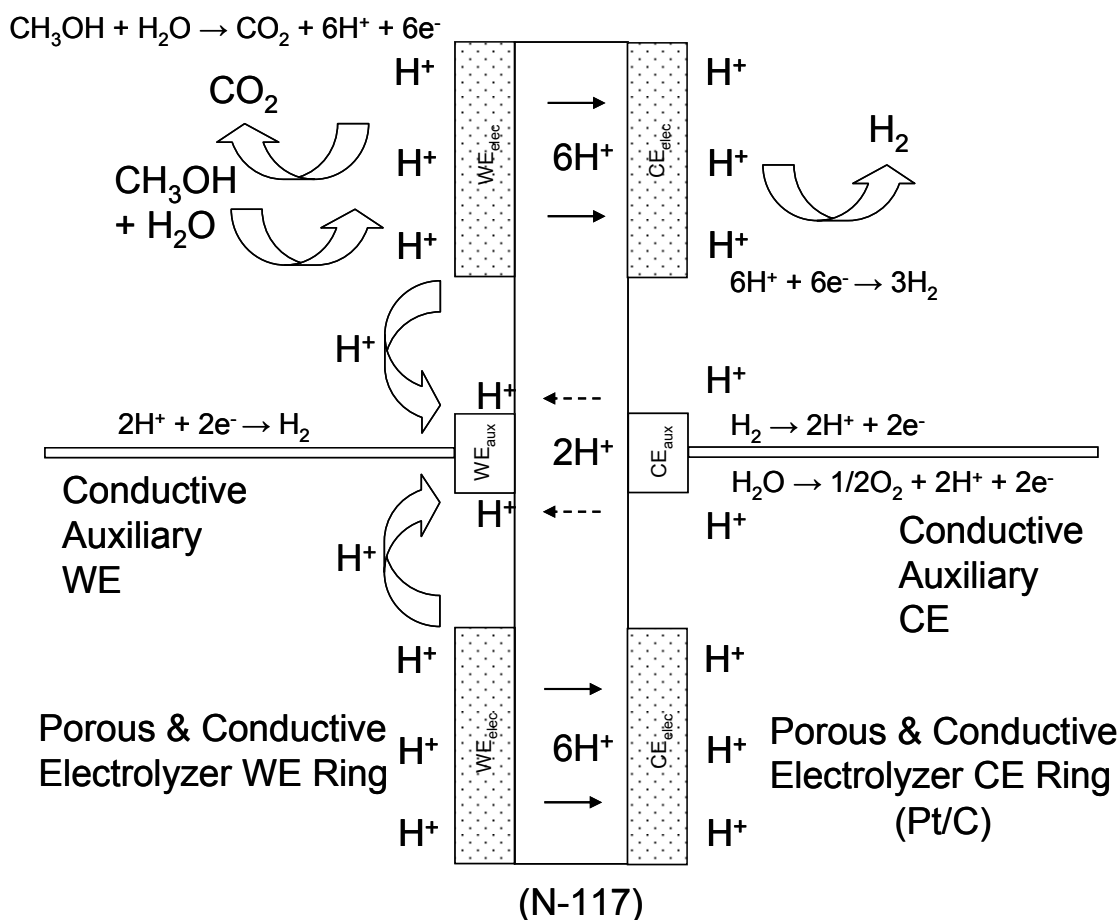


Figure 3.36: Schematic diagram of the proposed triode/tetrode mechanism in reverse electrolysis operation.

The tests conducted in this study were meant to elucidate some of the interactions occurring between the auxiliary  $\text{WE}_{\text{aux}}$  and the electrolyzer ring  $\text{WE}_{\text{elec}}$  surfaces located in the  $\text{CH}_3\text{OH}$  or  $\text{H}_2\text{O}$  oxidation compartment. The electrochemical triode or tetrode enhancement was only observed when the operation of the auxiliary was opposite to that of the electrolyzer circuit. It was proportional to the current/potential of the auxiliary circuit and was reproducible. The effect was beneficial to the electrolyzer potential only when the auxiliary circuit was operating in reduction. Similar results were obtained for both the triode and the tetrode configuration. In the tetrode configuration, the auxiliary and electrolyzer circuits were completely independent with no electronic contact or interaction. The electrolyzer ring electrode did not require a precious group metal (PGM) electrocatalyst to achieve an electrolyzer current/potential enhancement in triode or tetrode operation. Although the magnitude of the

electrocatalytic rate enhancement ratio obtained depended on the electrolyzer ring  $WE_{elec}$  material, neither carbon oxidation nor hydrogen oxidation was responsible for the rate enhancement.

The same triode or tetrode effect was obtained using non-catalytic materials for the auxiliary  $WE_{aux}$  (e.g., Au plated SS, etc.), which just forces protons through the membrane but with no surface electrochemical reaction, i.e., no  $H_2$  is produced. It was observed that the auxiliary  $WE_{aux}$  needed to be in physical contact with the membrane for a significant triode or tetrode effect to occur. Pulling the auxiliary  $WE_{aux}$  away from the membrane surface, further confirmed that the triode improvement is mainly caused by the electrochemical pumping of protons rather than by the generation of molecular  $H_2$  from a catalytic auxiliary  $WE_{aux}$ . Finally, it was determined that the performance enhancement obtained in triode and tetrode operation was linked to the working electrode surfaces rather than a change in the intrinsic membrane or solution conductivity. All these observations appear to agree with a triode or tetrode mechanism involving localized  $H^+$  species rather than molecular  $H_2$ .

In this study, it was shown that the  $H^+$  flux to the auxiliary  $WE_{aux}$  surface in cathodic operation had a promotional effect which proportionally affected the properties of the electrolyzer ring electrode surface. It appears that the localized in-situ migration of mobile promoting  $H^+$  species, either from the auxiliary  $WE_{aux}$  to the anodic active electrocatalyst surface of the electrolyzer or vice-versa, is responsible for the effect observed. Surface charge differences are likely the driving force which makes the  $H^+$  ions migrate to/from the auxiliary  $WE_{aux}$  surface from/to the electrolyzer ring electrode surface. However, in the case of water or methanol electrolysis, the triode or tetrode improvement was only observed when the proton flux was directed from the  $WE_{elec}$  to the  $WE_{aux}$ . The local removal of  $H^+$  from the  $WE_{elec}$  surface appears to drive the electrochemical oxidation reaction consistent with Le Châtelier's principle and a change in work function for galvanostatic control, thus improving the electrolysis charge transfer rate. It also explains why the gap between the  $WE_{aux}$  and the  $WE_{elec}$  has to be kept as small as possible. This is analogous to the EPOC effect where there is a backspillover of promoting ions occurring from the support to the metal surface. The main difference here is that the promoted reaction is an electrochemical reaction and not a chemical reaction.

### 3.6 Summary

The triode and tetrode operation of a low temperature H<sub>2</sub>O or CH<sub>3</sub>OH PEM electrolyser, running under non-flowing conditions was observed under various operating modes. The electrolyser and the auxiliary circuits were both galvanostatically, or both potentiostatically controlled. In tetrode operation, it was even possible to use potentiostatic control for the electrolyser circuit while using galvanostatic control for the independent auxiliary circuit.

Under some electrochemical promotion conditions obtained via triode or tetrode operation, the electrolysis performance improved with a decrease in energy required, i.e., less current/potential was needed in the electrolysis circuit when the auxiliary circuit was in operation. It was demonstrated that the effect was durable, reproducible, stable and reliable over periods of times up to 5 hours and upon multiple start-up and shut-down cycles of the auxiliary circuit. It was proposed that triode and tetrode operation enhanced the CH<sub>3</sub>OH electro-oxidation rate through electrochemical pumping and backspillover of protons. Therefore, the effect observed is the electrochemical promotion of electrocatalysis (EPOE) and not the electrochemical promotion of catalysis (EPOC). The only case where the latter might have been observed was when both circuits were controlled galvanostatically. Nevertheless, triode or tetrode operation appear to be a potential way to reduce the cost of electrolytic H<sub>2</sub> production processes. By operating the auxiliary circuit electrolyser in the opposite direction to the main circuit electrolyser, it is possible to use a non-precious anodic electrode materials and to reduce the energy requirement for the main electrolysis process. Hence, with this new electrolysis configuration, capital cost reductions may be achievable as the working electrodes can be made non-precious materials, while maintaining or reducing the operating cost by improving the performance of the H<sub>2</sub> production process. The electrochemical promotion of catalysis and the electrochemical promotion of electrocatalysis are both emerging areas which offer a number of potential advantages for H<sub>2</sub> production. The promotional effect obtained under triode and tetrode operation represents an alternative technological approach to other research efforts aiming to maximize the electrochemical surface area and develop new catalytic materials with improved properties.

## Chapter 4: Catalysis and Electrochemical Promotion of Catalysis (EPOC)

### 4.1 Synopsis

As seen in the prior Chapters, the catalyst carbon support has a high surface area and good electronic conductivity, but its corrosion limits the operating conditions of the electrochemical system under study. Various metal oxide catalyst supports were found to possess a higher oxidation resistance than C, and a better Pt adhesion [203]. Titanium dioxide ( $\text{TiO}_2$ ) is known for its high catalytic activity, good mechanical properties, stability in acidic solutions, non-toxic properties, and low cost. It can be used as a catalyst or support in electrocatalysis or catalysis. It can also be used as a photocatalyst under UV light in photocatalysis. Furthermore, in reducing atmospheres,  $\text{TiO}_2$  tends to lose oxygen and becomes an n-type semi-conducting material.

To study the electrochemical promotion of catalysis (EPOC) phenomenon, the catalyst chosen not only needs to be a catalyst to the chemical reaction, but also needs to be an electrocatalyst to the electrochemical reaction used to promote the catalytic reaction. As discussed in *Section 1.3.1* in *Chapter 1*, a high activity towards liquid  $\text{CH}_3\text{OH}$  catalytic reforming at low temperature has been reported with Pt-Ru/ $\text{TiO}_2$  [16]. However, to the author's knowledge, no low temperature  $\text{CH}_3\text{OH}$  catalytic reforming studies have been conducted with Pt-Ru/C. The catalyst support may play a significant role in the activity of noble metals toward a certain catalytic reaction. Strong metal-support interactions (SMSI), which decrease the  $\text{H}_2$  and CO chemisorption capacity of the  $\text{TiO}_2$ -supported metals, may exist when a  $\text{TiO}_2$  supported catalyst is reduced at a temperature between 200 and 500°C [204]. It was noted that SMSI interactions only occurred when  $\text{H}_2$  adsorption on the supported metal was dissociative and that they were not due to change in the metal particle sizes. An accepted explanation for this is that at temperatures greater than 300°C, the titania is partially reduced and a suboxide phase migrates onto the metal particles, blocking the metal surface partially covered by  $\text{TiO}_x$ , which decreases the chemisorption capacity of the metal and suppresses structure-sensitive reactions [204]. At higher reduction temperatures, partial or complete encapsulation of the metal particles in titania may occur, and above

800°C, the formation of intermetallic compounds and alloys was reported [204]. These interactions may improve the performance of precious metal catalysts by surface improvements and/or limitation of poisoning effects.

Typical electrocatalyst requirements include being electrically conductive, high surface area, high electrocatalytic activity, and low cost. Proton-conducting hydrophilic TiO<sub>2</sub> was shown to improve the stability of PEMFC electrodes when present in the catalyst layer [61] or as the catalyst support [205]. Using Pt-TiO<sub>2</sub>/C was shown to result in a greater electrochemical active surface area and fuel cell performance than using Pt/C [206]. Although the TiO<sub>2</sub> support is not sufficiently electronically conductive at low precious metal loadings (10<sup>-5</sup> S/cm at <10 % Pt), it was shown that increasing the weight percent of precious metal on this support may increase the electronic conductivity of the material to levels sufficient to sustain an electrochemical reaction (1.26 S/cm at 60 % Pt) [207]. Also, the addition of Nb metal to the TiO<sub>2</sub> support can increase its conductivity enough to make it suitable for electrochemistry. It was reported that the activity of Pt-Ru supported on Nb-TiO<sub>2</sub> increased the electrochemical activity by 83 % compared to the same electrocatalysts supported on carbon Vulcan XC-72R and by 64 % compared to the same metal catalyst but supported on TiO<sub>2</sub> only, for the electro-oxidation of CH<sub>3</sub>OH [207]. Nevertheless, as explained in *Section 1.3.4.1*, only low currents or potentials need to be applied to study the effect of EPOC. Therefore, the addition of Nb to the TiO<sub>2</sub> support is not necessary to study the effect of electrochemical promotion.

The preparation of most TiO<sub>2</sub>-supported metal catalyst starts by depositing precursor metal salts followed by a reduction of the metal ions. The catalytic performance is often affected by the average metal particle size and by the homogeneity of the distribution of the two metals. The metal particle size and structure is affected by both, the pre-reduction and reduction treatments [204]. Many techniques exist for the preparation of TiO<sub>2</sub> supported bimetallic catalysts, such as impregnation [208], sputtering [209], sol-gel [210], and ion exchange [211]. In this study, an impregnation synthesis method was developed based on previous work available in the literature [14, 16, 29, 210, 212]. The ratio of Pt to Ru, the solution pH and composition, the heat treatment, the hydration level of the precursor salts, and the recrystallization conditions and pressure, are all factors which could influence the formation of the Pt-Ru/TiO<sub>2</sub> catalyst. However, they were not investigated in this study.

The catalyst powder synthesized was characterized by Scanning Electron Microscopy with Energy dispersive X-ray Spectroscopy (SEM-EDX), Transmission Electron Microscopy (TEM), X-ray Diffraction (XRD), X-ray Photoelectron Spectroscopy (XPS), Inductively Coupled Plasma Mass Spectrometry (ICPMS), and Brunauer-Emmett-Teller (BET) surface area, before and after ball-milling. Once the targeted composition for the Pt-Ru/TiO<sub>2</sub> was obtained, cyclic voltammetry was employed to determine the CH<sub>3</sub>OH oxidation activity of the Pt-Ru/TiO<sub>2</sub> catalyst, and compare it to that of Pt and commercial Pt-Ru/C catalyst.

In *Chapter 2*, it was shown that the theoretical thermodynamic efficiency and theoretical cell voltage of CH<sub>3</sub>OH electrochemical or chemical reforming become positive at a temperature of about 41°C. Catalytic CH<sub>3</sub>OH reforming experiments reported in the literature were carried out at temperatures ranging from 72 to 105°C with Pt-Ru/TiO<sub>2</sub>. Catalysis was first conducted using catalyst powders in a three port round-bottom glass cell for comparison with low temperature CH<sub>3</sub>OH reforming data available in the literature. It was the first time the low temperature catalytic reforming of CH<sub>3</sub>OH was conducted using a commercial fuel cell catalyst, i.e., Pt-Ru/C. Catalysis was also carried out on gas diffusion electrodes prepared using the method described in *Chapter 2*. The effect of EPOC was investigated in the galvanostatic mode, in order to find out if a non-Faradaic effect could enhance the catalytic activity and selectivity towards H<sub>2</sub> production. If successful, the application of EPOC to the catalytic reforming of CH<sub>3</sub>OH has the potential of reducing the operating temperature and energy requirements, as well as shortening the start-up time of the catalytic CH<sub>3</sub>OH reformer.

## 4.2 Experimental

### 4.2.1 Materials

The catalyst support used was a TiO<sub>2</sub> nanopowder (P25, Degussa Co., 99.995%, average primary particle size of 20 nm, BET surface area of 50 ± 15 m<sup>2</sup>/g, 70% anatase, 30% rutile). The platinum and ruthenium precursor salts were chloroplatinic acid hexahydrate (H<sub>2</sub>PtCl<sub>6</sub>.xH<sub>2</sub>O, ACS reagent, 99.999%, ≥ 37.5% metal), and ruthenium (III) chloride hydrate, (RuCl<sub>3</sub>.xH<sub>2</sub>O, ReagentPlus<sup>®</sup>, 99.99%, 40 to 49% metal) both from Sigma Aldrich. In some experiments, ultra high purity (5.0) helium from Praxair was used as a carrier gas. All other materials used are the same as the ones described in prior Chapters.

### 4.2.2 Catalyst synthesis

Initially, two methods were employed to synthesize the Pt-Ru/TiO<sub>2</sub>: an impregnation procedure followed by calcination and reduction in H<sub>2</sub>, and a chemical reduction procedure followed by calcination in Ar. Since the first procedure resulted in a more homogeneous distribution of precious metal nanoparticles, it was preferred over the chemical reduction method. Information on both procedures can be found in *Section E.7 of Appendix E*. However, only results obtained by the impregnation method are discussed.

The first step of the impregnation is to suspend the TiO<sub>2</sub> in an aqueous solution of precursor salts. A quantity of TiO<sub>2</sub> was added to DI water and sonicated for an hour. The Ru metal precursor salt was then added to the aqueous TiO<sub>2</sub> suspension, and the mixture was sonicated for another hour before the Pt metal precursor salt was added, followed by another hour of sonication. The slurry formed was then heated to 80°C in an oil bath under continuous stirring until all water was evaporated. After this, the slurry was evaporated to dryness in a vacuum oven in air at 110°C overnight. The hardened particles were then crushed using a pestle and mortar.

The loading of Pt and Ru metal was adjusted to the desired wt% with a molar ratio of Pt/Ru equal to unity. For comparison with the catalytic CH<sub>3</sub>OH reforming literature, the targeted catalyst precious metal

loading was initially 10 wt% for the preliminary catalytic reforming tests carried out with Pt-Ru/TiO<sub>2</sub> powder. However, difficulties were encountered for the cyclic voltammetry tests as the catalyst's substrate electrical conductivity was too low. Therefore, in order to increase the catalyst conductivity, and for ease of comparison with the commercial Pt-Ru/C catalyst used in prior thesis Chapters, the catalyst precious metal loading was increased to 20 wt%. An example of the catalyst composition is located in Table E.4 in *Appendix E*.

The catalyst synthesized was calcined and reduced in a H<sub>2</sub> atmosphere in 20 ml alumina (99.6%) combustion boats (AdValue Technology, LLC) using a programmable Barnstead International tube furnace (model F21135, 120 V, 11.3 A, 1350 W). The tube furnace was first flushed by passing H<sub>2</sub> and Ar for a minimum of 2 hours to remove air/O<sub>2</sub>. The gas flow rates were adjusted to obtain 10% H<sub>2</sub> in Ar (10 sccm H<sub>2</sub> and 90 sccm Ar). The temperature was ramped up at a rate of 5°C/min to a dwell temperature of 500°C for 2 hours. This time period was selected to avoid extensive particle growth. Following this, the furnace was cooled down to room temperature at a rate of 5°C/min. The total time for the reduction was about 7 hours and 30 minutes.

Although the calcination temperature has an influence on the structure, morphology, crystallinity and particle size [213], the effect of the heat treatment on the microstructure of the bi-metallic material catalyst particles was not investigated. At calcination temperatures closer to 600°C, the TiO<sub>2</sub> support conductivity would increase, however its SA would decrease, as the transition from the anatase phase to the rutile phase starts to occur near 550°C. The reduced and calcined catalyst powder was ball milled for an hour and 30 min. at a time, using a 0.25" OD tungsten carbide milling ball (Spex 8004A) in a ball milling barrel inserted in a ball mill (Spex Sample Prep 8000-D).

For the catalysis and EPOC experiments, inks of the Pt-Ru/TiO<sub>2</sub> and Pt-Ru/C catalyst powder were sprayed on TGPH-60 using the same composition and technique as described in *Chapter 2*. The catalyst loading was 4 mg/cm<sup>2</sup> of Pt-Ru/TiO<sub>2</sub> or Pt-Ru/C at the electrolyser anode, and 2 mg/cm<sup>2</sup> of Pt/C at the electrolyser cathode. The same ink composition and catalyst loading resulted in thicker electrodes for the Pt-Ru/TiO<sub>2</sub> catalyst (0.34 mm), than for the Pt-Ru/C catalyst (0.23 mm).

### **4.2.3 Pt-Ru/TiO<sub>2</sub> physicochemical characterization**

Specimens of the different Pt-Ru/TiO<sub>2</sub> powders produced were physicochemically characterized using various techniques: SEM, EDX or EDS, XPS or ESCA, TEM, XRD and BET. In some cases, commercial 20 wt% Pt-Ru/C, Vulcan X72-R carbon, and TiO<sub>2</sub> were used as standards for comparison with the Pt-Ru/TiO<sub>2</sub> catalyst powder specimens. The characterization techniques employed are briefly described in this section.

#### **4.2.3.1 Scanning electron microscopy**

Scanning Electron Microscopy (SEM) images were taken using an Hitachi model S-3000N system to obtain information about the catalyst's surface morphology. Most precipitate crystallographic morphologies were observed at low scanning speed in the low vacuum mode. The vacuum pressure was 20 Pa and the accelerating voltage was either 20, 80 or 100 kV. The high resolution surface images, which are produced by scanning the sample with a high energy beam of electrons, reveals information about the surface topography, composition and electrical conductivity. Aluminum alloy mounts (SPI Supplies) covered with a double sided carbon tape coupon was used for sample mounting.

#### **4.2.3.2 Energy-dispersive X-ray spectroscopy**

In addition to the secondary electron (SE) and the back-scattering electron (BSE) detectors of the Hitachi model S-3000N system, an energy-dispersive X-ray spectroscopy (EDX or EDS) detector was also employed. The SEM EDX capability permits the detection of light elements having atomic numbers greater than 4. The visualization of the material surface with this technique generates a spectrum which allows one to obtain information on the elemental analysis or chemical characterization of the specimen.

#### **4.2.3.3 Transmission-electron microscopy**

Transmission-electron microscopy (TEM) was employed to estimate the average particle size and visualize the shape of the Pt and Ru deposits. In this type of microscopy, the electron beam interacts with the sample as it passes through it. The Hitachi H800 TEM used was operated at an acceleration voltage of 200 kV. A suspension of 20 mg of catalyst powder in 5 ml of DI water was prepared. After sonication, about 2  $\mu$ l of the suspension was extracted and deposited on polymer plated Cu grids which was then dried under a lamp.

#### **4.2.3.4 X-ray diffraction**

X-ray diffraction (XRD) measurements were taken with a Bruker AEX D8 advanced powder X-ray diffractometer using Cu radiation to obtain information about the catalyst's structure, composition and particle size. The diffraction patterns were recorded at 40 kV and 40 mA in the angular range of  $\theta=5-90^\circ$ , with a continuous scan speed of 1.2 to 2.8 $^\circ$ /min. and a sampling width of 0.02 or 0.04 $^\circ$ . The intensities observed were corrected for background noise, and peaks were determined using the EVA 10.0 (2004) Differac Plus basic evaluation package which has access to the Cambridge Structural Database and the Inorganic Crystal Structure Database. A qualitative XRD analysis required about 1 g of catalyst powder evenly spread out in a thin layer over a 1x1 cm<sup>2</sup> surface. This technique permits the identification of phases in a sample by comparing them with standard patterns available in the literature. It is also used to estimate the relative proportions of the different phases present in a multi-phase material sample by comparing the peak intensities associated with the phases identified. A quantitative characterization permits the determination of the quantity of the different phases in a multi-phase sample, but requires about 4 to 5 g of catalyst powder (2 g for a semi-quantitative test), and was not carried out for this study because the quantities of catalyst prepared were too small.

#### **4.2.3.5 X-ray photoelectron spectrometry**

X-ray photoelectron spectrometry (XPS), also referred to as electron spectroscopy for chemical analysis (ESCA), was used to analyze the material's elemental surface chemistry for atomic numbers of 3 and greater. Measurements were obtained with a Leybold model MAX 200 to determine the surface atomic ratio of the synthesized Pt-Ru/TiO<sub>2</sub>.

#### **4.2.3.6 Inductively coupled plasma optical emission spectrometry**

Inductively coupled plasma (ICP) optical emission spectrometry (OES) or atomic emission spectroscopy (AES) is a sensitive and robust technique for the determination of trace elements in a solution. ICP-OES analysis was carried out by Exova Canada Inc. using a Thermo Fisher IRIS Intrepid II. Two different analyses were conducted and required different liquid sample preparation procedures. The total metal content was determined by alkaline fusion for oxide dissolution, while the physical, and the aggregate properties were determined by acid digestion. The liquid samples were sprayed into an ICP source obtained by inductively heating a flow of Ar gas to about 10000°C. Under the plasma conditions, the sample's elements become ionized and excited, and their electrons emit electromagnetic radiation at characteristic wavelengths. The light emission intensity is measured by OES and is indicative of a particular element's concentration in the sample. A minimum of 0.4 g of sample was required to perform the two analysis.

#### **4.2.3.7 Brunauer, Emmett and Teller surface area, and Barrett-Joyner-Halenda pore size and volume analysis**

Brunauer, Emmett and Teller (BET) developed a theory pertaining to the physical adsorption of gaseous molecules on a solid surface and which allowed for the measurement of the specific surface area of a material [214]. Some characterization tests were carried out with a single point Micromeritics Flow Sorb II (model 2300FC) with Ar at liquid N<sub>2</sub> temperatures. Before each surface area measurement, the apparatus was calibrated twice by injecting a known volume of N<sub>2</sub> gas. The catalyst sample to be characterized was degassed and dried at 250°C overnight. A multi-point Belkman Coulter surface area

analyzer (model SA3100) was also used to obtain the Pt-Ru/TiO<sub>2</sub> nanopowder BET surface area, as well as to perform a Barrett-Joyner-Halenda (BJH) analysis to obtain surface porosity and particle size information. In this case, degassing was performed at 120°C for 15 minutes. About 0.5 to 1 g of catalyst powder was sufficient to carry out the tests and obtain reliable results.

#### 4.2.4 Pt-Ru/TiO<sub>2</sub> electrochemical characterization

Cyclic Voltammetry (CVs) were used to evaluate electrochemical activity of the noble metal oxide catalysts synthesized. A five-port single compartment glass cell was used to conduct CVs with a Pine Instrument Company bi-potentiostat (model AFCBP1). The CVs were corrected for resistance with measurements obtained using an impedance meter (LCR-821, GW Instek) at a frequency of 200 kHz. Experiments were conducted in 0, 2 and 16 M CH<sub>3</sub>OH in 0.5 M H<sub>2</sub>SO<sub>4</sub> at 23 ±2 °C, 50 and 75 ±1 °C. The glass cell was submerged in an oil bath on a magnetic heating plate. The reference electrodes and Pt flag counter electrode were the same as the ones used in *Chapter 2* and *3*. All potential scans are reported vs. SHE.

The working electrodes tested were a Pt disk electrode (AFE1XFG030PTR, 3 mm disk OD, Pine Research Instrumentation), and Pt-Ru/C or Pt-Ru/TiO<sub>2</sub> inks deposited on a glassy carbon disk electrode (GC, AFE1XFP030GCR, 3 mm disk OD, Pine Research Instrumentation) which was not rotated. A quantity of catalyst powder was soaked by 0.5 ml of DI water first, then 9.5 ml of IPA was added as the solvent. After 30 min. of sonication, a quantity of 5 wt% Nafion<sup>®</sup> solution was added, followed by another 30 min. of sonication, to ensure a uniform dispersion. Using a micropipette, an aliquot of the dispersion was drop coated onto a clean and polished GC disk electrode, which was dried in air for solvent evaporation. Preliminary ink composition optimization work was required as the Pt-Ru/TiO<sub>2</sub> catalyst particles had a tendency to come off the disk electrode. In an attempt to overcome this, the mass of catalyst in the ink was varied between 10 and 40 mg, different Nafion<sup>®</sup> contents ranging between 5 to 40 wt% were tested, and the volume of catalyst ink deposited on the disk electrode surface was in the range of 2 to 10 µl. The final ink composition used contained 40 mg of catalyst with 20 wt% Nafion<sup>®</sup> for Pt-Ru/C and 5 wt% Nafion for Pt-Ru/TiO<sub>2</sub>, and 2 µl was sufficient to cover the GC surface uniformly, resulting in a thin film

loading of 28.5 mg/cm<sup>2</sup>. More details on the ink preparation procedure can be found in *Section E.6* of *Appendix E*.

The solution in the glass cell was degassed with N<sub>2</sub> for a few minutes and the working electrode surface was conditioned prior to carrying out the CVs by running ten scans at 100 mV/s between 0.2 and 1.2 V vs. SHE. As no significant differences in the CVs were noted for the Pt-Ru/TiO<sub>2</sub> tests conducted in ambient light vs. dark conditions, all remaining tests were conducted in ambient light.

## **4.2.5 Apparatus**

### **4.2.5.1 Powder catalysis**

Preliminary heterogeneous catalytic CH<sub>3</sub>OH reforming tests were conducted in the closed semi-batch reactor system shown in Fig. 4.1.

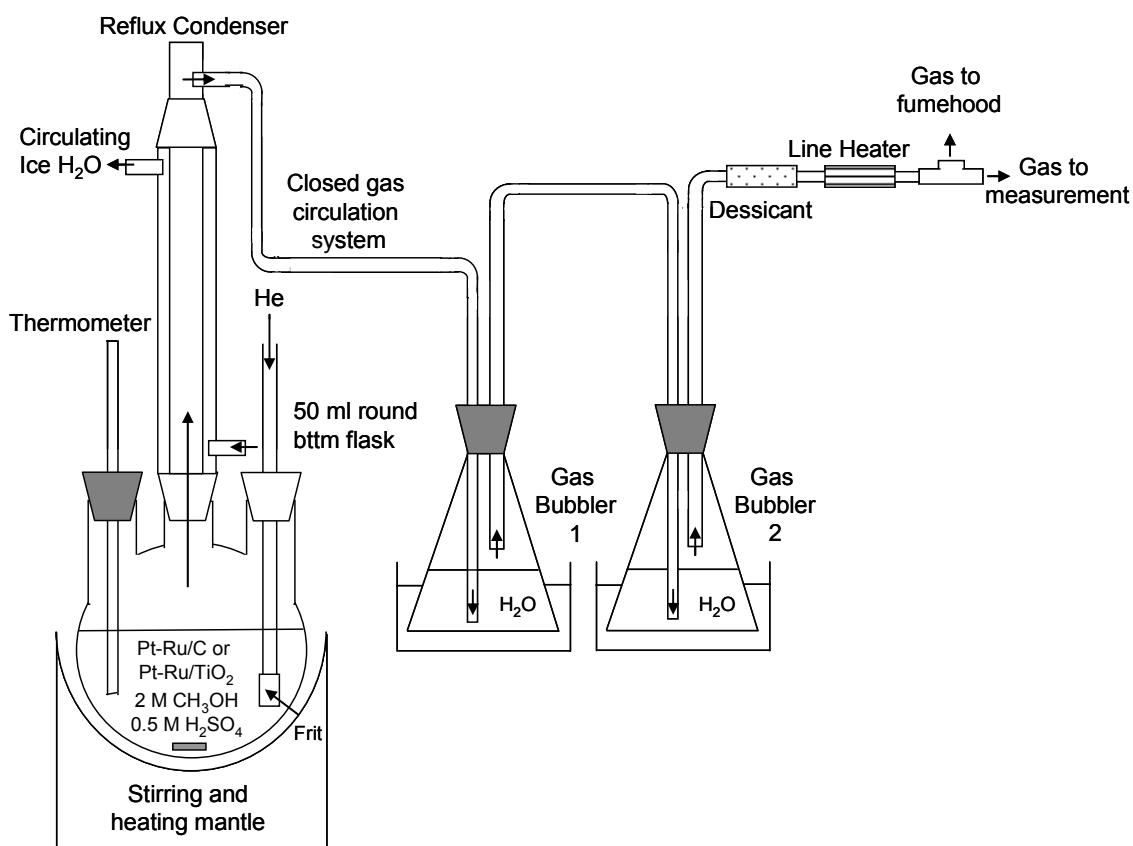


Figure 4.1: Schematic diagram of the experimental set-up used for the catalytic reforming of liquid CH<sub>3</sub>OH using catalyst powders.

A three-port single compartment 50 ml round bottom borosilicate glass flask (14/20 connections, Kontes, batan-ware) acted as the reaction vessel. One side-port was occupied by a Viton septum enclosing a thermometer; the other side-port was used for carrier gas injection using a glass frit gas sparger, while the center port was connected to a double walled condenser (14/20 connections). Vacuum grease (Apiezon AP-101) was spread on all glass joint connections to ensure gas tightness. The solution and the catalyst powder were both added at ambient temperature before the carrier gas flow was turned on, and the total liquid volume of each test was kept the same. The condensing water temperature was kept at  $2^{\circ}\text{C} \pm 1^{\circ}\text{C}$  using an ice water circulation bath (Haake DC-30). The condenser gas exit was connected to two gas bubblers containing DI water at room temperature, which allowed for the condensation of H<sub>2</sub>O and CH<sub>3</sub>OH entrained vapours in the He flow. Before entering the MS capillary, the gas also went through a desiccant to remove any entrained H<sub>2</sub>O vapours and a line heater, maintained at  $110^{\circ}\text{C}$ . A

stirring and heating mantle (EMA0050/CEBX1, Thermoscientific) was used to uniformly stir the reacting solution and maintain the single-compartment glass cell reactor at the desired reaction temperature.

Preliminary powder catalysis tests were carried out to confirm the validity of the methodology employed. For the preparations tests, the volume of gas generated was monitored by using an inverted burette, located on the reflux condenser exit line after one gas bubbler, by water displacement, and in some cases, N<sub>2</sub> was used as a carrier gas. The catalyst powder sample and/or the CH<sub>3</sub>OH solution were either added separately or together at room temperature or at the reacting temperature. It was assumed that the relative quantity of H<sub>2</sub> and CO<sub>2</sub> gas generated was stoichiometric. As mentioned in *Chapter 2*, the boiling point of a CH<sub>3</sub>OH equimolar solution is 76.7°C. To verify the CH<sub>3</sub>OH evaporation rate during the course of the powder catalysis experiment, tests were carried out under the same experimental conditions as for the powder catalysis experiments, but without any catalyst. At the end of the experiment, an aliquot of the reacting solution was analyzed for CH<sub>3</sub>OH concentration using the K<sub>2</sub>Cr<sub>2</sub>O<sub>7</sub> - spectrophotometric method described in *Chapter 2, 3* and *Appendix E*. It was confirmed that, using a cold water condenser, the CH<sub>3</sub>OH concentration of the reacting solution did not change by less than 5% over an hour. It confirmed that most of the CH<sub>3</sub>OH vapours were effectively condensed by the condenser.

Preliminary tests were also carried out to confirm that no H<sub>2</sub>SO<sub>4</sub> would be entrained in the gas to the MS capillary. During these tests, the pH of the first gas bubbler water was monitored over time using a calibrated pH meter and electrode (Oakton Ph 110 series, ±0.01 pH, 35811-98), while passing a N<sub>2</sub> carrier gas at a rate of 150-175 bubbles/min. under powder catalytic reforming conditions similar to the ones used in the final powder catalysis experiments. Experiments involved one hour of N<sub>2</sub> purging, followed by a 30 min. ramp-up to 75°C, where conditions were held for 5 hours. In the first experiment, the pH of 40 ml of DI water in a single bubbler increased by 1.8% from 4.98 to 5.07 over the course of the experiment. In the second experiment, two 200 ml DI water bubblers were used. The pH of the second bubbler decreased by 3% from 5.93 to 5.75 during the experiment. The pH fluctuations measured fall within experimental error, and indicate that entrained acid should not cause issues to the MS and its capillary. These preliminary tests confirmed the validity of the experimental method.

For all final experiments, the exit gas composition was continuously monitored using a quadrupole mass spectrometer (MS, RGA-200, Jerome & Francis Co. Ltd.) which was controlled using RGA 3 software. In these cases, the carrier gas was He, which was controlled with a mass flow controller (model 5878, Brooks Instrument Division, Emerson Electric Co) to generate a flow rate of 170 ml/min. at standard temperature and pressure (STP) to continuously remove the produced gases and to reduce the lag time as much as possible. Before entering the MS capillary, the gas stream was split into two flows: (i) a portion of the gas was sent to analysis to the mass spectrometer capillary, and (ii) the other portion of the gas was vented to a fumehood. This is because the total gas flow can not be directed into the MS due to its vacuum limit. Therefore, only a small portion of the exit total flow goes to the MS and the rest is vented off to a fumehood. Although the partial pressures of CH<sub>3</sub>OH, H<sub>2</sub>O, CO<sub>2</sub>, H<sub>2</sub>, CO, CH<sub>4</sub> and air were monitored, the MS was only calibrated for various partial pressures of H<sub>2</sub> relative to the total flow, making it possible to determine the flow rate of H<sub>2</sub> but not of the other gases monitored. Since the H<sub>2</sub> gas is quantified using a calibration curve obtained from the partial pressures related to the total flow, the portion of the total flow which goes to the MS is not used in the calculations. Knowing the He flow rate and the partial pressures of He and H<sub>2</sub>, it was possible to determine the production rate of H<sub>2</sub> using the following expression:

$$\frac{Fr_{He}}{Fr_{H_2}} = Cal \cdot \frac{P_{p,He}}{P_{p,H_2}} \quad (4.1)$$

Where  $Fr$  is the molar flow rate in mmol/min.,  $Cal$  is a dimensionless calibration number, and  $P_p$  is the gas partial pressure in torr. The MS has a partial pressure precision of  $5 \times 10^{-14}$  torr. The calibration number comprises a factor for the conversion of the He volumetric flow rate,  $Vr$ , to a molar flow rate,  $Fr$ , using the ideal gas law at STP, as well as a dimensionless calibration factor,  $cal_f$ , to convert the ratio of the partial pressures to a molar ratio. The calibration factor,  $cal_f$ , was determined experimentally to be 10.714 from the slope of the calibration curve as per the following equation:

$$\frac{P_{P,H_2}}{P_{P,He}} = cal_f \cdot \frac{Y_{H_2}}{Y_{He}} \quad (4.2)$$

Knowing  $cal_f$  and  $Cal$ , it is possible to determine the generation rate of  $H_2$  using Eq. 4.1, as the He molar flow rate is known and the respective gas  $P_p$  are measured by the MS. The hydrogen production rate calculated from Eq. 4.1 is equivalent to the unpromoted or promoted catalytic reaction rate,  $r$  or  $r_o$  in mol/s in Eq. 1.33, 1.36 and 1.37.

The solution and catalyst were introduced into the reaction vessel at ambient conditions. Prior to starting an experiment, the air was flushed out of the system and the solution de-aerated by flowing He gas for 5 min. under stirring. The filament was then turned on and the MS valve was opened. It usually took about half an hour for the air partial pressure to drop below  $1 \times 10^{-7}$  torr. Once this low air level was reached, the experiment was started by heating the reaction vessel under a He atmosphere until the desired reaction temperature was reached. Once reflux started, it was checked that no droplets were forming in the upper part of the condenser, but only in the lower part. Even though the lines between the gas sampling point and the mass spectrometer injection point were as short as possible (about 125 cm), there was a delay of about 2 min. between the an electrochemical current was imposed at the MEA and a response was seen in the MS measurement. The MS measurements were taken every 10 s, and the data collected was corrected to take the retention time into account.

#### 4.2.5.2 GDE catalysis and electrochemical promotion of catalysis

The experimental set-up used for the GDE catalysis and EP of catalysis tests is similar to the one used for the powder catalytic reforming tests, except that as shown in Fig. 4.2 and 4.3, the double-wall 2-compartment glass cell used in *Chapter 3*, was employed as the reactor instead of a single compartment round bottom flask.

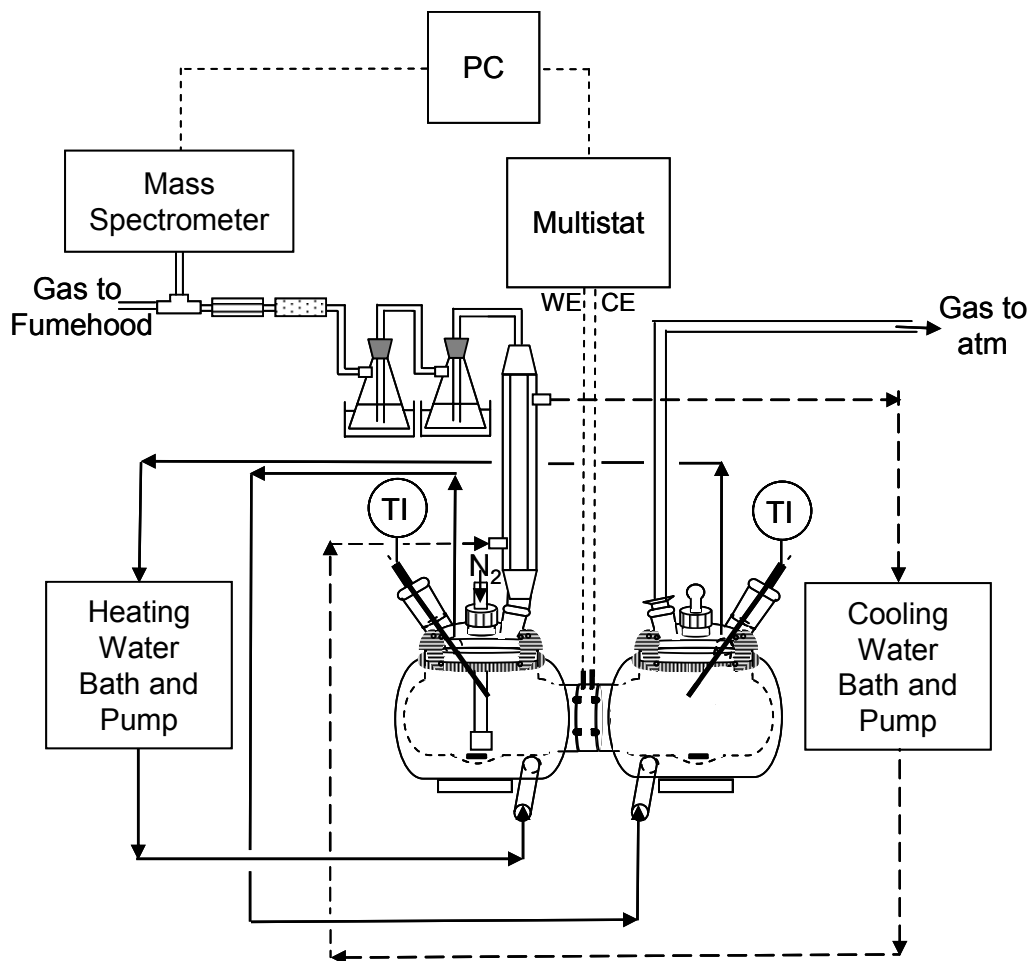


Figure 4.2: Schematic diagram of the experimental set-up used for the catalytic  $\text{CH}_3\text{OH}$  reforming and the electrochemical promotion of catalytic  $\text{CH}_3\text{OH}$  reforming using GDEs.

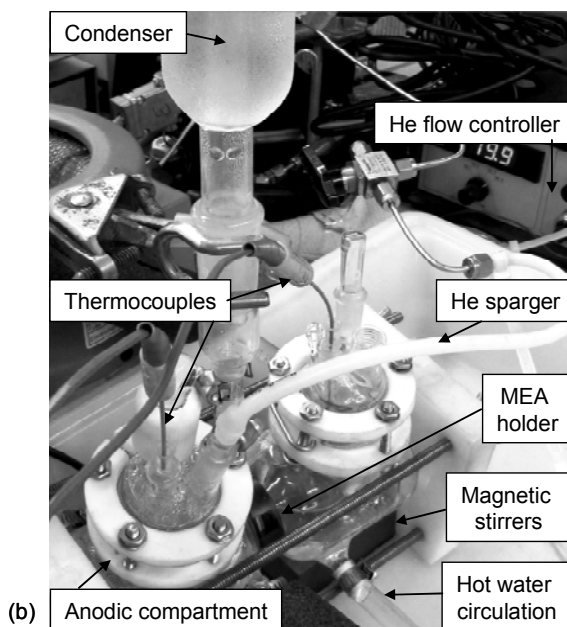
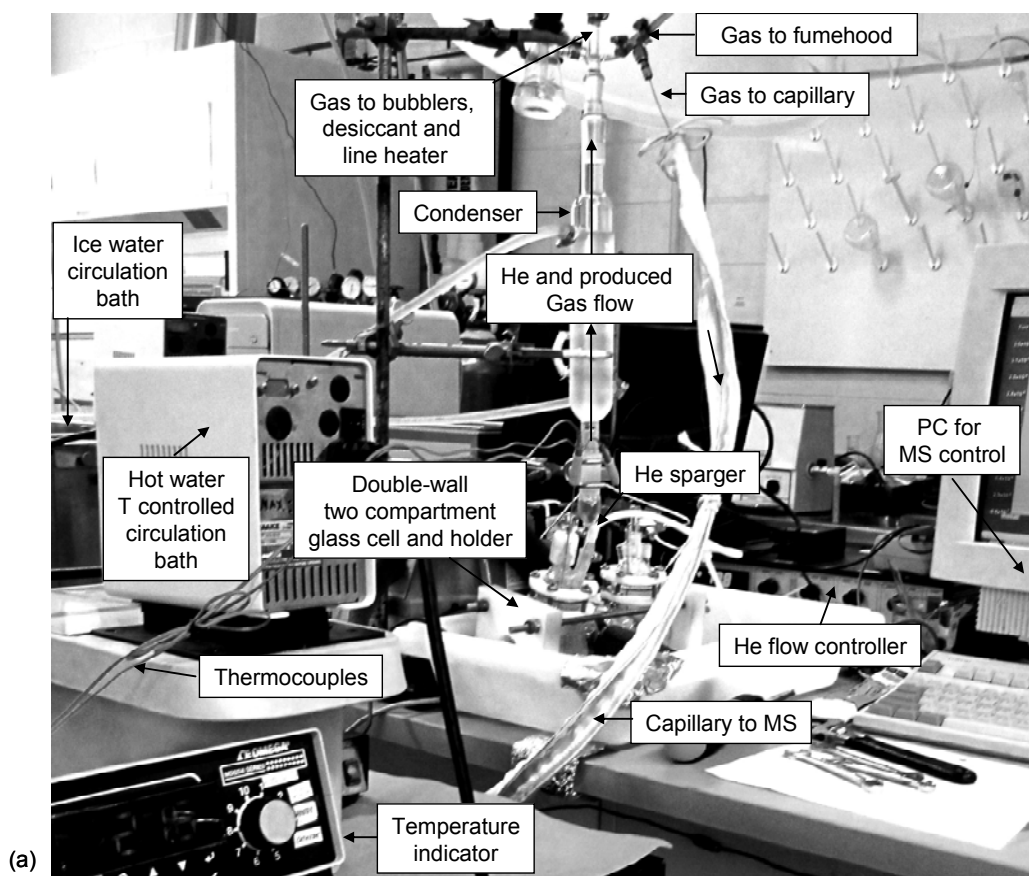


Figure 4.3: Picture of the experimental set-up used for the catalytic  $\text{CH}_3\text{OH}$  reforming and the electrochemical promotion of catalytic  $\text{CH}_3\text{OH}$  reforming using GDEs (a) auxiliary equipment (b) glass cell configuration.

A sparger permitted the distribution of He bubbles in the anolyte. The cap port of the anodic glass cell compartment which is closest to the MEA was connected to the condenser. The cathodic glass cell compartment gas was vented to the atmosphere. Both glass cell compartments had ports for thermocouples. A water circulation bath (Haake DC-10) was provided to heat and maintain the two-compartment glass cell at  $75^{\circ}\text{C} \pm 0.5^{\circ}\text{C}$ , while an ice water circulation bath (Haake DC-30) cooled the condenser to  $2^{\circ}\text{C} \pm 1^{\circ}\text{C}$ . The MEA composition and assembly was similar to the one used in *Chapter 2*. The WE GDE was  $4 \text{ mg/cm}^2$  Pt-Ru/C or Pt-Ru/TiO<sub>2</sub> and the CE GDE was  $2 \text{ mg/cm}^2$  Pt/C.

## 4.3 Results and Discussion

### 4.3.1 Pt-Ru/TiO<sub>2</sub> physicochemical characterization

#### 4.3.1.1 SEM images

SEM images permitted the visual observation of the synthesized Pt-Ru/TiO<sub>2</sub> particles shape, structure, composition and surface morphology. Figure 4.4 shows an image obtained for the 20 wt% metal Pt-Ru/TiO<sub>2</sub> catalyst.

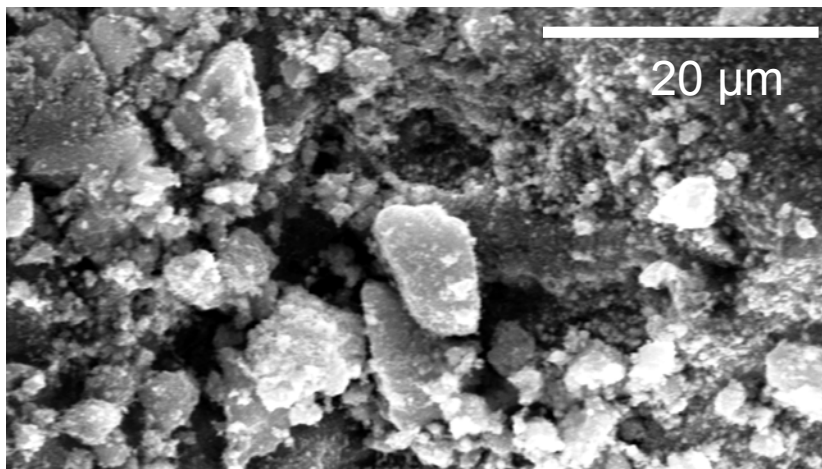


Figure 4.4: SEM image of 20 wt% metal Pt-Ru/TiO<sub>2</sub> (WD 15.2 mm, 20.0 kV, x2.0 k).

The Pt-Ru/TiO<sub>2</sub> catalyst powder is composed of scattered clusters or agglomerations constituted of small individual particles. It seems like the catalyst particle's surface had a low porosity. The Pt and Ru precious metal particles are spread out at the surface, and are represented by conductive white spots. However, the SEM images do not allow to distinguish between the Pt and Ru particles.

#### 4.3.1.2 EDX measurements

The EDX spectrum gave information about the elemental composition of the catalyst samples. An example of a typical EDX spectra conducted on a 10 wt% metal Pt-Ru/TiO<sub>2</sub> catalyst sample and a 20 wt% metal Pt-Ru/TiO<sub>2</sub> catalyst sample are presented in Fig. 4.5. The spectra exhibited peaks at 2 keV and 2.5 keV, which were assigned to Pt and Ru respectively. There were two peaks assigned to Ti at 4.5 and 5 keV. These binding energies are in close agreement with the ones reported in the literature for similar catalysts [215]. Hence, the EDX measurements confirmed the presence of Pt, Ru and Ti.

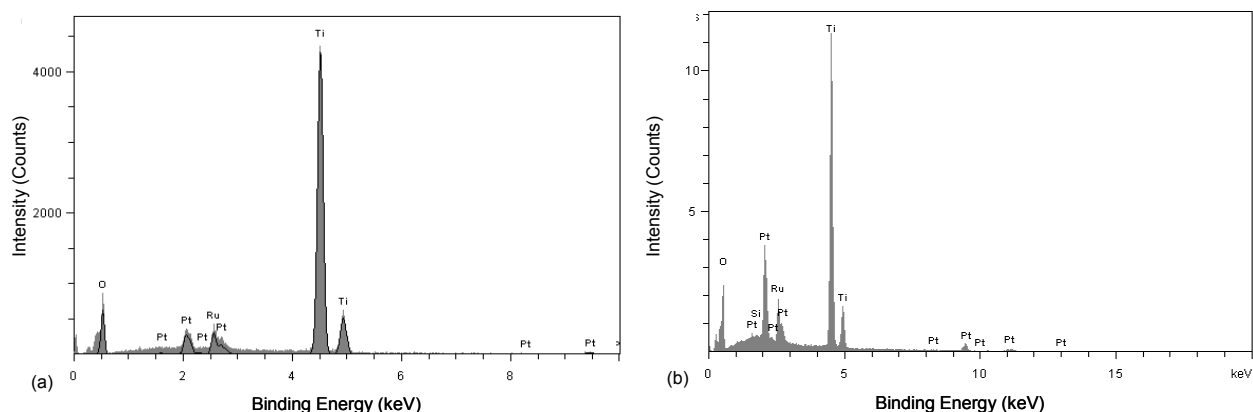


Figure 4.5: EDX spectra for Pt-Ru/TiO<sub>2</sub> (a) 10 wt% metal, (b) 20 wt% metal.

For the 10 wt% metal spectrum shown in Fig. 4.5 (a), the Ru content was 3 wt% and the Pt content was 4 wt% which translates into 7 wt% metal. This is about 30 % lower than the targeted metal loading of 10 wt%. Various EDX measurements were taken on 10 wt% metal Pt-Ru/TiO<sub>2</sub> and in average the Pt and Ru metal content was about 8 wt%, i.e., 4-6 wt% of Pt, and 2-3 wt% of Ru. In general, the Ru wt% was

about 47% lower than the Pt wt%. It is possible that the Ru precursor salts impregnation is more difficult than the Pt precursor salt impregnation, or that the Ru particles attached to the substrate more easily detach than the Pt ones. In order to compensate for this, an excess of Ru precursor salt was used to synthesize the 20 wt% metal Pt-Ru/TiO<sub>2</sub> catalyst samples. For the 20 wt% metal spectrum shown in Fig. 4.5 (b), the Ru content was 5 wt% and the Pt content was 12 wt%, according to which the total metal content was about 15% lower than the targeted loading of 20 wt%.

For the commercial 20 wt% metal Pt-Ru/C, which has a Pt:Ru 1:1 a/o, EDX results on an atomic % basis were 0.34 for Pt and 0.29 for Ru, which resulted in a Pt to Ru atomic ratio of about 1.2 instead of 1. The accuracy of the EDX spectrum may have been reduced by raising the over-voltage on the SEM, overlapping peaks, and the nature of the sample. For inhomogeneous and rough samples, the results tend to be less precise. Therefore, it appears that this material characterization technique was not sufficiently accurate to precisely determine the metal content of the catalyst sample.

#### **4.3.1.3 TEM images**

TEM images were taken to allow for the estimation of the nanoparticles size and the observation of the metal catalyst dispersion over the TiO<sub>2</sub> substrate surface. Two Pt-Ru/TiO<sub>2</sub> TEM images of different magnifications are shown in Fig. 4.6.

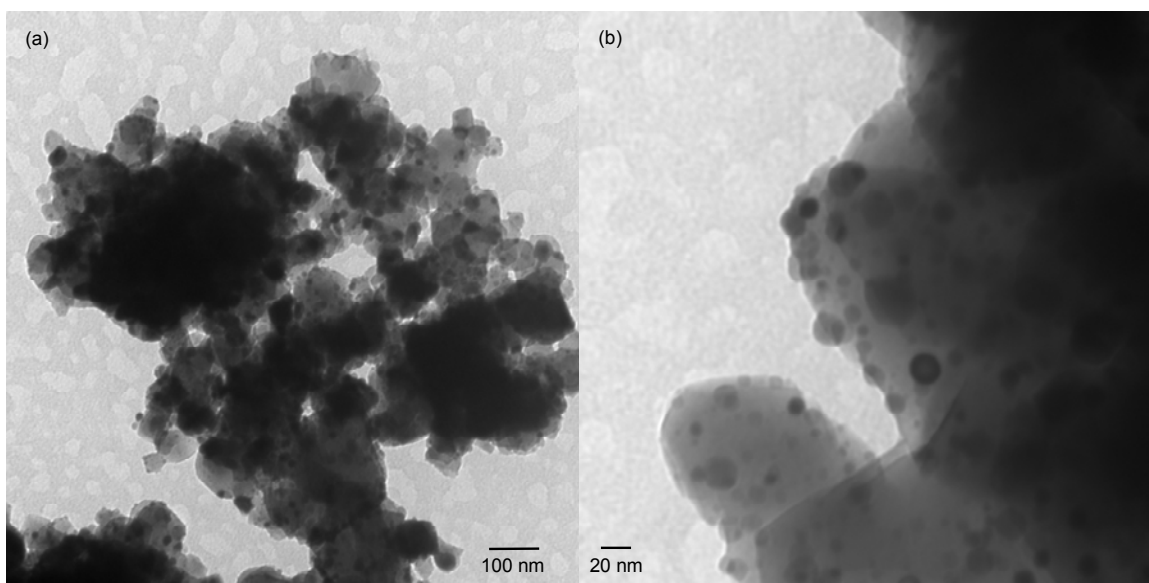


Figure 4.6: TEM images of 20 wt% Pt-Ru/TiO<sub>2</sub> (a) direct mag. 200000x and (b) direct mag. 600000x (20 wt% Pt-Ru, H<sub>2</sub> reduction method, ball milled 60 min., HV = 100.0 kV).

The Pt-Ru/TiO<sub>2</sub> catalyst formed multilayer agglomerations of small irregular flakes. The variation in contrast seen on the TEM images result from overlapping of the TiO<sub>2</sub> particles and their different thicknesses. High agglomerations have also been obtained for Ru/TiO<sub>2</sub> formed using a similar wetness impregnation technique [216]. The TiO<sub>2</sub> catalyst support was homogeneously decorated with Pt and Ru nanoparticles. The TiO<sub>2</sub> flakes were about 150 nm and larger, which is at least 7.5 times larger than the original average primary particle size of 20 nm. Small particle sizes can cause melting point depression compared to bulk materials, therefore, the TiO<sub>2</sub> nanoparticles may depress the melting point in such a way that the TiO<sub>2</sub> nanoparticles melted together during the H<sub>2</sub> reduction step. However, since the melting point of TiO<sub>2</sub> is 1640°C, a depression of the melting point below 500°C (the temperature used for the H<sub>2</sub> reduction step) is unlikely. Therefore, the adherence of the TiO<sub>2</sub> particles most likely results from sintering during the H<sub>2</sub> reduction process.

From the visual observation of various TEM images, the metal nanoparticles size seems to range from 5 to 10 nm, which falls into the reported range size for metallic nanoparticles for other similar materials (3 to 10 nm) [215, 217], but which is slightly greater than the average particle size reported for 20 wt% Pt/C (E-TEK) which is 2.6 nm [218]. Usually, smaller metal particles result in larger exposed surface area,

and in a more uniform distribution on the substrate. For photocatalysis, it would be desirable to have the  $\text{TiO}_2$  surface exposed with smaller metal particles. However, for the electrochemical oxidation of  $\text{CH}_3\text{OH}$ , it may be preferable to have a high portion of the  $\text{TiO}_2$  surface area covered by the metals particles in order to enhance the electrocatalyst's conductivity. Even if the 20 wt% Pt and Ru metal particles seem to be homogeneously distributed, it does not look like they will have sufficient connectivity to permit the conduction of current with a non-conductive support. The nanoparticles size of the metal will affect  $\text{CH}_3\text{OH}$  adsorption and the activity of the catalyst towards  $\text{CH}_3\text{OH}$  oxidation as the reaction is structure sensitive.

#### 4.3.1.4 XRD measurements

While electron microscope techniques allowed the examination of the Pt-Ru/ $\text{TiO}_2$  particles, XRD allows the identification of the Pt-Ru/ $\text{TiO}_2$  crystal structure and the proportion of the different crystal phases. In addition to identifying the microstructure of the catalyst synthesized, the average particle size can also be calculated. Figure 4.7 shows representative diffraction patterns for commercial Vulcan X72-R carbon, Pt-Ru/C,  $\text{TiO}_2$  powders and the 20 wt% metal Pt-Ru/ $\text{TiO}_2$  prepared by the  $\text{H}_2$  reduction method after an hour of ball milling.

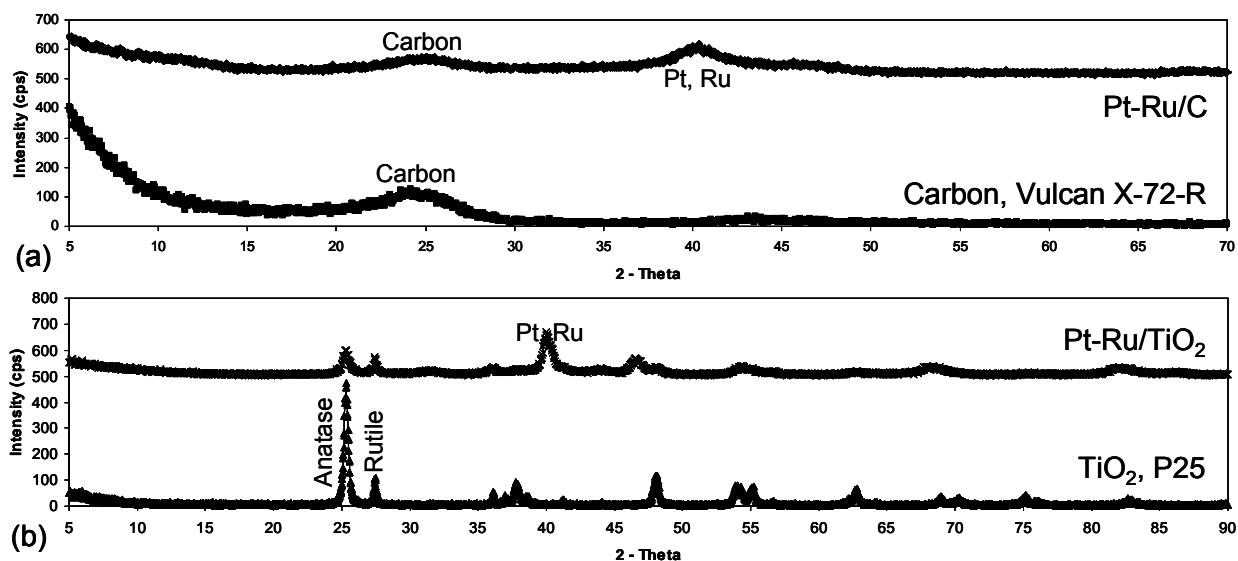


Figure 4.7: X-ray diffraction data for (a) Carbon and 20 wt% Pt-Ru/C, and (b)  $\text{TiO}_2$  and 20 wt% Pt-Ru/ $\text{TiO}_2$ .

The carbon peak was located at the same  $2\theta$  value of 25 for the carbon sample and the Pt-Ru/C sample. The Pt and Ru peaks located at a  $2\theta$  of about 40 were present in the Pt-Ru/C sample and in the Pt-Ru/TiO<sub>2</sub> sample. The Pt and Ru peaks slightly overlap making them more difficult to distinguish. The peak position and intensity also indicate that the crystalline structure of the anatase and rutile form were both present in the Pt-Ru/TiO<sub>2</sub> sample, and that the crystalline anatase phase was predominant (~60 %), although its content was lower than in the original TiO<sub>2</sub> P25 sample. The original anatase phase of the TiO<sub>2</sub> P25 sample was determined to be about 79%, which is almost 10% greater than the manufacturer's specification. The sintering temperature was low enough to retain much of the anatase structure of the original TiO<sub>2</sub> powder. The intensity of the rutile phase did not change considerably between the Pt-Ru/TiO<sub>2</sub> sample and the original TiO<sub>2</sub> P25 sample. In catalysis, the anatase phase is mostly used as there is a predominant molecular adsorption of alcohols and water on the anatase surface and a predominant dissociative adsorption on the rutile surface [2]. The anatase crystal structure is also known to be more active for electrochemical oxidation reactions than the rutile crystal structure [207].

Scherrer's equation for nanoparticles, for grains less than 0.1  $\mu\text{m}$ , correlates the size of particles to the broadening of a peak in the diffraction pattern. It defines  $\tau$  as the mean size of the crystalline domains in nm, which may be smaller or equal to the grain size:

$$\tau = \frac{k \cdot W}{\sqrt{FWHM^2 - W_o} \cdot \cos \theta_B} \quad (4.3)$$

Where  $k$  is the shape factor, a dimensionless constant which depends on the crystal size and is assumed to be 0.89 for spherical crystals with a cubic crystallographic structure,  $W$  is the X-ray wavelength, which was 0.154 nm,  $FWHM$  is the line broadening at the maximum intensity, i.e., full width half max in radians, and  $\theta_B$  is the Bragg angle in radians. The Scherrer equation typically leads to results within an accuracy of 20 to 30 %. Correcting the  $FWHM$  value for the instrumentation broadening,  $W_o$ , which was of  $0.05^\circ 2\theta$  did not increase the  $\tau$  values by more than 5%. Table 4.1 lists selected peak  $2\theta$

values, corresponding *FWHM* values, and average size of the crystallites based on Scherrer's equation for the XRD patterns shown in Fig. 4.3.

Table 4.1: Scherrer's crystallite size for selected peaks from the carbon, Pt-Ru/C, TiO<sub>2</sub> and Pt-Ru/TiO<sub>2</sub> XRD patterns.

| XRD pattern                   | Peak ID                  | $2\theta$ [°]<br>± 0.06 | FWHM [°] | $\tau$ [nm] |
|-------------------------------|--------------------------|-------------------------|----------|-------------|
| VulcanX-72-R                  | carbon                   | 25                      | 4.152    | 19          |
| 20 wt% Pt-Ru/C                | carbon                   | 25                      | 3.419    | 23          |
| 20 wt% Pt-Ru/C                | Pt                       | 40.5                    | 2.395    | 32          |
| 20 wt% Pt-Ru/C                | Ru                       | 41.3                    | 2.440    | 32          |
| P25 TiO <sub>2</sub>          | TiO <sub>2</sub> anatase | 25.25                   | 0.364    | 216         |
| P25 TiO <sub>2</sub>          | TiO <sub>2</sub> rutile  | 27.5                    | 0.208    | 392         |
| 20 wt% Pt-Ru/TiO <sub>2</sub> | TiO <sub>2</sub> anatase | 25.4                    | 0.496    | 158         |
| 20 wt% Pt-Ru/TiO <sub>2</sub> | TiO <sub>2</sub> rutile  | 27.6                    | 0.278    | 287         |
| 20 wt% Pt-Ru/TiO <sub>2</sub> | Pt <sub>3</sub> Ti       | 40.4                    | 0.763    | 102         |
| 20 wt% Pt-Ru/TiO <sub>2</sub> | RuO <sub>2</sub>         | 54.4                    | 0.563    | 139         |

As can be seen in Table 4.1, smaller crystals results in broader XRD peaks. The crystallites of the commercial Pt-Ru/C powder were an order of magnitude smaller than the ones of the synthesized Pt-Ru/TiO<sub>2</sub> powder. The carbon crystallite thickness of the Vulcan X-72 sample was 37.77% smaller than the average particle size reported from the manufacturer, which is 30 nm. However, it was similar to that obtained for the carbon crystallites in the commercial Pt-Ru/C sample. The Pt and Ru crystallites of the commercial Pt-Ru/C sample had about the same size (32 nm). The P25 TiO<sub>2</sub> support anatase and rutile crystals were about 10 to 20 times larger than the Vulcan X-72-R carbon support ones. As expected, the anatase TiO<sub>2</sub> had larger crystals than the rutile TiO<sub>2</sub> for both, the commercial P25 TiO<sub>2</sub> and the synthesized Pt-Ru/TiO<sub>2</sub>. The commercial TiO<sub>2</sub> P25 anatase and rutile crystallites were about 25 to 27 % larger than the ones in the synthesized Pt-Ru/TiO<sub>2</sub> sample. Thus, it seems like the TiO<sub>2</sub> crystallites did not grow upon the H<sub>2</sub> reduction at 500°C. It seems like the TiO<sub>2</sub> anatase crystallite size estimated in

Table 4.1 (158 nm) corresponded to the TiO<sub>2</sub> particle size observed on the TEM picture (about 150 nm and greater) shown in Fig. 4.6. However, the Pt and Ru crystallite size estimated via Scherrer's equation for the Pt-Ru/C catalyst (32 nm) is at least two times greater than the Pt and Ru particle size observed for Pt-Ru/TiO<sub>2</sub> in Fig. 4.6 (5-10 nm). Therefore, it is possible that the agglomeration of crystals resulted in broader XRD peaks than expected. In the Pt-Ru/TiO<sub>2</sub> sample, the precious metal particles and the titanium may form intermetallic compounds. For example, the formation of TiPt<sub>3</sub> is thermodynamically favourable at 500°C [217]:



As most of the Ru present was in the oxide form, it seems that the chosen reduction temperature was unfavourable to the segregation of Ru or its alloying with TiO<sub>2</sub>.

#### 4.3.1.5 XPS measurements

XPS measurements are used to generate the valence-band spectra at the material's conduction band. This gives information about the elemental composition of the surface, the empirical formula of pure materials, and the chemical and electronic states of elements in the surface. Elements associated with the XPS peaks can be identified with binding energies available in handbooks or databases. The XPS surface quantitative measurements ( $\pm 5\%$ ) along with a chemical identification of the main peaks is presented in Fig. 4.8.

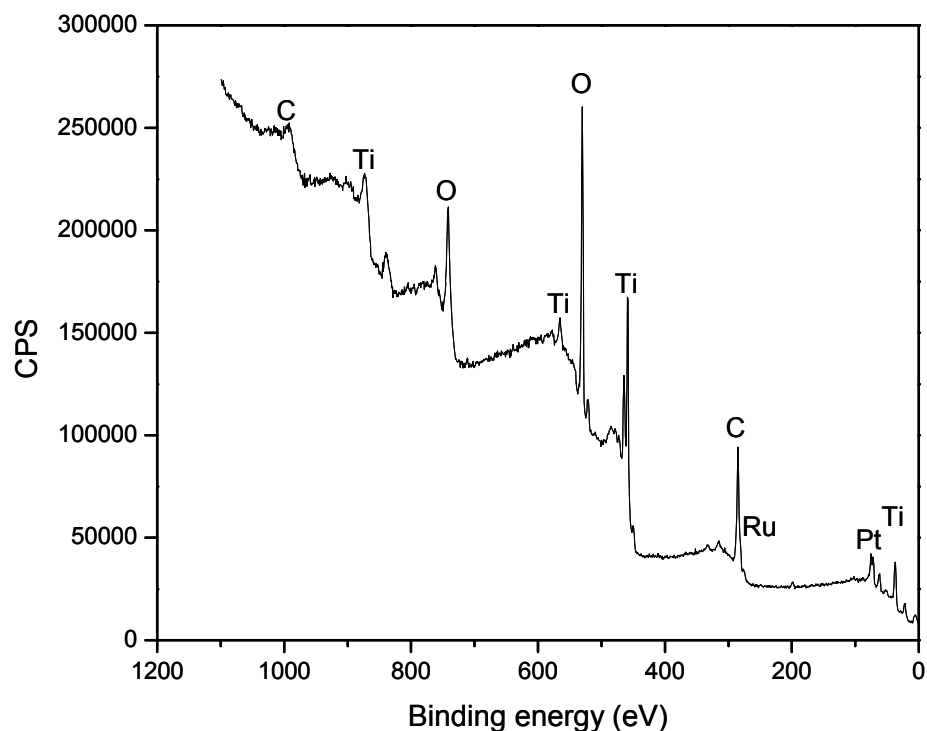


Figure 4.8: Survey XPS spectrum of 20 wt% Pt-Ru/TiO<sub>2</sub>.

The main elements identified were Ti, O, C, Pt and Ru. The C peak, resulting from CO from the air, interfered with the Ru peak, which rendered the identification of the Ru peak difficult. From the literature, the Ru peak is at 280 eV, RuO<sub>2</sub> is at 281 eV and RuO<sub>3</sub> is at 282.5 eV. The Pt-Ru/TiO<sub>2</sub> spectra yielded a Ru peak at 281.28 eV, indicating that most Ru is present in the oxide form. From the literature, the Pt peak is at about 71 eV, while the ones for Pt oxides vary between 72 and 75 eV. The Pt-Ru/TiO<sub>2</sub> spectra yielded Pt peaks at 71.5 and 75 eV, indicating that Pt is present in the metallic and oxide form. Based on the XPS surface analysis, which gives the % distribution amongst the different compounds detected at the sample surface, the precious metal loading was 16 wt%, which is lower than the targeted metal loading of 20 wt%. However, it was confirmed that the atomic ratio of Pt/Ru was 0.95, which is very close to the targeted atomic ratio of 1.

#### 4.3.1.6 ICP-OES measurements

Among the different methods taken to determine the metal content of the catalyst powder prepared, ICP-OES was the most accurate one ( $\pm 0.01$  wt%). This quantitative technique was used for the

determination of the catalyst Pt, Ru and Ti metal content, as well as the PtOx, RuOx and TiO<sub>2</sub> content. The ICP-OES analysis results were converted to weight percentage in terms of total Pt, Ru and Ti content for ease of comparison. Selected results are shown in Table 4.2.

Table 4.2: ICP-OES results for H<sub>2</sub> reduced Pt-Ru/TiO<sub>2</sub> before and after ball milling and Pt-Ru/C.

| Sample description             | Excess Pt salt [%] | Excess Ru salt [%] | Ball milling time [min.] | Total Pt [wt%] | Total Ru [wt%] |
|--------------------------------|--------------------|--------------------|--------------------------|----------------|----------------|
| 20 wt% Pt-Ru/TiO <sub>2</sub>  | 30                 | 60                 | 0                        | 13.77          | 13.37          |
| 20 wt % Pt-Ru/TiO <sub>2</sub> | 30                 | 60                 | 30                       | 11.68          | 10.77          |
| 20 wt % Pt-Ru/TiO <sub>2</sub> | 15                 | 50                 | 60                       | 10.85          | 8.12           |
| 20 wt% Pt-Ru/C                 | -                  | -                  | 0                        | 8.45           | 8.79           |

An excess of precursor salt was needed to obtain the desired metal loading. It is possible that some experimental error is caused by a loss of the precursor salt's crystallization water due to evaporation, or that the Ru salt did not dissolve as well as the Pt salt, and for this reason, the excess of Pt was less than the excess of Ru. Ball milling gradually resulted in a larger partial loss of metal loading from the support. The composition of the Pt-Ru/TiO<sub>2</sub> sample which was ball milled for 60 min. resulted in a metal loading 5% within that of the desired metal loading target (20 wt%). The commercial Pt-Ru/C catalyst ICP-OES total metal loading was 17.3% lower than the supplier quoted 20 wt%. Based on these results, the composition of the Pt-Ru/TiO<sub>2</sub> catalyst prepared by the H<sub>2</sub> reduction method was judged to be adequate for the purposes of this study.

#### 4.3.1.7 BET surface area and BJH pore size and volume analysis

The surface area (SA) is a key factor in catalysis and electrocatalysis as it has a strong effect on the overall rate of reaction. Therefore, it is desired to obtain a catalyst with a high specific SA. Also, the desorption area resulting from the N<sub>2</sub> evaporation from the sample pores was always slightly greater than the prior adsorption area resulting from the liquefaction of N<sub>2</sub> in the sample pores. Three measurements

taken on a same sample resulted in an error of 3%. The BET SA experimental results are listed in Table 4.3 along with the TiO<sub>2</sub> and Pt-Ru/C BET SA values given in the manufacturer's certificate of analysis.

Table 4.3: BET surface areas of the Pt-Ru/TiO<sub>2</sub> materials synthesized, as well as commercial TiO<sub>2</sub> and Pt-Ru/C materials.

| Sample description                                                                                           | BET SA [m <sup>2</sup> /g] |
|--------------------------------------------------------------------------------------------------------------|----------------------------|
| Pt-Ru/TiO <sub>2</sub><br>(NaBH <sub>4</sub> reduction, 10 wt%)                                              | 30.23                      |
| Pt-Ru/TiO <sub>2</sub><br>(H <sub>2</sub> reduction, after 60 min. ball milling, 20 wt%, 1 point method)     | 19.69                      |
| Pt-Ru/TiO <sub>2</sub><br>(H <sub>2</sub> reduction, after 60 min. ball milling, 20 wt%, multi-point method) | 15.74                      |
| P 25 TiO <sub>2</sub>                                                                                        | 50.00*                     |
| carbon VulcanX-72-R                                                                                          | 240.00*                    |
| 20 wt% Pt-Ru/C                                                                                               | 130.00*                    |

\* From certificate of analysis

As expected, increasing the metal loading decreased the catalyst's SA. Also, the one point method resulted in a surface area 20% greater than the multi-point method. This may be because a longer sample degassing period and higher drying temperature were used in the one point method. On average, after an hour of ball milling, the 20 wt% Pt-Ru/TiO<sub>2</sub> synthesized by the H<sub>2</sub> reduction method had an average SA about 60% lower than that of the commercial TiO<sub>2</sub> and about 86% lower than the commercial Pt-Ru/C catalyst. This reduction in SA may partly be attributed to incorporation of metal particles in the pores of the TiO<sub>2</sub> support and the fact that the carbon support has a SA 4.8 times greater than the TiO<sub>2</sub> support.

The BJH pore size and pore volume is a widely accepted model, which characterizes the pore size distribution independently from external area due to the particle size of the sample. The multi-point BET method allowed for the measurement of the porosity. Micropores have a diameter less than 2 nm,

mesopores, a diameter between 2 and 50 nm, and macropores, a diameter greater than 50 nm. Figure 4.9 shows the BJH desorption pore size distribution for the 20 wt% Pt-Ru/TiO<sub>2</sub> nanopowder.

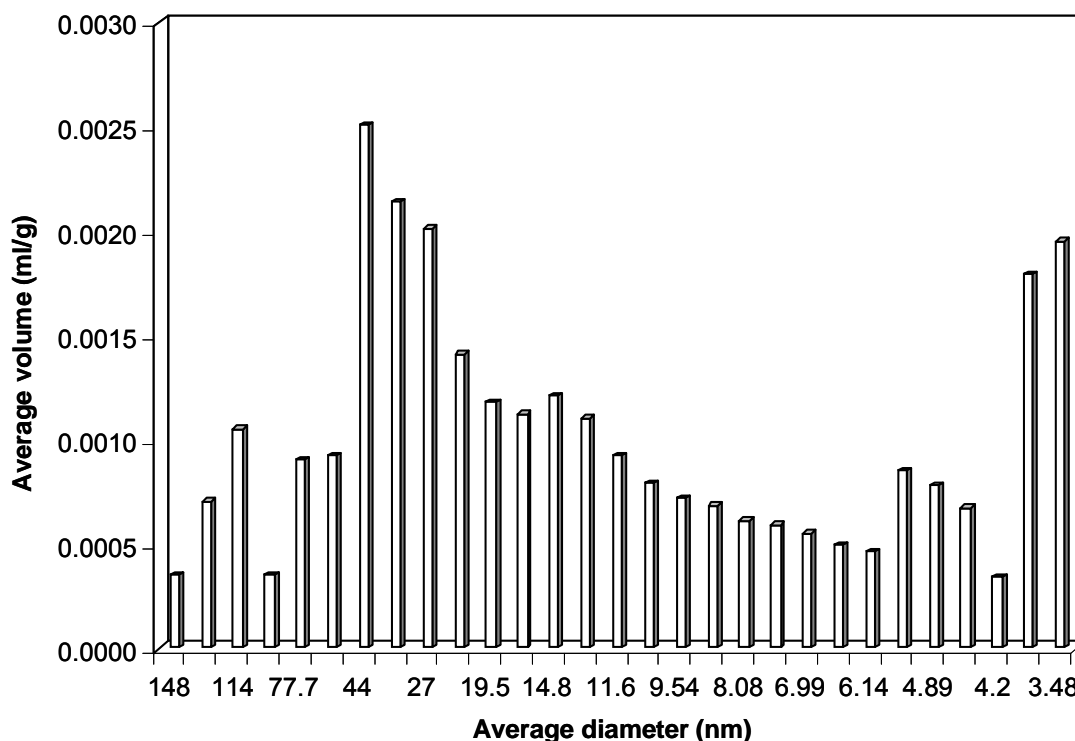


Figure 4.9: Pt-Ru/TiO<sub>2</sub> BJH desorption pore volume distribution.

From the diagram, it can be seen that the average pore volume of the Pt-Ru/TiO<sub>2</sub> sample with the greatest cumulative volume is 44 nm, indicating that the prominent pores are mesopores. From the TEM images shown in Fig. 4.6, it was determined that the surface metal nanoparticles size ranged between 5 to 10 nm. Thus, it may be possible that smaller metal nanoparticles were inside the TiO<sub>2</sub> pores, reducing the surface area. The catalyst activity towards the species involved in the electrochemical or chemical reaction will be greater for a material which has a high porosity.

#### 4.3.2 Pt-Ru/TiO<sub>2</sub> electrochemical characterization

The electrochemical response was obtained for a Pt RDE and Pt-Ru/C or Pt-Ru/TiO<sub>2</sub> thin films coated on a GC RDE in 0, 2 or 16 M CH<sub>3</sub>OH acidic solutions. Cyclic voltammetry was carried out in the absence of O<sub>2</sub> at ambient temperature, 50 and 75°C over the potential range of 0.2 to 1.2 V vs. SHE, at a scan rate

of 50 mV/s, without rotation. From the thermodynamic analysis carried out in *Chapter 2*, it was determined that the catalytic CH<sub>3</sub>OH reforming reaction becomes spontaneous at 41°C. Thus, at 75°C, the catalytic CH<sub>3</sub>OH reforming reaction is thermodynamically spontaneous making it possible to study the electrochemical promotion of catalysis (EPOC). Results obtained for the oxidation of 2 M CH<sub>3</sub>OH in 0.5 M H<sub>2</sub>SO<sub>4</sub> are illustrated in Fig. 4.10 and discussed in this section.

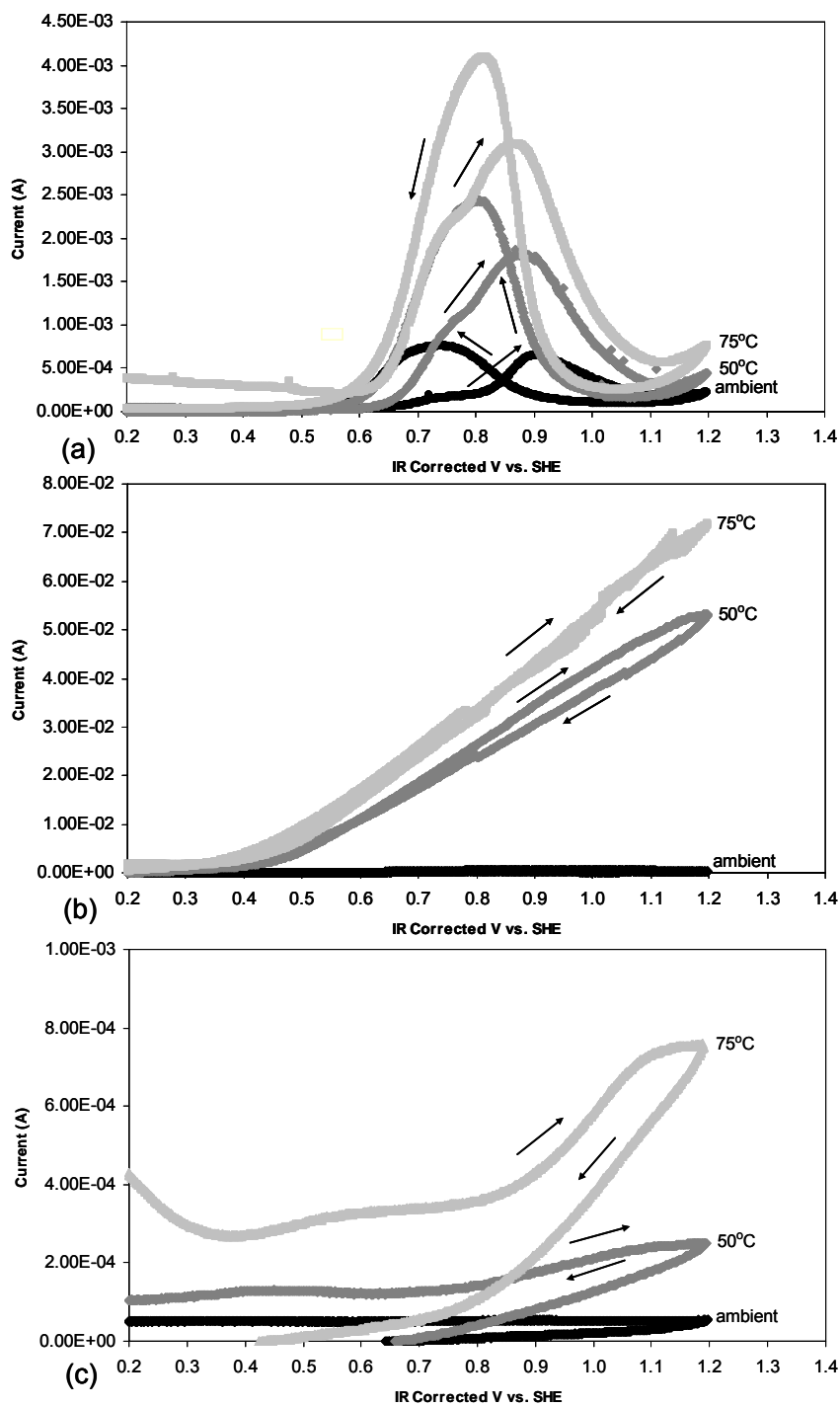


Figure 4.10: Cyclic voltammograms of (a) Pt, (b) Pt-Ru/C on GC, and (c) Pt-Ru/TiO<sub>2</sub> on GC (2 M CH<sub>3</sub>OH in 0.5 M H<sub>2</sub>SO<sub>4</sub>, 23 ± 2°C, 50 and 75 ± 1°C, 50 mV/s, no rotation).

The CH<sub>3</sub>OH oxidation on-set potentials and peak potentials,  $E_p$ , for the forward and reverse scans are summarized in Table 4.4 and 4.5 respectively. Table 4.6 lists the conditions of relevant CV studies

which were carried-out in the literature using similar electrocatalysts and conditions. Direct comparison with data available in the literature was difficult due to the varying CV test conditions.

Table 4.4: On-set potentials for the forward and reverse CH<sub>3</sub>OH oxidation on different catalytic surfaces (2 M CH<sub>3</sub>OH in 0.5 M H<sub>2</sub>SO<sub>4</sub>).

| Temperature<br>Electrode                     | 23 ±2°C        |                | 50 ±1°C        |                | 75 ±1°C        |                |
|----------------------------------------------|----------------|----------------|----------------|----------------|----------------|----------------|
|                                              | Forward<br>[V] | Reverse<br>[V] | Forward<br>[V] | Reverse<br>[V] | Forward<br>[V] | Reverse<br>[V] |
| Pt                                           | 0.63           | 0.94           | 0.65           | 0.93           | 0.75           | 0.90           |
| Pt-Ru/C - GC, 20 wt%<br>Nafion               | 0.6            | 1              | 0.5            | 0.45           | 0.4            | 0.4            |
| Pt-Ru/TiO <sub>2</sub> - GC, 5 wt%<br>Nafion | 0.73           | -              | 0.68           | 0.82           | 0.82           | 0.82           |

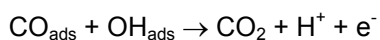
Table 4.5: Peak potentials for the forward and reverse CH<sub>3</sub>OH oxidation on different catalytic surfaces (2 M CH<sub>3</sub>OH in 0.5 M H<sub>2</sub>SO<sub>4</sub>).

| Temperature<br>Electrode                     | 23 ±2°C        |                | 50 ±1°C        |                | 75 ±1°C        |                |
|----------------------------------------------|----------------|----------------|----------------|----------------|----------------|----------------|
|                                              | Forward<br>[V] | Reverse<br>[V] | Forward<br>[V] | Reverse<br>[V] | Forward<br>[V] | Reverse<br>[V] |
| Pt                                           | 0.90           | 0.74           | 0.88           | 0.80           | 0.87           | 0.81           |
| Pt-Ru/C - GC, 20 wt%<br>Nafion               | 0.93           | 0.79           | 1.2            | -              | 1.2            | -              |
| Pt-Ru/TiO <sub>2</sub> - GC, 5 wt%<br>Nafion | 0.87           | -              | 1.2            | -              | 1.2            | -              |

As can be seen in Fig. 4.10 (a), on Pt, a CH<sub>3</sub>OH oxidation peak is present on the positive (anodic) potential scan. At the onset potential of about 0.6 V vs. SHE, the CH<sub>3</sub>OH adsorbed on Pt starts to oxidize and dissociate to CO, increasing the anodic current:



The complete CH<sub>3</sub>OH oxidation can also occur, further increasing the current:



(Eq. 4.6)

Table 4.6: List of CV studies on unsupported and supported Pt, Pt-Ru and TiO<sub>2</sub> available in the literature.

| Electrode<br>Material                               | Description                              | Concentration [M]              |                                         | Scan<br>Rate<br>[mV/s] | Potential Range<br>[V vs. SHE] |              | T<br>[°C]        | Ref.  |
|-----------------------------------------------------|------------------------------------------|--------------------------------|-----------------------------------------|------------------------|--------------------------------|--------------|------------------|-------|
|                                                     |                                          | H <sub>2</sub> SO <sub>4</sub> | CH <sub>3</sub> OH                      |                        | Low                            | High         |                  |       |
| Pt (110)                                            |                                          | 0.1                            | 0.2                                     | 50                     | -0.1                           | 1            | 20               | [179] |
| Pt(110 and<br>111)                                  |                                          | 0.1                            | 0.2                                     | 50                     | 0                              | 1            | 20               | [181] |
| Pt                                                  |                                          | 0.5                            | 0.1                                     | 12.5                   | 0.1                            | 1.5          |                  | [219] |
| Pt                                                  |                                          | 0.1(HClO <sub>4</sub> )        | 0.1                                     | 50                     | 0                              | 1.5          | 25               | [220] |
| Pt                                                  |                                          | 1 (HClO <sub>4</sub> )         | 0.1                                     | 100                    | 0                              | 1.8          |                  | [221] |
| Pt/C                                                | 40 wt% Pt                                | 0.5                            | 0.1, 0.5,<br>1, 2                       | 50                     | 0                              | 1            | 30,<br>60,<br>80 | [184] |
| Pt/C                                                | 45.9 wt%                                 |                                |                                         |                        |                                |              | 25 -<br>80       | [222] |
| Pt/C                                                | 20 wt%,<br>Pt:Ru 1:1 a/o                 | 0.5                            | 0 - 3                                   | 20                     | 0.1                            | 0.8          |                  | [223] |
| Pt/C                                                | 0.2 mg/cm <sup>2</sup>                   | 0.3                            | 0                                       | 50                     | -0.1                           | 1            |                  | [224] |
| Pt/C                                                |                                          | 0.3                            | 0.2                                     |                        | 0                              | 1            |                  | [224] |
| Pt/C                                                | 0.1 - 0.8 mg/cm <sup>2</sup>             |                                | 0.1 - 1.2                               | 5 - 50                 |                                | 0.7 -<br>1.2 | 25 -<br>65       | [224] |
| Pt/C                                                | 47.5 wt% Pt<br>15-20 μg/cm <sup>2</sup>  | 0.5                            | 0.5                                     | 10                     | 0.1                            | 1.1          | 22,<br>60        | [225] |
| Pt(100)/Ru,<br>Pt(110)/Ru and<br>Pt(111)/Ru         |                                          | 0.1<br>(HClO <sub>4</sub> )    | 0.6                                     | 50                     | 0                              | 0.6          |                  | [192] |
| PtRu                                                | Pt:Ru 7/3 a/o                            | 1 (HClO <sub>4</sub> )         | 0.1                                     | 100                    | 0                              | 1.8          |                  | [221] |
| Pt-Ru/C                                             | 40 wt% Pt-Ru,<br>Pt:Ru 1:1 a/o           | 0.5                            | 0.5                                     | 20                     | 0                              | 1            | 23               | [177] |
| Pt-Ru/C                                             | 27.87 mg/cm <sup>2</sup><br>29.8 wt% Pt, | 0.5                            | 0 - 2                                   | 20                     | 0                              | 1            |                  | [222] |
| Pt-Ru/C                                             | 23.1 wt% Ru,<br>Pt:Ru 2:3 a/o            | 0.5                            | 0.5                                     |                        | 0.2                            | 1.4          |                  | [226] |
| Pt-Ru/C                                             | 54 wt% Pt-Ru<br>15-20 μg/cm <sup>2</sup> | 0.1                            | 0.5                                     | 10                     | 0.1                            | 1.1          | 22,<br>60        | [225] |
| Pt (111)<br>Ru modified<br>Pt(111)                  |                                          | 0.1<br>(HClO <sub>4</sub> )    | 0.5                                     | 50                     | 0.1                            | 0.9          | 25               | [227] |
| Pt-Ru/TiO <sub>2</sub>                              |                                          | 0.08<br>(HClO <sub>4</sub> )   | 4.67                                    | 200                    | -0.2                           | 0.8          | 20               | [228] |
| Pt-Ru/C-TiO <sub>2</sub>                            | 30 μg/cm <sup>2</sup>                    | 1                              | 0.5                                     | 50                     | 0                              | 1.4          | 25               | [229] |
| TiO <sub>2</sub><br>nanotubes<br>(TNT)/Pt/C -<br>Au | TiO <sub>2</sub> :Pt 1:1 a/o             | 1<br>(HClO <sub>4</sub> )      | 1<br>(C <sub>2</sub> H <sub>5</sub> OH) | 50                     | -0.2                           | 1            | 25               | [230] |
| TiO <sub>2</sub> /carbon<br>nanotubes<br>(CNT)/Pt   | 0.042 to 1.15<br>mg/cm <sup>2</sup>      | 0.5                            | 1                                       | 100                    | 0                              | 1            | Room<br>T        | [231] |
| Pt-TiO <sub>2</sub> /CNT                            | 20 wt% Pt<br>Pt:TiO <sub>2</sub> 1:1 a/o | 1<br>(HClO <sub>4</sub> )      | 1<br>(C <sub>2</sub> H <sub>5</sub> OH) | 50                     | -0.2                           | 1            | 25               | [232] |

The formation of  $\text{OH}_{\text{ads}}$  on Pt occurs between 0.5 to 0.8 V vs. SHE [233]. The electro-oxidation of CO occurs at about 0.2 V lower on Pt-Ru [234]. At potentials greater than about 0.9 V vs. SHE, the rate of  $\text{CH}_3\text{OH}$  oxidation decreases as the formation of Pt oxides starts to occur. The formation of PtO film, which deactivates the catalyst's surface is:



The scan potential was reversed at 1.2 V vs. SHE to avoid oxygen evolution which starts to occur at 1.23 V vs. SHE. A reduction peak appeared on the negative (cathodic) potential scan due to the dissolution of the Pt oxide film to Pt:



After the PtO is reduced,  $\text{CH}_3\text{OH}$  is oxidized on the clean Pt particles surface and another  $\text{CH}_3\text{OH}$  oxidation peak appears. This reverse oxidation peak current depends on the amount of poisoning species removed from the Pt surface. The  $\text{CH}_3\text{OH}$  oxidation decreases due to an increase in adsorbed CO species. The  $\text{CH}_3\text{OH}$  oxidation current is always greater on the forward scan than on the reverse scan because of the large irreversibilities involved in the surface oxidation and oxide reduction processes [181]. These forward and reverse scan observations are in agreement with similar studies reported for  $\text{CH}_3\text{OH}$  oxidation on Pt/C in acidic  $\text{CH}_3\text{OH}$  solutions [224, 226]. The  $\text{CH}_3\text{OH}$  oxidation peak current depends on the catalyst loading, the acid concentration, scan rate, temperature, and the amount of poisoning species formed at the catalyst surface [224]. In this study, only the effect of temperature was looked at. Although there may have been a shift in the MSE reference electrode potential of about -0.04 V at 75°C, based on a temperature coefficient of  $-8.1 \times 10^{-4} \text{ V}/^\circ\text{C}$ , it was clear that the kinetics of  $\text{CH}_3\text{OH}$  oxidation improved with temperature. The forward  $\text{CH}_3\text{OH}$  oxidation peak current was an order of magnitude greater at 75°C than at 23°C, indicating that the electrocatalytic activity increases at higher temperature as the removal of the CO species poisoning the Pt surface becomes easier.

The CVs obtained for CH<sub>3</sub>OH oxidation on 20 wt% metal Pt-Ru/C-GC with 20 wt% Nafion are shown on Fig. 4.10 (b). At potentials greater than 0.8 V vs. SHE, Ru dissolution (oxidation) may start to occur [235], however, conditioning has shown that the CVs obtained were stable and that no working electrode degradation occurred. On Pt-Ru/C, the forward and reverse CH<sub>3</sub>OH oxidation on-set potentials were shifted to lower potentials compared to that observed on Pt. Although Ru itself is inactive towards CH<sub>3</sub>OH oxidation, its presence results in a bi-functional CH<sub>3</sub>OH oxidation mechanism, which lowers the oxidation potential of CO oxidation via the formation of adsorbed hydroxide ions [226]. It was reported that OH adsorption on Ru starts at 0.2 V vs. SHE [236], and that it shifts the CH<sub>3</sub>OH oxidation onset potential on Pt-Ru/C negatively compared to Pt/C.

Nevertheless, at ambient temperature, the activity of Pt for CH<sub>3</sub>OH oxidation was comparable to that of Pt-Ru/C. The forward CH<sub>3</sub>OH oxidation peaks current obtained on Pt-Ru/C was the same as the forward CH<sub>3</sub>OH oxidation peak current obtained on Pt under similar conditions ( $6.45 \times 10^{-4}$  A). The reverse oxidation peak current obtained on Pt-Ru/C ( $3.27 \times 10^{-4}$  A) was only slightly smaller than the reverse peak current obtained on Pt ( $7.53 \times 10^{-4}$  A). This agrees with studies according to which Ru is not very active for CH<sub>3</sub>OH adsorption and dehydrogenation at ambient temperatures [225]. The difference in the peak potentials obtained at ambient temperature for the Pt-Ru/C and Pt catalyst is due to the formation of Pt oxide on the forward scan, which occurs at a potential slightly higher on Pt-Ru/C than on Pt, and on the reverse scan, the reduction of Pt oxide, which occurs at a potential slightly higher on Pt-Ru/C than on Pt.

Temperature had a strong effect on the activity of Pt-Ru/C for CH<sub>3</sub>OH oxidation. As expected, at higher temperatures, the CH<sub>3</sub>OH oxidation rate was faster, and the onset potential for CH<sub>3</sub>OH oxidation was shifted to lower values on Pt-Ru/C, as can be seen in Table 4.4. In accordance with the literature, increasing the temperature activated the Ru sites and resulted in improvements in the adsorption and dehydrogenation steps of CH<sub>3</sub>OH oxidation, which exceeded that achievable on Pt [225]. At 50°C, the forward CH<sub>3</sub>OH oxidation peak on Pt-Ru/C - GC is at a much greater current than that observed on Pt at the same temperature due to improvements in the CO oxidation kinetics (Eq. 4.6). Initially, on the forward scan, the Pt-Ru/C surface is covered by CO. Once the onset potential for CO oxidative removal is reached, most CO is stripped from the surface. It seems like an insignificant amount of inactive Pt oxides were formed in parallel as the CO oxidation effect of Ru was not significantly hindered. Also, on

the reverse scan, CH<sub>3</sub>OH re-oxidation occurred right away as the Pt surface was already cleared of Pt oxides. The CO eventually re-accumulated on the surface, and the CH<sub>3</sub>OH oxidation gradually diminished. At 75°C however, the Pt-Ru/C - GC CH<sub>3</sub>OH oxidation and re-oxidation peaks completely overlapped. At this temperature, the Ru surface very effectively oxidized CO from the Pt sites, and was able to sustain the decomposition of CH<sub>3</sub>OH, after the CH<sub>3</sub>OH oxidation onset potential was reached. The adsorption of OH on Ru occurred at an even lower potential, but the adsorbed OH also desorbs faster. As the CO poison does not occupy the Pt active sites, the Pt surface is clean to oxidize CH<sub>3</sub>OH. Again, it seems like the CO removal effect of Ru surpassed the formation and reduction of the oxides, which should also be accelerated at higher temperature. Forward and reverse scans almost overlapped for a Pt/C catalyst in 0.5 M CH<sub>3</sub>OH in 0.5 M H<sub>2</sub>SO<sub>4</sub> at 80°C due to very fast reaction kinetics [226]. According to Tremiliosi-Filho *et al.*, overlapping indicated that the catalyst surface did not experience considerable CO poisoning in both scan directions, and that no other surface effects were involved [192].

The CVs obtained for 20 wt% metal Pt-Ru/TiO<sub>2</sub> - GC with 5 wt% Nafion are shown in Fig. 4.10 (c). The ECSA of the Pt electrode is close to its geometric surface area, and is much smaller than the ECSA of the GC Pt-Ru/C or Pt-Ru/TiO<sub>2</sub> ink coated electrodes, and therefore it could be expected that the currents would be greater for both ink coated GCs. However, the polarization of the Pt-Ru/TiO<sub>2</sub> - GC was poor, likely because of the low conductivity of the TiO<sub>2</sub> support. Forward and reverse oxidation peaks have been observed on conductive TiO<sub>2</sub> catalyst containing carbon and carbon nanotubes, such as for TiO<sub>2</sub>/Pt/C, and Pt-Ru/C-TiO<sub>2</sub>, and TiO<sub>2</sub>/CNT/PtRu in acidic CH<sub>3</sub>OH solutions [229-231]. For Pt/Nb-TiO<sub>2</sub>, (Nb:Ti 0.1:0.9), Pt loadings less than 10 wt% resulted in conductivity of about 10<sup>-5</sup> S/cm, while with Pt loading of 60 wt% the conductivity increased to 1.26 S/cm [207]. The poor response of synthesized Pt-Ru/TiO<sub>2</sub> may also be due to the larger particles compared to that of the commercial Pt-Ru/C, as observed in the material characterization *Section 4.3.1*. Generally, the activity is greater on smaller particles. Therefore the activity of the synthesized Pt-Ru/TiO<sub>2</sub> may be improved by lowering the calcination temperature to reduce particle growth. It was also reported that the predominant face present in small supported catalyst particles, Pt(111), is more active towards CH<sub>3</sub>OH oxidation [237]. Hepel *et al.* [228], observed forward and reverse CH<sub>3</sub>OH oxidation peaks on Pt-Ru supported on basal TiO<sub>2</sub> films formed by a voltammetric procedures which prevented the formation of compact non-conductive TiO<sub>2</sub> films. To obtain CVs showing a large current loop extending the CH<sub>3</sub>OH anodic oxidation currents to

very low potentials, they first applied an anodization potential greater than the  $\text{CO}_{\text{ad}}$  oxidative desorption potential to clean and activate the catalyst surface. The current Pt-Ru/ $\text{TiO}_2$  ink composition was based on an ink composition used for Pt-Ru/C inks and further ink optimization may be required as  $\text{TiO}_2$  is hydrophilic. Furthermore, the hydrophilic nature of  $\text{TiO}_2$  may affect the  $\text{CH}_3\text{OH}$  bonding ability on the Pt surface.  $\text{CH}_3\text{OH}$  may not absorb as easily to the Pt surface as extra energy may be required to displace water molecules which are in the way, making the electrochemical process slower and less efficient.

Strong metal-support interactions (SMSI) can occur in catalysts systems comprising metal particles dispersed on the surface of inorganic oxides after reduction at certain temperatures [217]. Therefore, it is possible that the interactions between the Pt and Ru metallic phase and the  $\text{TiO}_2$  support affected the intrinsic activity of the Pt-Ru/ $\text{TiO}_2$  electrocatalyst. The chemisorption ability of the precious metals may have been altered by interactions with the  $\text{TiO}_2$  surface and the  $\text{TiO}_2$  support may have shifted the  $\text{CH}_3\text{OH}$  oxidation onset potential to a more positive value. In addition to Ru, the  $\text{TiO}_2$  support may also provide hydroxide ions to remove CO poisoning from the Pt surface. Based on the CVs obtained, it is not possible to conclude that the  $\text{CH}_3\text{OH}$  electrochemical oxidation mechanism observed on Pt-Ru/ $\text{TiO}_2$  - GC is similar to the one observed on Pt-Ru/C. Nevertheless, catalytic reforming tests were successful using Pt-Ru/ $\text{TiO}_2$  in the literature, and a low electrocatalytic activity (low electrode polarization) is actually preferred to carry out EPOC experiments. This is because the currents or potentials involved in EPOC experiments are usually very small, and because the rate enhancement factor,  $\Lambda$ , is inversely proportional to the electrode exchange current,  $i_0$  as per Eq. 1.38.

#### 4.3.3 Powder catalysis

The mass spectrometer provided a real-time analysis of catalytic  $\text{CH}_3\text{OH}$  reforming  $\text{H}_2$  production rate using either 0.5 g of Pt-Ru/C or 0.5 g Pt-Ru/ $\text{TiO}_2$  catalyst powders. In preliminary tests, the  $\text{H}_2$  formation rate was measured as a function of time as the temperature was continuously increased from ambient temperature to  $100 \pm 1^\circ\text{C}$ . The  $\text{H}_2$  formation rates hence obtained were transient values and not steady-state equilibrium values. An example is shown in Fig. 4.11.

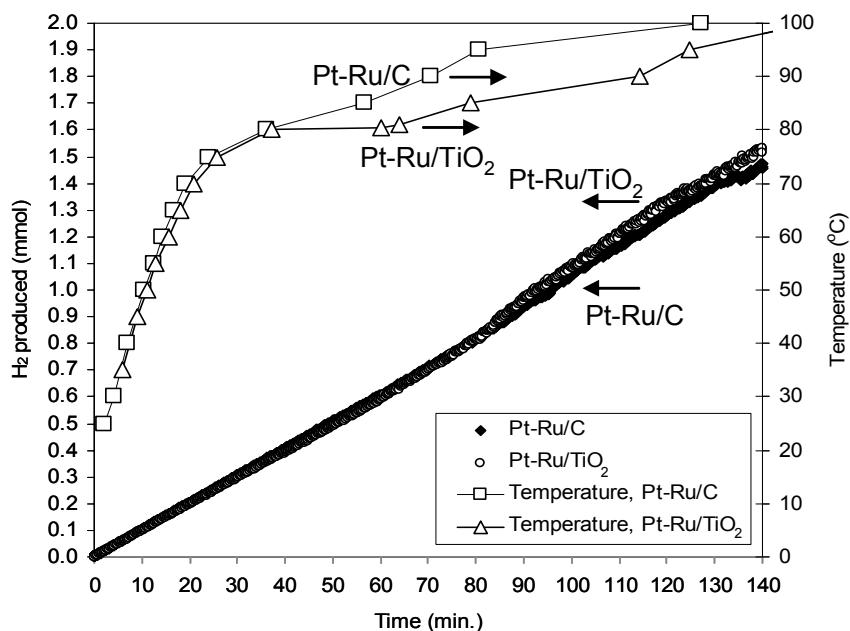


Figure 4.11: H<sub>2</sub> produced as a function of time (ambient to 100 ±1°C, 0.5 g catalyst, 20 wt% Pt-Ru, Pt:Ru 1:1 a/o, 20 ml of 2 M CH<sub>3</sub>OH in 0.5 M H<sub>2</sub>SO<sub>4</sub>).

It was found that, for both catalysts, some H<sub>2</sub> was produced at temperatures below 41°C, the temperature at which the catalytic reforming of CH<sub>3</sub>OH in the liquid phase becomes thermodynamically spontaneous for an equimolar CH<sub>3</sub>OH - water solution. However, the system studied here is not at thermodynamic equilibrium. To be at thermodynamic equilibrium, the catalytic system studied would need to be at chemical and thermal equilibrium. For example, reaction rates are not taken into account in equilibrium thermodynamics calculations. The powder catalysis system evaluated in Fig. 4.11 is not at thermal equilibrium as the temperature is constantly changing over time. Nevertheless, a steeper increase in the quantity of H<sub>2</sub> produced was observed from 80 to 85°C with Pt-Ru/C and from 80 to 90°C with Pt-Ru/TiO<sub>2</sub>. Improvements in the H<sub>2</sub> production rate are expected as temperature increases as the catalytic reaction rate constant depends exponentially on the temperature as per Arrhenius's law:

$$k_A = A_r \cdot \exp\left(\frac{-E_A}{RT}\right) \quad (4.9)$$

where  $k_A$ , the reaction rate constant and  $A_r$ , the pre-exponential factor, both have units of 1/s for a first order reaction, and  $E_A$  is the activation energy. For the purpose of this study, the temperature region between 80 to 90°C was avoided in all subsequent tests in order to keep the conversion rate low and increase the sensitivity to the effect of EPOC. A temperature of 75°C was chosen to carry out the powder catalysis and GDE catalysis experiments, as well as to study the effect of EP. Results obtained for the baseline powder catalysis tests carried out from ambient temperature to 75 ±1°C, until a steady-state H<sub>2</sub> production rate was reached at that temperature are presented as shown in Fig. 4.12.

It took about 30 to 40 minutes to reach 75 ±1°C, and the catalytic reforming experiment was held for about 70 minutes at this temperature. For both catalysts, the H<sub>2</sub> production rate did not increase significantly from ambient temperature to 75 ±1°C. For a semi-batch reactor, it is expected that the longer the reactant is in the reactor, the more reactant is converted until either equilibrium is reached, or the reactant is exhausted. Therefore, the CH<sub>3</sub>OH catalytic conversion to H<sub>2</sub> will depend on the time spent in the reactor. It may be possible that equilibrium was not reached over the duration of the powder catalysis experiment. To evaluate this, the rate of H<sub>2</sub> production was plotted as a function of temperature in Fig. 4.13.

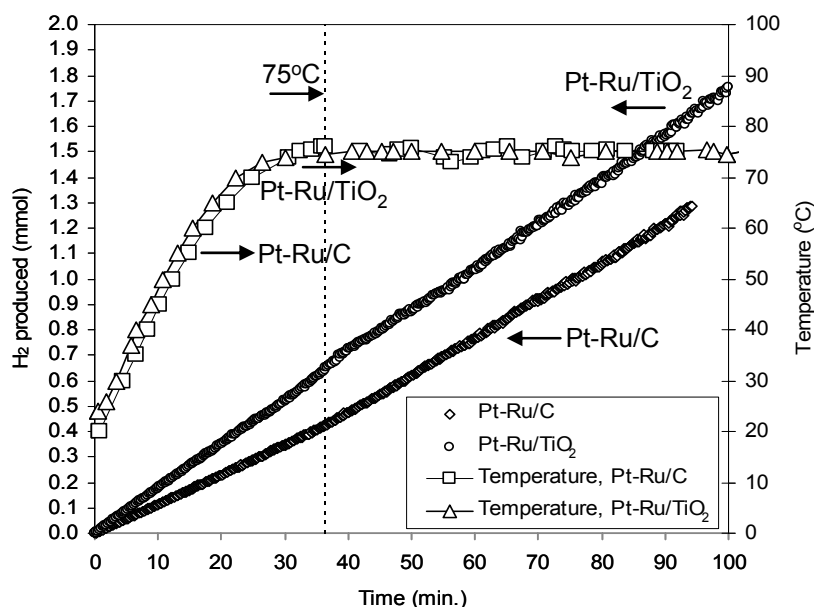


Figure 4.12: H<sub>2</sub> produced as a function of time (ambient to 75 ±1°C, 0.5 g catalyst, 20 wt% Pt-Ru, Pt:Ru 1:1 a/o, 20 ml of 2 M CH<sub>3</sub>OH in 0.5 M H<sub>2</sub>SO<sub>4</sub>).

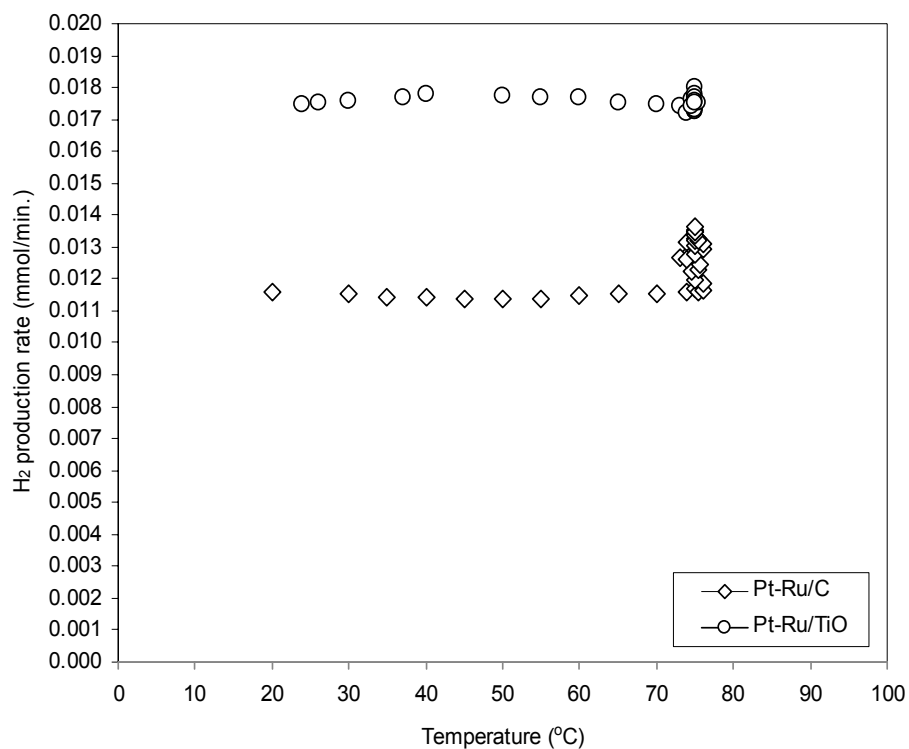


Figure 4.13: H<sub>2</sub> production rate as a function of temperature (0.5 g catalyst, 20 wt% Pt-Ru, Pt:Ru 1:1 a/o, 20 ml of 2 M CH<sub>3</sub>OH in 0.5 M H<sub>2</sub>SO<sub>4</sub>).

Once 75 ±1°C was reached, the H<sub>2</sub> production rate kept increasing slowly at this temperature with increasing run time. The Pt-Ru/C test was kept at 75 ±1°C for an hour and 30 min. and the Pt-Ru/TiO<sub>2</sub> test was kept at 75 ±1°C for an hour. The average H<sub>2</sub> production rate at 75 ±1°C on Pt-Ru/TiO<sub>2</sub> (0.017 mmol/min.) was 36.6% greater than on Pt-Ru/C (0.013 mmol/min.) under the same experimental conditions. The average H<sub>2</sub> formation rates obtained at 75 ±1°C were converted to μmol/h.g catalyst and x10<sup>6</sup> ml/h.g catalyst for comparison with experimental results available in the literature, which are summarized in Table 4.7.

Table 4.7: Literature powder catalysis CH<sub>3</sub>OH reforming production rates at low temperature (0.5 g Pt-Ru/TiO<sub>2</sub>, 10 wt% metal, Pt:Ru 1:1 a/o, 60 ml of 2 M CH<sub>3</sub>OH).

| H <sub>2</sub> reduction<br>T<br>[°C] | Reaction<br>T<br>[°C] | Molar flow rate ( $F_r$ )             |      |                 | Volumetric flow rate ( $V_r$ ) |      |                                                           | Ref   |      |
|---------------------------------------|-----------------------|---------------------------------------|------|-----------------|--------------------------------|------|-----------------------------------------------------------|-------|------|
|                                       |                       | H <sub>2</sub><br>[μmol/h.g catalyst] | CO   | CO <sub>2</sub> | H <sub>2</sub>                 | CO   | CO <sub>2</sub> Gas<br>[x10 <sup>6</sup> ml/h.g catalyst] |       |      |
| -                                     | 72                    | 102.9                                 | -    | -               | 2.91                           |      | 2.91                                                      | [29]  |      |
| 400                                   | 77-84                 | 105.6                                 | 4.2  | 30.6            | 3.06                           | 0.12 | 0.89                                                      | 4.07  | [14] |
| 200                                   | 105                   | 59.8                                  | 12   | 4               | 1.86                           | 0.37 | 0.12                                                      | 2.35  | [16] |
| 200                                   | 105                   | 158.6                                 | 21.2 | 29.8            | 4.92                           | 0.66 | 0.92                                                      | 6.50  | [16] |
| 400                                   | 105                   | 205.8                                 | 6.6  | 66              | 5.96                           | 0.19 | 1.91                                                      | 8.07  | [16] |
| 450                                   | 105                   | 321.6                                 | 9.6  | 106.8           | 9.98                           | 0.30 | 3.31                                                      | 13.59 | [16] |

All catalytic CH<sub>3</sub>OH reforming experiments reported in the literature used powder catalysts with a precious metal content of 10 wt%, and a metal catalyst mass (0.5 g) to solution volume (60 ml) ratio of  $8 \times 10^{-4}$ . The experiments carried out in this study were conducted using catalysts with double the precious metal content (20 wt%), and a metal catalyst mass (0.5 g) to solution volume (20 ml) ratio of 0.005. Results obtained in the current study are summarized in Table 4.8. In the last two columns of Table 4.8, the experimental results were normalized to the metal catalyst mass to solution volume ratio of  $8 \times 10^{-4}$  for better comparison with the results available in the literature.

Table 4.8: Powder catalysis CH<sub>3</sub>OH reforming production rates (0.5 g catalyst, 20 wt% Pt-Ru, Pt:Ru 1:1 a/o, 20 ml of 2 M CH<sub>3</sub>OH in 0.5 M H<sub>2</sub>SO<sub>4</sub>, 75 ± 1°C).

| Catalyst                                | H <sub>2</sub> reduction<br>T<br>[°C] | Reaction<br>T<br>[°C] | Molar flow rate ( $F_r$ )             | Volumetric flow rate ( $V_r$ )                       | Normalized $F_r$                      | Normalized $V_r$                                     |
|-----------------------------------------|---------------------------------------|-----------------------|---------------------------------------|------------------------------------------------------|---------------------------------------|------------------------------------------------------|
|                                         |                                       |                       | H <sub>2</sub><br>[μmol/h.g catalyst] | H <sub>2</sub><br>[x10 <sup>6</sup> ml/h.g catalyst] | H <sub>2</sub><br>[μmol/h.g catalyst] | H <sub>2</sub><br>[x10 <sup>6</sup> ml/h.g catalyst] |
| Pt-Ru/C<br>(commercial)                 | Unknown                               | 75 ± 1                | 1531                                  | 44                                                   | 255                                   | 7                                                    |
| Pt-Ru/TiO <sub>2</sub><br>(synthesized) | 500                                   | 75 ± 1                | 2090                                  | 60                                                   | 348                                   | 10                                                   |

The H<sub>2</sub> production rate or formation volume was 36.5 % greater for the Pt-Ru/TiO<sub>2</sub> catalyst than for the Pt-Ru/C catalyst under the same reaction conditions. Thus, the synthesized Pt-Ru/TiO<sub>2</sub> had a greater activity for the catalytic reforming of CH<sub>3</sub>OH than the commercial Pt-Ru/C. As the precious metal content was the same for both catalysts studied, it may be possible that the larger H<sub>2</sub> production rate observed with the Pt-Ru/TiO<sub>2</sub> catalyst is linked to strong metal-support interactions (SMSI). The normalized Pt-Ru/TiO<sub>2</sub> H<sub>2</sub> formation rate and the H<sub>2</sub> formation volume were about three times greater than the results reported by Miyao *et al.* for the same catalyst, but reduced at 400°C and at reaction temperatures of 77-84°C [14]. The normalized Pt-Ru/TiO<sub>2</sub> H<sub>2</sub> formation rate was 69 % greater and the H<sub>2</sub> formation volume was 22.8 % greater than the results reported by Miyao *et al.* for the same catalyst, but reduced at 400°C and a reaction temperature of 105°C [16]. However, when comparing with the same catalyst, but reduced at 450°C and at a reaction temperature of 105°C, the H<sub>2</sub> formation rate was 8% greater and the H<sub>2</sub> formation volume was 3.7% smaller in this study. The differences in the rates may arise from the fact that their catalyst reduction temperature was slightly lower (400-450°C) and their reaction temperature, slightly greater (77-105°C) than the one used in this study (500°C, 75 ±1°C). Greater reaction temperatures would improve the CH<sub>3</sub>OH conversion and result in greater H<sub>2</sub> production. Also, the experiments reported in the literature were conducted for 5 hours, and a longer run time will result in more H<sub>2</sub> production. Nevertheless, since the powder catalysis production rates obtained in this study are good and generally in a similar range as the ones reported in the literature under similar conditions, the H<sub>2</sub> rate measurement method was determined to be adequate to conduct further catalytic studies and evaluate the effect of EPOC.

Further confirmation of the validity of the experimental H<sub>2</sub> monitoring method was obtained by looking at the CH<sub>3</sub>OH partial pressure monitored by the MS over time. Based on the preliminary CH<sub>3</sub>OH evaporation test described in *Section 4.2.5*, it can be estimated that, over a period of 2 hours at 75°C, the loss of CH<sub>3</sub>OH concentration due to evaporation could be up to 10%. Lower H<sub>2</sub> production rates would result if there would be a significant loss of unreacted CH<sub>3</sub>OH by evaporation. Figure 4.14 shows the CH<sub>3</sub>OH partial pressure measured during the catalytic reforming experiments shown on Fig. 4.12 and 4.13.

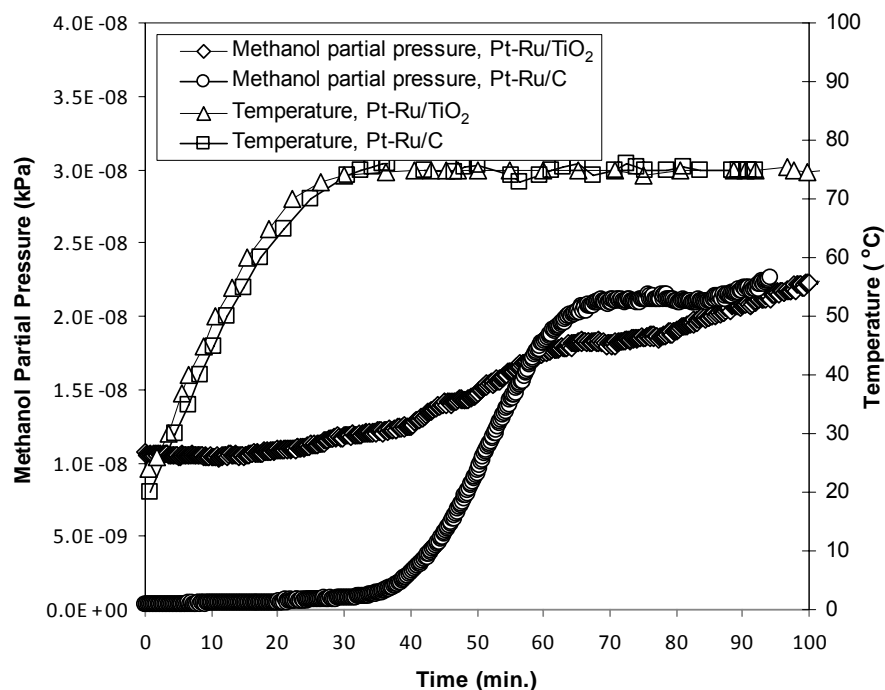


Figure 4.14: CH<sub>3</sub>OH partial pressure as a function of time (a) Pt-Ru/C, (b) Pt-Ru/TiO<sub>2</sub> (ambient to 75 ±1°C, 0.5 g catalyst, 20 wt% Pt-Ru, Pt:Ru 1:1 a/o, 20 ml of 2 M CH<sub>3</sub>OH in 0.5 M H<sub>2</sub>SO<sub>4</sub>).

The CH<sub>3</sub>OH partial pressure was very low and did not increase significantly during the course of the catalytic reforming experiment, indicating that the gas bubbler was effective at preventing CH<sub>3</sub>OH vapours from entering the MS. The MS also recorded the partial pressure of CO<sub>2</sub> during the catalytic reforming experiment. It would be expected that the partial pressure of CO<sub>2</sub> would increase proportionally to the partial pressure of H<sub>2</sub>. However, this was not the case and the partial pressure of CO<sub>2</sub> detected by the MS did not change significantly during the course of the experiment. This is may be due to the large solubility of CO<sub>2</sub> in water which is 3.4 g/l at 0°C, i.e., 0.578 g of CO<sub>2</sub> in the 170 ml of H<sub>2</sub>O contained in the two gas bubblers. Assuming the molar flow rate of CO<sub>2</sub> is 1/3 of the H<sub>2</sub> molar flow rate, when using 0.5 g of Pt-Ru/TiO<sub>2</sub>, it can be calculated that 0.015 g of CO<sub>2</sub> is generated per hour, which is much less than the solubility limit of the water contained in the chilled gas bubblers. The DI water in the gas bubblers was changed between each experiment.

Knowing the catalytic CH<sub>3</sub>OH reforming H<sub>2</sub> formation rate at open-circuit and the exchange current, it is possible to estimate the magnitude of the absolute Faradaic efficiency on Pt-Ru/C at 75 ±1°C using Eq. 1.38. As per Table 2.3 in *Chapter 2*, the exchange current for 2M CH<sub>3</sub>OH at 75 ±1°C was estimated to

be  $8.1 \times 10^{-6}$  A using a GDE, and as per Table 4.8, the unpromoted catalytic rate is  $4.25 \times 10^{-7}$  mol/s using catalyst powder. Hence,  $|A|$  is estimated to be approximately 5067, which is two orders of magnitude larger than that reported for most low temperature EPOC studies using Nafion, which range from 20 to 28. The large  $|A|$  calculated may have been caused by discrepancies in the exchange current density estimation, and the use of an unpromoted catalytic rate obtained for a catalyst powder reforming experiment rather than one using a GDE.

#### 4.3.4 GDE catalysis and electrochemical promotion of catalysis

The EPOC tests were carried out in the two-compartment glass cell and required the use of gas diffusion electrodes. The anodic compartment of the electrolyser served also as the catalytic reaction chamber. Therefore, in EPOC experiments, the anodic GDE acted as a catalyst and as an electrocatalyst at the same time. The  $H_2$  produced in the cathodic compartment during the EPOC tests was vented to atmosphere and was not included in the  $H_2$  generation rate values reported. Only the gases evolving from the anodic compartment were sent to the MS for measurements. The anode GDE was a  $2.01 \text{ cm}^2$  disk coupon of a  $4 \text{ mg/cm}^2$ , 20 wt% metal Pt-Ru/C or Pt-Ru/TiO<sub>2</sub>. The anodic compartment was filled with 80 ml of 2 M CH<sub>3</sub>OH acidic solution. The resulting metal catalyst mass to volume ratio was of  $2 \times 10^{-5}$ , which is many orders of magnitude smaller than that used in the prior powder catalysis experiments (0.005). Nevertheless, this should keep the conversion rates sufficiently low (below 5 %) and improve the sensitivity of the EPOC effect on the catalytic reaction rate. The helium carrier gas flow rate was kept at the same rate as for the powder catalysis experiments.

The range of imposed currents or potentials evaluated for selected chemical reactions for which EPOC was studied in the literature are listed in Table 4.9. As can be seen, the range of current imposed in the literature varied widely depending on the type of conducting electrolyte used, the chemical reaction studied, and the reaction temperature. Values were only reported on a current basis in the literature, and as not all geometric surface areas were available, they could not be converted to current densities. All chemical reactions using cationic conductors studied for the EPOC effect have been using gaseous reactants, even at low reaction temperature. Based on prior Pt-Ru/C polarization curves shown in Fig. 2.12 c) of *Chapter 2*, at 75°C for 2 M CH<sub>3</sub>OH, it can be expected that electrocatalysis should start at

currents between 100 and 500  $\mu\text{A}$ , i.e., current densities of 0.05 and 0.25  $\text{mA}/\text{cm}^2$ . When currents smaller than this were imposed, the electrolyser cell voltage,  $U_{WC}$ , remained positive for the entire experiment. Larger currents were also evaluated for the electrochemical reforming of 2 M  $\text{CH}_3\text{OH}$  using Pt-Ru/C, but they did not surpass the limiting current density of 75  $\text{mA}/\text{cm}^2$ , i.e., 0.15 A.

Table 4.9: Imposed currents or potentials on selected chemical reactions subjected to EPOC.

| Electrolyte type | Chemical Reaction                | Catalyst and protonic electrolyte                        | T [ $^{\circ}\text{C}$ ] | Imposed current [ $\mu\text{A}$ ] | Imposed potential [V vs. SHE] | Ref   |
|------------------|----------------------------------|----------------------------------------------------------|--------------------------|-----------------------------------|-------------------------------|-------|
| Oxide            | Methanol oxidation               | Pt-YSZ                                                   | 350-650                  | -                                 | 0 to 12.5, and 0 to -12.5     | [238] |
|                  | Methanol oxidation               | Ag-YSZ                                                   | 500                      | 0 to -2000                        | -                             | [138] |
|                  | Methanol dehydrogenation         | Ag-YSZ                                                   | 600-680                  | -2000                             | -                             | [139] |
|                  | Methane reforming                | Ni-YSZ                                                   | 750-950                  | 300000                            | -                             | [239] |
|                  | $\text{C}_2\text{H}_4$ oxidation | Pt-YSZ                                                   | 370                      | 1                                 | -                             | [240] |
|                  | $\text{C}_2\text{H}_4$ oxidation | $\text{IrO}_2/\text{YSZ}$                                | 380                      | 10                                | -                             | [241] |
|                  | $\text{C}_2\text{H}_4$ oxidation | Rh-YSZ                                                   | 350                      | 400                               | -                             | [242] |
| Protonic         | Hydrogen oxidation               | Pt black-N117                                            | room T                   | 5000                              | -                             | [147] |
|                  | $\text{C}_2\text{H}_4$ oxidation | $\text{Pt-CaZr}_{0.9}\text{In}_{0.1}\text{O}_{3-\alpha}$ | 450                      | 3                                 | -                             | [243] |
|                  | CO oxidation                     | $\text{Pt-}\beta\text{-Al}_2\text{O}_3$                  | 350                      | -20                               | -                             | [244] |
|                  | 1-butene isomerization           | Pt black/N-117/Pd/C                                      | 70                       | -                                 | -0.05 to 0.38                 | [245] |
| Liquid           | Hydrogen oxidation               | Pt in 0.1 M KOH                                          | 25-50                    | -10000 to 15000                   | -                             | [246] |
|                  | Hydrogenation of maleic acid     | Platinized Pt in 0.5 M $\text{HClO}_4$                   | 26                       | -                                 | 0.05 to 1.8                   | [247] |

Each EPOC test was conducted using a different MEA of similar composition. For each test, three different EP currents were sequentially applied. In general, it took about 30 min. to attain the desired temperature of  $75 \pm 1^\circ\text{C}$ , as indicated by the first vertical dash line of the graph. Once at the desired reaction temperature, the catalytic reaction rate was measured for about 2.5 hours under OCV before the first galvanostatic current was applied to obtain the unpromoted catalytic reaction  $\text{H}_2$  production rate value,  $r_o$ . The galvanostatic currents were applied for 30 min. and ranged from -0.15 to 0.01 A ( $-75.63$  to  $5 \text{ mA/cm}^2$ ). In EPOC studies with oxide conductors, the current  $I$  is positive when  $\text{O}^{2-}$  is pumped to the catalyst surface and negative when  $\text{O}^{2-}$  is pumped away from the catalyst surface [238]. Based on this convention, for a protonic conductor,  $I$  was taken as positive when  $\text{H}^+$  is removed from the surface and as negative when  $\text{H}^+$  is supplied to the catalyst surface. The system was brought back to OCV for 30 min. between each galvanostatic current application. Vertical dashed lines indicate the time at which the galvanostatic current application periods started and stopped. The promoted catalytic reaction  $\text{H}_2$  production rate obtained during the EPOC portion of the test were averaged as  $r$  values. The unpromoted catalytic reaction rate during the other OCV portions of the test were averaged as  $r'$  values. These  $r'$  values should be the same as the  $r_o$  values, if 30 min. was sufficient for the chemical reaction system to attain equilibrium again. An EPOC test conducted with Pt-Ru/ $\text{TiO}_2$  is shown in Fig. 4.15 and one conducted on Pt-Ru/C is shown in Fig. 4.16.

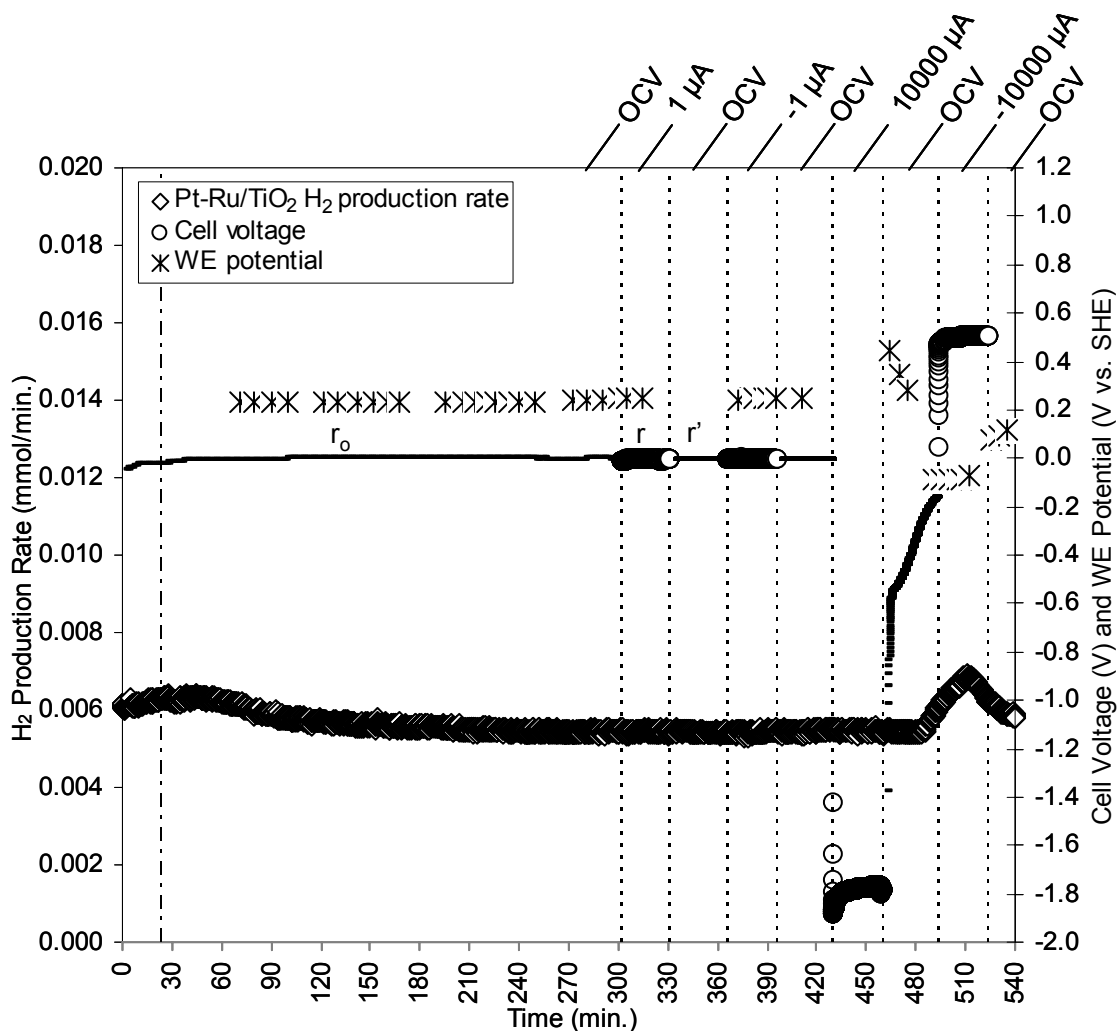


Figure 4.15: H<sub>2</sub> production rate and electrolysis cell voltage as a function of time during unpromoted and promoted catalysis (2.01 cm<sup>2</sup>, 4 mg/cm<sup>2</sup> Pt-Ru/TiO<sub>2</sub>, 20 wt% Pt-Ru, Pt:Ru 1:1 a/o, 80 ml of 2 M CH<sub>3</sub>OH in 0.5 M H<sub>2</sub>SO<sub>4</sub> electrolyser anolyte, 80 ml of 0.5 M H<sub>2</sub>SO<sub>4</sub> electrolyser catholyte, 75 ±1°C).

It appeared that 300 min. (5 hours) was sufficient for the catalytic reaction to reach steady-state under open circuit conditions. The catalysis conditioning profiles were similar for other MEAs evaluated in our research with Pt-Ru/TiO<sub>2</sub> or Pt-Ru/C. It was calculated that a steady state H<sub>2</sub> production rate of 0.006 mmol/min corresponded to an electrolysis current density of about 30 mA/cm<sup>2</sup>. At this current density, CH<sub>3</sub>OH would be electrolysed on the WE of the electrolyser as per earlier 2 M CH<sub>3</sub>OH electrolysis results on 4 mg/cm<sup>2</sup> Pt-Ru/C at 75°C (Fig. 2.12). This calculated current density is unlikely at open circuit voltage. It is possible that the MS has a poor sensitivity at detecting low flow rates of H<sub>2</sub> compared to the sensitivity of the Multistat at controlling currents or potentials.

The experiments carried out in this section were conducted using a geometric area of  $2.01 \text{ cm}^2$  with a loading of  $4 \text{ mg/cm}^2$  catalysts with a precious metal content (20 wt%), and, hence, a metal catalyst mass ( $0.0016 \text{ g}$ ) to solution volume ( $80 \text{ ml}$ ) ratio of  $2 \times 10^{-5}$ . The  $\text{H}_2$  formation rates for the unpromoted catalytic reaction,  $r_o$ , obtained with GDEs were normalized to a metal catalyst mass to solution volume ratio of  $8 \times 10^{-4}$  for comparison with the powder catalysis tests results discussed in Section 4.3.4. The average unpromoted catalytic  $\text{H}_2$  production rates obtained with the GDEs are listed in Table 4.10 along with the normalized rates for comparison with the powder catalysis test results. Similar to the powder catalysis cases, the unpromoted catalytic  $\text{H}_2$  production rate using Pt-Ru/ $\text{TiO}_2$  was about 27 % greater than the average unpromoted catalytic  $\text{H}_2$  production rate obtained using various Pt-Ru/C based MEAs.

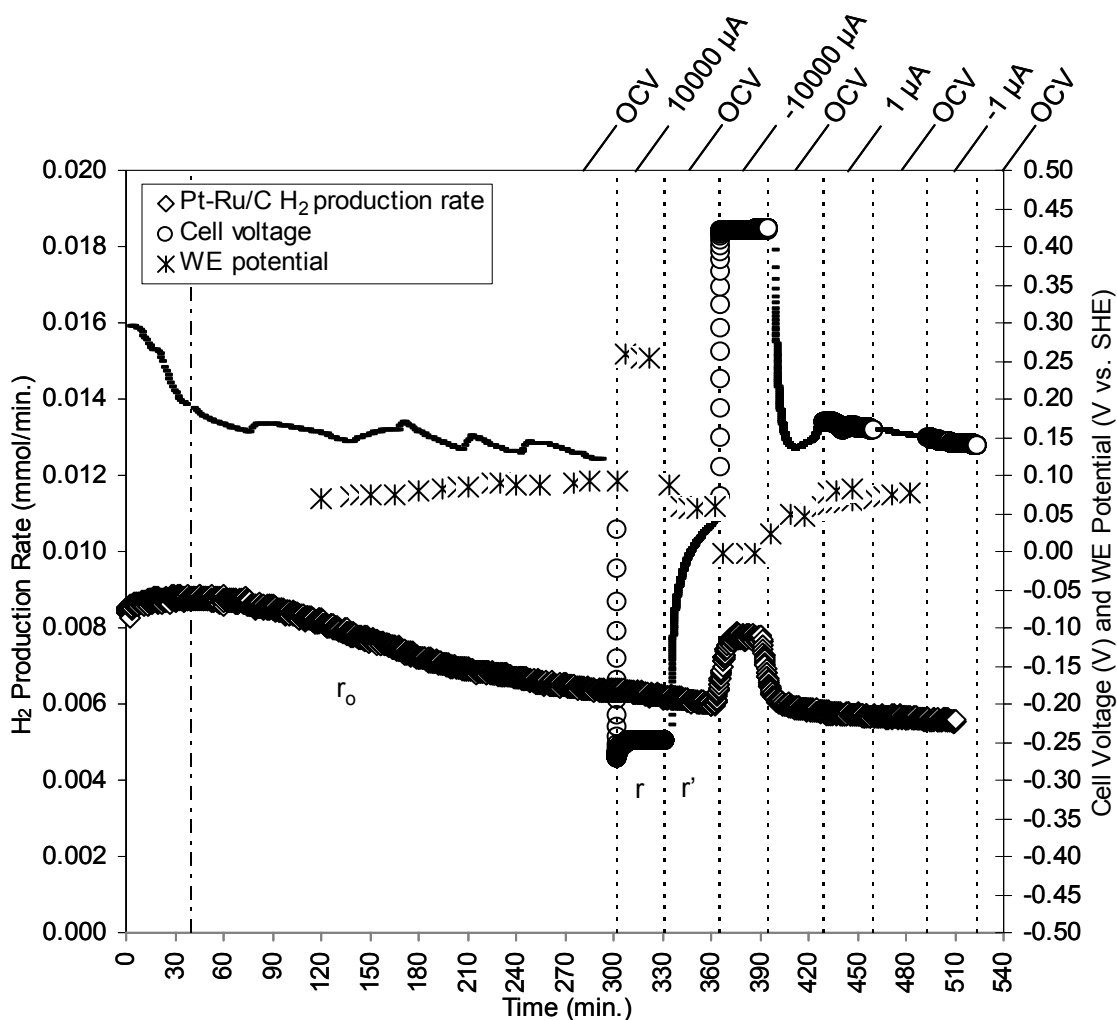


Figure 4.16:  $\text{H}_2$  production rate and electrolysis cell voltage as a function of time during unpromoted and promoted catalysis ( $2.01 \text{ cm}^2$ ,  $4 \text{ mg/cm}^2$  Pt-Ru/C, 20 wt% Pt-Ru, Pt:Ru 1:1 a/o, 80 ml of 2 M  $\text{CH}_3\text{OH}$  in 0.5 M  $\text{H}_2\text{SO}_4$  electrolyser anolyte, 80 ml of 0.5 M  $\text{H}_2\text{SO}_4$  electrolyser catholyte,  $75 \pm 1^\circ\text{C}$ ).

Table 4.10: Average H<sub>2</sub> unpromoted production rates for GDE catalysis of CH<sub>3</sub>OH at low temperature (2.01 cm<sup>2</sup>, 4 mg/cm<sup>2</sup> Pt-Ru/C or Pt-Ru/TiO<sub>2</sub>, 20 wt% Pt-Ru, Pt:Ru 1:1 a/o, 80 ml of 2 M CH<sub>3</sub>OH in 0.5 M H<sub>2</sub>SO<sub>4</sub> electrolyser anolyte, 80 ml of 0.5 M H<sub>2</sub>SO<sub>4</sub> electrolyser catholyte, 75 ± 1°C).

| Catalyst               | Molar flow rate ( <i>Fr</i> ) H <sub>2</sub><br>[μmol/h.g catalyst]<br>± 10184 μmol/h.g catalyst<br><i>r<sub>o</sub></i> | Normalized <i>Fr</i> H <sub>2</sub><br>[μmol/h.g catalyst]<br>± 407360 μmol/h.g catalyst<br><i>r<sub>o</sub></i> |
|------------------------|--------------------------------------------------------------------------------------------------------------------------|------------------------------------------------------------------------------------------------------------------|
| Pt-Ru/C                | 36582                                                                                                                    | 1463280                                                                                                          |
| Pt-Ru/TiO <sub>2</sub> | 42163                                                                                                                    | 1686520                                                                                                          |

The standard deviation values were calculated based on tests conducted with three different MEAs with Pt-Ru/C GDEs. The un-normalized molar flow rates measured were adjusted to 1 g of catalyst, while the normalized results were adjusted for the metal catalyst mass to solution volume ratio. It was verified that, without the catalyst mass adjustment and without the metal catalyst mass to solution volume ratio, more H<sub>2</sub> was evolved in the powder catalysis cases than for the GDE catalysis cases, as expected. However, it can be seen that the normalized H<sub>2</sub> formation rates for the unpromoted catalytic CH<sub>3</sub>OH reforming reaction obtained with GDEs are several orders of magnitude greater than the ones obtained for powder catalysis in Table 4.8. Different reactor configurations were used to carry the powder catalysis tests (single-compartment glass cell reactor) and the GDE tests (2-compartment glass cell reactor). It is possible that EPOC was induced at the GDE in the 2-compartment reactor without the application of external current to stimulate the catalytic reaction. It has been reported that, for certain configurations, a current or potential difference may developed between the catalyst WE surface and CE at open circuit due to the occurrence of the catalytic reaction on the catalyst WE surface [132]. This may be possible as the H<sub>2</sub> production rate measurements have shown that the GDE Pt-Ru/C catalyst WE was not completely inert to catalytic activity even at ambient temperature where there is no thermodynamic driving force for H<sub>2</sub> production. This could be further verified by measuring the quantity of H<sub>2</sub> produced during a test carried out in the single-compartment reactor using a non-conductive connection to a GDE catalyst sample immersed in the reacting solution. This value would results in the true *r<sub>o</sub>* value, i.e., without the wireless application of a small current or potential due to the 2-compartment cell MEA. If the H<sub>2</sub> production rate obtained in the single-compartment reactor case, *r<sub>o</sub>*, is indeed lower than that obtained

for the equivalent test carried out in the double-compartment reactor,  $r$ , then a wireless EPOC effect exist when using the 2-compartment reactor. Knowing the electrochemical cell internal current at open circuit voltage in the 2-compartment cell would then allow the determination of the Faradaic efficiency for this self-driven wireless EPOC case.

As shown in Fig. 4.15 and 4.16, during the application of 1 or -1  $\mu\text{A}$  (0.5 or -0.5  $\mu\text{A}/\text{cm}^2$ ), the electrolyser cell voltage,  $U_{WC}$  remained approximately zero and no effect on the  $\text{H}_2$  production rate were observed. It was found that larger negative currents, i.e. -0.01 A (-5  $\text{mA}/\text{cm}^2$ ) with a positive cell voltage, were required to observe an effect. For Pt-Ru/ $\text{TiO}_2$  or Pt-Ru/C, only the application of a negative current resulted in an increase in the  $\text{H}_2$  production rate. The proposed electrochemical enhancement mechanism for the catalytic reforming of  $\text{CH}_3\text{OH}$  is described in Fig. 4.17.

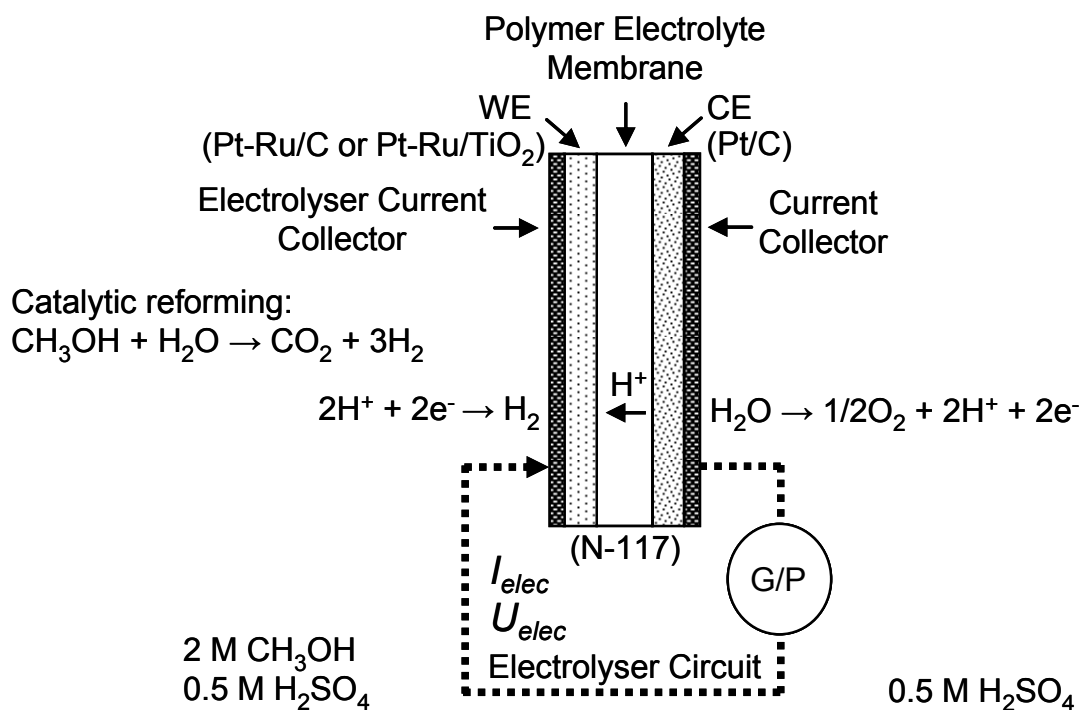


Figure 4.17: Schematic diagram of the reverse electrolyser electrical circuit and of the proposed EPOC mechanism for the catalytic reforming of methanol.

When a negative current is applied to the electrolyser circuit,  $\text{H}^+$  ions are supplied to the WE surface. Water is oxidized in the catholyte compartment of the glass cell and the electrolyser operated in reverse.

No CH<sub>3</sub>OH or water is electro-oxidized in the catalytic reaction compartment of the glass cell. However, the reverse electrolyser may generate H<sub>2</sub> in the catalytic reaction compartment. Under the experimental conditions studied, only providing H<sup>+</sup> to the catalyst surface was beneficial to the catalytic CH<sub>3</sub>OH reforming reaction rate, and removing H<sup>+</sup> from the catalyst surface did not increase the catalytic CH<sub>3</sub>OH reforming reaction rate.

At an applied current of -0.01 A (-5 mA/cm<sup>2</sup>), the electrochemical promotion effect was about 20 % lower when using Pt-Ru/TiO<sub>2</sub> than when using Pt-Ru/C. This is likely due to the low electronic conductivity the Pt-Ru/TiO<sub>2</sub> for CH<sub>3</sub>OH electro-oxidation compared to that of Pt-Ru/C, as was discussed in *Section 4.3.2*. Based on the powder catalysis tests, it was shown that Pt-Ru/C did possess a lower catalytic activity than Pt-Ru/TiO<sub>2</sub> for the electrochemical oxidation of CH<sub>3</sub>OH. However, using a GDE, to obtain a same enhancement as for the Pt-Ru/C catalyst, more current may need to be applied with the Pt-Ru/TiO<sub>2</sub> catalyst to obtain a similar effect on the work function of the working electrode. Consequently, all further EPOC experiments were conducted with commercial Pt-Ru/C catalyst GDEs. Figure 4.18 demonstrates the reproducibility of the catalytic rate enhancement was investigated by applying multiple negative current consecutively.

Again, it can be seen that application of negative currents smaller than -0.01 A (-5 mA/cm<sup>2</sup>) did not impact the catalytic H<sub>2</sub> production rate significantly. The consecutive application of a current of -0.01 A following OCV showed that the effect was reversible, i.e., the catalytic H<sub>2</sub> production rate always returned to the unpromoted rate upon interruption of the current. The average promoted H<sub>2</sub> production rate,  $r$ , for the four consecutive current applications of -0.01 A with Pt-Ru/C as the working electrode was of 46469 ±456 μmol/h.g catalyst and the average unpromoted H<sub>2</sub> production rate,  $r'$ , was of 35131 ±1172 μmol/h.g catalyst. The average  $r'$  did not change significantly (6 %) from the initial  $r_0$  value of 33057 μmol/h.g catalyst, indicating a reproducible process.

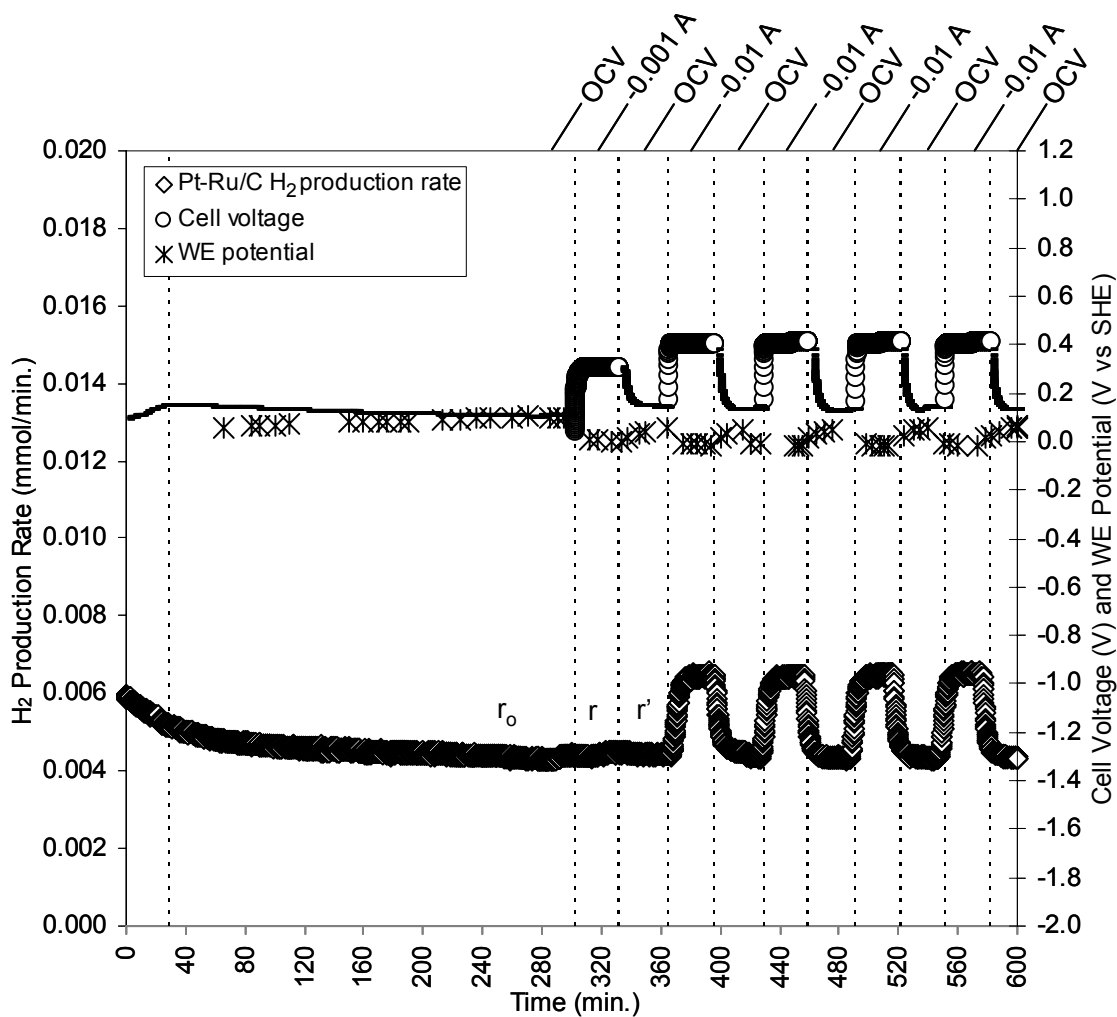


Figure 4.18: H<sub>2</sub> production rate and electrolyser current as a function of time during unpromoted and promoted catalysis (2.01 cm<sup>2</sup>, 4 mg/cm<sup>2</sup> Pt-Ru/C, 20 wt% Pt-Ru, Pt:Ru 1:1 a/o, 80 ml of 2 M CH<sub>3</sub>OH in 0.5 M H<sub>2</sub>SO<sub>4</sub> electrolyser anolyte, 80 ml of 0.5 M H<sub>2</sub>SO<sub>4</sub> electrolyser catholyte, 75 ±1°C).

The application of consecutively larger negative currents was also investigated with Pt-Ru/C and the results are shown in Figure 4.19. The application of greater negative currents resulted in greater increases in the catalytic H<sub>2</sub> production rate. As shown in Fig. 2.12 c), the limiting current for normal water electrolysis with 4 mg/cm<sup>2</sup> Pt-Ru/C at the anode was 25 mA/cm<sup>2</sup> (0.05 A) when the electrolyser cell voltage reached values greater than -2 V in normal electrolysis with 2 mg/cm<sup>2</sup> Pt/C at the cathode at 75 ±1°C. Although currents of -0.1 A (-0.05 A/cm<sup>2</sup>) and -0.15 A (-0.075 A/cm<sup>2</sup>) were imposed, the reverse electrolyser cell voltage during the EPOC tests carried out in Fig. 4.19 did not reach values greater than 2 V. At reverse electrolysis cell voltages greater than 2 V, carbon oxidation would start to

occur on the counter electrode, where the electrochemical oxidation of water occurs. It was checked that the reverse electrolyser returned to cell voltages close to its original OCV value between each test, indicating that there was no electrode degradation.

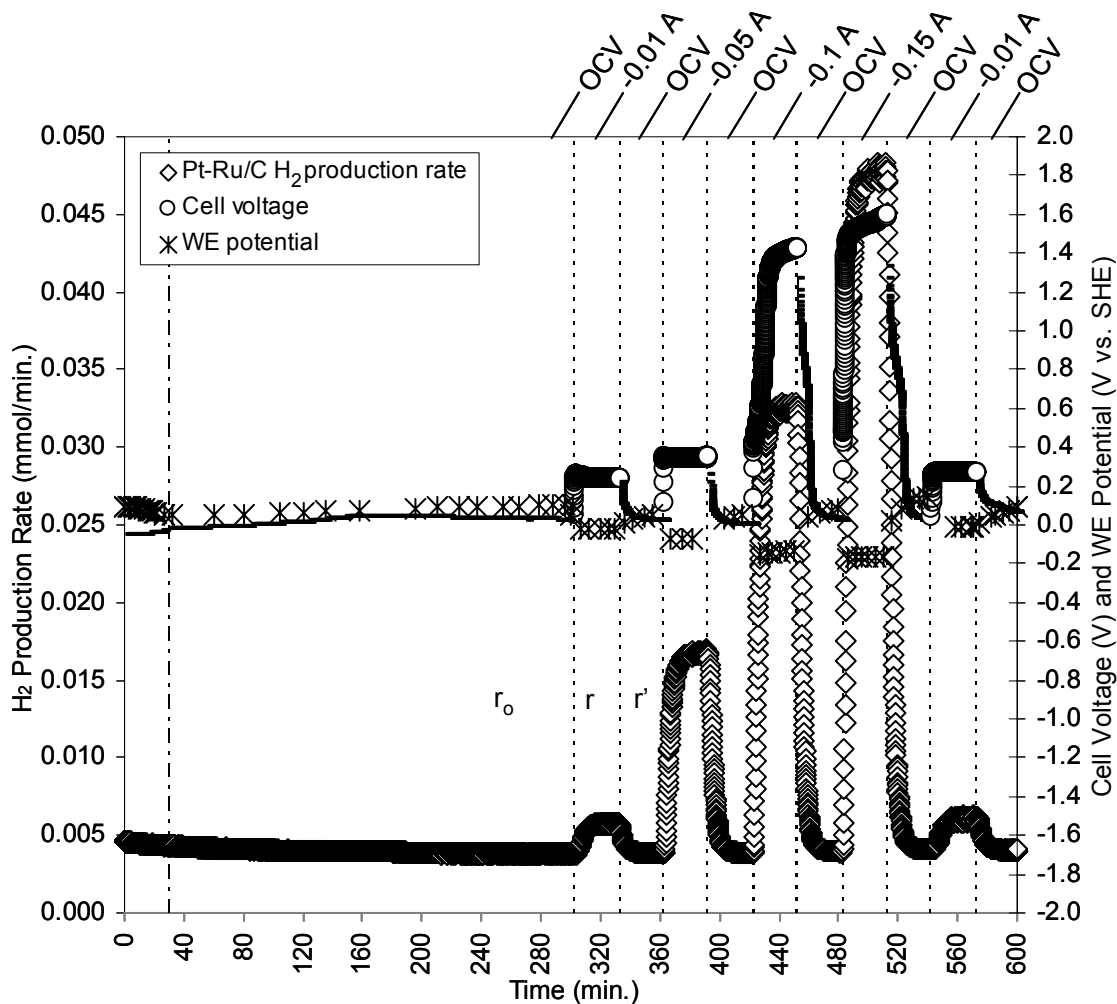


Figure 4.19:  $\text{H}_2$  production rate and electrolyser current as a function of time during unpromoted and promoted catalysis ( $2.01 \text{ cm}^2$ ,  $4 \text{ mg/cm}^2$  Pt-Ru/C, 20 wt% Pt-Ru, Pt:Ru 1:1 a/o, 80 ml of 2 M  $\text{CH}_3\text{OH}$  in 0.5 M  $\text{H}_2\text{SO}_4$  electrolyser anolyte, 80 ml of 0.5 M  $\text{H}_2\text{SO}_4$  electrolyser catholyte,  $75 \pm 1^\circ\text{C}$ ).

The average  $\text{H}_2$  formation rates for each EPOC test segment carried out in Fig. 4.18 and 4.19 are reported in Table 4.11. The calculated theoretical Faradaic  $\text{H}_2$  production rate based on the imposed current,  $r_F$ , along with the Faradaic efficiencies,  $\lambda$ , and the EPOC production rate efficiency,  $\eta_{\text{EPOC}}$ . The  $\text{H}_2$  production Faradaic efficiencies (Eq. 1.37) were calculated using  $n = 2$  and the initial test  $r_0$  values obtained at steady-state for each respective test. The  $r_0$  value was taken as the average of the  $\text{H}_2$

formation rate over the 30 min. period before the first EPOC galvanostatic current was imposed. Equation 1.32 can be rewritten in terms of production rates as follows:

$$\Lambda = \frac{r - r_o}{r_F} \quad (4.10)$$

where  $r_F$  is the Faradaic production rate. The dimensionless EPOC production rate efficiency was evaluated by comparing the promoted catalytic reaction rate to the electrochemical Faradaic production rate as follows:

$$\eta_{EPOC} = \frac{r}{r_F} \quad (4.11)$$

As the  $r^o$  for the different MEAs is not exactly the same, it makes it difficult to compare the promoted  $H_2$  production rates,  $r$ , for the different test directly. However, as the relative differences between the  $r_o$  and  $r$ , for a particular EPOC test are similar and the efficiencies are calculated on the basis of  $r_o$  and  $r$  values, it is possible to compare the Faradaic efficiencies obtained for the different cases. For all EPOC tests for which negative currents were applied,  $r$  was greater than  $r_o$ , and the difference between  $r$  and  $r_o$  was greater than the theoretical Faradaic  $H_2$  production rate calculated based on the current imposed. Typically,  $r'$  exceeded  $r_o$ , especially for the EPOC tests carried out at currents  $> -0.01$  A ( $5 \text{ mA/cm}^2$ ), for which the unpromoted  $H_2$  production rate,  $r'$ , did not have time to return to its original unpromoted  $H_2$  production rate,  $r_o$ , over the 30 min. relaxation period.

Table 4.11: Faradaic H<sub>2</sub> production rate, measured H<sub>2</sub> production rates, Faradaic efficiencies and EPOC efficiencies for the GDE catalytic reforming of CH<sub>3</sub>OH at low temperature (2.01 cm<sup>2</sup>, 4 mg/cm<sup>2</sup> Pt-Ru/C, 20 wt% Pt-Ru, Pt:Ru 1:1 a/o, 80 ml of 2 M CH<sub>3</sub>OH in 0.5 M H<sub>2</sub>SO<sub>4</sub> electrolyser anolyte, 80 ml of 0.5 M H<sub>2</sub>SO<sub>4</sub> electrolyser catholyte, 75 ±1°C).

| Applied current<br>[μA] | Applied current density<br>[μA/cm <sup>2</sup> ] | Faradaic H <sub>2</sub> molar flow rate<br>[μmol/s.g catalyst]<br><i>r<sub>F</sub></i> | Measured H <sub>2</sub> molar flow rate ( <i>Fr</i> )<br>[μmol/s.g catalyst] |          |           | Faradaic efficiency (Λ)<br><i>(r-r<sub>o</sub>)/r<sub>F</sub></i> | EPOC efficiency ( <i>η<sub>EPOC</sub></i> )<br><i>r/r<sub>F</sub></i> |
|-------------------------|--------------------------------------------------|----------------------------------------------------------------------------------------|------------------------------------------------------------------------------|----------|-----------|-------------------------------------------------------------------|-----------------------------------------------------------------------|
|                         |                                                  |                                                                                        | <i>r<sub>o</sub></i>                                                         | <i>r</i> | <i>r'</i> |                                                                   |                                                                       |
| -1000                   | -497.51                                          | 0.65                                                                                   | 9.18                                                                         | 9.24     | 9.26      | -0.08                                                             | -14.24                                                                |
| -10000                  | -4975.12                                         | 6.49                                                                                   | 9.18                                                                         | 12.73    | 9.71      | -0.55                                                             | -1.96                                                                 |
| -10000                  | -4975.12                                         | 6.49                                                                                   | 9.18                                                                         | 13.01    | 9.56      | -0.59                                                             | -2.01                                                                 |
| -10000                  | -4975.12                                         | 6.49                                                                                   | 9.18                                                                         | 12.91    | 9.80      | -0.58                                                             | -1.99                                                                 |
| -10000                  | -4975.12                                         | 6.49                                                                                   | 9.18                                                                         | 12.99    | 10.16     | -0.59                                                             | -2.00                                                                 |
| -10000                  | -4975.12                                         | 6.49                                                                                   | 7.95                                                                         | 11.22    | 8.40      | -0.50                                                             | -1.73                                                                 |
| -15000                  | -7462.69                                         | 32.43                                                                                  | 7.95                                                                         | 31.42    | 10.85     | -0.72                                                             | -0.97                                                                 |
| -100000                 | -49751.24                                        | 64.66                                                                                  | 7.95                                                                         | 60.37    | 14.18     | -0.81                                                             | -0.93                                                                 |
| -150000                 | -74626.87                                        | 97.29                                                                                  | 7.95                                                                         | 88.45    | 17.76     | -0.83                                                             | -0.91                                                                 |
| -10000                  | -4975.12                                         | 6.49                                                                                   | 7.95                                                                         | 11.77    | 8.86      | -0.59                                                             | -1.81                                                                 |

Applying a negative current, i.e., supplying H<sup>+</sup> to the WE, resulted in a negative Λ. For all cases listed in Table 4.11, the low temperature catalytic reforming of CH<sub>3</sub>OH was electrochemically promoted, as the absolute value of Λ was less than unity. The average Faradaic efficiency for all the EPOC tests carried out at -0.01 A (5 mA/cm<sup>2</sup>) was and -0.56 ±0.03. It is important to note that the Faradaic efficiency became closer to 1, i.e. indicating a Faradaic process, as the imposed current increased. Also at a current of -0.01 A (5 mA/cm<sup>2</sup>), the average EPOC efficiency was -1.92 ±0.12. The largest EPOC efficiency (-14.24) was obtained at the smallest current applied (-0.001 A or 0.5 mA/cm<sup>2</sup>). Vayenas and Neophytides [238] have shown that, in general, dehydrogenation or decomposition reactions exhibit negative Λ values for EPOC. The Λ values obtained for the tests carried out in Fig. 4.19 were plotted as

a function of the reverse electrolyser cell voltage and the working electrode potential measured during the EPOC experiment as shown in Fig. 4.20.

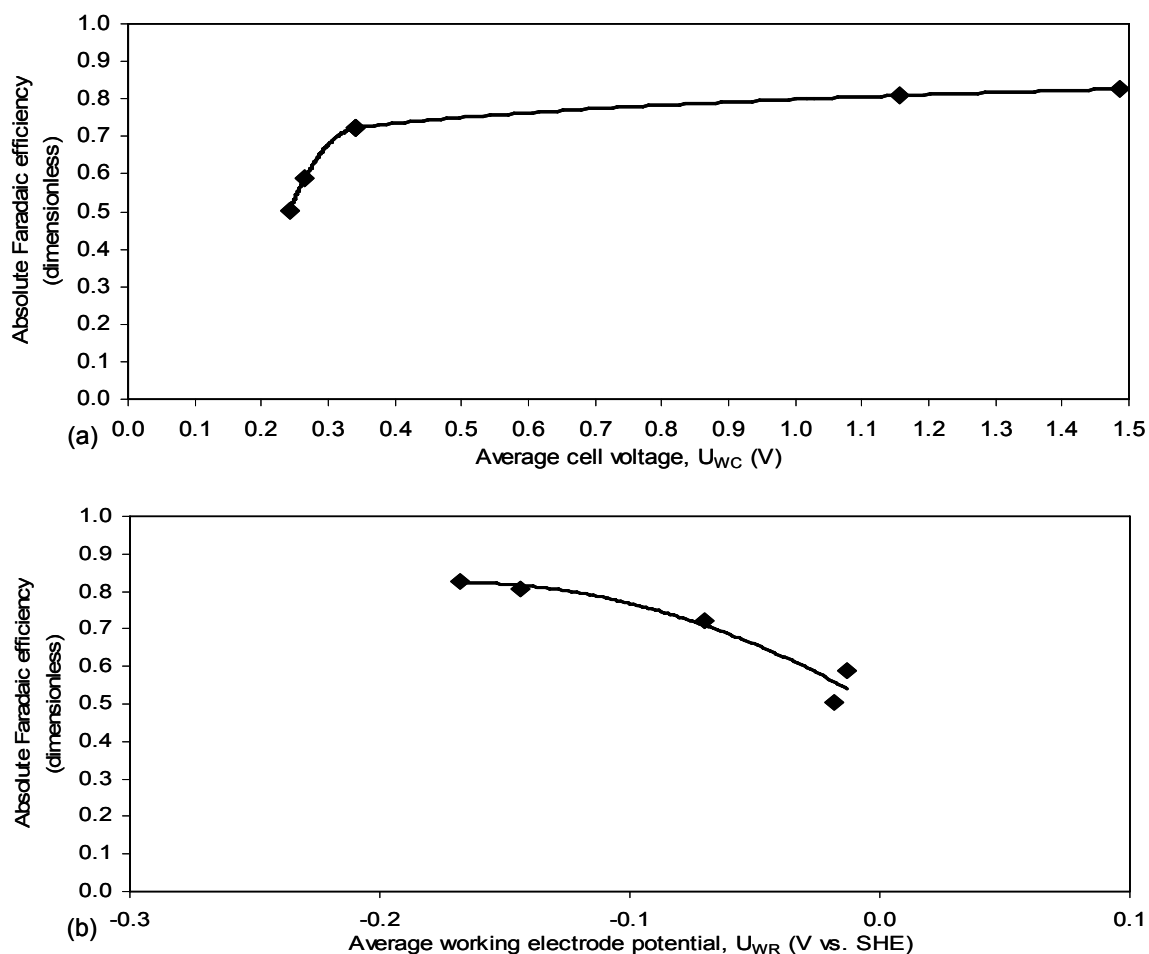


Figure 4.20: Absolute Faradaic efficiency as a function of (a) average cell voltage, and (b) average working electrode potential (2.01 cm<sup>2</sup>, 4 mg/cm<sup>2</sup> Pt-Ru/C, 20 wt% Pt-Ru, Pt:Ru 1:1 a/o, 80 ml of 2 M CH<sub>3</sub>OH in 0.5 M H<sub>2</sub>SO<sub>4</sub> electrolyser anolyte, 80 ml of 0.5 M H<sub>2</sub>SO<sub>4</sub> electrolyser catholyte, 75 ±1°C).

As shown in Fig. 4.20 (a), the greatest change in the absolute Faradaic efficiency appears to be at cell voltages < 0.5 V. At greater  $U_{WC}$  values, the change in the absolute  $\Lambda$  was not as significant. Non carbon-containing GDE at the reverse electrolyser anode (CE) would be required to evaluate greater EPOC currents (with greater cell voltages, i.e., > 1.23 V) to avoid carbon oxidation. As Fig. 4.20 (b) indicates, decreasing the potential of the working electrode,  $U_{WR}$ , enhanced the absolute Faradaic efficiency.

Figure 4.21 shows that, as is expected, the catalytic  $H_2$  production rate,  $r$ , depended exponentially on the working electrode potential [238]. The measured promoted catalytic reaction rate increased exponentially with decreasing working electrode potential. When small currents were applied, the measured promoted catalytic  $H_2$  production tended to get closer to the unpromoted catalytic  $H_2$  production rate. However, promoted catalytic  $H_2$  production rate matched closely the absolute Faradaic  $H_2$  production rate calculated. It seems like the effect observed is mostly Faradaic and that the increase in the promoted  $H_2$  production rate observed can mainly be attributed to the electrochemical reaction. Therefore, applying currents resulting in working electrode potentials more negative than the working electrode potential at OCV only caused a Faradaic enhancement in the  $H_2$  production rate.

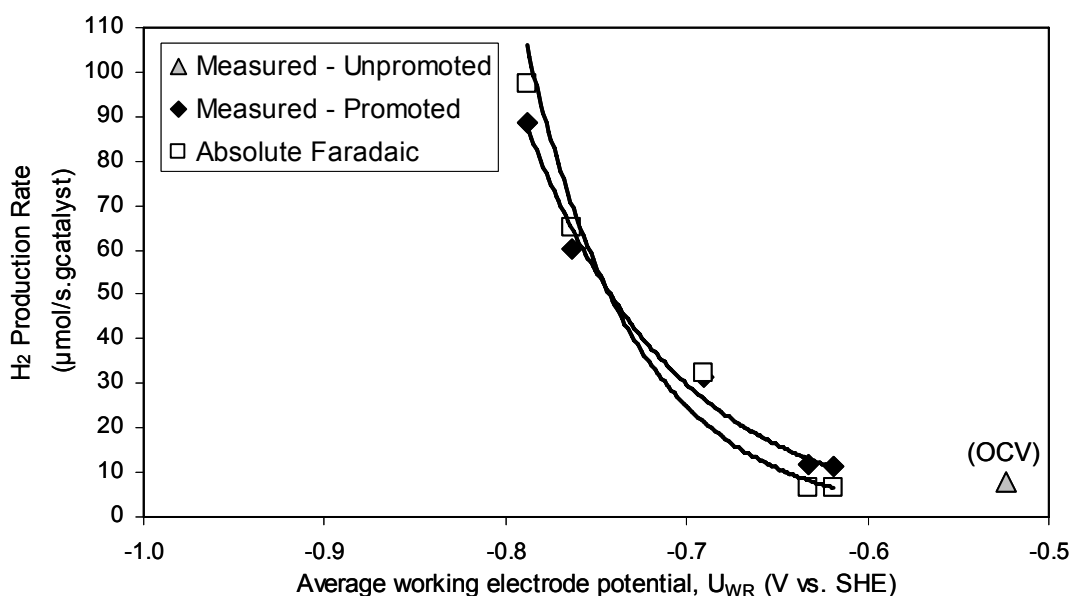


Figure 4.21: Catalytic  $H_2$  production rate as a function of average working electrode potential ( $2.01 \text{ cm}^2$ ,  $4 \text{ mg/cm}^2$  Pt-Ru/C, 20 wt% Pt-Ru, Pt:Ru 1:1 a/o, 80 ml of 2 M  $\text{CH}_3\text{OH}$  in 0.5 M  $\text{H}_2\text{SO}_4$  electrolyser anolyte, 80 ml of 0.5 M  $\text{H}_2\text{SO}_4$  electrolyser catholyte,  $75 \pm 1^\circ\text{C}$ ).

As per Eq. 1.29, the working electrode potential,  $U_{WR}$ , is proportional to the catalyst work function,  $\Phi_W$ . Under promoted conditions over the working electrode potential range of Fig. 4.21, the  $H_2$  evolution reaction is occurring at the working electrode catalyst surface as shown in Fig. 4.17. It is known that supplying  $H^+$ , an electropositive adsorbate, to the catalyst surface with a protonic conductor is equivalent to removing an electronegative promoter ( $O^{2-}$ ) with an oxide conductor, and both decrease the catalyst

work function [18]. Under small negative catalyst working electrode potentials, the catalytic reforming of  $\text{CH}_3\text{OH}$  appears to have an electrophilic behaviour, for which the catalytic reaction rate increases with decreasing work function ( $\partial r/\partial\Phi < 0$ ). This behaviour was reported for the dehydrogenation of  $\text{CH}_3\text{OH}$  on Ag with an oxide conductor at high temperature ( $> 400^\circ\text{C}$ ) and a partial pressure of  $\text{CH}_3\text{OH}$  up to 7 kPa, which had a Faradaic efficiency of -25 [18, 138]. It was also reported for the non-redox isomeration of 1-butene ( $1-\text{C}_4\text{H}_8$ ) on Pd using Nafion<sup>TM</sup> as the protonic conductor at  $70^\circ\text{C}$ , which had a  $\Lambda$  of -28 [18, 147]. Large  $\Lambda$  values for the removal of  $\text{O}^{2-}$  from the catalyst surface (supply of  $\text{H}^+$  for a proton conductor), rather than for the supply of  $\text{O}^{2-}$ , were reported for EPOC studies on the oxidation of  $\text{CH}_3\text{OH}$  on Pt/ZrO at  $350\text{-}650^\circ\text{C}$  [248]. Hence, the EPOC behaviour observed for the low temperature catalytic reforming of  $\text{CH}_3\text{OH}$  appears to be as illustrated in Fig. 4.22.

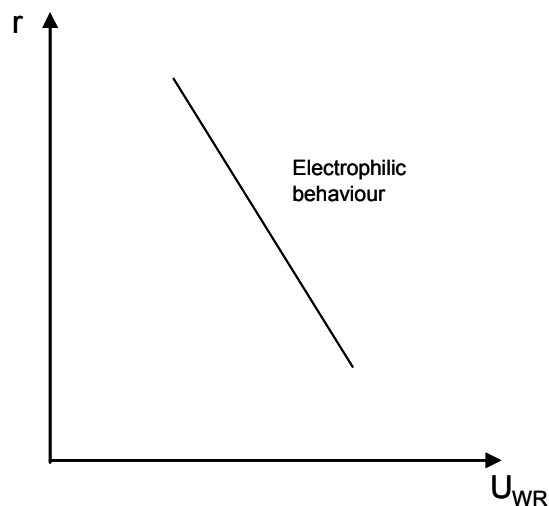


Figure 4.22: Electrophilic behaviour of the catalytic reaction rate as a function catalyst WE potential (Modified from Vayenas *et al.* [18] with permission from Springer).

The possible wireless enhancement in the catalytic activity at OCV could result from an  $\text{H}^+$  spill-over mechanism between the supported precious metal nanoparticles and the electrolyte similar to the one illustrated in Fig. 1.4. Decreasing the catalyst working electrode work function for electrophilic reactions was reported to strengthen the metal-adsorbate chemisorptive bond of methoxy intermediates and thus weaken the intra-adsorbate  $\text{C}=\text{O}$  bonds, the cleavage of which is usually rate-limiting [137]. In their study, Neophytides and Vayenas reported that the resulting weakening in the intra-adsorbate  $\text{C}-\text{H}$  bonds facilitated the dehydrogenation of  $\text{CH}_3\text{OH}$  on Ag using an oxide-conducting electrolyte [138]. They also

mentioned that, while the application of EPOC enhanced the rate of the surface dehydrogenation and decomposition reaction, it did not affect the rate of CH<sub>3</sub>OH adsorption. Therefore, a plausible explanation for the wireless improvement in the catalytic activity observed in the 2-compartment reactor is an enhancement in the formation of CO<sub>2</sub>, which is likely the rate-limiting step of the low temperature CH<sub>3</sub>OH catalytic reforming mechanism.

#### 4.4 Summary

A Pt-Ru/TiO<sub>2</sub> catalyst was synthesized and a commercially available Pt-Ru/C catalyst was used, and both were characterized physico-chemically and electrochemically. The Pt-Ru/TiO<sub>2</sub> electrocatalytic activity for the electrochemical reforming of CH<sub>3</sub>OH was lower than that of a commercial Pt-Ru/C catalyst of the same composition, because of the TiO<sub>2</sub> support poor conductivity and large particle size. Its catalytic activity for the low temperature catalytic reforming of CH<sub>3</sub>OH was compared to that of Pt-Ru/C in the powder form, using a MS to record the partial pressure of H<sub>2</sub>, which was converted to a catalytic H<sub>2</sub> production rate. For the same quantity of catalyst and precious metal content, the Pt-Ru/TiO<sub>2</sub> catalyst had a greater activity towards the CH<sub>3</sub>OH catalytic reforming reaction than the Pt-Ru/C catalyst. This was attributed to the different properties of the catalyst support. The normalized results obtained for the Pt-Ru/TiO<sub>2</sub> catalyst were comparable to those reported in the literature under similar conditions. This appears to be the first time that low temperature catalytic CH<sub>3</sub>OH reforming has been conducted on Pt-Ru/C. Catalytic CH<sub>3</sub>OH reforming tests were also carried out using GDEs under similar conditions, but in a two-compartment cell including a MEA. The normalized H<sub>2</sub> catalytic reaction rates obtained in this manner were much greater than the ones obtained for powder catalysis in the single-compartment cell. It appears that the small current or potential which developed through the MEA may have been sufficient to induce a wireless EPOC effect to the working electrode surface.

The effect of EPOC was also evaluated while applying an electrochemical stimulus in the galvanostatic mode using a Multistat, while recording the transient effect on the catalytic H<sub>2</sub> production rate with the MS. It was determined that the reaction's kinetic regime influenced the extent of the EPOC enhancement caused by the addition or removal of H<sup>+</sup> ions. Under the EPOC conditions studied, the

catalytic reforming of CH<sub>3</sub>OH was Faradaic in nature as the absolute values of the Faradaic efficiencies were close to unity. However, it appears that supplying H<sup>+</sup> to the working electrode surface at OCV improved the H<sub>2</sub> production rate of the low temperature catalytic CH<sub>3</sub>OH reforming reaction. This appears to be the first time EPOC experiments have been conducted for a catalytic reaction using liquid reactants. This Chapter has demonstrated that the effect of EPOC could play an important role in improving the catalyst performance and the efficiency for the low temperature catalytic reforming of CH<sub>3</sub>OH for H<sub>2</sub> production.

## Chapter 5: Conclusions

The main goal of the research presented in this thesis was to contribute to the advancement of electrochemical reforming of CH<sub>3</sub>OH (and H<sub>2</sub>O) for H<sub>2</sub> production. Two different approaches for low temperature H<sub>2</sub> production were investigated: the electrochemical promotion of electrocatalysis and the electrochemical promotion of catalysis. These approaches are different from other research efforts which aim at maximizing the catalyst surface area and performance, and at developing new catalytic materials with improved properties. The following conclusions were drawn from the work carried-out in *Chapters 2 to 4* and summarize the major contributions of the thesis. In addition, potential applications are discussed, the significance and impact of the research work reported are highlighted, and recommendations for future work are provided.

### 5.1 Electrocatalysis baseline study

The first thesis objective was to evaluate the performance of a PEM CH<sub>3</sub>OH electrolyser and compare it with a PEM water electrolyser under the same conditions. This work was carried out in *Chapter 2*. It provided a baseline for the subsequent thesis Chapters, and will serve as a ground work for future organic fuel depolarized PEM water electrolysis research.

- A theoretical thermodynamic evaluation demonstrated that the CH<sub>3</sub>OH depolarized electrolysis or electrochemical reforming becomes thermodynamically-favourable at a temperature of 41°C, while water electrolysis does not become thermodynamically favourable over the temperature range studied.
- GDE characterization by H<sub>2</sub> adsorption and UPD showed that the catalyst ESCA decreased with increasing usage and carbon oxidation.
- IR corrected polarization curves were obtained for various CH<sub>3</sub>OH concentrations and different anode electrocatalysts. At high geometric current densities, lower overpotentials were obtained for

greater CH<sub>3</sub>OH concentrations. The largest limiting geometric current density for CH<sub>3</sub>OH electrolysis was obtained with Pt-Ru/C, while that for water electrolysis was obtained with a well-defined Pt disk.

- AC impedance measurements confirmed that the MEA resistance increased with increasing CH<sub>3</sub>OH concentration, MEA usage, and MEA oxidation.
- The anode and cathode potentials were measured and reported separately for acidic aqueous CH<sub>3</sub>OH electrolysis for the first time. The change in cathode potential was insignificant compared to the change in the anode potential.
- The performance of Pt/C and Pt black catalyst was compared on an ECSA basis. Carbon oxidation started at a lower real current density on Pt/C than for Pt black, suggesting that the carbon of the supported catalyst start to oxidize before the carbon of the CFP.
- It was demonstrated that the CH<sub>3</sub>OH electro-oxidation should be conducted at conditions that avoid water electrolysis and other undesirable secondary electrochemical reactions. In acidic aqueous media and at ambient conditions, carbon oxidation can cause a premature catalyst degradation which prevents the DMR from sustaining high current densities.
- Operating the PEM electrolyser with a dry cathode, purged with N<sub>2</sub> resulted in lower cell voltage requirements and may be a practical method of operation provided there are no durability issues.
- Increasing the temperature improved the electrolyser performance for all electrocatalysts studied. There was no significant change in the limiting current density between 50 and 75°C.
- Tafel parameters were determined for various CH<sub>3</sub>OH concentrations, catalysts and temperature. In general, Pt-Ru/C is more favourable for the electrolysis of CH<sub>3</sub>OH and water than Pt/C. However, as Tafel kinetic analysis indicated, this may depend on the electrolyser operating conditions. The Tafel slopes obtained at  $\eta_a < 0.6$  V vs. SHE and CH<sub>3</sub>OH  $\leq 2$  M on 2 mg/cm<sup>2</sup> Pt black were in agreement with values reported in the literature. Other comparisons with values available in the literature were difficult due to differences in the experimental conditions and whether geometric or real surface area was used.
- The apparent activation energy was estimated for Pt-Ru/C. It increased with increasing CH<sub>3</sub>OH concentration and indicated that CO surface diffusion was the rate determining step for the electrolysis of 2 and 16 M CH<sub>3</sub>OH.

Based on these results, CH<sub>3</sub>OH depolarized PEM water electrolysis represents an energy efficient alternative to PEM water electrolysis. The remaining part of the thesis focused on the application of electrochemical promotion.

## **5.2 Electrochemical promotion of electrocatalysis (EPOE)**

The second thesis objective was to study the effect of EPOE on the PEM water electrolyser, and on the CH<sub>3</sub>OH depolarized PEM water electrolyser or electrochemical CH<sub>3</sub>OH reformer. The effect of EPOE was examined as an advancement of the PEM electrolysis systems evaluated in *Chapter 2*. This work is reported in *Chapter 3*. The research presented led to a variety of findings regarding the application of EPOE via triode and tetrode operation and the mechanism behind the enhancement.

### **5.2.1 Galvanostatic and potentiostatic characterization**

- It was determined that triode and tetrode effects are only obtained when the electrolyser and the auxiliary circuits were operating in reverse and not when they were operating in parallel. In reverse operation, the system comprises two electrolysers working in different directions.
- It was confirmed that carbon corrosion of the electrolyser working electrode was not an issue under the system's operating conditions, and was not responsible for the enhancement observed.
- Triode and tetrode operation effects were observed in the galvanostatic and potentiostatic mode with working electrode rings made of noble electrocatalysts, as well as non-catalytic materials like carbon.
- A triode and tetrode effect was obtained independently of the electrolyser working electrode material tested, and of the electrolysis process being tested, i.e., water electrolysis or CH<sub>3</sub>OH electrolysis.
- Normal and inverted operation galvanostatic tests indicated that the current line distribution on the WE plane affected the auxiliary circuit cell potential.
- There is a capacitive effect when using a noble electrocatalyst at the electrolyser working electrode.
- Triode or tetrode operation may be used as a measure to prevent electrode damage from carbon oxidation or other material corrosion.

- The electrolyser triode or tetrode voltage ratio, power enhancement ratio and power gain ratio were determined in galvanostatic control. Triode or tetrode operation allowed electrolysis operation at voltages lower than the reversible cell voltage, which is not possible in normal electrolysis. The power enhancement ratio and the power gain ratio showed that the power required to operate in triode or tetrode was less than the power required to operate in normal electrolysis. Under certain operating conditions, the reduction in the power requirements in triode or tetrode electrolysis can exceed that consumed in the auxiliary circuit.
- Electrolyser triode or tetrode current gain ratio, rate enhancement ratio, power gain ratio and Faradaic efficiency were measured in potentiostatic control. The rate enhancement ratios were large and reached a maximum which occurred at different auxiliary working electrode potential depending on the electrolyser working electrode surface. Operation at the maximum rate enhancement ratio was stable and durable. The power gain ratios indicated that the power required to operate in triode or tetrode electrolysis was less than that required to operate in normal electrolysis. The Faradaic efficiencies were close to unity indicating that the enhancement is not non-Faradaic in nature, but electrocatalytic.
- The current or potential of the electrolyser circuit in triode or tetrode operation exceeded what is expected according to Faraday's law for normal electrolysis.

### 5.2.2 Durability investigations

- Tetrode operation allows for mixed independent control of the electrolyser and auxiliary circuits, i.e., one circuit in galvanostatic mode and the other in the potentiostatic mode.
- Long-term triode and tetrode tests shown that the enhancement effect is stable, durable, and reversible.
- The change in  $\text{CH}_3\text{OH}$  concentration over time during normal electrolysis was consistent with Faraday's law. The change in  $\text{CH}_3\text{OH}$  concentration over time in triode and tetrode operation exceeded what was predicted from Faraday's law for normal electrolysis and was consistent with the electrochemical parameters measured.

### 5.2.3 Mechanism investigations

- The auxiliary  $WE_{aux}$  needs to be in direct physical contact with the membrane to observe a triode or tetrode effect. In tetrode operation, a weaker effect can be obtained even if the independent auxiliary  $CE_{aux}$  is not in direct contact with the membrane surface. The triode or tetrode effect is related to the generation of  $H^+$  rather than  $H_2$  generation.
- An increase in the intrinsic membrane conductivity or an increase in the localized  $H^+$  concentration of the electrolyte in the vicinity of the WE electrode provide no effect or a small effect, and does not account the triode or tetrode effects observed.
- The membrane conductivity does not improve due to the  $H^+$  flux produced by the auxiliary circuit and the beneficial effect observed for triode or tetrode operation is limited to the electrode surface.
- There appear to be a linear relationship between the auxiliary current/potential and the electrolyser current/potential, as more electrolyser current/potential requires more auxiliary current/potential stimulation to attain an EPOE enhancement.
- Larger triode and tetrode effects are observed when the gap between the electrolyser ring  $WE_{elec}$  and the auxiliary  $WE_{aux}$  is reduced.
- Intersecting proton flux lines by inverting the CEs or inverting the WEs in tetrode operation resulted in an insignificant triode or tetrode effect.
- Increasing the surface area of the electrolyser ring CFP did not significantly improve the triode effect obtained.
- The on-set potential of non-catalytic and non-carbon containing materials, e.g., Au plated 316 SS  $WE_{elec}$  and  $WE_{aux}$  components were determined and compared with that of noble metal and carbon-containing materials studied in triode and tetrode operation.
- It was demonstrated that the effect of triode or tetrode operation can be successfully obtained using non-precious and carbon-free electrolyser and auxiliary WEs material combinations. In triode or tetrode operation, the only catalyst required to carry out the triode electrolysis is then the  $2\text{ mg/cm}^2$  Pt/C at the common electrolyser CE.

- With a Pt WE<sub>aux</sub>, the rate enhancement ratio was greater when using a CFP WE<sub>elec</sub> ring than when using an Au plated 316 SS mesh, due to the differences in the WE<sub>elec</sub> material surface properties, conductivity, porosity, and geometry.
- The power gain ratio values obtained indicated that, under certain operating conditions, less power is needed to operate in triode or tetrode electrolysis than in normal electrolysis.
- The Faradaic efficiency ratio indicated that, under the operating conditions studied, triode or tetrode electrolysis with precious or non-precious WEs is Faradaic and electrocatalytic in nature.
- Like for the case of carbon containing precious metal WEs, the current or potential of the electrolyser circuit in triode or tetrode operation for the carbon-free non-precious WEs exceeded what is expected according to Faraday's law for normal electrolysis.
- It was proposed that the triode and tetrode effects observed are due to a mechanism which influences the electrolysis charge transfer rate at the WE<sub>elec</sub>, by the in-situ migration of mobile promoting H<sup>+</sup> ions from the WE<sub>aux</sub> to the WE<sub>elec</sub> which is driven by surface charge differences.
- The triode and tetrode EPOE effect is analogous to the EPOC effect which relies on the backspillover of promoting ions from the support to the metal catalyst surface, except that in this case, the promoted reaction is an electrochemical reaction instead of a chemical one.

These findings add to the current knowledge of the mechanism behind EPOE. These contributions may serve as a basis for the development of new circuit designs and WE configurations for controlling the potential or current of an electrode surface, and improving the efficiency of electrocatalytic processes.

### 5.3 Electrochemical promotion of catalysis (EPOC)

The third and last objective of this thesis was to determine the effect of EPOC on the catalytic reforming of CH<sub>3</sub>OH using a commercial fuel cell catalyst, Pt-Ru/C, and a synthesized Pt-Ru/TiO<sub>2</sub> catalyst. The overall reaction of CH<sub>3</sub>OH catalytic reforming is the same as the overall CH<sub>3</sub>OH electrolysis reaction. To study EPOC, the catalyst/electrocatalyst working electrode material had to be both, a catalyst to the CH<sub>3</sub>OH catalytic reforming reaction and an electrocatalyst to the CH<sub>3</sub>OH electrolysis reaction. The application of EPOC was studied for the oxidation of CH<sub>3</sub>OH at low temperature, using a protonic

conductor, and liquid phase reactants for the first time. The work function of the catalyst working electrode surface was affected by applying currents in galvanostatic mode through the use of a PEM electrolyser configuration. The ground work carried out in *Chapter 4* is valuable in the evaluation of the application of EPOC in low temperature systems using liquid reactants.

### 5.3.1 Catalyst synthesis and characterization

- A Pt-Ru/TiO<sub>2</sub> catalyst was synthesized by an impregnation method with calcination and reduction in H<sub>2</sub> because it was not available commercially.
- The synthesized Pt-Ru/TiO<sub>2</sub> catalyst was characterized physicochemically by SEM, EDX or EDS, XPS or ESCA, TEM, XRD and BET, and electrochemically by cyclic voltammetry, and compared to commercially available Pt-Ru/C catalyst.

### 5.3.2 Powder catalysis

- Hydrogen was catalytically produced by the low temperature reforming of 2 M CH<sub>3</sub>OH using Pt-Ru/C or Pt-Ru/TiO<sub>2</sub> catalysts powders.
- H<sub>2</sub> was produced at low levels even at temperatures below 41°C, temperature at which the catalytic reforming of CH<sub>3</sub>OH in the liquid phase becomes thermodynamically spontaneous for an equimolar CH<sub>3</sub>OH - water solution.
- The H<sub>2</sub> production rate did not increase significantly from ambient temperature to 75°C. Once 75°C was reached, the H<sub>2</sub> production rate increased slightly as run time increased.
- At 75°C, the average H<sub>2</sub> production rate for Pt-Ru/TiO<sub>2</sub> was about 36% greater for Pt-Ru/C under the same experimental conditions. The larger H<sub>2</sub> production rate observed with the Pt-Ru/TiO<sub>2</sub> catalyst may be linked to strong metal-support interactions (SMSI).
- Due to the greater precious metal content and larger catalyst to solution volume ratio, the H<sub>2</sub> generation rates obtained in this study were normalized for comparison with values reported in the literature, which were the similar to the ones reported in this thesis.

### 5.3.3 GDE catalysis and electrochemical promotion of catalysis

- The application of EPOC was studied for the oxidation of  $\text{CH}_3\text{OH}$  at low temperature for the first time. The work function of the catalyst working electrode surface was affected by applying currents in galvanostatic mode through the use of a PEM electrolyser double-compartment cell configuration with an MEA.
- Under the chemical reaction conditions studied and using a GDE catalyst working electrode, it took about 300 min. for the catalytic reaction to reach steady-state.
- The normalized catalytic  $\text{H}_2$  production rate measured at open circuit with the GDE exceeded that obtained for the powder catalysis test in the single-compartment cell. It appears that the small current/potential gradient which developed in the MEA may have been sufficient to induce a wireless EPOC effect on the catalytic  $\text{H}_2$  production rate. Similar effects have been previously observed in the literature [132].
- The absolute Faradaic efficiency exceeded unity for all currents applied, indicating that the process was non-Faradaic. Supplying  $\text{H}^+$  to the catalyst working electrode surface resulted in a non-Faradaic catalytic  $\text{H}_2$  rate enhancement for the low temperature catalytic reforming of  $\text{CH}_3\text{OH}$ . It was demonstrated that EPOC can be applied to heterogeneous reactions using liquid reactants at low temperature for the first time.
- Catalytic rate enhancement was increasingly significant as the catalyst work function was decreasing. The low temperature catalytic reforming of  $\text{CH}_3\text{OH}$  on Pt-Ru/C appears to exhibit an electrophilic behaviour.
- The predominant mechanistic effect explaining the rate enhancement when  $\text{H}^+$  is supplied to the catalyst working electrode is likely due to an enhancement in the formation of  $\text{CO}_2$ , which is likely the rate-limiting step of the low temperature  $\text{CH}_3\text{OH}$  catalytic reforming mechanism.

## 5.4 Potential applications, significance and impact

### 5.4.1 Potential applications

Some applications for CH<sub>3</sub>OH depolarized PEM electrolyzers were discussed in Section 1.3.3.2 and the development of practical reactors for the application of EP for various catalytic reactions was reviewed in Section 1.3.4.5. The applications of electrochemically promoted CH<sub>3</sub>OH depolarized PEM electrolyzers will be similar to the ones discussed for normal CH<sub>3</sub>OH depolarized PEM electrolyzers. Likewise, the applications for electrochemically promoted or normal low temperature CH<sub>3</sub>OH catalytic reformers will also be similar to the applications discussed for electrochemically promoted or normal CH<sub>3</sub>OH depolarized PEM electrolyzers.

Just like for the normal CH<sub>3</sub>OH depolarized PEM electrolyser, triode or tetrode CH<sub>3</sub>OH depolarized PEM electrolysis, and EP low temperature CH<sub>3</sub>OH catalytic reforming would be adaptable to small or large H<sub>2</sub> production processes. They could be developed into portable fuelling modules producing H<sub>2</sub> for combustion vehicles or fuel cell vehicles (FCV), or for PEMFCs and micro-fuel cells (e.g., Angstrom Power Inc.) powering small electronic devices. They could also be developed into a stationary large-scale H<sub>2</sub> fuelling station, to be part of off-grid electricity generator systems for back-up and remote power applications, or into off-peak H<sub>2</sub> storage devices used for electricity production during high grid loads or blackouts. Nevertheless, based on the work carried-out in this thesis, it is still too early to establish which of these advanced electrochemical H<sub>2</sub> production options would be the most advantageous for each of these practical applications.

Both low temperature H<sub>2</sub> production processes studied, i.e., the CH<sub>3</sub>OH depolarized water PEM electrolysis and the catalytic reforming of CH<sub>3</sub>OH, have potential advantages over conventional H<sub>2</sub> production methods such as steam reforming, as they both can result in reduced energy consumption. Furthermore, it was shown that the efficiency of these low temperature H<sub>2</sub> production processes may be improved by applying the principles of EP. Usually, improving efficiency directly results in reduced energy losses, hence, greater environmental benefits. It was also demonstrated that the application of

EPOE and EPOC may result in cost reductions, such as the use of non-precious metals, which may lead to more affordable H<sub>2</sub> production.

EPOE can reduce the cost and operating energy requirements, as well as increase the efficiency of electrolytic H<sub>2</sub> production processes. It was shown that under certain EPOE conditions attained via triode or tetrode operation, the electrolyzer performance improved with a decrease in energy required, i.e., less current/potential was needed in the electrolysis circuit when the auxiliary circuit was in operation. Triode and tetrode operation permitted the use of non-precious and carbon-free electrolyzer and auxiliary working electrode material combinations, limiting the need for precious metal electro-catalyst to the counter electrode(s) only. While material degradation in acidic media imposed some limitations on the current/potential operating range of the triode and tetrode PEM electrolyser, it may be possible to operate the triode or tetrode electrolyser over a wider range of currents/potentials with suitable non-precious carbon-free working electrode materials. The fact that EPOE can be obtained using a variety of WE<sub>elec</sub> materials, and that the auxiliary WE<sub>aux</sub> H<sub>2</sub> production can be purely ionic and does not require being catalytic adds flexibility to the overall system design.

Scaling-up the triode or tetrode operation approach to meet the requirements of large commercial electrocatalytic applications could potentially be achieved by new electrolyser and auxiliary WEs designs. These new WE designs and configurations could be easily interchanged with the WEs currently used in commercial PEM water electrolysers, without requiring significant modifications. Figure 5.1 shows an example of a working electrode design that could be scaled-up for triode or tetrode operation.

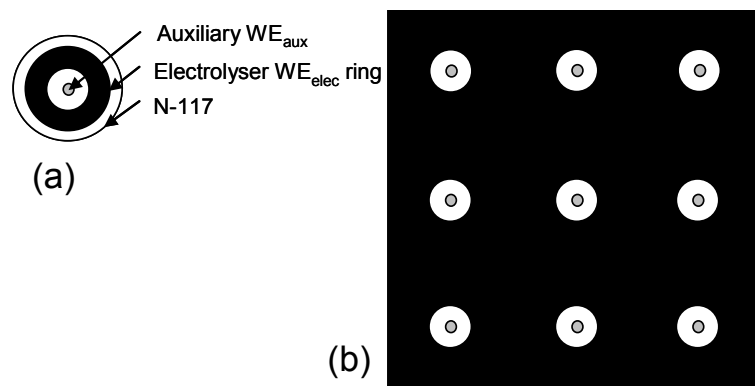


Figure 5.1: Example of working electrode scale-up design for triode or tetrode operation (a) single auxiliary working electrode, (b) multiple auxiliary working electrodes.

Moreover, the tetrode configuration may offer additional advantages over the triode configuration. It allows for the independent mixed control of the electrolyser and of the auxiliary circuits, results in more concentrated auxiliary current lines, and does not require the auxiliary counter electrode to be in contact with the membrane. This configuration may open the door to the development of a novel electrolyser or fuel cell architectures, which have not been considered before. It may also allow more opportunities for the synergetic juxtaposition of various electrochemical systems, such as the one presented in Fig. 1.1.

In some cases, triode and tetrode electrolysis could effectively cogenerate chemical energy and electrical energy by itself, or in various system combinations, which may include a H<sub>2</sub> PEMFC, as long as the amount of energy required for H<sub>2</sub> generation does not exceed the energy resulting from using the H<sub>2</sub> produced. An example of this is shown in Fig. 5.2:

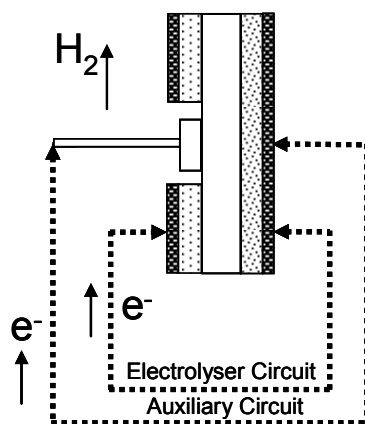


Figure 5.2: Diagram showing possible electrolysis circuit current reversal under triode or tetrode operation.

Electrochemical promotion has been applied to an aqueous phase catalytic reaction using liquid phase reactants for the first time. Much work remains to be accomplished to confirm that the application of EPOC has benefits on the low temperature catalytic reforming of  $\text{CH}_3\text{OH}$ . However, the ability to use a commercially available catalyst such as Pt-Ru/C, instead of a synthesized Pt-Ru/ $\text{TiO}_2$  catalyst to carry out the low temperature catalytic  $\text{CH}_3\text{OH}$  reforming reaction will reduce the process's capital cost. Generating  $\text{H}_2$  from the catalytic reforming of  $\text{CH}_3\text{OH}$  at low temperature requires only a very small electric-power consumption rate to electrochemically promote the catalytic reaction. EPOC may improve the low temperature  $\text{CH}_3\text{OH}$  catalytic reforming system start-up time and result in a better response to  $\text{H}_2$  requirements. As seen in *Section 1.3.4.5*, EPOC reactors with simple electrical connections and using inexpensive materials are being developed and attempts to scale-up attempts are being undertaken. A scalable high temperature single chamber membrane electrochemically promoted reactor (MEPR) design is underway. However, the EP catalytic reaction studied in this thesis was carried out in a low temperature dual chamber reactor, which may be more difficult to scale-up than the proposed single chamber MEPR. The successful development and manufacturing of a single or dual chamber MEPR may make the application of EPOC to the low temperature catalytic reforming of  $\text{CH}_3\text{OH}$  commercially possible.

The application of EPOC may be transferrable to other electrochemical and chemical reactions. To the author's knowledge, there are currently no commercial applications using the benefits of electrochemical promotion for electrocatalysis or catalysis.

#### **5.4.2 Significance and impact**

Sustainable energy is of growing importance due to a combination of environmental and socio-economical issues. As the demand for energy keeps increasing, finding ways to provide a sustainable supply of clean energy to guarantee ecological safety without resulting in a negative impact on society is becoming more and more crucial. Efficient H<sub>2</sub> generation from renewable sources is a key energy path to the future. A H<sub>2</sub> economy is a compelling solution to lower pollution GHG climate change, increase energy security, and sustainability. It encompasses efficient electrochemical methods for the transformation of renewable sources to H<sub>2</sub>, as well as efficient energy production through fuel cells. Even though many political, societal, and technological issues still remain to be resolved before H<sub>2</sub> becomes the sustainable fuel of the future, it is anticipated that there will be a growing demand for H<sub>2</sub> production in the interim. This will gradually become more evident as gasoline prices continue to rise, and society starts to recognize the long term benefits of a reduced fossil fuel dependency for a cleaner environment.

Research efforts on the practical application of new fuelling technologies in the market place and closure of existing technology gaps, such as H<sub>2</sub> production, transportation and storage, will help to overcome the remaining issues and facilitate the introduction of alternative fuels for fuel cells and other applications to the general public. This thesis brought together core competencies from various areas of chemical engineering, which can be directly involved in alternative fuel, H<sub>2</sub> production, and fuel cell research. The experiments conducted required the use of a variety of chemical, electrochemical and material characterization techniques. As the knowledge in the field of EPOC is still limited, the work carried out in this thesis has significantly increased the understanding of the application of this new approach to low temperature electrochemical and chemical systems for H<sub>2</sub> production.

The technological development of efficient low temperature H<sub>2</sub> production may have a significant impact on the energy sector including the transportation sector. The EP of low temperature electrocatalytic or

catalytic reforming of  $\text{CH}_3\text{OH}$  may provide a way to surpass the Department of Energy (DOE) 2012 technical target of 69% electrolyser efficiency, and 66.2%  $\text{H}_2$  generation system efficiency for a 1500kg/day water electrolysis refuelling station, while reducing the capital cost and operating cost of the electrolyser. Efficient low temperature  $\text{H}_2$  production processes could provide  $\text{H}_2$  on-demand and eliminate the need to transport and store  $\text{H}_2$  in the liquid or gaseous phase. This research complements the existing high level of hydrogen and fuel cell research in Canada and may help the development of a broader research outlook in automotive fuel cells and other fuel cell applications.

Although the operating costs of electrochemical processes are affordable where electricity prices are low, the capital cost needs to be reduced and the operating efficiency needs to be increased. If the cost of precious metals keeps increasing, the precious metal loadings presently required to meet the needed catalytic activity for electrochemical reactions may eventually become impractical for commercialization. In this regards, electrochemical promotion may represent a viable option to achieve material cost reduction while maintaining or enhancing the performance of conventional electrochemical or chemical systems. The principles of EP are versatile since they can be applied to a variety of electrochemical and chemical processes. Thus, there may well be many future opportunities for electrochemical promotion technology transfer.

In addition, the electrochemical promotion processes studied in this thesis can be applied to different fuels. This fuel flexibility is a socio-economic advantage as there are a wide variety of fuels available throughout the world. Hence, the field of electrochemical promotion could play a role in technology development in rural and urban areas, as well as in developing and industrialized countries. Fuel Cell Energy Inc., Idatech LLC, Methanex Corporation, and the General Hydrogen Corporation are only a few examples of existing businesses which might be interested in the commercialization of technologies using electrochemical promotion in North America and abroad.

This thesis has demonstrated some of the potential benefits that advanced electrochemical processes may have in a  $\text{H}_2$  or  $\text{CH}_3\text{OH}$  economy. It was shown that  $\text{H}_2$  production from renewable fuels, such as  $\text{CH}_3\text{OH}$ , may be a viable option in some sustainable energy systems of the future. More importantly, this research work suggests that EPOE and EPOC may represent a cost-effective solution to tap into the

hidden capacity of existing electrochemical or chemical processes, respectively. Therefore this approach may play an important role in the development of a new energy era.

## **5.5 Recommendations for further research**

Collectively, this thesis's contributions will be extremely valuable for further studies on PEM electrolysis, as well as on the application of EP to electrocatalysis and catalysis at low temperature. During the completion of this work, different aspects of the research were identified as requiring more investigation. The proposed research directions mainly concern the optimization of the approach taken and supplemental experiments, or refinement of the experimental methods. These recommendations will help address remaining technical challenges. They may open the door to new research areas, as well as bring the application of the principles of EP of electrocatalysis or catalysis closer to commercialization.

### **5.5.1 Electrocatalysis baseline study**

- To mitigate carbon corrosion issues, anode catalysts supported on a non-carbon containing material, such as  $\text{TiO}_2$ , should be investigated. However, the electrical conductivity of the  $\text{TiO}_2$  support needs to be increased and a possible way of doing this is by adding a metal, such as Nb, to the  $\text{TiO}_2$  support.
- The polarization curves for  $\text{CH}_3\text{OH}$  and water electrolysis using Pt-Ru/ $\text{TiO}_2$  and Pt-Ru/Nb- $\text{TiO}_2$  GDEs, as well as using fine porous Pt or Nb meshes of known surface areas, should be established. When the support contains  $\text{TiO}_2$ , the effect of applying UV light during electrolysis could be evaluated.
- The polarization effect of using a different carbon-containing PEM water electrolysis depolarization fuel, such as ethanol, could be investigated. Similarly, the effect of using no supporting electrolyte, or of using a different acid than  $\text{H}_2\text{SO}_4$  could be evaluated.
- Although acidic PEM are generally more robust, it may also be useful to evaluate depolarized PEM electrolysis in alkaline media as no  $\text{CO}_2$  would be generated, and cheaper materials could be used. While water electrolysis in alkaline media is a well established process, other processes, such as

CH<sub>3</sub>OH [110] or ammonia electrolysis, could also be evaluated in an alkaline environment. The application of EPOE could then be evaluated in alkaline media for the first time.

- Experiments with humidified N<sub>2</sub> in the cathode compartment should be carried out in the static and flowing mode. Long-term stability tests using a dried or humidified N<sub>2</sub> purged cathode compartment should also be carried out. This would further confirm the practicality of the proposed PEM electrolyser design simplification.
- The effect of temperature and activation energy should be determined for all electrocatalyst investigated to find out which catalyst results in the lowest activation energy for the electro-oxidation of CH<sub>3</sub>OH.
- Different polymeric membrane materials, e.g. PBI, could be used to evaluate the PEM electrolyser at higher temperatures. The CH<sub>3</sub>OH and CO<sub>2</sub> crossover rates should be measured and the effect of polymeric membrane thickness and composition should be evaluated as a measure to decrease fuel losses.
- The CH<sub>3</sub>OH depolarized PEM water electrolysis should be evaluated in a flowing system using a carrier gas in the anolyte and/or catholyte cell compartment to allow for the determination of the CO<sub>2</sub> and/or H<sub>2</sub> gas evolution rates.

### 5.5.2 Electrochemical promotion of electrocatalysis (EPOE)

- The EP study should be expanded to evaluate the effect of CH<sub>3</sub>OH concentration (16 M CH<sub>3</sub>OH) and temperature (50 and 75°C) on the electro-oxidation of CH<sub>3</sub>OH in triode and tetrode operation. Triode or tetrode operation could be evaluated using ring WE<sub>elec</sub> composed of TiO<sub>2</sub>, Nb-TiO<sub>2</sub>, Pt-Ru/TiO<sub>2</sub> or Pt-Ru/Nb-TiO<sub>2</sub>. The effect of applying UV light on the electrolyser working electrode containing TiO<sub>2</sub> could be evaluated during triode or tetrode operation.
- It may be insightful to evaluate the Tafel kinetics data from polarization curves obtained in triode and tetrode operation, and compare them with that obtained for normal electrolysis operation as shown in *Chapter 2*. Similarly, kinetic data as a function of temperature could be used to determine the activation energy in triode or tetrode operation, and compare with that obtained for the same electrolyser working electrode catalyst material in normal electrolysis operation as in *Chapter 2*.

- The effect of the auxiliary ECSA should be investigated by platinising the Pt WE<sub>aux</sub> tip or using a Pt black or Pt/C GDE. The use of WE materials resistant to degradation, such as electrochemically etched Nb or Ti meshes for the WE<sub>elec</sub> rings and an Nb rod for the WE<sub>aux</sub>, should be also be evaluated to widen the triode or tetrode electrolyser operating potential or current range.
- In triode or tetrode electrolysis, the effect of activating the auxiliary circuit only should be evaluated on the electrolyser circuit, when a non-catalytic material is used as the WE<sub>elec</sub>. To do this, the electrolyser circuit would be left at OCV while the current or potential of the auxiliary circuit would be varied in increments, and its effect on WE<sub>elec</sub> potential would be monitored as well as the CH<sub>3</sub>OH concentration in the electrolyser anolyte. This test could clarify the direction of the spillover H<sup>+</sup> between the WEs.
- It would be helpful to use a reference electrode in galvanostatic control as well as in potentiostatic control to track the individual electrolyser and auxiliary electrode potentials in triode or tetrode operation. In some cases, this may require the use of two reference electrodes, one in each cell compartments. For this, the glass cell caps may need to be modified. Similarly, tracking the local pH in the electrolyser working electrode compartment would be useful.
- The effect of EPOE in triode or tetrode operation could be applied to the electrolyser cathode rather than to the electrolyser anode could be investigated in triode or tetrode operation. It should also be more thoroughly verified if the tetrode independent circuit configuration offers operating advantages over the triode configuration, such as having concentrated current lines (tetrode) vs. spread out current lines (triode).
- Other materials which just forces protons through the membrane but with no surface electrochemical reaction, i.e., no H<sub>2</sub> is produced, should be evaluated for triode and tetrode operation.
- The MEA holder and WE<sub>elec</sub> current collector design should be modified to allow for multiple concentric electrolyser WE rings connections and/or multiple auxiliary WE<sub>aux</sub> connections.
- A carrier gas could be used to continuously monitor the H<sub>2</sub> gas being produced with an MS or micro-GC in the WE or CE compartment during triode or tetrode operation. The gas production rates (especially H<sub>2</sub>) obtained in triode or tetrode operation in the WE compartment as well as in the CE compartment should be compared to that obtained in normal electrolysis, and with that predicted by

Faraday's law under the same normal electrolysis operating conditions. This may help further clarify the proposed enhancement mechanism.

- In tetrode electrolysis, the PEM should be replaced by a non-ion conducting material, such as capton, to further confirm if the  $H^+$  generated at the auxiliary  $WE_{aux}$  are going through the PEM or are just produced at the  $WE_{aux}$  surface. Similarly, both circuits could have their own membranes: the electrolyser circuit PEM would be a ring and the auxiliary PEM a disk having the same dimensions as the auxiliary electrode tip. The respective circuit membranes could then be alternatively replaced with capton to determine the path of the  $H^+$  species.
- The electrolyser WE ring surface could be partially masked by ring of capton of different sizes to evaluate the extent of  $H^+$  spillover species when using a non-catalytic material as the  $WE_{elec}$  in triode or tetrode operation.
- A  $WE_{elec}$  current or potential mapping techniques could be developed to evaluate the distribution of the  $WE_{aux}$  spillover  $H^+$  on the  $WE_{elec}$  surface. This may be useful in the evaluation of localized gradients around the WE surfaces during triode or tetrode operation and in the evaluation of new designs. For example, modeling of equipotential lines could be conducted using the COMSOL Inc. multiphysics software.
- Different electrolyser  $WE_{elec}$  and auxiliary  $WE_{aux}$  geometries and alternative configurations should be investigated. The fact that the electrolyser cathode does not need to be in contact with the membrane in tetrode operation could be exploited in new designs.
- A new WE scaled-up configuration with multiple auxiliary electrodes, such as the one suggested in Fig. 5.1 should be developed. Ideally, it should be easy to manufacture and be interchangeable with the WE currently used in commercial PEM electrolyzers.
- A PEM electrolyser WE scaled-up design should be evaluated in a state-of-the-art commercial PEM electrolyser in the active mode. Its response to varying  $H_2$  demand should be evaluated in normal electrolysis, as well as in triode and tetrode electrolysis operation. Tests should be performed under extended time periods under different operating cycles to understand the long-term effects of using EPOE on the scaled-up PEM electrolyser. Assess if the  $CH_3OH$  depolarized PEM water electrolyser and PEM water electrolyser would meet or exceed the 2011 DOE electrolyser technical targets in normal electrolysis, and in triode or tetrode operation.

- Active systems comprising combinations of PEMFCs, triode or tetrode PEM electrolyzers, and triode or tetrode electrochemical synthesis, such as the one described in Fig. 1.1, should be evaluated through modeling studies.

### 5.5.3 Electrochemical promotion of catalysis (EPOC)

- A catalytic reforming test should be carried out by using a non-conductive material to hang a GDE catalyst coupon in the solution in the single-compartment catalytic glass cell reactor used for the powder catalysis test to determine and verify the true  $r_o$  value. The resulting  $H_2$  production rate should then be compared to that obtained for the test carried out in the 2-compartment reactor using a MEA when no external current or potential is applied. This will confirm if a wireless EPOC effect is induced by a gradient developing between the catalyst working electrode and the counter electrode due to the catalytic reaction occurring at the catalyst working electrode. If this is the case, the catalytic rate determined when the 2-compartment cell at OCV is in fact a promoted  $r$  value, and the internal current developing in the 2-compartment cell at open circuit voltage should be determined to allow for the calculation of the Faradaic efficiency for this wireless EPOC case.
- Longer relaxation time periods between each promoted tests segments should be evaluated to ensure the  $H_2$  production rate eventually returns to its equilibrium value between each EPOC test.
- The final  $CH_3OH$  concentration of the un-reacted solution should be measured after the GDE catalysis experiments and compared to that after long-term EPOC experiments tests. It should also be compared with the  $CH_3OH$  consumption rate calculated based on the measured  $H_2$  production rates during the same experiments.
- The effect of  $H_2SO_4$  concentration (pH) on the powder catalysis, and unpromoted and promoted GDE catalysis reaction rate should be evaluated. Similarly, various concentrations of  $CH_3OH$  should be evaluated.
- The catalytic reaction rate should be evaluated at different temperatures under unpromoted (powder and GDE) and promoted conditions (GDE). This would allow for the determination and comparison of the activation energy under various unpromoted and promoted conditions.
- The effect of applying UV light could be explored when using a Pt-Ru/ $TiO_2$  GDE.

- It should be determined if the application EPOC had an effect on the catalytic reaction order. For this, the catalytic reaction order, the reaction rate constant and the rate determining step would need to be established.
- An investigation should be carried out to see if the low temperature CH<sub>3</sub>OH reforming EPOC experiment could be scaled up to a single or dual chamber membrane electrochemically promoted reactor (MEPR).
- The synergetic effects of EPOE (triode or tetrode operation) and EPOC should be further investigated. As mentioned in *Section 3.5.3*, in triode or tetrode operation, it may be possible to carry out the low temperature catalytic reforming of CH<sub>3</sub>OH using non-precious materials at the electrolyser ring WE<sub>elec</sub>.

The high level H<sub>2</sub> production process efficiency and economic comparison carried out in *Appendix C* should be expanded to include the low temperature electrocatalytic and catalytic reforming of CH<sub>3</sub>OH and the effect of electrochemical promotion on the different processes.

## References

- [1] S. Sorrella, J. Speirsb, R. Bentleyc, A. Brandt, and R. Millere, "Global oil depletion: a review of the evidence, energy policy", 38(9), (2010) 5290-5295.
- [2] D. Hart, "Hydrogen - a truly sustainable transport fuel?", *Front. Ecol. Environ.*, 1(3), (2003)138-145.
- [3] D. Sperling, and N. Lutsey, "Energy efficiency in passenger transportation", *The Bridge*, 39(2), (2009) 22-30.
- [4] C. Lamy, J.-M. Leger, and S. Srinivasan, "Direct methanol fuel cells: from a twentieth century electrochemist's dream to a twenty-first century emerging technology", *Modern aspects of electrochemistry*, John O'M. Bockris J. O'M., Conway B. E., White R. E., editors. New York, NY: Kluwer Academic Publishers, 34 (2001) 53-117.
- [5] B. I. Podlovchenko, and T. D. Gladysheva, "Copper ion-catalysed electrochemical synthesis of methanol from carbon monoxide on palladium electrodes", *Mendeleev Commun.*, 16(4), (2006) 232-233.
- [6] J. Li, and G. Prentice, "Electrochemical synthesis of methanol from CO<sub>2</sub> in high-pressure electrolyte", *J. Electrochem. Soc.*, 144(12), (1997) 4284-4288.
- [7] Z. Hu, M. Wu, Z. Wei, S. Song, and P. K. Shen, "Pt-WC/C as a cathode electrocatalyst for hydrogen production by methanol electrolysis", *J. Power Sources*, 166, (2007) 458-461.
- [8] J. W. Phair, and S. P. S. Badwal, "Review of proton conductors for hydrogen separation", *Ionics*, 12, (2006) 103-115.
- [9] S. Ishikura, and C. F. Maciel, "Steam reforming of renewable feedstock's for the production of hydrogen", [http://www.ecodesarrollo.cl/descargas/Caio\\_Ishikura\\_Diploma\\_hidrogeno.pdf](http://www.ecodesarrollo.cl/descargas/Caio_Ishikura_Diploma_hidrogeno.pdf) , (2007) 55 pp.
- [10] Department of Energy (DOE) decision team committee report. "On-board fuel processing go/no-go decision", [http://www1.eere.energy.gov/hydrogenandfuelcells/news\\_fuel\\_processor.html](http://www1.eere.energy.gov/hydrogenandfuelcells/news_fuel_processor.html), (2004) 1-7.
- [11] P.-K. Shen, S.-L. Wang, Z.-L. Hu, Y.-L. Li, R. Zeng, and Y.-Q. Li, "Hydrogen production by alcohol electrolysis", *Acta Phys. - Chim. Sin.*, 23(1), (2007) 107-110.
- [12] T. Tetsuo, T. Kazuhiko, and U. Minoru, "Hydrogen production by methanol-water solution electrolysis", *J. Power Sources*, 164, (2007) 9-16.
- [13] N. Meng, T. Yamakawa, and S. Shinoda, "Methanol dehydrogenation in the liquid phase with Ru/activated carbon catalyst", *React. Kinet. Catal. Lett.*, 58(2), (1996) 341-348.
- [14] T. Miyao, M. Yamauchi, and S. Naito, "Liquid phase methanol reforming with water over silica supported Pt-Ru catalysts", *Catalysis Today*, 87, (2003) 227-235.
- [15] T. Miyao, Y. Watababe, M. Teramoto, and S. Naito, "Catalytic activity of various supported Ir-Re catalysts for liquid phase methanol reforming with water", *Catalysis Communications*, 6, (2003) 113-117.
- [16] T. Miyao, M. Yamauchi, H. Narita, and S. Naito, "Remarkable support effect for liquid phase methanol reforming with water over supported Pt-Ru catalysts", *Appl. Catal. A: Gen.*, 299, (2006) 285-291.
- [17] J. Qu, X. Zhang, Y. Wang, and C. Xie, "Electrochemical reduction of CO<sub>2</sub> on RuO/TiO<sub>2</sub> nanotubes composite modified Pt electrode", *Electrochim. Acta*, 50(16-17), (2005) 3576-3580.

- [18] C. G. Vayenas, S. Bebelis, C. Pliangos, S. Brosda, and D. Tsiplakides, "Electrochemical activation of catalysis - promotion, electrochemical promotion and metal-support interactions", Kluwer Academic / Plenum Publishers, (2001) 574 pp.
- [19] S. P. Balomenou, and C. G. Vayenas, "Triode fuel cells and batteries", *J. Electrochem. Soc.*, 151(11), (2004) A1874-A1877.
- [20] D. P. Wilkinson, "Fuel cells", *The Electrochemical Society Interface*, 10(1), (2001) 22-25.
- [21] S. Leclerc, R. F. Mann, and B. A. Peppley, "Evaluation of the catalytic ethanol-steam reforming process as a source of hydrogen-rich gas for fuel cells", CANMET Energy Technology Center (CETC), (1998) 37 pp.
- [22] R. O. Idem, and N. N. Bakhshi, "Production of hydrogen from methanol. 2. Experimental studies", *Industrial Engineering Chemistry Research*, 33(9), (1994) 2056-2065.
- [23] S. R. Segal, K. B. Anderson, K. A. Carrado, and C. L. Marshall, "Low temperature steam reforming of methanol over layered double hydroxide-derived catalysts", *Appl. Cat. A*, 231, (2002) 215-226.
- [24] M. M. Natile and A. Glisenti, "WO<sub>3</sub>/CeO<sub>2</sub>/YSZ nanocomposite as a potential catalyst for methanol reforming", *J. Power Sources*, 145, (2005) 644-651.
- [25] R. R. Davda, J. W. Shabaker, G. W. Huber, R. D. Cortright, and J. A. Dumesic, "A review of catalytic issues and process conditions for renewable hydrogen and alkanes by aqueous-phase reforming of oxygenated hydrocarbons over supported metal catalysts", *Applied Catalysis B: Environmental*, 56, (2005) 171-186.
- [26] G. W. Huber, J. W. Shabaker, and J. A. Dumesic, "Raney Ni-Sn catalyst for H<sub>2</sub> production from biomass-derived hydrocarbons", *Science*, 300, (2003) 2075-2077.
- [27] J. W. Shabaker, R. R. Davda, G. W. Huber, R. D. Cortright, and J. A. Dumesic, "Aqueous-phase reforming of methanol and ethylene glycol over alumina-supported platinum catalysts", *Journal of Catalysis*, 215, (2003) 344-352.
- [28] G. W. Huber, and J. A. Dumesic, "An overview of aqueous-phase catalytic processes for production of hydrogen and alkanes in a biorefinery", *Catalysis Today*, 111, (2006) 119-132.
- [29] S. Naito, "Market effect of various supports and additives upon liquid phase methanol reforming with water over supported group 8-10 metal catalysts", *Catalysis Surveys from Asia*, 9(4), (2006) 243-258.
- [30] W. Curtis Conner Jr., and J. L. Falconer, "Spillover in heterogeneous catalysis", *Chem. Rev.*, 95, (1995) 759-788.
- [31] F. Roessner, and U. Roland, "Hydrogen spillover in bifunctional catalysis", *J. of Molecular Catalysis A: Chemical*, 112, (1996) 401-412.
- [32] U. Roland, T. Braunschweig, and F. Roessner, "On the nature of spilt-over hydrogen", *J. of Molecular Catalysis A: Chemical*, 127, (1997) 61-84.
- [33] H. Chang, and J. Phillips, "Catalytic synergism in physical mixtures on supported iron-cerium and supported noble metal for hydro-isomerization of 1, 3-butadiene", *Langmuir*, 13, (1997) 477-482.
- [34] J. C. Weigle, and J. Phillips, "Novel dual-bed reactors: utilization of hydrogen spillover in reactor design", *Langmuir*, 20, (2004) 1189-1193.
- [35] E. Baumgarten, and I. Niemeyer, "On the role of surfaces in hydrogenation reactions with gas phase spillover hydrogen", *React. Kinet. Catal. Lett.*, 70(2), (2000) 371-377.

- [36] E. Baumgarten, and G. Meyer, "Hydrogen spillover through the gas phase. Some kinetic aspects", *React. Kinet. Catal. Lett.*, 71(2), (2000) 325-333.
- [37] E. Baumgarten, and L. Maschke, "Hydrogen spillover through the gas phase reaction with graphite and activated carbon", *Applied catalysis A: General*, 202, (2000) 171-177.
- [38] P. C. H. Mitchell, A. J. Ramirez-Cuesta, S. F. Parker, J. Tomkinson, and D. Thompsett, "Hydrogen spillover on carbon-supported metal catalysts studied by inelastic neutron scattering. Surface vibrational states and hydrogen riding modes", *J. Phys. Chem. B*, 107, (2003) 6838-6845.
- [39] B. Miremedi, T. Yadav, J. Z. Zhang, and J. L. Falconer, "Low-temperature hydrogen production using electrically activated catalysts", *Chem. Comm.*, (2000) 1875-1876.
- [40] C. K. Narula, A. Arbor, J. H. Visser, and A. A. Adamczyk, Jr., "Electrically heatable catalyst device using electrically conductive non-metallic materials", US 5480622, (1996).
- [41] Y. Tapes, and M. Bijan, "Processes for electrically activated transformation of chemical and material compositions", WO 02046130, (2002).
- [42] J. Z. Zhang, M. Still, T. Yadav, and G. T. Gaudet, "Low-temperature hydrogen production from steam reforming of methane using electrically activated catalyst", *ECS Transactions*, 5(1), (2007) 673-676.
- [43] S. Kundu, L. C. Simon, M. Fowler, and S. Grot, "Mechanical properties of Nafion electrolyte membranes under hydrated conditions", *Polymer*, 46(25), (2005) 11707-11715.
- [44] M. J. Kelly, G. Faflek, J. O. Besenhard, H. Kronberger, and G. E. Nauer, "Contaminant absorption and conductivity in polymer electrolyte membranes", *J. Power Sources*, 145(2), (2005) 249-252.
- [45] T. Higuchi, T. Tsukamoto, N. Sata, M. Ishigame, K. Kobayashi, S. Yamaguchi, and S. Shin, "Electronic structures of protonic conductors SrTiO<sub>3</sub> and SrCeO<sub>3</sub> by O 1s x-ray absorption spectroscopy", *Solid State Ionics*, 145-155, (2002) 735-739.
- [46] T. Schober, and H. G. Bohn, "Water vapour solubility and electrochemical characterization of the high temperature proton conductor BaZr<sub>0.9</sub>Y<sub>0.1</sub>O<sub>2.95</sub>", *Solid State Ionics*, 127(3-4), (2001) 351-360.
- [47] N. Bonanos, and M. Mogensen, "H<sub>2</sub> oxidation at the interface Ni/Sr<sub>0.995</sub>Ce<sub>0.95</sub>Y<sub>0.05</sub>O<sub>2.975</sub>", *Solid State Ionics*, 97(1-4), (1997) 483-488.
- [48] H. Iwahara, K. Uchida, K. Ono, and K. Ogaki, "Proton conduction in sintered oxides based on BaCeO<sub>3</sub>", *J. Electrochem. Soc.*, 135(2), (1988) 529-533.
- [49] K. Katahira, Y. Kohchi, T. Shimura, and H. Iwahara, "Protonic conduction in Zr-substituted BaCeO<sub>3</sub>", *Solid State Ionics*, 138(1-2), (2000) 91-98.
- [50] A. S. owick, and Y. Du, "High-temperature protonic conductors with perovskite-related structures", *Solid State Ionics*, 77, (1995) 137-146.
- [51] J. A. Kosek, G. Jose, and A. B. Laconti, "Method and system for producing high-pressure hydrogen", WO 2005014468, (2005).
- [52] R. Lawson, C. Wang, J. Hong, J. Ma, B. Fang, and D. Chu, "Nafion-bimevox composite membrane for fuel cell applications", *J. Electrochem. Soc.*, 154(1), (2007) B48-B52.
- [53] I. Honma, S. Nomura, and H. Nakajima, "Protonic conducting organic inorganic nanocomposites for polymer electrolyte membrane", *Journal of Membrane Science*, 185, (2001) 83-94.

- [54] V. Antonucci, A. Di Blasi, V. Baglio, R. Ornelas, F. Matteucci, J. Ledesma-Garcia, L. G. Arriaga, and A. S. Arico, "High temperature operation of a composite membrane-based solid polymer electrolyte water electrolyser", *Electrochim. Acta*, 53, (2008) 7350-7356.
- [55] L. Xiao, H. Zhang, E. Scanlon, L. S. Ramanathan, E.-W. Choe, D. Rogers, T. Apple, and B. C. Benicewicz, "High-temperature polybenzimidazole fuel cell membranes via a sol-gel process", *Chem. Mater.*, 17, (2005) 5328-5333.
- [56] L. Quingfeng, H. A., Hjuler, and N. J. Bjerrum, "Phosphoric acid doped polybenzimidazole membranes: physicochemical characterization and fuel cell applications", *J. of Appl. Electrochem.*, 31, (2001) 773-779.
- [57] X. Glipa, M. E. Haddad, D. J. Jones, and J. Roziere, "Synthesis and characterization of sulphonated polybenzimidazole: a highly conducting proton exchange polymer", *Solid State Ionics*, 97, (1997) 323-331.
- [58] N. Ito, S. Aoyama, T. Nakata, M. Lijima, and H. Sato, "Hydrogen-permeable membrane and manufacturing method of the same", US 7049008, (2006).
- [59] R. E. Buxbaum, "Hydrogen permeable membrane and hydride composition", US 6576350, (2003).
- [60] S. A. Grigoriev, P. Millet, and V. N. Fateev, "Evaluation of carbon-supported Pt and Pd nanoparticles for the hydrogen evolution reaction in PEM water electrolyzers", *J. Power Sources*, 177, (2008) 281-285.
- [61] J. Tian, G. Sun, M. Cai, Q. Mao, and Q. Xin, "PtTiOx/C electrocatalysts with improved durability in H<sub>2</sub>/O<sub>2</sub> PEMFCs without external humidification", *J. Electrochem. Soc.*, 155 (2), (2008) B187-B193.
- [62] M. Goetz, and H. Wendt, "Composite electrocatalysts for anodic methanol and methanol-reformate oxidation", *J. of Appl. Electrochem.*, 31, (2001) 811-817.
- [63] P. Paunovic, I. Radev, A. T. Dimitrov, O. Popovski, E. Lefterova, E. Slavcheva, and S. H. Jordanov, "New nanostructure and interactive supported composite electrocatalysts for hydrogen evolution with partially replaced platinum loading", *Int. J. H<sub>2</sub> Energy*, 34, (2009) 2866-2873.
- [64] M. Wilson, and S. Gottesfeld, "High performance catalyzed membranes of ultra-low Pt loadings for polymer electrolyte fuel cells", *J. Electrochem. Soc.*, 139, (1992) L28-L30.
- [65] T. Frey, and M. Linardi, "Effects of membrane electrode assembly preparation on the polymer electrolyte membrane fuel cell performance", *Electrochim. Acta*, 50, (2004) 99-105.
- [66] Y. J. Zhang, C. Wang, N. F. Wan, Z. X. Liu, and Z. Q. Mao, "Study on a novel manufacturing process of membrane electrode assemblies for solid polymer electrolyte water electrolysis", *Electrochem. Commun.*, 9, (2007) 667-670.
- [67] J. Larminie, and A. Dikes, "Fuel cell system explained", John Wiley & Sons Ltd., England, (2003) 406pp.
- [68] S. Gilman, "The mechanism of electrochemical oxidation of carbon monoxide and methanol on platinum. 1. Carbon monoxide adsorption and desorption and simultaneous oxidation of the platinum surface at constant potential", 67, (1963) 1898-1905.
- [69] S. Gottesfeld, "Preventing CO poisoning in fuel cells", US 4910099, (1990).
- [70] X. Yan, S. Wang, X. Li, M. Hou, Z. Yuan, D. Li, L. Pan, C. Zhang, J. Liu, P. Ming, and B. Yi, "A 75 kW methanol reforming fuel cell system", *J. Power Sources*, 162(2), (2006) 1265-1269.
- [71] J. Zhang, and R. Datta, "Electrochemical preferential oxidation of CO in reformate", *J. Electrochem. Soc.*, 152(6), (2005) A1180-1187.

- [72] T. Iwasita, "Fuel cells: spectroscopic studies in the electrocatalysis of alcohol oxidation", *Journal of the Brazilian Chemical Society*, 13(4), (2002) 1-19.
- [73] N. Munichandraiah, K. McGrath, G. K. S. Prakash, R. Aniszfeld, and O. G. A. Robert, "A potentiometric method of monitoring methanol crossover through polymer electrolyte membranes of direct methanol fuel cells", *J. Power Sources*, 117(1-2), (2003) 98-101.
- [74] A. Hamnett, B. J. Kennedy, and S. A. Weeks, "Base metal oxides as promoters for the electrochemical oxidation of methanol", *J. Electroanal. Chem.*, 240, (1988) 349-353.
- [75] P. K. Shen, and A. C. C. Tseung, "Anodic oxidation of methanol on Pt/WO<sub>3</sub> in acidic media", *J. Electrochem. Soc.*, 141(11), (1994) 3082-3090.
- [76] E. Kjeang, J. Goldak, M.R. Golriz, J. Gub, D. James, and K. Kordes, "A parametric study of methanol crossover in a flowing electrolyte-direct methanol fuel cell", *J. Power Sources*, 153, (2006) 89-99.
- [77] J. A. Drake, W. Wilson and K. Killeen, "Evaluation of the Experimental Model for Methanol Crossover in DMFCs", *J. Electrochem. Soc.*, 151(3), (2004) A413-A417.
- [78] R. Jiang, C. Rong, and D. Chu, "Fuel cross-over and energy conversion in lifetime operation of direct methanol fuel cells", *J. Electrochem. Soc.*, 154(1), (2007) B13-B19.
- [79] F. J. Rodriguez-Varela, and O. Savadogo, "Ethanol-tolerant oxygen reduction reaction (ORR) cathodes for direct ethanol fuel cell applications", *The Electrochemical Society Interface, Conference Proceedings, 208<sup>th</sup> ECS Meeting*, 1(6), (2005) 331-338.
- [80] M. K. Ravikumar, and A. K. Shukla, "Effect of methanol crossover in a liquid-feed polymer-electrolyte direct methanol fuel cell", *J. Electrochem. Soc.*, 143(8), (1996) 2601-2606.
- [81] A. Heinzl, and V. M. Barragan, "A review of the state-of-the-art of the methanol crossover in direct methanol fuel cells", *J. Power Sources*, 84(1), (1999) 70-74.
- [82] Y.-L. Ma, J. S. Wainright, M. H. Litt, and R. F. Savinell, "Conductivity of PBI membranes for high-temperature polymer electrolyte fuel cells", *J. Electrochem. Soc.*, 151(1), (2004) A8-A16.
- [83] J.-T. Wang, J. S. Wainright, R. F. Savinell, and M. Litt, "A direct methanol fuel cell using acid doped polybenzimidazole as polymer electrolyte", *J. Appl. Electrochem.*, 26, (1996) 751-756.
- [84] S. R., Narayan, and T. K. Valdez, "High-energy portable fuel cell power sources", *The Electrochemical Society, Interface*, 17(4), (2008) 40-45.
- [85] S. Ramaswamy, M. Sundaresan, A. Eggert, and R. M. Moore, "System dynamics and efficiency of the fuel processor for an indirect methanol fuel cell vehicle", *35<sup>th</sup> Intersociety Energy Conversion Engineering Conference*, 24-28, (2000) 2000-3048.
- [86] K.-H. Hauer, "Dynamic interactions between the electric drive train and fuel cell system for the case of an indirect methanol fuel cell vehicle", *AIAA-2000-3039, American Institute of Aeronautics and Astronautics Inc.*, (2000) 1317-1325.
- [87] S. A. Fateen, "Fuel cell systems for personal and portable power applications", *Symposium 2001: Highlighting Student and Postdoctoral Research, ESA-EPE, Los Alamos National Laboratory*, (2001) 5 pp.
- [88] A. Ishihara, S. Mitsushima, N. Kamiya, and K.-I. Ota, "Exergy analysis of polymer electrolyte fuel cell systems using methanol", *J. Power Sources*, 126, (2004) 34-40.
- [89] L. F. Brown, "A comparative study of fuels for on-board hydrogen production for fuel-cell-powered automobiles", *Int. J. H<sub>2</sub> Energy*, 26, (2001) 381-397.

- [90] J. R. Lattner, and M. P. Harold, "Comparison of methanol-based fuel processors for PEM fuel cell systems", *Applied Catalysis B: Environmentla* 56, (2005) 149-169.
- [91] S. A. Grigoriev, V. I. Porembsky, and V. N. Fateev, "Pure hydrogen production by PEM electrolysis for hydrogen energy", *Int. J. H<sub>2</sub> Energy*, 31, (2006) 171-175.
- [92] E. Rasten, G. Hagen, and R. Tunold, "Electrocatalysis in water electrolysis with solid polymer electrolyte", *Electrochim. Acta*, 48, (2003) 3945-3852.
- [93] D. Stolten (Ed.), "Hydrogen and fuel cells, fundamentals, technologies and applications", Wiley-VCH Verlag GMBh & Co., Weinbeim, (2010) 908 pp.
- [94] T. M., Maloney, "An electrolysis-based pathway towards hydrogen fuelling", *Vehicle Power and Propulsion*, 2005 IEEE Conference, (2005) 652 - 656.
- [95] T. M. Maloney, "Vehicle power and propulsion", *IEEE Conference*, (2005) 487-491.
- [96] S. Song, H. Zhang, B. Liu, P. Zhao, Y. Zhang, and B. Yi, "An improved catalyst-coated membrane structure for PEM water electrolyzer", *Electrochemical and Solid-State Letters*, 10(8), (2007) B122-B125.
- [97] A. Fujishima, and K. Honda, "Electrochemical photolysis of water at a semiconductor electrode", *Nature*, 238, (1972) 37-38.
- [98] V. Baglio, R. Ornelas, F. Matteucci, F. Martina, G. Ciccarella, I. Zama, L. G. Arriaga, V. Antonucci, and A. S. Arico, "Solid polymer electrolyte water electrolyser based on Nafion-TiO<sub>2</sub> composite membrane for high temperature operation", *Fuel Cells*, 9(3), (2009) 247-252.
- [99] V. Antonucci, A. Di Blasi, V. Baglio, R. Ornelas, F. Matteucci, J. Ledesma-Garcia, L. G. Arriaga, and A. S. Arico, "High temperature operation of a composite membrane-based solid polymer electrolyte water electrolyzer", *Electrochim. Acta*, 53, (2008) 7350-7356.
- [100] Hydrogenics Corporation, HyLYZER™ Annex, "HyLYZER™ 1Nm<sup>3</sup>/h PEM hydrogen generation technology", <http://www.hydrogenics.com/assets/pdfs/ANNEX%201%20-%20HyLYZER-1.pdf>, 7 pp.
- [101] H-tec Wasserstoff-Energie-Systeme GmbH, "EL 30 electrolyzers for distributed hydrogen production", [http://h-tec-electrolyser.com/downloads/htec\\_EL30\\_Electrolyser.pdf](http://h-tec-electrolyser.com/downloads/htec_EL30_Electrolyser.pdf), 1 p.
- [102] A. H. Shaaban, "Pulsed DC and anode depolarization in water electrolysis for hydrogen generation", Engineering Research Division, HQ Air Force Civil Engineering Support Agency, Final Report, ESL-TR-92-55, (1994) 69 pp.
- [103] R.W. Coughlin, and M. Farooque, "Electrochemical gasification of coal – simultaneous production of hydrogen and carbon dioxide by a single reaction involving coal, water and electrons", *Ind. Eng. Chem. Process Des. Dev.*, 19, (1980) 211-219.
- [104] M. R. St. John, A. J. Furgala, and A. F. Sammells, "Hydrogen generation from glucose depolarized water electrolysis", *J. Electrochem. Soc.*, 129, (1986)1174-1981.
- [105] A. J. Appleby, and B. Pinchon, "Electrochemical aspects of the H<sub>2</sub>SO<sub>4</sub>-SO<sub>2</sub> thermo-electrochemical cycle for hydrogen production", *Int. J. H<sub>2</sub> Energy*, 5, (1980) 253-267.
- [106] J. A. O'Brien, J. T. Hinkley, and S. W. Donne, "The electrochemical oxidation of aqueous sulphur dioxide. I. Experimental parameter influences on electrode behaviour", *J. Electrochem. Soc.*, 157(9), (2010) F111-F115.
- [107] C. R. Cloutier, and D. P. Wilkinson, "Electrolytic production of hydrogen from aqueous acidic methanol solutions", *Int J. H<sub>2</sub> Energ.*, 35, (2010) 3967-3984.

- [108] R. R. Adzic, W. E. O'Grady, and S. Srinivasan, "Oxidation of HCOOH and CH<sub>3</sub>OH on platinum modified by foreign metal adatoms in 85% phosphoric acid", J. Electrochem. Soc., 128(9), (1981)1913-1919.
- [109] L. Soler, J. Macanas, M. Munoz, and J. Casado, "Electrocatalytic production of hydrogen boosted by organic pollutants and visible light", Int. J. H<sub>2</sub> Energy, 31, (2006) 129-139.
- [110] B. Reichman, and W. Mays, "Electrolytic production of hydrogen", US 6890419, (2005).
- [111] R. Woods, I. Root, R. H. Lyer, and B. F. Porter, "Electrochemical reformer and fuel cell system", WO 2004046408, (2004).
- [112] I. Busenbender, V. Peinecke, H. Dohle, and T., Kels, "Process for reforming methanol", DE 197007384, (1998).
- [113] K. Teruo, K. Yuichi, H. Tatsuo, and T. Seiji, "Hydrogen production", JP 63219593, (1988).
- [114] S. Takayuki, and A. Yoshikawa, "Fuel cell", JP 2003308869, (2003).
- [115] T. Toshiki, and F. Toshio, "Organic electrolytic synthesis method and organic electrolytic synthesis device", JP 2005256033, (2005).
- [116] S. R. Narayanan, and W. Chun, B. Jeffries-Nakamura and T. I. Valdez, "Hydrogen generation by electrolysis of aqueous organic solutions", US 6299744, (2001).
- [117] S. R. Narayanan, W. Chun, B. Jeffries-Nakamura, and T. I. Valdez, "Hydrogen generation by electrolysis of aqueous organic solutions", US 7056428, (2006).
- [118] T. Take, K. Tsurutani, and M. Umeda, "Hydrogen production by methanol-water solution electrolysis", J. Power Sources, 164, (2007) 9-16.
- [119] J. W. Tester, E. M. Drake, M. W. Golay, and A. P. William, "Sustainable energy choosing among options". Cambridge, MA: MIT Press, (2005).
- [120] D. P. Bloomfield, and A. N. Rabe, "Electrochemical autothermal reformer", US 6143159, (2000).
- [121] D. P. Bloomfield, "Electrochemical hydrogen compressor with electrochemical autothermal reformer", US 6068673, (2000).
- [122] C. G. Vayenas, University of Patras, Department of Chemical Engineering, (2006)  
<http://www.chemeng.upatras.gr/index.htm>.
- [123] M. Stoukides, and C. G. Vayenas, "Solid electrolyte aided study of the ethylene oxide oxidation on Silver", Journal of Catalysis, 64, (1980) 18-28.
- [124] C. G. Vayenas, S. Bebelis, and S. Neophytides, "Non-Faradaic electrochemical modification of catalytic activity", J. Phys. Chem., 92(18), (1988) 5083-5085.
- [125] N. A. Anastasijevic, "NEMCA - From discovery to technology", Catalysis Today, 146, (2009) 308-311.
- [126] A. J. Bard, and L. R. Faulkner, "Electrochemical Methods Fundamentals and Applications", Second Edition, John Wiley & Sons, Inc., USA, (2001) 833 pp.
- [127] C. G. Vayenas, M. M., Jaksic, S. I., Bebelis, and S., G. Neophytides, "The electrochemical activation of catalytic reactions", Modern Aspects of Electrochemistry, Edited by John O'M. Bockris et al., 29, (1996) 57-202.

- [128] P. H. Chiang, and M. Stoukides, "Solid electrolyte aided direct coupling of methane", *Journal of Catalysis*, 139(2), (1993/2) 683-687.
- [129] C. Sanchez, and E. Leiva, "Theoretical aspects of some prototypical fuel cell reactions", *Handbook of fuel cells - fundamentals, technology and applications, Volume 2: Electrocatalysis*, W. Vielstich, H. A. Gasteiger, and A. Lamm (Ed), John Wiley & Sons, Ltd., England, Chapter 11, (2003) 93-131.
- [130] E. P. M. Leiva, and C. G. Sanchez, "NEMCA effect: why are the work function changes of the gas exposed catalyst-electrode surface one-to-one related to the changes in the catalyst working electrode potential?", *Solid State Electrochem.*, 7, (2003) 588-592.
- [131] H. Matsumoto, T. Shimura, T. Higushi, H. Tanaka, K. Katahira, T. Otake, T. Kudo, K. Yashiro, A. Kaimai, T. Kawada, and J. Mizusaki, "Protonic-electronic mixed conduction and hydrogen permeation in  $\text{BaCe}_{0.9-x}\text{Y}_{0.1}\text{Ru}_x\text{O}_{3-\alpha}$ ", *J. Electrochem. Soc.*, 152(3), (2005) A488-A492.
- [132] M. Marwood, S. Balomenou, A. Tsiliras, C. A. Cavalca, C. Pliangos, and C. G. Vayenas, "Electrochemical promotion of electronically isolated and dispersed Pt catalysts", *Ionics*, 4, (1998) 207-214.
- [133] P. E. Tsiakaras, S. L. Douvartzides, A. K. Demin, and V. A. Sobyenin, "The oxidation of ethanol over Pt catalyst-electrodes deposited on  $\text{ZrO}_2$  (8 mol%  $\text{Y}_2\text{O}_3$ )", *Solid State Ionics*, 152-153, (2002) 721-726.
- [134] S. L. Douvartzides, and P. E. Tsiakaras, "Electrochemically promoted catalysis: the case of ethanol oxidation over Pt", *Journal of Catalysis*, 211(2), (2002) 521-529.
- [135] S. G. Neophytides, D. Tsiplakides, P. Stonehart, M. Jasksic, and C. G. Vayenas, "Non-Faradaic electrochemical modification of the catalytic activity of Pt for  $\text{H}_2$  oxidation in aqueous alkaline media", *J. Phys. Chem.*, 100, (1996) 14803-14814.
- [136] C. A. Cavalca, G. Larsen, C. G. Vayenas, and G. L. Haller, "Electrochemical modification of  $\text{CH}_3\text{OH}$  oxidation selectivity and activity on a Pt single-pellet catalytic reactor", *J. Phys. Chem.*, 97, (1993) 6115-6119.
- [137] J. K. Hong, I.-H. Oh, S.-A. Hong, and W. Y. Lee, "Electrochemical oxidation of methanol over a silver electrode deposited on Ytria-stabilized zirconia electrolyte", *Journal of Catalysis*, 163(1), (1996) 95-105.
- [138] S. Neophytides, and C. G. Vayenas, "Non-Faradaic electrochemical modification of catalytic activity 2. The case of methanol dehydration and decomposition on Ag", *Journal of Catalysis*, 118, (1989) 147-163.
- [139] A. Thursfield, S. Brosda, C. Pliangos, T. Schober, and C. G. Vayenas, "Electrochemical promotion of an oxidation reaction using a proton conductor", *Electrochim. Acta*, 48(25-26), (2003) 3779-3788.
- [140] C. G. Yiokari, G. E. Pitselis, D. G. Pollydoros, A. D. Katsanounis, and C. G. Vayenas, "High-pressure electrochemical promotion of ammonia synthesis over an industrial iron catalyst", *J. Phys. Chem. A*, 104, (2000) 10600-10602.
- [141] G. Marnellos, S. Zisekas, and M. Stoukides, "Synthesis of Ammonia at Atmospheric Pressure with the Use of Solid State Proton Conductors", *Journal of Catalysis*, 193(1), (2000), 80-87.
- [142] G. Karagiannakis, S. Zisekas, and M. Stoukides, "Hydrogenation of carbon dioxide on copper in an  $\text{H}^+$  conducting membrane-reactor", *Solid State Ionics*, 162-163, (2003) 313-318.
- [143] D. Poulidi, M. A. Castillo-del-Rio, R. Salar, and I. S. Metcalfe, "Electrochemical promotion of catalysis using solid-state proton-conducting membranes", *Solid State Ionics*, 162-163, (2003) 305-311.

- [144] I. Politova, V. A. Sobyenin, and V. D. Belyaev, "Ethylene hydrogenation in electrochemical cell with solid proton-conducting electrolyte", *React. Kinet. Catal. Lett.*, 41(2), (1989) 321-326.
- [145] Salazar, and E. S. Smotkin, "Electrochemically promoted olefin isomerization reactions at polymer electrolyte fuel cell membrane electrode assemblies", *J. Appl. Electrochem.*, 36, (2006) 1237-1240.
- [146] D. Tsiplakides, S. G. Neophytides, O. Enea, M. Jaksic, and C. G. Vayenas, "Non-Faradaic electrochemical modification of the catalytic activity of Pt-black electrodes deposited on Nafion 117 solid polymer electrolytes", *J. Electrochem. Soc.*, 144(6), (1997) 2072-2078.
- [147] L. Ploense, M. Salazar, B. Gureau, and E. S. Smotkin, "Proton spillover promoted isomerization of n-butylenes on Pd-black cathodes/Nafion 117", *J. Am. Chem. Soc.*, 119, (1997) 11550-11551.
- [148] L. Ploense, M. Salazar, B. Gureau, and E. S. Smotkin, "Spectroscopic study of NEMCA promoted alkene isomerizations at PEM fuel cell Pd-Nafion cathodes", *Solid State Ionics*, 136-137, (2000) 713-720.
- [149] D. Tsiplakides, and S. Balomenou, "Electrochemical promoted catalysis: towards practical utilization", *Chemical Industry & Chemical Engineering Quarterly*, 14(2), (2008) 97-105.
- [150] G. Marnellos, and M. Stoukides, "Catalytic studies in electrochemical membrane reactors", *Solid State Ionics*, 175, (2004), 597-603.
- [151] M. Marwood, and C. G. Vayenas, "Electrochemical promotion of electronically isolated Pt catalysts on stabilized zirconia", *Journal of Catalysis*, 168, (1997) 538-542.
- [152] C. G. Vayenas, S. Bebelis, I. V. Yentekakis, and P. E. Tsiakaras, "Metal-solid electrolyte catalysts", EP 0480116, (1992).
- [153] M. A. Priestnall, M. J. Evans, and M. S. P. Shaffer, "Mixed reactant fuel cells", US 20040058203, (2004).
- [154] C. G. Yiokari, G. E. Pitselis, D. G. Polydoros, A. D. Katsaounis, and C. G. Vayenas, "High-pressure electrochemical promotion of ammonia synthesis over an industrial iron catalyst", *J. Phys. Chem. A*, 104, (2000) 10600-10602.
- [155] J. St-Pierre, D. P. Wilkinson, and S. A. Campbell, "Method and device for improved catalytic activity in the purification of fluids", US 20030010629, (2003).
- [156] S. P. Balomenou, D. Tsiplakides, A. Katsaounis, S. Brosda, A. Hammad, G. Foti, C. Comninellis, S. Thiemann-Handler, B. Cramer, and C. G. Vayenas, "Novel monolithic electrochemically promoted catalytic reactor for environmentally important reactions", *Applied Catalysis*, 52, (2004) 181-196.
- [157] S. P. Balomenou, D. Tsiplakides, A. Katsaounis, S. Brosda, A. Hammad, G. Foti, C. Comninellis, S. Thiemann-Handler, B. Cramer, and C. G. Vayenas, "Monolithic electrochemically promoted reactors: a step for the practical utilization of electrochemical promotion", *Solid State Ionics*, 177(26-32), (2006) 2201-2204.
- [158] L. Kriksunov, and C. G. Vayenas, "Method and device for treating automotive exhaust", US 2006177365, (2006)
- [159] C. A. Cacalca, "Method for low temperature, high activity and selectivity catalytic conversion using electrochemical (NEMCA) cells", US 20060131179, (2006).
- [160] Y. Ding, and J. C. Burba, "Fuel cell power plant with electrochemical enhanced carbon monoxide removal", US 6733909, (2004).
- [161] J. M. Naber, "Fuel cell power plant with electrochemical enhanced carbon monoxide removal", US 20020164507, (2002).

- [162] M. Salazar, and E. S. Smotkin, "Electrochemically promoted olefin isomerization reactions at polymer electrolyte fuel cell membrane electrode assemblies", *J. Appl. Electrochem.*, 36, (2006) 1237-1240.
- [163] F.M. Sapountzi, M.N. Tsampas, and C.G. Vayenas, "Methanol reformat treatment in a PEM fuel cell-reactor", *Catalysis Today*, 127, (2007) 295–303.
- [164] Q. Fan, "Biofuel production by high-temperature non-Faradaic electrochemical modification of catalysis", US 20100258447 (2010).
- [165] S. P. Balomenou, F. Sapountzi, D. Presvytes, M. Tsampas, and C. G. Vayenas, "Triode fuel cells", *Solid State Ionics*, 177(19-25), (2006) 2023-2027.
- [166] C. G., Vayenas, and S. Balomenou, "Triode fuel cell and battery and method for conducting exothermic chemical reactions", WO 2005/008820 (2005).
- [167] M. Behmann, S.-H. Kim, H.-J. Kob, and K. Lucas, "Experimental and theoretical investigations at the system  $\text{CH}_3\text{OH} + \text{H}_2\text{SO}_4 + \text{H}_2\text{O}$ ", *Thermodynamic Properties of Complex Fluid Mixture*, (2004) 3-25.
- [168] J. M. Dona Rodriguez, J. A. Herrera Melian, and J. Perez Pena, "Determination of the real surface area of Pt electrodes by hydrogen adsorption using cyclic voltammetry", *J. Chem. Educ.*, 77(9), (2000)1195-1197.
- [169] T. Ralph, G. A. Hards, J. E. Keating, S. A. Campbell, D. P. Wilkinson, M. Davis, J. St-Pierre, and M. C. Johnson. "Low cost electrodes for proton exchange membrane fuel cells", *J. Electrochem. Soc.*, 144(11), (1997) 3845-3857.
- [170] C. L. Green., and A. Kucernak, "Determination of the platinum and ruthenium surface areas in platinum-ruthenium alloy electrocatalysts by underpotential deposition of copper, I. Unsupported Catalysts", *J. Phys. Chem. B*, 106, (2002) 1036-1047.
- [171] J. A. Dean, "Lange's handbook of chemistry", New York, NY, McGraw Hill, (1999) 8.2, 8.7.
- [172] D. R. Lide, "CRC handbook of chemistry and physics", Boca Raton, FL, CRC Press LLC, (2006-2007).
- [173] A. Katsaounis, S. Balomenou, D. Tsiplakides, S. Brosda, S. Neophytides, and C. G. Vayenas, "Proton tunnelling-induced bistability, oscillations and enhanced performance of PEM fuel cells", *Appl. Catal. B Environ.*, 56, (2006) 251-258.
- [174] T.R. Ralph, S. Hudson, and D. P. Wilkinson, "Electrocatalyst stability in PEMFCs and the role of fuel starvation and cell reversal tolerant anodes", *ECS Transactions*, 1(8), (2006) 67-84.
- [175] T. T. H. Cheng, V. Colbow, S. Wessel, C. Chuy, and P. He, "Impacts of Ru dissolution and crossover on polymer electrolyte membrane fuel cell performance and anode functionality", *ECS Transactions*, 28 (23), (2010) 243-251.
- [176] E. Gileadi, "Electrode kinetics for chemists, chemical engineers, and materials scientists", VCH Publishers Inc., USA, (1993) 597 pp.
- [177] G. Wu, L. Li, and B.-Q. Xu, "Effect of electrochemical polarization of PtRu/C catalysts on methanol electrooxidation", *Electrochim. Acta*, 50, (2004) 1-10.
- [178] W. F. Gale, and T. C. Totemeier., "Smithells metals reference book", 8<sup>th</sup> edition, Oxford, Elsevier, (2004) 2080 pp.
- [179] K. Kinoshita, "Electrochemical oxygen technologies", The electrochemical society series. New York, NY, John Wiley & Sons Inc., (1992) 431 pp.

- [180] E. Herrero, K. Franaszczuk, and A. Wieckowski, "Electrochemistry of methanol at low index crystal planes of platinum: an integrated voltammetric and chronoamperometric study", *J. Phys. Chem.*, 98 (1994) 5074-5083.
- [181] K. Franaszczuk, E. Herrero, P. Zelenay, and A. Wieckowski, "A comparison of electrochemical and gas-phase decomposition of methanol on platinum surfaces", *J. Phys. Chem.*, 96, (1992) 8509-8516.
- [182] T. J. Schmidt, H. A. Gasteiger, and R. J. Behm., "Methanol electrooxidation on a colloidal PtRu-alloy fuel cell catalyst", *Electrochem. Comm.*, 1, (1999) 1-4.
- [183] A. Aramata, T. Kodera, and M. Masuda, "Electrooxidation of methanol on platinum bonded to solid polymer electrolyte, Nafion", *J. Appl. Electrochem.*, 18, (1998) 577-582.
- [184] L. Zhang, X. Cheng, H. Tu, M. You, Y. Zhang, and Q. Fan, "Kinetic analysis of methanol oxidation on Pt/C and PtRu/C catalysts", *ECS Transactions*, 11(1), (2007) 1347-1357.
- [185] R. Baker, Z. Xie, J. Zhang, and D. P. Wilkinson., "Kinetic study for methanol oxidation at different temperatures using a new and improved electrochemical cell design", *Proceedings of the International Symposium on Fuel Cell and Hydrogen Technologies.1<sup>st</sup>*, Calgary, AB, Canada, (2005) 3.
- [186] L. Dubau, C. Coutanceau, E. Garnier, J.-M. Leger, and C. Lamy, "Electrooxidation of methanol at platinum-ruthenium catalysts prepared from colloidal precursors: atomic composition and temperature effects", *J. Appl. Electrochem.* 33(5), (2003) 419-429.
- [187] H. Guoyan, and J. Prakash, "Rotating rate dependency of methanol oxidation on a smooth polycrystalline platinum surface", *ECS Transactions*, 1(14), (2006) 27-33.
- [188] T. H. Madden, N. Arvindan, and E. M. Stuve, "Development of an electrochemical flow-cell technique for studying methanol electro-oxidation at elevated temperatures", *J. Electrochem. Soc.*, 150(1), (2003) E1-E10.
- [189] H. N. Dinh, X. Ren, F. H. Garzon, P. Zelenay, and S. Gottesfeld, "Electrocatalysis in direct methanol fuel cells: li-situ probing of PtRu anode catalyst surfaces", *J. Electroanal. Chem.*, 491(1), (2000) 222-233.
- [190] P. Waszczuk, A. Wieckowski, P. Zelenay, S. Gottesfeld, C. Coutanceau, J.-M. Leger, and C. Lamy, "Adsorption of CO poison on fuel cell nanoparticle electrodes from methanol solutions: a radioactive labelling study", *J. Electroanal. Chem.*, 511(1-2), (2001) 55-64.
- [191] M. H. Miles, E. A. Klaus, B. P. Gunn, J. R. Locker, and W. E. Serafin, "The oxygen evolution reaction on platinum, Iridium, ruthenium and their alloys at 80°C in acid solutions", *Electrochim. Acta*, 23, (1978) 521-526.
- [192] G. Tremiliosi-Filho, H. Kim, W. Chrzanowski, A. Wieckowski, B. Grzybowska, and P. Kulesza, "Reactivity and Activation parameters in methanol oxidation on platinum single crystal electrodes "decorated" by ruthenium adlayers", *J. Electroanal. Chem.*, 467, (1999) 143-156.
- [193] K. H. Lim, H.-S. Oh, S.-E. Jang, Y.-J. Ko, H.-J. Kim, and H. Kim, "Effect of operating conditions on carbon corrosion in polymer electrolyte membrane fuel cells", *J. Power Source*, 193, (2009) 575-579.
- [194] L. M. Roen, C. H. Paik, and T. D. Jarvi, "Electrocatalytic corrosion of carbon support in PEMFC cathodes", *Electrochem. and Solid-State Lett*, 7(1), (2004) A19-A22.
- [195] A. Zawodzinski, M. Neeman, L. O. Sillerud, and S. Gottesfeld, "Determination of water diffusion coefficients in perfluorosulfonate ionomeric membranes", *J. Phys. Chem.*, 95, (1991) 6040-6044.
- [196] M. M. Mench, "Fuel Cell Engines", John Wiley & Sons Inc., (2008) 528 pp.
- [197] H. E. Darling, "Conductivity of sulphuric acid solutions", *J. Chem. Eng. Data*, 9(3) (1964) 421-426.

- [198] M. N. Tsampas, A. Pikos, S. Brosda, A. Katsaounis, and C. G. Vayenas, "The effect of membrane thickness on the conductivity of Nafion", *Electrochim. Acta*, 51, (2006) 2743-2755.
- [199] P. R. Roberge, *Handbook of Corrosion Engineering*, McGraw-Hill Companies, USA, Appendix F, (2000) 1101-1123.
- [200] N. P. Finkelstein, and R. D. Hancock, "A New Approach to the Chemistry of Gold", *Gold bulletin*, 7(3), (1974) 72-77.
- [201] P. Tengvall, and I. Lundstrom, "Physico-chemical considerations of titanium as a biomaterial", *Clin. Mater*, 9, (1992)115-134.
- [202] E. Asselin, T. M. Ahmed, and A. Alfantazi, "Corrosion of niobium in sulphuric acid and hydrochloric acid solutions at 75 and 95°C", *Corrosion Sci.*, 49, (2007) 649-710.
- [203] Wesselmark, M., Wickman, B., Lagergren, C., and Lindbergh, G., "Electrochemical performance and stability of thin film electrodes with metal oxides in polymer electrolyte fuel cells", *Electrochim. Acta*, 55, (2010) 7590-7596.
- [204] K. I. Hadjiivanov, and D. G. Klissurski, "Surface chemistry of titania (anatase) and titania-supported catalysts", *Chemical Society Reviews*, (1996) 61-69.
- [205] T. Ioroi, H. Senoh, S.-I. Yamazaki, Z. Siroma, N. Fujiwara, and K. Yasuda, "Stability of corrosion-resistant magneli-phase  $Ti_4O_7$ -supported PEMFC catalysts at high potentials", *J. Electrochem. Soc.*, 155(4), (2008) B321-B326.
- [206] J. Shim, C.-R. Lee, H.-K. Lee, J.-S. Lee, and E. J. Cairns, "Electrochemical characteristics of Pt- $WO_3/C$  and Pt- $TiO_2/C$  electrocatalysts in a polymer electrolyte fuel cell", *J Power Sources*, 102, (2001) 172-177.
- [207] R. E. Fuentes, B. L. Garcia, and J. W. Weidner, "Effect of Titanium Dioxide Supports on the Activity of Pt-Ru toward Electrochemical Oxidation of Methanol", *J. Electrochem. Soc.*, 158(5), (2011) B461-B466.
- [208] G. R. Bamwenda, S. Tsubota, T. Nakamura, M. Haruta, "Photoassisted Hydrogen Production from a Water-Ethanol Solution: A Comparison of Activities of Au- $TiO_2$  and Pt- $TiO_2$ ", *Journal of Photochemistry and Photobiology A: Chemistry*, 89, (1995) 177-189.
- [209] K. Hirakawaa, M. Inoueb, and T. Abea, "Methanol oxidation on carbon-supported Pt-Ru and  $TiO_2$  (Pt-Ru/ $TiO_2/C$ ) electrocatalyst prepared using polygonal barrel-sputtering method", *Electrochim. Acta*, 55 (20), (2010) 5874-5880.
- [210] S.Lj. Gojkovića, B.M. Babićb, V.R. Radmilovićc and N.V. Krstajića, "Nb-doped  $TiO_2$  as a support of Pt and Pt-Ru anode catalyst for PEMFCs", *Journal of Electroanalytical Chemistry*, 639 (1-2), (2010) 161-166.
- [211] P. Claus, S. Schimpfb, R. Schödelc, P. Kraakc, W. Mörked, and D. Hönickeb, "Hydrogenation of crotonaldehyde on Pt/ $TiO_2$  catalysts: Influence of the phase composition of titania on activity and intramolecular selectivity", *Applied Catalysis A: General*, 165 (1-2), (1997) 429-441.
- [212] P. Pnangiotopoulou, and D. I. Kondarides, "Effect of Morphological Characteristics of  $TiO_2$ -supported noble metal catalysts on their activity for the water-gas shift reaction", *Journal of Catalysis*, 225, (2004) 327-336.
- [213] F. L. S. Purgato, L. A. Montoro, J. Riberiro, K. B. Kokoh, and P. Olivi, "The effect of heat treatment on the preparation of Pt-RuO<sub>2</sub>/C electrocatalysts.", *Electrocatal*, (2010).
- [214] S. Brunauer, P.H. Emmett, and E. Teller, *J. Am. Chem. Soc.*, 1938, 60, 309.

- [215] A. S. Polo, M. C. Santos, R. F. B. De Souza, W. A. Alves, "Pt-Ru-TiO<sub>2</sub> photoelectrocatalysts for methanol oxidation", *J. Power Sources*, 196, (2011) 872-876.
- [216] N. Perkas, Z. Zhong, L. Chen, M. Besson, and A. Gedanken, "Sonochemically prepared high dispersed Ru/TiO<sub>2</sub> mesoporous catalyst for partial oxidation of methane to syngas", *Catalysis Letters*, 103(1-2), (2005) 9-14.
- [217] S. J. Tauster, S. C. Fung, and R. L. Garten, "Strong metal-support interactions, group 8 noble metals supported on TiO<sub>2</sub>", *Journal of the American Chemical Society*, 100(1), (1978) 170-175.
- [218] E. Antolini, L. Giorgi, F. Cardellini, and E. Passalacqua, "physical and morphological characteristics and electrochemical behaviour in PEM fuel cells of Pt-Ru/C catalysts", *J. Solid State Electrochem.*, 5, (2001) 131-140.
- [219] J. Willsau, and J. Heitbaum, "Analysis of adsorbed intermediates and determination of surface potential shifts by DEMS", *Electrochim. Acta*, 31(8), (1986) 943-948.
- [220] C. Lamy, E. M. Belgsir, and J.-M. Leger, "Electrocatalytic oxidation of aliphatic alcohols: application to the direct alcohol fuel cell (DAFC).", *J. of Appl. Electrochem.*, (31), (2001) 799-809.
- [221] M. Metikos-Hukovic, R. Babic, and Y. Piljac, "Kinetics and electrocatalysis of methanol oxidation on electrodeposited Pt and Pt<sub>70</sub>Ru<sub>30</sub> catalysts.", *J. of New Materials for Electrochemical Systems*, 7, (2004) 179-190.
- [222] N. Karthikeyan, V. V. Giridhar, and D. Vasudevan, "Surfactant effects on methanol oxidation at Pt-Ru/C coated glassy carbon electrode", *J. Solid State Electrochem*, 14(5), (2010) 877-881.
- [223] W. H. Iizcano-Valbuena, V. A. Paganin, and E. R. Gonzalez, "Methanol electro-oxidation on gas diffusion electrodes prepared with Pt/Ru/C catalysts", *Electrochim. Acta*, 47(22-23), (2002) 3715-3722.
- [224] A. N. Golikand, M. G. Maragheh, S. S. Sherehjini, K. M. Taghi-Ganji, M. Yari, "Carbon-supported Pt particles as a catalyst for electrooxidation of methanol and cyclic voltammetry studies under acidic conditions", *Electroanalysis*, 18(9), (2006) 911-917.
- [225] A. V. Tripkovic, K. D. Popovic, B. N. Grgur, B. Blizanac, P. N. Ross, and N. M. Markovic, "Methanol electrooxidation on supported Pt and PtRu catalysts in acid and alkaline solutions.", *Electrochim. Acta*, 47, (2002) 3707-3714.
- [226] C.-G. Lee, M. Umeda, and I. Uchida, "Cyclic voltammetric analysis of C<sub>1</sub>-C<sub>4</sub> alcohol electrooxidations with Pt/C and Pt-Ru/C microporous electrodes", *J. Power Sources*, 160, (2006) 78-89.
- [227] T. Iwasita, H. Hoster, A. John-Anacker, W. F. Lin, and W. Vielstich, "Methanol oxidation on PtRu electrodes. Influence of surface structure and Pt-Ru atom distribution", *Langmuir*, 16, (2000) 522-529.
- [228] M. Hepel, I. Kumarihamy, and C. J. Zhong, "Nanoporous TiO<sub>2</sub>-supported bimetallic catalysts for methanol oxidation in acidic media.", *Electrochem. Comm.*, 8, (2006) 1439-1444.
- [229] Z. Wang, G. Chen, D. Xia, and L. Zhang, "Studies on the electrocatalytic properties of PtRu/C-TiO<sub>2</sub> toward the oxidation of methanol.", *J. of Alloys and Compounds*, 450, (2008) 148-151.
- [230] H. Song, X. Qui, X. Li, F. Li, W. Zhu, and L. Chen, "TiO<sub>2</sub> nanotubes promoting Pt/C catalysts for ethanol electro-oxidation in acidic media.", *J. Power Sources*, 170, (2007) 50-54.
- [231] D. He, L. Yang, S. Kuang, and Q. Cai, "Fabrication and catalytic properties of Pt and Ru decorated TiO<sub>2</sub>/CNTs catalyst for methanol electrooxidation", *Electrochem. Comm.*, 9, (2007) 2467-2472.
- [232] H. Song, Z. Qiu, F. Li, W. Zhu, and L. Chen, "Ethanol electro-oxidation on catalysts with TiO<sub>2</sub> coated carbon nanotubes as support", *Electrochem. Comm.*, 9, (2007) 1416-1421.

- [233] B. N. Grgur, N. M. Markov, C. A. Lucas, and P. N. Ross, "Electrochemical oxidation of carbon monoxide: from platinum single crystals to low temperature fuel cells catalysts. Part I: Carbon monoxide oxidation onto low index platinum single crystals", *J. Serb. Chem. Soc.*, 66(11–12), (2001) 785-797.
- [234] J. Zhang, "PEM fuel cell electrocatalysts and catalyst layers, Fundamentals and Applications", Springer-Verlag London Limited, (2008) 1137 pp.
- [235] I. D. Santos, F. Colmati, E. R. Gonzales, "Preparation and characterization of supported Pt-Ru catalysts with a high Ru content.", *J. Power Sources*, 159 (2006) 869-877.
- [236] E. Ticanelli, J. G. Beery, M. T. Paffett, S. Gottesfeld, "An electrochemical, ellipsometric, and surface science investigation of the Pt-Ru bulk alloy surface", *J. Electroanal. Chem.*, 258(1), (1989) 61-77.
- [237] P. Stonehart, "Development of alloy electrocatalysts for phosphoric acid fuel cells (PAFC)", *J. Applied Electrochem*, 22(11), (1992) 995-1001.
- [238] C. G. Vayenas, and S. Neophytides, "Non-Faradaic electrochemical modification of catalytic activity: 3. the case of methanol oxidation on Pt", *J. Catal.*, 127, (1991) 645-664.
- [239] I. V. Yentekakis, Y. Jiang, S. Neophytides, S. Bebelis, and C. G. Vayenas, "Catalysis, electrocatalysis and electrochemical promotion of the steam reforming of methane over Ni film and Ni-YSZ cermet anodes, *Ionics*, 1, (1995) 491-498.
- [240] S. Bebelis, and C. G. Vayenas, "Non-Faradaic electrochemical modification of catalytic activity: 1. the case of ethylene oxidation on Pt", *J. Catal.*, 118, (1989) 125-146.
- [241] D. Tsiplakides, J. Nicole, C. G. Vayenas, and C. Comninellis, "Work function and catalytic activity measurements of an IrO<sub>2</sub> film deposited on YSZ subjected to in situ electrochemical promotion", *J. Electrochem. Soc.*, 145(3), (1998) 905-908.
- [242] C. Pliangos, I. V. Yentekakis, X. E. Verykios, and C. G. Vayenas, "Non-Faradaic electrochemical modification of catalytic activity: 8. Rh-catalyzed C<sub>2</sub>H<sub>4</sub> oxidation, *J. Catal.*, 154, (1995) 124-136.
- [243] M. Makri, A. Buekenhoudt, J. Luyten, and C. G. Vayenas, "Non-Faradaic electrochemical modification of the catalytic activity of Pt using a CaZr<sub>0.9</sub>In<sub>0.1</sub>O<sub>3-α</sub> proton conductor", *Ionics* 2, (1996) 282-288.
- [244] I. V. Yentekakis, G. Moggridge, C. G. Vayenas, and R. M. Lambert, "In-situ controlled promotion of catalyst surfaces via NEMCA: the effect of Na on the Pt-catalyzed CO oxidation, *J. Catal.*, 146, (1994) 292-305.
- [245] L. Ploense, M. Salazar, B. Gurau, and E. S. Smotkin, "Spectroscopic study of NEMCA promoted alkene isomerizations at PEM fuel cell Pd-Nafion cathodes, *Solid State Ionics*, 136-137, (2000) 713-720.
- [246] S. Neophytides, D. Tsiplakides, P. Stonehart, M. Jaksic, and C. G. Vayenas, "Electrochemical enhancement of a catalytic reaction in aqueous solutions, *Nature*, 370, (1994), 292-294.
- [247] E. Lamy-Pitawa, S. E. Mouahid, and J. Barbier, "Effect of anions on catalytic and electrocatalytic hydrogenations and on the electrocatalytic oxidation and evolution of hydrogen on platinum", *Electrochim. Acta*, 45, (2000), 4299-4308.
- [248] C. G. Vayenas, S. Bebelis, I. V. Yentekakis, P. Tsiakaras, and H. Karasali, "Non-Faradaic electrochemical modification of catalytic activity, Reversible promotion of platinum metals catalysts." *Platinum Metals Rev.*, 34(3), (1990) 122-130.

## Appendix A: Publications, Presentations, and Posters

### A.1 Publications

- C. R. Cloutier, and D. P. Wilkinson, "Electrochemical Promotion of Aqueous Acidic Methanol PEM Electrolysis in Triode and Tetraode Operation", (submitted).
- C. R. Cloutier, and D. P. Wilkinson, "Triode Operation of a Proton Exchange Membrane (PEM) Electrolyser", ECS Transactions, 25 (23), (2010) 47-57.
- C. R. Cloutier, and D. P. Wilkinson, "Electrolytic Production of Hydrogen from Aqueous Acidic Methanol Solutions", Int. J. H<sub>2</sub> Energy, 35, (2010) 3967-3984.

### A.2 Presentations

- Hydrogen and Fuel Cells Conference, Hydrogen production, storage and utilisation – from nanomaterials to demonstrators, Presentation, (2011), Cancun, Mexico.
- Catalysis Society of South Africa (CATSA), Invited Keynote Presentation, (2011), Gauteng, South Africa.
- 3<sup>rd</sup> International Training School on the Electrochemical Promotion of Catalysis, Short Communication, (2009), Université Claude Bernard Lyon 1, Villeurbanne, Lyon, France.
- 216<sup>th</sup> ECS Meeting, Electrochemistry: Symposium on Interfacial Electrochemistry in Honour of Brian E. Conway, Presentation, (2009), Vienna, Austria.
- T. Jang, C. R. Cloutier, K. Matsuzawa, S. Mitsushima, and K.-I. Ota, Industrial Electrolysis Symposium, Presentation, (2008), Kobe, Japan.
- Department of Energy and Safety Engineering, Chemical Energy Laboratory Conference, Yokohama National University, Presentation, (2008), Yokohama, Kansai, Japan.

### A.3 Posters

- The Graduate University of Advanced Studies, JSPS Summer Program, Poster, June 20 (2008), Zushi, Kansai, Japan.
- 58<sup>th</sup> Annual Meeting of the International Society of Electrochemistry, Poster, September 9-14 (2007), Banff, AB, Canada.

## Appendix B: Methanol Electro-oxidation Mechanism

### B.1 Methanol electro-oxidation parallel pathways

The schematic representation of the parallel pathways for methanol electro-oxidation is described in Fig.

B.1.

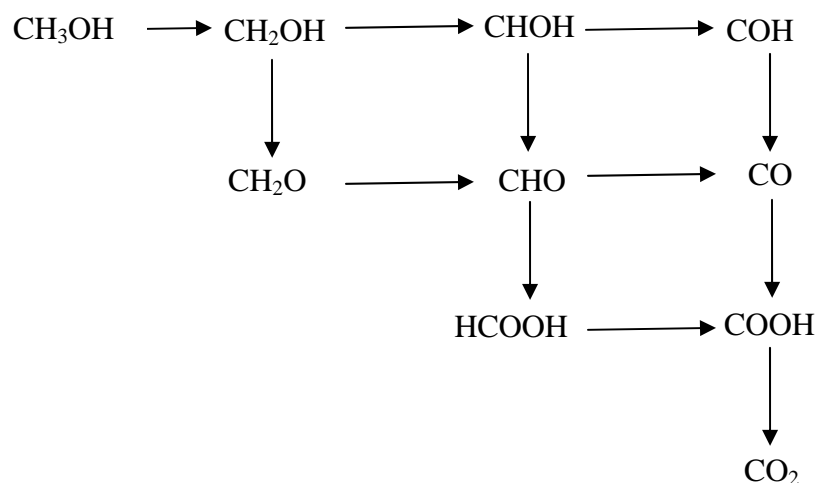
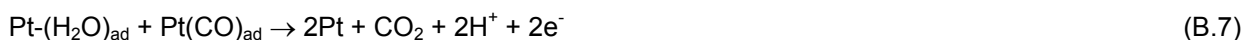


Figure B.1: Methanol electro-oxidation parallel pathways.

### B.2 Methanol electro-oxidation mechanism on Pt

The generally accepted reaction sequence of the mechanism of the electro-oxidation of methanol on Pt-based catalysts is described as follows [1].





### B.3 Methanol electro-oxidation mechanism on Pt-Ru

The bi-functional mechanism illustrating the enhancement effect of Pt-Ru on the electro-oxidation of methanol is described as follows [2].



The schematic representation of the bi-functional mechanism of Pt-Ru on the electro-oxidation of methanol is shown on Fig. B.2 [3].

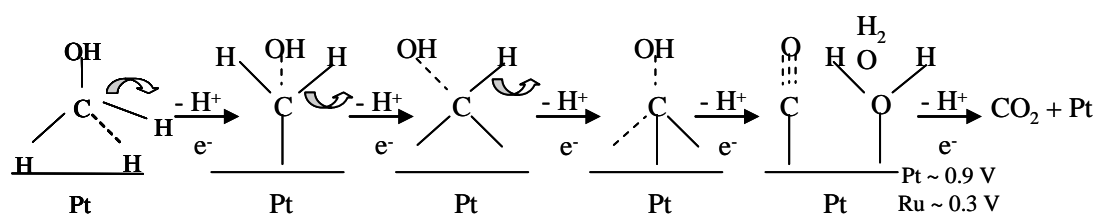


Figure B.2: Methanol electro-oxidation bi-functional mechanism on Pt-Ru.

### B.4 References

[1] N. A. Tapan, W. E. Mustain, B. Gurau, G. Sandi and J. Prakash, "Investigation of Methanol Oxidation Electrokinetics on Pt Using the Asymmetric Electrode Technique", *Journal of New Materials for Electrochemical Systems*, 7 (2004) pp. 281-286.

[2] T. Iwassita, H. Hoster, A. John-Anacker, W. F. Lin and W. Vielstich, "Methanol Oxidation on PtRu Electrodes. Influence of Surface Structure and Pt-Ru Atom Distribution", *Langmuir*, 16 (2000) p. 522-529.

[3] Presentation: "Nanostructured Architectures for Solar Energy and Beyond", Radiation Laboratory, Dept. of Chemical and Biomolecular Engineering, University of Notre Dame, Nore Dame, Indiana, 46556-0579.

## **Appendix C: Efficiency and Economic Comparison of H<sub>2</sub> Production**

### **C.1 Objective**

Determine the merits of the overall direct methanol electrochemical reforming system approach compared to other H<sub>2</sub> generation approaches. This will be accomplished by conducting a high level analysis composed of an efficiency and economic comparison of different methods of H<sub>2</sub> production.

### **C.2 System definition**

Hydrogen can be produced in various ways. In this study, three production process schemes for the manufacturing of H<sub>2</sub> are compared: electrolysis, catalytic steam reforming, and chemical hydride hydrolysis. Three fuels were considered: methanol, water, and sodium borohydride. These processes are only ecologically feasible if the fuels are originating from renewable resources. Hence, only production from renewable raw material sources was examined: biomass (methanol), water, and borax mineral ore (sodium borohydride). The four process combinations evaluated are: methanol PEM electrolysis or direct methanol electrochemical reforming (DMR), water PEM electrolysis, methanol catalytic steam reforming, and sodium borohydride hydrolysis. Other H<sub>2</sub> production processes and similar comparative studies have been provided elsewhere [1, 2].

### **C.3 Block Diagrams**

Block Diagrams of the H<sub>2</sub> production processes compared are shown in Fig. C.1. For the purpose of this high level evaluation, all processes were compared on a stationary basis and only the most important processing steps were considered. Purification processes such as water filtration and deionization, biosyngas purification and methanol sulphur removal, as well as passive devices such as liquid/gas separators were all ignored. In all cases, the end product is pure H<sub>2</sub> (99.9%). The produced H<sub>2</sub>

compression, storage and application requirements were not included in the analysis. The same applied for the pipelines and infrastructure required for the transportation of materials.

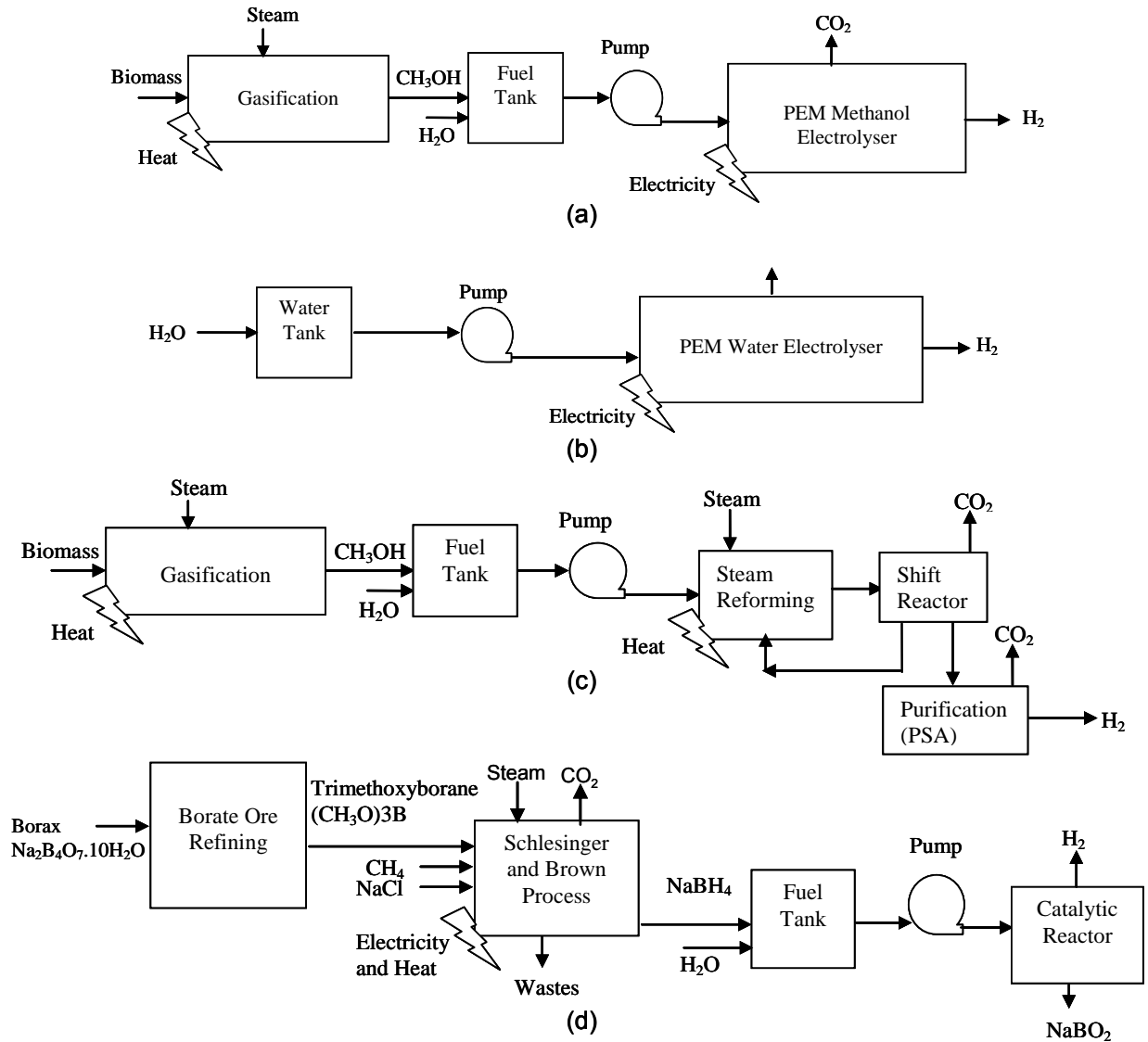


Figure C.1: Block diagrams of four  $H_2$  generation process schemes (a) PEM methanol electrolyser, (b) PEM water electrolyser, (c) methanol steam reforming, and (d) sodium borohydride hydrolysis.

## C.4 Feedstock processing

### C.4.1 Methanol production

Biomass is renewable organic matter available through natural processes or as a by-product of processes using renewable resources [3]. It represents a large potential feedstock for sustainable processes generating chemicals or electricity. The exact source of biomass was not specified. Pre-treatment of biomass feedstock typically includes processes such as drying and chipping which were not taken into account in this evaluation. After pre-treatment, the biomass is converted to biosyngas through sequential steps, which usually include a pressurized gasification, a gas conditioning, a catalytic reaction, and a distillation step. The gasification is the most crucial step and is the only process considered in this study. It is a thermochemical process usually carried at high temperature and pressure, during which all the biomass is converted to biosyngas. Indirect gasification is of interest for methanol synthesis as it does not require an oxygen plant [4]. The biosyngas produced requires cleaning as it contains contaminants. This purification process was ignored in the evaluation. Methanol is exothermically synthesised from the biosyngas as per:



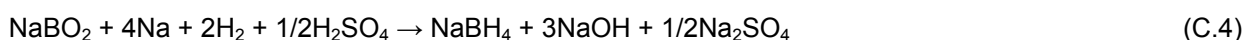
The overall production of methanol by the gasification of biomass can be described by the following general reaction:



The methanol generated contains water, and, as some side reactions are possible, it also contains minor amounts of by-products. For this reason, the methanol produced is usually purified to the required final purity by multistage distillation. Again, this purification step was not taken into account.

### C.4.2 Sodium borohydride production

Most NaBH<sub>4</sub> is produced by the Schlesinger and Brown process, which is based on the reduction of trimethoxyborane ((CH<sub>3</sub>O)<sub>3</sub>B) obtained from borate ore refining. The borate ore refining process is relatively simple and typically includes four basic steps to transform the raw ore into refined borates: dissolution, purification, crystallization and drying. The Schlesinger and Brown process is quite energy extensive as it includes the electrolysis of NaCl to produce Na and the catalytic steam reforming of methane to generate H<sub>2</sub>. The overall chemical reaction is:



The electrolysis of NaCl is the reaction step having the highest activation energy requirements and is the most energy consuming of the entire process [5]. There is also a large amount of by-products (Na<sub>2</sub>SO<sub>4</sub>), wastes (Cl<sub>2</sub>) and greenhouse gases (CO<sub>2</sub>) generated by the overall process.

### C.5 Hydrogen production

Table C.1 shows a high level comparison of the H<sub>2</sub> generation processes discussed below.

Table C.1: High level comparison of four H<sub>2</sub> generation process schemes.

| System Description                 | DMR                                                                               | PEM Water Electrolyser                                     | Methanol Steam Reformer                                                           | Sodium Borohydride                                                                                      |
|------------------------------------|-----------------------------------------------------------------------------------|------------------------------------------------------------|-----------------------------------------------------------------------------------|---------------------------------------------------------------------------------------------------------|
| System Type                        | Electrochemical                                                                   | Electrochemical                                            | Chemical                                                                          | Others                                                                                                  |
| Fuel                               | Methanol and water mixture                                                        | Pure Water                                                 | Pure Methanol                                                                     | NaBH <sub>4</sub> and water mixture                                                                     |
| Fuel Safety                        | Flammable                                                                         | Non-flammable                                              | Flammable                                                                         | Non-flammable                                                                                           |
| H <sub>2</sub> Production Reaction | $\text{CH}_3\text{OH} + \text{H}_2\text{O} \rightarrow \text{CO}_2 + 3\text{H}_2$ | $2\text{H}_2\text{O} \rightarrow 2\text{H}_2 + \text{O}_2$ | $\text{CH}_3\text{OH} + \text{H}_2\text{O} \rightarrow \text{CO}_2 + 3\text{H}_2$ | $\text{NaBH}_4 + 4\text{H}_2\text{O} \rightarrow 4\text{H}_2 + \text{NaBO}_2 \cdot 2\text{H}_2\text{O}$ |
| Operating T (°C)                   | 80                                                                                | 80                                                         | 270                                                                               | 90                                                                                                      |
| Start-up time                      | minutes                                                                           | minutes                                                    | 30 min.                                                                           | less than 30 seconds                                                                                    |
| Footprint                          | Small                                                                             | Small                                                      | Large                                                                             | Small                                                                                                   |
| CO <sub>2</sub> :H <sub>2</sub>    | 1:3                                                                               | -                                                          | 1:3                                                                               | -                                                                                                       |
| Type of CO <sub>2</sub> emissions  | Localized                                                                         | -                                                          | Non-localized                                                                     | Non-localized                                                                                           |
| Major Processing steps             | 2                                                                                 | 1                                                          | 4                                                                                 | 3                                                                                                       |

### C.5.1 Electrolysis

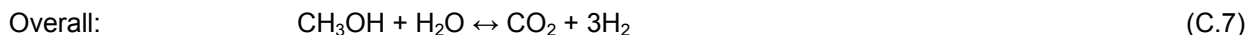
In general, PEM water electrolyzers are cleaner, safer and result in a higher H<sub>2</sub> purity than traditional water-alkaline electrolyzers. The PEM electrolysis of methanol will consume less electricity than the PEM electrolysis of water. This is based on the fact that the standard potential for the electro-oxidation of alcohol in the liquid phase is only 0.02 V vs. SHE for methanol, compared to the 1.23 V vs. SHE for the electro-oxidation of water. It was reported that the cost of methanol electrolysis is about half of the cost of water electrolysis, even when the cost of methanol is taken into account [6]. However, no details were provided on this calculation and the source used for the production of the methanol was not specified.

A drawback of methanol electrolysis over water electrolysis is that CO<sub>2</sub>, a greenhouse gas, is emitted while in water electrolysis useful O<sub>2</sub> is released. However, it is important to note that the CO<sub>2</sub> emissions

from the electrochemical reformer are localized and can be more easily controllable and captured than the non-localized emissions resulting from other processes.

### C.5.2 Catalytic steam reforming

The catalytic SR of methanol is an endothermic reaction carried out at temperatures between 250 and 350 °C which produces H<sub>2</sub> [7]. Ideally, the process starts by the splitting of methanol into CO and H<sub>2</sub> in the reformer. It is followed by the splitting of the water into H<sub>2</sub> and O<sub>2</sub> through the exothermal water gas shift (WGS) reactor, where CO is combined with O<sub>2</sub> to form CO<sub>2</sub>. The chemical reactions are:



The maximum H<sub>2</sub> production efficiency of 78 mol % was obtained for the SR reaction at 250 °C using a catalyst containing 27.8 wt% Cu and calcined at 700°C [8].

A gas clean-up sub-system is required to obtain pure H<sub>2</sub>. Pressure swing adsorption (PSA) is a cost-effective and reliable industrial process based on selective adsorbent beds, which is commonly used for the purification of H<sub>2</sub> from catalytic reformer off-gas. The gas mixture is introduced in the bed at an elevated pressure and the solid adsorbent selectively adsorbs certain components of the gas mixture. The un-adsorbed components pass through the bed as purified produced gas. Multiple beds are cycled in the process, allowing for the adsorbed pollutants to be periodically desorbed, cleaning the beds for the next cycle [9]. PSA results in pure H<sub>2</sub> (>99.9%) and has recovery rates of 90% or higher [4].

### **C.5.3 Sodium borohydride hydrolyser**

The overall reaction is exothermic and liberates 75 kJ/mole of H<sub>2</sub> formed at 25°C [10]. Hence, the reaction is very energetically favourable and no energy input is required to produce H<sub>2</sub>. The hydrolysis of NaBH<sub>4</sub> liberates a determined amount of H<sub>2</sub> at ambient temperature and pressure with no side reactions or by-product. The H<sub>2</sub> generation system comprises two storage tanks for NaBH<sub>4</sub> and NaBO<sub>2</sub> respectively, a pump, a catalyst chamber reactor, a liquid/gas separator, and a heat exchanger. The last two units were ignored in this evaluation. The release of H<sub>2</sub> from the NaBH<sub>4</sub> alkaline solution occurs by pumping the fluid mixture through a reactor containing a catalyst. The heat supplied by the exothermic reaction partially humidifies the H<sub>2</sub> gas by evaporating water. The H<sub>2</sub> produced contains less than 0.5 ppm of CO, and no NO<sub>x</sub> or SO<sub>x</sub> [5]. The H<sub>2</sub> is usually cooled down in a heat exchanger before being used.

### **C.6 Efficiency analysis**

The efficiency was estimated for each major processing step. The overall efficiency of the H<sub>2</sub> production process was obtained by multiplying the efficiency of the individual processing steps. It was assumed that the stoichiometry was one in all case, i.e. no feed was provided in an excess of the required stoichiometric amounts. The electrolyser current efficiencies were assumed to be equal to unity. Compression efficiencies were ignored. The efficiencies obtained from the literature represent various process conditions. For example, the range of efficiencies reported for water electrolysis varied from 30 to 90%. The results are summarized in Table C.2.

Table C.2: Efficiency comparison of four H<sub>2</sub> generation process schemes.

| Process                       | Major Steps                      | Efficiency (%) | Notes                                                                                                                          | Ref.        | Overall Efficiency (%) |
|-------------------------------|----------------------------------|----------------|--------------------------------------------------------------------------------------------------------------------------------|-------------|------------------------|
| Methanol Electrolyser         | Gasification from biomass        | 57             | Upper average of reported efficiencies                                                                                         | [11, 12]    | 36                     |
|                               | Liquid Pump                      | 90             |                                                                                                                                | [13]        |                        |
|                               | Electrolysis                     | 70             | Assumed methanol electrolyser would have an efficiency 10% higher than the water electrolyser due to higher energy efficiency. |             |                        |
| Water Electrolyser            | Liquid Pump                      | 90             |                                                                                                                                | [13]        | 54                     |
|                               | Electrolysis                     | 60             | Vary between 30 to 90%                                                                                                         | [14, 15-17] |                        |
| Methanol Steam Reforming      | Gasification from biomass        | 57             | Upper average of reported efficiencies                                                                                         | [11, 12]    | 30                     |
|                               | Gas Pump                         | 75             |                                                                                                                                |             |                        |
|                               | Steam reformer and shift reactor | 78             | 78% reported maximum, 77% generally accepted                                                                                   | [15, 8]     |                        |
|                               | PSA Purification                 | 90             |                                                                                                                                | [4]         |                        |
| Sodium Borohydride Hydrolysis | Borate refining                  | 55             |                                                                                                                                | [19]        | 22                     |
|                               | Schlesinger and Brown process    | 47             | Na manufacture energy efficiency of 50%, borohydride generation reaction yield of 94%                                          | [20]        |                        |
|                               | Liquid Pump                      | 90             |                                                                                                                                | [13]        |                        |
|                               | Catalytic reactor                | 93             | Fuel input volume efficiency of 95% and yield of H <sub>2</sub> of 98%                                                         | [13]        |                        |

The efficiency calculated indicates that the sodium borohydride hydrolysis process is the least efficient of the processes reviewed while water electrolysis is the most efficient of the process reviewed. The results give the general idea that the electrolysis processes are more efficient. However, due to the low efficiency of the gasification of biomass to generate methanol, the methanol electrolysis process fall behind the water electrolysis process.

If the storage and dispensing efficiency are taken into account the results would be significantly altered. The storage and dispensing efficiency was reported to be 65 % for H<sub>2</sub> and 99.8 % for methanol [15]. This would result in an overall efficiency of 35 % for H<sub>2</sub> electrolysis and of 36 % for methanol electrolysis. Hence, it might be appropriate to have the methanol production facility at a remote central location, and the methanol electrolyser at distributed locations. The water electrolysis would have to be at distributed locations, as the transport of hydrogen has a low efficiency.

## C.7 Economic analysis

The economic analysis was high level. No complex statistical or modelling methods were used to determine the individual contributions to the cost of H<sub>2</sub>. The cost of hydrogen production was simply broken down in the feedstock cost, the capital cost, the operation and maintenance cost and the carbon cost as per this basic formula:

$$C_{H_2} = C_{CAP} * FCR + C_{OM} + C_F / E_{ff} + C_C * P_C \quad (C.8)$$

where  $C_{H_2}$  is the hydrogen cost (\$/GJ),  $C_{CAP}$  is the capital cost (\$-y/GJ), FCR is the fixed charge rate on capital (1/y),  $C_{OM}$  is the operation and maintenance cost (\$/GJ),  $C_F$  is the feedstock cost (\$/GJ),  $E_{ff}$  is the efficiency (GJ of Hydrogen Produced / GJ of Potential Energy in Feedstock),  $C_C$  is the carbon tax (\$/ton C), and  $P_C$  is the carbon emissions (tons of C / GJ of hydrogen produced) [21].

The  $C_{CAP}$  includes only the cost of the essential equipment of the facility. The practical standard in capital cost evaluation in the energy industry is to include an interest rate of 8 %, depreciation period of 15 years, i.e., about 50 % of the expected technical lifetime of the plant. However, for the purpose of this high level analysis, the FCR, which encompasses the investment return rate, income taxes, insurance charges, interest during construction, start-up expenses, working capital and other costs, was assumed to be equal to one. Little if any information pertaining to the  $C_{OM}$ , i.e., operating and maintenance costs, could be found in the literature, and these costs were not considered. The efficiency effect on the

feedstock costs was neglected and the  $E_{ff}$  value was assumed to be unity. The resulting simplified formula is as follows:

$$C_{H_2} = C_{CAP} * FCR + C_F + C_E + C_C * P_C \quad (C.9)$$

where  $C_E$  is the energy cost (\$/GJ). A cost should also be added to take the cost of waste disposal into account as well as the credits for any useful by-products resulting from the process. However, as these costs are difficult to establish, they were neglected in this simple cost analysis.

Cost estimates for each component were found from the literature. There is a wide range of costs reported in the literature as they are all based on different assumptions. Major factors affecting the  $H_2$  production cost include the feedstock and the energy source from which the  $H_2$  is produced, the size of the  $H_2$  production facility and the transportation requirements for delivery it to the customer, the state of the technology used, and whether or not the  $CO_2$  by-product is sequestered.

In this simplified cost analysis, it is assumed that all electricity is generated from hydro-electric power plants and does not include any costs associated with the various hydro-electric power plant capacities and unit operation sizes. The  $H_2$  production plant cost is proportional to its capacity, and plants with smaller footprints should result in lower real-estate, installation and maintenance costs. However, these issues were not taken into account in this analysis. The cost estimate values found from the different studies were assumed to be all on the same plant capacity basis. Furthermore, no costs associated with transportation were taken into account.

Lastly, the cost estimates were not adjusted to current dollar amounts using inflation rates and the costs were not normalized to the current year. They were left in the year of publication of the data. Historical correction of the currency conversion between US\$ and CAN\$ was not conducted and it was assumed that 1\$US was equal to 1\$CAN. Units were converted from \$/kg  $H_2$  produced to \$/GJ or vice-versa using the energy density of  $H_2$ , which is about 120000 KJ/kg  $H_2$ .

### C.7.1 Capital cost

The capital cost of an electrolyser depends on its H<sub>2</sub> generation capacity and its rated current density [22]. The cost of commercial PEM water electrolysers vary from 13 to 159 \$/GJ depending on the size of the unit [23]. For a distributed plant, the cost of water electrolysis was reported as being between 7.36 and 6.82 \$/kg H<sub>2</sub> [16]. This leads to an average of 59.08 \$-y/GJ. It was assumed that the capital cost of the PEM methanol electrolyser would be very similar to that of the PEM water electrolyser. The capital cost of methanol production from biomass by thermal gasification and by supercritical water gasification are 1.5 and 4.5x10<sup>3</sup> US\$/kW, respectively [11]. This results in an average capital cost of 95.13 \$/GJ. The capital cost of H<sub>2</sub> production by methanol reforming is reported as 4.65x10<sup>3</sup> US\$/kW [11]. This is equivalent to 28.54 \$/GJ. For simplicity, it will be assumed that the steam reformer, the shift reactor and the PSA unit are all included in this cost.

As described earlier, the extraction and production of borates is quite simple and the mining costs only vary by the depth of the pit and the amount of overburden to be removed to expose the ore [24]. However, one of the most difficult things to determine in the borate market is the cost of production of each supplier. About 75 % of the borate market is controlled by its two major producers, and there are strong indications that capacity is restricted and there is collusion on pricing [25]. For this reason, the capital cost associated with borate mining was ignored in this high level cost estimate. The capital cost needed for the production of NaBH<sub>4</sub> through the Schlesinger and Brown process could not be found in the literature. However, it is expected to be very high as it includes an electrolyser, a reformer and a reactor. For estimation purposes, the electrolyser was assumed to be the same cost as the PEM water electrolyser, the reformer and the reactor the same as the methanol steam reformer. This would result in a capital cost estimate of 116.16 \$/GJ. The cost of the hydrolysis reactor could not be found in the literature either as it is a new technology still under development. For estimation purposes, it was assumed as being a third of the cost of the PEM water electrolyser as it is a one chamber reactor, does not contain any membrane and likely uses non-noble catalyst. This would give an estimated capital cost of 19.19 \$/GJ.

### C.7.2 Feedstock cost

The cost of methanol made from biomass was reported as being 75 US\$/MWh or 20.83 US\$/GJ [26]. In all cases, it was assumed that the cost of water usage and water demineralization was negligible. The listed price of NaBH<sub>4</sub> is about \$50US/kg for industrial quantities. Based on this feed price, it would cost \$230US to produce 1 kg of H<sub>2</sub> from NaBH<sub>4</sub>. This is equivalent to 19166.67 \$/GJ.

### C.7.3 Energy cost

All electricity was assumed to originate from hydroelectric power plants. The cost of electricity at BC Hydro is about 0.05 \$/kWh [27]. The energy requirements for water electrolysis was reported to be between 53.4 and 70.1 kWh/kg of H<sub>2</sub> produced [16]. Taking the average and using the assumed electricity cost, this results in an energy cost of 25.67 \$/GJ. Based on the preliminary experiments conducted, there is about 1 V difference between the voltage that needs to be supplied for the electrolysis of methanol compared to the voltage required for the electrolysis of water at the same conditions. Hence, for estimation purposes, the methanol electrolyser was assumed to cost about 1/3 of the energy cost of the water electrolyser, i.e. 8.56 \$/GJ.

The energy requirement of the gasification process largely depends on the type of biomass used. In some cases, the net electrical output is null or positive [12]. This is because the gross electricity produced by gas turbine and/or steam turbine can be equal or greater than the internal electricity use from pumps, compressors, oxygen separator, and other units operations. An average value of 28.78 kWh/GJ was calculated based on the electricity requirements of four different types of gasifiers [28]. Using the assumed electricity cost, this results in an energy cost of 1.44 \$/GJ. No values could be found for the energy requirements of the methanol steam reforming process. Hence, a generic energy requirement value of 40 kWh/kg H<sub>2</sub> produced, based on hydrocarbon steam reforming, was used. This corresponds to a cost of 166.66 \$/GJ.

The most energy consuming process of the manufacture of NaBH<sub>4</sub> is the electrolysis of Na. The electrolysis of Na requires 9.7 kWh per kg of Na produced [29]. As it takes 4 moles of Na to produce one

mole of  $\text{NaBH}_4$ , which in turn can produce 4 moles of  $\text{H}_2$ , this results in 111.55 kWh/kg  $\text{H}_2$ . Based on the electricity cost, and converting using the energy density of  $\text{H}_2$ , this can be converted to an energy cost of 464.79\$/GJ. It was assumed that the catalytic reactor does not require any energy input as the sodium borohydride hydrolysis reaction is exothermic.

#### **C.7.4 Carbon cost**

The emissions from manufacturing the  $\text{H}_2$  production facility become of interest when renewable resources are used. Cost of the renewable  $\text{H}_2$  production paths becomes more comparable when the cost of environmental damage is taken into account. This cost can be evaluated by assuming a carbon tax or by estimating the capture and sequestration cost of  $\text{CO}_2$ . Capture and sequestration only makes economical sense if it costs less than the imposed cost of releasing carbon to the atmosphere. The cost of  $\text{CO}_2$  sequestration includes the costs for drying and compressing the  $\text{CO}_2$  to the pressure required for  $\text{CO}_2$  transport and injection, the costs of pipelines for transporting the  $\text{CO}_2$  to the sequestering sites and the costs for wells and surface facilities at the storage sites [30]. For simplicity, a carbon tax,  $C_C$ , of 20 \$/tonC was assumed in this high level cost analysis.

As the quantity of  $\text{CO}_2$  emitted from the electric power generation plants was not taken into account, the water electrolyser system results in no  $\text{CO}_2$  emissions. The total emissions resulting from the production of methanol from biomass, i.e. emission from fuel extraction, transportation and conversion was reported as 30 gC/kWh or 0.08 tonC/GJ [27]. Using the carbon tax, this can be converted to a carbon cost of 1.66 \$/GJ. As the methanol electrolyser and the methanol steam reforming have the same overall reaction, the total carbon emissions can be assumed to be similar in both cases if the efficiencies are not taken into account. Based on a feed stoichiometry of 1, there will be one mol of  $\text{CO}_2$  produced for every three moles of  $\text{H}_2$  generated. This represents an emission rate of 7333 g  $\text{CO}_2$  per kg  $\text{H}_2$  or 0.61 tonC/GJ, which results in a carbon cost of 12.22 \$/tonC. In the Schlesinger and Brown process, four moles of  $\text{H}_2$  are needed to generate one mole of  $\text{NaBH}_4$ . It can be that the  $\text{H}_2$  used originates from the steam reforming of bio-methanol. In this case, for the four moles of  $\text{H}_2$  needed to generate a mole of  $\text{NaBH}_4$ , there will be 1.33 mol of  $\text{CO}_2$  produced. This still results in a  $\text{CO}_2$  emission rate of 0.61 tonC/GJ or a carbon cost of 12.22 \$/ton C.

### C.7.5 Economic analysis summary

The results of the simplified cost analysis are shown in Table C.3. It gives a general idea of the relative cost ranking of the different processes. As expected, the most expensive H<sub>2</sub> production process is the sodium borohydride hydrolysis, followed by the methanol steam reforming process, the methanol electrolysis and the water electrolysis, which is the cheapest.

The H<sub>2</sub> production cost could play a key role in deciding which of the process evaluated has an overall advantage. It appears that the cost of the methanol electrolysis process would cost about twice the cost of water electrolysis. This cost difference is largely due to the fact that producing H<sub>2</sub> from a sustainable biomass based methanol is substantially higher than producing H<sub>2</sub> from the electrolysis of water. The most interesting outcome of this high level economic analysis is that it revealed that the methanol and water electrolysis H<sub>2</sub> production cost could meet the 2008 US DOE H<sub>2</sub> pre-tax target at refuel pump station is \$US3/kg H<sub>2</sub> or \$US250/GJ [31].

Table C.3: Cost comparison of four H<sub>2</sub> generation process schemes.

| Process                       | Major Steps                        | C <sub>CAP.FCR</sub><br>(\$/GJ) | C <sub>F</sub><br>(\$/GJ) | C <sub>E</sub><br>(\$/GJ) | C <sub>C</sub> * P <sub>C</sub><br>(\$/GJ) | C <sub>H2</sub><br>(\$/GJ) |
|-------------------------------|------------------------------------|---------------------------------|---------------------------|---------------------------|--------------------------------------------|----------------------------|
| Methanol Electrolyser         | Methanol from biomass              | 95                              | 21                        | 1                         | 2                                          | 199                        |
|                               | Electrolysis                       | 59                              |                           | 9                         | 12                                         |                            |
| Water Electrolyser            | Electrolysis                       | 59                              | -                         | 26                        | -                                          | 85                         |
| Methanol Steam Reforming      | Methanol from biomass              | 95                              | 21                        | 1                         | 2                                          | 326                        |
|                               | Steam reformer, shift reactor, PSA | 29                              |                           | 167                       | 12                                         |                            |
| Sodium Borohydride Hydrolysis | Schlesinger and Brown process      | 116                             | 19167                     | 465                       | 12                                         | 19779                      |
|                               | Catalytic reactor                  | 19                              |                           | -                         |                                            |                            |

## C.8 Conclusion

The electrolysis of methanol or the direct methanol electrochemical reformer might represent an economical way to produce H<sub>2</sub> for use in PEM fuel cells and other energy-consuming systems under certain conditions and might be more suitable for portable applications rather than stationary ones. However, considering the high level of this comparison and the large number of assumptions made to carry out this efficiency and economic analysis, there is some uncertainty in the estimated values, and one should be cautious in ranking the concepts compared based on this evaluation. A more precise evaluation would include mass and heat balance modelling of each H<sub>2</sub> generation process flow sheets, using Hysis or Aspen. Based on the resulting dimensions of the unit operations, a proper statistical economic analysis could be carried out. However, this type of detailed analysis lies outside of the scope of the proposed doctorate thesis.

## C.9 References

- [1] J. M., Ogden, M. M. Steinbugler, T. G. Kreutz, A comparison of hydrogen, methanol, and gasoline as fuels for fuel cell vehicles: implications for vehicle design and infrastructure development, *J. Power Sources*, 19, (1999) 143-168.
- [2] R. G. Lemus, and J. M. M. Duart, Updated hydrogen production costs and parities for conventional and renewable technologies, *International J. of H<sub>2</sub> energy*, in press, (2010) 1-8.
- [3] D. A. Bowen, F. Lau, R. Zabransky, R. Remick, R. Slimane, S. Doong, and M. Paster, "Techno-Economic Analysis of Hydrogen Production by Gasification of Biomass", *Hydrogen, Fuel Cells, and Infrastructure Technologies*, Progress Report, (2003) 4 pp.
- [4] D. C. C. Barranon, "Methanol and Hydrogen Production, Energy and Cost Analysis", Master's Thesis, Department of Applied Physics and Mechanical Engineering, Division of Energy Engineering, (2006) 58 pp.
- [5] R. M. Mohring, and Y. Wu, *American Institute of Physics Conference Proceedings*, 671, (2003) 90-100.
- [6] Z. Hu, M. Wu, Z. Wei, S. Song and P. K. Shen, "Pt-WC/C as a Cathode Electrocatalyst for Hydrogen Production by Methanol electrolysis", *J. Power Sources*, 166, (2007) 458-461.
- [7] J. W. Phair and S. P. S. Badwal, "Review of Proton Conductors for Hydrogen Separation", *Ionics*, 12, (2006) 103-115.
- [8] R. O. Idem and N. N. Bakhshi, "Primary: Production of Hydrogen from Methanol. 2. Experimental Studies", *Industrial Engineering Chemistry Research*, 33(9), (1994) 2056-2065.
- [9] D. B. Myers, G. D., Ariff, B. D. James, J. S. Lettow, C. E. Thomas and R. C. Kuhn, "Cost and Comparison of Stationary Hydrogen Fuelling Appliances", *Proceedings of the 2002 US DOE Hydrogen Program Review*, NREL/CP-610-32405, (2002) 8 pp.
- [10] S. C. Amendola, S. L. Sharp-Goldman, M. Saleem Janjua, N. C. Spencer, M. T. Kelly, P. J. Petillo, and M. Binder, "A Safe, Portable, Hydrogen Gas Generator using Aqueous Borohydride Solution and Ru Catalyst", *Int. J. H<sub>2</sub> Energy*, 25, (2000) 969-975.
- [11] Y. Yoshisa, K. Diwaki, Y. Matsumura, R. Matsushashi, D. Li, H. Ishitani, and H. Komiyama, "Comprehensive comparison of efficiency and CO<sub>2</sub> emissions between biomass energy conversion technologies - position of supercritical water gasification in biomass technologies", *Biomass and Energy*, 25, (2003) 257-272.
- [12] C. N. Hamelinck, and A. P. C. Faaij, "Future Prospects for Production of Methanol and Hydrogen from Biomass", *J. Power Sources*, 111, (2002) 1-22.
- [13] D. Gervasio, "Fuel Cell for Hand-Carried Portable Power", Presentation, Arizona State University, Incheon, Korea (2005).
- [14] J. Larminie, and A. Dicks, "Fuel Cell Systems Explained", John Wiley & Sons Ltd., UK, Second Edition, (2003), 406 pp.
- [15] K. A. Adamson, P. Pearson, "Hydrogen and Methanol: A Comparison of Safety, Economics, Efficiencies and Emissions", *J. Power Sources*, 86, (2000) 548-555.
- [16] A. Haryanto, S. Fernando, N. Murali, and S. Adhikari, "Current Status of Hydrogen Production Techniques by Steam Reforming of Ethanol: A Review", *Energy and Fuels*, 19 (2005).

- [18] M. A. Rosen, "Thermodynamic Investigation and Comparison of Selected Production Processes for Hydrogen and Hydrogen-Derived Fuels", *Energy*, 21(12), (1996) 1079-1094.
- [19] BCS, Incorporated, U.S. Department of Energy, Office of Energy Efficiency and Renewable Energy, "Mining, Industry of the Future, Energy and Environmental Profile of the US Mining Industry", Chapter 3, Potash, Soda Ash and Borates, (2002) 3-1.
- [20] Y. Wu, M. T. Kelly, and J. V. Ortega, "Review of Chemical Processes for the Synthesis of Sodium Borohydride", Millennium Cell Inc., Under DOE Cooperative Agreement DE-FC36-04GO14008, (2004) 21 pp.
- [21] G. Brinkman, "Economics and Environmental Effects of Hydrogen Production Methods", (2003) 29 pp.
- [22] T. Oi, and K. Wada, "Feasibility Study on Hydrogen Refuelling Infrastructure for Fuel Cell Vehicles Using the Off-peak Power in Japan", *Int. J. H<sub>2</sub> Energy*, 29, (2004) 347-354.
- [23] C.E.G. Padro, and V. Putsche, "Survey of the Economics of Hydrogen Technologies", National Renewable Energy Laboratory, NREL/TP-570-27079, (1999).
- [24] V.C.Y. Kong, F. R. Foulkes, D.W.Kirk, J.T. Hinatsu, *Int. J. H<sub>2</sub> Energy*, 24, (1999) 665-675.
- [25] P.S.E. Cave, "Why the borate industry must respond to the market in order to avoid substitution", *Editörün Görüşü*, (2007), <http://www.boraxtr.com/boraxtr/Etihol/cave2.htm>.
- [26] B. Johansson, "The Economy of Alternative Fuels when Including the Cost of Air Pollution", *Transportation Research, Part D4*, (1999) 91-108.
- [27] BC Hydro for Generations - Involvement in Education, [http://www.bchydro.com/education/8-12/8-12\\_2676.html](http://www.bchydro.com/education/8-12/8-12_2676.html).
- [28] R. H. Williams, E. D. Larson, R. E. Katofsky, and J. Chen, "Methanol and Hydrogen from Biomass for Transportation", *Energy for Sustainable Development*, 1, (1995) 18-34.
- [29] Y. Wu, "Hydrogen Storage via Sodium Borohydride", Presentation, GCEP Hydrogen Workshop, Stanford University, CA, USA, (2003), [http://gcep.stanford.edu/pdfs/hydrogen\\_workshop/Wu.pdf](http://gcep.stanford.edu/pdfs/hydrogen_workshop/Wu.pdf).
- [30] R. U. Ayres, and P. M. Weaver, "Eco-Restructuring: Implications for Sustainable Development", United Nations University Press, (1998), <http://www.unu.edu/unupress/unupbooks/uu24ee/uu24ee0f.htm>.
- [31] Department of Energy (DOE), "Controlled H<sub>2</sub> Fleet and Infrastructure Demonstration and Validation Project", Draft Revision 3, (2003) A1-A25.

## Appendix D: Supplemental EPOC and EPOE Theory

### D.1 EPOC rules

Promoters are usually not consumed during a catalytic reaction. If a promoter is consumed, it is referred too as a sacrificial promoter. An electropositive promoter is an electron donor and causes a decrease in the catalyst work function, while an electronegative promoter is an electron acceptor and causes an increase in the catalyst work function. Some of the most important EPOC rules are listed below [1]:

Rule 1: Electropositive (electron donor) promoters enhance the chemisorption of electron acceptor adsorbates and weaken the chemisorption of electron donor adsorbates.

Rule 2: Electronegative (electron acceptor) promoters enhance the chemisorption of electron donor adsorbates and weaken the chemisorption of electron acceptor adsorbates.

Rule 3: In the presence of a strong electron donor (electropositive) adsorbate (e.g. K, Na) a weaker electron donor (e.g. NO on Pt(111)) behaves as an electron acceptor.

Rule 4: In the presence of a strong electron acceptor (electronegative) adsorbate (e.g. O) a weaker electron acceptor (e.g. CO on Pt(111)) behaves as an electron donor.

Rule P1: If a catalyst surface is predominantly covered by an electron acceptor reactant (e.g. O) then an electron acceptor promoter (e.g.  $O^{2-}$ ) is recommended.

Rule P2: If a catalyst surface is covered predominantly by an electron donor reactant (e.g.  $C_6H_6$ ,  $C_2H_4$ ), than an electron donor promoter (e.g.  $Na^+$ ) is recommended.

Rule P3: If both reactants are weakly adsorbed on the catalyst surface, then both electron acceptor and electron donor promoters can enhance the rate.

Rule F1: Increasing work function (via the addition of electronegative promoters) strengthens the chemisorptive bond of electron donor adsorbates and weakens the chemisorptive bond of electron acceptor adsorbates.

Rule F2: Decreasing work function (via the addition of electropositive promoters) weakens the chemisorptive bond of electron donor adsorbates and strengthens the chemisorptive bond of electron acceptor adsorbates.

Rule G1: A reaction exhibits purely electrophobic behaviour when the kinetics are positive order in the electron donor reactant and negative or zero order in the electron acceptor reactant.

Rule G1': A reaction exhibits purely electrophobic behaviour when the electron acceptor reactant is strongly adsorbed and much more strongly adsorbed on the catalyst surface than the electron donor reactant.

Rule G2: A reaction exhibits purely electrophilic behaviour when the kinetics are positive order in the electron acceptor reactant and negative or zero order in the electron donor reactant.

Rule G2': A reaction exhibits purely electrophilic behaviour when the electron donor reactant is strongly adsorbed and much more strongly adsorbed on the catalyst surface than the electron acceptor reactant.

Rule G3: A reaction exhibits volcano-type behaviour when both the electron donor and electron acceptor are strongly adsorbed on the catalyst surface.

Rule G4': A reaction exhibits inverted volcano-type behaviour when the kinetics are positive order in both the electron acceptor and the electron donor reactant.

Rule G5: The above rules G1-G4 apply also when the electron donor and the electron acceptor are both electron acceptors or electron donors. In this case the electron donor is always the stronger electron donor or weaker electron acceptor and the electron acceptor is always the weaker electron donor or stronger electron acceptor.

Rule G6: A mononuclear reaction is electrophobic for an electron donor adsorbate and electrophilic for an electron acceptor adsorbate.

Rule G7: The maximum rate modification obtained under electrochemical promotion conditions increases for every fixed overpotential with increasing difference in the electron acceptor-electron donor character of the two reactants.

## **D.2 Chemisorption on a transition metal**

When adsorbed on a transition metal, CO can exhibit electron acceptor or electron donor characteristics. The example illustrated in Fig. D.1 is based on quantum mechanical calculations [2]. Fig. D.1 (a) shows the sp and d bands of a transition metal, such as Pt, i.e., the density of states (DOS) as a function of electron energy,  $E$ . The outer orbital energy levels of a gaseous CO molecule is also shown: orbitals  $4\sigma$ ,  $1\pi$  and  $5\sigma$  are occupied as indicated by the arrows, while orbital  $2\pi^*$  is empty [2]. The geometry of these molecular orbitals is shown in Fig. D.1 (b). Fig. D.1 (c) and (d) show the energy and density of states of the resonances (adsorbed molecular orbitals) formed upon CO adsorption due to the interaction of the  $2\pi^*$  orbitals and  $5\sigma$  orbitals with the metal surface [2].

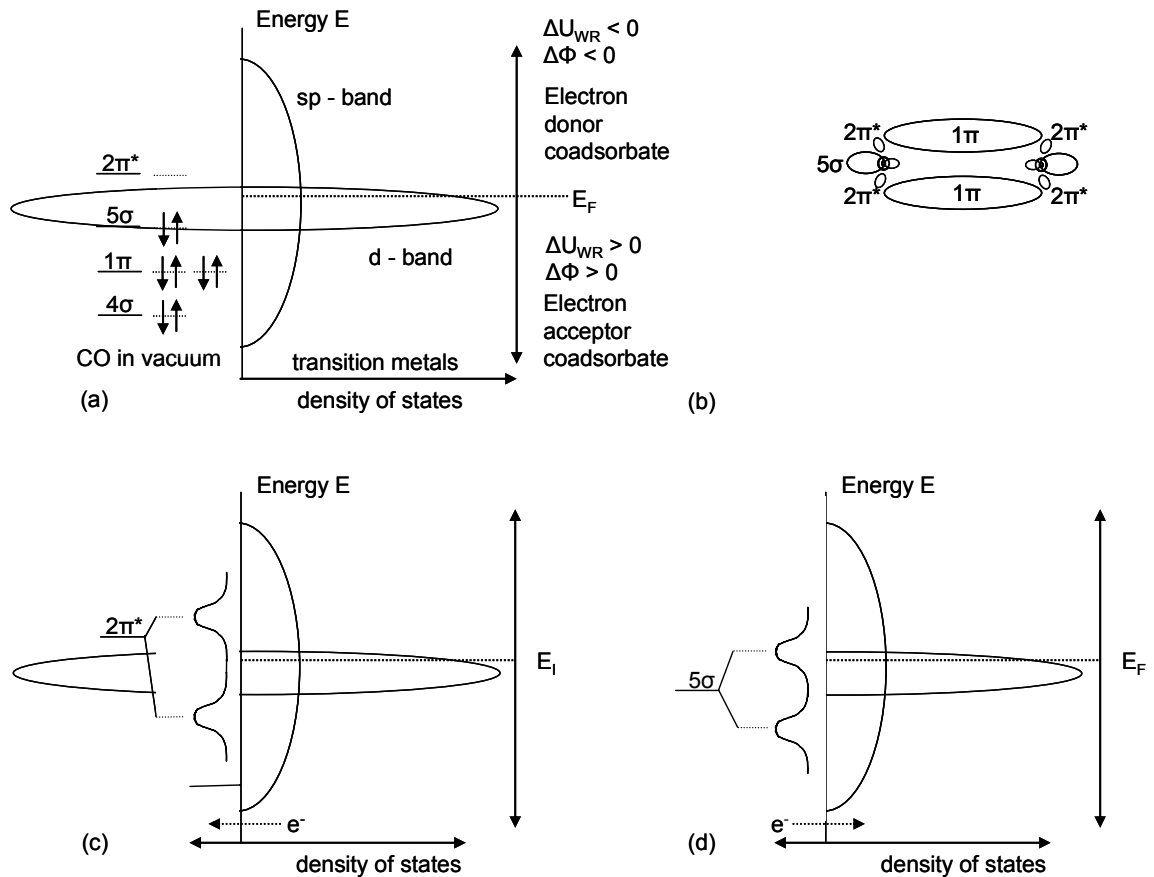


Figure D.1: CO chemisorption on a transition metal. Molecular orbitals and density of states before (a, b) and after (c, d). Effect of varying  $\Phi$  and  $E_F$  on electron back donation (c) and donation (d) (Modified from Vayenas *et al.* [1] with permission from Springer).

Fig. D.1 (c) shows the electron backdonation interaction, i.e., electrons are transferred from the Fermi level of the metal to the hybridized  $2\pi^*$  molecular orbital which was originally [2]. Fig. D.1 (d) shows the electron donation interactions, i.e., electrons are transferred from the initially fully occupied  $5\sigma$  molecular orbitals to the Fermi level of the metal [2]. Fig. D.1 (c), demonstrates the electron acceptor character for which  $E_F$  decreases and  $\Phi$  increases. Lowering the work function or increasing the Fermi level enhances electron backdonation to the  $2\pi^*$  orbitals and diminishes electron donation from the  $5\sigma$  orbitals. Fig. D.1 (d) demonstrates the electron donor character for which  $E_F$  increases and  $\Phi$  decreases. It is now experimentally and theoretically established that CO behaves as an electron acceptor on most

transition metal surfaces [2]. The enhance backdonation of electrons to the  $2\pi^*$  orbitals results in a strengthening of the Pt=CO bond, which eventually may lead to the weakening in the C=O bond [2].

### D.3 Kirchhoff's first law for triode and tetrode operation

Equation 3.1 originates from the one used in triode fuel cell operation [3]. For the case of parallel electrolysis operation, the sign of the electrolyser current would be the same as the sign of the auxiliary circuit current (+). In triode operation, the electrolyser current would be greater than in normal electrolysis. In the case of reverse electrolysis operation, the sign of the electrolyser circuit current (+) would be opposite to the sign of the auxiliary circuit current (-). According to this, in triode operation, the electrolyser circuit current would be less than that in normal electrolysis.

Please note that in Eq. 3.1, the Faradaic current was defined as the total fuel-consuming current and not a cathodic current as the reviewer is suggesting. It is stated in the paper that this equation is based on Kirchhoff's first law. According to this law, the current entering a point must be equal to the current leaving the point. The current always flow from the positive terminal to the negative one. The triode and tetrode diagrams below (Fig. D.3.2 to D.3.5) illustrate how Eq. 3.4 was derived for the fuel cell and electrolyser cases.

#### D.3.1 Triode fuel cell

In a fuel cell, the anode is negative, the cathode is positive and current is generated at the  $WE_{fc}$  (out).

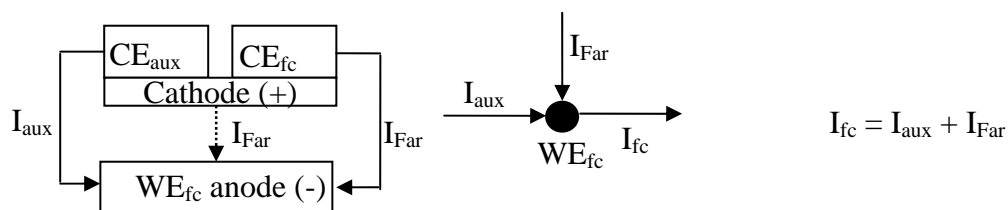


Figure D.2: Application of Kirchhoff's first law for fuel cell triode operation.

### D.3.2 Triode electrolyser

In electrolysis, the anode is positive, the cathode is negative and current is needed at the WE<sub>elec</sub> (in).

Taking into account the signs, for parallel operation, the auxiliary current and the electrolyser current are both positive.

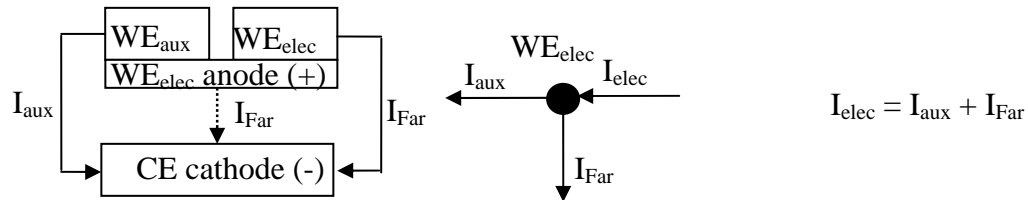


Figure D.3: Application of Kirchhoff's first law for triode electrolysis in parallel operation.

In reverse operation, the electrolyser current is positive and the auxiliary current is opposite.

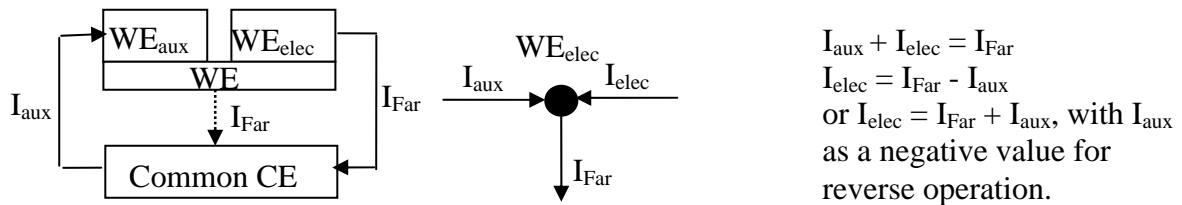


Figure D.4: Application of Kirchhoff's first law for triode electrolysis in reverse operation.

### D.3.3 Tetraode electrolyser

In reverse tetraode operation, the electrolyser current is positive and the auxiliary current is opposite, like in the reverse triode case. The only difference is that two separate counter electrodes are used and that the electrolyser and the auxiliary circuits are completely independent.

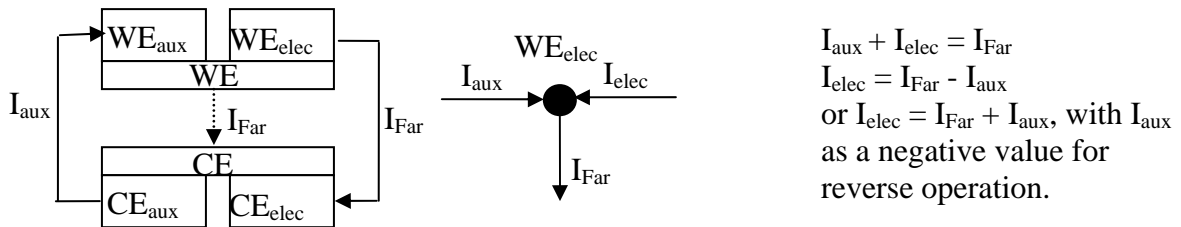


Figure D.5: Application of Kirchhoff's first law for tetrode electrolysis in reverse operation.

#### D.4 References

- [1] C. G. Vayenas, S. Bebelis, C. Pliangos, S. Brosda and D. Tsiplakides, "Electrochemical Activation of Catalysis - Promotion, Electrochemical Promotion and Metal-Support Interactions", Kluwer Academic / Plenum Publishers, (2001) 574 pp.
- [2] M. T. M. Koper, and R. A. van Santen, "Electric field effects on CO and NO adsorption at the Pt(111) surface", J. Electroanal. Chem., 476, (1999) 64-70.
- [3] S. P. Balomenou, and C. G. Vayenas, Triode Fuel Cells and Batteries, Journal of The Electrochemical Society, 151 (11), (2004) A1874-A1877.

## Appendix E: Experimental procedures

### E.1 Catalyst electrode preparation

#### E.1.1 Cathode carbon sublayer composition calculation

1. Choose a desired carbon sublayer loading ( $L_{Csub}$ ). It is typically 1 mg/cm<sup>2</sup>
2. Choose the fraction of PTFE required ( $f_{PTFE}$ ). It is typically 20 wt% (i.e. 0.2)
3. Calculate the amount of carbon ( $m_{carbon}$ ) required. For the automated sprayer allow for an excess of 2x, for hand spraying allow for an excess of 3x

$$m_{Carbon} (g) = 2 L_{Csub} A_{Geom} \left( \frac{1g}{1000 mg} \right) \quad (E.1)$$

4. Calculate the amount of PTFE solution required. PTFE solution typically supplied at 60%

$$m_{PTFE\_Sol} (g) = \frac{f_{PTFE} m_{Carbon}}{1 - f_{PTFE}} \left( \frac{1}{0.6} \right) \quad (E.2)$$

5. Clean an appropriate-sized beaker with isopropanol
6. Using an analytical balance, weigh the amount of carbon and PTFE solution calculated in step 3. & 4. and add to the beaker
7. Add water and isopropanol to the beaker
8. Follow the procedure for the automated sprayer
9. Oven dry for 40 min. at 350°C

Table E.1: Cathode carbon sublayer calculation spreadsheet.

| Carbon in Sublayer Required           | Cathode |                      |
|---------------------------------------|---------|----------------------|
| Desired Loading [mg/cm <sup>2</sup> ] | 1       |                      |
| Area [cm <sup>2</sup> ]               | 121     |                      |
| Carbon [wt%]                          | 1       | pure carbon powder   |
| Excess                                | 3       | hand spraying excess |
| m carbon [g]                          | 0.363   |                      |

| PTFE in Sublayer Required | Cathode |                      |
|---------------------------|---------|----------------------|
| Desired f PTFE            | 0.2     |                      |
| % PTFE in Solution        | 0.6     | bottle specification |
| m PTFE [g]                | 0.15125 |                      |

| Final Mass of GDL w/ Sublayer        | Cathode |                   |
|--------------------------------------|---------|-------------------|
| m GDE (initial) [g]                  | 2.12196 | weight            |
| m GDE (final) [g]                    | 2.27321 | target mass       |
| m GDE (Actual) [g]                   | 2.25556 | mass after drying |
| Actual Loading [mg/cm <sup>2</sup> ] | 0.88331 |                   |

### E.1.2 Anode and cathode catalyst ink composition calculation

1. Choose a desired catalyst loading ( $L_{cat} = \text{mg/cm}^2$ ) and Nafion® wt% ( $f_{Nafion}$ )
2. Calculate the amount of supported catalyst ( $m_{cat-VulcanXCR}$ ) based on the total weight percentage of the purchased catalyst. For the automated sprayer allow for an excess of 2x, for hand spraying allow for an excess of 3x

$$m_{Cat-VulcanXCR} (g) = 2 L_{cat} A_{Geom} \left( \frac{1}{Wt \%_{cat}} \right) \left( \frac{1 g}{1000 mg} \right) \quad (E.3)$$

3. Calculate the amount of Nafion® solution required. Nafion® solution typically supplied as 5 wt%

$$m_{Naf-Sol} (g) = \frac{f_{Nafion} m_{Cat+VulcanXCR}}{1 - f_{Nafion}} \left( \frac{1}{0.05} \right) \quad (E.4)$$

4. Clean an appropriate sized beaker with isopropanol

5. Using an analytical balance, weigh the amount of catalyst calculated in step 2. and add to the beaker
6. Add enough DI water to cover the supported catalyst powder
7. Using an analytical balance, weigh the amount of Nafion<sup>®</sup> solution calculated in step 3. and add to the beaker
8. Add isopropanol to the beaker
9. Sonicate the catalyst ink solution for 90 minutes
10. Follow the procedure for the automated sprayer
11. Mass of substrate with loading can be expressed by the following:

$$m_{GDE,f} (g) = \frac{L_{cat} \times A_{Geom}}{1000mg \times Wt\%_{cat} \times (1 - f_{Nafion})} + m_{GDE,i} \quad (E.5)$$

Table E.2: Anode catalyst ink composition calculation spreadsheet.

| Catalyst Required                     | Anode |
|---------------------------------------|-------|
| Desired Loading [mg/cm <sup>2</sup> ] | 4     |
| Area [cm <sup>2</sup> ]               | 121   |
| Catalyst [wt%]                        | 0.2   |
| Excess                                | 3     |
| m cat + vulcan [g]                    | 7.26  |

| Nafion Required                | Anode |
|--------------------------------|-------|
| Desired f Nafion               | 0.3   |
| m Nafion <sup>®</sup> soln [g] | 62.23 |

bottle specification  
hand spraying excess

| Final Mass of GDE                    | Anode |
|--------------------------------------|-------|
| m GDE (initial) [g]                  | 2.19  |
| m GDE (final) [g]                    | 5.64  |
| m GDE (Actual) [g]                   | 5.65  |
| Actual Loading [mg/cm <sup>2</sup> ] | 4     |

weight  
target mass  
mass after drying

|                       | 1     | 4     | 8      | Total  |
|-----------------------|-------|-------|--------|--------|
| m cat + vulcan        | 1.82  | 7.26  | 14.52  | 9.08   |
| m Nafion <sup>®</sup> | 15.56 | 62.23 | 124.46 | 77.786 |

Table E.3: Cathode catalyst ink composition calculation spreadsheet.

| Catalyst Required                     | Cathode | Nafion Required                | Cathode  |
|---------------------------------------|---------|--------------------------------|----------|
| Desired Loading [mg/cm <sup>2</sup> ] | 2       | Desired f Nafion               | 0.3      |
| Area [cm <sup>2</sup> ]               | 121     | m Nafion <sup>®</sup> soln [g] | 31.11429 |
| Catalyst [wt%]                        | 0.2     | bottle specification           |          |
| Excess                                | 3       | hand spraying excess           |          |
| mM cat + vulcan [g]                   | 3.63    |                                |          |

| Final Mass of GDE                    | Cathode |                   |
|--------------------------------------|---------|-------------------|
| m GDE (initial) [g]                  | 2.25556 | (GDE w/ Sublayer) |
| m GDE (final) [g]                    | 3.98413 | target mass       |
| m GDE (Actual) [g]                   | 3.99312 | mass after drying |
| Actual Loading [mg/cm <sup>2</sup> ] | 2.0104  |                   |

### E.1.3 Catalyst ink preparation procedure

1. On the Pt-loading spread sheet
  - a. Insert desired loading (1, 2, 4 mg/cm<sup>2</sup>)
  - b. Insert desired area (121 cm<sup>2</sup>) (11 x 11 cm = max. plate area)
  - c. Insert mass or required supported catalyst (20%)
  - d. Insert desired Nafion<sup>®</sup> wt% (30%)
2. Mix in a beaker
  - a. Add catalyst powder as required by the spreadsheet (M cat + Vulcan (g))
  - b. Add water just enough to cover the catalyst powder and protect the carbon from isopropyl alcohol attack
  - c. Add Nafion<sup>®</sup> solution as required by the spreadsheet (M Nafion<sup>®</sup> soln (g))
  - d. Add isopropyl alcohol (IPA, CH<sub>3</sub>CHOHCH<sub>3</sub>) (enough so it does not stick)
3. Parafilm beaker and sonicate for 90 minutes
4. Bring the balance to spraying area in the fumehood

#### E.1.4 Electrode spraying procedure

1. Weight CFP (TGPH-060) & record as  $M_{\text{GDE}}(\text{initial})$
2. Clean out spray gun, plate and ink reservoir with IPA
3. Place CFP between metal frame and tape to the metal frame with masking tape to ensure it does not move
4. Turn on hot plate to  $\sim 80^{\circ}\text{C}$  for one hour if spraying catalyst or at  $100^{\circ}\text{C}$  for one hour if spraying a carbon sub-layer
5. Attach gun to air line, open air fully and set pressure to  $\sim 15$  psi (14.696 psi or 1,1013 bar) adjust spraying while holding sprayer air trigger while adjusting spraying pressure
6. Ensure nozzle is parallel to the handle or to the spraying direction
7. Test spray gun adjustment on paper towel
8. Spray catalyst Ink
  - a. Adjust first back knob clockwise to make spray finer (adjust spray to  $\sim 2$  cm)
  - b. First stage of trigger is air. Second stage of trigger is catalyst ink.
  - c. Load reservoir with about  $2/3$  of the solution
  - d. Spray evenly (turn sheet around for even coating distribution)
  - e. Use air pass between each spraying passes for better drying
  - f. Change metal frame and GDL orientation every two pass
9. Weight GDL & repeat step 9-10 as needed
10. Dry for one hour at  $80^{\circ}\text{C}$  in an oven (or at  $350^{\circ}\text{C}$  for 40 min. for sub-layer preparation)
11. Turn off air and bleed air gun
12. Clean air gun tip, remove with wrench, sonicate tip in IPA for one hour
13. 17. Determine final GDL weight

## E.2 Platinization procedure

This platinization procedure was extracted from Janz and Ives "Reference Electrodes" [1].

1. Clean substrate with warm concentrated nitric acid. It is also recommended to briefly immerse the substrate in dilute aqua regia:

- 1) 4 volumes of DI water
- 2) 1 volume of 16 M (~70%)  $\text{HNO}_3$
- 3) 3 volumes of 12 M (~40%)  $\text{HCl}$

So for 24 ml of solution, one needs 12 ml of DI water, 3 ml of 16 M  $\text{HNO}_3$ , and 9 ml of 12 M  $\text{HCl}$ . If dilute aqua regia is used, it must be followed by treatment with concentrated  $\text{HNO}_3$ . Wash the substrate with DI water prior to platinization.

2. Cathodic cleaning prior to platinization is also recommended to remove the platinum oxides ( $\text{PtO}_x$ ). This is performed by using the substrate as the cathode for water electrolysis in dilute sulphuric acid using a 9 volt battery for a period of ten minutes. Use a Pt wire as the cathode and a Pt mesh as the anode. Hydrogen should be evolved in small bubbles over the cathode's whole surface. If not, the surface is not clean enough.

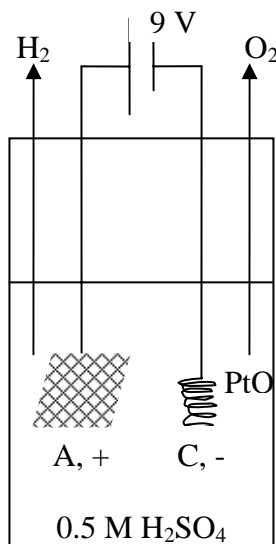


Figure E.1: Electrolysis in dilute sulphuric acid.



3. Grab a small plastic container and weight it on the balance. "Zero" the balance once the container has been weighted.
4. Pour some curing agent (around 1.6 grams) and weigh it on the balance.
5. Once the curing agent is weighed, "zero" the balance and put the corresponding amount of silicone inside the plastic container (i.e. around 16 grams). Make sure that the ratio is met (10:1) as accurate as possible by weighing the total content. Mix the two substances.
6. Put the mix in the oven/vacuum, turn the vacuum pump on and pressurize the chamber to around 30inHg. At this point the silicone will expand and return to its normal size. This is done so that no air bubbles are in the silicone. Make sure that you do not put a lot of silicone and curing agent inside the container to avoid any spills when they expand in the vacuum.
7. Repeat steps 3 to 5 (using other containers) based on how much silicone is necessary. For the seal 4cm<sup>2</sup> fuel cell around 17-20 grams of the final mixture are needed.
8. Take all the seal plates (cleaned with acetone) and pour the silicone onto the grooves (a small spatula or/and a syringe could be used). Make sure that the silicone covers all the grooves.
9. If any bubbles are seen put more silicone beside them (not on top of them). Once all the silicone has covered all the corresponding surfaces and no bubbles are evident, use a straight edge (or spatula) and slide it over the plates in order to remove all the silicone excess.
10. The silicone can be cured overnight or if it is necessary the plates can be heated up to 100°C for around 1 hour.
11. Once the silicone is cured, remove the seals slowly without breaking them.
12. Clean the mold plates with Acetone.

#### **E.4 Nafion membrane conditioning**

1. Cut membrane in squares
2. Boil in 3% H<sub>2</sub>O<sub>2</sub> for 30 min.
3. (3.4% H<sub>2</sub>O<sub>2</sub>, bp. of pure H<sub>2</sub>O<sub>2</sub> = 151.4°C)
4. Rinse with DI H<sub>2</sub>O
5. Boil in DI H<sub>2</sub>O for 30 min.

6. Rinse with DI H<sub>2</sub>O
7. Boil in 0.5 M H<sub>2</sub>SO<sub>4</sub> for 30 min.
8. Store in DI H<sub>2</sub>O
9. Cut membranes in circles with the die-cutter

### **E.5 Determination of CH<sub>3</sub>OH concentration**

The concentration of alcohol crossover to the cathode in a DMFC can be determined using various techniques. First, the amount of alcohol crossover at the cathode can be established by determining the steady-state concentration of CO<sub>2</sub> in the cathode exhaust by gas chromatography [2]. From the amount of CO<sub>2</sub> produced at the cathode exhaust, it is possible to determine the oxidation current density equivalent to the alcohol crossover. Another common way of determining the alcohol crossover is to use an optical infra-red CO<sub>2</sub> sensor to monitor the flow of CO<sub>2</sub> in the cathode exit gas. However, this method requires precise calibrations, and overestimation of the alcohol crossover is possible at high current density [3, 4]. This is because, in a DMFC, the total cathodic CO<sub>2</sub> includes a non-negligible amount of permeated CO<sub>2</sub> from the anodic electro-oxidation [5, 6].

In the liquid phase, it is possible to measure alcohol partitioning and transport in the proton-conducting membrane under the electrochemical system operating conditions by using voltammetric methods while correcting for electro-osmotic drag effects [4]. In this method, the diffusion coefficient and CH<sub>3</sub>OH concentration in the membrane were determined by measuring the transient limiting current density following a potential step. The rate of CH<sub>3</sub>OH transport induced by electro-osmotic drag can also be estimated by using a limiting-current technique [7]. A potentiometric method was also developed to determine the alcohol crossover [3]. In this method, the potential of the catalyst working electrode is recorded during the CH<sub>3</sub>OH crossover. It was shown that the slope of the plot of the potential vs. time is proportional to the crossover rate. Crossover determinations were also carried out by using a dynamic hydrogen electrode (DHE) on the cathode for single electrode potential measurements [8]. The DHE allowed for the measurement of the mixed potential due to a simultaneous CH<sub>3</sub>OH oxidation and O<sub>2</sub> reduction in a DMFC.

Methanol permeability through a membrane can be determined in a two-compartment diffusion cell by using a refractive index infra-red (I-R) detector [7, 9]. One compartment is filled with a mixture of alcohol and DI water while the other is filled with DI water. It is connected to a computer with software which calculates methanol permeability. A Waters IR detector model 2414 and a Shimadza liquid chromatograph pump are available. However, the internals are all made of SS and hence, it cannot be used with an acid electrolyte, which would be present in the systems presently studied.

In the gas phase, methanol crossover could be determined by purging the cathode compartment with N<sub>2</sub> or Ar and analyzing the gas composition through the use of a previously calibrated gas chromatograph, if column contamination from H<sub>2</sub>SO<sub>4</sub> is not a concern. If it is, the cathode compartment gas would have to be condensed and analysed in the liquid phase. High-performance liquid chromatography (HPLC) could be used to determine the CH<sub>3</sub>OH concentration in the cathode compartment as a function of time and for different electrode potentials [10].

More conveniently, there exists a method to determine the methanol content of aqueous solutions based the reduction of potassium dichromate (K<sub>2</sub>Cr<sub>2</sub>O<sub>7</sub>) and using a UV spectrophotometer. The ionic reduction of potassium disulphate is:



A sample is added to excess K<sub>2</sub>Cr<sub>2</sub>O<sub>7</sub> in acid and incubated at 65°C for 30 minutes. As the reaction proceeds, the orange color of Cr<sub>2</sub>O<sub>7</sub><sup>2-</sup> decreases while the blue-violet color of Cr<sup>3+</sup> increases. A spectrophotometer is used to measure either the disappearance of Cr<sub>2</sub>O<sub>7</sub><sup>2-</sup> at a wavelength of 430 nm or the appearance of Cr<sup>3+</sup> at a wavelength of 580 nm. The concentration of CH<sub>3</sub>OH in the solution is determined by using Beer's law:

$$A = \epsilon Cl, \quad (\text{E.7})$$

where  $A$  is the dimensionless absorbance,  $\epsilon$  is the molar extinction coefficient (l/mol.cm),  $C$  is the concentration (M) and  $l$  is the path length of the light in the solution (cm). The value of  $A$  is directly proportional to the aqueous  $\text{CH}_3\text{OH}$  concentration up to 1 wt%, after which  $A$  remains about constant for all  $\text{CH}_3\text{OH}$  concentrations. Hence, if the  $\text{CH}_3\text{OH}$  concentration is too high, the solution will need to be diluted to preferably close to 0.5 wt% in order to use this method effectively. In addition to being used for monitoring crossover in the electrochemical reformer, this method could also be used to determine the change in  $\text{CH}_3\text{OH}$  concentration in an aqueous acidic  $\text{CH}_3\text{OH}$  solution over time, at a temperature close or greater than the pure alcohol's boiling point. The detailed procedure is as follows:

1. Prepare 500 ml of a stock solution of 0.04 M  $\text{K}_2\text{Cr}_2\text{O}_7$  in 3 M  $\text{H}_2\text{SO}_4$ 
  - a) Weigh 5.8838 g of the  $\text{K}_2\text{Cr}_2\text{O}_7$  salt and dissolve in a 500 ml volumetric flask
  - b) Slowly add 80 ml concentrated  $\text{H}_2\text{SO}_4$  and dilute close to the mark with de-ionized water. Be careful not to allow the flask to get hot
  - c) After allowing the solution to cool to room temperature, dilute with the de-ionized water to the mark
2. Dilute the sample(s) into a 50 ml or 100 ml volumetric flask with de-ionized water so as to ensure that the resulting methanol concentration lies between 0 and 1 wt%, preferably near 0.5 wt%
3. Pipette 2.5 ml into a 25 ml volumetric flask and dilute to the mark with the prepared 0.04 M  $\text{K}_2\text{Cr}_2\text{O}_7$  in 3 M  $\text{H}_2\text{SO}_4$
4. Prepare a reagent blank in the same manner using 2.5 ml de-ionized water instead of the diluted samples
5. Place both solutions into a water bath at 65°C for at least 30 minutes but not more than an hour, and then allow to cool to room temperature

A UV Vis spectrophotometer model 1240 by Shimadza was used, and the  $K_2Cr_2O_7$  was a reagent plus grade from Sigma-Aldrich. It was calculated that 29.78 ml  $H_2O$  needed to be added to a 2.5 ml aliquot sample of a 2 M  $CH_3OH$  solution in 0.5 M  $H_2SO_4$  in order to get a concentration of 0.5 wt%  $CH_3OH$ . Using solutions of known  $CH_3OH$  concentrations (0 to 2 M) and  $H_2SO_4$  concentrations (0 to 0.5 M), it was established that this  $CH_3OH$  concentration determination technique gave results within 10%. The random error was within 9% on many multiple dilutions of a same sample.

## E.6 RDE catalyst ink preparation

### 1. RDE preparation:

- a. Clean RDE
- b. Polish the RDE with 0.05 mm  $Al_2O_5$ . If electrode is rough start polishing with the 3 mm and go down to 1 mm, 0.3 mm and 0.05 mm.
- c. Dry

### 2. Materials:

- a. 40 mg of nanocatalyst powder
- b. Nafion ionomer (~200 mg 5% Nafion solution). Use 10 mg of to obtain a Nafion content of 20 w%.
- c. IPA

### 3. Procedure:

- a. Weigh nanocatalyst powder in a disposable beaker
- b. Disperse the nanocatalyst in a volume of solvent
  - i. Add DI water to wet the nanocatalyst powder
  - ii. Add 20 to 40% IPA and sonicate to disperse the nanocatalyst powder  
(Typically 500 to 1000  $\mu g$  nanocatalyst/ml solvent)
- c. Add 200 mg 5% Nafion ionomer solution and IPA to reach a total volume of 5 ml  
(Typically 32ml of Nafion ionomer for 8 ml of catalyst solution)
- d. Sonicate 60 min. to create an uniform dispersion

- e. Drop coat the RDE using a micro-pipette (5  $\mu\text{L}$  of ink) and dry in air for 30 min. in a casting enclosure

(Typically 20  $\mu\text{l}$  of dispersion for a 5 mm OD disk electrode)

- f. Heat dry in air for an hour or in an oven at 50-80°C for 10 min. After solvent evaporation, a thin Nafion film ( $\sim 0.1 \mu\text{m}$ ) should remain on the disk. Estimate the amount of catalyst in the film from the concentration of the catalyst in the dispersion and the volume dispensed. Thick films ( $> 0.5 \mu\text{m}$ ) should be avoided to prevent interference with ideal solution flow at a RDE

#### 4. Cleaning:

- a. wipe with a Kimwipe dipped with acetone
- b. Polish the RDE with 0.05 mm  $\text{Al}_2\text{O}_3$

### E.7 Pt-Ru/ $\text{TiO}_2$ preparation

#### 1. Impregnation procedure for 0.25 g Pt-Ru/ $\text{TiO}_2$ 20 wt% (g metal or catalyst) 1:1 a/o

1. Add  $\text{TiO}_2$  to 20 ml aqueous solution and sonicate for an hour
2. Add the Ru precursor salt, adjusted to the desired metal loading and molar ratio
3. Sonicate the mixture for an hour
4. Add the Pt precursor salt, adjusted to the desired metal loading and molar ratio
5. Sonicate the mixture for an hour
6. Heat the impregnated slurry to 80°C under continuous stirring until complete water evaporation
7. Leave sample in the beaker, cover with Al foil, and dry in over overnight at 110°C
8. Place catalyst in a ceramic boat.
9. Follow-up with reduction heat treatment (See procedure for reduction in 10%  $\text{H}_2$  in Ar)

#### 2. Chemical reduction procedure for 0.25 g Pt-Ru/ $\text{TiO}_2$ 20 wt% (g metal or catalyst) 1:1 a/o

1. Weigh 0.2 g  $\text{TiO}_2$
2. Sonicate the  $\text{TiO}_2$  in 100 ml Millipore DI water for an hour

3. Add 0.08591 g of  $\text{H}_2\text{PtCl}_6 \cdot 6\text{H}_2\text{O}$  (38.34%Pt) and 0.04265 g of  $\text{RuCl}_3 \cdot n\text{H}_2\text{O}$  (40.01%Ru) precursors
4. Sonicate the mixture for an hour
5. Heat the suspension to 80°C (225°C on hot plate) in an oil bath under constant stirring and bubbling of Ar (or  $\text{N}_2$ ) with reflux condenser
6. Prepare the reducing agent by dissolving 95 mg  $\text{NaBH}_4$  and 200 mg  $\text{NaOH}$  in 25 ml Millipore DI water
7. After cooling to room T, add excess reducing agent drop-wise over a period of 2h while sonicating the suspension with  $\text{N}_2$  bubbling
8. After the reduction process, filter and wash the catalyst several times with pure water and dry at 110°C overnight
9. Place the catalyst in a ceramic boat
10. Follow-up with heat treatment (See procedure for calcination in Ar)

Table E.4: Precursor salt addition calculation spreadsheet for the impregnation method.

| Description            | Quantity | Units  | Material                                            |
|------------------------|----------|--------|-----------------------------------------------------|
| Dry Pt content         | 47.6052  | wt%    | $\text{H}_2\text{PtCl}_6$                           |
| Dry Ru content         | 48.7249  | wt%    | $\text{RuCl}_3$                                     |
| Wet Pt content         | 38.05    | wt%    | $\text{H}_2\text{PtCl}_6 \cdot 6\text{H}_2\text{O}$ |
| Wet Ru content         | 39       | wt%    | $\text{RuCl}_3 \cdot n\text{H}_2\text{O}$           |
| Final mass of catalyst | 0.25     | g      | Pt-Ru/ $\text{TiO}_2$                               |
| Final metal content    | 0.2      | wt (%) | Pt-Ru                                               |
| Mass of metal          | 0.05     | g      | Pt-Ru                                               |
| Mass of support        | 0.2      | g      | $\text{TiO}_2$                                      |
| Mol of metal           | 1.69E-04 | mol    | Pt-Ru                                               |
| Pt:Ru a/o ratio        | 1        |        | Pt:Ru                                               |
| Mol of Pt              | 1.69E-04 | mol    | Pt                                                  |
| Mol of Ru              | 1.69E-04 | mol    | Ru                                                  |
| Mass of Pt             | 3.29E-02 | g      | Pt                                                  |
| Mass of Ru             | 1.71E-02 | g      | Ru                                                  |
| Mass of dry salt       | 0.06919  | g      | $\text{H}_2\text{PtCl}_6$                           |
| Mass of dry salt       | 0.03502  | g      | $\text{RuCl}_3$                                     |
| Mass of wet salt       | 0.08656  | g      | $\text{H}_2\text{PtCl}_6 \cdot 6\text{H}_2\text{O}$ |
| Mass of wet salt       | 0.04375  | G      | $\text{RuCl}_3 \cdot n\text{H}_2\text{O}$           |

### 3. Calcination in Ar

1. Insert sample from the left hand side of the tube on top of thermocouple. Center sample boat with wire and flashlight. Insert isolating wool and close tube furnace ends
2. Turn on Ar gas tank. Set Ar flow rate to full flow for purging. Check if exhaust gas is flowing and the pressure drop across tube furnace. Check for leaks with snoop, especially at the inlet.
3. Purge with Ar for a min. of three air changes (1 hour at room T)
4. Program safety s/d temperature. Program ramp-up rate ( $5^{\circ}\text{C}/\text{min}$ ) and dwell time ( $500^{\circ}\text{C}$  for 2 hrs)
5. Reduce the Ar flow rate a set rate of 10 ml/min and start the temperature operation of the furnace
6. Once program is finished, let cool down to room T
7. Turn off Ar gas tank, open tube, retrieve sample
8. Crush particles with mortar and pestle, ball mill for one hour

### 4. Reduction in 10% H<sub>2</sub> in Ar

1. Insert sample from the left hand side of the tube on top of thermocouple. Center sample boat with wire and flashlight. Insert isolating wool and close tube furnace ends
2. Turn on Ar gas tank. Set Ar flow rate to full flow for purging. Check if exhaust gas is flowing and the pressure drop across tube furnace. Check for leaks with snoop, especially at the inlet.
3. Purge with Ar for a min. of three air changes (1 hour at room T)
4. Turn on 10% H<sub>2</sub> in Ar gas tank. Set to 10% H<sub>2</sub> in Ar flow rate. Turn off Ar gas tank. Check for leaks with H<sub>2</sub> sensor, especially at the inlet.
5. Purge with 10% H<sub>2</sub> in Ar for a min. of three air changes
6. Program safety s/d temperature. Program ramp-up rate ( $5^{\circ}\text{C}/\text{min}$ ) and dwell time ( $500^{\circ}\text{C}$  for 2 hrs).
7. Reduce the flow rate a set rate of 100 cm<sup>3</sup> STP/min and Start the temperature operation of the furnace.
8. Once program is finished, turn on Ar gas tank and turn off 10% H<sub>2</sub> in Ar gas tank, let cool down to room T
9. Turn off Ar gas tank, open tube, retrieve sample

10. Crush particles with mortar and pestle, ball mill for one hour

5. Tube furnace programming procedure: ramp to a set-point, hold for a fixed time, then turn off

1. Setup the program

- a. Press SCROLL button to choose 'm - A', use  $\uparrow\downarrow$  button to choose 'MAN'
- b. Press PAGE button until 'SP' is shown
- c. Press the SCROLL button so 'SPrr' is shown, then using the  $\uparrow\downarrow$  button set your ramp rate. Ramp rate units are in degrees per minute.
- d. Press SCROLL so that 'tm.OP' is displayed, then by using the  $\uparrow\downarrow$  button select Opt.1
- e. Press the SCROLL button so 'dwElI' is shown, then using the  $\uparrow\downarrow$  button select your desired dwell time. Dwell time units are in minutes.
- f. Press the PAGE button until the actual temperature is displayed
- g. Use the  $\uparrow\downarrow$  button to set the 'dwElI' temperature ( $^{\circ}\text{C}$ )

2. Run the program

- a. Press the SCROLL button until 'StAt' is displayed and then using the  $\uparrow\downarrow$  button choose 'run'
- b. Press the PAGE button to show the actual temperature. Temperature should start rising now.
- c. Stopping the program
- d. Press the SCROLL button until 'StAt' is displayed and then using the  $\uparrow\downarrow$  button choose 'oFF'

## E.8 References

- [1] D. J. G. Ives and G. J. Janz, "Reference Electrodes, Theory and Practice", Academic Press Inc, New York and London, (1961) 65 pp.
- [2] H. Uchida, Y. Mizuno and M. Watanabe, "Suppression of Methanol Crossover in Pt-Dispersed Polymer Electrolyte Membrane for Direct Methanol Fuel Cells", *Chemical Letters*, (2000) p. 1268-1269.
- [3] N. Munichandraiah, K. McGrath, G. K. S. Prakash, R. Aniszfeld and O. G. A. Robert, "A Potentiometric Method of Monitoring Methanol Crossover through Polymer Electrolyte Membranes of Direct Methanol Fuel Cells", *Journal of Power Sources*, 117(1-2) (2003) p. 98-101.
- [4] X. Ren, T. E. Springer, T. A. Zawodzinski and S. Gottesfeld, "Methanol Transport through Nafion Membranes - Electro-osmotic Drag Effects on Potential Step Measurements", *Journal of the Electrochemical Society*, 147(2) (2000) p. 466-474.
- [5] J. A. Drake, W. Wilson and K. Killeen, "Evaluation of the Experimental Model for Methanol Crossover in DMFCs", *Journal of the Electrochemical Society*, 151(3) (2004) p. A413-A417.
- [6] H. Dohle, J. Divisek, J. Mergel, H. F. Oetjen, C. Zingler and D. Stolten, "Recent Developments of the Measurement of the Methanol Permeation in a Direct Methanol Fuel Cell", *Journal of Power Sources*, 105 (2002) p. 274-282.
- [7] B. Bae, H. Y. Ha and D. Kim, "Preparation and Characterization of Nafion/Poly(1-vinylimidazole) Composite Membrane for Direct Methanol Fuel Cell Application", *Journal of the Electrochemical Society*, 152(7) (2005) p. A1366-A1372.
- [8] V. A. Paganin, E. Sitta, T. Iwasita and W. Vielstich, "Methanol Crossover Effect on the Cathode Potential of a Direct PEM Fuel Cell", *Journal of Applied Electrochemistry*, 35 (2005) p. 1239-1243.
- [9] K. Y. Cho, J.-Y. Eom, H.-Y. Jung, N.-S. Choi, Y. M. Lee, J.-L. Park, J.-H. Choi, K.-W. Park and Y.-E. Sung, "Characteristics of PVdF Copolymer/Nafion Blend Membrane for Direct Methanol Fuel Cell (DMFC)", *Electrochim. Acta*, 50 (2004) p. 583-588.
- [10] C. Lamy, J.-M. Leger and S. Srinivasan, "Direct Methanol Fuel Cells: From a Twentieth Century Electrochemist's Dream to a Twenty-first Century Emerging Technology", *Modern Aspects of Electrochemistry*, Edited by John O'M. Bockris et al., 34 (2001), p. 53-117.

## Appendix F: Electrochemical Techniques

### F.1 Cyclic voltammetry

Cyclic voltammetry (CV) is a controlled potential technique in which the potential of the working electrode is slowly and linearly cycled or scanned between a high and a low voltage limit while the resulting current is measured. A cyclic voltammogram is obtained by plotting the current measured at the working electrode versus the voltage. A three-electrode cell, like the one shown in Fig. F.1, is typically used to conduct cyclic voltammetric studies.

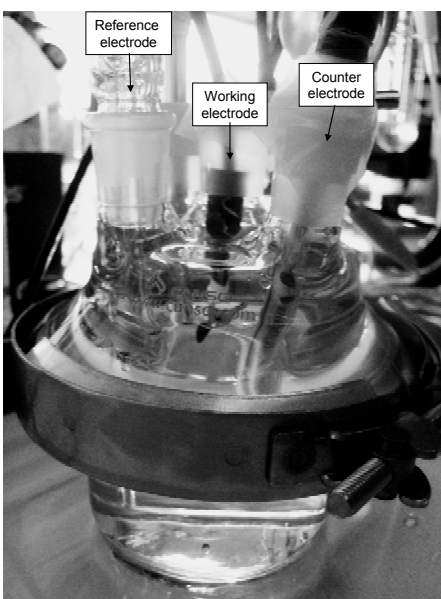


Figure F.1: Picture of a three-port glass cell for cyclic voltammetry.

A potentiostat is used to control and apply the voltage between the WE and CE. This drives a current to flow between the WE and CE. As the voltage is scanned in the positive direction, the reduced compound is oxidized at the electrode surface, then, at a certain voltage value, the scan is reversed and the material that was oxidized is then reduced. Hence, the forward scan represents the electro-oxidation reaction and the reverse scan represents the electro-reduction reaction. At the beginning of the scan, the current is dominated by the electron kinetics. As the potential increases, the limiting current

decreases and diffusion begins to affect the current. At the peak, both influences are equal. At higher potentials, diffusion control dominates: the concentration of species near the electrode surface is depleted, and the diffusion is too slow to replenish the species near the electrode surface. The current measured at a given potential during the anodic scan is often different from the current during the cathodic scan.

Cyclic voltammetry can be used to investigate the redox behaviour of electrode reactions such as potentials and diffusion vs. adsorption behaviour, as well as to elucidate kinetics and mechanisms of electrode reactions, such as reversibility and electron transfer rates. CV can be used to determine the electrochemical surface area (ECSA) of supported or unsupported precious metal electrocatalysts. The ECSA available for the electrochemical reaction is larger than the total noble metal particle area. The three ports glass cell were first cleaned with aqua regia, a concentrated acid solution of HCl:HNO<sub>3</sub> 3:1, to eliminate possible contaminants, then rinsed with DI water, followed by a final rinse with the electrolytic solution. A catalyst coupon, acting as the WE, a platinized Pt flag CE and an MSE were immersed in the unstirred solution. The platinized Pt flag electrodes were cleaned using a concentrated solution of 30 wt% H<sub>2</sub>O<sub>2</sub>:H<sub>2</sub>SO<sub>4</sub> 1:1 while the catalyst coupon was cleaned in a 3 wt% H<sub>2</sub>O<sub>2</sub> solution. Nitrogen gas was bubbled in the solution for 15 minutes prior to the measurements and a N<sub>2</sub> blanket was maintained throughout the scans to prevent O<sub>2</sub> ingress into the solution. Details on the voltammetric procedure used to determine the ECSA of the Pt/C catalyst and on the copper underpotential deposition (UPD) method used to determine the ECSA of the Pt-Ru/C catalyst follows.

#### **F.1.1 Pt/C catalyst electrochemical surface area determination**

The Pt/C and Pt black catalyst ECSAs were determined by recording CV's in the presence of deoxygenated 0.5 M H<sub>2</sub>SO<sub>4</sub> at ambient conditions [1, 2]. The circular 2 cm<sup>2</sup> GDE sample was held in the cell by a Cu alligator clip model BU-34C from Mueller Electric Company Inc., which was gold plated by Acme Plating Inc. with a 2.5 micron sub-layer of nickel and a 5 micron layer of 24K gold. The electrode was first activated with an extended sweep to more positive values to eliminate impurities by cycling 20 times at a fast scan rate of 250 mV/s. The potential was then scanned at a potential step rate of 5 mV/s

between 0 and 1.2 V vs. SHE to obtain a stable CV. It is assumed that each Pt surface atom absorbs about one H<sub>2</sub> atom as per:



Hence, the charge associated with H<sub>2</sub> adsorption indicates the number of surface Pt atoms and hence, the real electrode surface area. It was established that the charge associated with a monolayer of H<sub>2</sub> atoms formed on a polycrystalline Pt surface is 210 μC/cm<sup>2</sup> [2]. The area under the cathodic part of the H<sub>2</sub> adsorption region was estimated in two different ways: by using the integration feature available in CorrView, and by exporting the data to Excel, re-plotting it and dividing the area in the H<sub>2</sub> adsorption region with squares. In the latter method, the time division, *t* (s), for one square was given by:

$$t = \frac{V}{v}, \quad (\text{F.2})$$

where *v* is the scan rate (mV/s) and *V* is the voltage of one square (mV). The charge of one square, *c* (C) is given by:

$$c = I \cdot t, \quad (\text{F.3})$$

where *I* represents the current division of one square (A). The H<sub>2</sub> adsorption charge, *Q<sub>cv</sub>* (C) is given by:

$$Q_{cv} = c \cdot N_s, \quad (\text{F.4})$$

where *N<sub>s</sub>* is the total number of squares. Finally, the following relationship was used to determine the total metal area (TMA) (cm<sup>2</sup>Pt) and the electrochemical surface area (ECSA) (cm<sup>2</sup>Pt/gPt):

$$TMA = \frac{Q_{cv}}{210} \quad (\text{F.5})$$

$$ECSA = \frac{Q_{cv}}{210 \cdot L_{cat}} \quad (F.6)$$

where,  $Q_{cv}$  is the  $H_2$  adsorption charge ( $\mu C$ ), and where  $L_{cat}$  is the catalyst electrode loading ( $g Pt/cm^2$ ).

Figure F.2 shows a CV example for the determination of the ECSA of a  $2.01 cm^2$  Pt/C catalyst sample.

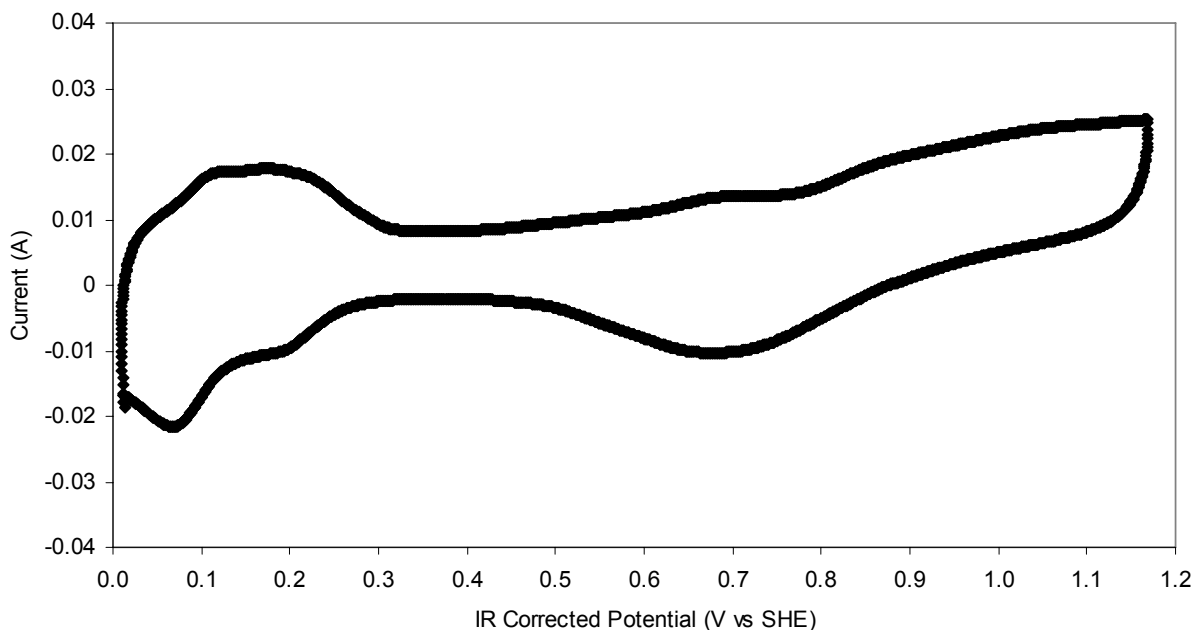


Figure F.2: Cyclic voltammogram ( $2.01 cm^2$ ,  $2 mg/cm^2$  Pt/C,  $5 mV/s$ ,  $0.5 M H_2SO_4$ , Pt flag CE,  $23 \pm 2^\circ C$ ).

The charge associated with the formation of a monolayer of  $H_2$  was first estimated using the CorrView software by integrating the cathodic part of the  $H_2$  adsorption region. The total charge  $Q_{cv}$  was estimated to be  $0.764 C$ . This resulted in a TMA of  $3638 cm^2$  and an ECSA of  $1819 cm^2/gPt$ . The graphical evaluation of the area under the curve was also carried out by importing the data in Excel and dividing the cathodic region of the  $H_2$  adsorption region in squares of  $0.01 A$  and  $0.002 V$ . At the scan rate of  $0.5 mV/s$ , each square represented  $2 s$  and  $0.004 C$ . It was estimated that  $N_s$  was  $184$ , which results in a charge  $Q_{cv}$  of  $0.736 C$ . This resulted in a TMA of  $3503 cm^2$  and an ECSA of  $1751 cm^2/gPt$ . There was only an error of about  $4\%$  between the CorrView and Excel ECSA estimation methods. For each catalyst material evaluated (Pt/C and Pt black), an average ECSA was obtained using different catalyst GDE samples of the same material.

The same technique was used to evaluate electrode degradation. Different catalyst samples were compared for surface area: a fresh unused catalyst sample, a used catalyst sample, which was previously employed to conduct galvanostatic measurements in CH<sub>3</sub>OH acidic solutions, and an oxidized catalyst sample, which carbon was oxidized at low voltages while conducting galvanostatic measurements in the same solutions, at high current densities. Figure F.3 shows the cyclic voltammograms obtained for the various catalyst samples.

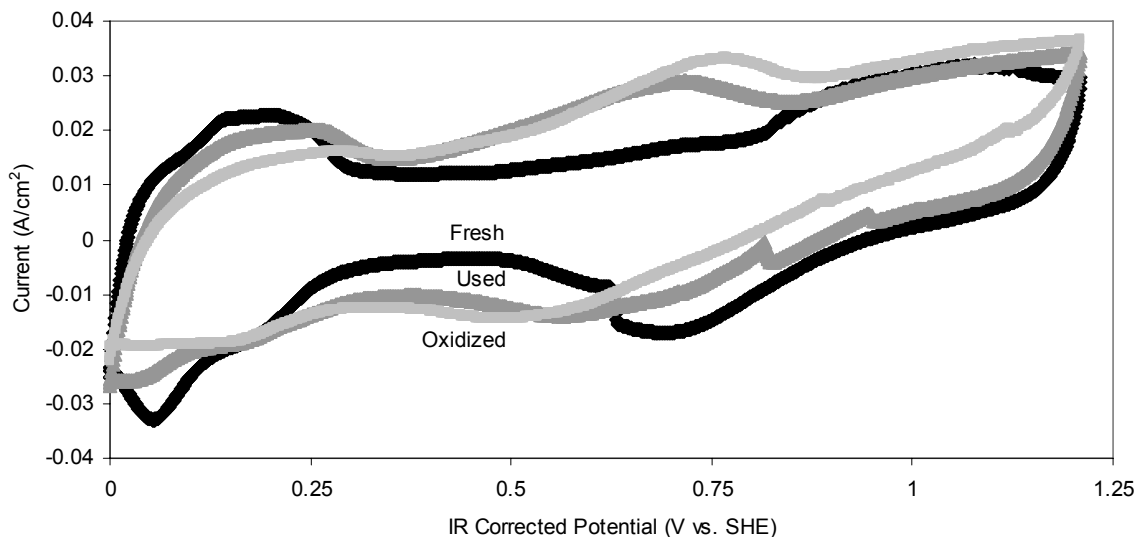


Figure F.3: Cyclic voltammograms for a fresh catalyst sample, a used catalyst sample, and an oxidized catalyst sample ( $2.01 \text{ cm}^2$ ,  $2 \text{ mg/cm}^2 \text{ Pt/C}$ ,  $5 \text{ mV/s}$ ,  $0.5 \text{ M H}_2\text{SO}_4$ , Pt flag CE,  $23 \pm 2^\circ\text{C}$ ).

As indicated on the cyclic voltammograms, the H<sub>2</sub> adsorption region for the fresh GDE was the greatest and decreased in size as the catalyst utilisation increased. Conversely, the Pt oxide peak height increased as the catalyst usage increased. It was at its highest value when the carbon in the catalyst was oxidized. Similarly, the double layer region became less defined and the H<sub>2</sub> adsorption region became smaller as catalyst usage increased. The coulombic charge,  $Q_{CV}$ , was calculated by estimating the area under the curve in the region illustrated on the scans. It was used to calculate the active Pt surface of the electrode. The estimated area under the curve determined in Excel was within 5% of the one determined in CorrView in all cases. Table F.1 compares the ECA results obtained for various Pt/C catalyst samples.

Table F.1: Total metal area results comparison for electrode degradation evaluation.

| Sample Description | TMA (cm <sup>2</sup> Pt) |
|--------------------|--------------------------|
| Fresh              | 3503                     |
| Used               | 2392                     |
| Oxidized           | 1433                     |

The used GDE sample lost 40% of its TMA when compared to the fresh sample. This loss in Pt from the catalyst surface might be due to its prolonged exposure to CH<sub>3</sub>OH acidic solution. The oxidized catalyst sample lost about 60% of its TMA. When the carbon paper of the GDE was oxidized, the carbon leached away with some of the Pt on its surface. This shows the importance of the effect of catalyst degradation on the TMA and ECSA and emphasizes the necessity to use fresh catalyst samples to ensure good reproducibility of electrochemical experiments which will be carried out in this study.

### F.1.2 Pt-Ru/C catalyst electrochemical surface area determination

The H<sub>2</sub> adsorption and stripping technique described above cannot be used to determine the ECA of the bi-metallic Pt-Ru/C electrocatalyst as the H<sub>2</sub> and Ru oxidation currents overlap. Hence, a CV technique based on the underpotential deposition (UPD) of copper was used to determine the ECSA of the Pt-Ru/C electrocatalyst [3, 4]. The underpotential deposition of a monolayer of metal atoms on an electrode surface is carried out at a potential more positive than that required for bulk deposition [4].

The potential is first pre-cycled between -0.68 V and 0.27 V vs. MSE by immersing the clean 4 mg/cm<sup>2</sup> Pt-Ru/C 2 cm<sup>2</sup> circular catalyst coupon in a 0.5 M H<sub>2</sub>SO<sub>4</sub> solution at a scan rate of 5 mV/s to obtain a background scan. The electrode surface oxides are reduced at a potential of -0.48 V vs. MSE for 300 s in the same electrolytic solution. Next, the three electrode cell is emptied and a solution composed of 2 mM CuSO<sub>4</sub> in 0.5 M H<sub>2</sub>SO<sub>4</sub> was transferred to it. A monolayer of Cu is then deposited on the catalyst coupon surface by a UPD adsorption transient at -0.38 V vs. MSE for 300 s after which a linear oxidative

sweep from the hold potential of -0.38 V to 0.27 V vs. MSE at a scan rate of 5 mV/s was applied to strip the Cu from the catalyst surface. The Cu deposited is hence oxidatively removed from the electrode surface in the scan. Other potential scans after this one will not detect any Cu on the surface. All of these steps were carried out at ambient conditions. It is assumed that one Cu atom adsorbs to each surface metal atom as per:



The total charged measured,  $Q_{\text{exp}}$  (C), is given by:

$$Q_{\text{exp}} = Q_{\text{UPD}} - Q_b, \quad (\text{F.8})$$

where  $Q_{\text{UPD}}$  is the copper UPD layer stripping charge ( $\mu\text{C}$ ), and  $Q_b$  is the charged obtained from the background scan in the absence of Cu ( $\mu\text{C}$ ) [201]. Two peaks should appear on the Cu stripping voltammogram: the first one, at about -0.3 V vs. MSE represents the Cu stripping mostly from Ru and the second one, at about -0.08 V vs. MSE, represents the Cu stripping from Pt only. The Ru oxide charge gained ( $\Delta Q_D$ ) and the  $\text{H}_2$  adsorption charge lost ( $\Delta Q_H$ ) of the catalyst working electrode can be obtained by comparing the background scan to the copper stripping voltammograms. It was established that the charge associated with a monolayer of Cu atoms formed on a polycrystalline Pt surface is  $420 \mu\text{C}/\text{cm}^2$  [3]. Hence, the ECSA is given by:

$$ECSA = \frac{Q_{\text{exp}}}{420 \cdot L_{\text{cat}}} \quad (\text{F.9})$$

This test is non-destructive as the electrode surface area can be fully recovered by cycling between -0.68 and 0.37 V vs. MSE [5].

Figure F.4 shows a CV example for the determination of the ECSA of a 2.01 cm<sup>2</sup> unsupported Pt-Ru catalyst sample.

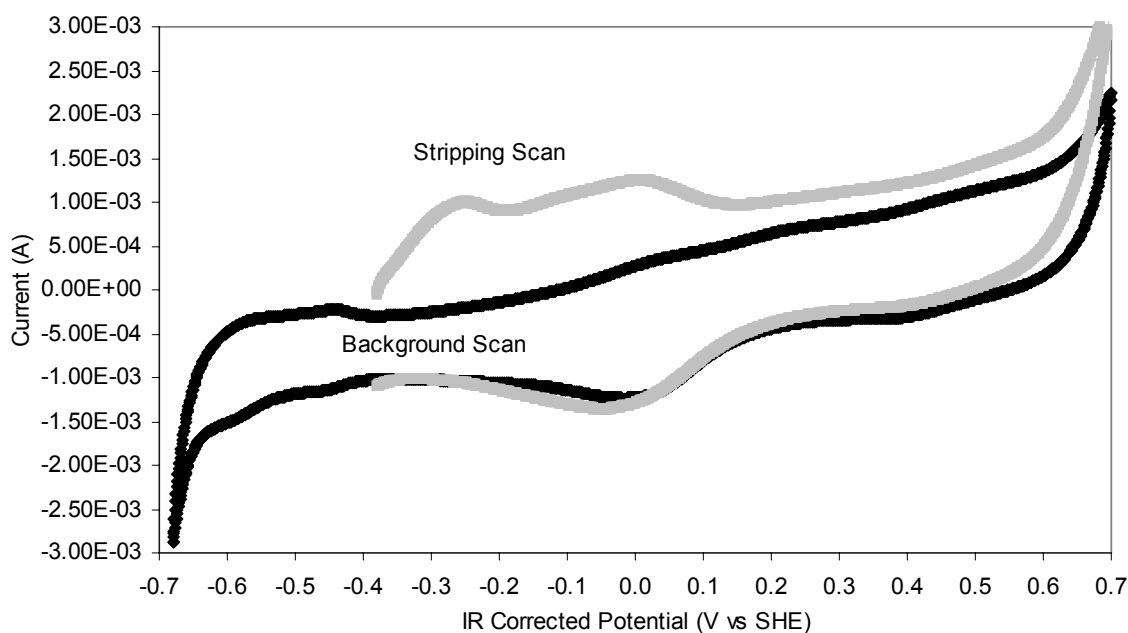


Figure F.4: Cyclic voltammogram (4 mg/cm<sup>2</sup> Pt-Ru, 5 mV/s, 0.5 M H<sub>2</sub>SO<sub>4</sub>, Pt flag CE, 23 ± 2°C).

For the Cu UPD method, the charge associated with the formation of a monolayer of Cu could only be estimated in Excel. The graphical evaluation of the area under the curve was also carried out by importing the data in Excel and dividing the graph in squares of  $1 \times 10^{-4}$  A and  $2 \times 10^{-2}$  V. At the scan rate of 0.5 mV/s, each square represented 2 s and 0.0002 C. It was estimated that  $N_{UPD} - N_b$  was 143, which results in a charge in the Cu desorption region  $Q_{exp}$  of 0.029 C. This results in a TMA of 68 cm<sup>2</sup> Pt-Ru and an ECSA of 17 cm<sup>2</sup>/gPt-Ru. For each catalyst material evaluated (Pt-Ru/C and Pt-Ru black), an average ECSA was obtained using different catalyst GDE samples of the same material.

## F.2 Electrochemical impedance spectroscopy

AC impedance or electrochemical impedance spectroscopy (EIS) is a powerful technique for characterizing and evaluating fuel cells [6]. Impedance is the resistance or resistivity in the alternating current (AC) version of Ohm's law and measures the inability of a material to carry an electrical current. A small sinusoidal voltage or current is applied in addition to a conventional DC voltage or current. The AC component of the resulting current or voltage is measured and used to calculate, by Fourier analysis, the resulting impedance, which is frequency-dependent. Hence, in this analog experiment, a wide spectrum of time responses is examined at one potential value. When plotted as a function of frequency, a semi-circle is obtained. In this plot, called the Nyquist plot, the x axis is the real part ( $Z'$ ) and the y-axis is the imaginary part ( $Z''$ ) of the impedance. The absolute value of the impedance is expressed as a complex number represented by  $Z$  (ohm), which is given by:

$$Z = ((Z')^2 + (Z'')^2)^{1/2} \quad (\text{F.10})$$

At low frequencies, the impedance is dominated by the resistor and the diameter of the semi circle is equal to the ohmic resistance,  $R_s$  (ohm). Hence,  $R_s$  is the real part of the impedance when the imaginary impedance is zero. Half-cell EIS measurements will be employed to determine  $R_s$  of the electrolyte, solution or MEAs utilized in the cells after various electrochemical measurements are carried out. Typically, in order to obtain a clear half circle intercept, the initial frequency scan must be in the range of 50000 Hz. The ohmic overvoltage,  $\eta_{ohm}$  (V), given by:

$$\eta_{ohm} = I \cdot R_s \quad (\text{F.11})$$

where  $I$  is the current (A), will be used to correct the voltage measurements for ohmic losses in order to pursue further data treatment to obtain kinetic information on the system studied.

In this thesis, the MEA and solution resistance measurements were obtained from AC impedance measurements performed at different final frequencies ( $1 \times 10^4$  to  $1 \times 10^7$  Hz) and at different initial

frequencies (0.001, 0.1 and 100 Hz) and at an AC amplitude of 10 mV, depending on the set-up for which the resistance was measured. The MEA or solution resistance was found by reading the real axis value at the high frequency intercept, near the origin of a Nyquist plot, a typical example of which is shown in Fig. F.5.

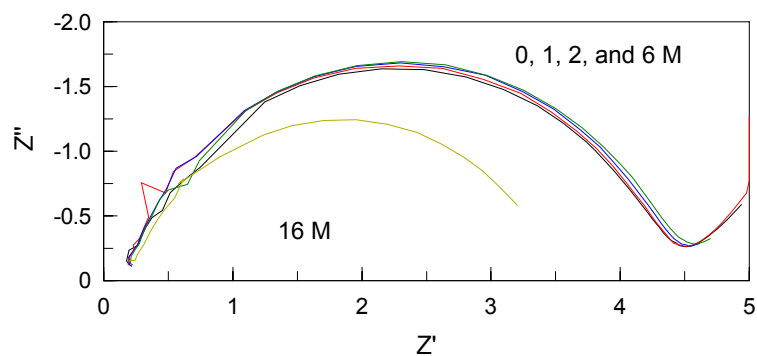


Figure F.5: Typical Nyquist plots for a fresh MEA at varying methanol concentration (initial frequency of  $1 \times 10^5$  Hz to final frequency of 0.01 Hz,  $4 \text{ mg/cm}^2$  Pt-Ru/C anode,  $2 \text{ mg/cm}^2$  Pt/C cathode, 0, 1, 2, 6 or 16 M  $\text{CH}_3\text{OH}$  in 0.5 M  $\text{H}_2\text{SO}_4$  electrolyser anolyte, 0.5 M  $\text{H}_2\text{SO}_4$  electrolyser catholyte).

The intercept was similar for all MEAs except when in the equimolar  $\text{CH}_3\text{OH}:\text{H}_2\text{O}$  solutions. The average resistance obtained for fresh, used and oxidized MEAs are shown in Fig. F.6 for different  $\text{CH}_3\text{OH}$  concentration. Each point represents the average of three measurements.

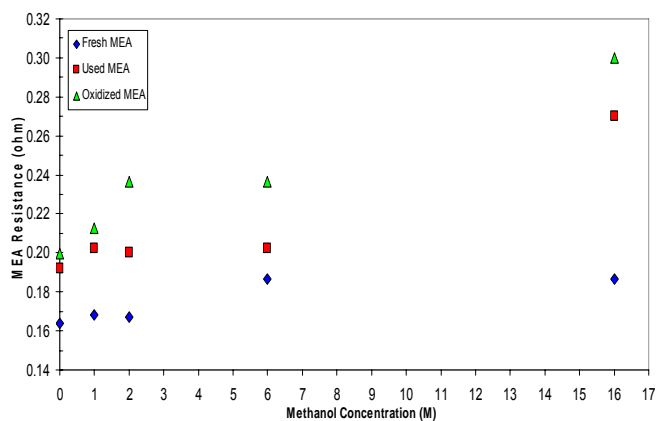


Figure F.6: MEA resistance as a function of methanol concentration for various MEA conditions ( $4 \text{ mg/cm}^2$  Pt/Ru anode,  $2 \text{ mg/cm}^2$  Pt cathode, N-117, 0.5 M  $\text{H}_2\text{SO}_4$  electrolyte and catholyte).

As can be seen, the MEA resistance increased slightly with the CH<sub>3</sub>OH concentration and MEA usage. Also, the polymeric membrane material became less flexible after usage in high CH<sub>3</sub>OH concentration. As there is less water in the solution as the CH<sub>3</sub>OH concentration increases, it is possible that the membrane lost some of its conductivity due to partial dehydration. For an oxidized sample in 16 M CH<sub>3</sub>OH at the highest current density studied, the ohmic drop will be of:

$$E_{ohm} = 0.3 \text{ ohm} (150 \times 10^{-3} \text{ A/cm}^2) (2.02 \text{ cm}^2) = 0.09 \text{ mV} \quad (\text{F.12})$$

This is slightly higher than what can be estimated for a N117 membrane, having an area resistance of 0.26 ohm.cm<sup>2</sup>, at 20°C and at the same current density:

$$E_{ohm} = 0.26 \text{ ohm.cm}^2 (150 \times 10^{-3} \text{ A/cm}^2) = 0.04 \text{ mV} \quad (\text{F.13})$$

The values of the measured potentials were corrected for the IR drop before kinetic parameter information was extracted. For example, an average value of 0.2 ohm was used to correct for the ohmic losses of an MEA having a 4 mg/cm<sup>2</sup> Pt-Ru/C anode in 0 to 6 M CH<sub>3</sub>OH in 0.5 M H<sub>2</sub>SO<sub>4</sub>. An average value of 0.25 ohm was used to correct for the ohmic losses for the same MEA but in 16 M CH<sub>3</sub>OH in 0.5 M H<sub>2</sub>SO<sub>4</sub>, while an average value of 0.07 ohm was used to correct for the ohmic losses of MEA's having a 2 mg/cm<sup>2</sup> anode in 0 and 2 M CH<sub>3</sub>OH in 0.5 M H<sub>2</sub>SO<sub>4</sub>.

### F.3 Determination of the open circuit voltage

An H-cell, as shown on Fig. F.7, was used to conduct open circuit voltage (OCV) measurements to determine the voltage under no-load conditions. To accomplish this, the electrical potential of an electrode is measured against a reference electrode when no current flows through the electrode.

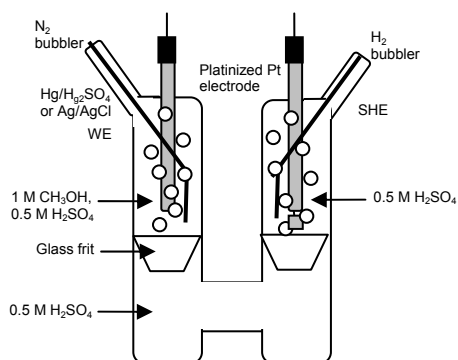


Figure F.7: H-cell set-up for OCV measurements.

A reference electrode, either MSE or SSE, was placed one of the H-cell compartment, where  $N_2$  was bubbled. A Pt flag electrode was platinized and placed in the other H-cell compartment, where  $H_2$  was bubbled, to act as an isothermal standard  $H_2$  reference electrode (SHE). The glass frit plugs were pre-wetted in 0.5 M  $H_2SO_4$ . The H-cell was first filled with 0.5 M  $H_2SO_4$ . The glass frit plugs were then put in place. The extra 0.5 M  $H_2SO_4$  solution above the glass frit in the WE compartment was removed. The compartment was rinsed with a 1 M  $CH_3OH$  solution in 0.5 M  $H_2SO_4$  and refilled with the same solution. All solutions were deoxygenated by bubbling  $N_2$  for 20 minutes and then degassed in a sonicator for 20 minutes prior to the measurements, as residual  $O_2$  could cause errors. The potential of the WE was recorded against the potential of SHE. For measuring the OCV at higher temperatures, a controlled temperature water bath will be used to circulate water at the appropriate temperature in the double wall of the H-cell.

#### F.4 Current - potential transients

The determination of the current-potential relationship under a certain set of fixed conditions, such as concentration and temperature, is a common electrochemical measuring technique [7]. It is used for electrochemical analysis or the determination of the kinetics and mechanism of electrode reactions. Multiple measurements, based on the control of the current flowing through the system, are made to obtain polarization curves, i.e. current vs. potential plots, over a range of changing conditions. These experiments can be carried out galvanostatically, by controlling the current and measuring the resulting potential, or potentiostatically, by controlling the potential and measuring the resulting current [7].

In a galvanostatic experiment, the potentiostat controls the current flowing between the working and counter electrode and externally controls the reaction rate. The potential of the working electrode is allowed to assume a value appropriate for the rate and is measured against a reference electrode at a constant current as a function of time. The potential measured must be corrected for the resistance, which can be determined by EIS. To conduct these experiments, two lines are required on the multistat, one for the galvanostatic loop between the anode and the cathode and one for an OCV loop between the reference electrode and the cathode. The first loop measures the cell voltage while the other measures the cathode potential vs. the reference electrode. The working electrodes of both loops are connected together. The reference electrode loop was always started prior to the galvanostatic loop so that interactions between the two lines are minimized. The OCV was also checked with an independent multimeter and the error was not significant.

In the alcohol electrolysis or electrochemical reforming mode, the current imposed on the galvanostatic loop will be negative and the resulting overall cell voltage measured will also be negative. It is the minimum cell voltage needed to be applied to drive the reaction at a given current. The cathode potential, which forces the electrons into reduction, is negative while the anode potential, which extracts the electrons from oxidation, is positive. Polarization curves obtained under various conditions will be corrected for the ohmic resistance and used to extract kinetic information on the electrochemical system being investigated.

In the case of pure kinetic control, the reaction is only limited by the rate of electron transfer between the electrode and active species. It is assuming the concentration overpotential due to diffusion, i.e. mass transfer limitations, is negligible. Hence, the overpotential is limited by charge transfer and is the surface activation or charge transfer overvoltage,  $\eta_s$ . It is the difference between the actual electrode potential and the equilibrium electrode potential and is the electrochemical reaction's driving force (from Eq. 1.13).

$$\eta_s = E - E_e \tag{F.14}$$

According to the Butler-Edvey-Gruz-Volmer (BEV) equation, the current is exponentially related to the overpotential:

$$i = i_o \left[ \exp\left(\frac{(1-\beta)nF}{RT} \eta_s\right) - \exp\left(\frac{\beta nF}{RT} \eta_s\right) \right], \quad (\text{F.15})$$

where  $\beta$  is the symmetry coefficient, and  $i_o$  is the exchange current density. The first term of the equation describes the anodic contribution and the second term describes the cathodic contribution. The exchange current density is the absolute value of oxidizing and reducing current density at null potential or equilibrium electrode potential. Its value usually depends on the electrode electrocatalytic properties, temperature and concentration as well as on the reaction mechanism and is related to the exchange current,  $I_o$ , as follows:

$$I_o = i_o \cdot A_{Geom} \quad (\text{F.16})$$

where  $A_{Geom}$  is the exposed catalyst geometric surface area. For large activation overpotentials, i.e.  $\eta_s > 50$  mV, the anodic reaction rate will be very high compared to that of the cathodic reaction rate, resulting in the high field approximation of the BEV equation:

$$i = i_o \exp\left(\frac{\alpha_a F}{RT} \eta_a\right) \quad (\text{F.17})$$

The Tafel equation is:

$$|\eta_s| = b \cdot \log|i| + a \quad (\text{F.18})$$

where in this case,  $|\eta_s| = \eta_a$  and  $|i| = i_a$ . The Tafel parameters are defined as:

$$b = \frac{2.303RT}{\alpha_a nF}, \quad (\text{F.19})$$

$$a = -b \log i_o, \quad (\text{F.20})$$

where  $\alpha_a$  is the anodic transfer coefficient which is a measure of the symmetry of the energy barrier,  $b$  is the Tafel slope, and  $a$  is the intercept. By plotting the  $\eta_a$  vs.  $\log i$ , the slope and the intercept can be determined. The experimental extrapolation of the Tafel line to obtain  $i_o$  is often challenging and as the result can vary widely on the region of the data used for the straight line fit.

## F.5 Rotating disk electrode

The rotating disk electrode (RDE) is a specialized hydrodynamic electrode which creates controllable flow conditions and a nearly uniform density distribution along the electrode, making it a powerful tool to investigate electrochemical reactions. It is used in the investigation of the kinetics of electro-oxidation and electro-reduction reactions, in the mechanistic analysis of electrode reactions and in electro-analytical applications to ensure a known and controllable flow of solution over the electrode. The RDE creates additional convection which enhances the rate of mass transport to the electrode and increases the current and sensitivity compared to voltammetric measurements in stagnant solution.

Flow control is achieved by bringing fresh reactant to the surface by a flat PTFE disc electrode which is rotated in the solution. The working electrode, Pt for example, is embedded in the top face of the PTFE shield. This permits a controlled variation in the electrochemical reaction rate by changing the convection rate in the solution. As the rotation speed is increased, the distance that a species must diffuse from the surface before it is removed by convection decreases. Hence, under the effect of rotation in the presence of a highly-concentrated electrolyte, the mass transport is dominated by diffusion and convection. A mass transport-limited current will arise when the system reaches a steady-state, once the equilibrium at the surface is driven to the product side.

A typical measurement used with the RDE is linear sweep voltammetry. The rotating disk electrode rotation speed is controlled so that there is a well-defined uniform transport of the solution phase reactant to the electrode surface resulting in a laminar flow of solution in the cell. This is the case when the dimensionless Reynolds number,  $Re$ , given by:

$$Re = \frac{\omega r^2}{\nu} \quad (F.21)$$

where  $\omega$  is the angular velocity (1/s),  $r$  is the disk radius (cm) and  $\nu$  is the kinematic fluid viscosity ( $\text{cm}^2/\text{s}$ ), is less than  $1 \times 10^5$  [7]. The angular velocity can also be expressed in revolutions per minute (rpm):

$$\omega = \frac{2\pi(\text{rpm})}{60} \quad (F.22)$$

When the flow is laminar in the cell, the fluid dynamics can be described by the Navier-Stokes equation, which represents the conservation of momentum in the system. This equation relates the mass transport limited current and the rotation speed for a reversible electron transfer reaction. It was solved by Levich for the RDE geometry. The properties of the limiting current,  $i_L$ , at the RDE can be described by the Levich equation:

$$i_L = 0.62nFD^{2/3}\nu^{-1/6}\omega^{1/2}C^o, \text{ or} \quad (F.23)$$

$$i_L = B\omega^{1/2} \quad (F.24)$$

where  $C^o$  is the bulk concentration (M),  $D$  is the diffusion coefficient ( $\text{cm}^2/\text{s}$ ) and  $B$  is the Levich parameter of Levich slope constant [8].

Typically, a set of current voltage curves are recorded for a reversible electron transfer reaction at different rotation speeds. The total current flowing depends on the rotation speed and as the rotation speed increases, the distance that the reactant can diffuse from the surface before being removed by

convection decreases. From polarization curves,  $i_L$  can be obtained for various rotation rates. By plotting  $i_L$  vs.  $\omega^{1/2}$  for a set of experimental data, a straight line will be observed if the reaction is reversible. From the slope,  $B$ , the diffusion coefficient can be obtained.

The mass transfer limiting current density,  $i_L$ , represents the condition when the surface concentration of the reactant is zero while the electrode activation kinetic current density,  $i_k$ , is the theoretical current that would be expected to flow in the absence of mass transfer limitations. The total current density,  $i$ , in the mixed control region, where activation and mass control are present, is a function  $i_k$  and  $i_L$ :

$$\frac{1}{|i|} = \frac{1}{|i_k|} + \frac{1}{|i_L|}. \quad (\text{F.25})$$

The Koutecky-Levich equation shows that as  $\omega$  goes to infinity, the current approaches  $i_k$ :

$$\frac{1}{|i|} = \frac{1}{|i_k|} + \frac{1}{|B\omega^{1/2}|}. \quad (\text{F.26})$$

A Koutecky-Levich plot can be obtained by choosing values of the overpotentials in the mixed activation and mass-transport control region. At every overpotential, the current density is found at each rotation rates. If each overpotential point is extrapolated to the y axis, the y intercepts represent the kinetic currents at every overpotential. Each line has the same slope of  $1/B$ . The plot of  $1/i$  vs.  $1/\omega^{1/2}$  should be a straight line intercept of  $1/i_k$  [7].

## F.6 References

- [1] J. M. D. Rodriguez, J. A. H. Melian and J. P. Pena, "Determination of the Real Surface Area of Pt Electrodes by Hydrogen Adsorption Using Cyclic Voltammetry", *Journal of Chemical Education*, 77(9), (2000) 1195-1197.
- [2] T. R. Ralph, G. A. Hards and J. E. Keating, "Low Cost Electrodes for Proton Exchange Membrane Fuel Cells", *Journal of the Electrochemical Society*, 144(11), (1997) 3845-3857.

- [3] C. L. Green and A. Kucernak, "Determination of the Platinum and Ruthenium Surface Areas in Platinum-Ruthenium Alloy Electrocatalysts by Underpotential Deposition of Copper. 1. Unsupported Catalysts", *Journal of Physical Chemistry B*, (106), (2002) 1036-1047.
- [4] C. L. Green and A. Kucernak, "Determination of the Platinum and Ruthenium Surface Areas in Platinum-Ruthenium Alloy Electrocatalysts by Underpotential Deposition of Copper. 2. Effect of Surface Composition on Activity", *Journal of Physical Chemistry B*, (106), (2002) 11446-11456.
- [5] S.-R. Wang and P. S. Fedkiw, "Pulsed-potential Oxidation of Methanol, 1. Smooth Platinum Electrode With and Without Tin Surface Modification", *J. Electrochemical Society*, 139(9), (1992) 2519-2525.
- [6] A. J. Bard and L. R. Faulkner, "Electrochemical Methods Fundamentals and Applications", Second Edition, John Wiley & Sons, Inc., USA (2001) 833 pp.
- [7] E. Gileadi, "Electrode Kinetics for Chemists, Chemical Engineers, and Materials Scientists", VCH Publishers Inc., USA (1993) 597 pp.
- [8] V. A. Paganin, E. Sitta, T. Iwasita and W. Vielstich, "Methanol Crossover Effect on the Cathode Potential of a Direct PEM Fuel Cell", *Journal of Applied Electrochemistry*, 35, (2005) 1239-1243.

## Appendix G: Thermodynamic data and sample calculations

### G.1 Thermodynamic data

Table G.1: Thermodynamic data.

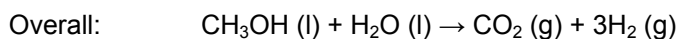
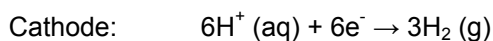
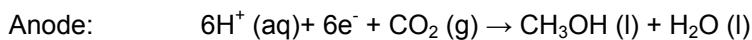
| Species            | State | $\Delta G_f^\circ$<br>[kJ/mol] | $\Delta H_f^\circ$<br>[kJ/mol] | $\Delta S_f^\circ$<br>[J/molK] | $C_p^\circ$<br>[J/molK] |
|--------------------|-------|--------------------------------|--------------------------------|--------------------------------|-------------------------|
| CH <sub>3</sub> OH | g     | -162.30                        | -201.00                        | 39.90                          | 44.10                   |
|                    | lq    | -166.60                        | -239.10                        | 126.80                         | 81.20                   |
| H <sub>2</sub> O   | g     | -228.61                        | -241.83                        | 188.80                         | 33.60                   |
|                    | lq    | -237.14                        | -285.83                        | 70.00                          | 75.35                   |
| H <sub>2</sub>     | g     | 0.00                           | 0.00                           | 130.70                         | 28.84                   |
| CO <sub>2</sub>    | g     | -394.40                        | -393.51                        | 213.80                         | 37.10                   |
| O <sub>2</sub>     | g     | 0.00                           | 0.00                           | 205.20                         | 29.40                   |

References [1, 2]

### G.2 Thermodynamic sample calculations

#### G.2.1 Liquid phase

The electrochemical reactions for the direct methanol reformer (DMR) in the liquid phase written in the reduction sense are as follows:



The Gibbs free energy associated with the electrochemical reaction at standard condition is:

$$\Delta G^{\circ} = \sum_i s_i \Delta G_{i,f}^{\circ} (\text{products} - \text{reactants}) \quad (\text{G.1})$$

$$\text{Anode:} \quad \Delta G_a^{\circ} = ((-166.6) + (-237.14) - (-394.4)) \cdot 1000 = -9340 \text{ J/mol}$$

$$\text{Cathode:} \quad \Delta G_c^{\circ} = ((3 \cdot 0) - 0) \cdot 1000 = 0 \text{ J/mol}$$

$$\text{Overall:} \quad \Delta G^{\circ} = \Delta G_c^{\circ} - \Delta G_a^{\circ} = 0 - (-9340) = 9340 \text{ J/mol}$$

Similarly, the enthalpy of formation associated with the electrochemical reaction at standard condition is:

$$\Delta H^{\circ} = \sum_i s_i \Delta H_{i,f}^{\circ} (\text{products} - \text{reactants})$$

$$\text{Anode:} \quad \Delta H_a^{\circ} = ((-239.1) + (-285.83) - (-393.51)) \cdot 1000 = -131420 \text{ J/mol}$$

$$\text{Cathode:} \quad \Delta H_c^{\circ} = ((3 \cdot 0) - 0) \cdot 1000 = 0 \text{ J/mol}$$

$$\text{Overall:} \quad \Delta H^{\circ} = \Delta H_c^{\circ} - \Delta H_a^{\circ} = 0 - (-131420) = 131420 \text{ J/mol}$$

The standard cell voltage or reversible cell voltage at standard conditions is:

$$E^{\circ} = -\frac{\Delta G^{\circ}}{nF} \quad (\text{G.2})$$

$$\text{Anode:} \quad E_a^{\circ} = -(-9340) / 6 \cdot 96485 = 0.016 \text{ V}$$

$$\text{Cathode:} \quad E_c^{\circ} = -(0) / 6 \cdot 96485 = 0 \text{ V}$$

$$\text{Overall:} \quad E^{\circ} = E_c^{\circ} - E_a^{\circ} = 0 - 0.016 = -0.016 \text{ V}$$

The maximum thermodynamic efficiency at standard condition is determined using the higher heating value (HHV) for the enthalpy of formation of liquid CH<sub>3</sub>OH at 25°C:

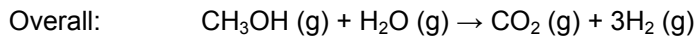
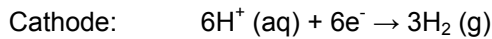
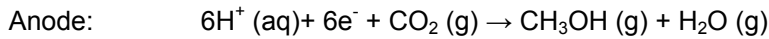
$$\eta_{\max} = \left( \frac{\Delta G^{\circ}}{\Delta H^{\circ}} \right) \cdot 100 \% \quad (\text{G.3})$$

$$\eta_{\max} = (9340/131420) \cdot 100 = 7.11\%$$

The thermodynamic efficiency is positive as work is required to generate H<sub>2</sub> under these conditions since the overall reaction is endothermic ( $\Delta H^\circ > 0$ ), and non-spontaneous ( $\Delta G^\circ > 0$ ).

### G.2.2 Gas phase

The electrochemical reactions for the direct methanol reformer (DMR) in the gas phase written in the reduction sense are as follows:



*Standard Gibbs free energy of formation:*

$$\Delta G^\circ = \sum_i s_i \Delta G_{i,f}^\circ (\text{products} - \text{reactants})$$

Anode:  $\Delta G_a^\circ = ((-162.3) + (-228.61) - (-394.4)) \cdot 1000 = 3490 \text{ J/mol}$

Cathode:  $\Delta G_c^\circ = ((3 \cdot 0) - 0) \cdot 1000 = 0 \text{ J/mol}$

Overall:  $\Delta G^\circ = \Delta G_c^\circ - \Delta G_a^\circ = 0 - (3490) = -3490 \text{ J/mol}$

*Standard cell theoretical cell voltage or reversible cell voltage:*

$$E^\circ = -\frac{\Delta G^\circ}{nF}$$

Anode:  $E_a^\circ = - (3490) / 6 \cdot 96485 = -0.006 \text{ V}$

Cathode:  $E_c^\circ = - (0) / 6 \cdot 96485 = 0 \text{ V}$

Overall:  $E^{\circ} = E^{\circ}_c - E^{\circ}_a = 0 - (-0.006) = 0.006 \text{ V}$

*Standard enthalpy of formation:*

$$\Delta H^{\circ} = \sum_i s_i \Delta H_{i,f}^{\circ} \quad (\text{G.4})$$

Anode:  $\Delta H^{\circ}_a = ((-201) + (-241.83) - (-393.51)) \cdot 1000 = -49316 \text{ J/mol}$

Cathode:  $\Delta H^{\circ}_c = ((3 \cdot 0) - 0) \cdot 1000 = 0 \text{ J/mol}$

Overall:  $\Delta H^{\circ} = \Delta H^{\circ}_c - \Delta H^{\circ}_a = 0 - (-49316) = 49316 \text{ J/mol}$

*Standard entropy of reaction:*

$$\Delta S^{\circ} = \sum_i s_i \Delta S_{i,f}^{\circ} \quad (\text{G.5})$$

Anode:  $\Delta S^{\circ}_a = ((39.9) + (188.8) - (-213.8)) \cdot 1000 = 15 \text{ J/mol.K}$

Cathode:  $\Delta S^{\circ}_c = ((3 \cdot 130.7) - 0) \cdot 1000 = 392 \text{ J/mol.K}$

Overall:  $\Delta S^{\circ} = \Delta S^{\circ}_c - \Delta S^{\circ}_a = 392 - (15) = 377 \text{ J/mol.K}$

*Temperature correction:*

Assuming constant pressure, the molar enthalpy and entropy at T are given by:

$$\Delta H_T = \Delta H^{\circ} + \int_{298}^T C_p dT$$

$$\Delta H_T = \Delta H^{\circ} + (T - 298)C_p \quad (\text{G.6})$$

$$\Delta S_T = \Delta S^{\circ} + \int_{298}^T \frac{1}{T} C_p dT$$

$$\Delta S_T = \Delta S^{\circ} + \ln(T) - \ln(298)C_p \quad (\text{G.7})$$

The Shomate equations and empirical coefficients for the heat capacity for the relevant species are available in the literature [3-6] and are summarized in Table G.2.

Table G.2: Empirical coefficients for Shomate equations.

| Species            | State | A        | B                       | C                      | D                      | E                        | T<br>Range<br>[°K] | Eq.<br>Form | Ref |
|--------------------|-------|----------|-------------------------|------------------------|------------------------|--------------------------|--------------------|-------------|-----|
| CH <sub>3</sub> OH | g     | 39250    | 87900                   | 1917                   | 53650                  | 897                      | 200-1500           | 1           | [4] |
|                    | lq    | 86.2     |                         |                        |                        |                          | 323                |             | [6] |
| H <sub>2</sub> O   | g     | 30.092   | 6.832514                | 6.793435               | -2.53448               | 0.082139                 | 500-1700           | 2           | [3] |
|                    | g     | 4.0700   | -0.6160/10 <sup>3</sup> | 1.2810/10 <sup>6</sup> | -0.508/10 <sup>9</sup> | 0.0769/10 <sup>12</sup>  | 300-1000           | 3           | [5] |
|                    | lq    | -203.606 | 1523.29                 | -3196.413              | 2474.455               | 3.855326                 | 298-500            | 2           | [3] |
| H <sub>2</sub>     | g     | 33.06618 | -11.363417              | 11.432816              | -2.772874              | -0.158558                | 298-1000           | 2           | [3] |
|                    | g     | 3.0570   | 1.4870/10 <sup>3</sup>  | -1.793/10 <sup>6</sup> | 0.9470/10 <sup>9</sup> | -0.1726/10 <sup>12</sup> | 300-1000           | 3           | [5] |
| CO <sub>2</sub>    | g     | 24.99735 | 55.18696                | -33.69137              | 7.948387               | -0.136638                | 298-1200           | 2           | [3] |
|                    | g     | 2.4010   | 4.8530/10 <sup>3</sup>  | -2.039/10 <sup>6</sup> | 0.3430/10 <sup>9</sup> | 0.0000                   | 300-1000           | 3           | [5] |
| O <sub>2</sub>     | g     | 3.6260   | -1.0430/10 <sup>3</sup> | 2.1780/10 <sup>6</sup> | -1.160/10 <sup>9</sup> | 0.2053/10 <sup>12</sup>  | 300-1000           | 3           | [5] |

Shomate equation form 1 [4]:  $C_p/K = A + B*((C/T)/\sinh(C/T))^2 + D*((E/T)/\cosh(E/T))^2$   
 Shomate equation form 2 [3]:  $C_p/K = (A + B*T + C*T^2 + D*T^3 + E*T^4)*8.314$   
 Shomate equation form 3 [5]:  $C_p/R = A + BT + CT^2 + DT^3 + ET^{12}$

As noted in Section 2.3.1, the heat capacity in a specific phase did not vary significantly over the temperature range studied (> 8 %). However, there is a more significant change in the heat capacity when the phase changes from liquid to gas.

Using the heat capacities determined as a function of temperature, it is possible to evaluate the enthalpy of formation and the entropy of formation at temperature T using Eq. G.6 and G. 7, respectively. For example, for methanol at 100°C in the gas phase:

$$\Delta H_{373} = (-201 \cdot 1000) + ((100+273.15)-298) \cdot 49.5315 = -197285.13 \text{ J/mol}$$

$$\Delta S_{373} = 39.9 + (\ln((100+273.15)-\ln(298)) \cdot 49.5315 = 51.02 \text{ J/mol}$$

It was determined that using the average heat capacity over the temperature range from 298 K to T did not have a significant impact (> 2 %) in the resulting enthalpy of formation and entropy of formation values. Like in the case of standard conditions, it is possible to determine the overall electrolysis enthalpy and entropy of reaction using the temperature corrected values. An example calculation is given for the CH<sub>3</sub>OH electrolyser at 100°C.

*Enthalpy of formation:*

$$\Delta H_{373} = \sum_i s_i \Delta H_{373,i,f} \quad (\text{G.8})$$

Anode:  $\Delta H_{a, 373} = ((-19785.13) + (-2397.1) - (-390489.54)) = -46067.7 \text{ J/mol}$

Cathode:  $\Delta H_{c, 373} = ((3 \cdot 181.59) - 0) = 6544.78 \text{ J/mol}$

Overall:  $\Delta H_{373} = \Delta H_{c, 373} - \Delta H_{a, 373} = 6544.78 - (-46067.7) = 5612.48 \text{ J/mol}$

*Entropy of reaction:*

$$\Delta S_{373} = \sum_i s_i \Delta S_{373,i,f} \quad (\text{G.9})$$

Anode:  $\Delta S_{a, 373} = ((51.02) + (196.44) - (222.84)) \cdot 1000 = 24.62 \text{ J/mol.K}$

Cathode:  $\Delta S_{c, 373} = ((3 \cdot 137.23) - 0) = 411.69 \text{ J/mol.K}$

Overall:  $\Delta S_{373} = \Delta S_{c, 373} - \Delta S_{a, 373} = 411.69 - (24.62) = 387.06 \text{ J/mol.K}$

The effect of temperature on the reversible electrode potential comes from the Gibbs-Helmholtz equation:

$$d\Delta G/dT = -\Delta S$$

$$nFdE/dT = \Delta S$$

$$nFdE^{\circ}/dT = \Delta S^{\circ}$$

Thus, assuming a small effect of temperature on S over the temperature range studied,

$$E_e = E^{\circ} + (T - 298) \cdot \left( \frac{\Delta S_T}{nF} \right) \quad (\text{G.10})$$

Typical values of  $\Delta E^{\circ}/\Delta T$  are of the order of  $\pm 1e^{-3}$  V/K. For the overall methanol electrolysis reaction, at 100°C and 1 atm:

$$\text{Overall: } E_{e, 373} = (0.006) + (373-298) \cdot ((387.06)/(6 \cdot 96485)) = 0.0562 \text{ V}$$

From this, the Gibbs free energy associated with the electrochemical reaction at temperature T is:

$$\Delta G_T = -nFE_{e,T} \quad (\text{G.11})$$

$$\text{Overall: } \Delta G_{373} = -6 (96485) 0.0562 = -32520.01 \text{ J/mol}$$

*Maximum thermodynamic efficiency:*

It was shown that the  $\Delta H$  and  $\Delta G$  values were corrected for the temperature using the heat capacity for the species involved. For the methanol electrolyser at 100°C and 1 atm:

$$\eta_{\max} = \left( \frac{\Delta G_T}{\Delta H_T} \right) \cdot 100 \% \quad (\text{G.12})$$

$$\eta_{\max,373} = -32520.01/5612.48 \cdot 100 = -61.81 \%$$

Note that the thermodynamic efficiency for the electrolyser is negative as, under these conditions, work is produced by the system.

For a PEMFC operating at similar conditions, (100°C, 1 atm), the thermodynamic efficiency would be:

$$\eta_{\max,373} = -225104.25/-242575.51 \cdot 100 = 92.80\%$$

### G.2.3 System efficiency calculation

$$\eta_{\max,system} = \left( \eta_{\max,1} \cdot \eta_{\max,2} \cdot \eta_{\max,3} \dots \right) \cdot 100 \quad (\text{G.13})$$

For a PEMFC in the liquid phase at 100°C and 1 atm combined with a DMR combination in the gas phase at 100°C and 1 atm:

$$\text{PEMFC thermodynamic efficiency} = \eta_{\max,1} = 92.80 \%$$

$$\text{Absolute DMR thermodynamic efficiency} = 61.81 \%$$

*System overall efficiency:*

$$\eta_{\max,system} = (0.9280 \cdot 0.6181) \cdot 100 = 57.36 \%$$

## G.2.4 Effect of pressure in the gas phase

From the Maxwell relation and based on the ideal gas law, the volume change of gaseous components is related to the change in the number of moles of gaseous components based on the reaction stoichiometry:

$$\frac{\partial \Delta G}{\partial P} = \Delta V_g = \left( \frac{\Delta N_{mol,g} RT}{P_{tot}} \right) \quad (\text{G.14})$$

Assuming that the total pressure of the gaseous species on the cathode and the anode side is

$$P_{H_2} + P_{CO_2} + P_{CH_3OH} + P_{H_2O} = P_1 = 1 \text{ atm}$$

and that the total pressure is increased to  $P_2 = 2.5 \text{ atm}$ :

$$E_e = E^o - \left( \frac{\Delta N_{mol,g} \cdot RT}{nF} \right) \cdot \ln \left( \frac{P_2}{P_1} \right) \quad (\text{G.15})$$

$$\Delta N_{mol,g} \text{ anode} = 1+1-1 = 1$$

$$\Delta N_{mol,g} \text{ cathode} = 3-0 = 3$$

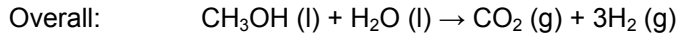
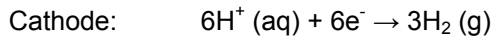
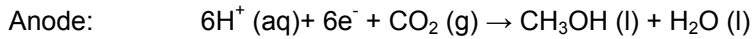
$$\Delta N_{mol,g} \text{ overall} = 3+1-1-1 = 2$$

$$\text{Anode:} \quad E_a = (-0.0596) - ((1 \cdot 8.314 \cdot 473)/(6 \cdot 96485)) \cdot \ln(2.5/1) = -0.07 \text{ V}$$

$$\text{Cathode:} \quad E_c = 0 - ((3 \cdot 8.314 \cdot 473)/(6 \cdot 96485)) \cdot \ln(2.5/1) = -0.02 \text{ V}$$

$$\text{Overall:} \quad E_e = E_c - E_a = (-0.02) - (-0.07) = 0.05 \text{ V}$$

### G.2.5 Effect of anode and cathode pressure in the liquid phase



Applying Nernst equation:

Anode: 
$$E_a = E^o - \frac{RT}{nF} \ln \left( \frac{[\text{CH}_3\text{OH}] \cdot [\text{H}_2\text{O}]}{[\text{H}^+]^6 \cdot P_{\text{CO}_2}} \right)$$

Cathode: 
$$E_c = E^o - \frac{RT}{nF} \ln \left( \frac{P_{\text{H}_2}^3}{[\text{H}^+]^6} \right)$$

Overall: 
$$E_e = E_c - E_a = E^o - \frac{RT}{nF} \cdot \ln \left( \frac{P_{\text{H}_2}^3}{[\text{H}^+]^6} \right) - \frac{RT}{nF} \ln \left( \frac{[\text{CH}_3\text{OH}] \cdot [\text{H}_2\text{O}]}{[\text{H}^+]^6 \cdot P_{\text{CO}_2}} \right)$$

Knowing that  $\ln a - \ln b = \ln a/b$ ,

$$E_e = E^o - \frac{RT}{nF} \cdot \ln \left( \frac{P_{\text{H}_2}^3 \cdot P_{\text{CO}_2}}{[\text{CH}_3\text{OH}]} \right)$$

Hence, as the  $\text{CO}_2$  pressure on the anode increases,  $E_e$  becomes more negative. Similarly, as the  $\text{H}_2$  pressure on the cathode increases,  $E_e$  becomes more negative. Therefore, increasing the anode or cathode compartment pressure is not beneficial to the cell voltage required for  $\text{CH}_3\text{OH}$  electrolysis.

### G.3 References

[1] Dean, J. A., "Lange's Handbook of Chemistry", 15<sup>th</sup> Edition, McGraw Hill, New York, (1999) Section 8.2 and 8.7.

[2] D. R. Lide, "CRC Handbook of Chemistry and Physics", 87<sup>th</sup> Edition, CRC Press LLC, (2006-2007) 2608 pp.

[3] M. W. Chase, "NIST-JANAF Thermodynamical Tables", Fourth edition, J. Phys. Chem. Ref. Data, Monograph 9, (1998) 1-1951.

[4] Perry, R.H.; and Green, D.W., "Perry's Chemical Engineers' Handbook", 7th edition, McGraw-Hill, (1997) 2581 pp., Table 2-198.

[5] M. J. Moran and H. N. Shapiro, "Fundamentals of engineering thermodynamics", Third Edition, John Wiley & Sons, Inc., (1995), 859pp.

[6] Hough, E.W.; Mason, D.M.; and Sage, B.H., "Heat capacities of several organic liquids", J. Am. Chem. Soc., 72, (1950) 5775-5777.

## Appendix H: Electrochemical Sample Calculations

### H.1 Power consumption

The electric power consumption of the electrochemical reformer,  $P_e$  (W), is given by:

$$P_e = E_{T,P} \cdot i \cdot A_{Geom}, \quad (\text{H.1})$$

where  $E_{T,P}$  is the operating cell voltage,  $i$  is the current density ( $\text{A}/\text{cm}^2$ ) and  $A_{Geom}$  is the cell geometric area which is  $2 \text{ cm}^2$ .

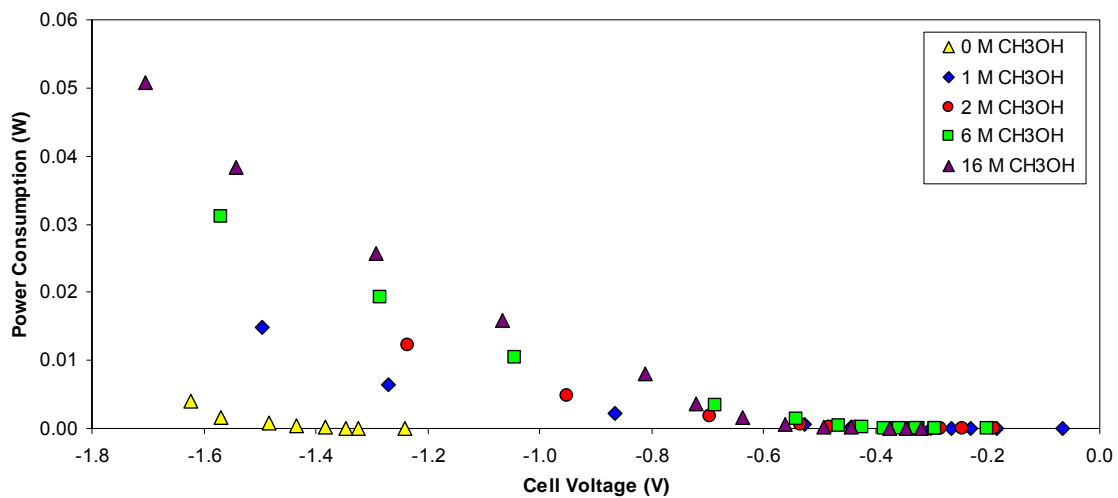


Figure H.1: Power consumption as a function of cell voltage for different CH<sub>3</sub>OH concentrations (0, 1, 2, 6 or 16 M CH<sub>3</sub>OH in 0.5 M H<sub>2</sub>SO<sub>4</sub> electrolyser anolyte, 0.5 M H<sub>2</sub>SO<sub>4</sub> electrolyser catholyte, 4 mg/cm<sup>2</sup> Pt-Ru anode, 2 mg/cm<sup>2</sup> Pt cathode, 23 ± 2°C).

### H.2 CO<sub>2</sub> emissions and H<sub>2</sub> production rate

For the CH<sub>3</sub>OH electrochemical reformer, 1 mol of CO<sub>2</sub> is emitted for every 3 moles of H<sub>2</sub> produced.

According to Faraday's law, the rate of CO<sub>2</sub> emissions,  $N_{CO_2}$  (mol/cm<sup>2</sup>s), is:

$$N_{CO_2} = \frac{1}{3} \cdot N_{H_2} = \frac{1}{3} \cdot \frac{i}{6F} = \frac{i}{18F}. \quad (\text{H.2})$$

This rate can be converted in the total mass rate of CO<sub>2</sub> emissions,  $M_{CO_2}$  (g/day), as per the following equation where  $t = 3600 \text{ s/h} \times 24 \text{ h} = 86400 \text{ s}$ :

$$M_{CO_2} = N_{CO_2} \cdot Mw_{CO_2} \cdot t \cdot A_{Geom} \quad (\text{H.3})$$

The rate of H<sub>2</sub> evolution,  $N_{H_2}$  (mol/m<sup>2</sup>s), is given by Faraday's law at STP is:

$$N_{H_2} = \frac{i}{6F}. \quad (\text{H.4})$$

By combining this expression with the ideal gas law,

$$PV_{H_2} = N_{H_2} \cdot A_{Geom} \cdot RT, \quad (\text{H.5})$$

where A is the electrode area and  $V_{H_2}$  is the volumetric H<sub>2</sub> evolution rate (m<sup>3</sup>/h), we can obtain that:

$$V_{H_2} = \left( \frac{i \cdot A_{Geom}}{6F} \right) \cdot \frac{RT}{P} \quad (\text{H.6})$$

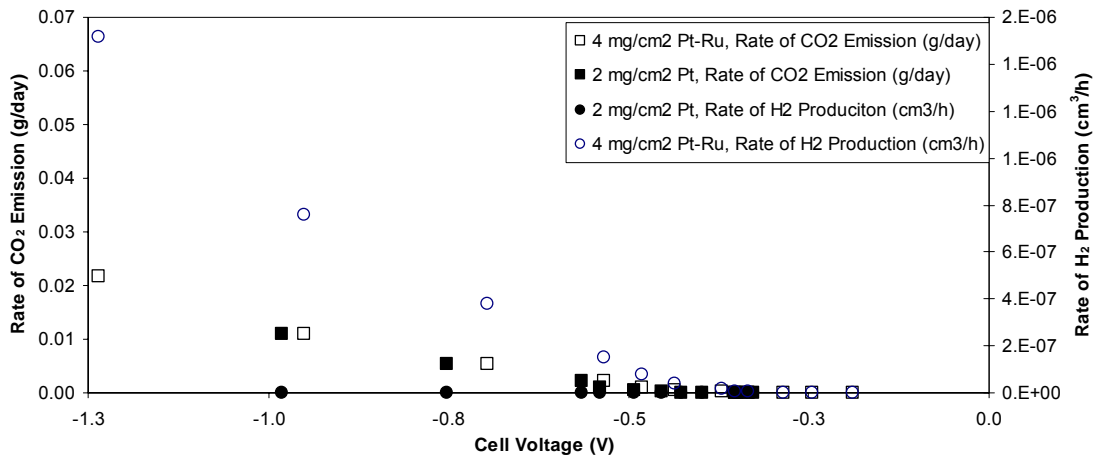


Figure H.2: Rate of CO<sub>2</sub> emission and volumetric rate of H<sub>2</sub> evolution rate in function of the cell Voltage (2 M CH<sub>3</sub>OH in 0.5 M H<sub>2</sub>SO<sub>4</sub> electrolyser anolyte, 0.5 M H<sub>2</sub>SO<sub>4</sub> electrolyser catholyte, 4 mg/cm<sup>2</sup> Pt-Ru or 2 mg/cm<sup>2</sup> Pt anode, 2 mg/cm<sup>2</sup> Pt cathode, 23 ± 2°C).

### H.3 Proton diffusion limited H<sub>2</sub> production – back envelope calculation

A PEMFC automotive system having a peak electric power,  $P_e$ , of 100 kW and a voltage of 0.6 V at peak power will have a current of  $I = P_e/E = 166.67$  A or C/s.

Generally, the diffusion coefficients of most ions in dilute aqueous solutions are similar and have values that at room temperature are in the range of  $0.6 \times 10^{-9}$  to  $2 \times 10^{-9}$  m<sup>2</sup>/s. Various values were found for the diffusion coefficient of protons. In a dilute aqueous solution, it is equal to  $9.31 \times 10^{-9}$  m<sup>2</sup>/s [1]. In a fully hydrated N-117 membrane, the proton diffusion coefficient was reported as  $1.92 \times 10^{-9}$  m<sup>2</sup>/s [2], in a fully hydrated Nafion<sup>®</sup> membrane, it was reported as  $8.36 \times 10^{-10}$  m<sup>2</sup>/s, and in N-117 at 80°C, it was reported as  $4.50 \times 10^{-9}$  m<sup>2</sup>/s [3]. These examples of proton diffusion coefficients show that there is a wide variability in the values reported.

A DMR operating temperature of 80°C (or 353.15 K) was assumed. The membrane thickness of 161 mm (or  $1.61 \times 10^{-4}$  m) for a hydrated N-115 membrane was used in the calculation [4]. The DMR voltage loss through MEA resistance,  $\eta_{ohm}$ , was taken to be equal to 0.21 V, based on the experimental values

obtained for a N-117, 4 mg/cm<sup>2</sup> Pt-Ru/C anode, a 2 mg/cm<sup>2</sup> Pt/C cathode, a 1 to 16 M CH<sub>3</sub>OH anode, and a 0.5 M H<sub>2</sub>SO<sub>4</sub> electrolyte. The DMR proton concentration, CH<sup>+</sup>, was assumed to be equal to 1 M (1000 mol/m<sup>3</sup>) based on 0.5 M H<sub>2</sub>SO<sub>4</sub>.

Assuming that 3H<sub>2</sub> is equivalent to 6H<sup>+</sup> and that the number of electrons transferred is equal to 6, the DMR proton rate,  $r_eH^+$ , can be calculated from Faraday's law for the PEMFC current determined above:

$$r_eH^+ = 6I / 6F = 166.67/96485 = 1.73 \times 10^{-3} \text{ mol/s} \quad (\text{H.7})$$

The proton flux by migration,  $NH^+$ , is equal to:

$$\begin{aligned} NH^+ &= (F \cdot CH^+ \cdot \eta_{ohm} \cdot DH^+) / (t \cdot RT) \\ &= (96485 \cdot 1000 \cdot 0.21 \cdot 9.31 \times 10^{-9}) / (1.61 \times 10^{-4} \cdot 8.314 \cdot 353.15) \\ &= 3.99 \times 10^{-4} \text{ mol/m}^2 \cdot \text{s} \end{aligned} \quad (\text{H.8})$$

Therefore, the DMR active geometric surface area can be obtained:

$$\begin{aligned} A_{Geom} &= r_eH^+ / NH^+ \\ &= 1.73 \times 10^{-3} / 3.99 \times 10^{-4} \\ &= 4.33 \text{ m}^2 \end{aligned} \quad (\text{H.9})$$

Table H.1 summarizes the results obtained for various proton diffusion coefficients. As can be seen, the DMR active surface area greatly depends on the proton diffusion in the membrane.

Table H.1: Direct methanol reformer electrochemical active surface area as a function of proton diffusion coefficient in Nafion, based on H<sub>2</sub> production for a 100 kW PEMFC at a voltage of 0.6 V.

| DH <sup>+</sup> [m <sup>2</sup> /s] | NH <sup>+</sup> [mol/m <sup>2</sup> .s] | A <sub>Geom</sub> [m <sup>2</sup> ] |
|-------------------------------------|-----------------------------------------|-------------------------------------|
| 9.31x10 <sup>-9</sup>               | 3.99x10 <sup>-4</sup>                   | 4.33                                |
| 1.92x10 <sup>-9</sup>               | 8.23x10 <sup>-5</sup>                   | 20.99                               |
| 1.92x10 <sup>-9</sup>               | 3.58x10 <sup>-5</sup>                   | 48.21                               |
| 4.50x10 <sup>-9</sup>               | 1.93x10 <sup>-4</sup>                   | 8.96                                |

#### H.4 Overall system efficiency

The calculation for the thermodynamic efficiency  $\eta_{max}$ , and the system thermodynamic efficiency,  $\eta_{max, system}$ , was demonstrated in *Appendix G*. A thermodynamic efficiency  $\eta_{max}$  of 7.11 % was obtained for the liquid DMR system at 25°C. The voltage efficiency,  $\eta_E$ , is obtained by dividing the cell voltage by the thermodynamic reversible cell voltage.

$$\eta_E = \frac{E}{E_e} \quad (H.10)$$

For the DMR in the liquid phase at 25°C, the reversible cell voltage,  $E_e$ , is equal to -0.016 V. At a current density of 50 mA/cm<sup>2</sup> and ambient conditions, the IR-corrected experimental liquid CH<sub>3</sub>OH electrolyser voltage was -1.22 V, when using N-117, 2 M CH<sub>3</sub>OH, a 4 mg/cm<sup>2</sup> Pt/Ru anode, and a 2 mg/cm<sup>2</sup> Pt cathode. Under these conditions, the voltage efficiency,  $\eta_E$ , can be calculated as:

$$\eta_E = \frac{-1.22}{-0.016} = 76.25, \quad (H.11)$$

assuming that the fuel utilization coefficient is one, i.e. that the mass of fuel reacted in the electrolyser equals the mass of fuel input in the electrolyser.

The Faradaic current efficiency,  $\eta_I$ , of an electrolyser is the fraction of the current (or charge) passed through the cell that is used for converting starting materials to products. It is obtained by dividing the current,  $i$ , by the reversible current,  $i_r$ , which is composed of the current and the cross-over current. In terms of current densities, this is given by:

$$\eta_I = \frac{i}{i + i_c} \quad (\text{H.12})$$

where  $i_c$  is the CH<sub>3</sub>OH cross-over current density. The concentration of CH<sub>3</sub>OH crossing over to the cathode was not determined in the preliminary experiments. From this value, it would be possible to obtain  $i_c$  using Faraday's law. For a DMFC, a realistic value for the Faradaic current efficiency is 0.8 [5].

The reactants are usually supplied in an amount exceeding the reaction stoichiometry. The fuel stoichiometry,  $\lambda$ , refers to the ratio of reactant supplied to the electrolyser over reactant consumed by the electrolyser. However, at a given concentration of CH<sub>3</sub>OH,  $\lambda$  will vary with the current. The fuel utilization efficiency,  $\eta_{fuel}$ , would be given by:

$$\eta_{fuel} = \frac{1}{\lambda} \quad (\text{H.13})$$

Assuming a fuel efficiency of 2, the overall system efficiency,  $\eta_{overall}$ , can be calculated by multiplying all the above efficiencies:

$$\eta_{overall} = \eta_{max} \cdot \eta_E \cdot \eta_I \cdot \eta_{fuel} \quad (\text{H.14})$$

$$\eta_{overall} = -0.013 \cdot 76.25 \cdot 0.8 \cdot 2 = -1.57$$

The operating overall system efficiency will vary widely based on the electrolyser operating conditions.

## H.5 References

[1] D. R. Lide, "CRC Handbook of Chemistry and Physics", 87<sup>th</sup> Edition, CRC Press LLC, (2006-2007) 2608 pp.

[2] S. J. Paddison, and S. Paul, "The Nature of Proton Transport in fully Hydrated Nafion", Phys. Chem. Chem. Phys., 4 (2002) p. 1158-1163.

[3] S. J. Paddison, S. Paul, and T. A. Jr. Zawodzinski, "A Statistical Mechanical Model of Proton and Water Transport in a Proton Exchange Membrane", Journal of the Electrochemical Society, 147(2) (2000) p. 617-626.

[4] S. Slade, S. A. Campbell, T. R. Ralph and F. C. Walsh, "Ionic Conductivity of an Extruded Nafion 1100 EW Series of Membranes", Journal of the Electrochemical Society, 149(12) (2002) pp. A1556-A1564.

[5] J. Larminie, and A. Dicks, "Fuel Cell Systems Explained", John Wiley & Sons Ltd., UK, Second Edition, (2003), 406 pp.